

JCTC

Journal of Chemical Theory and Computation

Conservative Algorithm for an Adaptive Change of Resolution in Mixed Atomistic/Coarse-Grained Multiscale Simulations

Andreas Heyden*[†] and Donald G. Truhlar*

Department of Chemistry and Supercomputing Institute,
University of Minnesota, 207 Pleasant Street S.E.,
Minneapolis, Minnesota 55455-0431

Received October 13, 2007

Abstract: We derive a Hamiltonian and present a simulation protocol for mixed-resolution systems that allows for a change in resolution of selected groups of atoms during a molecular dynamics simulation. The Hamiltonian uses a low-resolution force field for the part of the system distant from an active site (for efficiency) and an atomistic force field for the active site and its direct environment (for accuracy). A microcanonical simulation protocol conserves energy and angular and linear momentum. The method is also applicable to simulations in other ensembles.

Understanding complex materials such as polymeric systems and biological functional units often requires investigating multiple and tightly coupled time and length scales. Neither atomistic nor coarse-grained simulations are able to adequately capture all the relevant scales, from the quantum mechanical to the meso- and macroscales. Atomistic models can capture the former but are too inefficient to model the latter. Coarse-grained models lump a group of atoms into a pseudoatom whose motion is governed by a simplified potential. Thus they require the evaluation of fewer interactions¹ that are often shorter ranged and “softer” than atomic interactions;^{2,3} this permits the use of longer and more efficient time steps in a molecular dynamics simulation.^{4,5} However, the loss of chemical detail and the difficulty in obtaining accurate coarse-grained potential energy parameters for strongly interacting systems, where atoms become polarized or react, limit the applicability of these models.⁶

To combine the efficiency of coarse-grained models with the accuracy of atomistic models for systems that require atomistic resolution only locally, for example at a reactive

group or defect (called the active zone), mixed-resolution models have been developed; these models use a low-resolution description for the part of the system distant from an active site and an atomistic description for the active site and its direct environment.^{7–18} The low-resolution description can be a coarse-grained model or a mixture of coarse-grained and atomistic models. Since the active zone may diffuse during a molecular simulation or ligands may exchange in and out of the inner coordination shell of the active site, the algorithm needs to permit an on-the-fly reclassification (from atomistic to low-resolution or vice versa) of atoms or groups as they transition between the high- and low-resolution regimes.

Previously, only the AdResS algorithm from Praprotnik et al.^{11,15–17} and the hybrid scheme from Ensing et al.¹⁸ permitted such a reclassification during a molecular dynamics simulation. The AdResS scheme defines an atomistic zone, a coarse-grained zone, and a mixed-resolution zone (in which the degrees of freedom are slowly switched on or off) in the simulation box and considers the reclassification of atoms or groups as a “geometry-induced first-order phase transition”. Using different force fields in each zone is equivalent to using a nonconservative force field for the whole system.¹⁹ As a result, there exists no potential energy function for the entire system, and simulations do not conserve either energy or angular momentum. The hybrid scheme from Ensing et al. integrates in essence the same force field as the AdResS scheme (a different smoothing function is used) and, to approximately conserve energy, adds or subtracts energy terms to or from the system energy whenever a group crosses a zone boundary. Considering that adding or subtracting energy terms does not alter the trajectory, the hybrid scheme from Ensing et al. does in principle not remove any of the limitations of the AdResS algorithm.

Recently, we introduced an adaptive partitioning (AP) method²⁰ for treating the potential energy function for systems with an active zone modeled at a high-level of theory (e.g., quantum mechanics) and a surrounding environmental zone modeled at a low-level of theory (e.g., molecular mechanics). This algorithm permits an on-the-fly change in level of theory of the potential energy function of an atomistic simulation as atoms or groups of atoms move between the active and environmental zones. In this letter, we present a new method called adaptive partitioning of the Lagrangian (APL) that extends our previous AP method from potential energy functions to Lagrangian functions and that can be used to derive a conservative Hamiltonian for a mixed-resolution system that allows for a change in resolution of selected groups during a simulation. Many-body force fields can be used (the AdResS method is limited to pair potentials),

* Corresponding author e-mail: heyden@engr.sc.edu (A.H), truhlar@umn.edu (D.G.T).

[†] Current address: Department of Chemical Engineering, University of South Carolina, Columbia, SC 29208.

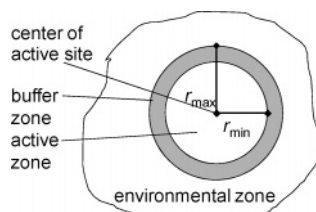


Figure 1. Partitioning of a multiscale system into an active zone, an environmental zone, and a buffer zone separating the active from the environmental zone. Groups of atoms in the active zone have a high (atomistic) resolution, groups in the environmental zone have a low (coarse-grained) resolution, and groups in the buffer zone have a mixed resolution.

multiple active zones can be present in the simulation system, a microcanonical-ensemble (NVE) simulation protocol conserves energy, angular, and linear momentum (conservation proofs including proofs of fulfillment of Newton’s third law and their group-definition requirements are presented in the Supporting Information), and the method is also well defined for any other thermodynamic ensemble. We note that both the AdResS and hybrid scheme integrate Newton’s equation of motion. Considering that the degrees of freedom of a group of atoms change depending on the coordinates of the group of atoms, the kinetic energy functional of the system is both velocity and coordinate dependent. It is well-known that for coordinate-dependent kinetic energies the equations of motion are not given by Newton’s equations but by the Euler–Lagrange equations (or Hamilton’s equations),²¹ and it is the Lagrangian or Hamiltonian that can describe a mixed-resolution system that we derive in this letter.

The APL method starts with an atomistic description of a system and classifies all atoms into groups with group coordinates that become the interaction sites for those groups that are coarse grained in the low-resolution description of the system. We define a particular atom or a group of atoms, called the active site, as the center of an active zone that needs to be modeled atomistically. Although the scheme can involve multiple active zones and each active zone can be defined very generally, including the possibility of the active zone boundary passing through a covalent bond, the discussion here is for a single spherical active zone surrounded by a spherical-shell buffer zone (defined with inner and outer radii, r_{\min} and r_{\max}) and an environmental zone (which comprises the rest of the system, which need not be spherical), and without loss of generality we illustrate the potential energy for the case where there are no covalent bonds between groups (e.g., when the low-resolution zone is a molecular liquid solvent). At any time, all of the atoms of a given group are always considered to be in the same zone. Groups of atoms located in the environmental zone are described only by their low-resolution interaction sites. The atomistic structure of these groups is not specified, and only the group coordinates are stored. In contrast, groups in the active zone and the buffer zone possess an explicit atomistic structure. The purpose of the buffer zone is to smooth the potential and kinetic energy of the system when groups are entering or leaving the active zone. The thickness of the buffer depends on the low-resolution and atomistic description but might be, for example, a few angstroms. Figure 1 illustrates the partitioning of the system into three zones.

To keep the notation simple, we will write the equations for the case where every group has the same number A of atoms, but the generalization to A_α atoms in group α is straightforward. In addition, all equations are written here for a system following classical particle dynamics, but an extension to mixed atomistic–continuum systems^{12–14,22,23} is possible. We define a Lagrangian for v coarse-grained and μ atomistic groups

$$L^{(\mu,v)} = \sum_{\alpha=1}^v \frac{1}{2} M_\alpha U_\alpha^2 + \sum_{k=1}^{A\mu} \frac{1}{2} m_k u_k^2 - V^{(\mu,v)} \quad (1)$$

where $M_\alpha = \sum_{k=1}^A m_k^{(\alpha)}$ is the mass of group α , U_α is the velocity of its group coordinate (which may be, but need not be, at the center of mass of the group), $m_k^{(\alpha)}$ is the mass of atom k in group α , \mathbf{u}_k is its velocity vector $(u_{kx}, u_{ky}, u_{kz})^T$, and $V^{(\mu,v)}$ is the potential energy describing all interactions between the low-resolution and atomistic sites. For the case considered here (no covalent bonds between groups), there is considerable freedom in the choice of the mixed-resolution potential energy functional, but one reasonable possibility is

$$V^{(\mu,v)} = V^{\mu+v} + (V_{AA}^\mu - V^\mu) + 3(A-1)v k_B T_0 \quad (2)$$

where $V^{\mu+v}$ is the potential energy of the entire system described by a low-resolution force field, V_{AA}^μ is the potential energy of the active groups described by an atomistic force field, and V^μ is the potential energy of the active groups as described by the low-resolution force field. All energies are calculated in the APL scheme with reference to a point in configuration space of the all-atomistic system with all momenta equal to zero. Since most low-resolution force fields do not include energy contributions of the implicit degrees of freedom at a finite temperature, eq 2 includes $k_B T_0$ for each implicit degree of freedom in the low-resolution description of the potential energy $V^{(\mu,v)}$ where T_0 is the average temperature of the system we plan to study in our simulation. Note that the choice of $k_B T_0$ per degree of freedom is motivated by considering all implicit degrees of freedom to be harmonic,²⁴ but this does not limit the treatment to harmonic potentials for either the atomistic or coarse-grained potential functions. Because of the dependence on T_0 , the APL force field is thermodynamic-state dependent. In general, the energy contributions of the implicit degrees of freedom are system dependent and not necessarily $k_B T_0$ per degree of freedom, but the following APL procedure is independent of the specific mixed-resolution potential energy functional.

If, at one instant in time during a molecular simulation, there are M groups of atoms in the active zone, K groups of atoms in the buffer zone, and N groups of atoms in the environmental zone, then we define the mixed-resolution Lagrangian, L^{AP} , as a linear combination of all possible combinations of Lagrangian functions that are obtained by treating the active zone and a subset of the K groups in the buffer zone at a high level of resolution (and the rest at a low level of resolution)

$$L^{\text{AP}} = L^{\text{AP}}(L^{[0]}, \{L^{[1]}\}, \dots, L^{[K]}) \quad (3)$$

where $\{L^{[J]}\}$ denotes all $K!/J!(K-J)!$ possible Lagrangian

functions that can be obtained by considering various choices of J buffer-zone groups to be atomistic. To simplify the notation, we will denote the Lagrangian as $L_{\alpha\beta\cdots\theta}$ when groups $\alpha, \beta, \cdots, \theta$ in the buffer zone are considered as atomistic and groups $\gamma, \delta, \cdots, K - \theta$ are considered as having a low resolution. In the APL method all high-resolution Lagrangian contributions from groups α in the buffer zone are smoothed according to their radial coordinate r_α (distance between group α and the center of the active site)

$$L^{\text{AP}} = L + \sum_{\alpha=1,\cdots,K} S_\alpha (L_\alpha - L) + \sum_{\substack{\alpha=1,\cdots,K-1 \\ \beta=\alpha+1,\cdots,K}} S_\alpha S_\beta \{L_{\alpha\beta} - [L + \sum_{\mu=\alpha,\beta} (L_\mu - L)]\} + \sum_{\substack{\alpha=1,\cdots,K-2 \\ \beta=\alpha+1,\cdots,K-1 \\ \gamma=\beta+1,\cdots,K}} S_\alpha S_\beta S_\gamma [L_{\alpha\beta\gamma} - (L + \sum_{\mu=\alpha,\beta,\gamma} (L_\mu - L) + \sum_{(\sigma,\tau)=(\alpha,\beta),(\alpha,\gamma),(\beta,\gamma)} (L_{\sigma\tau} - [L + \sum_{\mu=\alpha,\beta} (L_\mu - L)]))] + \cdots \quad (4)$$

where L corresponds to $\theta = 0$, S_α is a fifth-order spline

$$S_\alpha(\Omega_\alpha) = -6\Omega_\alpha^5 + 15\Omega_\alpha^4 - 10\Omega_\alpha^3 + 1 \quad (5)$$

and Ω_α is given by

$$\Omega_\alpha = \frac{r_\alpha - r_{\min}}{r_{\max} - r_{\min}}, \quad \text{for } r_{\min} < r_\alpha < r_{\max} \quad (6)$$

The Supporting Information shows that eq 4 can be written as

$$L^{\text{AP}} = T^{\text{AP}} - V^{\text{AP}} = \sum_{w=x,y,z} \left[\sum_{\alpha=1}^N \frac{1}{2} M_\alpha U_{\alpha,w}^2 + \sum_{k=1}^{AM} \frac{1}{2} m_k u_{k,w}^2 + \sum_{\beta=1,\cdots,K} \frac{1}{2} (u_{1,w}^{(\beta)} \cdots u_{A,w}^{(\beta)}) \mathbf{\Lambda}^{(\beta)} \begin{pmatrix} u_{1,w}^{(\beta)} \\ \vdots \\ u_{A,w}^{(\beta)} \end{pmatrix} \right] - V^{\text{AP}} \quad (7)$$

where T^{AP} is the kinetic energy, V^{AP} is the potential energy calculated with the permuted AP method²⁰ applied to the mixed atomistic and low-resolution potential energy functions, $V^{(\mu,v)}$, $u_k^{(\beta)}$ is the velocity of atom k of group β in the buffer zone, and $\mathbf{\Lambda}^{(\beta)}$ is a coordinate-dependent mass matrix of group β . The mass matrix $\mathbf{\Lambda}^{(\beta)}$ is nonsingular for $S_\beta > 0$, and the Supporting Information shows that

$$\mathbf{\Lambda}^{(\beta)} = [(1 - S_\beta) \mathbf{M}_D^{(\beta)} + S_\beta \mathbf{M}_M^{(\beta)}] \quad (8)$$

with

$$\mathbf{M}_D^{(\beta)} \equiv \left[\frac{1}{M_\beta} \begin{pmatrix} m_1^{(\beta)} \\ \vdots \\ m_A^{(\beta)} \end{pmatrix} (m_1^{(\beta)} \cdots m_A^{(\beta)}) \right] \quad (9)$$

and

$$\mathbf{M}_M^{(\beta)} \equiv \begin{bmatrix} m_1^{(\beta)} & \cdots & 0 \\ \vdots & \ddots & \vdots \\ 0 & \cdots & m_A^{(\beta)} \end{bmatrix} \quad (10)$$

Having defined a mixed-resolution Lagrangian function, we

can calculate²¹ the generalized momenta $p_i = \partial L / \partial u_i$ and the mixed-resolution Hamiltonian function H^{AP} . We obtain

$$H^{\text{AP}} = \sum_i u_i p_i - L^{\text{AP}} = \sum_{w=x,y,z} \left[\sum_{\alpha=1}^N \frac{P_{\alpha,w}^2}{2M_\alpha} + \sum_{k=1}^{AM} \frac{P_{k,w}^2}{2m_k} + \sum_{\beta=1,\cdots,K} \frac{1}{2} (p_{1,w}^{(\beta)} \cdots p_{A,w}^{(\beta)}) (\mathbf{\Lambda}^{(\beta)})^{-1} \begin{pmatrix} p_{1,w}^{(\beta)} \\ \vdots \\ p_{A,w}^{(\beta)} \end{pmatrix} \right] + V^{\text{AP}} \quad (11)$$

where P_α is the total momentum of group α .

We note that for K groups in the buffer zone, 2^K potential energy functions have to be evaluated to determine the AP potential energy, V^{AP} . (For classical mixed-resolution force fields that consist of additive many-body interaction terms the computational overhead of the APL procedure is usually negligible, which is why we based our APL scheme on the permuted AP method (that scales as $O(2^K)$) and not on the sorted AP method (that scales as $O(K)$).²⁰ For example, for pairwise potentials the computational effort scales as $[1/2(AM + N + K)(AM + N + K - 1) + 1/2AK(AM + N) + 1/2AK(AK - 1)]$ where the computational overhead of the APL procedure, $[1/2AK(AM + N) + 1/2AK(AK - 1)]$, is negligible if the number of atoms in the buffer zone, AK , is small in comparison to the number of interaction sites in the active and environmental zone, $AM + N$.)

Equation 11 shows that the mixed-resolution Hamiltonian for the system allows for a change in resolution of selected groups of atoms during a simulation by making the kinetic energy part of the adaptively partitioned Hamiltonian a functional of the splines. There are no explicit symplectic integrators for coordinate-dependent kinetic energies, but the Supporting Information presents an implicit symplectic generalization of the leapfrog algorithm²⁵ that solves Hamilton's equation of motion with a single force evaluation per time step.

APL simulations can be performed with an all-atomistic resolution in all zones (the force field has still different resolutions). In this case, the Hamiltonian propagates the atomistic structure of groups in the environmental zone in parallel to the group coordinates, and the APL scheme is time-reversible. The main disadvantage of this approach is that the all-atomistic system (including the atomistic structure of groups in the environmental zone) needs to be equilibrated using an all-atomistic force field, a step that is often computationally unfeasible. To eliminate this extra requirement, we propose to use the algorithm with reduced-dimensionality in the environmental zone, integrate only the group coordinates of groups in the environmental zone, and only insert the atomistic structure of a group as it enters the buffer zone from the environmental zone. Thus, we need an algorithm for determining atomistic structure of a group during the simulation. There are two requirements: (i) The procedure should generate appropriate atomic coordinates for the simulation conditions without changing the group coordinate. (ii) The configuration space should be sampled with a probability corresponding to that of an all-atomistic simulation. One possible procedure is to place the group coordinate on one of the atoms of the group, to generate an

atomistic configuration for the group entering the buffer zone that satisfies requirement (i), and then to perform a constrained molecular dynamics simulation to relax the newly placed atoms in the force field of all the other atoms and groups. During this process only the newly placed atoms move, and all atoms in the buffer and core zone are considered explicit. Furthermore, all group coordinates are fixed during this process. We note that in the mixed-resolution potential energy functional of eq 2, there is no change in the interaction of the environmental zone with the active and buffer zones when the group coordinates are fixed, and this interaction does not have to be evaluated. Other procedures for inserting atomistic structure based on Monte Carlo methods^{26,27} are also possible.

A notable advantage of the APL scheme is that only atomic coordinates (and not velocities) have to be generated when a group enters the buffer zone from the environmental zone. For groups on the boundary between the buffer and environmental zone the atomic velocities are the same as the velocity of the group coordinate. The Hamiltonian automatically reintroduces intragroup (vibrational) velocities as a group in the buffer zone moves toward the active zone (and it removes intragroup kinetic energy as a group in the buffer zone moves toward the environmental zone). Furthermore, the AP potential energy is independent of the atomistic structure of a group on the boundary between buffer and environmental zone so that the insertion of atomic structure yields both a continuous kinetic energy and a continuous potential energy.

Finally, we illustrate how to extend the APL algorithm to perform simulations in the NVT ensemble. The average temperature, $\langle T \rangle$, during a simulation is calculated as

$$\langle T \rangle = 2 \left\langle \frac{T^{\text{AP}}}{D} \right\rangle \quad (12)$$

where $\langle \dots \rangle$ denotes a phase space average, and D is the effective number of degrees of freedom of the system for a specific configuration (time) that is calculated as

$$D = 3N + 3AM + 3K + 3 \sum_{\alpha=1, \dots, K} S_{\alpha}(A - 1) \quad (13)$$

We note that the temperature is configuration-space dependent since the kinetic energy is explicitly dependent on coordinates. The AP Hamiltonian, eq 11, is quadratic in the conjugate momenta, so that we can, for example, use the Berendsen thermostat²⁸ to perform simulations in the NVT ensemble and scale all momenta, p_i , according to

$$p_i^{\text{new}} = \sqrt{1 + \frac{\Delta t}{\tau} \left(\frac{T_{\text{desired}}}{T_{\text{instantaneous}}} - 1 \right)} p_i^{\text{old}} \quad (14)$$

where Δt is the time step, τ is a coupling parameter, and T_{desired} and $T_{\text{instantaneous}}$ are the desired and instantaneous temperature of the simulation, respectively.

The main difference between the new APL method and previous mixed resolution algorithms^{7–18} is that we define a single Lagrangian for a mixed-resolution system that allows for a change in resolution of selected groups of atoms instead of defining multiple Hamiltonians or force fields (that possess different resolutions) for different areas in space that are connected by boundary conditions. In addition, the phase

space dimensionality of a system is constant during an APL simulation and equal to the all-atomistic phase space dimensionality. Only the number of interaction sites and degrees of freedom are reduced and vary during an APL simulation. Unlike previous mixed-resolution methods, the APL scheme is therefore currently the only algorithm that solves the Euler–Lagrange equations of motion for a mixed-resolution system and that can be easily extended to any thermodynamic ensemble. The main disadvantage of the APL scheme is the need to define a mixed-resolution potential energy functional that uses the same reference state for the zero of energy for both the coarse-grained and atomistic part of the potential energy functional. In contrast, in the AdResS method the zero of energy can be defined independently for the coarse-grained and atomistic force fields.

In conclusion, we have derived a Hamiltonian and presented a simulation protocol for mixed-resolution systems that allows for a change in resolution of selected groups of atoms during a simulation. An NVE simulation protocol with this Hamiltonian conserves kinetic and potential energy and angular and linear momentum. For systems that require atomistic resolution only for a small part or parts of the simulation system, the APL algorithm permits a simulation with accuracy comparable to an atomistic one at the computational cost of a coarse-grained one.

As an application of this novel algorithm we are currently studying the structure and diffusion of hexane molecules surrounding a water molecule.

ACKNOWLEDGMENT.

This work is supported in part by the Defense-University Research Initiative in Nanotechnology (DURINT) of the U.S. Army Research Laboratory and the U.S. Army Research Office under agreement number DAAD190110503 and by the office of Naval Research under award number N00014-05-1-0538. A.H. gratefully acknowledges the Minnesota Supercomputing Institute for a research scholarship.

Supporting Information Available: Derivation of the mixed-resolution Hamiltonian; conservation of energy and linear and angular momentum; constraints on low-resolution group coordinates and Newton's third law; generalized leapfrog algorithm for mixed-resolution simulations; and references. This material is available free of charge via the Internet at <http://pubs.acs.org>.

REFERENCES

- (1) Mueller-Plathe, F. *ChemPhysChem* **2002**, *3*, 754.
- (2) Klapp, S. H. L.; Diestler, D. J.; Schoen, M. *J. Phys.: Condens. Matter* **2004**, *16*, 7331.
- (3) Izvekov, S.; Voth, G. A. *J. Chem. Phys.* **2005**, *123*, 134105.
- (4) Lopez, C. F.; Moore, P. B.; Shelley, J. C.; Shelley, M. Y.; Klein, M. L. *Comput. Phys. Commun.* **2002**, *147*, 1.
- (5) Depa, P. K.; Maranas, J. K. *J. Chem. Phys.* **2005**, *123*, 94901.
- (6) Muller, M.; Katsov, K.; Schick, M. *Phys. Rep.* **2006**, *434*, 113.
- (7) Delle Site, L.; Abrams, C. F.; Alavi, A.; Kremer, K. *Phys. Rev. Lett.* **2002**, *89*, 156103.
- (8) Villa, E.; Balaeff, A.; Mahadevan, L.; Schulten, K. *Multiscale Modell. Simul.* **2004**, *2*, 527.
- (9) Neri, M.; Anselmi, C.; Cascella, M.; Maritan, A.; Carloni, P. *Phys. Rev. Lett.* **2005**, *95*, 218102.
- (10) Abrams, C. F. *J. Chem. Phys.* **2005**, *123*, 234101.
- (11) Praprotnik, M.; Delle Site, L.; Kremer, K. *J. Chem. Phys.* **2005**, *123*, 224106.
- (12) Dupuy, L. M.; Tadmor, E. B.; Miller, R. E.; Phillips, R. *Phys. Rev. Lett.* **2005**, *95*, 060202.
- (13) Rudd, R. E.; Broughton, J. Q. *Phys. Rev. B* **2005**, *72*, 144104.

- (14) Diestler, D. J.; Zhou, H.; Feng, R.; Zeng, X. C. *J. Chem. Phys.* **2006**, *125*, 064705.
- (15) Praprotnik, M.; Delle Site, L.; Kremer, K. *Phys. Rev. E* **2006**, *73*, 66701.
- (16) Praprotnik, M.; Kremer, K.; Delle Site, L. *Phys. Rev. E* **2007**, *75*, 17701.
- (17) Praprotnik, M.; Kremer, K.; Delle Site, L. *J. Phys. A: Math. Theor.* **2007**, *40*, F281.
- (18) Ensing, B.; Nielsen, S. O.; Moore, P. B.; Klein, M. L.; Parrinello, M. *J. Chem. Theor. Comput.* **2007**, *3*, 1100.
- (19) The curl of a force field is zero if the force field is conservative, but it can be shown that the curl of the force field in the AdResS scheme is in general not equal to zero for groups in the buffer zone.
- (20) Heyden, A.; Lin, H.; Truhlar, D. G. *J. Phys. Chem. B* **2007**, *111*, 2231.
- (21) Goldstein, H.; Poole, C. P.; Safko, J. L. *Classical mechanics*, 3rd ed.; Addison Wesley: San Francisco, 2002.
- (22) Tadmor, E. B.; Phillips, R.; Ortiz, M. *Langmuir* **1996**, *12*, 4529.
- (23) E, W.; Huang, Z. Y. *J. Comput. Phys.* **2002**, *182*, 234.
- (24) Huang, K. *Statistical mechanics*; Wiley: New York, 1963.
- (25) Leimkuhler, B.; Reich, S. *Simulating Hamiltonian dynamics*; Cambridge University Press: New York, 2004.
- (26) Peslherbe, G. H.; Wang, H. B.; Hase, W. L. *Adv. Chem. Phys.* **1999**, *105*, 171.
- (27) DePablo, J. J.; Escobedo, F. A. *Adv. Chem. Phys.* **1999**, *105*, 337.
- (28) Berendsen, H. J. C.; Postma, J. P. M.; van Gunsteren, W. F.; DiNola, A.; Haak, J. R. *J. Chem. Phys.* **1984**, *81*, 3684.

CT700269M

Quantum Chemistry on Graphical Processing Units. 1. Strategies for Two-Electron Integral Evaluation

Ivan S. Ufimtsev and Todd J. Martínez*

Department of Chemistry and The Beckman Institute, 600 S. Mathews, University of Illinois, Urbana, Illinois 61801

Received October 13, 2007

Abstract: Modern videogames place increasing demands on the computational and graphical hardware, leading to novel architectures that have great potential in the context of high performance computing and molecular simulation. We demonstrate that Graphical Processing Units (GPUs) can be used very efficiently to calculate two-electron repulsion integrals over Gaussian basis functions—the first step in most quantum chemistry calculations. A benchmark test performed for the evaluation of approximately 10^6 (ss|ss) integrals over contracted s-orbitals showed that a naïve algorithm implemented on the GPU achieves up to 130-fold speedup over a traditional CPU implementation on an AMD Opteron. Subsequent calculations of the Coulomb operator for a 256-atom DNA strand show that the GPU advantage is maintained for basis sets including higher angular momentum functions.

1. Introduction

The past decade has seen a tremendous increase in the computing requirements of consumer videogames, and this demand is being met through novel hardware architectures in the form of proprietary consoles and graphics cards. Offerings such as the Sony PlayStation 3 (designed around IBM's Cell processor¹) and the nVidia GeForce 8800 GTX graphics card are excellent examples, both of which may be characterized as stream processors.² Stream processing is a generalization of the single instruction multiple data (SIMD) vector processing model which formed the core of the Cray-1 supercomputer.³ Applications are organized into streams and kernels, representing blocks of data and code transformations, respectively. The kernel is typically comprised of a tight loop of relatively few instructions. Streams of data are then processed in pipelined and parallel fashion by many processors executing a small number (possibly only one) of kernels. In the case of the nVidia 8800 GTX, there are 128 total processors organized as 16 multiprocessor units comprised of 8 processing units each. These run at a clock speed of 1.35 GHz, which is comparable to the conventional CPUs commonly used as the basis for scientific computing clusters.

Since a graphics card typically costs less than a single CPU used in conventional scientific clusters, it is tempting to consider the use of graphics cards for computational chemistry. The earliest attempts to use graphics processing units (GPUs) for nongraphical computing in fields outside of chemistry^{4–6} were largely stymied by limited precision and difficulty of programming. The former problem has been partially remedied, and the latest GPUs support 32-bit floating point arithmetic. The next generation of GPUs and stream processors from nVidia and AMD have already been announced and will extend this support to 64-bit. The latter problem of programming difficulty has been largely removed by nVidia's recent introduction of the Compute Unified Device Architecture (CUDA), which provides a relatively simple programming interface that can be called from the standard C language. A few groups have recognized the potential of GPUs in the context of computational chemistry,^{7–9} with some recent implementations within the CUDA framework.^{8–10} Much of the focus has been on questions of accuracy associated with 32-bit single precision arithmetic, but we discuss this only very briefly here since the precision problem will be much less important with the advent of 64-bit GPUs and stream processors. Instead, our paper focuses

* Corresponding author e-mail: tjm@spawn.scs.uiuc.edu.

on the implementation of quantum chemistry algorithms in the context of stream processors.

In this paper, we propose and test three different algorithms to solve one of the bottleneck problems of most ab initio calculations, the two-electron integral evaluation part, entirely on the GPU. Yasuda has recently demonstrated that that GPU evaluation of two-electron integrals is feasible with up to $10\times$ speedups compared to conventional CPUs.⁹ He introduced a novel scheme that calculates the largest integrals on the CPU in double precision and others on the GPU in single precision. In contrast, we explore several computational organizations for the problem, determining which are most appropriate for the GPU architecture. We formulate three different approaches, each with its own strong and weak points. By taking the architectural details of the GPU into account, we are able to achieve speedups of more than $100\times$ compared to mature algorithms on conventional CPUs. One of the algorithms is particularly suitable for direct SCF methods,¹¹ where the integrals are recomputed every SCF iteration, while the others are better for conventional SCF methods, where primitive integrals have to be contracted and stored (usually on disk) before the SCF procedure starts.

To assess the relative performance of these three algorithms, we have chosen a relatively simple test system consisting of 64 H atoms organized on a $4 \times 4 \times 4$ cubic lattice with nearest-neighbor spacing of 0.74 Å using the STO-6G and 6-311G basis sets. In this test system, only (*ss|ss*) type integrals need to be evaluated. Having identified the algorithm which is most suitable for direct SCF calculations, we then use it to construct (entirely on the GPU) the Coulomb contribution to the Fock matrix (the *J*-matrix) for a much larger system including both *s*- and *p*-type basis functions—a 256-atom DNA strand using the 3-21G basis set (1699 basis functions). Comparison of the corresponding CPU and GPU timings confirms that the GPU architecture is well-suited for use in quantum chemistry calculations. The algorithms presented here, and to a large extent also the code, will be directly applicable to double-precision GPUs and stream processors with little or no modification.

This paper is organized in the following way. Section 1 is the Introduction; section 2 outlines the problem background; section 3 provides a brief overview of the GPU architecture and some programming basics required for understanding the further material; the integral computation algorithms on GPU are described in section 4; and section 5 includes the benchmark timing results as well as a brief discussion concerning the impact of 32-bit precision in the GPU calculations.

2. Two-Electron Repulsion Integrals

The first step in any ab initio Molecular Orbital (MO) or Density Functional Theory (DFT) treatment of electronic structure is the evaluation of a large number of two-electron repulsion integrals over *N* atom-centered one-electron basis functions φ

$$(pq|rs) = \int \int \varphi_p(\vec{r}_1) \varphi_q(\vec{r}_1) \frac{1}{|\vec{r}_1 - \vec{r}_2|} \varphi_r(\vec{r}_2) \varphi_s(\vec{r}_2) d\vec{r}_1 d\vec{r}_2 \quad (1)$$

where \vec{r} refers to the electronic coordinates. In practice, these basis functions are typically linear combinations of primitive atom-centered Gaussian basis functions:

$$\varphi_p(\vec{r}) = \sum_{k=1}^K c_{pk} \chi_k(\vec{r}) \quad (2)$$

The primitive basis functions χ are centered at the coordinates $\vec{R}_A = (X_A, Y_A, Z_A)$ of the *A*th nucleus:

$$\chi(\vec{r}) = N(x - X_A)^{n_x} (y - Y_A)^{n_y} (z - Z_A)^{n_z} \exp(-\alpha|\vec{r} - \vec{R}_A|^2) \quad (3)$$

The two-electron integrals in the contracted basis are thus evaluated as

$$(pq|rs) = \sum_{k_1=1}^{K_p} \sum_{k_2=1}^{K_q} \sum_{k_3=1}^{K_r} \sum_{k_4=1}^{K_s} c_{pk_1} c_{qk_2} c_{rk_3} c_{sk_4} [\chi_{k_1} \chi_{k_2} | \chi_{k_3} \chi_{k_4}] \quad (4)$$

where we use brackets to denote two-electron integrals over primitive basis functions and parentheses to denote such integrals over contracted basis functions. The angular momentum of the basis functions is given by the sum of the three integer parameters, $\lambda = n_x + n_y + n_z$, in the usual way. The primitive integrals can be evaluated analytically as originally shown by Boys.¹² Since Boys' seminal work, numerous computational approaches have been developed to minimize the effort in this N^4 bottleneck.^{13–17} However, even if the most efficient algorithm is being used, the two-electron integral evaluation phase still takes much of the computation time.

3. Overview of GPU Hardware and CUDA API

All calculations throughout this project were performed on one nVidia GeForce 8800 GTX graphical processor running under the Windows XP operating system. The Compute Unified Device Architecture (CUDA) Application Programming Interface (API) provided by nVidia¹⁸ was used to develop the GPU-side code. Perhaps the most detailed descriptions of the nVidia GeForce GPU architecture and the CUDA API are provided in the CUDA Programming Guide available for download free of charge.¹⁹ We briefly outline some features of the hardware and programming models that are needed to understand our implementation of two-electron integral evaluation.

In the beta version of the CUDA implementation which we used for this work, all GPU functions (those functions which are executed on the GPU, not on the CPU) are called synchronously. In other words, when the CPU reaches the point where a GPU function (“kernel”) is called, the CPU waits until this function returns and only then can proceed further.²⁰ From this point of view, the GPU can be considered as a coprocessor to the CPU—a fast processor that is responsible for executing the most computationally intensive parts of a program which can be efficiently processed in parallel. The processors of the GPU are not able to access CPU memory directly. Therefore, before a GPU kernel is executed, the CPU (using functions provided by the CUDA host runtime component) must copy required data from CPU memory to GPU memory. Likewise, if desired, the results

in GPU memory may be copied to CPU memory after GPU processing is completed.

The GeForce 8800 is able to process a large number of parallel threads. Within the CUDA framework, the whole batch of threads is arranged as a one- or two-dimensional grid of blocks with up to 65 535 blocks in each dimension. Each block of threads can be one-, two-, or three-dimensional depending on the problem being solved. The number of threads in a block must be specified explicitly in the code and should not be more than 512 in the current CUDA implementation. The best performance is obtained if the number of threads in a block is a multiple of 32, for scheduling reasons discussed below. The CUDA framework assigns a unique serial number (*threadIdx*) to each thread in a block. Likewise, each block of threads is assigned a unique identification number (*blockIdx*). For a two-dimensional grid of blocks, *blockIdx* consists of two numbers, *blockIdx_x* and *blockIdx_y*. Using both *threadIdx* and *blockIdx*, one can completely identify a given thread. This makes it possible for each thread to identify its share of the work in a Single Program Multiple Data (SPMD) application.

The GeForce 8800 GTX consists of 16 independent stream multiprocessors (SM). Each SM has a Single Instruction Multiple Data (SIMD) implementation with eight scalar processors and one instruction unit. At each clock cycle, the instruction unit of an SM broadcasts the same instruction to all eight of its scalar processor units, which then operate on different data. Each SM can process several blocks concurrently, but all the threads in a given block are guaranteed to be executed on a single SM. Threads within the same block are thereby able to communicate with each other very efficiently using fast on-chip shared memory and are furthermore able to synchronize their execution. In contrast, threads belonging to different blocks are not able to communicate efficiently nor to synchronize their execution. Thus, interblock communication must be avoided in an efficient GPU algorithm.

Since the number of threads in a typical GPU application is much larger than the total number of scalar processing units, all the threads are executed using time slicing. All blocks are split into 32-thread groups (which is why the number of threads in a block should be a multiple of 32) called warps. Each warp is then processed in SIMD fashion (all 32 threads are executed by 8 processor units in 2 clock cycles). The thread scheduler periodically switches the active warps to maintain load balancing, maximizing the overall performance.

4. GPU Algorithms for Two-Electron Integrals

Most parallel programs use one of two general organizational schemes: the master–slave model or the peer model. In the master–slave model, there is one master node which executes a common serial program but distributes the most computationally intensive parts among the slave nodes. After the slave nodes are done, the master node gathers the results and uses them in further computations. In the case of the two-electron integral evaluation problem, a common implementation^{21–23} of the master–slave model is as follows: the master node loops over all atomic orbitals, generating lists

of (*pq|rs*) integrals (i.e., index ranges) and the required input data (exponents, contraction coefficients, and atomic coordinates). These lists are sent to the slave nodes, which then evaluate the corresponding integrals. In the peer model, there is no master node, and all computational nodes execute the same program.

There are two levels of parallelism in a typical GPU code. The first is between the CPU and the GPUs, which is handled in the master–slave model. The CPU is the master node which calls one or more GPUs as slave nodes. The second level of parallelism is within the GPU itself, which is implemented in the peer model, where each thread executes the same program and must use its *threadIdx* and *blockIdx* to determine precisely what work it is to perform.

Because of the relatively slow 2Gb/s transfer speeds between the CPU and GPU, it is important to avoid CPU–GPU data transfer as much as possible. Below, we present several algorithms for two-electron integral evaluation. We test them on a simple system consisting of 64 H atoms. Finally, we show that these algorithms preserve their efficiency for much more complex systems, specifically a 256-atom DNA strand, containing 685 contracted *s*- and 1014 *p*-type basis functions.

4a. Mapping Integrals to the GPU Threads. The mapping procedure starts by enumerating all the N atomic orbitals φ_p in the system ($p=1\dots N$) and then constructing corresponding *bra*- and *ket*-arrays $\varphi_p\varphi_q$ of length $M = N(N + 1)/2$. The two-electron integrals can then be generated as (*pq|rs*) *bra*- and *ket*-vector element combinations. This is schematically represented in Figure 1. Each light green square represents one (*bra|ket*) integral out of M^2 total integrals. The (*bra|ket*)=(*ket|bra*) symmetry reduces these M^2 integrals to the final set of $M(M + 1)/2$ unique two-electron integrals represented by the upper-right triangle submatrix in Figure 1. Several different integral↔GPU thread mappings can be envisioned. The two-dimensional square grid of contracted integrals in Figure 1 can be naturally mapped to a two-dimensional grid of GPU thread blocks. In this case, there are two possibilities—either each block of GPU threads calculates a contracted integral as depicted in Figure 1, or each GPU thread calculates a contracted integral as depicted in Figure 2. In the first case, the primitive integrals contributing to the same contracted integral are cyclically mapped to the threads of a block (the predefined number of threads in a block is the same for all blocks). Following the calculation of the primitive integrals, a block sum reduction performs the final summation leading to the contracted integral. In the second case, each individual GPU thread calculates its own contracted integral by looping over all contributing primitive integrals and accumulating the result in a local variable. A third possible mapping is shown in Figure 3, where each thread calculates just one primitive integral, no matter to which contracted integral it contributes. In this case, additional overhead is needed to perform a series of local sum reductions converting the grid of primitive integrals to the grid of contracted integrals.

These three approaches cover a wide range of possible mapping schemes. The third mapping (one thread ↔ one primitive integral) is very fine-grained with perfect computa-

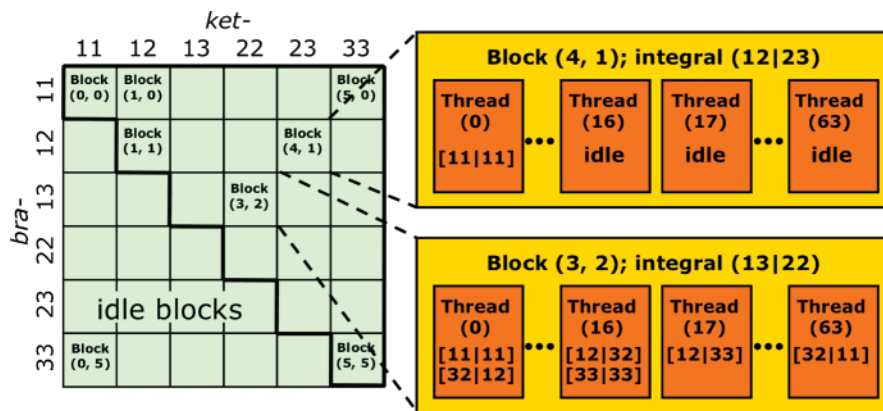


Figure 1. “One Block \leftrightarrow One Contracted Integral” (1B1CI) mapping. The green squares represent the contracted integrals as well as one-dimensional 64-thread blocks mapped to them. To the right, the GPU thread to primitive integral mapping is illustrated for two contracted integrals containing 1 and $3^4 = 81$ primitive integrals. After all the primitive integrals are calculated, a block sum reduction leads to the final result.

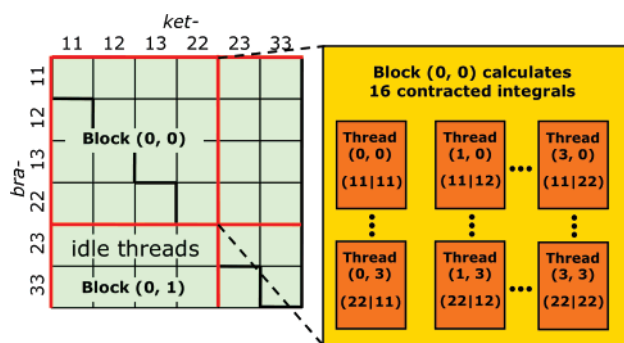


Figure 2. “One Thread \leftrightarrow One Contracted Integral” (1T1CI) mapping. Green squares represent the contracted integrals as well as individual GPU threads mapped to them. A two-dimensional 4×4 thread block is outlined in red. Each thread calculates its integral by looping over all primitive integrals and accumulating the result in a local variable.

tion load balancing but relatively large data reduction overhead. In contrast, the second mapping (one thread \leftrightarrow one contracted integral) is very coarse-grained with imperfect load balancing. This is because different threads can have different loop lengths, depending on the degree of contraction of each of the four basis functions in the integral. On the other hand, this mapping has no data reduction overhead (summation of data held in different threads). The first mapping, (one thread block \leftrightarrow one contracted integral) is intermediate in terms of the grain of parallelism. Load imbalancing can decrease the performance significantly, for example in basis sets with low average degree of contraction. However, the load is balanced more effectively than in the second mapping. Additionally, the data reduction overhead is small because the threads that need to communicate are all located in the same thread block (and hence reside on the same SM).

We have tested all these three approaches on a system of 64 hydrogen atoms using the STO-6G^{24,25} and 6-311G²⁶ basis sets, representing highly contracted and relatively uncontracted basis set cases, respectively.

4b. One Thread Block \leftrightarrow One Contracted Integral Mapping. The “One Block \leftrightarrow One Contracted Integral” mapping (1B1CI) is schematically represented in Figure 1.

The green squares represent the contracted integrals as well as the blocks of computational GPU threads mapped to them. Because of $(bra|ket)=(ket|bra)$ symmetry, those integrals lying below the main diagonal should be disregarded. This is easily done with a logic statement at the beginning of thread execution. If the thread is assigned to an integral in the lower triangle, it simply exits without computing anything—this is indicated in Figure 1 by the designation “idle blocks”. This “outscheduling” has little effect on performance since the scheduler switches between GPU warps very quickly (once all threads in a warp have completed processing, they are removed from the scheduling list and do not impose any load balancing penalty). After each contracted integral is mapped to the corresponding block of GPU threads, the primitive integrals contributing to the particular contracted integral are assigned to the threads constituting this block. Different schemes can be used here—in our program we use a cyclic mapping to a one-dimensional block of 64 threads (orange rectangles in Figure 1). Each successive term in the sum of eq 4 is then mapped to a successive GPU thread, i.e., [11|11] to thread 0, [11|12] to thread 1, and so on. If the number of primitive integrals is larger than the number of GPU threads in the block, the procedure repeats: the 65th primitive integral is mapped to thread 0, the 66th to thread 1, and so on until all primitive integrals have been assigned to a GPU thread. Depending on the number of terms in eq 4 for the contracted integral under consideration, two situations are possible as shown on the right in Figure 1. Block (4,1) represents the case when some threads have no integrals mapped to them. This can happen, for example, when there is only one term in the sum of eq 4, i.e. the contraction length for all basis functions involved in the integral is unity. Since the number of threads in a block is fixed and is the same for all the blocks, the number of threads in Block (4,1) will be 64, of which only one will do useful work—the others will just waste the computational resources executing unnecessary instructions. Thus, the 1B1CI mapping is more efficient for highly contracted basis sets. Direct computational tests confirm this conclusion and show that for low-contracted basis sets the performance drops by a factor of 2–3. Note that the

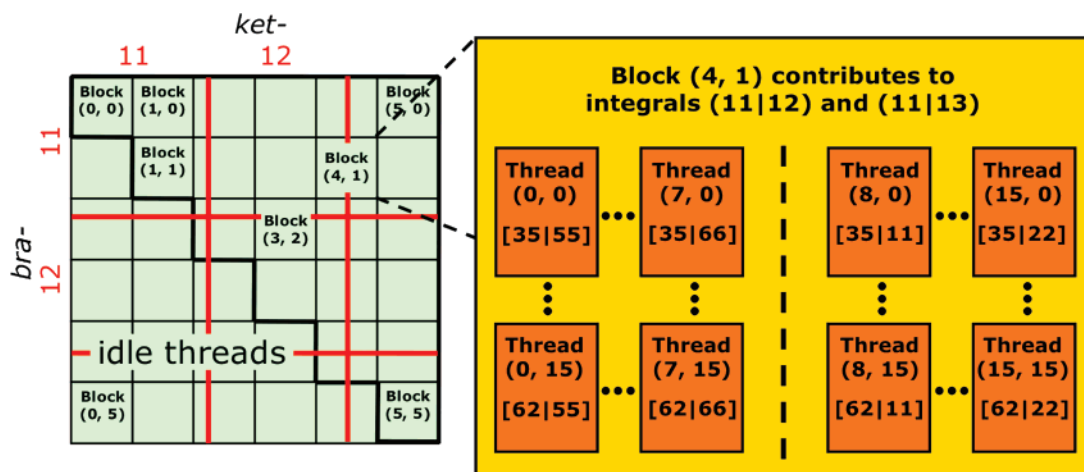


Figure 3. “One Thread ↔ One Primitive Integral” (1T1PI) mapping. The two-dimensional 16×16 thread blocks are represented by green squares, while the red squares represent contracted integrals. To the right, we show an example where the primitives calculated by one thread block contribute to more than one contracted integral.

performance penalty is less than might have been expected. This is partly because of the efficient scheduling and organization of threads into warps as discussed above. When all of the threads in a warp are idle, the entire warp wastes only one clock cycle, after which the GPU “outschedules” the warp, i.e., it is removed from consideration for further scheduling. Block (3, 2) represents the case when the number of primitive integrals is not a multiple of the number of threads in a block. In this case, there is also performance degradation since threads 17–31 are only calculating one primitive integral, while threads 0–16 calculate two primitive integrals. However, in general the effect is much smaller than in the previous case. Again, the efficient scheduling of the GPU and organization of threads into warps is the reason for relatively minor effects of load imbalance. Given the current lack of performance monitoring tools for the GPU, the only way to assess the impact of load imbalancing is by direct experimentation for realistic test cases.

4c. One Thread ↔ One Contracted Integral Mapping.

The “One Thread ↔ One Contracted Integral” (1T1CI) mapping is shown schematically in Figure 2. Again, the green squares represent the contracted integrals, while the blocks of threads are sketched in red. In contrast to the previous model, the blocks of threads are now two-dimensional. Figure 2 shows a block of 16 threads arranged as a 4×4 grid for illustrative purposes, while in our test calculations we found the 16×16 configuration to be optimal. Each thread now has its own contracted integral to calculate. It does this by looping over all primitive integrals and accumulating the result. Figure 4 presents a detailed flowchart of the procedure. As mentioned above, the 1T1CI mapping scheme can suffer from load balancing problems since there may be a different number of terms in each of the sums of primitive integrals. This results in a different number of loop cycles needed to calculate each contracted integral and a corresponding imbalance in the computational work per thread. The effect of this load imbalance can be minimized by organizing the contracted integrals into subgrids, so that each subgrid contains contracted integrals involving the same number of

primitive integrals. The computation threads are then assigned over all the subgrids serially through a series of synchronous function calls from the CPU. This provides all GPU threads in each subgrid exactly the same amount of work, which is nonetheless different for different subgrids. The sorting step to divide the work into subgrids is done on the CPU prior to integral evaluation by the GPU.

4d. One Thread ↔ One Primitive Integral Mapping.

The “One Thread ↔ One Primitive Integral” (1T1PI) mapping exhibits the finest grained parallelism of all the mappings we consider here. The mapping scheme is shown schematically in Figure 3, where it can be seen that each individual GPU thread calculates only one primitive integral, no matter which contracted integral it contributes to. In Figure 3, two-dimensional blocks of threads are represented by green squares, while the red squares represent contracted integrals. Individual primitive integrals are not displayed. The situation shown in Figure 3 corresponds to the STO-6G basis set (with 1296 primitive integrals in each contracted integral) and a block size of 16×16 threads. Since 16 is not a multiple of 36, some blocks like block (4, 1) calculate primitive integrals which belong to different contracted integrals like (11|12) and (11|13). From the computational point of view, this is the fastest version because of ideal load balancing. However, the following sum reduction stage, which converts the calculated primitive integral grid to the final contracted integral grid, is the most expensive part in this model and can decrease the ultimate performance. As depicted in Figure 3, the reduction to contracted integrals will sometimes require summation over values from threads in different blocks, and these therefore may reside on different SMs, necessitating expensive communication.

4e. The $(ss|ss)$ Integral Computation Algorithm. The general formula for primitive $[ss|ss]$ integral evaluation is¹²

$$[s_1s_2|s_3s_4] = \frac{\pi^3}{AB\sqrt{A+B}} K_{12}(\vec{\mathbf{R}}_{12}) K_{34}(\vec{\mathbf{R}}_{34}) F_0\left(\frac{AB}{A+B} |\vec{\mathbf{R}}_P - \vec{\mathbf{R}}_Q|^2\right) \quad (5)$$

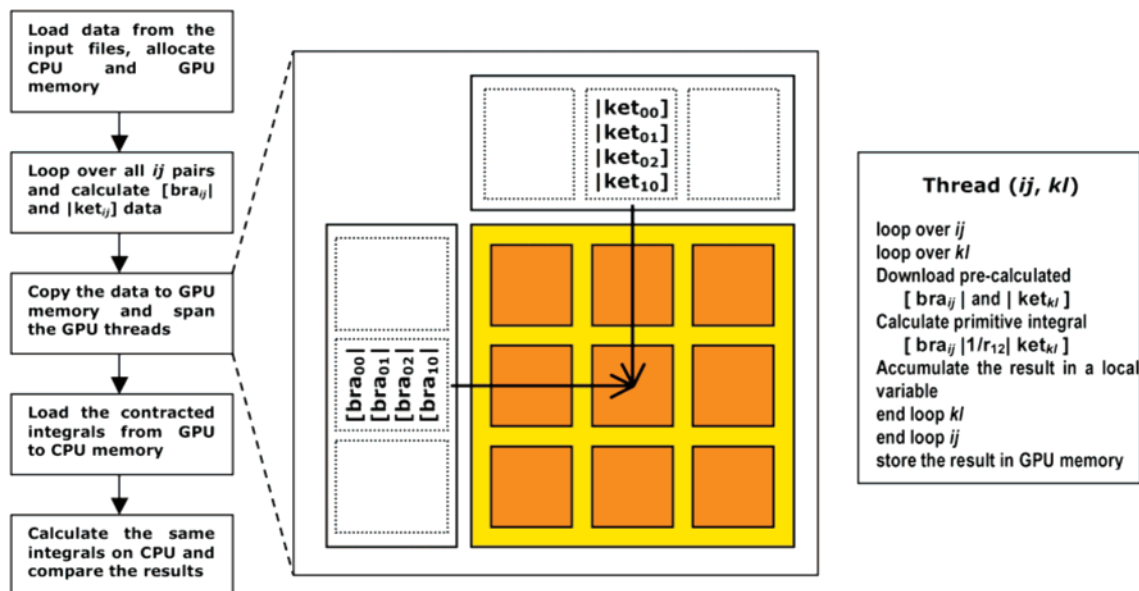


Figure 4. Flowchart for the 1T1CI mapping algorithm. The small orange boxes represent individual threads, each calculating a contracted integral. The whole block of threads (large yellow box) thus calculates a number of contracted integrals (nine in the example shown). The “bra-” and “ket-” rectangles on the top left of the thread block represent the pairwise quantities precalculated on the CPU.

where

$$A = \alpha_1 + \alpha_2; \quad B = \alpha_3 + \alpha_4 \quad (6)$$

$$K_{ij}(\vec{\mathbf{R}}_{ij}) = \exp\left(-\frac{\alpha_i \alpha_j}{\alpha_i + \alpha_j} [\vec{\mathbf{R}}_i - \vec{\mathbf{R}}_j]^2\right) \quad (7)$$

$$\vec{\mathbf{R}}_p = \frac{\alpha_1 \vec{\mathbf{R}}_1 + \alpha_2 \vec{\mathbf{R}}_2}{\alpha_1 + \alpha_2}; \quad \vec{\mathbf{R}}_q = \frac{\alpha_3 \vec{\mathbf{R}}_3 + \alpha_4 \vec{\mathbf{R}}_4}{\alpha_3 + \alpha_4} \quad (8)$$

$$\vec{\mathbf{R}}_{kl} = \vec{\mathbf{R}}_k - \vec{\mathbf{R}}_l \quad (9)$$

$$F_0(t) = \frac{\text{erf}(\sqrt{t})}{\sqrt{t}} \quad (10)$$

In eqs 5–10, α_k and $\vec{\mathbf{R}}_k$ denote the exponent and atomic center of the k th primitive basis function in the integral. Instead of having each GPU thread calculate a primitive integral directly through eqs 5–10, we precalculate all pair quantities on the host CPU. Alternatively, this could be done on the GPU, if desired. The following terms are precalculated and stored in the GPU memory: $\alpha_1 + \alpha_2$, $\pi^{3/2} c_1 c_2 / (\alpha_1 + \alpha_2) \exp(-\alpha_1 \alpha_2 / (\alpha_1 + \alpha_2) \vec{\mathbf{R}}_{12}^2)$, and $(\alpha_1 \vec{\mathbf{R}}_1 + \alpha_2 \vec{\mathbf{R}}_2) / (\alpha_1 + \alpha_2)$. Having loaded these pair quantities for both *bra* and *ket* parts, each GPU thread is then able to calculate the required primitive integrals.

4f. Extension to Basis Sets with Higher Angular Momentum Functions. The algorithm presented for $(ss|ss)$ integral calculations is easily generalized to allow for higher angular momentum functions. We discuss some of the relevant considerations here. Consider an example of a system consisting of five uncontracted basis shells: four s -shells and one p -shell. The total number of basis functions is thus seven. First, the shells can be sorted from the lowest angular momentum to the highest angular momentum. In our

example, this would lead to $\{1,2,3,4,5\} \leftrightarrow \{s,s,s,s,p\}$. The integral grid can now be generated in exactly the same way as previously discussed. This is shown for the given example in Figure 5, where now each individual square represents an integral batch rather than a single integral. For example, every $(ss|pp)$ batch (pink squares in Figure 5) contains nine integrals. The resulting grid for this example contains 120 unique two-electron integral batches as shown in Figure 5. Different colors represent different types of batches: orange – $(ss|ss)$, blue – $(ss|sp)$, yellow – $(sp|sp)$, pink – $(ss|pp)$, green – $(sp|pp)$, and dark red – $(pp|pp)$. Typical integral evaluation programs have separate routines for each class of integrals represented as different colors in Figure 5. A straightforward method to calculate all the integrals would be the following: a) each of 6 functions spawns a 15×15 grid of blocks to cover the whole integral batch grid (Figure 5a); b) depending on its type $[(ss|ss), (ss|sp), \text{etc.}]$, each routine (“kernel”) has its own set of rules to extract only those batches (small squares of the same color in Figure 5a) which it is responsible to calculate and schedules out the others; c) the result is then stored in the GPU memory and another function, responsible for another type of batch is called on the same 15×15 grid. However, such an approach has one serious drawback—the batches of the same type are scattered over the whole grid (Figure 5a). As a result, the rules each integral evaluation kernel needs to apply to outschedule the unsuitable batches will be rather complicated. In addition, the number of such integral batches rapidly increases with the system size, which will ultimately decrease computational performance.

The integral batch grid shown in Figure 5a was generated by a conventional loop structure as shown in Figure 6a. If one instead adopts a less conventional loop structure as shown in Figure 6b, one obtains the integral batch grid shown

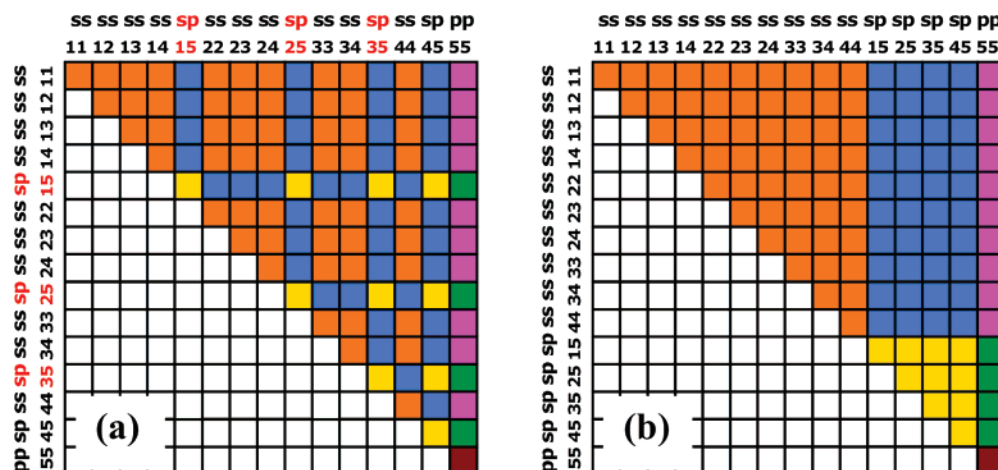


Figure 5. a) The integral grid generated by a conventional loop over shells ordered according to their angular momentum (s , then p , etc.). b) Rearranged loop sequence that leads to a well-ordered integral grid, suitable for calculations on the GPU. Different colors represent different integral types such as $(ss|ss)$, $(ss|sp)$, etc. as discussed in section 4f.

Version (a).	Version (b).
loop i over s -shells	loop i over s -shells
loop j over s -shells	loop j over s -shells
loop j over p -shells	loop i over s -shells
loop j over d -shells	loop j over s -shells
loop i over p -shells	loop i over s -shells
loop j over p -shells	loop j over d -shells
loop j over d -shells	loop i over p -shells
loop i over d -shells	loop j over p -shells
loop j over d -shells	loop i over p -shells
	loop j over d -shells
	loop i over d -shells
	loop j over d -shells

Figure 6. Pseudocode for the loop arrangement corresponding to Figure 5.

in Figure 5b. This new integral grid, or *supergrid*, has very well defined *subgrids* of integral batches of the same type. Calculation on the GPU is now straightforward—all the different integral type calculation functions are called on their own subgrids. In this case, the off-diagonal integral types, i.e., $(ss|sp)$, $(ss|pp)$, and so on, do not require any block out-scheduling, since the corresponding subgrids have rectangular shape. The diagonal integral types still need the very inexpensive “main-diagonal” out-scheduling, as discussed previously in the context of the $(ket|bra)=(bra|ket)$ symmetry (section 4b). Any of the three different thread-integral mapping schemes discussed above can now be directly applied.

4g. Considerations for Direct Self-Consistent Field Calculations. The next step after generation of the two-electron integrals is the assembly of the Fock operator for direct SCF calculations. In this context, there is no need to generate the contracted integrals explicitly—instead, one can use the primitive integrals directly to generate the desired Coulomb and exchange operators. Thus, the best of the three integral mappings considered above for direct SCF will be the 1T1PI scheme, since it exhibits ideal load balancing and the problematic inter-SM communication requirements are completely alleviated if the contracted integrals are never explicitly formed.

Given the considerations listed above when angular momenta higher than s functions are involved, we have extended the 1T1PI scheme such that each individual GPU thread evaluates an entire batch of integrals (the small squares

in Figure 5) instead of a single primitive integral (which was the case when only s functions were being considered above). Thus, when angular momenta higher than s are involved, this scheme might be better denoted as “One Thread \leftrightarrow One Batch” (1T1B). Once every integral batch is assigned to a corresponding computation thread, the thread first evaluates the integral Schwartz upper bound.²⁷ If this upper bound is larger than some predefined threshold (we used the value of 10^{-9} au), the thread calculates all the integrals in the batch and accumulates them in the corresponding elements of the Coulomb matrix.

We have used the Rys-quadrature approach²⁸ for evaluating integrals involving basis functions of higher angular momenta than s functions because it requires little memory for intermediate quantities. This is an important consideration because the amount of memory available to each thread during the computation is limited on the GPU—for optimal performance, one should stay within the register space of each SM as much as possible. On the 8800 GTX, there are 8192 32-bit registers per SM, and this register space must be evenly distributed among all threads executing on the SM. Thus, decreasing memory usage per thread is important to ensure that a large number of threads can execute in parallel on each SM (streaming processors exploit this parallelism to hide latency associated with memory-access). Six different GPU kernels were hand-coded, each capable of handling one of the six unique batch types— $(ss|ss)$, $(ss|sp)$, $(ss|pp)$, $(sp|sp)$, $(sp|pp)$, and $(pp|pp)$. We are developing a program that will generate the source code for basis sets including angular momenta higher than p functions.

5. Results and Discussion

First, we have benchmarked these three different mapping schemes on a relatively simple system consisting of 64 hydrogen atoms organized on a $4 \times 4 \times 4$ atom cubic lattice with 0.74 Å nearest-neighbor interatomic distance. The STO-6G and 6-311G basis sets were used, representing highly contracted and relatively uncontracted basis sets, respectively. All GPU computations were performed on one nVidia Geforce 8800 GTX card. For comparison, all reference

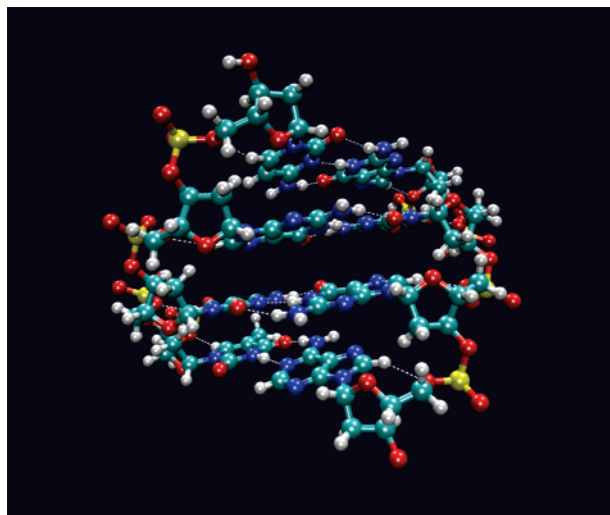
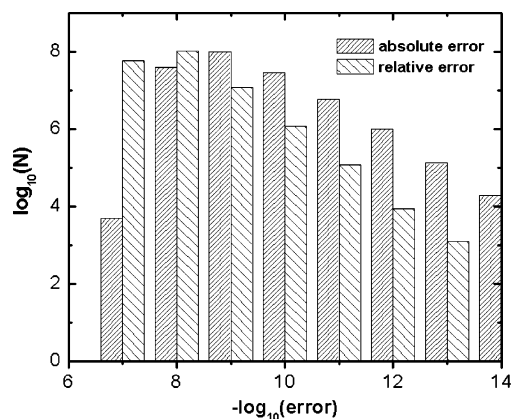
Table 1. Timings for the 64 H Atom System Two-Electron Integral Evaluation on the GPU Using the Algorithms (1B1CI, 1T1CI, 1T1PI) Described in the Text^a

	GPU 1B1CI (s)	GPU 1T1CI (s)	GPU 1T1PI (s)	CPU pre- calculation (s)	GPU-CPU transfer (s)	GAMESS
6-311G	7.086	0.675	0.428	0.009	0.883	170.8
STO-6G	1.608	1.099	2.863	0.012	0.012	90.6

^a The “CPU precalculation” column lists the amount of time required to generate pair quantities on the CPU, and the “GPU-CPU transfer” column lists the amount of time required to copy the contracted integrals from the GPU to CPU memory. Timings for the same test case using the GAMESS program package on a single Opteron 175 CPU are provided for comparison.

timing data was generated by GAMESS^{29,30} running on a single AMD Opteron 175 processor. The GAMESS source code was modified to prevent it from storing the computed integrals on the hard drive, avoiding all I/O and ensuring fair timing comparisons. The results are presented in Table 1. Note that the time required to transfer the integrals from the GPU to CPU memory can be significant, especially for weakly contracted basis sets. In fact, this transfer time can be comparable to the integral evaluation time. The GPU-CPU transfer time is determined by the speed of the host bus, and straightforward calculation from the data in Table 1 (only unique integrals are transferred) gives a speed of 0.7 Gbytes per second, consistent with the expected speeds³¹ on the PCI Express x8 bus used (unidirectional peak speed of 2 Gb/s). For the 6-311G basis set, the GPU-CPU transfer time exceeds the integral evaluation itself. Thus, it is clearly desirable to implement a direct SCF approach¹¹ entirely on the GPU.

As mentioned in section 4, we have chosen the 1T1PI (or 1T1B) mapping for future work in generating a direct SCF algorithm. For a realistic benchmark, we have chosen a 256-atom DNA strand shown in Figure 7. The 3-21G basis set is used, with a total of 1699 basis functions, including both *s* and *p* angular momenta. Although our direct SCF implementation is still under development, we are able to provide significant timing comparisons based on the formation of the Coulomb contribution to the Fock matrix. We compare the GPU time for Coulomb matrix construction to the time GAMESS requires to evaluate all two-electron integrals. For both our GPU implementation and GAMESS, the integral upper bound used for Schwartz inequality prescreening was 10^{-9} Hartree. The GPU implementation does not utilize prescreening based on the density matrix elements, i.e., all two-electron integrals which are not prescreened are calculated and contracted with density matrix elements. The current version of the GPU code for Coulomb matrix construction evaluates $O(N^4/4)$ integrals, while the total number of unique two-electron integrals is $O(N^4/8)$. In other words, each integral is calculated twice. In spite of this fact, the GPU algorithm demonstrates impressive performance—the time required to calculate the Coulomb matrix for the DNA molecule described above (Figure 7) is 19.8 s. Further elimination of the redundant integrals calculated in the GPU algorithm is expected to improve its performance. For comparison, GAMESS requires 1600 s (on an AMD Opteron 175) just to evaluate all the two-electron integrals (which

**Figure 7.** The 256-atom DNA strand used for the Coulomb matrix formation benchmark. The chemical formula of the molecule is $C_{77}P_8N_{31}H_{91}O_{49}$. Our GPU algorithm calculates the Coulomb matrix for this molecule in 19.8 s compared to 1600 s required by GAMESS (on a single AMD Opteron 175 CPU) for evaluation of the two-electron integrals (which need to be further contracted to form the Coulomb matrix).**Figure 8.** Absolute and relative error distribution of two-electron integrals generated on the GPU for the test system of 64 H atoms on a $4 \times 4 \times 4$ cubic lattice using the 6-311G basis set.

need to be further contracted with the density matrix elements to generate the Coulomb matrix).

An additional issue that merits some discussion is the fact that the 8800 GTX hardware supports only single precision floating point operations. As a result, all the integrals calculated on the GPU have single precision (7-digit) accuracy. Figure 8 presents the number of two-electron integrals calculated for the 64 H atom test system using the 6-311G basis set with given absolute and relative errors as determined by comparison with double precision CPU results. The relative error distribution demonstrates typical behavior for single precision calculations (relative error of 10^{-7} – 10^{-8}). However, electronic structure calculations are often held to an absolute accuracy standard, since it is energy differences that are important. The absolute error distribution has a maximum at 10^{-8} – 10^{-10} Hartree. In order to save CPU

time, electronic structure codes often neglect two-electron integrals less than 10^{-9} or 10^{-10} Hartree. Thus, the accuracy achieved by the GPU is somewhat worse than what is usually required in quantum chemistry calculations. Yasuda has discussed this in detail and outlined a solution which calculates large integrals (where higher precision is needed) on the CPU and others on the GPU.⁹ This is definitely a fruitful approach when confronted with hardware limited to single precision. However, the introduction of double precision support in upcoming GPUs from nVidia and AMD's FireStream processor makes it unclear whether such mixed CPU-GPU schemes will be worth the extra effort in the future. Certainly, it will not be necessary to adopt such a strategy. Only minor revisions of our current single-precision accuracy code will be needed for these 64-bit stream processors, and the relative effectiveness of the algorithms presented here will not be affected at all.

6. Conclusions

We have demonstrated that graphical processors can significantly outpace the usual CPUs in one of the most important quantum chemistry problems bottlenecks—the evaluation of two-electron repulsion integrals. We have achieved speedups of more than $130\times$ for two-electron integral evaluation in comparison to the GAMESS program package running on a single Opteron 175 CPU. One can easily anticipate the possibility of using GPUs in parallel, and hardware support for 4 GPUs per CPU has already been announced by nVidia. Parallelization of electronic structure calculations over GPUs is an obvious next step that is expected in the near future. We have demonstrated the calculation of the Coulomb matrix for a chemically significant test molecule corresponding to a 256-atom DNA strand, showing that the speedups we have obtained are representative of what can be expected on realistic systems.

The integrals generated on the GPU in single precision have a relatively large absolute error of $\approx 10^{-8}$ Hartree. Possible accuracy problems can be addressed by using effective core potentials for medium sized molecules to reduce the dynamic range of the one- and two-electron integrals used to construct the Fock matrix. Alternatively, a hybrid strategy evaluating some of the integrals on the GPU and others on the CPU could be used, as previously demonstrated.⁹ However, both nVidia and AMD have already announced GPUs with hardware support for double precision, so this will likely be a moot point within the next few months. Consequently, we are focusing on the development of a complete electronic structure code running almost entirely on the GPU, in anticipation of the coming hardware improvements.

Acknowledgment. This work has been supported by the National Science Foundation (CHE-06-26354 and DMR-03-25939) and the Department of Energy (DEFG02-00ER-15028 and DEFG02-05ER-46260).

References

(1) Kahle, J. A.; Day, M. N.; Hofstee, H. P.; Johns, C. R.; Mauerer, T. R.; Shippy, D. Introduction to the Cell Multi-processor. *IBM J. Res. Dev.* **2005**, *49*, 589.

(2) Kapasi, U. J.; Rixner, S.; Dally, W. J.; Khailany, B.; Ahn, J. H.; Mattson, P.; Owens, J. D. Programmable Stream Processors. *Computer* **2003**, *36*, 54.

(3) Russel, R. M. The Cray-1 Computer System. *Comm. ACM* **1978**, *21*, 63.

(4) Fatahalian, K.; Sugerma, J.; Hanrahan, P. Understanding the Efficiency of GPU Algorithms for Matrix-Matrix Multiplication. In *Graphics Hardware*; Akenine-Moller, T., McCool, M., Eds.; A. K. Peters: Wellesley, 2004.

(5) Hall, J.; Carr, N.; Hart, J. *Cache and Bandwidth Aware Matrix Multiplication on the GPU*; University of Illinois Computer Science Department Web Site, 2003. <http://graphics.cs.uiuc.edu/~jch/papers/UIUCDCS-R-2003-2328.pdf> (accessed December 1, 2007).

(6) Bolz, J.; Farmer, I.; Grinspun, E.; Schroder, P. Sparse matrix solvers on the GPU: Conjugate gradients and multigrid. *ACM Trans. Graph.* **2003**, *22*, 917.

(7) Anderson, A. G.; Goddard, W. A., III.; Schroder, P. Quantum Monte Carlo on graphical processing units. *Comput. Phys. Commun.* **2007**, *177*, 265.

(8) Stone, J. E.; Phillips, J. C.; Freddolino, P. L.; Hardy, D. J.; Trabuco, L. G.; Schulten, K. Accelerating molecular modeling applications with graphics processors. *J. Comput. Chem.* **2007**, *28*, 2618.

(9) Yasuda, K. Two-electron integral evaluation on the graphics processor unit. *J. Comput. Chem.* **2007**, *00*, 0000.

(10) Kermes, S.; Olivares-Amaya, R.; Vogt, L.; Shao, Y.; Amador-Bedolla, C.; Aspuru-Guzik, A. Accelerating Resolution of the Identity Second Order Moller-Plesset Calculations with Graphical Processing Units. *J. Phys. Chem. A* **2007**, in press.

(11) Almlöf, J.; Faegri, K.; Korsell, K. Principles for a direct SCF approach to LCAO-MO ab initio calculations. *J. Comput. Chem.* **1982**, *3*, 385.

(12) Boys, S. F. Electronic Wave Functions. I. A General Method of Calculation for the Stationary States of Any Molecular System. *Proc. R. Soc. London, Ser. A* **1950**, *200*, 542.

(13) McMurchie, L. E.; Davidson, E. R. One- and two-electron integrals over cartesian gaussian functions *J. Comput. Phys.* **1978**, *26*, 218.

(14) Gill, P. M. W.; Head-Gordon, M.; Pople, J. A. An Efficient Algorithm for the Generation of Two-Electron Repulsion Integrals over Gaussian Basis Functions. *Int. J. Quantum Chem.* **1989**, *23S*, 269.

(15) Dupuis, M.; Marquez, A. The Rys quadrature revisited: A novel formulation for the efficient computation of electron repulsion integrals over Gaussian functions. *J. Chem. Phys.* **2001**, *114*, 2067.

(16) Pople, J. A.; Hehre, W. J. Computation of electron repulsion integrals involving contracted Gaussian basis functions. *J. Comput. Phys.* **1978**, *27*, 161.

(17) Obara, S.; Saika, A. Efficient recursive computation of molecular integrals over Cartesian Gaussian functions. *J. Chem. Phys.* **1986**, *84*, 3963.

(18) <http://developer.nvidia.com/cuda> (accessed June 1, 2007).

(19) NVIDIA CUDA. *Compute Unified Device Architecture Programming Guide Version 1.0*; nVidia Developer Web Site. 2007. http://developer.download.nvidia.com/compute/cuda/1_0/NVIDIA_CUDA_Programming_Guide_1.0.pdf (accessed December 1, 2007).

- (20) In the latest implementation of CUDA, GPU functions are called asynchronously.
- (21) Harrison, R. J.; Kendall, R. A. *Theo. Chim. Acta* **1991**, 79, 337.
- (22) Colvin, M. E.; Janssen, C. L.; Whiteside, R. A.; Tong, C. H. *Theo. Chim. Acta* **1993**, 84, 301.
- (23) Brode, S.; Horn, H.; Ehrig, M.; Moldrup, D.; Rice, J. E.; Ahlrichs, R. Parallel Direct SCF and Gradient Program for Workstation Clusters. *J. Comput. Chem.* **1993**, 14, 1142.
- (24) Hehre, W. J.; Stewart, R. F.; Pople, J. A. *J. Chem. Phys.* **1969**, 51, 2657.
- (25) Hehre, W. J.; Ditchfield, R.; Stewart, R. F.; Pople, J. A. *J. Chem. Phys.* **1970**, 52, 2769.
- (26) Krishnan, R.; Binkley, J. S.; Seeger, R.; Pople, J. A. *J. Chem. Phys.* **1980**, 72, 650.
- (27) Whitten, J. L. Coulombic potential energy integrals and approximations. *J. Chem. Phys.* **1973**, 58, 4496.
- (28) Dupuis, M.; Rys, J.; King, H. F. Evaluation of molecular integrals over Gaussian basis functions. *J. Chem. Phys.* **1976**, 65, 111.
- (29) Schmidt, M. W.; Baldrige, K. K.; Boatz, J. A.; Elbert, S. T.; Gordon, M. S.; Jensen, J. H.; Koseki, S.; Matsunaga, N.; Nguyen, K. A.; Su, S.; Windus, T. L.; Dupuis, M.; Montgomery, J. A. General Atomic and Molecular Electronic Structure System. *J. Comput. Chem.* **1993**, 14, 1347.
- (30) Gordon, M. S.; Schmidt, M. W. Advances in electronic structure theory: GAMESS a decade later. In *Theory and Applications of Computational Chemistry: the first forty years*; Dykstra, C. E., Frenking, G., Kim, K. S., Scuseria, G. E., Eds.; Elsevier: Amsterdam, 2005; p 1167.
- (31) The GPU-CPU transfer was not done in page-locked mode for technical reasons related to the version of CUDA we used. Tests using page-locked mode show transfer speeds much closer to the 2Gb/s peak speed.

CT700268Q

Investigations into the Nature of Halogen Bonding Including Symmetry Adapted Perturbation Theory Analyses

Kevin E. Riley and Pavel Hobza*

Institute of Organic Chemistry and Biochemistry, Academy of Sciences of the Czech Republic and Center for Biomolecules and Complex Molecular Systems, Flemingovo nám. 2, 166 10 Prague 6, Czech Republic

Received August 24, 2007

Abstract: In recent years it has been recognized that, because of their unique properties, halogen bonds have tremendous potential in the development of new pharmaceutical compounds and materials. In this study we investigate the phenomenon of halogen bonding by carrying out *ab initio* calculations on the halomethane-formaldehyde complexes as well as the fluorine substituted $F_nH_{3-n}CX\cdots OCH_2$ dimers, where the halogen bonding halogens (X) are chlorine, bromine, and iodine. Coupled cluster (CCSD(T)/aug-cc-pVTZ) calculations indicate that the binding energies for these type of interactions lie in the range between -1.05 kcal/mol ($H_3CCl\cdots OCH_2$) and -3.72 kcal/mol ($F_3CI\cdots OCH_2$). One of the most important findings in this study is that, according to symmetry adapted perturbation theory (SAPT) analyses, halogen bonds are largely dependent on both electrostatic and dispersion type interactions. As the halogen atom involved in halogen bonding becomes larger the interaction strength for this type of interaction also gets larger and, interestingly, more electrostatic (and less dispersive) in character. Halogen bonding interactions also become stronger and more electrostatic upon substitution of (the very electronegative) fluorines onto the halomethane molecule.

Introduction

In recent years halogen bonding has been implicated as an important type of interaction in many different types of physical systems and are especially interesting within the fields of biochemistry^{1–11} and material science.^{12–23} These interactions play roles in a wide variety of biochemical phenomena such as protein–ligand complexation^{1,2,4–6,9,19} and are responsible for many novel properties of materials;^{14,17,19–21} these types of interactions, many believe, promise to be of great importance in the design of novel drugs and materials.

A halogen bond is defined as a short-range $C - X\cdots Y - Z$ interaction (where X is typically chlorine, bromine, or iodine, Y is an electron donor such as oxygen, nitrogen, or sulfur, and $Y - Z$ represents a side group such as a hydroxyl or carbonyl group), where the $X\cdots Y$ distance is less than sum of the van der Waals radii of X and Y .¹ Halogen bonds share

numerous physical properties with the more commonly encountered hydrogen bonds and are often treated analogously to their ubiquitous counterparts.^{1,19} There is a broad range of reported halogen bond interaction energies with values varying from about 1.2 kcal/mol ($Cl\cdots Cl$) to about 43.0 kcal/mol ($I_3^-\cdots I_2$).¹⁹

Considering the fact that halogen atoms as well as halogen bond electron donors (Y) are negatively charged, the existence of halogen bonds is surprising and counterintuitive. However, studies of the electrostatic potentials of halogen bonding systems by Auffinger et al.,¹ Clark et al.,²⁴ and Politzer et al.²⁵ show that a large halogen bound to carbon tends to form an electropositive crown, which is distal to the carbon, an electroneutral ring, which surrounds the crown, and an electronegative belt, which goes around the circumference of the halogen atom in the plane that is perpendicular to the $C - X$ bond (see Figure 3). In the works by Clark and Politzer, the electropositive crown is referred to as the

* Corresponding author e-mail: pavel.hobza@uochb.cas.cz.

σ -hole to denote the region of positive charge on the halogen surface. Halogen bonding can be, at least partially, attributed to the favorable interaction that exists between a halogen's electropositive σ -hole and an electronegative atom, such as oxygen.^{1,19,24–27} A halogen's σ -hole becomes larger and gains a higher degree of electropositivity as the size of the halogen increases, with a corresponding tendency for the halogen bond to become stronger. Fluorine, the smallest (and most electronegative) halogen, does not form an electropositive crown and thus does not participate in halogen bonding.^{1,24,25} It has also been observed that the size and charge of the σ -hole tends to increase as electronegative substituents are added to a halogen containing molecule.^{1,24,25}

There have been several theoretical^{1,23–40} and experimental^{16,17,28,41–54} studies seeking to characterize the geometric and energetic properties of halogen bonds. For example, Valerio et al. performed *ab initio* calculations on the $CH_{n-3}F_nX\cdots NH_3$ ($X = I, Br, Cl$) halogen bonded complexes, and it was found in this study that substitution of successive fluorines substituents results in $X\cdots N$ halogen bonds that are shorter and stronger.⁴⁰ The strongest halogen bond found in this study occurs for the $CF_3I\cdots NH_3$ complex with a binding energy of 5.8 kcal/mol. Riley and Merz characterized halogen bonds involving chlorine, bromine, and iodine, and carbonyl oxygens as a function of the halogen bonding distance and the $X\cdots O - C$ halogen bonding angle. In this work it was found that the optimum halogen bond angle is generally within the range from 95° to 115° , corresponding to an interaction between the halogen σ -hole and the lone pair of electrons on oxygen.²⁷ Lommerse et al. carried out intermolecular perturbation theory calculations on several halogen bonding systems containing chlorine as the halogen bond donor and both nitrogen and oxygen as the halogen bond acceptors.²⁶ In this study it is concluded that the attractive nature of halogen bonds is mostly attributable to electrostatic effects although dispersion, polarization, and charge-transfer effects seem to also play a role in these interactions. It should be pointed out that these studies were carried out with the 6-31G basis set, which is not large enough to describe dispersion effects, and it would be expected that the use of this small basis set would result in an underestimation of the dispersion energy by about an order of magnitude. On the experimental side, Corradi et al. determined the binding energy for a halogen bonded complex of 1-iodoperflouorohexane and 2,2,6,6-tetramethylpiperidine to be 7.4 kcal/mol.¹⁷

Halogen bonds involving oxygen as the halogen bond acceptor are especially interesting in biochemistry because they are, by a large margin, the most common types of halogen bonds involved in protein–ligand interactions. Recently Auffinger and co-workers carried out a database survey of short halogen-oxygen interactions, and in this study it was found that 81 out of 113 $X\cdots O$ interactions involved carbonyl oxygens (the data set contained 66 protein structures and 6 nucleic acid structures from the protein data bank).¹ These interactions generally involved a protein's backbone carbonyl group (78 out of 81 interactions). Interactions involving hydroxyl groups were also fairly common, with 18 $X\cdots O$ interactions involving hydroxyl oxygens. As has

been shown in several studies, a nitrogen atom can act as an efficient halogen bond acceptor, and one might expect that nitrogen atoms found in proteins (both in the backbone and in sidechains) might tend to be involved in halogen bonding with roughly the same frequency as oxygen atoms. Auffinger's work shows that there are only a handful of halogen bonds involving nitrogen, and seemingly these atoms are somehow inaccessible to halogen atoms. Our main interest is in halogen bonds as they pertain to biological systems, and for this reason we have chosen to focus on $X\cdots O$ halogen bonds in this study, as they seem to be the most biologically relevant examples of these types of interactions.

In this work we carry out systematic studies of $C - X\cdots O - Z$ halogen bonds, where the $O - Z$ group represents a carbonyl group. The model systems used here are the halomethane-formaldehyde dimers. Because the binding energies of halogen bonds are comparable to those of hydrogen bonding, very accurate quantum mechanical procedures should be adopted to describe them. It has recently been shown that the CCSD(T) method, extrapolated to the complete basis set limit (CBS), provides a very accurate description of intermolecular interactions.⁵⁵ In order to more fully understand the nature of halogen bonding we need, in addition to accurate binding energies, physically meaningful, well-defined interaction energy components, which can be obtained using symmetry adapted perturbation theory (SAPT).⁵⁶ We have also obtained accurate interaction energies and performed SAPT analyses of the fluorine substituted halogen bonding dimers ($F_nH_{3-n}CX\cdots O - Z$) in order to gain insight into the effects of electron withdrawing substituents on the strength and character of halogen bonds. In order to compare these, relatively poorly characterized, interactions with their more ubiquitous counterparts, hydrogen bonds, we have performed SAPT calculations on the methane-formaldehyde and ethyne-water dimers, which exemplify $C - H\cdots O$ type hydrogen bonds.

The recently developed density functional theory combined with the symmetry adapted perturbation theory (DFT-SAPT) method uses electronic densities determined using DFT methods (instead of Hartree–Fock).^{57–61} This method promises to yield results that are similar to those of the Hartree–Fock based scheme with a much smaller computational cost. In this work we have performed calculations using both SAPT and DFT-SAPT in order to compare the results obtained with each method.

Methods

In order to gain insight into the origin and nature of halogen bonds we have employed several computational methods in this study. Very accurate interaction energies are obtained with the coupled cluster method (CCSD(T)) using several different basis sets, the largest of which is the aug-cc-pVQZ quadruple- ζ basis of Dunning. Møller-Plesset (MP2) and Hartree–Fock (HF) interaction energies are also computed with several basis sets. Symmetry adapted perturbation theory calculations are carried out in order to discern the relative contributions of the interaction energy components. Natural bond order (NBO) analyses are done for some halogen

bonded dimers so that the role of electron sharing effects, such as hyperconjugation, can be studied.⁶²

The geometries of the halomethane-formaldehyde complexes were optimized on the counterpoise corrected geometric hypersurface at the MP2 level. For systems containing chlorine and bromine the cc-pVTZ basis⁶³ was used for optimization, while for complexes containing iodine a mixed basis set approach was used; here the large halogens are described using the pseudopotential based cc-pVTZ-PP basis,^{64–67} and the other atoms are described using the cc-pVTZ basis set. The MP2/cc-pVTZ method is used for these optimizations because it has been shown that the cc-pVTZ basis set yields the most well balanced description of intermolecular interactions, in terms of describing electrostatic and dispersion type interactions, when paired with MP2.⁶⁸ In the case of fluorine substituted systems, the positions of the carbon, oxygen, and halogen bonding halogen atom were kept fixed (at the positions obtained for the unsubstituted complexes), while the positions of the hydrogen and fluorine atoms were optimized at the B3LYP/3-21G* level of theory.

Interaction energies for all halogen bonding systems have been computed using the HF, MP2, and CCSD(T) methods. The CCSD(T) method describes correlation effects very well and is the most accurate modern technique for the determination of interaction energies of noncovalently bound complexes; when combined with large basis sets this method provides accurate values for molecular properties such as stabilization energies, geometries, and vibrational frequencies. The MP2 method describes some correlation effects and is much less computationally intensive than higher order techniques such as the configuration interaction and coupled cluster methods. HF describes interactions derived from electrostatic forces fairly well but greatly underestimates the binding energies of dispersion bound systems. Thus, HF interaction energies can be used to qualitatively determine whether an interaction is attributable chiefly to electrostatic or dispersive forces.

For complexes containing chlorine, the aug-cc-pVxZ (x = D,T,Q) basis sets of Dunning have been employed.⁶³ For systems containing iodine we have used a somewhat different strategy, whereby the iodine atom is treated using the pseudopotential based aug-cc-pVxZ-PP^{64–67} (x = D,T,Q) bases, while all other atoms in these systems are described using the standard aug-cc-pVxZ basis sets. There are two main reasons that this strategy has been adopted, first, there are very few high quality all-electron basis sets available for iodine, and, second, the aug-cc-pVxZ-PP basis implicitly takes relativistic effects into account. Given the large size of an iodine atom, it seems that relativistic effects might play a role in its halogen bonding behavior. For systems containing bromine calculations have been carried out using both the aug-cc-pVxZ (on all atoms) and mixed aug-cc-pVxZ-PP/aug-cc-pVxZ (for bromine/all other atoms) basis sets. This is done in order to estimate the role that relativistic effects play in these halogen bonding complexes. For all of these systems the MP2 and CCSD(T) interaction energies have also been determined at the extrapolated complete basis set limit (CBS). The electronic energies of all monomers and

dimers were extrapolated to the complete basis set limit from aug-cc-pVTZ and aug-cc-pVQZ values using the technique of Helgaker and co-workers.⁶⁹

The SAPT method allows for the separation of interaction energies into physically meaningful components such as those arising from dispersion, electrostatics, induction, and exchange. The SAPT interaction energy is given as

$$E_{\text{int}} = E_{\text{pol}}^1 + E_{\text{ex}}^1 + E_{\text{ind}}^2 + E_{\text{ex-ind}}^2 + E_{\text{disp}}^2 + E_{\text{ex-disp}}^2$$

Some of these terms can be combined in order to define values that correspond to commonly understood physical quantities. In this work we define the following equalities

$$E(\text{elec.}) = E_{\text{pol}}^1$$

$$E(\text{ind.}) = E_{\text{ind}}^2 + E_{\text{ex-ind}}^2$$

$$E(\text{disp.}) = E_{\text{disp}}^2 + E_{\text{ex-disp}}^2$$

and

$$E(\text{exch.}) = E_{\text{ex}}^1$$

These four quantities refer to the electrostatic, induction, dispersion, and exchange contributions (respectively) to the overall interaction energy.

In this work we have carried out SAPT analyses for all of the halogen bonding systems. Calculations were carried out using the aug-cc-pVxZ and aug-cc-pVxZ/aug-cc-pVxZ-PP basis sets (x = D,T,Q). Estimated complete basis set results were also obtained by extrapolating each of the interaction energy terms (as well as the SAPT interaction energy) from values obtained with aug-cc-pVTZ and aug-cc-pVQZ using the extrapolation technique of Helgaker and co-workers.⁶⁹

We have performed NBO analyses for all of the halogen bonding systems considered in this work at the DFT/B3LYP/aug-cc-pVDZ level of theory. The interaction between filled orbitals in one subsystem and unfilled orbitals of another represents a deviation of the complex from its Lewis structure and can be used as a measure of the intermolecular delocalization, also called hyperconjugation. The hyperconjugative interaction energy can be deduced from the second-order perturbation approach

$$E(2) = -\eta_{\sigma} \frac{\langle \sigma^* | F | \sigma \rangle}{\epsilon_{\sigma^*} - \epsilon_{\sigma}} = \eta_{\sigma} \frac{F_{ij}^2}{\Delta E}$$

where F_{ij} is the Fock matrix element between the i and j NBO orbitals, ϵ_{σ} and ϵ_{σ^*} are the energies of σ and σ^* , and n_{σ} is the population of the donor σ orbital.

The DFT-SAPT method provides the same type of interaction energy decomposition as SAPT but at a much lower computational cost, which makes it a useful tool for computations on very large systems. The DFT-SAPT interaction energy is given as

$$E_{\text{int}} = E_{\text{pol}}^1 + E_{\text{ex}}^1 + E_{\text{ind}}^2 + E_{\text{ex-ind}}^2 + E_{\text{disp}}^2 + E_{\text{ex-disp}}^2 + \delta HF$$

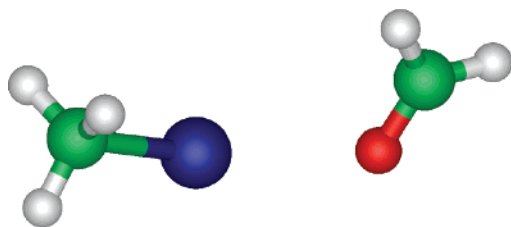


Figure 1. Geometrical configuration of the iodomethane-formaldehyde dimer.

where all but the last term are identical to the SAPT interaction energy components. The δHF term is a Hartree–Fock correction for higher order contributions to the interaction energy that are not included within the other DFT-SAPT terms.

In order to compare DFT-SAPT to SAPT we have performed DFT-SAPT calculations on the bromomethane-formaldehyde complex. These computations were carried out using the aug-cc-pVxZ/aug-cc0pVxZ-PP ($x = D, T, Q$) basis sets.

All single point CCSD(T), MP2, HF, SAPT, and DFT-SAPT calculations were performed using the MOLPRO version 2006.1 suite of molecular electronic structure programs,⁷⁰ while the NBO analysis and geometry optimizations were carried out using the Gaussian electronic structure package.⁷¹ Here we will note that binding energies are given as the negative value of interactions (i.e. $\Delta E(\text{binding}) = -\Delta E(\text{interaction})$), so that a positive binding energy refers to a bound complex.

Results and Discussion

In this article we describe computations carried out for the set of halomethane-formaldehyde dimers. We will note here that some calculations were also done for the halomethane-methanol dimers and that the results for these complexes were very similar to those obtained for the halomethane-formaldehyde dimers. Tables and figures describing the halomethane-methanol data are given as Supporting Information. Most of the data presented for the bromomethane-formaldehyde dimer described in this text refer to calculations carried out using the aug-cc-pVDZ/aug-cc-pVDZ-PP mixed basis set approach, and results computed using the aug-cc-pVDZ basis set (on all atoms) are also available as Supporting Information.

Geometries. Figure 1 shows the optimized structure of the iodomethane-formaldehyde dimer, and in this figure it can be seen that the iodine atom is positioned in such a way that its σ -hole can interact with the lone pair electrons on the methanol oxygen atom. The geometrical structures of the bromomethane-methanol and chloromethane-methanol complexes are similar to that of the iodomethane-methanol system, with the halogen atom σ -holes pointing in the direction of the oxygen lone pair electrons. Table 1 gives the important geometric quantities for the halomethane-formaldehyde complexes. One interesting aspect of the data presented in this table is the fact that the bonding distance of the systems tends to increase as the size of the halogen increases, with the bromine and iodine substituted systems having roughly the same bond distance. The $C-X\cdots O$ angle

Table 1. Geometric Parameters (Å and deg) for Optimized Structures of Halogen Bonding Complexes Considered in This Work

	$H_3CCl\cdots OCH_2$	$H_3CBr\cdots OCH_2$	$H_3CI\cdots OCH_2$
$d(X\cdots O)$	3.26	3.29	3.30
$\theta(C-X\cdots O)$	166.8	171.2	172.9
$\theta(X\cdots O-C)$	91.3	97.1	107.6

Table 2. Interaction Energies (kcal/mol) for $H_3CX\cdots OCH_2$ Complexes (kcal/mol)^a

	a-pVDZ	a-pVTZ	a-pVQZ	CBS
$H_3CCl\cdots OCH_2$ (a-pVxZ)				
HF	0.63	0.66	0.65	
MP2	-0.86	-1.11	-1.19	-1.25
CCSD(T)	-0.78	-1.05	-1.12	-1.18
$H_3CBr\cdots OCH_2$ (a-pVxZ)				
HF	0.29	0.36	0.37	
MP2	-1.37	-1.61	-1.69	-1.75
CCSD(T)	-1.24	-1.49	-1.58	-1.64
$H_3CBr\cdots OCH_2$ (a-pVxZ-PP)				
HF	0.20	0.27	0.28	
MP2	-1.44	-1.68	-1.76	-1.82
CCSD(T)	-1.32	-1.57	-1.65	-1.71
$H_3CI\cdots OCH_2$ (a-pVxZ-PP)				
HF	-0.33	-0.21	-0.21	
MP2	-2.08	-2.34	-2.43	-2.50
CCSD(T)	-1.87	-2.15	-2.25	-2.32

^a Note that a-pVxZ denotes a aug-cc-pVxZ basis set, parenthetical notation refers to the basis set used to describe the halogen atom, and CBS refers to the extrapolated complete basis set limit.

for bromine and iodine containing complexes is about the same ($\approx 172^\circ$), while it is smaller for the chlorine system ($\approx 167^\circ$). This trend may be attributable to the fact that the interaction between chlorine and oxygen is the weakest among those seen in halogen bonding and is largely based on dispersion forces (see below). Thus, the alignment of the σ -hole with the oxygen lone pair is not as critical as in the case of bromine and iodine based halogen bonds. Increasing the size of the halogen bonding halogen results in an increase in the $X\cdots O-C$ angle from 91.3° (for chlorine) to 107.6° (for iodine).

Interaction Energies. The halogen bonding interaction energies for all of the $H_3CX\cdots OCH_2$ complexes are shown in Table 2. As expected, the magnitudes of the binding energies increase with increasing halogen size. Focusing on the CCSD(T)/aug-cc-pVQZ (aug-cc-pVTZ/aug-cc-pVTZ-PP for the bromine and iodine substituted complexes) results, which are available for each type of system considered, it can be seen that the $H_3CI\cdots OCH_2$ complex is bound about 27% more strongly than $H_3CBr\cdots OCH_2$, which binds about 32% more strongly than $H_3CCl\cdots OCH_2$.

Considering the halogen-bonded complexes discussed above, the HF method greatly underestimates all of the binding energies and, in the cases of chlorine and bromine substituted systems, predicts the dimers to be unbound. This indicates that dispersion must play a large role in the stabilization of halogen bonded complexes. The fact that HF interaction energies for iodine containing halogen bonding

Table 3. SAPT Decomposition of the Interaction Energies (kcal/mol) for the $H_3CCl\cdots OCH_2$, $H_3CBr\cdots OCH_2$, and $H_3CI\cdots OCH_2$ Complexes^a

	aug-cc-pVDZ	aug-cc-pVTZ	aug-cc-pVQZ	CBS
$H_3CCl\cdots OCH_2$				
$E(elec.)$	-1.01	-0.96	-0.96	-0.96
$E(ind.)$	-0.22	-0.23	-0.23	-0.23
$E(disp.)$	-1.55	-1.81	-1.89	-1.96
$E(exch.)$	2.03	2.02	2.02	2.02
ΔE_{int}^{SAPT}	-0.75	-0.98	-1.07	-1.13
$H_3CBr\cdots OCH_2$				
$E(elec.)$	-1.56	-1.47	-1.46	-1.45
$E(ind.)$	-0.36	-0.37	-0.37	-0.37
$E(disp.)$	-1.69	-1.98	-2.08	-2.15
$E(exch.)$	2.12	2.12	2.11	2.11
ΔE_{int}^{SAPT}	-1.49	-1.70	-1.80	-1.86
$H_3CI\cdots OCH_2$				
$E(elec.)$	-2.77	-2.61	-2.61	-2.60
$E(ind.)$	-0.77	-0.78	-0.78	-0.79
$E(disp.)$	-1.91	-2.31	-2.44	-2.54
$E(exch.)$	3.01	3.01	2.98	2.96
ΔE_{int}^{SAPT}	-2.45	-2.67	-2.85	-2.96

^a Chlorine is described using the aug-cc-pVxZ basis sets, while bromine and iodine are described using the aug-cc-pVxZ-PP basis sets; CBS refers to the extrapolated complete basis set limit.

complexes are negative suggests that these interactions may depend more on electrostatic effects than those occurring between the smaller halogen atoms and oxygen. It should also be noted that the MP2 binding energies are all slightly higher than those of CCSD(T) as computed using any given basis set and that the difference between MP2 and CCSD(T) binding energies increases as the size of the halogen substituent increases.

In terms of basis sets, it can be seen that for all of the $H_3CX\cdots OCH_2$ complexes that the MP2 and CCSD(T) binding energies display convergent behavior. One interesting aspect of the data presented here is that, for all of the chlorine and bromine containing halogen bonding systems, the difference between the MP2 and CCSD(T) interaction energies remains roughly constant (within 0.02 kcal/mol) for each of the basis sets employed here.

The binding energies obtained for the bromomethane-formaldehyde complex with the mixed aug-cc-pVxZ/aug-cc-pVxZ-PP basis sets are consistently higher (by about 0.1 kcal/mol) than those computed using the aug-cc-pVxZ bases. This indicates that relativistic effects do play a non-negligible role in halogen bonding complexes involving bromine. The binding energy for this complex as computed using the aug-cc-pVQZ/aug-cc-pVQZ-PP mixed bases is 0.07 kcal/mol higher than that obtained with the aug-cc-pVQZ basis on all atoms.

SAPT Interaction Energy Decomposition. Table 3 gives the symmetry adapted perturbation theory interaction energy decomposition results for the halomethane-formaldehyde complexes. One of the most striking features of these data is the fact that the stabilities of the $Cl\cdots O$ and $Br\cdots O$ halogen bonds are predicted to be attributable chiefly to dispersion, while electrostatic forces, which have been widely believed to be responsible for these types of interactions, play a

smaller role in stabilizing these complexes. In contrast to the $Cl\cdots O$ and $Br\cdots O$ type halogen bonds, for the $I\cdots O$ halogen bond, the most stabilizing interaction energy component is the electrostatic one.

Considering the results obtained with the large aug-cc-pVQZ (aug-cc-pVQZ/aug-cc-pVQZ-PP) basis set, dispersion forces account for about 61% and 52% of the overall attraction in the chlorine and bromine substituted dimers respectively. By comparison, the electrostatic components of these interactions represent about 31% and 39% of the total attractive forces, while induction contributes 7% and 10% to the stability of these complexes (for $X = Cl, Br$ respectively). Thus it can be said that the halogen bonding interactions that occur for the chloromethane-formaldehyde and bromomethane-formaldehyde complexes are dependent on both electrostatic and dispersive forces, with dispersion playing the largest role in their stability. For the iodomethane-formaldehyde dimer the electrostatic term accounts for 54% of the attractive interaction, while dispersion represents about 33% of the attractive forces within this dimer. Induction plays a larger role in the $I\cdots O$ halogen bonding interaction than in the cases of the $Cl\cdots O$ and $Br\cdots O$ type halogen bonds, accounting for about 13% of the overall attractive interaction. It is interesting to note that, although these types of interactions are largely dependent on dispersive forces, the electrostatic interaction between the halogen σ -hole and the oxygen lone pair electrons seems to play a large role in determining the geometric structures of these complexes.

As the size of the halogen substituent increases the dispersion interaction would be expected to increase, whereas the larger halogen substituents should also allow for a larger sigma-hole, which would tend to increase the magnitude of the electrostatic interaction. Comparing the data for the chlorine, bromine, and iodine substituted halogen bonding systems, it can be seen that both the dispersion and electrostatic components of the interaction energy increase with increasing halogen size. Interestingly, there is a larger increase in the electrostatic interaction, going from chlorine to bromine to iodine, than in the dispersion interaction.

The quality of results obtained with the SAPT method, like those of other molecular structure methods, is highly dependent on the size of basis set employed. In terms of halogen bonding, Table 3 shows that the overall SAPT interaction energies as well as the interaction energy components tend to converge as larger basis sets are used. While the induction and exchange parts of the interaction energies vary very little with basis set size, the dispersion and, to a lesser extent, electrostatic components display more basis set dependence. For each of the systems considered here the electrostatic portion of the interaction energy decreases by about 5% going from aug-cc-pVDZ to aug-cc-pVTZ but does not decrease any more when the aug-cc-pVQZ basis is used. The dispersion component of the interaction energies, for each of these halogen-bonded complexes, decreases significantly (by between 10% and 15%) going from aug-cc-pVDZ to aug-cc-pVTZ and then decreases by about 5% going from aug-cc-pVTZ to aug-cc-pVQZ. Looking at the extrapolated complete basis set limit results it can be seen that each of the SAPT interaction energy

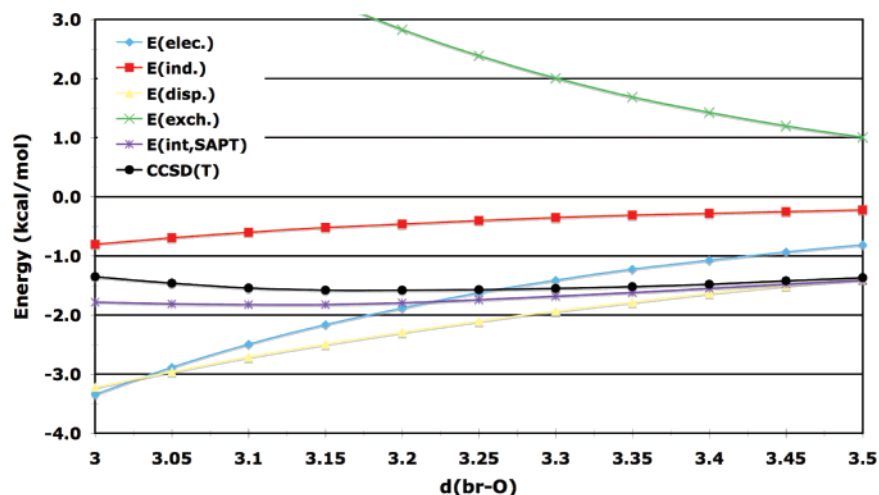


Figure 2. CCSD(T) and SAPT interaction energies as well as SAPT interaction energy components, for the bromomethane-formaldehyde dimer as a function of the bromine-oxygen separation distance $d(\text{Br}\cdots\text{O})$.

components, with the exception of the dispersion term, converges (to within 0.01 kcal/mol) at the aug-cc-pVQZ basis set. The CBS dispersion terms are about 0.06–0.08 kcal/mol lower than the aug-cc-pVQZ dispersion values; this is not a surprising result, as it is well-known that it is necessary to use very large basis sets to treat dispersion properly.

The SAPT interaction energies for the chloromethane-formaldehyde complex (for which no pseudopotential based basis sets are used) are generally in good agreement with those obtained using the CCSD(T) method. The SAPT interaction energies for complexes containing larger halogens generally do not agree with CCSD(T) results as well. The SAPT results for the iodomethane-formaldehyde complex compare particularly poorly to CCSD(T), with the SAPT/aug-cc-pVQZ(aug-cc-pVQZ-PP) binding energy being 0.60 kcal/mol higher than that calculated using the CCSD(T) with the same basis set. It is interesting to note that, in the case of the $\text{Cl}\cdots\text{O}$ type halogen bond, all SAPT binding energies are underestimated in relation to CCSD(T), while binding energies for the $\text{Br}\cdots\text{O}$ and $\text{I}\cdots\text{O}$ halogen bonds are always overestimated. It should also be noted that when standard (nonpseudopotential based) basis sets are used for the bromomethane-formaldehyde complex the SAPT and CCSD(T) interactions energies are generally in much better agreement, with SAPT binding energies always being lower than those of CCSD(T) (see the Supporting Information).

Distance Dependence of Halogen Bonds. Figure 2 shows the CCSD(T) interaction energies and SAPT interaction energy components, as calculated with the aug-cc-pVTZ/aug-cc-pVTZ-PP basis set, for several points near the potential energy minimum of the $\text{H}_3\text{CBr}\cdots\text{OCH}_2$ complex. Here it can be seen that the potential energy curve for this interaction is fairly shallow with a minimum CCSD(T) binding energy of -1.58 at a $d(\text{Br}\cdots\text{O})$ distance of 3.20 Å. The SAPT interaction energies are in relatively good agreement with those determined using CCSD(T), although they tend to deviate at small values of $d(\text{Br}\cdots\text{O})$.

One of the most interesting aspects of the data depicted in Figure 2 is the increasing contribution of the electrostatic interaction to the overall stability of the complex with decreasing halogen bond distances. At a separation distance

Table 4. Interaction Energies (kcal/mol) of the $F_n\text{H}_{3-n}\text{CX}\cdots\text{OCH}_2$ Complexes as a Function of the Number of Fluorine Substituents^a

	n=0	n=1	n=2	n=3
<i>F_nH_{3-n}CCl</i> ⋯OCH ₂ (aug-cc-pVTZ)				
HF	0.66	0.32	-0.03	-0.45
MP2	-1.11	-1.34	-1.58	-1.87
CCSD(T)	-1.05	-1.29	-1.54	-1.84
<i>F_nH_{3-n}CBr</i> ⋯OCH ₂ (aug-cc-pVTZ-PP)				
HF	0.27	-0.18	-0.69	-1.24
MP2	-1.68	-1.98	-2.28	-2.61
CCSD(T)	-1.57	-1.89	-2.23	-2.58
<i>F_nH_{3-n}Cl</i> ⋯OCH ₂ (aug-cc-pVTZ-PP)				
HF	-0.21	-0.89	-1.60	-2.50
MP2	-2.34	-2.72	-3.22	-3.77
CCSD(T)	-2.15	-2.58	-3.16	-3.72

^a aug-cc-pVTZ for Cl complexes, aug-cc-pVTZ/aug-cc-pVTZ-PP for Br and I complexes.

of 3.50 Å the electrostatic contribution to the interaction energy (-0.81 kcal/mol) is about half that of the dispersion contribution (-1.39 kcal/mol), while at a separation of 3.00 kcal/mol the contributions of these two binding components are roughly the same (electrostatic = -3.34 kcal/mol, dispersion = -3.22 kcal/mol). The contribution from induction effects also increases with decreasing values of $d(\text{Br}\cdots\text{O})$, with a minimum value of -0.22 at a separation of 3.50 Å and a maximum value of -0.80 kcal/mol at a separation of 3.00 Å. The different behavior of the electrostatic and dispersion interaction terms can likely be explained on the basis of the difference in their dependence on reciprocal distances (i.e. r^{-3} for electrostatic and r^{-6} for dispersion).

Effects of Fluorine Substitution. Fluorine is a very electronegative atom and, when substituted onto halogen bonding systems, such as the set of $F_n\text{H}_{3-n}\text{CX}\cdots\text{OCH}_2$ complexes, has the effect of drawing electron density away from the halogen bonding halogen. The HF, MP2, and CCSD(T) interactions for the fluorine substituted halomethane-formaldehyde complexes, as calculated with the aug-cc-pVTZ basis set, are given in Table 4. Here it can be seen that successive fluorine substitution results in a continuous

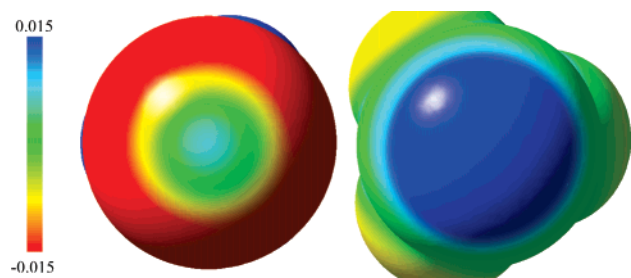


Figure 3. Molecular electrostatic potential for H_3CBr (left) and F_3CBr (right) at the 0.001 electrons Bohr^{-3} isodensity surface.

decrease in the interaction energies of these systems. It is expected that this decrease in the binding energy is caused by an increase in the electrostatic interaction between the halogen's σ -hole and the oxygen's lone pair electrons. The fact that the HF binding energies go from being positive, for the unsubstituted chlorine and bromine containing complexes, to being negative as fluorine substituents are added indicates that this assertion is correct. Figure 3 shows electrostatic potential isosurfaces for H_3CBr and F_3CBr ; here it can be seen that the σ -hole for the fluorine substituted system is significantly larger than that of the unsubstituted molecule.

Inspection of Table 4 shows the MP2 and CCSD(T) interaction energies for the $F_nH_{3-n}CX\cdots OCH_2$ complexes as a function of the number of substituted fluorines. Two features of these data that are clearly depicted in this figure are that the steepness of the curves increases with increasing halogen size and that the MP2 interaction energies approach those of CCSD(T) as more fluorine substituents are added. The most likely explanation for the stronger effect of fluorine substitution on the interactions of systems containing larger halogens is that, because the electronegativity of halogens decreases with size, the larger ones tend to lose electron density more easily and are able to form larger σ -holes. The MP2 method, when paired with a large basis set, is known to yield accurate results for electrostatically bound complexes, such as in the case of hydrogen bonding. The fact that the MP2 interaction energies become increasingly accurate (compared to those of CCSD(T)) with successive fluorine substitution is another indicator that fluorine substitution into these types of halogen bonding systems produces interactions that are more electrostatic in nature.

Table 5 gives the SAPT interaction energy decompositions for the sets of $F_nH_{3-n}CX\cdots OCH_2$ complexes. One key aspect of these results is the fact that, as expected, the electrostatic interactions are strongly modulated by the addition of fluorine substituents in these types of systems. Somewhat surprisingly, there are also non-negligible changes in the exchange and dispersion terms upon successive fluorine substitution. The exchange terms decrease with an increasing number of fluorine substituents, a trend that is probably caused by the decrease in electron density on the halogen bonding halogen, and tends to stabilize structures containing more fluorines. The addition of fluorine substituents tends to cause a decrease in the dispersion interaction terms, which tends to destabilize the fluorinated halogen bonding complexes. This increase in the dispersion term may be related to a change in the polarizability of the halomethane upon fluorine substitution.

Table 5. SAPT Interaction Decomposition Terms (kcal/mol) for the $F_nH_{3-n}CCL\cdots OCH_2$ and $F_nH_{3-n}CCBr\cdots OCH_2$ Complexes as a Function of the Number of Fluorine Substituents^a

	n=0	n=1	n=2	n=3
$F_nH_{3-n}CCL\cdots OCH_2$				
$E(elec.)$	-0.96	-1.22	-1.47	-1.73
$E(ind.)$	-0.22	-0.21	-0.22	-0.24
$E(disp.)$	-1.81	-1.77	-1.73	-1.68
$E(exch.)$	2.02	1.93	1.81	1.70
ΔE_{int}^{SAPT}	-0.98	-1.27	-1.60	-1.96
$F_nH_{3-n}CBr\cdots OCH_2$				
$E(elec.)$	-1.47	-1.84	-2.17	-2.50
$E(ind.)$	-0.37	-0.38	-0.4	-0.45
$E(disp.)$	-1.98	-1.94	-1.89	-1.83
$E(exch.)$	2.12	2.04	1.90	1.74
ΔE_{int}^{SAPT}	-1.70	-2.12	-2.56	-3.04
$F_nH_{3-n}Cl\cdots OCH_2$				
$E(elec.)$	-2.61	-3.11	-3.62	-4.04
$E(ind.)$	-0.78	-0.82	-0.88	-0.95
$E(disp.)$	-2.30	-2.26	-2.21	-2.14
$E(exch.)$	3.01	2.90	2.73	2.48
ΔE_{int}^{SAPT}	-2.68	-3.29	-3.98	-4.65

^a aug-cc-pVTZ for Cl Complexes aug-cc-pVTZ/aug-cc-pVTZ-PP for Br and I Complexes.

It is interesting to note that the magnitudes of the electrostatic interaction energy components for the $F_3CCL\cdots OCH_2$, $F_2H_1CBr\cdots OCH_2$, and $F_3CBr\cdots OCH_2$ complexes as well as for all of the halogen bonding systems containing iodine exceed those of the dispersion components.

NBO Analysis. We would like to note that extensive NBO analyses of halogen bonding systems have been carried out by Clark and co-workers, who show that the electronic configuration of the unshared electron pairs on a halogen bonding halogen approximates $s^2p_x^2p_y^2$ (where the $C - X$ bond lies along the z -axis).²⁴ This electronic configuration leads to an electron density deficiency in the region of the halogen that is distal to the carbon in the $C - X$ bond and leads to the formation of the halogen's σ -hole. The goal of the NBO analysis carried out here is to determine the role of hyperconjugation in halogen bonding. We will note here that the concept of hyperconjugation has successfully been used to interpret the electronic structure and properties of hydrogen bonds.⁷² In hydrogen bonding the main contribution to hyperconjugation is derived from charge transfer between the proton acceptor's lone pair orbital and the $X - H$ antibonding orbital.

Natural bond order analysis of the $F_nH_{3-n}CX\cdots OCH_2$ halogen bonding complexes reveals non-negligible values of the Fock matrix elements, F_{ij} , between the $C - X$ antibonding and oxygen lone pair natural orbitals, indicating a delocalization, or hyperconjugation, of the electron density between these orbitals. It is interesting to note that the hyperconjugation observed for these halogen bonds is of the same type as that seen in the case of hydrogen bonding. Table 6 shows the F_{ij} matrix element values for these complexes, where i represents the $C - X$ antibonding orbital and j represents the oxygen lone pair orbital. Here it can be seen that the degree of hyperconjugation increases with increasing

Table 6. NBO Fock Matrix Elements (kcal/mol) between the C–X Antibonding Orbital and the Oxygen Lone Pair Orbital for the $F_nH_{3-n}CX\cdots OCH_2$ and $F_nH_{3-n}CX\cdots OHCH_3$ Complexes and the Changes of Electron Density in the C–X σ^* Antibonding Orbital upon Complexation of Halogen Bonding Pairs^a

	$F_nH_{3-n}CX\cdots OCH_2$			
	n = 0	n = 1	n = 2	n = 3
X = Cl	0.31 (0.0020)	0.33 (0.0014)	0.35 (0.0010)	0.40 (0.0007)
X = Br	0.65 (0.0044)	0.69 (0.0029)	0.76 (0.0019)	0.87 (0.0020)
X = I	1.23 (0.0095)	1.36 (0.0070)	1.51 (0.0054)	1.76 (0.0071)

^a Given in parentheses (B3LYP/aug-cc-pVDZ).

halogen size and with higher degree of fluorination. The hyperconjugation increase leads to a decrease in the interaction energy. In the SAPT decomposition this increase is reflected primarily in the decrease of the induction term, which includes charge transfer.

C–H \cdots X hydrogen bonds exhibit both red and blue shifts of the C–H stretching frequency upon formation of the hydrogen bond. Vibrational shifts for the present (unfluorinated) halogen bonded complexes have been computed, and we have found that these shifts are negligible (maximum $\pm 3\text{ cm}^{-1}$). All of the halomethane monomers exhibit a positive derivative of the dipole moment as a function of the C–X distance (i.e., the dipole moment increases when the C–X bond is elongated), which indicates a red shift of the C–X stretching frequencies. The electron density of the σ^* antibonding orbital of the C–X bond systematically increases upon complexation, which also indicates a red shift of the C–X stretching frequencies. On the other hand the s-character of the carbon atom in the C–X bond increases upon dimerization, which indicates a blue shift of the C–X stretching frequencies. Evidently, the cumulative effect of all the factors considered above is to leave the C–X stretching frequencies largely unchanged upon complexation of these halogen bonding dimers.

Comparison of Halogen Bonds to Hydrogen Bonds.

Halogen bonds are often compared to, the much more ubiquitous, hydrogen bonds, with which they share some properties. Here we will compare the SAPT (aug-cc-pVTZ) interaction energy decomposition results for the, halogen bonding, $H_3CCl\cdots OCH_2$, $H_3CBr\cdots OCH_2$, $F_1H_2Cl\cdots OCH_2$, and $F_3Cl\cdots OCH_2$ complexes to those obtained for $H_3CH\cdots OCH_2$ and $HCCH\cdots OH_2$, which exemplify typical C–H \cdots O type hydrogen bonds.

Table 7 gives the SAPT interaction energy decomposition values for $H_3CCl\cdots OCH_2$, $H_3CBr\cdots OCH_2$, $F_1H_2Cl\cdots OCH_2$, and $F_3Cl\cdots OCH_2$, $H_3CH\cdots OCH_2$, and $HCCH\cdots OH_2$. The binding energy of the ethyne-water dimer (-3.25 kcal/mol) is roughly comparable to that of $F_1H_2Cl\cdots OCH_2$ (-3.29 kcal/mol) and is higher than that of $H_3CBr\cdots OCH_2$ (-1.70 kcal/mol). Overall, the C–H \cdots O interaction is more electrostatic (and less dispersive) in nature than the C–X \cdots O interactions, with the electrostatic term accounting for 68.5% of the overall attractive interaction in the $HCCH\cdots OH_2$ complex. For the

$F_1H_2Cl\cdots OCH_2$ complex, to which the hydrogen-bonding systems can be most closely compared, the electrostatic component is responsible for 50.2% of the attractive interaction, while for the (unfluorinated) bromomethane-formaldehyde dimer, this term yields only 38.5% of the attractive interaction. When the SAPT decomposition results for the $HCCH\cdots OH_2$ (68.5% electrostatic) dimer are compared to those of the $F_3Cl\cdots OCH_2$ (56.8% electrostatic) complex, which exemplifies the strongest halogen bonding complex considered in this work (SAPT binding energy of -4.65 kcal/mol), it can be seen that the hydrogen-bonding complex displays much more of an electrostatic character.

The hydrogen bonding $H_3CH\cdots OCH_2$ complex, with a binding energy of -0.70 kcal/mol , can most closely be compared to the $H_3CCl\cdots OCH_2$ complex, which has a binding energy of -0.98 kcal/mol . The interaction between methanol and formaldehyde is not dominated by the electrostatic interaction as in the case of the ethyne-water complex; nonetheless, electrostatics play a larger role in the $H_3CH\cdots OCH_2$ complex (38.5% of the attractive interaction) than in the $H_3CCl\cdots OCH_2$ complex (32.2% of the attractive interaction). In terms of SAPT interaction energy contributions the methane-formaldehyde complex is most similar to the bromomethane-formaldehyde system, whose electrostatic term corresponds to 38.5% of the total attractive interaction.

Overall it can be said that, in terms of SAPT interaction energy components, halogen bonds are similar in character to the weak C–H \cdots O type hydrogen bond found in the $H_3CH\cdots OCH_2$ complex. Both halogen bonds and this weak hydrogen bond depend largely on both electrostatic and dispersive forces. The strong C–H \cdots O hydrogen bond found in the $HCCH\cdots OH_2$ complex is very electrostatic in nature and, in terms of the SAPT interaction decomposition, does not resemble a halogen bonding interaction.

Comparison of DFT-SAPT and SAPT. Table 8 gives the DFT-SAPT and SAPT interaction energy decomposition results with the aug-cc-pVxZ/aug-cc-pVxZ-PP basis set for the $H_3CBr\cdots OCH_2$ complex. The binding energies obtained by SAPT and DFT-SAPT agree remarkably well, with the largest deviation of 0.05 kcal/mol occurring for the aug-cc-pVDZ/aug-cc-pVDZ-PP basis set. Here it can be seen that, for a given basis set, the DFT-SAPT method slightly overestimates the electrostatic and dispersion values, while it slightly underestimates the exchange values compared to standard SAPT. The DFT-SAPT values for the induction components of the binding energies agree with those of SAPT perfectly (out to two decimal places). In terms of basis sets, the same trends are seen for the DFT-SAPT method as for SAPT, as the basis set becomes larger the interaction between the two molecules within a complex gets stronger, the dispersion component increases and the electrostatic term decreases.

At present it is only possible to use the DFT-SAPT/aug-cc-pVDZ method to treat large systems, such as biological complexes. While this method can be used to obtain a qualitative description of these types of interactions, it should be kept in mind that dispersion contributions are generally underestimated by 15%–20% and that electrostatic contributions are usually overestimated by 5%–10%.

Table 7. Comparison of SAPT Results for Several Halogen Bonding and Hydrogen Bonding Complexes^a

	$H_3CCl\cdots OCH_2$	$H_3CBr\cdots OCH_2$	$F_1H_2Cl\cdots OCH_2$	$F_3Cl\cdots OCH_2$	$H_3CH\cdots OCH_2$	$HCCH\cdots OH_2$
$E(elec.)$	-0.96 (32.2)	-1.47 (38.5)	-3.11 (50.2)	-4.04 (56.7)	-0.55 (38.5)	-3.78 (68.5)
$E(ind.)$	-0.23 (7.5)	-0.37 (9.7)	-0.82 (13.2)	-0.95 (13.3)	-0.16 (11.0)	-0.51 (9.3)
$E(dis.)$	-1.81 (60.3)	-1.98 (51.8)	-2.26 (36.5)	-2.14 (30.0)	-0.72 (50.5)	-1.23 (22.2)
$E(exch.)$	2.02	2.12	2.90	2.48	0.72	2.27
ΔE_{int}^{SAPT}	-0.98	-1.70	-3.29	-4.65	-0.70	-3.25

^a kcal/mol (numbers in parentheses indicate the relative contribution (in %) to the total attractive interaction).

Table 8. Comparison of SAPT and DFT-SAPT Results for the $H_3CBr\cdots OCH_2$ Complex^a

DFT-SAPT	$H_3CBr\cdots OCH_2$			
	a-pVDZ	a-pVTZ	a-pVQZ	CBS
$E(elec.)$	-1.63	-1.56	-1.56	-1.56
$E(ind.)$	-0.36	-0.37	-0.37	-0.37
$E(dis.)$	-1.74	-2.06	-2.13	-2.18
$E(exch.)$	2.29	2.29	2.26	2.23
δHF	0.00	-0.01	-0.01	-0.01
ΔE_{int}^{SAPT}	-1.44	-1.71	-1.81	-1.89

SAPT	a-pVDZ	a-pVTZ	a-pVQZ	CBS
$E(elec.)$	-1.56	-1.47	-1.46	-1.45
$E(ind.)$	-0.36	-0.37	-0.37	-0.37
$E(dis.)$	-1.69	-1.98	-2.08	-2.15
$E(exch.)$	2.12	2.12	2.11	2.11
ΔE_{int}^{SAPT}	-1.49	-1.70	-1.80	-1.86

^a kcal/mol (note that a-pVxZ = aug-cc-pVxZ/aug-cc-pVxZ-PP).

Conclusions

In this work we have performed HF, MP2, CCSD(T), NBO, SAPT, and DFT-SAPT calculations, using several large basis sets, on the (fluorinated and unfluorinated) halomethane-formaldehyde complexes. It is found that, as the halogen bonding halogen's size increases, the halogen bond becomes stronger and longer. SAPT analyses of halogen bonds in systems containing chlorine and bromine indicate that halogen bonding interactions involving these halogen atoms are principally dispersive in nature, although electrostatic contributions to halogen bonds are not negligible. The electrostatic contribution to the interaction energy in halogen bonding increases as the size of the halogen bonding halogen increases. The most dominant physical component of interactions for systems containing iodine is the electrostatic one, which accounts for slightly more than half of the total binding energy. Upon substitution of fluorine atoms, which are very electronegative, onto the halomethanes, halogen bonds become more stable and more electrostatic (and less dispersive) in nature. The weakest halogen bond observed in this study is for the $H_3CCl\cdots OCH_2$ complex, whose CCSD(T)/aug-cc-pVTZ binding energy is -1.05 kcal/mol. The strongest halogen bond occurs for the $F_3Cl\cdots OCH_2$ complex, with a CCSD(T)/aug-cc-pVTZ interaction energy of -3.72 kcal/mol.

The most significant result obtained in this study is the fact that, according to SAPT analysis, halogen bonds are largely dependent on both electrostatic and dispersion forces. The electrostatic nature of halogen bonds increases with the increasing size of the halogen involved, while the dispersive contribution to the halogen bonding interaction decreases

with increasing halogen size. The largest SAPT interaction energy component for (unfluorinated) systems containing chlorine and bromine is dispersion, while the electrostatic term accounts for slightly more than half of the attractive interaction for the iodomethane-formaldehyde complex. It should be noted that, even in cases where the electrostatic contribution to the interaction energy is smaller than that of dispersion, electrostatic effects probably play a large role in determining the geometries of halogen bonding systems, as the halogen's positive σ -hole tends to line up with the negative lone electron pair on oxygen. The contribution of induction effects to halogen bonding interactions is relatively small and generally accounts for about 5%-15% of the attractive interaction.

The addition of fluorine substituents to the halomethane molecules in our model complexes tends to draw electron density away from the halogen bonding halogen atoms, which results in halogen atoms that have significantly larger (and more positive) σ -holes. The overall effect of successive fluorine substitution onto the halomethane systems is to produce halogen bonds that are both stronger and more electrostatic in character.

Halogen bonds are often compared to, the much more commonly encountered, hydrogen bonds. Here we have shown that, in terms of SAPT interaction energy terms, halogen bonds share many common features with weak $C-H\cdots O$ type hydrogen bonds. Halogen bonds are not very similar to strong $C-H\cdots O$ hydrogen bonds, which exhibit interactions that are much more electrostatic in nature. One common feature of halogen bonds and hydrogen bonds is the hyperconjugation that occurs between the $C-X$ (where X represents either a halogen or hydrogen) antibonding orbital and the oxygen lone pair orbital. The magnitude of this hyperconjugation increases with larger halogen atoms and with the addition of fluorine substituents onto the halomethane systems.

Among the many scientific fields in which halogen bonds have been implicated as important types of interactions is the study of protein-ligand interactions. It has been shown in this work, and in several other studies, that halogen bonding interactions are sufficiently strong to be considered as relevant in biological complexes and that, because of their unique properties, halogen bonds might be used in the development of, for example, new pharmaceutical compounds.

Acknowledgment. This project was supported by grants from the Ministry of Education, Youth and Sports of the Czech Republic (LC 512) and The Grant Agency of the Academy of Sciences of the Czech Republic (A400550510) and was also part of Research Project No. Z40550506. The

support of the Premium Academiae awarded to P.H. 2007 is also acknowledged. A portion of the research described in this paper was performed in the Environmental Molecular Sciences Laboratory, a national scientific user facility sponsored by the Department of Energy's Office of Biological and Environmental Research and located at Pacific Northwest National Laboratory.

Supporting Information Available: Tables and figures describing the halomethane-methanol data and results computed using the aug-cc-pVDZ basis set (on all atoms). This material is available free of charge via the Internet at <http://pubs.acs.org>.

References

- (1) Auffinger, P.; Hays, F. A.; Westhof, E.; Ho, P. S. *Proc. Natl. Acad. Sci. U.S.A.* **2004**, *101*, 16789.
- (2) Battistutta, R.; Mazzorana, M.; Sarno, S.; Kazimierczuk, Z.; Zanotti, G.; Pinna, L. A. *Chem. Biol.* **2005**, *12*, 1211.
- (3) Brouwer, a.; Morse, D. C.; Lans, M. C.; Schuur, A. G.; Murk, A. J.; Klasson-Wehler, E.; Bergman, A.; Visser, T. J. *Toxicol. Ind. Health* **1998**, *14*, 59.
- (4) Ghosh, M.; Meerts, I. A. T. M.; Cook, A.; Bergman, A.; Brouwer, A.; Johnson, L. N. *Acta Crystallogr., Sect. D: Biol. Crystallogr.* **2000**, *56*, 1085.
- (5) Himmel, D. M.; Das, K.; Clark, A. D.; Hughes, S. H.; Benjahad, A.; Oumouch, S.; Guillemont, J.; Coupa, S.; Poncelet, A.; Csoka, I.; Meyer, C.; Andries, K.; Nguyen, C. H.; Grierson, D. S.; Arnold, E. *J. Med. Chem.* **2005**, *48*, 7582.
- (6) Jiang, Y.; Alcaraz, A. A.; Chen, J. M.; Kobayashi, H.; Lu, Y. J.; Snyder, J. P. *J. Med. Chem.* **2006**, *49*, 1891.
- (7) Lans, M. C.; Klassonwehler, E.; Willemsen, M.; Meussen, E.; Safe, S.; Brouwer, a. *Chem.-Biol. Interact.* **1993**, *88*, 7.
- (8) Lans, M. C.; Spiertz, C.; Brouwer, a.; Koeman, J. H. *Eur. J. Pharmacol.* **1994**, *270*, 129.
- (9) Lopez-Rodriguez, M. L.; Murcia, M.; Benhamu, B.; Viso, A.; Campillo, M.; Pardo, L. *J. Med. Chem.* **2002**, *45*, 4806.
- (10) Trogdon, G.; Murray, J. S.; Concha, M. C.; Politzer, P. J. *Mol. Model.* **2007**, *13*, 313.
- (11) Voth, R.; Hays, F. a.; Ho, P. S. *Proc. Natl. Acad. Sci. U.S.A.* **2007**, *104*, 6188.
- (12) Bertani, R.; Chau, F.; Gleria, M.; Metrangolo, P.; Milani, R.; Pilati, T.; Resnati, G.; Sansotera, M.; Venzo, A. *Inorg. Chim. Acta* **2007**, *360*, 1191.
- (13) Boubekour, K.; Syssa-Magale, J. L.; Palvadeau, P.; Schollhorn, B. *Tetrahedron Lett.* **2006**, *47*, 1249.
- (14) Cariati, E.; Forni, A.; Biella, S.; Metrangolo, P.; Meyer, F.; Resnati, G.; Righetto, S.; Tordin, E.; Ugo, R. *Chem. Commun.* **2007**, 2590.
- (15) Caronna, T.; Liantonio, R.; Logothetis, T. A.; Metrangolo, P.; Pilati, T.; Resnati, G. *J. Am. Chem. Soc.* **2004**, *126*, 4500.
- (16) Chopra, D.; Thiruvengatam, V.; Manjunath, S. G.; Row, T. N. G. *Cryst. Growth Des.* **2007**, *7*, 868.
- (17) Corradi, E.; Meille, S. V.; Messina, M. T.; Metrangolo, P.; Resnati, G. *Angew. Chem., Int. Ed.* **2000**, *39*, 1782.
- (18) Marras, G.; Metrangolo, P.; Meyer, F.; Pilati, T.; Resnati, G.; Vij, A. *New J. Chem.* **2006**, *30*, 1397.
- (19) Metrangolo, P.; Neukirch, H.; Pilati, T.; Resnati, G. *Acc. Chem. Res.* **2005**, *38*, 386.
- (20) Metrangolo, P.; Resnati, G.; Pilati, T.; Liantonio, R.; Meyer, F. *J. Polym. Sci., Part A: Polym. Chem.* **2007**, *45*, 1.
- (21) Sourisseau, S.; Louvain, N.; Bi, W. H.; Mercier, N.; Rondeau, D.; Boucher, F.; Buzare, J. Y.; Legein, C. *Chem. Mater.* **2007**, *19*, 600.
- (22) Xu, J. W.; Liu, X. M.; Ng, J. K. P.; Lin, T. T.; He, C. B. *J. Mater. Chem.* **2006**, *16*, 3540.
- (23) Politzer, P.; Murray, J. S.; Concha, M. C. *J. Mol. Model.* **2007**, *13*, 643.
- (24) Clark, T.; Hennemann, M.; Murray, J. S.; Politzer, P. *J. Mol. Model.* **2007**, *13*, 291.
- (25) Politzer, P.; Lane, P.; Concha, M. C.; Ma, Y. G.; Murray, J. S. *J. Mol. Model.* **2007**, *13*, 305.
- (26) Lommerse, J. P. M.; Stone, A. J.; Taylor, R.; Allen, F. H. *J. Am. Chem. Soc.* **1996**, *118*, 3108.
- (27) Riley, K. E.; Merz, K. M. *J. Phys. Chem. A* **2007**, *111*, 1688.
- (28) Glaser, R.; Chen, N. J.; Wu, H.; Knotts, N.; Kaupp, M. J. *Am. Chem. Soc.* **2004**, *126*, 4412.
- (29) Lu, Y. X.; Zou, J. W.; Wang, Y. H.; Yu, Q. S. *J. Mol. Struct. THEOCHEM* **2006**, *776*, 83.
- (30) Lu, Y. X.; Zou, J. W.; Wang, Y. H.; Yu, Q. S. *J. Mol. Struct. THEOCHEM* **2006**, *767*, 139.
- (31) Poleshchuk, O. K.; Branchadell, V.; Brycki, B.; Fateev, A. V.; Legon, A. C. *J. Mol. Struct. THEOCHEM* **2006**, *760*, 175.
- (32) Poleshchuk, O. K.; Kalinina, E. L.; Legon, A. *Russ. J. Coord. Chem.* **2003**, *29*, 60.
- (33) Poleshchuk, O. K.; Legon, A. C. *Z. Naturforsch., A: Phys. Sci.* **2002**, *57*, 537.
- (34) Romaniello, P.; Lelj, F. *J. Phys. Chem. A* **2002**, *106*, 9114.
- (35) Wang, W. Z.; Tian, A. M.; Wong, N. B. *J. Phys. Chem. A* **2005**, *109*, 8035.
- (36) Wang, W. Z.; Wong, N. B.; Zheng, W. X.; Tian, A. M. *J. Phys. Chem. A* **2004**, *108*, 1799.
- (37) Wang, Y. H.; Zou, J. W.; Lu, Y. X.; Yu, Q. S. *J. Theor. Comput. Chem.* **2006**, *5*, 719.
- (38) Zou, J. W.; Jiang, Y. J.; Guo, M.; Hu, G. X.; Zhang, B.; Liu, H. C.; Yu, Q. S. *Chem.-Eur. J.* **2005**, *11*, 740.
- (39) Zou, J. W.; Lu, Y. X.; Yu, Q. S.; Zhang, H. X.; Jiang, Y. J. *Chin. J. Chem.* **2006**, *24*, 1709.
- (40) Valerio, G.; Raos, G.; Meille, S. V.; Metrangolo, P.; Resnati, G. *J. Phys. Chem. A* **2000**, *104*, 1617.
- (41) Bilewicz, E.; Rybarczyk-Pirek, A. J.; Dubis, A. T.; Grabowski, S. J. *J. Mol. Struct.* **2007**, *829*, 208.
- (42) Borowiak, T.; Wolska, I.; Brycki, B.; Zielinski, A.; Kowalczyk, I. *J. Mol. Struct.* **2007**, *833*, 197.
- (43) Castellote, I.; Moron, M.; Burgos, C.; Alvarez-Builla, J.; Martin, A.; Gomez-Sal, P.; Vaquero, J. *J. Chem. Commun.* **2007**, 1281.
- (44) Forni, A.; Metrangolo, P.; Pilati, T.; Resnati, G. *Cryst. Growth Des.* **2004**, *4*, 291.
- (45) Larsen, D. W.; Allred, A. L. *J. Am. Chem. Soc.* **1965**, *87*, 1216.
- (46) Larsen, D. W.; Allred, A. L. *J. Am. Chem. Soc.* **1965**, *87*, 1219.
- (47) Larsen, D. W.; Allred, A. L. *J. Phys. Chem.* **1965**, *69*, 2400.

- (48) Lucassen, A. C. B.; Karton, A.; Leitus, G.; Shimon, L. J. W.; Martin, J. M. L.; van der Boom, M. E. *Cryst. Growth Des.* **2007**, *7*, 386.
- (49) Lucassen, A. C. B.; Vartanian, M.; Leitus, G.; van der Boom, M. E. *Cryst. Growth Des.* **2005**, *5*, 1671.
- (50) Mossakowska, I.; Wojcik, G. *Acta Crystallogr., Sect. C: Cryst. Struct. Commun.* **2007**, *63*, O123.
- (51) Mugnaini, V.; Punta, C.; Liantonio, R.; Metrangolo, P.; Recupero, F.; Resnati, G.; Pedulli, G. F.; Lucarini, M. *Tetrahedron Lett.* **2006**, *47*, 3265.
- (52) Russo, L.; Biella, S.; Lahtinen, M.; Liantonio, R.; Metrangolo, P.; Resnati, G.; Rissanen, K. *CrystEngComm* **2007**, *9*, 341.
- (53) Zordan, F.; Brammer, L. *Cryst. Growth Des.* **2006**, *6*, 1374.
- (54) Zordan, F.; Espallargas, G. M.; Brammer, L. *CrystEngComm* **2006**, *8*, 425.
- (55) Lee, E. C.; Kim, D.; Jurecka, P.; Tarakeshwar, P.; Hobza, P.; Kim, K. S. *J. Phys. Chem. A* **2007**, *111*, 3446.
- (56) Jeziorski, B.; Moszynski, R.; Szalewicz, K. *Chem. Rev.* **1994**, *94*, 1887.
- (57) Hesselmann, A.; Jansen, G. *Chem. Phys. Lett.* **2002**, *362*, 319.
- (58) Hesselmann, A.; Jansen, G. *Chem. Phys. Lett.* **2002**, *357*, 464.
- (59) Hesselmann, A.; Jansen, G. *Phys. Chem. Chem. Phys.* **2003**, *5*, 5010.
- (60) Hesselmann, A.; Jansen, G.; Schutz, M. *J. Chem. Phys.* **2005**, *122*.
- (61) Jansen, G.; Hesselmann, A. *J. Phys. Chem. A* **2001**, *105*, 11156.
- (62) Reed, E.; Curtiss, L. a.; Weinhold, F. *Chem. Rev.* **1988**, *88*, 899.
- (63) Dunning, T. H. *J. Chem. Phys.* **1989**, *90*, 1007.
- (64) Metz, B.; Schweizer, M.; Stoll, H.; Dolg, M.; Liu, W. J. *Theor. Chem. Acc.* **2000**, *104*, 22.
- (65) Metz, B.; Stoll, H.; Dolg, M. *J. Chem. Phys.* **2000**, *113*, 2563.
- (66) Peterson, K. A. *J. Chem. Phys.* **2003**, *119*, 11099.
- (67) Peterson, K. A.; Figgen, D.; Goll, E.; Stoll, H.; Dolg, M. *J. Chem. Phys.* **2003**, *119*, 11113.
- (68) Riley, K. E.; Hobza, P. *J. Phys. Chem. A* **2007**, *111*, 8257.
- (69) Halkier, a.; Helgaker, T.; Jorgensen, P.; Klopper, W.; Koch, H.; Olsen, J.; Wilson, A. K. *Chem. Phys. Lett.* **1998**, *286*, 243.
- (70) Werner, H. J.; Knowles, P. J.; Lindh, R.; Manby, F. R.; Schütz, M.; Celani, P.; Korona, T.; Rauhut, G.; Amos, R. D.; Bernhardsson, A.; Berning, A.; Cooper, D. L.; Deegan, M. J. O.; Dobbyn, A. J.; Eckert, F.; Hampel, C.; Hetzer, G.; Lloyd, A. W.; McNicholas, S. J.; Meyer, W.; Mura, M. E.; Nicklass, A.; Palmieri, P.; Pitzer, R.; Schumann, U.; Stoll, H.; Stone, A. J.; Tarroni, R.; T., T. Molpro version 2006.1, a package of *ab initio* programs, 2006.
- (71) Frisch, M. J.; Trucks, G. W.; Schlegel, H. B.; Scuseria, G. E.; Robb, M. A.; Chesseman, J. R.; Zakrzewski, V. G.; Montgomery, J. A., Jr.; Stratmann, R. E.; Burant, J. C.; Dapprich, S.; Millam, J. M.; Daniels, A. D.; Kudin, K. N.; Strain, M. C.; Farkas, O.; Tomasi, J.; Barone, V.; Cossi, M.; Cammi, R.; Mennucci, B.; Pomelli, C.; Adamo, C.; Clifford, S.; Ochterski, J.; Petersson, G. A.; Ayala, P. Y.; Cui, Q.; Morokuma, K.; Malick, D. K.; Rabuck, A. D.; Raghavachari, K.; Foresman, J. B.; Cioslowski, J.; Ortiz, J. V.; Baboul, A. G.; Stefanov, B. B.; Liu, G.; Liashenko, A.; Piskorz, P.; Komaromi, I.; Gomperts, R.; Martin, R. L.; Fox, D. J.; Keith, T.; AlLoham, M. A.; Peng, C. Y.; Nanayakkara, A.; Gonzalez, C.; Challacombe, M.; Gill, P. M. W.; Johnson, B. G.; Chen, W.; Wong, M. W.; Andres, J. L.; Head-Gordon, M.; Replogle, E. S.; Pople, J. A. Gaussian 03; Gaussian Inc.: Wallingford, CT, 2003.
- (72) Chocholousova, J.; Spirko, V.; Hobza, P. *Phys. Chem. Chem. Phys.* **2004**, *6*, 37.

CT700216W

JCTC

Journal of Chemical Theory and Computation

Monoligand Zn(II) Complexes: Ab Initio Benchmark Calculations and Comparison with Density Functional Theory Methodologies

Víctor M. Rayón,^{*,†} Haydee Valdés,[‡] Natalia Díaz,[§] and Dimas Suárez^{*,§}

Departamento de Química Física y Química Inorgánica, Facultad de Ciencias, Universidad de Valladolid, 47005 Valladolid, Spain, Center for Biomolecules and Complex Molecular Systems, Institute of Organic Chemistry and Biochemistry, Academy of Sciences of the Czech Republic, 16610 Prague 6, Czech Republic, and Departamento de Química Física y Analítica, Facultad de Química, Universidad de Oviedo, 33007 Oviedo, Spain

Received September 11, 2007

Abstract: A systematic theoretical study on several models of Zn(II) complexes has been carried out employing both ab initio correlated wave function and density functional methods. The performance of five different functionals namely PW91, PBE, B3LYP, MPWLYP1M, and TPSS in the prediction of metal–ligand bond distances, binding energies, and proton affinities has been assessed comparing the results to those obtained with the MP2 and CCSD(T) wave function methodologies. Several basis sets ranging from double- ζ up to quintuple- ζ quality have been used, including the recently developed all-electron correlation consistent basis sets for zinc. It is shown that all the tested functionals overestimate both the metal–ligand bond distances and the binding energies, being that the B3LYP and TPSS functionals are the ones that perform the best. An analysis of the metal–ligand interaction energy shows that induction and charge-transfer effects play a prominent role in the bonding of these systems, even for those complexes with the less polarizable ligands. This finding highlights the importance of a correct description of the polarization of the monomers' charge densities by any theoretical method which aims to be applied to the study of Zn(II) complexes.

Introduction

Zinc, following iron, is the second-most abundant transition metal in biology and plays a prominent role in many structural and reactive biochemical processes.¹ It is present in more than 120 enzymes involved in the metabolism of nucleic acids, proteins, and carbohydrates. A combination of different factors, flexible coordination geometry, lack of redox activity, intermediate polarizability, and borderline hard–soft character, makes divalent zinc, Zn(II), capable of

satisfactorily coordinating with the broad spectrum of “hard” and “soft” ligands present in metalloenzymes. Thus, an accurate and well-balanced theoretical description of the ligand binding ability and hydration of Zn(II) ions is required in order to increase our understanding of zinc enzymology using the tools of computational quantum chemistry.

In principle, ab initio quantum mechanical (QM) methodologies provide the most accurate results, specially if coupled-cluster (CC) methods² are combined with correlation-consistent basis sets, which allow the systematic extension of one-particle basis set calculations of molecular properties toward the complete basis set (CBS) limit.^{3,4} Until recently, accurate ab initio calculations with correlation consistent basis sets were feasible only for main group elements. Fortunately, a similar strategy is now possible for

* Corresponding author fax: 34-983-423013; e-mail: vmrr@qf.uva.es (V.M.); fax: 34-985-103125; e-mail: dimas@uniovi.es (D.S.).

[†] Universidad de Valladolid.

[‡] Academy of Sciences of the Czech Republic.

[§] Universidad de Oviedo.

systems containing first-row transition metals thanks to Peterson and co-workers,⁵ who developed a family of nonrelativistic and relativistic correlation basis sets for Sc–Zn that are expected to facilitate accurate and reliable calculations for metal complexes. However, the large computational cost of the highly correlated QM methods determines that their applicability is limited to small systems. This is not the case, however, of the density functional theory (DFT),⁶ which offers quite accurate results for about the price of a Hartree–Fock (HF) calculation. For this reason, DFT has become the most popular correlated methodology for the study of biomolecules including zinc-enzymes.^{7,8} Additionally, the development of linear scaling techniques^{9–11} and tight-binding models^{12,13} have pushed further the applicability of DFT. Since the design of the most commonly used density functionals is ultimately based on parametrization procedures, the question of the applicability of a given functional outside the scope for which it was developed is always a matter of concern. This is particularly true when dealing with systems containing transition metal atoms because most functionals have not been parametrized to fit data for inorganic or organometallic molecules.¹⁴

Several computational studies on zinc-containing biomolecules have been published^{15–18} in which the application of DFT or semiempirical methodologies was assessed by performing ab initio calculations on small zinc complexes. In general the model systems considered in these studies were limited to what was required for the particular problem being analyzed as in a recent comparative study of semiempirical, ab initio, and DFT methods in Zn-biomimetic complexes,¹⁹ which is focused on models of histidine side chains. In addition, most of the previous ab initio calculations were carried out using the HF and the second-order Møller-Plesset (MP2) methods with medium-sized basis sets. Nevertheless, either DFT or MP2 methods have been employed to provide reference data in order to derive optimum parameters for Zn(II) ions within the context of approximate methodologies like the semiempirical PM3 method,²⁰ the approximate tight binding DFT method,²¹ and the molecular mechanics “Sum of Interactions Between Fragments Ab initio Computed” (SIBFA) method.^{22–24}

The first goal of this study is to provide reliable high-level benchmark ab initio results for a set of 1:1 complexes in order to improve the energetic, structural, and electronic description of the ligand binding ability of Zn(II), which we think is a convenient first step for the assessment of DFT or parametrized methods. Thus, a set of 18 complexes modeling the typical Zn(II)-ligand interactions existing in living systems was characterized by means of high level ab initio calculations. The following ligands were chosen: water, formaldehyde, methanol, acetic acid, formamide, ammonia, methanimine, methylamine, 1H-imidazole, hydrogen sulfide, methanethiol, benzene, hydroxide, methanolate, acetate, imidazolate, hydrosulfide, and methanethiolate. Taking into account the prevalence of Zn(II) ions in biomolecular systems and the efficacy with which DFT methods can be applied to large systems, we also carried out a systematic analysis of the performance of DFT on Zn(II)-ligand interactions by comparing the results obtained from several density func-

tionals with those provided by the correlated wave function methods. A third goal of this study is the analysis of the nature of the metal–ligand bond in the Zn(II) complexes by means of an energy decomposition method. This provides information on the relative importance of the electrostatic, induction, and dispersive contributions to the interaction energy. Altogether our results could be particularly useful for the refinement of molecular mechanics force fields as well as comparison with other partitioning schemes used for the calibration of some molecular mechanics potentials.

Computational Methods

Ab Initio Calculations. Ab initio benchmark calculations of the monoligand Zn(II) complexes examined in this work were carried out assuming the frozen core approximation in all the correlated calculations and using correlation consistent basis sets for valence electron correlation. The basis sets were constructed by employing the Dunning’s correlation consistent basis^{25,26} on the main group atoms and the nonrelativistic all-electron basis from Balabanov and Peterson on zinc.⁵

Molecular geometries were optimized at the MP2/aug-cc-pVTZ level. Harmonic frequency calculations were performed to check whether the optimized geometries are local minima on the Potential Energy Surfaces (PES) and to obtain the Zero-Point Vibrational Energies (ZPVE). Electronic energies were refined by performing single-point calculations at the CCSD(T)/aug-cc-pVTZ level of theory (coupled cluster single and double excitation augmented with a noniterative treatment of triple excitations)²⁷ on the MP2/aug-cc-pVTZ optimized geometries. To estimate the effect of larger basis sets on the ab initio energies, single-point MP2/aug-cc-pVnZ ($n=4, 5$) calculations were also performed on the MP2/aug-cc-pVTZ geometries.

As above-mentioned, the fundamental advantage in using a sequence of correlation consistent basis sets is the possibility of extrapolating the results toward the CBS limit and, thereby, removing basis set truncation errors. As proposed by Peterson and Puzzarini,²⁸ we used two extrapolation formulas

$$E_n = E_{\text{CBS}} + An^{-3} \quad (1)$$

$$E_n = E_{\text{CBS}} + An^{-(n-1)} + Be^{-(n-1)^2} \quad (2)$$

where n is the cardinal number of the basis set and E_{CBS} , A , and B are fitting parameters, with E_{CBS} being the resulting estimate of the CBS limit. The average E_{CBS} value obtained from these two expressions has been reported as a conservative estimate of the actual CBS limit.^{5,28} Herein, extrapolations using eqs 1 and 2 with the aug-cc-pVnZ ($n=4, 5$) basis sets were used systematically on the MP2 correlation energies. The HF energies were not extrapolated, and the 5Z HF values were simply taken as the most accurate estimates of the HF limits.

In general, the calculation of the CCSD(T) CBS limit for all the complexes considered in this work is impractical. Then we decided to approximate the corresponding CCSD(T) CBS values by means of the following “composite” formula

$$E_{\text{CCSD(T) CBS}} \approx E_{\text{CCSD(T)/aug-cc-pVTZ}} + (E_{\text{MP2/CBS}} - E_{\text{MP2/aug-cc-pVTZ}}) \quad (3)$$

which basically summarizes the computational scheme adopted in this work for computing the high-level benchmark energies of the Zn(II) monoligand complexes.

The sensitivity of the computed binding energies and molecular properties with respect to basis set effects and/or the method employed for geometry optimization were assessed by carrying out further ab initio calculations for some of the Zn(II)-*L* complexes (*L*=OH⁻, H₂O, HS⁻, and H₂S). For these small complexes, molecular geometries were reoptimized at the CCSD/aug-cc-pVTZ level and binding energies were recomputed on the new geometries using the “composite” approximation in eq 3. Moreover, the CBS limit of the CCSD(T) energies was also estimated by means of single-point CCSD(T)/aug-cc-pVnZ (*n*=4, 5) calculations and using eqs 1 and 2. We also tested that the same CBS-limit is consistently attained from both electronic energies that included the Counterpoise (CP) correction for Basis Set Superposition Error (BSSE)²⁹ and uncorrected energies. Finally, the quality of the frozen core approximation was assessed by performing full electron correlation calculations with basis sets optimal for correlating the outer-core 3*s* and 3*p* electrons, which are generally needed to compute accurate dissociation energies involving 3*d* elements and second-row main group elements. In these calculations, we employed the aug-cc-pwVnZ basis set for Zn,⁵ aug-cc-pV(*n*+*d*)Z for S,³⁰ and the standard aug-cc-pVnZ for H and O.

Density Functional Calculations. Five density functionals were selected for this study: two generalized gradient approximation (GGA) functionals, PW91³¹ and PBE;³² two hybrid functionals, B3LYP^{33–36} and MPWLYP1M;³⁷ and one meta-GGA functional, TPSS.³⁸ The MPWLYP1M functional has been developed recently, and it consists of the modified Perdew–Wang exchange functional and the Lee–Yang–Parr (LYP) correlation functional. It has one parameter (the percentage of HF exchange) optimized for metals (though not specifically for Zn). Note that both PBE and TPSS are nonempirical functionals, whereas PW91, B3LYP, and MPWLYP1M contain explicitly empirical parameters. These functionals were used to fully optimize the geometries of the Zn(II) complexes and the isolated ligands followed by analytical frequency calculations. The default integration grid (75 radial shells and 302 angular points) was used for all the DFT calculations. For test purposes we also carried out optimizations and frequency calculations on the whole set of complexes using a larger (“UltraFine”) integration grid with 99 radial shells and 590 angular points. These test calculations have been performed using the PBE functional and the aug-cc-pVTZ basis set.

We employed different basis sets for the DFT calculations ranging from double- ζ up to triple- ζ valence quality: 6-31G(*d*), 6-31+G(*d*), 6-31+G(2*d,p*), 6-311+G(*d*), and aug-cc-pVTZ. The double- ζ sets consists of the Pople basis for main group atoms and first-row transition metals.³⁹ The first two selected sets include one set of *d*-type polarization functions on the main group atoms and one set of *f*-type polarization functions on Zn. The 6-31+G(2*d,p*) basis include two sets of *d*-type and *f*-type functions along with one set of *p*-type

functions on the hydrogen atoms. All the basis, except the smallest 6-31G(*d*), additionally include one set of *s*- and *p*-type diffuse functions on the main group atoms and one set of *s*- and *d*-type and two sets of *p*-type functions on Zn. Cartesian functions were used for the 6-31G Pople basis set. On the other hand, the 6-311+G(*d*) basis is constructed by employing the triple- ζ valence 6-311G⁴⁰ basis set for the main group atoms and the Wachters⁴¹ and Hay⁴² basis set for Zn with the scaling factors of Raghavachari and Trucks.⁴³ This basis includes 5 *d*-type and 7 *f*-type pure functions. For the sake of completeness, geometrical and energetic parameters were also obtained by means of the MP2 method combined with the 6-31G(*d*), 6-31+G(*d*), 6-31+G(2*d,p*), and 6-311+G(*d*) basis sets. Besides, the aug-cc-pVQZ basis set was used to check the basis set truncation error in the DFT calculations. This has been done on the whole set of complexes using the B3LYP and the TPSS functionals. Finally, we would like to remind the reader that the applicability of DFT to the study of molecular anions has been debated in the literature specially in the past decade. For a recent review we refer to the work of Rienstra-Kiracofe et al.⁴⁴ It is shown in this review that DFT, in the form of inexact functionals, in conjunction with basis sets of at least double- ζ quality including diffuse functions is applicable to anionic species. We therefore believe that the functionals and basis sets tested in this work are adequate for the study of Zn²⁺ complexes with anionic ligands.

All of the calculations in this paper were performed with the Gaussian03 program package.⁴⁵ Finally, we would like to point out that we did not include solvent effects in our calculations since we are not aiming at reproducing the Zn(II) environment in biomolecular systems but rather to compare the performance of our tested functionals and basis sets.

SAPT Analyses. In order to analyze the nature of the bonding interactions in the Zn(II) complexes we used the Symmetry Adapted Perturbation Theory (SAPT) approach.^{46,47} SAPT computes the interaction energy as a sum of physically meaningful contributions, namely, electrostatic, induction, dispersion, and exchange. If we group these contributions in terms arising at the noncorrelated and correlated levels we can write

$$E_{\text{int}}^{\text{HF}} = E_{\text{elst}}^{(10)} + E_{\text{exch}}^{(10)} + E_{\text{ind,r}}^{(20)} + E_{\text{exch-ind,r}}^{(20)} + \delta E_{\text{int}}^{\text{HF}} \quad (4)$$

$$E_{\text{int}}^{\text{corr}} = E_{\text{elst,r}}^{(12)} + E_{\text{exch}}^{(11)} + E_{\text{exch}}^{(12)} + {}^t E_{\text{ind}}^{(22)} + {}^t E_{\text{exch-ind}}^{(22)} + E_{\text{disp}}^{(20)} + E_{\text{exch-disp}}^{(20)} \quad (5)$$

where $E_{\text{int}}^{\text{HF}}$ represents the supermolecular (SP) HF interaction energy, and $E_{\text{int}}^{\text{corr}}$ contains all the correlated contributions (up to second order, i.e., the so-called SAPT2 approach). The term $\delta E_{\text{int}}^{\text{HF}}$ in eq 4 contains third and higher order (noncorrelated) induction and exchange-induction terms and is defined as the difference between the SAPT noncorrelated first- and second-order energy and the supermolecular HF interaction energy. We further point out that $E_{\text{int}}^{\text{corr}}$ as defined in eq 5 is approximately equivalent to the supermolecular MP2 correlation energy.⁴⁸ All the contributions in eqs 4 and 5 have a clear physical interpretation: $E_{\text{elst}}^{(10)} +$

$E_{\text{elst},r}^{(12)} = E_{\text{elst}}^{(1)}$ represents the electrostatic interaction of the charge densities of the unperturbed monomers, $E_{\text{exch}}^{(10)} + E_{\text{exch}}^{(11)} + E_{\text{exch}}^{(12)} = E_{\text{exch}}^{(1)}$ takes into account the repulsion of the (unperturbed) charge densities of the monomers due to the Pauli exclusion principle, $E_{\text{ind},r}^{(20)} + {}^tE_{\text{ind}}^{(22)} = E_{\text{ind}}^{(2)}$ collects the interactions of the permanent multipole moments of one monomer with the induced moments of the other, $E_{\text{disp}}^{(20)} = E_{\text{disp}}^{(2)}$ represents the interaction of the instantaneous multipole moments of the monomers, and, finally, $E_{\text{exch-ind},r}^{(20)} + {}^tE_{\text{exch-ind}}^{(22)} = E_{\text{exch-ind}}^{(2)}$ and $E_{\text{exch-disp}}^{(20)} = E_{\text{exch-disp}}^{(2)}$ take into account the exchange effects associated with the induction and dispersion interactions, respectively. In this work we will group the SAPT components in two terms as follows:

$$E^{(1)} = E_{\text{elst}}^{(10)} + E_{\text{exch}}^{(10)} + E_{\text{elst},r}^{(12)} + E_{\text{exch}}^{(11)} + E_{\text{exch}}^{(12)} \quad (6)$$

$$E^{(2)} = E_{\text{ind},r}^{(20)} + E_{\text{exch-ind},r}^{(20)} + {}^tE_{\text{ind}}^{(22)} + {}^tE_{\text{exch-ind}}^{(22)} + E_{\text{disp}}^{(20)} + E_{\text{exch-disp}}^{(20)} \quad (7)$$

The first term, $E^{(1)}$, collects all contributions at first order with respect to the intermolecular interaction operator, whereas the second term collects all contributions at second order. We are interested in this partitioning because in this way we can separate those components arising from the interaction of the unperturbed fragments from those associated with the relaxation of the charge densities of the monomers (caused by the interaction with the partner). Thus, $E^{(1)}$ represents the classical electrostatic interaction energy, whereas $E^{(2)}$ collects all polarization and charge-transfer effects.

Finally, the SAPT interaction energy can be represented as

$$E_{\text{int}}(\text{SAPT}) = E^{(1)} + E^{(2)} + \delta E_{\text{int}}^{\text{HF}} \quad (8)$$

which should be roughly equivalent to the supermolecular MP2 (SP-MP2) interaction energy as commented before. For more details about this methodology see ref 49 and references therein. All SAPT calculations were performed with the SAPT2002 program.⁴⁶ We would finally like to remind the reader that the interaction energies are related to the bond dissociation energies (D_e) by means of the deformation energies of the fragments, that is, the energy required to bring the fragments from their isolated geometry to the geometry they have in the complex, namely

$$-D_e = E_{\text{int}} + E_{\text{def}} \quad (9)$$

Results and Discussion

Ab Initio Calculations. Figures 1 and 2 show the optimized structures for the monoligand complexes formed between Zn(II) and the neutral ligands ($L =$ water, ammonia, hydrogen sulfide, formaldehyde, methylimine, methanol, methylamine, methanethiol, acetic acid, formamide, imidazole, and benzene) and anionic ligands ($L =$ hydroxide, hydrosulfide, methanolate, methanethiolate, acetate, and imidazolate), respectively. All the structures were characterized as energy minima on the MP2/aug-cc-pVTZ potential energy surface, excepting the $[\text{Zn}(\text{imidazolate})]^+$ complex with C_s

symmetry that corresponded to a transition structure. For each complex shown in Figures 1 and 2, the equilibrium Zn- L distance involving the Zn atom and the donor atom(s) of the ligand, the Natural Population Analysis (NPA) charge⁵⁰ of the Zn atom, and the harmonic frequency of the stretching normal mode associated with the Zn- L bond are also reported. As mentioned in the Methods section, the consistency of the computational scheme employed for computing the binding energies was tested in the case of the complexes of Zn(II) with water, hydrosulfide, hydroxide, and sulfide by using more elaborated computational schemes as well (see Table 1). We will analyze first these validation calculations, and then we will present the benchmark data for all the Zn(II) complexes.

Validation Calculations. To ensure that the benchmark calculations performed for the 18 Zn(II)-complexes are accurate and could replace missing experimental data, we report in Table 1 some test calculations that assess the adequacy of the various choices made in the computational scheme defined in eqs 1–3 (i.e., “composite” approximation, MP2 geometries, valence correlation, CBS extrapolation, ...). For example, by carrying out single-point CCSD(T)/aug-cc-pVnZ ($n=4, 5$) calculations on the four test complexes, we found that the D_e values computed with the “composite” method are nearly identical ($\sim \pm 0.10$ kcal/mol) to those obtained with the CCSD(T)/CBS method. We also found that the binding energies are rather insensitive to small changes on the equilibrium geometries: although the structures optimized at the CCSD/aug-cc-pVTZ level have slightly larger Zn-ligand distances by 0.01–0.03 Å than the MP2 structures, practically the same D_e values were obtained using the MP2/aug-cc-pVTZ and the CCSD/aug-cc-pVTZ optimized geometries (see Table 1). In addition, we see in Figure 1 that the NPA charges of the Zn atom computed from the MP2 and CCSD electronic densities match closely to each other ($\pm 0.01 e^-$) and that the MP2 and CCSD harmonic stretching frequencies for the Zn-ligand bond are very similar.

Of particular interest can be to determine the relevance of core-valence correlation effects. The small Zn(II)- L complexes and their ligands were reoptimized by carrying out full electron MP2 calculations with enlarged basis sets for explicitly including core-valence correlation effects. The resulting molecular geometries and the NPA charge of the Zn atom hardly differ from the frozen-core MP2 results. On the other hand, the changes in the “composite” binding energies, D_e , computed correlating all the electrons, with respect to the frozen core values are -1.11 , -0.96 , -1.25 , and -1.81 kcal/mol for $L = \text{H}_2\text{O}$, H_2S , OH^- , and HS^- , respectively. Thus, we estimate that core-valence correlation effects should range between 1 and 2 kcal/mol for the monoligand Zn^{2+} complexes. This relatively small influence of core-valence correlation could be related to the fact that binding between the Zn(II) cation and a ligand donor atom results in a small accumulation of charge in the interatomic region, that is, zinc-ligand bonds are essentially closed-shell interactions with only a partial covalent character.¹⁷

In order to assess now the reliability of the CBS extrapolation, we computed the change in the binding energies when going from MP2/aug-cc-pVQZ to MP2/aug-cc-pV5Z and

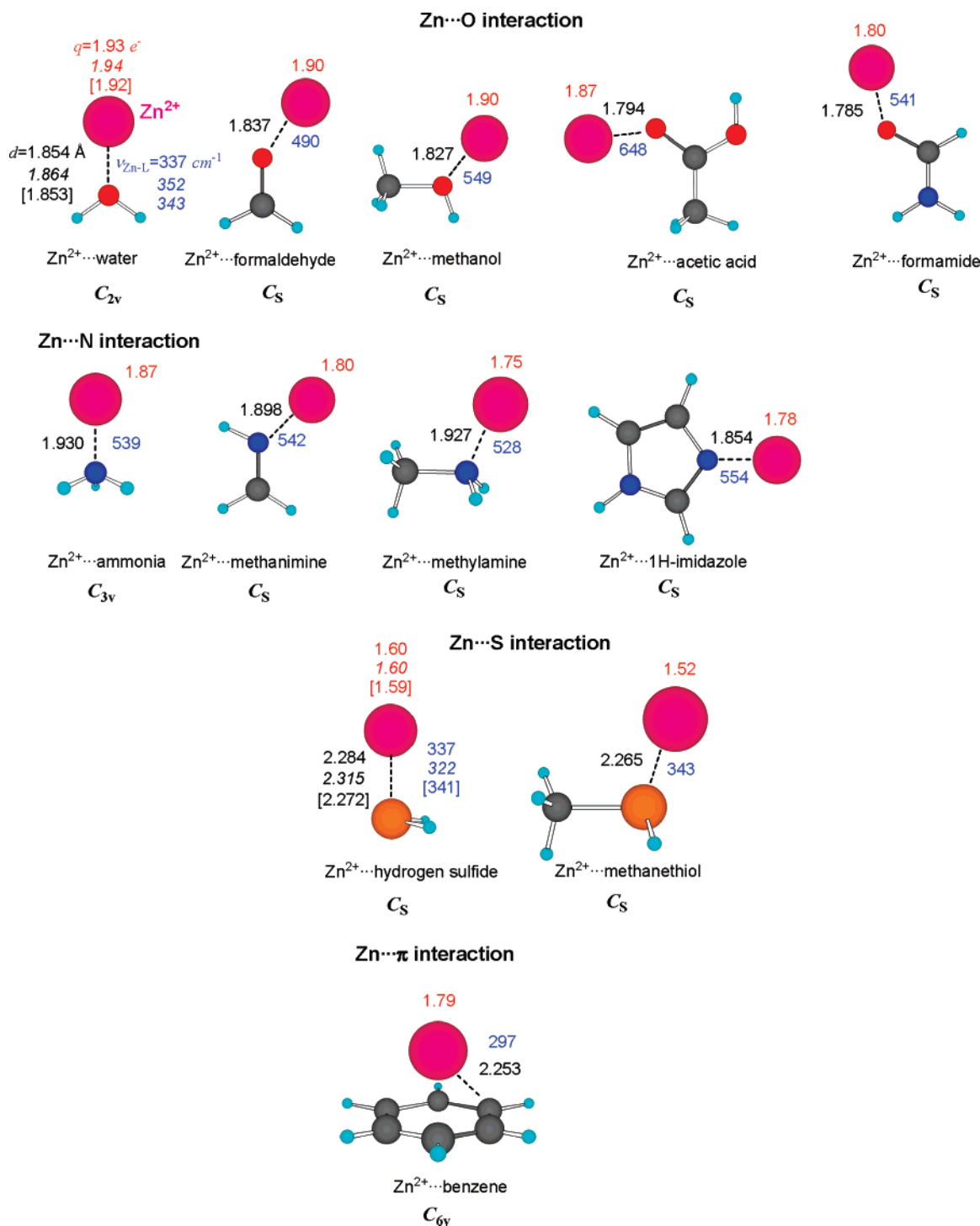


Figure 1. Geometrical arrangement of the studied Zn(II) complexes with neutral ligands along with the most important geometrical parameters as computed at the MP2/aug-cc-pVTZ level of theory. For water and hydrogen sulfide, CCSD/aug-cc-pVTZ and full electron MP2 data are given in italics and in squared brackets, respectively. All distances are given in angstroms.

from MP2/aug-cc-pV5Z to MP2/CBS for the set of four selected complexes. The differences are smaller than 0.50 kcal/mol (the average is 0.27 kcal/mol for the set of both neutral and anionic ligands) and 0.21 kcal/mol (average: 0.16 kcal/mol), respectively. When the core-valence correlation is taken into account, these differences are smaller than 0.73 kcal/mol and 0.13 kcal/mol, respectively. We also estimated for these four systems the CBS limit extrapolating the CP-corrected binding energies. The final “composite” D_e values are within 0.17 kcal/mol of the uncorrected ones.

Overall, we conclude that the larger factor that could affect the benchmark “composite” energies are the core-valence correlation effects which, as commented before, should be within 1–2 kcal/mol for these systems. Therefore, we believe that limiting to valence correlation effects in the benchmark calculations represents a reasonable compromise between cost and accuracy, which should be close to chemical accuracy (~ 1 kcal/mol).

Ab Initio Benchmark Data. Table 2 contains the ab initio binding energies for the full set of Zn(II) complexes that

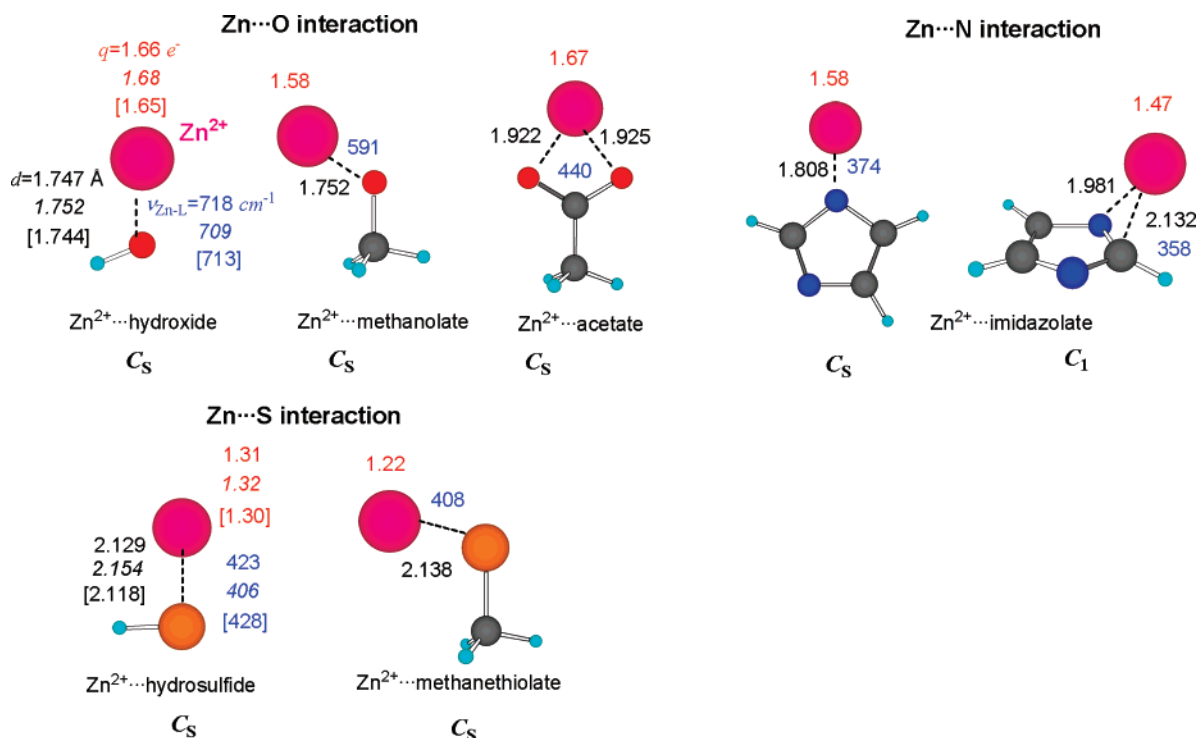


Figure 2. Geometrical arrangement of the studied Zn(II) complexes with anionic ligands along with the most important geometrical parameters as computed at the MP2/aug-cc-pVTZ level of theory. For hydroxide and sulfide, CCSD/aug-cc-pVTZ and full electron MP2 data are given in italics and in squared brackets, respectively. All distances are given in angstroms.

Table 1. Binding Energies (in kcal/mol) for the Small Zn(II) Complexes Obtained with Different Ab Initio Computational Protocols

ligand	MP2/aug-cc-pVTZ	CCSD(T)/aug-cc-pVTZ	MP2/CBS ^a	composite method ^b	CCSD(T)/CBS ^a
Frozen Core, MP2/aug-cc-pVTZ Geometries					
water	-98.02	-97.43	-98.78	-98.19	-98.27
hydrogen sulfide	-113.05	-112.36	-114.29	-113.59	-113.55
hydroxide	-424.21	-425.16	-425.37	-426.32	-426.36
hydrosulfide	-408.48	-407.92	-410.44	-409.87	-409.68
Frozen Core, MP2/aug-cc-pVTZ Geometries, CP-Corrected Energies					
water	-97.41	-96.84	-98.67	-98.10	
hydrogen sulfide	-112.41	-111.78	-114.15	-113.52	
hydroxide	-423.08	-424.05	-425.19	-426.15	
hydrosulfide	-407.37	-406.89	-410.20	-409.73	
Frozen Core, CCSD/aug-cc-pVTZ Geometries					
water	-98.00	-97.45	-98.73	-98.18	-98.26
hydrogen sulfide	-112.95	-112.44	-114.11	-113.60	-113.55
hydroxide	-424.15	-425.19	-425.30	-426.34	-426.38
hydrosulfide	-408.37	-408.03	-410.23	-409.89	-409.69
Full Electron, MP2 Geometries, aug-cc-pwVnZ for Zn, aug-cc-pV(n+d)Z for S					
water	-98.98	-98.08	-100.21	-99.30	-
hydrogen sulfide	-115.26	-113.79	-116.01	-114.55	-
hydroxide	-426.32	-426.46	-427.43	-427.57	-
hydrosulfide	-412.16	-410.27	-413.57	-411.68	-

^a Obtained from CBS extrapolation of the correlation energy based on eqs 1 and 2 and using the HF/aug-cc-pV5Z energies. ^b Using an additive combination of electronic energies.

are examined in this work. The “composite” D_e values in Table 2 provide the benchmark data. Nevertheless, the MP2/aug-cc-pVTZ level shows a good performance as compared with the “composite” energy calculations. In fact the computed binding energies using the MP2/aug-cc-pVTZ geometries are quite similar regardless of the correlated method (CCSD(T) vs MP2) or the basis set (see Table 2)

employed to perform the corresponding single-point calculations. With respect to the MP2/aug-cc-pVTZ energy values, inclusion of energy corrections due to higher correlated methods and larger basis sets cancel each other partially, so that the average difference between the MP2/aug-cc-pVTZ calculations and the more accurate “composite” energy values is only 0.7 kcal/mol for neutral ligands or 2.1 kcal/mol for

Table 2. Binding Energies (in kcal/mol) for the Zn(II) Complexes Optimized at the MP2/aug-cc-pVTZ Level Obtained with the MP2 and CCSD(T) Methods

ligand	MP2/ aug-cc- pVTZ D_e	CCSD(T)/ aug-cc- pVTZ D_e	MP2/ CBS ^a D_e	composite method ^b D_e	composite method ^c D_0
water	-98.02	-97.43	-98.78	-98.19	-96.56
ammonia	-129.08	-128.08	-129.81	-128.82	-126.11
hydrogen sulfide	-113.05	-112.36	-114.29	-113.59	-111.72
formaldehyde	-108.32	-108.62	-108.98	-109.28	-107.49
methanimine	-139.63	-138.56	-140.48	-139.42	-137.32
methanol	-116.35	-115.55	-116.83	-116.03	-115.26
methylamine	-143.50	-142.54	-144.01	-143.05	-141.10
methanethiol	-134.45	-133.95	-135.73	-135.22	-134.15
acetic acid	-132.94	-133.43	-133.61	-134.09	-133.28
formamide	-148.30	-148.76	-149.01	-149.48	-147.29
1H-imidazole	-172.87	-172.04	-173.55	-172.72	-171.34
benzene	-160.20	-157.20	-161.19	-158.19	-156.64
hydroxide	-424.21	-425.16	-425.37	-426.32	-424.14
hydrosulfide	-408.48	-407.92	-410.44	-409.87	-408.28
methanolate	-423.07	-423.46	-424.12	-424.52	-421.10
methanethiolate	-420.22	-419.73	-422.14	-421.66	-419.92
acetate	-413.31	-414.45	-414.81	-415.95	-413.97
imidazolate (C_5)	-379.09	-381.80	-380.19	-382.89	-381.93
imidazolate (C_1)	-386.96	-387.19	-384.82	-385.05	-383.98

^a Obtained from CBS extrapolation of the MP2 correlation energy based on eqs 1 and 2 and using the HF/aug-cc-pV5Z energies.

^b Using an additive combination of electronic energies (CCSD(T)/aug-cc-pVTZ+ MP2/CBS - MP2/aug-cc-pVTZ). ^c Using an additive combination of electronic energies and including MP2/aug-cc-pVTZ ZPVE energies

anionic ligands whose complexes have much larger binding energies. The largest differences arise in benzene and imidazolate (C_5) that are within 3 kcal/mol, still in very good agreement. All these results suggest that predictions obtained at the MP2/aug-cc-pVTZ level for Zn(II) complexes should already be quite reliable. This is gratifying because both CCSD(T)/aug-cc-pVTZ and MP2/aug-cc-pVnZ ($n=4, 5$) calculations are much more computationally demanding. We also note in passing that the MP2/aug-cc-pVTZ level has also been found to produce an accurate and balanced description of hydrogen-bonded and dispersion-bound complexes.⁵¹

For the neutral ligands, the optimized structures correspond to monodentate Zn(II) complexes that can be characterized by a single interatomic Zn-X distance of $\sim 1.82, 1.90,$ and 2.27 \AA for $X = O, N,$ and $S,$ respectively. For a given type of donor atom, it turns out that the binding energy (D_e) correlates well with the Zn-X distance (e.g., the linear correlation coefficient, r , between the Zn-X distances and the composite D_e values amounts to 0.987 and 0.909 for $X = O$ and $N,$ respectively). In the case of benzene, a typical cation- π complex is formed in which the Zn(II) ion is equidistant with respect to the six C atoms. The metal-ligand bond in the complexes with neutral ligands implies a significant charge transfer within the $0.07\text{--}0.48 e^-$ range according to the NPA charges. The amount of charge transfer, which depends on the electronegativity and hybridization of the donor X atom, is quite well correlated with the D_e energies ($r \sim 0.90\text{--}0.94$), suggesting thus that the charge-transfer interaction plays an important role in the total

Table 3. Protonation Energies (PEs in kcal/mol) for Various Acid-Base Pairs Both in Their Isolated Form and in the Corresponding Zn(II) Complexes^c

acid-base pair	MP2/ aug-cc- pVTZ	CCSD(T)/ aug-cc- pVTZ	MP2/ CBS ^a	composite method ^b	
A/B					
H ₂ O/OH ⁻	-393.26	-397.15	-393.13	-397.02	(-389.01)
H ₂ S/HS ⁻	-353.60	-355.99	-353.38	-355.77	(-349.97)
CH ₃ OH/CH ₃ O ⁻	-388.27	-391.13	-388.11	-390.98	(-381.09)
CH ₃ SH/CH ₃ S ⁻	-360.25	-362.65	-360.18	-362.58	(-356.17)
CH ₃ COOH/ CH ₃ COO ⁻	-352.13	-354.85	-351.90	-354.63	(-346.06)
1H-imidazol/ 1H-imida zolate	-352.91	-356.78	-352.89	-356.76	(-348.01)
Zn-A/Zn-B					
H ₂ O/OH ⁻	-67.08	-69.42	-66.55	-68.89	(-61.43)
H ₂ S/HS ⁻	-58.17	-60.43	-57.23	-59.49	(-53.41)
CH ₃ OH/CH ₃ O ⁻	-81.55	-83.23	-80.81	-82.49	(-75.25)
CH ₃ SH/CH ₃ S ⁻	-74.48	-76.86	-73.76	-76.15	(-70.40)
CH ₃ COOH/ CH ₃ COO ⁻	-71.76	-73.83	-70.70	-72.77	(-65.36)
1H-imidazol/ 1H-imida zolate	-146.69	-147.03	-146.25	-146.59	(-137.42)

^a Obtained from CBS extrapolation of the MP2 correlation energy based on eqs 1 and 2 and using the HF/aug-cc-pV5Z energies.

^b Using an additive combination of electronic energies (CCSD(T)/aug-cc-pVTZ+ MP2/CBS - MP2/aug-cc-pVTZ). Values in parentheses include the MP2/aug-cc-pVTZ ZPVE energies. ^c Molecular geometries were obtained at the MP2/aug-cc-pVTZ level.

binding. It may be interesting to note that the frequency of the stretching motion of the Zn-X bond is uncorrelated with the strength of the metal-ligand bond expressed in terms of binding energies.

The strong interaction between the Zn(II) cation and the anionic ligands is reflected in the magnitude of the computed binding energies (from -420 to -380 kcal/mol), which is accompanied by a typical shortening of the Zn-X distances of $\sim 0.10 \text{ \AA}$ with respect to the neutral ligands and an important charge transfer from ligand to Zn(II) ($0.36\text{--}0.68 e^-$). The two complexes formed between Zn(II) and imidazolate deserve some specific comments. One of these complexes corresponds to a planar monodentate structure (C_5 complex), which is characterized as a transition structure with an imaginary frequency of 120 cm^{-1} for an out-of-plane movement of the Zn-N bond. This transition structure leads to a true energy minimum (C_1 symmetry), which corresponds to a bidentate Zn(II) complex that can be better described as an asymmetric π -complex between Zn(II) and one of the C=N double bonds. In spite of their quite dissimilar coordination geometry and electronic features, the C_5 complex is only 2.05 kcal/mol above the C_1 one.

Since the catalytic mode of action of many zinc-enzymes involves proton-transfer events to and from zinc-ligands (water molecules and amino acid side chains), we also derived the protonation energies (PE) of some of the ligands studied in this work at the different correlated levels of theory. According to the PE values reported in Table 3, the nature of the correlated method (CCSD(T) vs MP2) has a more pronounced effect (~ 2 kcal/mol) on the computed PEs than in the case of the Zn-L binding energies, whereas the

Table 4. Mean Signed Errors (MSE) and Standard Deviations (Å) in the Metal–Ligand Bond Distances of the Monoligand Zn(II) Complexes Studied in This Work with Respect to the MP2/aug-cc-pVTZ Reference Values

basis set		PW91	PBE	B3LYP	MPWLYP1M	TPSS	MP2
6-31G(<i>d</i>)	MSE	−0.017	−0.016	−0.010	−0.013	−0.018	−0.024
	SD	0.016	0.017	0.012	0.014	0.015	0.009
6-31+G(<i>d</i>)	MSE	0.032	0.034	0.029	0.032	0.027	−0.004
	SD	0.019	0.020	0.015	0.018	0.016	0.005
6-31+G(2 <i>d</i> , <i>p</i>)	MSE	0.036	0.038	0.034	0.037	0.030	0.005
	SD	0.020	0.020	0.015	0.019	0.016	0.004
6-311+G(<i>d</i>)	MSE	0.052	0.055	0.046	0.050	0.047	0.010
	SD	0.023	0.023	0.016	0.021	0.018	0.003
aug-cc-pVTZ	MSE	0.041	0.044	0.035	0.041	0.036	
	SD	0.018	0.019	0.017	0.018	0.015	

CBS limit of the MP2 PEs is very similar to the MP2/aug-cc-pVTZ values. When comparing the PEs of the isolated A/B pairs with those of their Zn-bound counterparts, we see that the Zn(II) cation decreases the PEs by 327.58, 296.56, 305.84, 285.77, 280.69, and 210.59 kcal/mol for the H₂O/OH[−], H₂S/HS[−], CH₃OH/CH₃O[−], CH₃SH/CH₃S[−], CH₃COOH/CH₃COO[−], and imidazole/imidazolate acid–base pairs, respectively (composite energy values including ZPVE). Thus, the actual impact on the acid–base strength of the Zn-ligands is quite variable, the water/hydroxide pair being the most affected one, which is in consonance with the important role that zinc-bound water molecules usually have in zinc-enzymes.

DFT Calculations. In principle, the performance of the tested DFT functionals will be assessed by mean signed errors (MSE), i.e., the averages of the deviations with respect to the reference results including the sign of the error. We will not discuss in general mean unsigned errors (MUE) because all the functionals have shown systematic deviations either overestimating or underestimating the reference values for a given basis set. Thus, MUE do not provide any additional information. We also report standard deviations in order to describe the spread of the error distribution with respect to the mean value. Notice that for the sake of simplicity, part of the results obtained in this study are included in tables presented in the Supporting Information. These tables will be labeled with “S” when referred throughout the text.

DFT Molecular Geometries of the Zn-L Complexes. Table 4 collects the mean signed standard errors (MSE) and standard deviations in the Zn-ligand bond distance for the different complexes. As commented above, we will take the MP2/aug-cc-pVTZ values as the reference. The mean values were computed for the whole set of complexes since similar errors were obtained for both neutral and anionic ligands. Before discussing the data collected in Table 4, we would like to point out that, in general, we found that MP2 and DFT agree in fact in the geometry of the lowest energy structure for most of the analyzed complexes. However, in few cases, we found qualitative differences which deserve to be commented. For example, the Zn(II)-H₂O complex has *C*_{2v} symmetry at the MP2 level of theory. At the DFT level, the nature of the *C*_{2v} stationary point depends on both the functional and the basis set. With the PBE functional and

the 6-31+G(*d*), 6-31+G(2*d*,*p*), and aug-cc-pVTZ basis sets it is a transition structure (the imaginary frequencies are 66i cm^{−1}, 227i cm^{−1}, and 159i cm^{−1}, respectively). The same happens at the PW91/6-31+G(2*d*,*p*), PW91/aug-cc-pVTZ, TPSS/6-31+G(2*d*,*p*), and TPSS/aug-cc-pVTZ levels (195i cm^{−1}, 133i cm^{−1}, 180i cm^{−1}, and 76i cm^{−1} respectively). A similar situation occurs in [Zn(CH₃OH)]²⁺. At the MP2 level with all basis sets this complex has *C*_s symmetry with the zinc cation lying in the methanol symmetry plane (see Figure 1). However, at the DFT level and with all basis sets, this structure has one imaginary frequency indicating that the symmetry of the lowest energy conformation is *C*₁. The imaginary frequency lies between 90 and 270 cm^{−1} depending on the functional and the basis set, except for B3LYP that predicts values between 66 and 99 cm^{−1}. We have nevertheless assumed a *C*_s symmetry for this complex as suggested by the MP2/aug-cc-pVTZ calculation. Different MP2/aug-cc-pVTZ and DFT minimum energy structures are also predicted for [Zn(CH₃COOH)]²⁺ and [Zn(CH₃COO)]⁺. In these two cases, however, the differences are related to the rotation of the methyl group. We considered a OCCH dihedral angle of 180 for the former and 0 for the later (see Figures 1 and 2). These are the values of the dihedral angles in the MP2/aug-cc-pVTZ equilibrium geometries. Finally, the [Zn(imidazolate)]⁺ complex has *C*₁ symmetry and a Zn²⁺··π(C=N) interaction at all levels except MPWLYP1M and TPSS, which predict a more favorable interaction between the Zn(II) ion and the nitrogen lone pair in the *C*_s complex. For comparative purposes, we considered a *C*_s symmetry for this complex. We would like to point out that these imaginary frequencies are associated with a particular functional and basis set and do not depend on the integration grid. We checked this point in the water complex with the 6-31+G(2*d*,*p*) basis set. The lowest frequency is reproduced within 6 cm^{−1} for the five functionals. As commented above in the Methods section, we also carried out optimizations and frequency calculations at the PBE/aug-cc-pVTZ level of theory using a larger integration grid. We obtained frequencies which were similar to those calculated with the default “medium” grid. Our conclusion is therefore that the Zn²⁺-L interaction can be in general accurately described by a ‘medium’ integration grid.

Table 4 shows that all the tested functionals give, for a given basis set, metal–ligand distances that are larger than the MP2 ones by about 0.03–0.04 Å. The five functionals behave similarly, being B3LYP and TPSS the ones that predict shorter bond lengths. The data collected in Table 4 also reveal that the smallest 6-31G(*d*) basis set gives the lowest MSEs due to an error cancellation between the overestimation of the metal–ligand bond distances by the tested functionals and the underestimation associated with the size of the basis set. At the MP2 level with the 6-31+G(*d*) basis, the MSE is already as small as 0.004 Å. With the tested functionals, this basis set performs also quite well predicting distances within 0.006–0.010 Å from the aug-cc-pVTZ ones. Let us also point out that metal–ligand bond distances obtained with a larger integration grid at the PBE/aug-cc-pVTZ level differ by less than 0.003 Å of the “medium” grid results (see Table S4). Finally, in order to

Table 5. Mean Signed Errors (MSE) and Standard Deviations (kcal/mol) in the Binding Energies of the $[\text{Zn-L}]^{2+}$ Complexes (Neutral Ligands $L = \text{H}_2\text{O}, \text{NH}_3, \text{H}_2\text{S}, \text{H}_2\text{CO}, \text{H}_2\text{CNH}, \text{CH}_3\text{OH}, \text{CH}_3\text{NH}_2, \text{CH}_3\text{SH}, \text{CH}_3\text{COOH}, \text{HCONH}_2, 1\text{H-Imidazole},$ and Benzene) with Respect to the Reference “Composite” Values

basis set		PW91	PBE	B3LYP	MPWLYP1M	TPSS	MP2
6-31G(d)	MSE	-24.20	-21.84	-16.79	-25.00	-17.11	-3.69
	SD	4.36	4.38	3.66	3.27	4.82	5.65
6-31+G(d)	MSE	-19.38	-18.07	-12.06	-18.08	-14.11	-3.32
	SD	3.14	3.15	2.37	3.37	1.80	2.17
6-31+G(2d,p)	MSE	-19.72	-18.41	-12.20	-18.39	-14.47	-1.58
	SD	3.99	4.00	2.82	3.99	2.65	1.89
6-311+G(d)	MSE	-16.03	-14.87	-8.94	-14.64	-10.02	0.73
	SD	3.45	3.51	3.02	3.81	2.06	3.17
aug-cc-pVTZ	MSE	-16.16	-15.56	-9.57	-15.14	-10.60	0.11
	SD	3.60	3.64	2.79	4.00	2.20	0.86

Table 6. Mean Signed Errors (MSE) and Standard Deviations (kcal/mol) in the Binding Energies of the $[\text{Zn-L}]^+$ Complexes (Anionic Ligands, $L = \text{OH}^-, \text{HS}^-, \text{CH}_3\text{O}^-, \text{CH}_3\text{S}^-, \text{CH}_3\text{COO}^-$, and Imidazolate) with Respect to the Reference “Composite” Values

basis set		PW91	PBE	B3LYP	MPWLYP1M	TPSS	MP2
6-31G(d)	MSE	-45.83	-42.91	-34.24	-48.69	-34.76	-14.16
	SD	14.08	14.20	12.86	12.55	14.75	13.07
6-31+G(d)	MSE	-27.62	-26.17	-16.69	-27.77	-20.56	-3.05
	SD	4.49	4.49	3.06	4.69	3.81	3.58
6-31+G(2d,p)	MSE	-28.72	-27.23	-17.56	-28.74	-21.80	-1.29
	SD	4.63	4.61	3.16	4.97	3.70	2.11
6-311+G(d)	MSE	-23.06	-21.58	-12.24	-23.17	-15.02	2.70
	SD	5.27	5.19	4.00	5.59	4.07	4.32
aug-cc-pVTZ	MSE	-23.68	-22.79	-13.77	-24.33	-16.13	2.14
	SD	5.08	5.04	3.27	5.18	3.91	0.87

check the basis set truncation error we have also carried out optimizations using the B3LYP and TPSS functionals with the aug-cc-pVQZ basis set on the whole set of complexes (see Table S5). For the TPSS functional the maximum deviation from the aug-cc-pVTZ values is 0.003 Å. For B3LYP the maximum deviation is 0.002 Å except for two complexes, namely, $\text{Zn}^{2+}\cdots\text{NH}_3$ and $\text{Zn}^{2+}\cdots\text{ImH}$, for which the difference between the TZ and QZ values is 0.03 and 0.02 Å, respectively. These results show that the geometries of the Zn(II) complexes are already well converged with the aug-cc-pVTZ basis set.

Regarding the rest of the geometrical parameters let us just point out that, with the exceptions already commented above, they are in general very similar with both MP2 and DFT methodologies. Furthermore, these values do not change much with the size of the basis set (except for the smallest one) and are very close to the reference aug-cc-pVTZ results.

DFT Binding Energies of Zn-L Complexes. Tables 5 and 6 show the mean signed errors (MSE) and standard deviations for the tested functionals and the MP2 method with the selected basis sets. Table 5 collects the results obtained for the neutral ligands, whereas Table 6 lists the results obtained for the anionic ones. We split this data because the magnitude of the binding energies for both type of ligands is quite different (see Table 3). Nevertheless, we

also list in Table S1 the mean errors calculated for the whole set of complexes.

From the data collected in Table 5, we see that all the tested functionals overestimate the binding energies. Notice that the MSEs diminish when increasing the basis set. Interestingly, we do not observe a quantitative improvement when going from 6-31+G(d) to 6-31+G(2d,p), but a clear reduction of the error is achieved with the 6-311+G(d) basis, which give results close to the aug-cc-pVTZ ones. With the aug-cc-pVTZ basis set, the deviation of the DFT values is still 10–16 kcal/mol, about 5–10% of the reference data, which correspond to the high level “composite” binding energies (D_e values in Table 2). The second conclusion that can be drawn from the data listed in Table 5 is that B3LYP and TPSS functionals perform the best, yielding MSEs that are about 33% smaller than those obtained with the other functionals.

Table 6 shows the MSEs obtained for the complexes with anionic ligands. Now, the magnitude of the deviations is larger, in agreement with the larger magnitude of the binding energies, but the conclusions are the same: all the functionals show a very similar systematic behavior, and the functionals B3LYP and TPSS perform the best. With the aug-cc-pVTZ basis, the tested functionals overestimate the binding energies by about 23 kcal/mol (14 kcal/mol and 16 kcal/mol at the B3LYP and TPSS levels, respectively) which represents about 5% of the reference “composite” value. We would like to add here that the binding energies of both neutral and anionic ligands obtained with a larger integration grid are within 0.1 kcal/mol from the ‘medium’ grid values. This shows that larger grids are in principle not required for the computation of binding energies. Besides, TPSS/aug-cc-pVQZ calculations (see Table S6) show that the TPSS/aug-cc-pVTZ binding energies are already converged within 0.4 kcal/mol. Interestingly, B3LYP/aug-cc-pVTZ energies appear to be underestimated still by 1.5–2.5 kcal/mol (see also Table S6). Notice then, that, with respect to the reference ab initio values, B3LYP/aug-cc-pVQZ binding energies are slightly more overestimated than B3LYP/aug-cc-pVTZ ones.

The MSE in the binding energies corrected for BSSE by means of the counterpoise (CP) method²⁹ are listed in Tables 7 and 8. Comparing the MSE collected in Tables 5 and 7, it is clear that all the functionals give very similar BSSE. With the smallest basis set, namely 6-31G(d), it is about 12 kcal/mol, 50% of the ‘uncorrected’ MSE. With the 6-31+G(d), 6-31+G(2d,p), and 6-311+G(d) basis sets, the BSSE is reduced to 1–2 kcal/mol, while with the aug-cc-pVTZ basis it is negligible. Since all the functionals overestimate the binding energies with MSE values larger than the BSSE, the CP-corrected energies are necessary closer to the composite results. At the MP2 level (last column in Table 7), the CP-corrected energies do not necessary get closer to the “composite” values. This is not an unexpected result because the MP2 energies are not far from the reference data. We remind the reader that the CP method does not correct for basis set incompleteness errors apart from the BSSE. Thus, it is possible that it yields too small binding energies compared to the CBS values, which do not suffer from any kind of basis set incompleteness. Table 8 shows the corre-

Table 7. Mean Signed Errors (MSE) and Standard Deviations (kcal/mol) in the Counterpoise (CP) Corrected Binding Energies of the [Zn-L]²⁺ Complexes (Neutral Ligands, L = H₂O, NH₃, H₂S, H₂CO, H₂CNH, CH₃OH, CH₃NH₂, CH₃SH, CH₃COOH, HCONH₂, Imidazole, and Benzene) with Respect to the Reference “Composite” Values

basis set	PW91	PBE	B3LYP	MPWLYP1M	TPSS	MP2	
6-31G(d)	MSE	-11.32	-9.18	-4.97	-12.72	-5.06	8.58
	SD	2.16	2.15	2.51	3.63	2.37	4.55
6-31+G(d)	MSE	-17.35	-16.17	-10.27	-16.25	-12.30	1.90
	SD	3.30	3.28	2.53	3.65	1.94	1.66
6-31+G(2d,p)	MSE	-18.24	-16.97	-10.82	-16.87	-13.14	1.70
	SD	4.05	4.04	3.01	4.22	2.69	1.28
6-311+G(d)	MSE	-14.62	-13.50	-7.65	-13.37	-8.71	4.94
	SD	3.56	3.59	2.94	3.90	2.12	2.24
aug-cc-pVTZ	MSE	-15.92	-15.32	-9.36	-14.91	-10.42	
	SD	3.62	3.65	2.84	4.04	2.20	

Table 8. Mean Signed Errors (MSE) and Standard Deviations (kcal/mol) in the Counterpoise (CP) Corrected Binding Energies of the [Zn-L]⁺ Complexes (Anionic Ligands, L = OH⁻, HS⁻, CH₃O⁻, CH₃S⁻, CH₃COO⁻, and Im⁻) with Respect to the Reference “Composite” Values

basis set	PW91	PBE	B3LYP	MPWLYP1M	TPSS	MP2	
6-31G(d)	MSE	-21.16	-18.53	-11.96	-24.50	-12.00	8.77
	SD	5.71	5.82	4.61	4.97	6.32	5.67
6-31+G(d)	MSE	-25.44	-24.01	-14.87	-25.76	-18.57	4.10
	SD	4.92	4.91	3.34	5.09	3.96	2.22
6-31+G(2d,p)	MSE	-26.62	-25.18	-15.81	-26.76	-19.91	3.35
	SD	4.99	4.98	3.39	5.23	3.87	1.76
6-311+G(d)	MSE	-21.77	-20.32	-11.18	-22.03	-13.81	8.97
	SD	5.62	5.54	4.19	5.88	4.30	2.99
aug-cc-pVTZ	MSE	-23.06	-22.20	-13.42	-23.75	-15.59	
	SD	5.31	5.26	3.34	5.31	4.07	

Table 9. Mean Signed Errors (MSE) and Standard Deviations (kcal/mol) in the Protonation Energies of the Anionic Ligands (L = OH⁻, HS⁻, CH₃O⁻, CH₃S⁻, CH₃COO⁻, and Imidazolate) with Respect to the Reference “Composite” Values

basis set	PW91	PBE	B3LYP	MPWLYP1M	TPSS	MP2	
6-31G(d)	MSE	-13.27	-12.75	-14.02	-17.32	-14.21	-12.13
	SD	10.22	10.37	9.51	9.26	9.58	9.23
6-31+G(d)	MSE	6.05	6.30	4.34	2.09	3.09	6.11
	SD	1.64	1.63	1.13	1.74	1.56	1.51
6-31+G(2d,p)	MSE	2.63	2.88	0.88	-1.41	-0.21	2.01
	SD	1.21	1.22	0.76	1.21	1.06	0.93
6-311+G(d)	MSE	6.42	6.69	4.64	2.27	3.36	5.86
	SD	2.19	2.16	1.56	2.11	1.94	1.38
aug-cc-pVTZ	MSE	3.07	3.32	1.06	-1.13	0.08	2.89
	SD	2.17	2.17	1.42	2.13	1.96	0.73

sponding MSE in the CP-corrected binding energies of the complexes with an anionic ligand. The conclusions that can be drawn are the same already commented. The BSSE is about 24 kcal/mol with the smallest basis set, again approximately 50% of the ‘uncorrected’ MSE. With the larger basis, it reduces to less than 2 kcal/mol.

DFT Protonation Energies. In Table 9 we report the MSE and standard deviations for the protonation energies of the

Table 10. Mean Signed Errors (MSE) and Standard Deviations (kcal/mol) in the Protonation Energies of the [Zn-L]⁺ Complexes (Anionic Ligands, L = OH⁻, HS⁻, CH₃O⁻, CH₃S⁻, CH₃COO⁻, and Imidazolate) with Respect to the Reference “Composite” Values

basis set	PW91	PBE	B3LYP	MPWLYP1M	TPSS	MP2	
6-31G(d)	MSE	10.31	10.28	5.02	7.70	5.60	0.60
	SD	3.67	3.70	1.39	3.11	3.16	3.34
6-31+G(d)	MSE	14.27	14.41	8.73	11.24	9.84	6.37
	SD	5.17	5.28	2.66	4.55	4.24	1.89
6-31+G(2d,p)	MSE	11.36	11.48	5.73	8.16	7.17	2.52
	SD	5.82	5.91	3.26	5.11	4.93	0.40
6-311+G(d)	MSE	12.87	12.83	7.06	9.64	8.05	3.60
	SD	4.92	5.09	2.42	4.18	4.01	2.11
aug-cc-pVTZ	MSE	9.94	9.96	4.43	6.74	5.29	1.11
	SD	5.75	5.89	3.29	4.99	4.93	0.69

isolated acid–base pairs as computed with the tested functionals and the MP2 method with the selected basis sets. The results obtained for the corresponding Zn-L complexes are shown in Table 10.

In consonance with expectations, the PEs computed with the small basis set (6-31G(d)) in the absence of the Zn(II) cation contain relatively large errors (>12 kcal/mol in absolute value). These results are much improved by including diffuse and/or further polarization functions in the basis set at all the methods. Particularly, the B3LYP calculations with the 6-31+G(2d,p) and aug-cc-pVTZ basis sets give PE values that are very close to the best ab initio values, with MSEs of only 0.88 and 1.06 kcal/mol, respectively. Although the performance of the rest of DFT methods and the MP2 method in the PE calculations for the free ligands is clearly worse, the magnitude of their MSEs is still lower than those associated with the Zn-ligand binding energies in Tables 4–8.

As above-mentioned, to find out whether a ligand is protonated or deprotonated when coordinated to the Zn(II) cation is an important question. Unfortunately, the quality of the PEs predicted by the DFT methods decreases significantly for the Zn-L complexes with respect to the isolated ligands as the MSEs collected in Table 10 are 3–4-fold larger than those in Table 9 for the more complete basis sets. The opposite trend arises in the MP2 calculations, whose MSE values in Tables 9 and 10 are more comparable to each other. These observations illustrate clearly the extra difficulty associated with the theoretical description of the zinc complexes. However, it is also clear that the average error in the DFT protonation energies is lower than in the metal–ligand binding energy calculations. Again we conclude that all the functionals show basically the same trends and that B3LYP and TPSS perform the best.

Correlation between DFT and Ab Initio Data. The MSE values collected in Tables 4–10 assess the overall accuracy of selected functionals in calculating metal–ligand distances, binding energies, and protonation energies of monoligand Zn(II) complexes with reference to the benchmark ab initio results. However, many applications of theoretical methods that are relevant to zinc enzymology involve the computation of only relative energies for ligand exchange processes and/or proton-transfer reactions. Of course, this type of calcula-

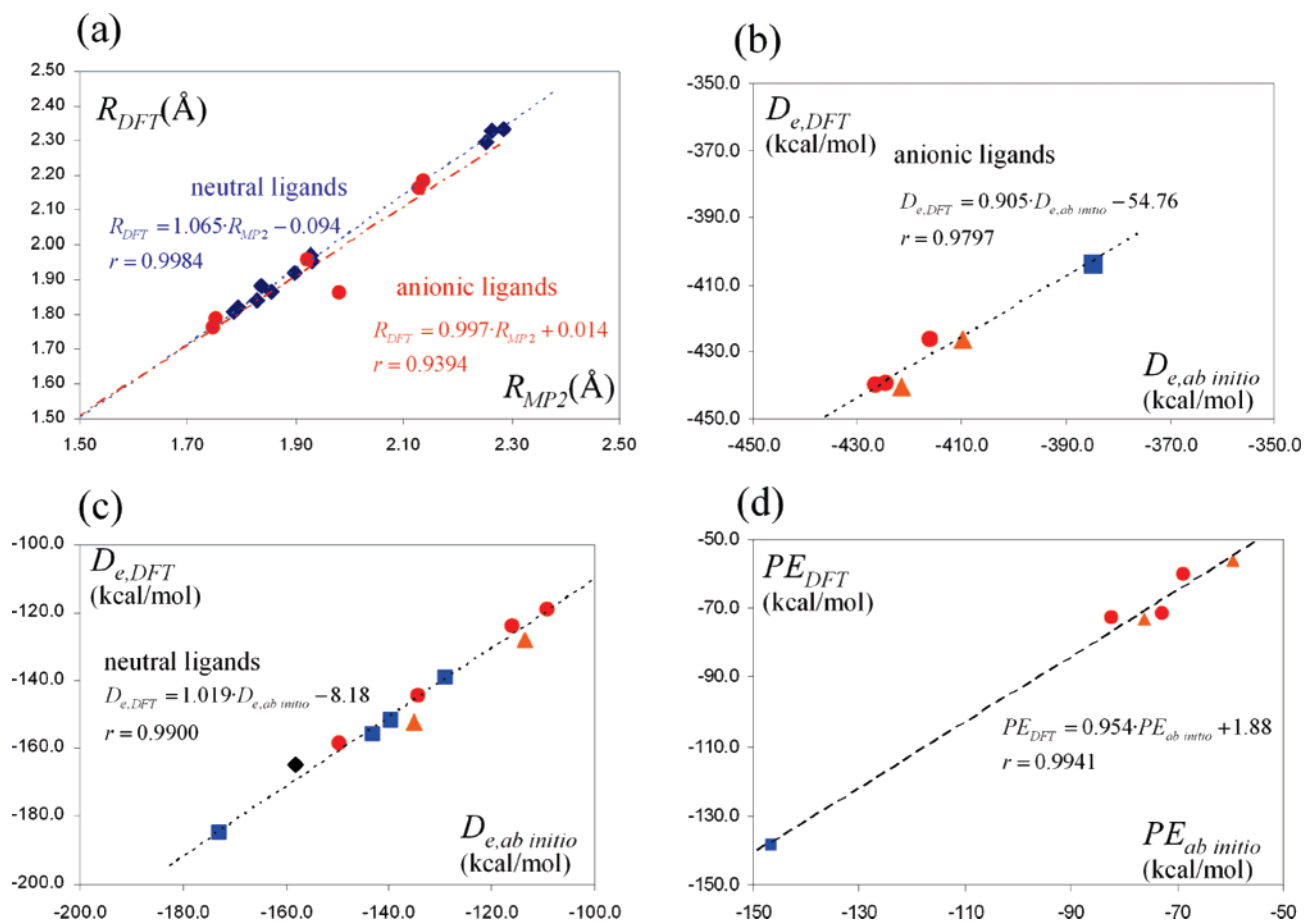


Figure 3. Linear regression plots of B3LYP/6-31+G(2d,p) data vs ab initio reference data: (a) zinc–ligand distances; (b) binding energies for anionic ligands; (c) binding energies for neutral ligands; and (d) protonation energies for zinc(II) complexes. Filled circles, squares, triangles, and diamond in plots (b–d) stand for oxygen-donor, nitrogen-donor, sulfur-donor, and benzene ligands, respectively.

tions can benefit from cancellation of “systematic” errors in the computed binding energies (D_e) and protonation energies (PEs) and, in general, the lower MSE of the D_e and PEs, the larger odds of cancellation of errors in the relative energies. Nevertheless, it may be interesting to examine some linear correlation plots of DFT results vs the ab initio reference results (discriminating between the neutral and the anionic ligands; see Figure 3) in order to ascertain more clearly the differences and similarities in the systematic deviations of the computed properties. For this purpose, we chose B3LYP/6-31+G(2d,p) as the DFT level of theory because this level shows a good balance between global accuracy and computational cost.

We see in Figure 3 that the best linear correlation between DFT and ab initio data corresponds to the protonation energies of the Zn-L complexes ($r = 0.994$), which is in consonance with the relatively low MSE of the B3LYP/6-31+G(2d,p) PEs. A reasonably good correlation coefficient is also obtained for the binding energies of neutral ligands ($r = 0.990$) although the corresponding MSE is larger than that of the PEs. However, the linear regression fit of the binding energies is less satisfactory in the case of the anionic ligands ($r = 0.980$). Similarly, the DFT zinc–ligand distances are better correlated with the ab initio data for the neutral ligands (see Figure 3a).

In terms of linear regression theory, the value of r^2 from plots (a–d) in Figure 3 can be interpreted as the fraction of the total variance of the DFT data that is “explained” by the variation in the corresponding ab initio data.⁵² For example, the uncertainty (as reflected in the variance) about a DFT PE energy value is reduced about 99.4% once we know its corresponding ab initio score and the correlation ratio ($r^2 = 0.994$) between the DFT and ab initio data. Reciprocally, the variance of the DFT data that remains “unexplained” by the linear regression fits is given by $1 - r^2$. Assuming that this latter variability is mainly due to the nonsystematic (i.e., erratic) errors, we propose to estimate the magnitude of the nonsystematic errors in the DFT calculations by multiplying the fraction of “unexplained” variation ($1 - r^2$) by 100.0 kcal/mol (an upper limit of the energy range covered by the regression analyses). In this way, we obtain that the approximate values of the nonsystematic errors for PEs, D_e for neutral ligands, and D_e for anionic ligands would be ~ 1.1 , ~ 2.0 , and ~ 4.0 kcal/mol, respectively, at the B3LYP/6-31+G(2d,p) level. In this scenario, both relative energies for processes involving the rupture of bonds between Zn(II) and neutral ligands and relative protonation energies of zinc-complexes, should be determined quite accurately using a hybrid DFT method combined with a flexible basis set like 6-31+G(2d,p) because the addition of the nonsystematic

Table 11. Contributions to the SAPT Interaction Energies (in kcal/mol) for the $[\text{Zn-L}]^{2+}$ Complexes (Neutral Ligands) with the 6-31+G(2*d*,*p*) Basis Set

ligand	$E_{\text{elst}}^{(1)}$	$E_{\text{ind}}^{(2)}$	$E_{\text{disp}}^{(2)}$	$E_{\text{exch}}^{(1)}$	$E_{\text{exch}}^{(2)}$	$E^{(1)a}$	$E^{(2)b}$	$\delta E_{\text{int}}^{\text{HF}}$	$E_{\text{int}}(\text{SAPT})$
H ₂ O	-88.0	-243.2	-6.5	55.7	175.3	-32.3	-74.4	10.3	-96.5
H ₂ CO	-85.3	-270.8	-7.0	58.5	183.3	-26.8	-94.5	9.4	-111.9
CH ₃ OH	-103.2	-313.8	-7.7	66.6	223.3	-36.6	-98.2	13.5	-121.3
CH ₃ COOH	-115.6	-362.3	-8.6	75.5	254.8	-40.1	-116.1	14.5	-141.7
HCONH ₂	-129.9	-375.3	-8.7	78.0	265.0	-51.9	-119.0	15.8	-155.1
NH ₃	-129.2	-461.1	-9.0	82.4	360.2	-46.8	-109.9	28.4	-128.3
H ₂ CNH	-126.7	-444.8	-9.0	79.1	333.1	-47.6	-120.7	23.6	-144.8
CH ₃ NH ₂	-132.5	-477.1	-8.9	80.3	366.0	-52.2	-120.2	26.0	-146.2
1H-imidazole	-155.9	-545.7	-10.7	95.3	407.6	-60.6	-148.8	29.9	-179.5
H ₂ S	-63.5	-375.6	-6.9	52.4	269.7	-11.1	-112.8	16.0	-107.9
CH ₃ SH	-78.9	-433.6	-7.6	59.4	313.1	-19.5	-128.1	18.0	-129.6
benzene	-71.3	-416.9	-15.5	77.8	262.5	6.5	-169.9	3.5	-159.9

$$^a E^{(1)} = E_{\text{elst}}^{(1)} + E_{\text{exch}}^{(1)}, \quad ^b E^{(2)} = E_{\text{ind}}^{(2)} + E_{\text{disp}}^{(2)} + E_{\text{exch}}^{(2)}$$

errors would amount to ~ 2 – 4 kcal/mol. However, the DFT relative energies for ligand rearrangement processes involving anions could have a larger error of ~ 8 kcal/mol. We note that these estimations are basically in agreement with the fact that, from previous computational experience in metal-containing systems,⁵³ the error on the relative energies computed by standard DFT methodologies is unlikely to exceed a range of 3–5 kcal/mol.

SAPT Analyses. In this section we will analyze the nature of the Zn(II)-ligand interaction by means of the Symmetry-Adapted Perturbation Theory. Table 11 collects the interaction energy components as well as the total intermolecular interaction energies for the Zn(II) complexes formed with the neutral ligands (see also Table S3 in the Supporting Information for a fully complete presentation of the SAPT data). For this analysis, we select again the 6-31+G(2*d*,*p*) basis set. We would also like to point out the fact that the interaction energies of these complexes range between 100 and 180 kcal/mol and, therefore, that the applicability of the SAPT2 methodology (that is, whether it can fully recover the SP-MP2 interaction energy) is here a matter of concern. As commented above in the Computational Methods section, terms of order higher than the second, which may well be important in these strongly bonded systems, can be obtained from a SP-HF calculation via the $\delta E_{\text{int}}^{\text{HF}}$ term. This is an easy and computationally cheap way of including these contributions, but this approximation does not come without a price since the physically meaningful components that comprise $\delta E_{\text{int}}^{\text{HF}}$ are of course not known. In the present case, $\delta E_{\text{int}}^{\text{HF}}$ represents in the worst case 10% of the total interaction energy, and, therefore, we think that we can provide a fairly correct qualitative picture of the nature of the interaction in these complexes by using SAPT2. However, we have not studied the anionic ligands because the interaction energy is in these cases far too large to be fully recovered by an intermolecular perturbation method without losing the physically meaningful picture of the interaction.

The results collected in Table 11 show that the electrostatic interaction $E_{\text{elst}}^{(1)}$ is not the largest attractive term in these complexes since it only represents 14–26% of the total attractive energy terms $E_{\text{elst}}^{(1)} + E_{\text{ind}}^{(2)} + E_{\text{disp}}^{(2)}$. The largest contribution to the interaction energy comes from $E_{\text{ind}}^{(2)}$,

whereas the dispersion energy clearly plays a minor role in the bonding of these systems. Of course, we also have to take into account that the induction component is partially quenched by its exchange counterpart (the same happens to the dispersion component, but the exchange-dispersion term is actually rather small, see Table S3). However, we do not think that it is particularly meaningful to sum up the induction and the exchange-induction components and conclude that these systems are stabilized mainly by $E_{\text{elst}}^{(1)}$. After all, if the $E_{\text{ind}}^{(2)}$ contribution were to be of a similar size of $E_{\text{elst}}^{(1)}$, the interaction energy would be repulsive. We think that a clearer picture of the interaction can be obtained by collecting all the components that contribute to a certain order in the intermolecular perturbation together, as described in the Computational Methods section. When using SAPT2, the two resulting terms are $E^{(1)}$ and $E^{(2)}$ which are also shown in Table 11. We see that in all cases $E^{(1)}$ is smaller than $E^{(2)}$ by more than 50%. Even in one particular case namely, $[\text{Zn}(\text{benzene})]^{2+}$, $E^{(1)}$ is repulsive. We interpret these results as indicating that the main stabilizing factor of the studied Zn(II) complexes is not the electrostatic attraction of the interacting fragments but the relaxation of the charge densities of the monomers through induction and charge transfer. This effect is far more important for the most polarizable ligands: hydrogen sulfide and methanethiol (see Table 11). The complex $\text{Zn}^{2+} \cdots \text{benzene}$ is a particular case because in this system the zinc atom is not pointing directly toward a negative local charge concentration of the base resulting in a relatively small electrostatic attraction and a positive first-order interaction energy. One important conclusion of this analysis is therefore that any methodology which is aimed to be applied to the study of Zn(II) complexes should give a correct description of the relaxation of the charge distribution of the interacting monomers. The systematic overestimation of the bond dissociation energies by different density functionals found in this work is actually related to this fact. Indeed, recent results obtained by Piquemal et al.⁵⁴ for the $[\text{Zn}(\text{imidazole})]^{2+}$ complex show that the larger interaction energy obtained with four different functionals (PW91, B3PW91, BLYP, and B3LYP) with respect to the MP2 value (13–26 kcal/mol with a DZVP2 basis set; we obtained in this work 13–22 kcal/mol with

the 6-31+G(2d,p) basis depending on the functional) is due to the overestimation of the charge-transfer effects, which is caused, in turn, by an overestimation of the imidazole polarizability.⁵⁴ This explanation is in complete agreement with our results, which highlight the importance of a correct description of the relaxation of the fragments' wave functions taking into account the important role played by the induction forces in the interaction of these complexes.

Implications for Molecular Mechanics Models. Besides its academic interest, the results of our SAPT calculations could be useful for the assessment of the so-called "non-bonded" molecular mechanics potentials that include electrostatic and van der Waals forces instead of covalent ones to maintain the Zn(II) coordination geometry during molecular dynamics simulations of zinc-enzymes. Thus, the simplest Zn(II) "nonbonded" models include merely a Coulombic term plus a Lennard-Jones term whose parameters are optimized either by fitting to ab initio interaction energies⁵⁵ or by reproducing relative experimental hydration free energies and the coordination number of Zn(II) in water.⁵⁶ However, in consonance with the importance of the induction and charge-transfer effects shown by the physically meaningful SAPT methodology, it has been found⁵⁷ that the "nonbonded" models should also include charge transfer from the donor atoms and local polarization of the Zn(II) ion and its ligands in order to properly describe the flexible coordination structure of the Zn(II) ions in proteins. We believe that further improvement of this or other extended "nonbonded" models²⁴ could be expected if these potentials are designed to reflect the underlying physical forces that govern the intermolecular interactions in monoligand complexes.

Conclusions

On the basis of the ab initio benchmark calculations for the 18 monoligand Zn(II)-complexes that are examined in this work, we can draw the following conclusions and/or recommendations: (a) Given that the MP2/aug-cc-pVTZ energies are in very good agreement with the "composite" CCSD(T) ones, this could be the ab initio level of choice in order to accurately predict the binding energies and/or PEs for polyligand Zn(II) complexes. (b) All the tested DFT functionals overestimate systematically the binding energy between the Zn(II) ion and the different ligands, the B3LYP and TPSS methods performing the best. (c) The Pople's 6-31+G(2d,p) basis set combined with the DFT or MP2 methods provides a good compromise between accuracy and computational cost for the systems studied here. (d) Using a hybrid DFT or a meta-GGA method, relative energies for ligand exchange and proton-transfer processes involving neutral ligands should be determined within a 2–4 kcal/mol accuracy, but larger errors should be expected for anionic ligands.

From the SAPT calculations, we find that, in the case of neutral ligands bound to the Zn(II) ion, 90% of their interaction energy can be assigned to well-defined and physically meaningful intermolecular forces. The SAPT calculations show that induction and charge-transfer interactions have a larger contribution than the classical electrostatic attraction between the fragments. This stresses the fact that

any theoretical methodology aimed to be applied to the study of Zn(II) complexes should be able to give a good description of the relaxation of the charge densities of the monomers upon complexation.

Acknowledgment. V.M.R. and N.D. gratefully acknowledge funds from the MEC within the "Ramón y Cajal" Program. This research has been partly supported by the Spanish MEC via grant CTQ2004-06309.

Supporting Information Available: Mean signed errors and standard deviations in the binding energies of the whole set of complexes included in this study, fully complete presentation of the SAPT data, metal–ligand bond distances obtained at the PBE/aug-cc-pVTZ level with an "ultrafine" grid, and metal–ligand bond distances and binding energies obtained with the B3LYP and TPSS functionals using a aug-cc-pVQZ basis set. This material is available free of charge via the Internet at <http://pubs.acs.org>.

References

- (1) Lipscomb, W. N. N. S. *Chem. Rev.* **1996**, *96*, 2375–2433.
- (2) Bartlett, R. J. *J. Phys. Chem.* **1989**, *93*, 1697–1708.
- (3) Dunning, T. H., Jr. *J. Phys. Chem. A* **2000**, *104*, 9062–9080.
- (4) Martin, J. M. L. Ab initio thermochemistry beyond chemical accuracy for first- and second-row compounds. In *Nato ASI Symposium Volume ASIC 535, Energetics of stable molecules and reactive intermediates*; Minas da Piedade, M. E., Ed.; Kluwer Academic Publishers: Dordrecht, 1999; pp 373–415.
- (5) Balabanov, N. B.; Peterson, K. A. *J. Chem. Phys.* **2005**, *123*, 064107.
- (6) Koch, W.; Holthausen, M. C. *A Chemist's guide to density functional theory*, 2nd ed.; Wiley-VCH: New York, 2001; p 528.
- (7) Estiu, G.; Suarez, D.; Merz, K. M. J. *J. Comput. Chem.* **2006**, *27*, 1240–1262.
- (8) Weston, J. *Chem. Rev.* **2005**, *105*, 2151–2174.
- (9) Strain, M. C.; Scuseria, G. E.; Frisch, M. J. *Science* **1996**, *271*, 51–53.
- (10) White, C. A.; Johnson, B. G.; Gill, P. M. W.; Head-Gordon, M. *Chem. Phys. Lett.* **1996**, *253*, 268–278.
- (11) Eichkorn, K.; Treutler, O.; Öhm, H.; Häser, M.; Ahlrichs, R. *Chem. Phys. Lett.* **1995**, *240*, 283–289.
- (12) Goringe, C. M.; Bowler, D. R.; Hernández, E. *Rep. Prog. Phys.* **1997**, *60*, 1447–1512.
- (13) Elstner, M. *Theor. Chem. Acc.* **2006**, *116*, 316–325.
- (14) Jensen, K. P.; Roos, B. O.; Ryde, U. *J. Chem. Phys.* **2007**, *126*, 014103.
- (15) Diaz, N.; Suarez, D.; Merz, K. M. J. *Chem. Phys. Lett.* **2000**, *326*, 288–292.
- (16) Tiraboschi Gresh, N.; Giessner-Pretre Pedersen, L. G.; Deerfield, D. W. *J. Comput. Chem.* **2000**, *12*, 1011–1039.
- (17) Diaz, N.; Suarez, D.; Merz, K. M. J. *J. Am. Chem. Soc.* **2000**, *122*, 4197–4208.
- (18) Yazal, J. E.; Pang, Y.-P. *J. Mol. Struct. (THEOCHEM)* **2001**, *545*, 271–274.

- (19) Frison, G.; Ohanessian, G. *J. Comput. Chem.* **2008**, *29*, 416–433.
- (20) Brothers, E. N.; Suarez, D.; Deerfield, D. W.; Merz, K. M. *J. J. Comput. Chem.* **2004**, *25*, 1677–1692.
- (21) Elstner, M.; Cui, Q.; Munih, P.; Kaxiras, E.; Frauenheim, T.; Karplus, M. *J. Comput. Chem.* **2003**, *24*, 565–581.
- (22) Gresh, N.; Garmer, D. J. *J. Comput. Chem.* **1996**, *17*, 1481–1495.
- (23) Rogalewicz, F.; Ohanessian, G.; Gresh, N. *J. Comput. Chem.* **2000**, *21*, 963–973.
- (24) Gresh, N.; Piquemal, J.-P.; Krauss, M. J. *J. Comput. Chem.* **2005**, *26*, 1113–1130.
- (25) Kendall, R. A.; Dunning, J. T. H.; Harrison, R. J. *J. Chem. Phys.* **1992**, *96*, 6796–6806.
- (26) Woon, D. E.; Dunning, T. H., Jr. *J. Chem. Phys.* **1993**, *98*, 1358–1371.
- (27) Raghavachari, K.; Trucks, G. W.; Pople, J. A.; Head-Gordon, M. *Chem. Phys. Lett.* **1989**, *157*, 479–483.
- (28) Peterson, K. A.; Puzzarini, C. *Theor. Chem. Acc.* **2005**, *114*, 283–296.
- (29) Boys, S. F.; Bernardi, F. *Mol. Phys.* **1970**, *19*, 553.
- (30) Dunning, T. H. J.; Peterson, K. A.; Wilson, A. K. *J. Chem. Phys.* **2001**, *114*, 9244–9253.
- (31) Perdew, J. P.; Burke, K.; Wang, Y. *Phys. Rev. B* **1996**, *57*, 14999–14999.
- (32) Perdew, J. P.; Burke, K.; Enzerhof, M. *Phys. Rev. Lett.* **1996**, *78*, 1396–1396.
- (33) Becke, A. D. *J. Chem. Phys.* **1986**, *95*, 7184–7187.
- (34) Becke, A. D. *J. Chem. Phys.* **1988**, *88*, 2547–2553.
- (35) Becke, A. D. *J. Chem. Phys.* **1988**, *88*, 1053–1062.
- (36) Lee, C.; Yang, R. G.; Parr, R. G. *Phys. Rev. B* **1988**, *37*, 785–789.
- (37) Schultz, N. E.; Zhao, Y.; Truhlar, D. G. *J. Phys. Chem. A* **2005**, *109*, 4388–4403.
- (38) Tao, J.; Perdew, J. P.; Staroverov, V. N.; Scuseria, G. E. *Phys. Rev. Lett.* **2003**, *91*, 146401.
- (39) Rassolov, V. A.; Ratner, M. A.; Pople, J. A.; Redfern, P. C.; Curtiss, L. A. *J. Comput. Chem.* **2001**, *22*, 976–984.
- (40) Krishnan, R.; Binkley, J. S.; Seeger, R.; Pople, J. A. *J. Chem. Phys.* **1980**, *72*, 4654–4655.
- (41) Wachters, A. J. H. *J. Chem. Phys.* **1970**, *52*, 1033.
- (42) Hay, P. J. *J. Chem. Phys.* **1977**, *66*, 4377–4384.
- (43) Raghavachari, K.; Trucks, G. W. *J. Chem. Phys.* **1989**, *91*, 1062–1065.
- (44) Rienstra-Kiracofe, J. C.; Tschumper, G. S.; Schaefer, H. F., III; Nandi, S.; Ellison, G. B. *Chem. Rev.* **2002**, *102*, 231–282.
- (45) Frisch, M. J.; Trucks, G. W.; Schlegel, H. B.; Scuseria, G. E.; Robb, M. A.; Cheeseman, J. R.; Montgomery, J. J. A.; Vreven, T.; Kudin, K. N.; Burant, J. C.; Millam, J. M.; Iyengar, S. S.; Tomasi, J.; Barone, V.; Mennucci, B.; Cossi, M.; Scalmani, G.; Rega, N.; Petersson, G. A.; Nakatsuji, H.; Hada, M.; Ehara, M.; Toyota, K.; Fukuda, R.; Hasegawa, J.; Ishida, M.; Nakajima, T.; Honda, Y.; Kitao, O.; Nakai, H.; Klene, M.; Li, X.; Knox, J. E.; Hratchian, H. P.; Cross, J. B.; Bakken, V.; Adamo, C.; Jaramillo, J.; Gomperts, R.; Stratmann, R. E.; Yazyev, O.; Austin, A. J.; Cammi, R.; Pomelli, C.; Ochterski, J. W.; Ayala, P. Y.; Morokuma, K.; Voth, G. A.; Salvador, P.; Dannenberg, J. J.; Zakrzewski, V. G.; Dapprich, S.; Daniels, A. D.; Strain, M. C.; Farkas, O.; Malick, D. K.; Rabuck, A. D.; Raghavachari, K.; Foresman, J. B.; Ortiz, J. V.; Cui, Q.; Baboul, A. G.; Clifford, S.; Cioslowski, J.; Stefanov, B. B.; Liu, G.; Liashenko, A.; Piskorz, P.; Komaromi, I.; Martin, R. L.; Fox, D. J.; Keith, T.; Al-Laham, M. A.; Peng, C. Y.; Nanayakkara, A.; Challacombe, M.; Gill, P. M. W.; Johnson, B.; Chen, W.; Wong, M. W.; Gonzalez, C.; Pople, J. A. *Gaussian 03, Revision C.02*; Gaussian, Inc.: Wallingford, CT, 2004.
- (46) Bukowski, B. R.; Cencek, W.; Jankowski, P.; Jeziorski, B.; Jeziorska, M.; Kucharski, S. A.; Misquitta, A. J.; Moszynski, R.; Patkowski, K.; Rybak, S.; Szalewicz, K.; Williams, H. L.; Wormer, P. E. S. *SAPT2002: An Ab Initio program for many-body symmetry-adapted perturbation theory calculations of intermolecular interaction energies. Sequential and parallel versions*; 2002. See http://www.Physics.Udel.Edu/_szalewic/sapt/sapt.html.
- (47) Jeziorski, B.; Moszynski, R.; Szalewicz, K. *Chem. Rev.* **1994**, *94*, 1887–1930.
- (48) Chalasiński, G.; Szczesniak, M. *Mol. Phys.* **1988**, *63*, 205–224.
- (49) Misquitta, A. J.; Bukowski, R.; Szalewicz, K. *J. Chem. Phys.* **2000**, *112*, 5308–5319.
- (50) Reed, A. E.; Curtiss, L. A.; Weinhold, F. *Chem. Rev.* **1988**, *88*, 899–926.
- (51) Riley, K. E.; Hobza, P. *J. Phys. Chem. A* **2007**, *111*, 8257–8263.
- (52) Frank, H.; Althoen, S. C. *Statistics: Concepts and applications*; Cambridge University Press: 1994.
- (53) Siegbahn, P. E. M. *Q. Rev. Biophys.* **2003**, *36*, 91–145.
- (54) Piquemal, J. P.; Marquez, A.; Parisel, O.; Giessner-Prettre, C. *J. Comput. Chem.* **2005**, *26*, 1052–1062.
- (55) Stote, R. H.; Karplus, M. *Proteins: Struct., Funct., Genet.* **1995**, *23*, 12–31.
- (56) Babu, C. S.; Lim, C. *J. Phys. Chem. A* **2006**, *110*, 691–699.
- (57) Sakharov, D. V.; Lim, C. *J. Am. Chem. Soc.* **2005**, *127*, 4921–4929.

CT700229E

JCTC Journal of Chemical Theory and Computation

New Algorithms for Optimizing and Linking Conical Intersection Points

Fabrizio Sicilia,[§] Lluís Blancafort,^{*,†} Michael J. Bearpark,[§] and Michael A. Robb^{*,§}

Department of Chemistry, Imperial College, London SW7 2AZ, United Kingdom, and Institut de Química, Computational and Departament de Química, Universitat de Girona, E-17071 Girona, Spain

Received September 21, 2007

Abstract: In this paper we present two new algorithms to study the extended nature of the crossing seam between electronic potential energy surfaces. The first algorithm is designed to optimize conical intersection geometries: both minima and saddle points. In addition, this method will optimize conical intersection geometries using arbitrary geometrical constraints. We demonstrate its potential on different crossing seams of benzene, z-penta-3,5-dieniminium, and 1,3-butadiene. The second algorithm is designed to explicitly compute the intersection-space minimum energy coordinate. Our computations show how an intersection seam and the energy along it can be unambiguously defined. A finite region of the S_0/S_1 1,3-butadiene crossing seam has been mapped out, and a new saddle point linked with two lower-lying geometries on the seam.

1. Introduction

In the past two decades conical intersection geometries have been shown to play a central role in our understanding of photochemical reactions (see for instance refs 1–3). Up to now, numerous conical intersection structures have been located and shown to be involved in several nonradiative processes (see for instance refs 1–4).

Conical intersections are not isolated points but rather are connected along an $(n-2)$ -dimensional hyperline, where n is the number of internal degrees of freedom. Recent studies have shown that decay can also occur at higher energy points along the crossing hyperline (see for example refs 5 and 6) away from its minimum. Thus, an accurate investigation of the intersection space,⁷ which is the space where the two electronic states are degenerate, becomes crucial.

In this spirit, we recently developed a new methodology to compute the curvature of the crossing seam energy, such that saddle points could be distinguished from minima within the intersection space.^{8,9} In addition, from these frequency

calculations we could compute the motions corresponding to any imaginary frequencies. These intersection-space vibrational modes⁹ were then used to suggest connections among several conical intersection points belonging to the same intersection space. In this paper, we describe two complementary tools to study the intersection space. The first is a new algorithm designed to optimize conical intersection structures with improved convergence and which can make use of analytic second derivatives of the seam energy. The second method is for computing the minimum energy path connecting three conical intersection structures, e.g., two minima and a saddle point along the crossing seam. Thus, with the new algorithms described in this paper we have a complete set of tools capable of investigating the energy within the intersection space in the same way that one would study a single Born-Oppenheimer potential energy surface, i.e., using geometry optimization, frequency calculation, and reaction path computations (see for instance ref 10).

Over the years, many different approaches have been proposed to optimize structures where two electronic states become degenerate. The algorithms currently available are based upon either Lagrange-Newton methods (see for example refs 11–13) or projection methods (see for instance refs 14 and 15). The algorithms belonging to the first class

* Corresponding author e-mail: mike.robb@imperial.ac.uk (M.A.R.), lluis.blancafort@udg.edu (L.B.).

† Universitat de Girona.

§ Imperial College.

have the common feature of using variations of the classical Lagrange multipliers method.^{16–18} Recently, it has been shown¹⁹ that this class of algorithms is generally very efficient. Together with a higher computational cost, these methods are, however, difficult to be efficiently implemented and improved.^{19–21} One of the main problems is related to the Lagrange Hessian, which is not positive definite, i.e., for each constraint a negative eigenvalue arises. Therefore efficient updating methods such as the Broyden-Fletcher-Goldfarb-Shanno (BFGS) scheme cannot be employed, and the overall algorithm may be affected in terms of efficiency and convergence rate (see for instance refs 16, 17, 19, 20, 22, and 23). In contrast, the projection methods are designed to reach the energy degeneracy by means of a displacement within the branching space,⁷ while optimizing simultaneously the energy of the excited state within the intersection space.⁷

A typical algorithm, based on projection matrices, uses a gradient composed of two distinct parts.¹⁴ The first part consists of the normalized gradient difference vector, which is one of the two first-order degeneracy lifting directions,¹ weighted by twice the energy gap. This term is responsible for minimizing the energy difference between the two crossing states. The second part of the gradient optimizes the excited-state energy within the intersection space. Thus a critical point on the intersection hyperline can be located.

The use of a projection matrix ensures the orthogonality between the two parts of the composite gradient. However, such orthogonality may be lost in computing a quasi-Newton–Raphson displacement, as a consequence of an ill-conditioned approximate Hessian (see for instance ref 24). In other words, the displacement computed may have components in both branching and intersection space. This problem becomes troublesome in the region where the two electronic states become almost degenerate, where the displacement components within the branching plane will lift the degeneracy. The algorithm described in this paper therefore uses a combination of displacements taken within the two orthogonal spaces rather than two gradients. Although this idea is related to the theoretical development originally proposed by Anglada et al.²² and recently reviewed and extended by De Vico et al.,²⁰ the actual implementation of the proposed algorithm is substantially different, as we will discuss in the next section.

In the present algorithm, as the energy difference drops below a set threshold, a Newton–Raphson displacement, taken within the intersection space, is combined with a step along the gradient difference vector. When the energy is above the given threshold, the standard projection method¹⁴ is used. As we will discuss in section 4, the proposed algorithm shows a faster and smoother overall convergence to the minimum conical intersection geometry when compared with two previously reported algorithms.^{14,22} In addition, our implementation enables one to optimize conical intersection geometries along a selected constrained redundant internal coordinate.^{25–27} Finally, this algorithm and the possibility of computing analytically an intersection-space Hessian⁹ can be combined with the transition state search

algorithm (for a recent review see for instance ref 10) implemented in the Gaussian package.²⁸ To summarize, the algorithm proposed in this paper is capable of locating both minima and saddle points within the intersection space, as well as of optimizing conical intersection points along a given constrained geometrical variable.

Using two independent displacements, one within the intersection space and one along the gradient difference vector, we have also designed a method to compute a coordinate analogous to the intrinsic reaction coordinate^{29–31} but confined to the intersection space. Although such a coordinate may be not physically meaningful (see for example ref 32 and following comments), it represents a unique way to define finite portions of the intersection space. In section 4, we will present the study carried out to link a new saddle point found on the S_0/S_1 crossing seam of 1,3-butadiene with two lower lying critical points on the conical intersection seam.

2. Theory

Optimization of Stationary Points along a Crossing Seam.

At a conical intersection point, a displacement along two directions is capable of lifting the degeneracy at first order: the gradient difference [eq 1a] and the interstate coupling [eq 1b] (see for example refs 1, 3, 11, 33, and 34).

$$\mathbf{x}_1 = \frac{\partial(E_2 - E_1)}{\partial \mathbf{q}} \quad (1a)$$

$$\mathbf{x}_2 = \left\langle \mathbf{C}_1 \left| \frac{\partial \mathbf{H}}{\partial \mathbf{q}} \right| \mathbf{C}_2 \right\rangle \quad (1b)$$

In eq 1, \mathbf{C}_1 and \mathbf{C}_2 are the CI eigenvectors in the MC–SCF problem. The vectors \mathbf{x}_1 and \mathbf{x}_2 span the branching plane,⁷ also referred to as the g - h plane.³ In the orthogonal (n -2) subspace, the intersection space,⁷ the degeneracy is retained at the first order.^{9,33,35,36} The adiabatic energies of the two electronic states are indicated by E_1 and E_2 , whereas \mathbf{H} and \mathbf{q} represent the electronic CI Hamiltonian matrix and the nuclear coordinates, respectively.

In the direct algorithm proposed by Bearpark et al.,¹⁴ the gradient used in the optimization is the following

$$\mathbf{g} = \mathbf{f} + \mathbf{g}_p \quad (2a)$$

where

$$\mathbf{f} = 2(E_2 - E_1) \frac{\mathbf{x}_1}{\delta \kappa} = 2\Delta E \hat{\mathbf{x}}_1 \quad (2b)$$

and

$$\mathbf{g}_p = \mathbf{P} \frac{\partial E_2}{\partial \mathbf{q}} \quad (2c)$$

In eq 2, $\delta \kappa$ is the length of the gradient difference vector, i.e., $\delta \kappa = \sqrt{\mathbf{x}_1^T \mathbf{x}_1}$; and \mathbf{P} represents the projector matrix which projects the gradient of the upper state ($\partial E_2 / \partial \mathbf{q}$) onto the subspace perpendicular to the plane ($\hat{\mathbf{x}}_1, \hat{\mathbf{x}}_2$):

$$\mathbf{P} = \mathbf{1} - \hat{\mathbf{x}}_1 \hat{\mathbf{x}}_1^T - \hat{\mathbf{x}}_2 \hat{\mathbf{x}}_2^T \quad (2d)$$

The “hat” notation indicates a normalized vector. Here, we assume that the two potential energy surfaces cross each other along an $(n-2)$ -dimensional intersection space, where n is the number of internal coordinates. However, this algorithm works also when the nonadiabatic interstate coupling vector [eq 1b] is zero by symmetry, e.g., the intersection space is of $(n-1)$ dimensionality. For what follows, it is also worth noting that the projected gradient of the excited-state energy is the same vector as that obtained by projecting the average of the two state gradients (for the proof see the Appendix). This equivalence will be crucial in defining the second-derivative matrix of the seam energy.

An updated Hessian can become ill-conditioned in certain regions of the potential energy surface, if the composite gradient [eq 2] is used throughout the optimization. When the energy difference is large, for instance, the Hessian is dominated by contributions arising from the branching plane.^{16,23,24} As a result, the degeneracy region is rapidly reached. However, when the seam is located, contributions from the branching plane to the approximate Hessian may not vanish and therefore the degeneracy is lifted.

To improve the convergence of this algorithm we therefore propose to project both gradient and Hessian when the seam region is approached, so that the possible branching-space contamination is avoided. When the energy difference is below a certain threshold, we will combine an intersection-space displacement with a step taken along the gradient difference.

For the combined step part, the potential energy within the intersection space can be described by a Taylor expansion truncated at the second-order:

$$E_{Seam} = E_{Seam}^0 + (\Delta\mathbf{q}_{IS}^0)^T \mathbf{g}_{IS}^0 + \frac{1}{2} (\Delta\mathbf{q}_{IS}^0)^T \mathbf{H}_{IS}^0 \Delta\mathbf{q}_{IS}^0 \quad (3a)$$

Notice that $\Delta\mathbf{q}_{IS}^0 = \mathbf{q}_{IS} - \mathbf{q}_{IS}^0$ is an n -dimensional vector. The zero-order term is taken as the reference point and set to zero. The seam energy gradient within the intersection space, \mathbf{g}_{IS} , is computed as the projected average gradient (see the Appendix). This gradient allows us to introduce the intersection-space Hessian, recently proposed elsewhere,^{8,9} as the second-derivative matrix of the seam energy. Defining the intersection-space Hessian of the seam energy as the projected “derivative” of the seam energy gradient, we obtain

$$\mathbf{W}_{IS} = \mathbf{P} \left[\frac{\partial}{\partial \mathbf{q}} \mathbf{g}_{IS} \right] \mathbf{P} = \frac{1}{2} \mathbf{P} \left[\frac{\partial}{\partial \mathbf{q}} \mathbf{P} \frac{\partial(E_2 + E_1)}{\partial \mathbf{q}} \right] \mathbf{P} \\ = \frac{1}{2} \mathbf{P} \left[\frac{\partial^2(E_2 + E_1)}{\partial \mathbf{q}^2} - \frac{\lambda_{x_1}}{\delta\kappa} \frac{\partial^2 \Delta E}{\partial \mathbf{q}^2} - \frac{\lambda_{x_2}}{\kappa_{12}} \frac{\partial^2 H_{12}}{\partial \mathbf{q}^2} \right] \mathbf{P} \quad (3b)$$

In the differentiation we have used the definition of projection matrix reported in eq 2d. We have also introduced $\lambda_{x_{1(2)}}$ to indicate the components of the average gradient along the unit gradient difference (nonadiabatic interstate coupling vector) and $\delta\kappa$ (κ_{12}) for the length of the gradient difference (nonadiabatic interstate coupling vector).

To compute the Newton–Raphson displacement, the inverse of this Hessian matrix is required. However due to the projection, \mathbf{W}_{IS} has two zero eigenvalues corresponding

Table 1. Relevant Quantities Used in the Presented Conical Intersection Optimization Algorithm

$\Delta E = E_2 - E_1$	>threshold ^a	<threshold
gradient ^b	$\mathbf{g} = \mathbf{f} + \mathbf{g}_{IS}^c$	$\mathbf{g} = \mathbf{g}_{IS}$
total displacement	$\Delta\mathbf{q} = -(\mathbf{W})^{-1}\mathbf{g}$	$\Delta\mathbf{q} = -(\mathbf{H}_{IS})^{-1}\mathbf{g}_{IS} + (\Delta E/\delta\kappa)\hat{\mathbf{x}}_1^d$

^a The default cutoff has been set to $5 \times 10^{-3} E_h$. ^b This gradient is used to both update the Hessian matrix and to compute the displacement. ^c Defined in eq 2. ^d Defined in eq 4.

to the branching plane directions and therefore its inverse is not defined. However, using the idea of Peng et al.,³⁷ one can use instead the following matrix

$$\mathbf{H}_{IS} = \mathbf{W}_{IS} + (\mathbf{1} - \mathbf{P})\mathbf{A}(\mathbf{1} - \mathbf{P}) \quad (3c)$$

where \mathbf{A} is diagonal matrix whose elements are set to a large constant (e.g., 1000) and \mathbf{P} is the usual projection matrix defined in eq 2d. Consequently, using the Newton–Raphson method, the intersection-space displacement can be computed as

$$\Delta\mathbf{q}_{IS}^0 = -(\mathbf{H}_{IS}^0)^{-1}\mathbf{g}_{IS}^0 \quad (4a)$$

Although the displacement is an n -dimensional vector, the possible contributions from the branching plane have been projected out.

To guarantee the degeneracy, the following step along the gradient difference

$$\Delta\mathbf{q}_{BS}^0 = (\Delta E_0/\delta\kappa_0)\hat{\mathbf{x}}_1^0 \quad (4b)$$

is added to $\Delta\mathbf{q}_{IS}^0$, so that the total displacement is given by

$$\Delta\mathbf{q}_0 = \Delta\mathbf{q}_{IS}^0 + \Delta\mathbf{q}_{BS}^0 \quad (4c)$$

Although in principle the Hessian matrix, \mathbf{W} , could be analytically computed,^{8,9} an approximated Hessian (\mathbf{F}) is initially used in practice. Using the Broyden–Fletcher–Goldfarb–Shanno (BFGS) scheme, this matrix is calculated as

$$\mathbf{W} \approx \mathbf{F} = \mathbf{F}^0 + \frac{\Delta\mathbf{h}_0(\Delta\mathbf{h}_0)^T}{\Delta\mathbf{h}_0^T \Delta\mathbf{q}_0} - \frac{\mathbf{F}^0 \Delta\mathbf{q}_0 \Delta\mathbf{q}_0^T \mathbf{F}^0}{\Delta\mathbf{q}_0^T \mathbf{F}^0 \Delta\mathbf{q}_0} \quad (5)$$

Here $\Delta\mathbf{h}_0$ is computed as the difference between the gradients evaluated at \mathbf{q} (current iteration) and at \mathbf{q}_0 (previous iteration). $\Delta\mathbf{q}_0$ represents instead the difference between the current and previous geometry. Depending on the energy gap, the gradient used in the update scheme varies as shown in Table 1.

In Table 1, we have reported the main features of the algorithm discussed in this paper. The reader may recognize some similarities between the proposed algorithm and the one obtained by Anglada et al.,^{20,22} who have suggested applying the Han–Powell method^{16,17,23,38} to optimize conical intersection geometries. In proximity to the crossing seam, the two methodologies, for instance, use the same gradient (see the Appendix) to update the Hessian matrix, \mathbf{F} [eq 5]. Moreover, the intersection-space Hessian \mathbf{W}_{IS} , used here, is similar to the reduced Hessian reported by Anglada et al.

Despite the various similarities, the proposed algorithm differs from the one reported by Anglada et al. in several crucial ways. First, their method uses the Hessian only to compute the intersection space displacement throughout the optimization. Consequently, the method is known (see for example refs 16, 20, and 23) to have a fairly slow convergence when one starts from a point too far away from the solution. In our algorithm, a composite gradient [eq 2] is used to compute both the displacement and to update the Hessian in regions far away from the degeneracy. Furthermore, in the seam region, the two proposed displacements differ in the form of the gradient used: we use the projected gradient [eq 2c], whereas Anglada et al. propose using the reduced gradient. However, as theoretically outlined by Nocedal et al.²³ and based on our own experience, the additional term present in the reduced gradient does not provide any benefit to the overall convergence, once the crossing region is reached. Finally, the intersection-space Hessian, \mathbf{W}_{IS} , shown in eq 3b, is a symmetric n by n matrix, whereas the reduced Hessian used by Anglada et al. has dimension $(n-2)$ by $(n-2)$. Nevertheless, it should be remarked that both matrices have the same $(n-2)$ rank, i.e., both matrices have $(n-2)$ nonzero eigenvalues.

Along with minimum energy crossing points, the proposed algorithm is also able to optimize different conical intersection structures along a constrained coordinate. We have recently proposed an implementation to carry out this type of optimization,²⁵ which prevents the possible occurrence of cancellation errors.^{25–27} In that study, we suggested to apply first the constraints and subsequently to project out the branching space directions from the gradient. This procedure allowed us to map out successfully a region of the S_0/S_1 fulvene crossing seam. Nevertheless in that study, we explicitly applied symmetry considerations to carry out the calculations. Here, we apply the constraints to both branching plane vectors [eq 1], and then we build the projection matrix \mathbf{P} [eq 2d]. Thus, the procedure has been generalized and implemented in a development version of Gaussian.²⁸ We recognize that other methodologies (see for example ref 18) which allow geometrical constraints in a conical intersection optimization algorithm have been previously reported. While these methods do not suffer from cancellation errors, they are computationally more demanding than the algorithm discussed in this paper.¹⁹

Finally, we have explored the possibility of combining this new algorithm with the methodology implemented in Gaussian to find transition state structures [see for example ref 10 and references therein]. Routinely, to compute a transition state structure, one must compute the Hessian at a point located close enough to the quadratic region of the first-order saddle point. This matrix must have one negative eigenvalue, and the corresponding eigenvector should be a suitable guess for the initial optimization direction. In this work, we follow the same procedure but it has been limited to the intersection space. Consequently, we begin by analytically computing the intersection-space Hessian^{8,9} at an approximately converged conical intersection geometry. During the rest of the optimization, the intersection-space Hessian, \mathbf{W}_{IS} , is updated using Bofill's scheme³⁹ implemented in Gaussian and then

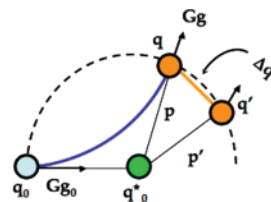


Figure 1. A graphical representation of the vectors used in the original IRC algorithm³¹ is shown.

Table 2. Terms Appearing in the Single-Surface, Minimum Energy Path Algorithm of Gonzalez et al.,³¹ and Their Equivalents in the Intersection-Space Version^a

single surface ²⁷	intersection space
$\Delta\mathbf{q}_M = \mathbf{G}^{-1/2}\Delta\mathbf{q}$	${}^{IS}\Delta\mathbf{q}_M = \mathbf{G}^{-1/2}\Delta\mathbf{q}_{IS}$
$\mathbf{g}'_M = \mathbf{G}^{1/2}\mathbf{g}'$	${}^{IS}\mathbf{g}'_M = \mathbf{P}\mathbf{G}^{1/2}\mathbf{g}'$
$\mathbf{H}'_M = \mathbf{G}^{1/2}\mathbf{H}'\mathbf{G}^{1/2}$	${}^{IS}\mathbf{H}'_M = \mathbf{P}\mathbf{G}^{1/2}\mathbf{W}_{IS}'\mathbf{G}^{1/2}\mathbf{P} + (1 - \mathbf{P})\mathbf{A}(1 - \mathbf{P})$
$\mathbf{p}'_M = \mathbf{G}^{-1/2}\mathbf{p}'$	${}^{IS}\mathbf{p}'_M = \mathbf{P}\mathbf{G}^{-1/2}\mathbf{p}'$

^a See eq 6. \mathbf{G} is the Wilson matrix;⁴¹ \mathbf{g} , \mathbf{H} , and $\Delta\mathbf{q}$ indicate the gradient, the Hessian, and the displacement, respectively.

used as described above. This methodology has allowed us to locate a new saddle point in the intersection space of 1,3-butadiene.

Computation of the Minimum Energy Path within the Intersection Space. We now move to discuss the second algorithm proposed in this paper. This method permits the computation of a coordinate analogous to the intrinsic reaction coordinate (IRC), confined to the intersection space (IS-IRC). Although several methods have been proposed to compute a segment of the intersection space [see for example ref 6, 20, 26, 32, and 40 and references therein], the algorithm that we have implemented is based upon the one proposed by Gonzalez et al.³¹ We will briefly present the ideas behind the original IRC algorithm, and then we will describe the modifications required to compute directly the IS-IRC.

As shown in Figure 1, the original IRC algorithm^{30,31} was designed such that starting from a point \mathbf{q}_0 , a $1/2s$ displacement along the gradient $\mathbf{G}\mathbf{g}_0$ is taken to locate point \mathbf{q}_0^* , defined as the *pivot point*. From this pivot point, a constrained optimization is carried out on the surface of a hypersphere of radius $1/2s$ and centered at \mathbf{q}_0^* . Thus, in Figure 1, \mathbf{q}_0 , \mathbf{q}' and \mathbf{q} are three points on the hypersphere and \mathbf{q}_0^* the center of it. Along the reaction path, at every \mathbf{q} the residual gradient is, by construction, parallel to the \mathbf{p} vector. Using this observation and the fact that the radius of the hypersphere must equal $1/2s$, one obtains the following set of equations

$$\Delta\mathbf{q}_M = -(\mathbf{H}_M - \sigma\mathbf{I})^{-1}(\mathbf{g}_M - \sigma\mathbf{p}_M) \quad (6a)$$

$$\Delta\mathbf{q}_M^T \Delta\mathbf{q}_M = [\mathbf{p}_M - (\mathbf{H}_M - \sigma\mathbf{I})^{-1}(\mathbf{g}_M - \sigma\mathbf{p}_M)]^T [\mathbf{p}_M - (\mathbf{H}_M - \sigma\mathbf{I})^{-1}(\mathbf{g}_M - \sigma\mathbf{p}_M)] = (1/2s)^2 \quad (6b)$$

where the scalar σ is the Lagrange multiplier, \mathbf{I} is the identity matrix and the remaining quantities are defined in Table 2.

In order to compute the intersection space path, we follow the same derivation. However, all the quantities previously

introduced are now projected onto the intersection space using the \mathbf{P} matrix defined in eq 2d. Thus, replacing the various terms in eq 6 (Table 2), the intersection-space displacement, $\Delta\mathbf{q}_{IS}$, can be computed. However, due to the curved nature of the intersection space (see for instance refs 1, 8, 9, 36, and 42), this displacement will in general make the two crossing surfaces split apart. To restore the degeneracy, an additional displacement within the branching space is finally added, in the spirit of the algorithm described above and in the way that has been defined in eq 4c. As we will discuss in the next section, we have imposed convergence criteria on both gradient and displacement computed. Consequently, the degeneracy condition is implicitly required from eq 4c, since a large displacement would correspond to a large energy gap.

3. Computational Details

The two algorithms described in the previous section have been implemented in a development version of the Gaussian package²⁸ and at the state averaged complete active space self-consistent field level of theory (SA-CASSCF). Nevertheless, they can be easily implemented at any other level of theory, provided that analytical energy gradients and the nonadiabatic interstate coupling vector are available. The overall convergence of the algorithm to optimize conical intersections has been tested on the S_0/S_1 crossing seam of benzene. The calculations have been carried out at the SA-CASSCF level of theory, with a six π electrons and six π orbitals active-space and an STO-3G basis set. An active space of $(6\pi, 6\pi)$ and one of $(4\pi, 4\pi)$ were instead used to investigate the S_0/S_1 crossing seams of z -penta-3,5-dieniminium and 1,3-butadiene, respectively. Also in these examples we have used the 2-SA-CASSCF level of theory, but with a 6-31G* basis set. All energies in the figures are reported in hartree (E_h).

In all the examples presented, the two crossing electronic states were equally weighted and the coupled perturbative MCSCF (CP-MCSCF) equations solved to evaluate the gradients (see for instance ref 43). However, tests have been also carried out using approximate gradients, i.e., without solving the CP-MCSCF equations, to guarantee the efficiency of the code implementation for molecules with either a large active space or a large number of atoms, where it may be too expensive to solve the CP-MCSCF equations. In these tests, the same structures (within $0.5 \text{ kcal mol}^{-1}$) were optimized with and without computing the corrections for the gradients. Nevertheless, we have noticed that away from the seam region, the two optimizations may differ significantly. This had some consequences for 1,3-butadiene, which has a complex intersection space with a large number of local minima. There the displacement computed with the approximate gradient can lead to a different stationary point if the optimization starts far away from the seam region.

In the examples considered in the next section, a conical intersection geometry is considered converged when the largest component of the intersection-space gradient, or of ${}^{IS}\mathbf{g}'_{\mathbf{M}}$ (Table 2) for the second algorithm, is smaller than

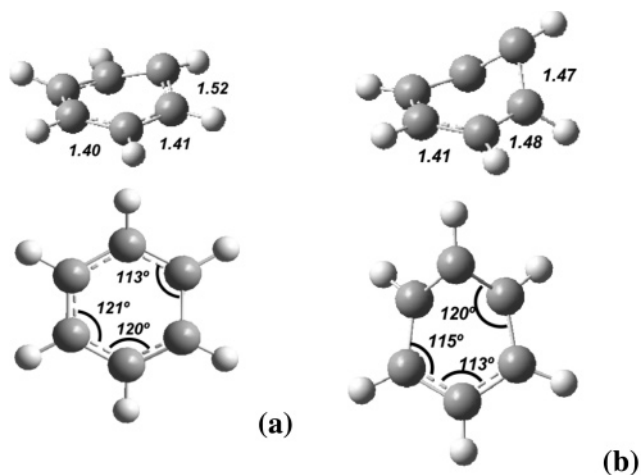


Figure 2. Starting benzene geometry (a) and optimized S_0/S_1 conical intersection geometry (b) at the SA-CASSCF(6,6)/STO-3G level. All the angles (*italic*) are reported in degrees, while C–C bonds are reported in Å.

4.5×10^{-4} au and with rms below 3.0×10^{-4} au. In addition to the gradient, also the maximum component of the total displacement is checked, $\Delta\mathbf{q}_0$ in eq 4c. A geometry is thus considered converged when the largest component of such a displacement is smaller than 1.8×10^{-3} au with rms 1.2×10^{-3} au.

In the last example reported below, we map out a finite portion of the S_0/S_1 1,3-butadiene crossing seam. Due to the complex morphology of the area around the conical intersection ${}^{\text{SP}}\text{CI}_{66}$, in our computations the step length was reduced. This explains the number of points on the left-hand side of the profile in Figure 9a.

Finally, we should point out all the conical intersection points discussed in this work have a peaked topology,⁷ but the algorithm reported has also been tested on sloped conical intersections.

4. Results and Discussions

The purpose of this section is to illustrate the potential of the two algorithms described in section 2. We begin by comparing the performance of the proposed conical intersection search algorithm using the S_0/S_1 and S_0/T_1 crossing seams of benzene. The z -penta-3,5-dieniminium crossing seam will be used as an example of constrained optimization. Finally, the S_0/S_1 crossing seam of butadiene is examined by optimizing a saddle point on this hyperline, then computing the associated intersection-space path.

Conical Intersection Algorithm. To evaluate the overall efficiency of the conical intersection algorithm, the S_0/S_1 conical intersection seam of benzene (see for example refs 44 and 45) has been used. We compare here the global convergence of the benzene S_0/S_1 conical intersection optimization computed by using the algorithm of Bearpark et al.,¹⁴ the one proposed by Anglada et al.²² and the one proposed in this paper. All the conical intersection optimizations were started from a slightly nonplanar benzene structure obtained by distorting the minimum geometry (Figure 2a) on the S_1 potential energy surface.⁴⁴

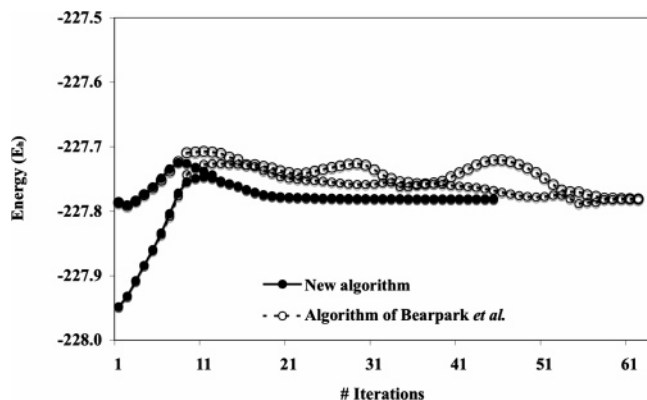


Figure 3. Global convergence of an S_0/S_1 conical intersection optimization of a benzene molecule: comparison between the energy profiles obtained by the algorithm of Bearpark et al. (open circles) and the proposed algorithm (filled circles).

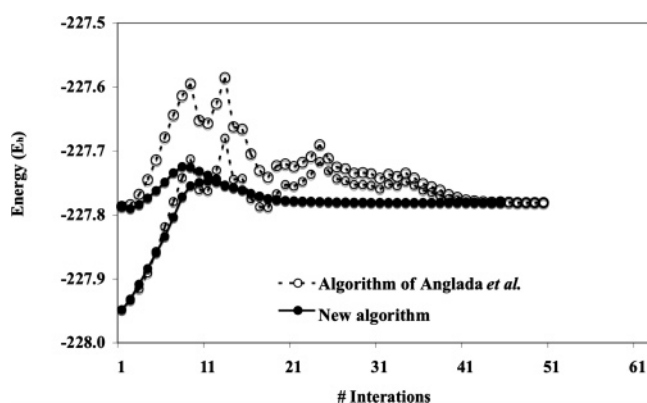


Figure 4. Global convergence of an S_0/S_1 conical intersection optimization of benzene: comparison between the method introduced by Anglada et al. (open circles) and the proposed algorithm (filled circles).

The same conical intersection geometry was optimized by the three different algorithms (Figure 2b), which is that previously reported by Bearpark et al.¹⁴ As noted in that study, a bigger basis set would, on one hand, provide a more accurate description of the molecular geometry. On the other hand, a bigger basis would not invalidate the results obtained regarding the convergence behavior. The objective of the test presented here is to discuss the total convergence of the new algorithm, so we used a relatively small basis set to speed up the tests.

In Figures 3 and 4 we show the energy changes of the two S_0 and S_1 crossing states for benzene computed with the three algorithms during the optimization. As discussed in section 2, the algorithm of Bearpark et al. (open circles in Figure 3) promptly reaches the crossing seam. However, once in that region, a poorly conditioned Hessian slows the overall convergence. On the other hand, the algorithm proposed by Anglada et al. has a slower convergence toward the crossing seam (open circles in Figure 4) but gives a much smoother profile in the degeneracy region. In addition to the low rate of convergence to the degeneracy region, this latter algorithm tends to take steps in high-energy regions, where

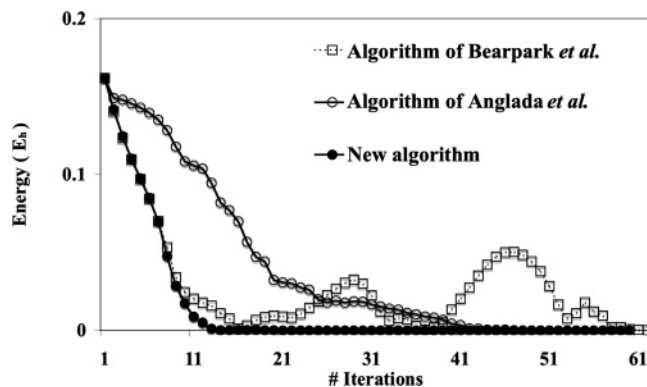


Figure 5. Energy difference between the S_0 and S_1 electronic states in benzene during the conical intersection optimization.

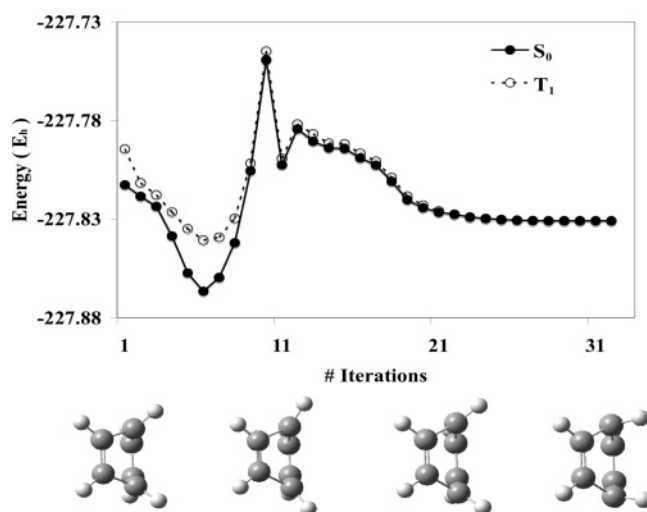
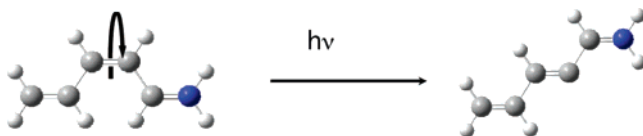


Figure 6. Global convergence of the optimization of an S_0/T_1 crossing geometry of benzene using the new algorithm presented here. Geometries for selected points (1, 11, 21, 31) along the optimization path are shown at the bottom of the figure.

Scheme 1



other molecules may, for example, dissociate and therefore be channeled toward high-energy portions of the intersection seam.

It is easily appreciated that the new algorithm (filled circles and solid line in both Figures 3 and 4) has a faster convergence, when compared with both the other methods. In addition, it is clear that the new algorithm combines the strengths of the two methods in different regions of the optimization: it has the fast convergence rate in the first part of the optimization, but it is also able to maintain the degeneracy between the two crossing electronic states once the crossing seam is reached.

To emphasize this last point, in Figure 5, the difference of the energies of the S_0 and S_1 states of benzene during the intersection optimization is shown. It should be noted that the starting geometry is very poor, since the initial energy

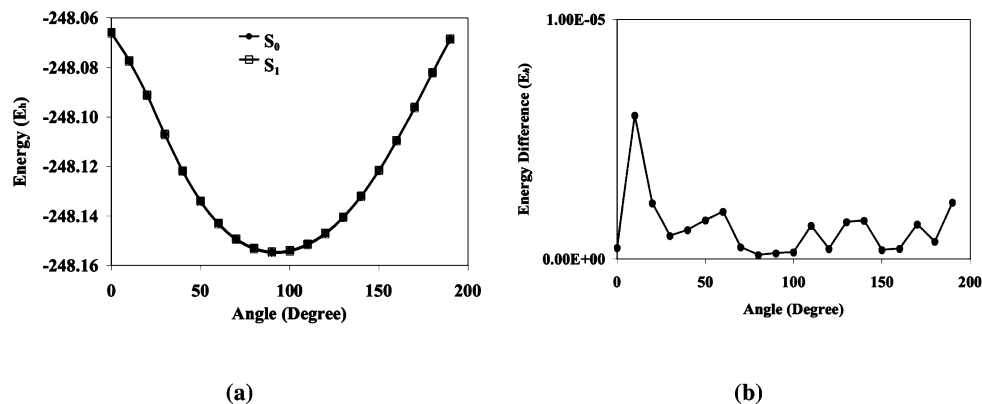


Figure 7. Energy profile obtained as a function of the z-penta-3,5-dieniminium cation central bond rotation **(a)**. The degeneracy is reached for all the examined angles as shown in panel **(b)**, where the energy difference is reported.

gap between the two states is over 100 kcal mol⁻¹. Such a difficult test demonstrates the robust global convergence of all three algorithms. The algorithm presented here shows a faster decrease of the energy gap.

Our new algorithm is also able to optimize crossing points along (*n*-1)-dimensional crossing seams. In Figure 6, we show, as an example, the energy separation and the geometrical changes during the optimization of a crossing point on the T₁/S₀ crossing seam of benzene. As initial geometry (iteration 1 in Figure 6), we have used a boat-like structure, resembling the transition state connecting benzene to Dewar benzene.^{44,46} Also in this type of crossing, the algorithm presented in this paper shows a robust overall convergence and promptly approaches the crossing seam. We note that the crossing point optimized in this test differs from the geometry obtained in our previous study,¹⁴ as a consequence of choosing a different starting geometry.

To illustrate the generality of our implementation, we now show a constrained conical intersection optimization within the S₀/S₁ intersection space of z-penta-3,5-dieniminium cation.^{26,47} We have carried out a relaxed scan of the central dihedral angle (Scheme 1), and in Figure 7a we report the energy profile computed. As previously reported,^{26,32,47,48} we have found the minimum crossing point to be in the region of 90°. However, it should be noted that the new algorithm can achieve a high level of degeneracy (see for instance refs 26 and 32) at all the optimized structures (Figure 7b).

Algorithm To Compute the Intersection-Space Minimum Energy Path. To further demonstrate the generality of the proposed conical intersection algorithm, we have optimized a saddle point along the S₀/S₁ crossing seam of 1,3-butadiene. Such a saddle point is then linked up with two structures lower in energy, along an intersection space minimum energy path computed with the second proposed algorithm.

Generally, in order to optimize a saddle point structure, one must start from a geometry that is close enough to the quadratic region of such a point. In addition, the Hessian at this initial structure must show a negative eigenvalue, and the corresponding eigenvector must be a suitable approximation for the direction connecting the two valleys. When one tries to optimize a saddle point within the

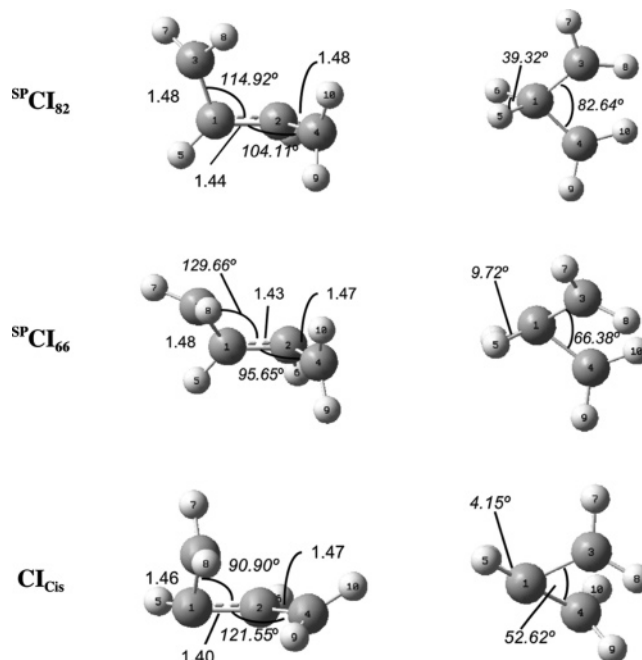


Figure 8. Important geometric parameters for the optimized butadiene CI geometries found along the S₀/S₁ 1,3-butadiene crossing seam. The bond lengths are expressed in Å, while the angles (in *italic*) are presented in degrees.

intersection space, the initial geometry should also be a point of degeneracy, since the intersection-space Hessian must be computed.

In our first studies^{13,49} on 1,3-butadiene, we optimized three stationary points along the S₀/S₁ crossing seam: the *cisoidal*, the *transoidal*, and the *central* structure. In the present study, starting from the *central* geometry we first re-optimized the energy gap between the two states along the gradient difference vector. At this point on the conical intersection seam, the intersection-space Hessian was computed and an imaginary frequency (with corresponding eigenvector) obtained. Finally, using the new algorithm presented in this paper, we were able to optimize a new saddle point not reported previously (^{SP}CI₈₂ in Figure 8). This structure shows an imaginary frequency of 639 *i* cm⁻¹ corresponding to a combination of a -CH₂ twisting mode and a symmetric rocking mode localized on H₅ and H₆. It closely resembles the ^{SP}CI_{cis/cis} structure previously reported

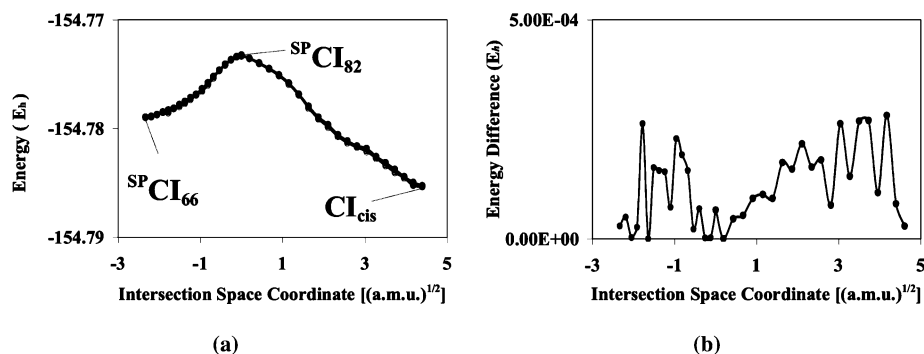


Figure 9. Minimum energy path connecting ${}^{\text{SP}}\text{CI}_{66}$ (negative part of the intersection space coordinate in panel a) to the CI_{cis} (positive intersection coordinate in panel a) through ${}^{\text{SP}}\text{CI}_{82}$. In panel (b), the energy difference computed at each point along the intersection space minimum energy coordinate is reported.

elsewhere,⁹ but where the C_2 symmetry has been broken and consequently a slightly lower (<1 kcal mol⁻¹) energy is obtained.

In Figure 9, we report the results obtained with the algorithm designed to compute the minimum energy path within the intersection space, discussed in section 2.

We started our intersection-space minimum energy path computation from the structure ${}^{\text{SP}}\text{CI}_{82}$ (Figure 8), and we have used as initial relaxation direction (see for instance refs 10, 30, 31, and 50) the eigenvector corresponding to the imaginary frequency. The accuracy of the algorithm proposed in this paper can be appreciated from Figure 9b, which shows that the energy difference at each optimized structure along the path is well below 1 kcal mol⁻¹.

Our results show that ${}^{\text{SP}}\text{CI}_{82}$ connects one of the *s-cisoidal* conical intersection isomers (CI_{cis} in Figure 8) with a new conical intersection saddle point (${}^{\text{SP}}\text{CI}_{66}$ in Figure 8). The absence of discontinuity in this profile (Figure 9a) is evidence of a single crossing seam. The calculated coordinate is somewhat unconventional as it ends at a saddle point, ${}^{\text{SP}}\text{CI}_{66}$, but the imaginary frequency at ${}^{\text{SP}}\text{CI}_{66}$ is perpendicular to the intersection space coordinate that connects ${}^{\text{SP}}\text{CI}_{82}$ to ${}^{\text{SP}}\text{CI}_{66}$. A similar case was described in our previous butadiene study,⁹ which is an indication of the complexity of the intersection space, even for an apparently simple example such as butadiene.

4. Conclusions

In this paper we presented two new algorithms to study the extended nature of the crossing seam between two electronic potential energy surfaces. The first algorithm represents an improvement over the algorithms already available. It combines fast convergence in reaching the seam region with flexibility in the degeneracy region itself. To demonstrate the potential of this algorithm, we have optimized both minima and saddle points on crossing seams as well as carried out conical intersection optimization with a frozen internal coordinate. In all cases, the results obtained show a fast and smooth convergence to an optimized conical intersection point.

The second algorithm has instead been designed to compute the intersection-space minimum energy path. Adapting one of the available algorithms³¹ to compute the reaction path on a single potential energy surface, we have imple-

mented an analogous method limited exclusively to the intersection space. We have shown its potential by explicitly mapping out a finite region of the S_0/S_1 1,3-butadiene crossing seam.

Acknowledgment. L.B. is financed by the Spanish/Ministerio de Educación y Ciencia/ for Project No. CTQ2005-04563 and the Ramón y Cajal program. F.S. is pleased to acknowledge the support of Gaussian, Inc. and the grant given by ESF-COST P9, Radiation Damage in Biological Systems, for sponsoring his visit to the University of Girona.

Appendix

In this Appendix, we will show the equivalence between the gradient of one of the two crossing states energy and the average gradients, once they are both projected onto the first-order intersection space. Using the definition of projection matrix given in eq 2c, the projected gradient, for instance, of the state 2 can be written as

$$\mathbf{P} \frac{\partial E_2}{\partial \mathbf{q}} \quad (\text{A.1})$$

On the other hand, the projected average gradient is defined as

$$\frac{1}{2} \mathbf{P} \frac{\partial (E_2 + E_1)}{\partial \mathbf{q}} \quad (\text{A.2})$$

Proving their difference zero is equivalent to show that they are the same vector. Thus

$$\frac{1}{2} \mathbf{P} \frac{\partial (E_2 + E_1)}{\partial \mathbf{q}} - \mathbf{P} \frac{\partial E_2}{\partial \mathbf{q}} = \frac{1}{2} \mathbf{P} \frac{\partial (E_1 - E_2)}{\partial \mathbf{q}} = \frac{1}{2} \mathbf{P} \mathbf{x}_1 = \frac{1}{2} (\mathbf{x}_1 - \mathbf{x}_1) = \mathbf{0} \quad (\text{A.3})$$

In eq A.3, we have used the definition of the projection matrix \mathbf{P} [eq 2] and exploited the fact that the gradient difference vector and the nonadiabatic interstate coupling vectors are chosen to be orthonormal to each other.

References

- (1) Domcke, W.; Yarkony, D. R.; Koppel, H. *Conical Intersections: Electronic Structure, Dynamics & Spectroscopy*; World Scientific Publishing Co.: Singapore, 2004.

- (2) Bernardi, F.; Olivucci, M.; Robb, M. A. *Chem. Soc. Rev.* **1996**, 25, 321; Klessinger, M.; Michl, J. *Excited States and Photochemistry of Organic Molecules*; Wiley-VCH: New York, 1995.
- (3) Yarkony, D. R. *Rev. Mod. Phys.* **1996**, 68, 985.
- (4) Toniolo, A.; Levine, B.; Thompson, A.; Quenneville, J.; Ben-Nun, M.; Owens, J.; Olsen, S.; Manohar, L.; Martinez, T. J. *Photochemistry from First Principles and Direct Dynamics in Computational Methods*. In *Computational Methods in Photochemistry*; Kutateladze, A., Ed.; CRC Press: Boca Raton, 2005; pp 166–234.
- (5) Ben-Nun, M.; Martinez, T. J. *Chem. Phys. Lett.* **1998**, 298, 57. Boggio-Pasqua, M.; Bearpark, M. J.; Hunt, P. A.; Robb, M. A. *J. Am. Chem. Soc.* **2002**, 124, 1456. Boggio-Pasqua, M.; Bearpark, M. J.; Ogliaro, F.; Robb, M. A. *J. Am. Chem. Soc.* **2006**, 128, 10533. Boggio-Pasqua, M.; Ravaglia, M.; Bearpark, M. J.; Garavelli, M.; Robb, M. A. *J. Phys. Chem. A* **2003**, 107, 11139.
- (6) Laino, T.; Passerone, D. *Chem. Phys. Lett.* **2004**, 389, 1.
- (7) Atchity, G. J.; Xantheas, S. S.; Ruedenberg, K. *J. Chem. Phys.* **1991**, 95, 1862.
- (8) Paterson, M. J.; Bearpark, M. J.; Robb, M. A.; Blancafort, L. *J. Chem. Phys.* **2004**, 121, 11562; Sicilia, F.; Blancafort, L.; Bearpark, M. J.; Robb, M. A. *Theor. Chem. Acc.* **2007**, 118, 241.
- (9) Sicilia, F.; Blancafort, L.; Bearpark, M. J.; Robb, M. A. *J. Phys. Chem. A* **2007**, 111, 2182.
- (10) Schlegel, H. B. *J. Comput. Chem.* **2002**, 24, 1514.
- (11) Yarkony, D. R. *J. Chem. Phys.* **1990**, 92, 2457.
- (12) Dallos, M.; Lischka, H.; Shepard, R.; Yarkony, D. R.; Szalay, P. G. *J. Chem. Phys.* **2004**, 120, 7330.
- (13) Ragazos, I. N.; Robb, M. A.; Bernardi, F.; Olivucci, M. *Chem. Phys. Lett.* **1992**, 197, 217.
- (14) Bearpark, M. J.; Robb, M. A.; Schlegel, H. B. *Chem. Phys. Lett.* **1994**, 223, 269.
- (15) Chachiyo, T.; Rodriguez, J. H., *J. Chem. Phys.* **2005**, 123, 094711; Yamazaki, S.; Kato, S. *J. Chem. Phys.* **2005**, 123, 114510. Izzo, R.; Klessinger, M. *J. Comput. Chem.* **2000**, 21, 52. Page, C. S.; Olivucci, M. *J. Comput. Chem.* **2003**, 24, 298.
- (16) Fletcher, R. *Practical Methods of Optimization*; Wiley & Sons: New York, 1981; Vol. 2.
- (17) Gill, P. E.; Murray, W. *Numerical Methods for Constrained Optimization*; Academic Press: London, 1974.
- (18) Manaa, M. R.; Yarkony, D. R. *J. Chem. Phys.* **1993**, 99, 5251.
- (19) Keal, T. W.; Koslowski, A.; Thiel, W. *Theo. Chem. Acc.* **2007**, 118, 837–844.
- (20) De Vico, L.; Olivucci, M.; Lindh, R. *J. Chem. Theory Comput.* **2005**, 1, 1029.
- (21) Yarkony, D. R. *J. Phys. Chem.* **2004**, 108, 3200.
- (22) Anglada, J. M.; Bofill, J. M. *J. Comput. Chem.* **1996**, 18, 992.
- (23) Nocedal, J.; Overton, M. L. *SIAM J. Num. Anal.* **1985**, 22, 821.
- (24) Toniolo, A.; Ben-Nun, M.; Martinez, T. J. *J. Phys. Chem. A* **2002**, 106, 4679.
- (25) Bearpark, M. J.; Blancafort, L.; Paterson, M. J. *Mol. Phys.* **2006**, 104, 1033.
- (26) Migani, A.; Robb, M. A.; Olivucci, M. *J. Am. Chem. Soc.* **2003**, 125, 2804.
- (27) Takahashi, O.; Sumita, M., *J. Chem. Phys.* **2004**, 121, 7030.
- (28) Frisch, M. J.; Trucks, G. W.; Schlegel, H. B.; Scuseria, G. E.; Robb, M. A.; Cheeseman, J. R.; Montgomery, J. A., Jr.; Vreven, T.; Scalmani, G.; Kudin, K. N.; Iyengar, S. S.; Tomasi, J.; Barone, V.; Mennucci, B.; Cossi, M.; Rega, N.; Petersson, G. A.; Nakatsuji, H.; Hada, M.; Ehara, M.; Toyota, K.; Fukuda, R.; Hasegawa, J.; Ishida, M.; Nakajima, T.; Honda, Y.; Kitao, O.; Nakai, H.; Li, X.; Hratchian, H. P.; Peralta, J. E.; Izmaylov, A. F.; Heyd, J. J.; Brothers, E.; Staroverov, V.; Zheng, G.; Kobayashi, R.; Normand, J.; Burant, J. C.; Millam, J. M.; Klene, M.; Knox, J. E.; Cross, J. B.; Bakken, V.; Adamo, C.; Jaramillo, J.; Gomperts, R.; Stratmann, R. E.; Yazyev, O.; Austin, A. J.; Cammi, R.; Pomelli, C.; Ochterski, J. W.; Ayala, P. Y.; Morokuma, K.; Voth, G. A.; Salvador, P.; Dannenberg, J. J.; Zakrzewski, V. G.; Dapprich, S.; Daniels, A. D.; Strain, M. C.; Farkas, O.; Malick, D. K.; Rabuck, A. D.; Raghavachari, K.; Foresman, J. B.; Ortiz, J. V.; Cui, Q.; Baboul, A. G.; Clifford, S.; Cioslowski, J.; Stefanov, B. B.; Liu, G.; Liashenko, A.; Piskorz, P.; Komaromi, I.; Martin, R. L.; Fox, D. J.; Keith, T.; Al-Laham, M. A.; Peng, C. Y.; Nanayakkara, A.; Challacombe, M.; Chen, W.; Wong, M. W.; Pople, J. A. *Gaussian Development Version, Revision F.01*; Gaussian, Inc.: Wallingford, CT, 2006.
- (29) Fukui, K. *Acc. Chem. Res.* **1981**, 14, 363.
- (30) Gonzalez, C.; Schlegel, H. B. *J. Chem. Phys.* **1989**, 90, 2154.
- (31) Gonzalez, C.; Schlegel, H. B. *J. Chem. Phys.* **1990**, 94, 5523.
- (32) Migani, A.; Sinicropi, A.; Ferre, N.; Cembran, A.; Garavelli, M.; Olivucci, M. *Faraday Discuss.* **2004**, 127, 179.
- (33) Yarkony, D. R. *J. Chem. Phys.* **2005**, 123, 204101.
- (34) Redmon, L. T. *Phys. Rev. A* **1982**, 25, 2453.
- (35) Mead, C. A. *J. Chem. Phys.* **1983**, 78, 807. Young, R. A.; Yarkony, D. R. *J. Chem. Phys.* **2006**, 125, 234301.
- (36) Yarkony, D. R. *J. Chem. Phys.* **2005**, 123, 134106.
- (37) Peng, C.; Ayala, P. Y.; Schlegel, H. B.; Frisch, M. J. *J. Comput. Chem.* **1996**, 17, 49.
- (38) Wright, S. J. Algorithms and Software for Linear and Nonlinear Programming. In *Foundations of Computer-Aided Process Design*; CACHE Publications: 1999.
- (39) Bofill, J. M. *J. Comput. Chem.* **1994**, 15, 1.
- (40) Passerone, D.; Laino, T. *Comput. Phys. Commun.* **2005**, 169, 305.
- (41) Wilson, E. B.; Decius, G. C.; Cross, P. C. *Molecular Vibrations*; McGraw-Hill: London, 1955.
- (42) Yarkony, D. R. *J. Chem. Phys.* **2005**, 123, 1234106.
- (43) Almlöf, J.; Taylor, P. *Int. J. Quantum Chem.* **1985**, 27, 743.
- (44) Palmer, I. J.; Ragazos, I. N.; Bernardi, F.; Olivucci, M.; Robb, M. A. *J. Am. Chem. Soc.* **1993**, 115, 673.
- (45) Domcke, W.; Sobolewski, A. L.; Woywod, C. *Chem. Phys. Lett.* **1993**, 203, 220; Sobolewski, A. L.; Woywod, C.; Domcke, W. *J. Chem. Phys.* **1993**, 98, 5627.

- (46) Turro, N. J. *Modern Molecular Photochemistry*; Benjamin Cummings: Menlo Park, CA, 1978.
- (47) Garavelli, M.; Celani, P.; Bernardi, F.; Robb, M. A.; Olivucci, M. *J. Am. Chem. Soc.* **1997**, *119*, 6891. Weingart, O.; Migani, A.; Olivucci, M.; Robb, M. A.; Buss, V.; Hunt, P. *J. Phys. Chem. A* **2004**, *108*, 4685. Vreven, T.; Bernardi, F.; Garavelli, M.; Olivucci, M.; Robb, M. A.; Schlegel, H. B. *J. Am. Chem. Soc.* **1997**, *119*, 12687.
- (48) Garavelli, M.; Bernardi, F.; Olivucci, M.; Vreven, T.; Klein, S.; Celani, P.; Robb, M. A. *Faraday Discuss.* **1998**, *110*, 51.
- (49) Olivucci, M.; Ragazos, I. N.; Bernardi, F.; Robb, M. A. *J. Am. Chem. Soc.* **1993**, *115*, 3710.
- (50) Celani, P.; Robb, M. A.; Garavelli, M.; Bernardi, F.; Olivucci, M. *Chem. Phys. Lett.* **1995**, *243*, 1.

CT7002435

On the Accuracy of Density Functional Theory to Predict Shifts in Nuclear Magnetic Resonance Shielding Constants due to Hydrogen Bonding

Jacob Kongsted*

*Department of Theoretical Chemistry, Chemical Center, University of Lund,
P.O. Box 124, S-221 00 Lund, Sweden*

Kestutis Aidas, Kurt V. Mikkelsen, and Stephan P. A. Sauer

*Department of Chemistry, University of Copenhagen, Universitetsparken 5,
DK-2100 Copenhagen Ø, Denmark*

Received October 25, 2007

Abstract: We present the first systematic investigation of shifts in the nuclear magnetic resonance (NMR) shielding constant due to hydrogen bonding using either the series of wave function based methods, Hartree–Fock (HF), second-order Møller-Plesset perturbation theory (MP2), Coupled Cluster Singles and Doubles (CCSD) and CCSD extended with an approximate description of triples (CCSD(T)), or Density Functional Theory (DFT) employing either the B3LYP, PBE0, or KT3 exchange correlation (*xc*) functionals. The molecular systems considered are (i) the water dimer and (ii) formaldehyde in complex with two water molecules. Specially for the ^{17}O in formaldehyde we observe significant differences between the DFT and CCSD(T) predictions. However, the extent of these deviations depends crucially on the applied *xc* functional. Compared to CCSD(T) we find the KT3 functional to provide accurate results, whereas both B3LYP and PBE0 are in significant error. Potential consequences of this observation are discussed in the context of general predictions of NMR shielding constants in condensed phase.

I. Introduction

Among the intermolecular forces acting between molecules in a condensed medium, the hydrogen bond is by far the strongest and plays in fact an important role when characterizing the chemical nature of a given molecular system. For example, hydrogen bonding is essential in determining the 3D geometries adopted by nucleic bases and proteins. In such large molecules, the hydrogen bonds between different regions within the same macromolecule may cause it to fold and thereby adapt a specific shape which partly determines its biochemical function.¹ In DNA the double helical structure is largely due to specific hydrogen bonding between base pairs, and in proteins hydrogen bonds form between the backbone oxygens and amide hydrogens. Hydrogen bonds are usually classified according to the strength, i.e., strong

(> 15 kcal/mol), moderate (4–15 kcal/mol), and weak (< 4 kcal/mol).² The strength of a hydrogen bond is closely related to the geometry or bond directionality, i.e., the angle (α) between D–H and H \cdots A, where D and A are the donor and acceptor groups, respectively.³ The preferable geometry of the hydrogen bond is found⁴ for $R(\text{H}\cdots\text{A}) \sim 2 \text{ \AA}$ and α in the range from 140° to 180°.

In recent years a lot of research has focused on the ability of DFT to describe the geometry and energetics of hydrogen bonds.³ DFT is for this application, due to the potential low scaling of this method, an obvious candidate. However, the accuracy of DFT in the description of hydrogen bonds depends strongly on the specific type of *xc* functional employed in the calculation. It has been found that local density approximation (LDA) functionals largely overestimate the strength of hydrogen bonds, while a much better description is provided by using either generalized gradient

* Corresponding author e-mail: Jacob.Kongsted@teokem.lu.se.

approximation (GGA) or general hybrid *xc* functionals (see for example the excellent paper by Ireta et al.³ and references therein).

In contrast to the large amount of data available on the performance of DFT versus high level wave function methods for the geometry and energetics of hydrogen bonds,³ only little is known about the accuracy of DFT in the calculation of changes in general spectroscopic properties due to the presence of hydrogen bonds in extended systems.⁵ Obviously, this is related to the fact that, due to the inherently large size of such systems, great difficulties are encountered when trying to base the quantum chemical description on correlated wave function approaches. However, the question is fundamental and requires attention. This should particularly be seen in light of the fact that DFT is now widely used and has become accepted in calculations of general molecular properties for isolated molecules.

In this paper we will present a systematic investigation of shifts in NMR shielding constants due to hydrogen bonding using either the series of wave function based methods HF, MP2, CCSD, and CCSD(T) or DFT employing either the B3LYP,⁶ PBE0,^{7,8} or KT3⁹ *xc* functionals. We consider either the water dimer or formaldehyde in complex with two water molecules. For these two small model systems we will present a systematic study of the effect of varying the electronic structure method with particular focus on the performance of the DFT based methods as compared to high level wave function methods like CCSD(T). It has previously been established that CCSD(T) is capable of predicting NMR shielding constants very accurately (see for example ref 10), and we will in this study use this model as the theoretical reference. The NMR shielding constants are known to be very sensitive to the chemical environment and specially hydrogen bonding may change the magnitude of the resonance frequency. In addition, it is well-known that NMR spectroscopy is a powerful tool for predicting protein structure and that *ab initio* calculations can provide important help in assigning experimental NMR spectra.^{11,12} It is therefore of both fundamental and practical interest to assess to what extent DFT may be used to predict NMR shielding constants in hydrogen-bonded molecular systems. Even though the molecular systems studied here are relatively small, they are appropriate model systems for more complex samples, e.g., acetone or other carbonyl compounds solvated by water, and bear the important chemistry characteristic for the class of carbonyl compounds. Moreover, these model systems are small enough for accurate quantum chemical methods to be applied. We therefore believe that our findings are of great importance for benchmarking solvent models for quantitative NMR predictions in particular in light of very recent progress within linear scaling methods applied to DFT¹³ calculations of NMR shielding constants, which opens the door for quantum chemical calculations of NMR properties on very large and complex chemical systems.

The rest of this paper is organized in the following way. In section II we outline the computational protocol. In section III we first present and discuss the results for the water dimer and then turn to the system composed of formaldehyde and

two water molecules. Finally, we end this paper by a discussion presented in section IV.

II. Computational Methods

The theoretical aspects of calculations of NMR shielding tensors are well-known and will not be repeated here. Instead we refer to ref 14 for a general and comprehensive review. Special theoretical aspects of the Coupled Cluster based calculations may be found in refs 15–18, whereas calculations of NMR shielding constants based on DFT are described in refs 19–23.

The molecular geometries of water and the water dimer were optimized using CCSD(T), whereas the geometries of formaldehyde and formaldehyde complexed with two water molecules were optimized using CCSD. In all cases we used the aug-cc-pVTZ basis set.²⁴ In all calculations the frozen core consisted of the 1s orbitals on the heavy atoms. The geometry optimizations were performed using the Dalton Quantum Chemistry Program.²⁵ The calculations of the NMR shielding constants at the HF, MP2, and CC level of theory were performed using the Mainz-Austin-Budapest version of ACES II.^{26,27} The CC calculations were run either at the CCSD or the CCSD(T) level of theory. In the property calculations based on MP2 or CC all electrons were correlated. The calculations based on DFT were carried out with the Dalton²⁵ program employing either the B3LYP,⁶ PBE0,^{7,8} or the KT3⁹ *xc* functionals. The B3LYP and PBE0 are general hybrid functionals, whereas KT3 belongs to the group of GGA *xc* functionals. KT3 has been designed with the specific aim of providing high quality NMR shielding constants for light, main-group nuclei.⁹ This has been accomplished by an increase in the HOMO–LUMO gap. We emphasize however that no environmental effects have been considered in the parametrization of the KT3 *xc* functional. Using the PBE0 *xc* functional we have considered basis set superposition errors using the counterpoise approach.²⁸ In order to ensure origin-independent results for the NMR shielding constants, we use Gauge Including Atomic Orbitals.^{29–33} In this work we only consider isotropic NMR shielding constants.

III. Results and Discussion

In this section we will present the results of the calculations described in the preceding section. We begin by discussing the results obtained for isolated water and the water dimer and then continue to discuss the case of formaldehyde and the complex of formaldehyde with two water molecules.

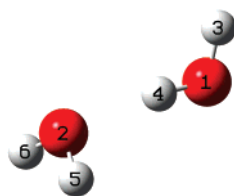
A. Water. 1. Basis Set Analysis. In Table 1 we present a basis set analysis for the NMR isotropic shielding constants $\sigma(^1\text{H})$ and $\sigma(^{17}\text{O})$ for the isolated water molecule. The calculations refer to CCSD(T) and various basis sets. As seen from Table 1 a reasonably fast basis set convergence is achieved when increasing the cardinal number (X) within the correlation consistent series of the aug-cc-pVXZ basis sets. The inclusion of the tight core functions in the aug-cc-pCVXZ basis sets is seen only to have an effect for the lowest cardinal number, i.e., X=D(2). In addition to the basis set analysis for the isolated water molecule, we present in Table 2 corresponding results for the water dimer (see Figure

Table 1. $\sigma(^1\text{H})$ and $\sigma(^{17}\text{O})$ NMR Isotropic Shielding Constants of Water (CCSD(T)/aug-cc-pVTZ Optimized Geometry) Calculated Using CCSD(T) and Various Basis Sets^a

basis	$\sigma(^1\text{H})$	$\sigma(^{17}\text{O})$
aug-cc-pVDZ	31.41	344.46
aug-cc-pCVDZ	31.39	342.79
aug-cc-pVTZ	30.89	336.67
aug-cc-pCVTZ	30.87	336.55
aug-cc-pVQZ	30.60	336.54
aug-cc-pCVQZ	30.59	336.15

^a Results are in units of ppm.**Table 2.** $\sigma(^1\text{H})$ and $\sigma(^{17}\text{O})$ NMR Isotropic Shielding Constants of Selected Nuclei in the Water Dimer (CCSD(T)/aug-cc-pVTZ Optimized Geometry) Calculated Using CCSD and Various Basis Sets^a

basis	$\sigma(^1\text{H4})$	$\sigma(^{17}\text{O1})$	$\sigma(^{17}\text{O2})$
aug-cc-pVDZ	28.45	340.63	337.25
aug-cc-pCVDZ	28.43	338.98	335.47
aug-cc-pVTZ	27.92	332.80	328.63
aug-cc-pCVTZ	27.90	332.54	328.58
aug-cc-pVQZ	27.58	332.36	328.59

^a Results are in units of ppm. See Figure 1 for the atom labeling.**Figure 1.** Atom labeling in the water dimer. (1,3,4) – proton donor, (2,5,6) – proton acceptor.

1 for the atom labeling). Due to computational demands the latter basis set analysis has been restricted to the CCSD level of theory. From Table 2 we observe the same trends as found from the calculation on the isolated water molecule, i.e., the NMR isotropic shielding constants are well converged using the aug-cc-pVTZ basis set. Based on the results presented in Tables 1 and 2, the aug-cc-pVTZ basis set was chosen for the rest of the calculations presented here for water and the water dimer.

2. Shifts in NMR Shielding Constants due to Hydrogen Bonding. Having found an appropriate basis set for the NMR shielding constant calculations, we now proceed to consider selected isotropic NMR shielding constants in the water dimer. Figure 1 shows the orientation of the individual water molecules within the dimer. In addition, it defines the atomic labels used in the following. The atoms 1, 3, and 4 constitute the proton donor, whereas the atoms 2, 5, and 6 define the proton acceptor. In the following we will restrict ourselves to consider atoms directly involved in the formation of the hydrogen bond, that is, atoms labeled 1, 2, and 4. For these atoms the absolute values of the isotropic NMR shielding constants are presented in Table 3. In addition, we have also included the results obtained for the isolated proton donor or acceptor using the same internal geometries as in the water dimer as well as the results for the isolated geometry

optimized water monomer. For the $\sigma(^{17}\text{O})$ we generally observe a good agreement between CCSD and CCSD(T), whereas the DFT based methods and HF tend to underestimate the shielding constants. On the other hand, the use of MP2 leads to overestimated results. At the CCSD(T) level of theory the difference in the donor–acceptor $\sigma(^{17}\text{O})$ amounts to around 4 ppm. Keeping the internal geometries of the water molecules, but otherwise treating them as isolated species, changes the same difference to around -1 ppm. We thereby observe that geometrical and polarization effects are in opposite directions. On average, the PBE0 functional is seen to perform slightly better than B3LYP or KT3, but the improvement is in any case small.

For $\sigma(^1\text{H})$ the inclusion of approximate triples is seen to have an almost negligible effect as compared to CCSD. In contrast to $\sigma(^{17}\text{O})$ both HF and MP2 now tend to underestimate the results, whereas the DFT based methods now give overestimated results with respect to CCSD(T) although the changes are much smaller than that found for $\sigma(^{17}\text{O})$.

Turning now to the core of this paper, we present DFT and wave function based results for the shifts in NMR shielding constants in Tables 4 and 5, respectively. In the following we will denote shifts due to hydrogen bonding by Δ . The shifts termed “Frozen” are calculated using the dimer geometry of the individual water molecules, whereas the shifts termed “Relaxed” are computed with respect to the isolated geometry optimized water molecule. The relaxed shifts are always more negative, i.e., the absolute values are larger than the corresponding frozen shifts. As seen from Table 4 only small deviations are found between the different *xc* functionals even though B3LYP seems to provide slightly larger magnitudes of the shifts. The BSSE corrected results based on the PBE0 *xc* functional are also listed in Table 4. Here we observe that the effect of BSSE is very small amounting to only around 2% of the total frozen shift for O2 and vanishes for H4 (i.e., the atoms defining the hydrogen bond). It has previously been stated that the effect of BSSEs are handled in an effective way using large and flexible basis sets including diffuse basis functions³⁴ which also is reflected by our findings. Comparing the shifts obtained with DFT to the corresponding results from the wave function calculations, we find a general decrease in the magnitude of the shifts. This is illustrated in Figure 2 which shows the “Frozen” and “Relaxed” $\Delta\sigma(^1\text{H4})$, $\Delta\sigma(^{17}\text{O2})$, and $\Delta\sigma(^{17}\text{O1})$ shifts for atoms in the water dimer with respect to the CCSD(T) predictions. Note that for O2 and H4 the HF model is found to provide surprisingly good results, whereas this model completely fails for O1. For this specific molecular system KT3 and PBE0 are seen to perform better than B3LYP, but no general improvement is seen on going from PBE0 to KT3.

In order to explore potential differences between the performance of PBE0 and KT3 in more detail, we have performed a series of calculations with varying lengths and angles of the hydrogen bond. In Figure 3 we have plotted the difference between the shifts due to hydrogen bonding in the NMR shielding constants for O2 obtained using PBE0 or KT3 and CCSD(T) as a function of the distance between the two oxygen atoms in the water dimer. The intramolecular

Table 3. $\sigma(^1\text{H})$ and $\sigma(^{17}\text{O})$ NMR Isotropic Shielding Constants of Water and the Water Dimer Calculated Using Various Electronic Structure Methods in Combination with the aug-cc-pVTZ Basis Set^a

	atom	site	B3LYP	PBE0	KT3	HF	MP2	CCSD	CCSD(T)
water dimer	O	1	322.09	324.64	322.93	326.08	340.04	332.80	333.27
	O	2	316.86	319.93	317.44	319.10	336.98	328.63	329.39
	H	4	28.08	28.02	28.46	27.52	27.75	27.92	27.95
proton donor	O	1	324.58	327.04	324.53	325.14	343.49	334.49	335.37
	H	4	30.92	30.82	31.23	30.34	30.38	30.63	30.65
proton acceptor	O	2	325.59	328.01	325.55	326.11	344.24	335.36	336.23
water monomer	O		326.09	328.50	326.05	326.58	344.64	335.80	336.67
	H		31.15	31.05	31.46	30.59	30.63	30.87	30.89

^a Results are in units of ppm. See Figure 1 for the atom labeling.

Table 4. $\Delta\sigma(^1\text{H})$ and $\Delta\sigma(^{17}\text{O})$ for the Atoms in the Water Dimer Computed Using DFT^a

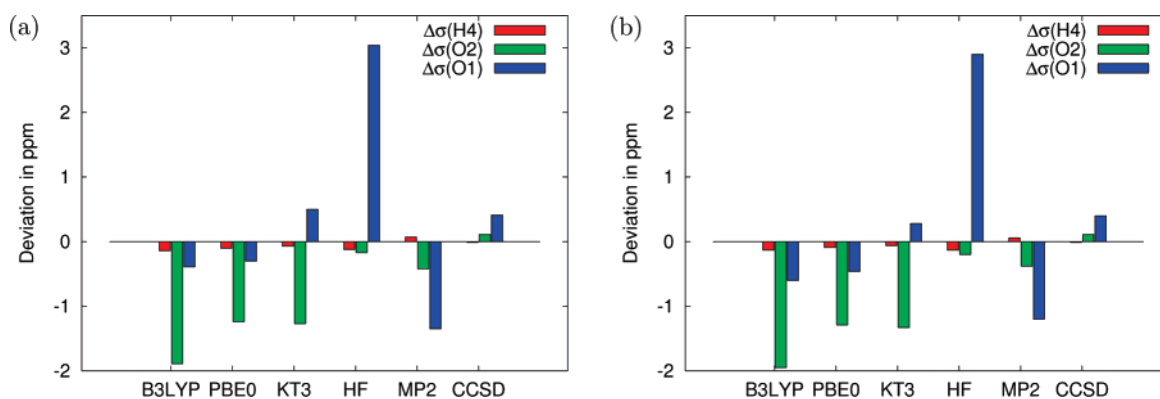
atom	site	B3LYP		PBE0		PBE0 (BSSE)	KT3	
		frozen	relaxed	frozen	relaxed	frozen	frozen	relaxed
O	1	-2.49	-4.00	-2.40	-3.86	-2.55	-1.60	-3.12
O	2	-8.73	-9.23	-8.08	-8.57	-7.87	-8.11	-8.61
H	4	-2.84	-3.07	-2.80	-3.03	-2.80	-2.77	-3.00

^a The shifts termed "Frozen" are calculated using the in-dimer geometry of the individual water molecules, whereas the shifts termed "Relaxed" are computed with respect to the isolated geometry optimized water molecule. The results indicated by PBE0(BSSE) have been corrected for BSSE. All molecular geometries have been optimized using CCSD(T)/aug-cc-pVTZ. Results are in units of ppm. See Figure 1 for the atom labeling.

Table 5. $\Delta\sigma(^1\text{H})$ and $\Delta\sigma(^{17}\text{O})$ for the Atoms in the Water Dimer Computed Using Various Wave Function Methods^a

atom	site	HF		MP2		CCSD		CCSD(T)	
		frozen	relaxed	frozen	relaxed	frozen	relaxed	frozen	relaxed
O	1	0.94	-0.50	-3.45	-4.60	-1.69	-3.00	-2.10	-3.40
O	2	-7.01	-7.48	-7.26	-7.66	-6.73	-7.17	-6.84	-7.28
H	4	-2.82	-3.07	-2.63	-2.88	-2.71	-2.95	-2.70	-2.94

^a The shifts termed "Frozen" are calculated using the in-dimer geometry of the individual water molecules, whereas the shifts termed "Relaxed" are computed with respect to the isolated geometry optimized water molecule. All molecular geometries have been optimized using CCSD(T)/aug-cc-pVTZ. Results are in units of ppm. See Figure 1 for the atom labeling.

**Figure 2.** (a) Frozen and (b) Relaxed shifts $\Delta\sigma(^1\text{H4})$, $\Delta\sigma(^{17}\text{O2})$, and $\Delta\sigma(^{17}\text{O1})$ for the atoms in the water dimer with respect to the corresponding CCSD(T) predictions. See Figure 1 for the atom labeling.

geometries of the individual water molecules have been kept frozen. From this figure we observe that results obtained using these two different *xc* functionals begin to diverge at O1–O2 separations shorter than the equilibrium geometry (2.914 Å). At O1–O2 distances within the range of the equilibrium values, the KT3 *xc* functional is seen to perform better than PBE0, i.e., it has smaller deviations with respect to the CCSD(T) predictions. A similar conclusion can be drawn from a set of similar calculations where now the hydrogen bond angle is changed. This is illustrated in Figure

4 which shows the difference between the shifts due to hydrogen bonding in the NMR shielding constants for O2 obtained using PBE0 or KT3 and CCSD(T) as a function of the deviation in the O1–H4–O2 angle with respect to the equilibrium geometry. The O1–H4–O2 angle in the equilibrium geometry is 171.6°. For very small changes in this angle, KT3 and PBE0 perform similarly, but for larger deviations KT3 tends to provide results in better agreement with CCSD(T). An important observation from Figure 4 is that the error, relative to CCSD(T), introduced using the KT3

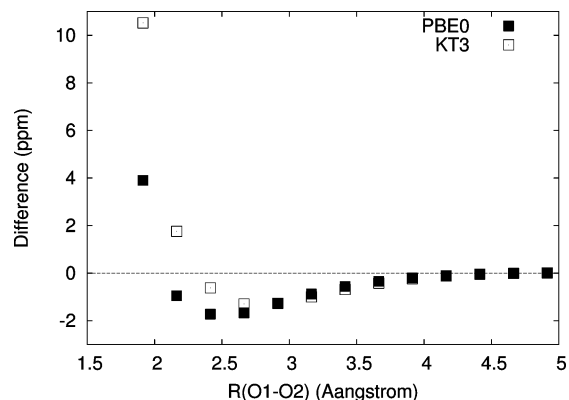


Figure 3. The intrinsic difference between DFT (PBE0 or KT3) and CCSD(T) with respect to the effect of hydrogen bonding on the isotropic NMR shielding constant of O2 (defined according to Figure 1) as a function of the distance between the two oxygen atoms in the water dimer. The intramolecular geometries of the individual water molecules have been kept frozen. The difference is defined as $\Delta\sigma_{DFT}^{O_2}(R) - \Delta\sigma_{CC}^{O_2}(R)$. The equilibrium distance in the water dimer is $R = 2.914 \text{ \AA}$. The basis set used is the aug-cc-pVTZ basis set.

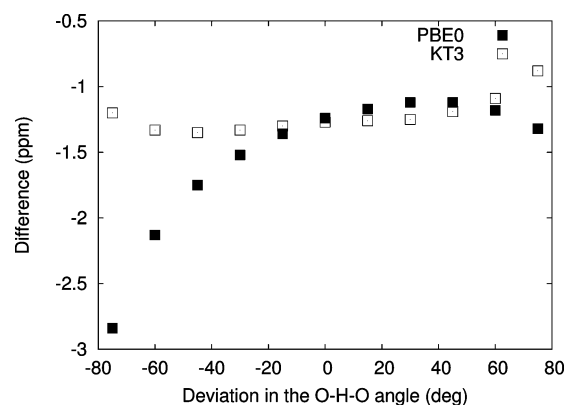


Figure 4. The intrinsic difference between DFT (PBE0 or KT3) and CCSD(T) with respect to the effect of hydrogen bonding on the isotropic NMR shielding of O2 (defined according to Figure 1) in the water dimer as a function of the deviation in the O1-H4-O2 angle (Θ) with respect to the equilibrium geometry. The intramolecular geometries of the individual water molecules have been kept frozen. The difference is defined as $\Delta\sigma_{DFT}^{O_2}(\Theta) - \Delta\sigma_{CC}^{O_2}(\Theta)$. The O1-H4-O2 angle in the equilibrium geometry is 171.6° . The basis set used is the aug-cc-pVTZ basis set.

xc functional is almost constant in a significant range. This is important since accurate models used to predict solvent effects on NMR shielding constants rely on a sampling over different solute-solvent configurations. For such a method to be valid it is important that the error in each calculation reflecting a specific configuration should be as constant as possible (and ideally equal to zero). Based on this reason we conclude that the most reliable xc functional to be considered in use for calculation of NMR shielding constants for systems like liquid water is likely to be KT3.

B. Formaldehyde. Having discussed the results for water and the water dimer we now turn to the case of formaldehyde and formaldehyde complexed with two water molecules.

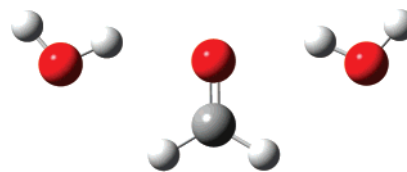


Figure 5. The hydrogen-bonded complex of formaldehyde and two water molecules as optimized using CCSD/aug-cc-pVTZ.

Table 6. $\sigma(^{13}\text{C})$ and $\sigma(^{17}\text{O})$ NMR Isotropic Shielding Constants of Formaldehyde Calculated Using CCSD^a

basis	$\sigma(^{13}\text{C})$	$\sigma(^{17}\text{O})$
aug-cc-pVDZ	29.25	-300.68
aug-cc-pCVDZ	24.78	-311.92
aug-cc-pVTZ	11.77	-354.20
aug-cc-pCVTZ	8.09	-363.60
aug-cc-pVQZ	6.02	-367.46
aug-cc-pCVQZ	3.74	-372.83
aug-cc-pV5Z	3.10	-374.52

^a The geometry used has been obtained from CCSD/aug-cc-pVTZ geometry optimization. Results are in units of ppm.

Apart from a purely academic point of view this system is interesting since formaldehyde is the smallest carbonyl compound thereby bearing the important chemistry of this class of systems. The structure of the complex of formaldehyde and 2 water molecules is illustrated in Figure 5. The complex possesses an overall C_{2v} symmetry.

1. Basis Set Analysis. In Table 6 we present a basis set analysis for the NMR isotropic shielding constants $\sigma(^{13}\text{C})$ and $\sigma(^{17}\text{O})$ of the isolated formaldehyde molecule. The calculations refer to CCSD and various basis sets and the geometry has been obtained from CCSD/aug-cc-pVTZ geometry optimization. As seen in Table 6, it is extremely difficult to get the shielding constants of formaldehyde converged. Thus, a significant change in shielding constant is observed on increasing the cardinal number from D(2) to T(3). But even when using the aug-cc-pV5Z basis set the results are not yet converged. For $\sigma(^{13}\text{C})$ this very slow basis set convergence has already been observed previously.¹⁰ However, in the present study our main interest is more in the effects induced by hydrogen bonds which means that we have to perform two separate calculations: one with and another without the hydrogen-bonding water molecules. Thereby, one could expect that, due to intrinsic error cancellation in the calculation of the shifts, converged results could be obtained using basis sets of modest size. In Table 7 we present results for the shifts due to hydrogen bonding (Δ) on the $\sigma(^{13}\text{C})$ and $\sigma(^{17}\text{O})$ NMR isotropic shielding constants of formaldehyde calculated using MP2. In addition we also list the absolute values of the shielding constants obtained for the isolated molecule or within the complex. In case of different basis sets used on formaldehyde or water, the nomenclature follows formaldehyde/water. From Table 7 we observe that even though the $\Delta\sigma(^{13}\text{C})$ is rather constant through the series of different basis sets, $\Delta\sigma(^{17}\text{O})$ changes significantly on increasing the cardinal number from D(2) to T(3). However, this is mainly due to the basis functions attached to formaldehyde as can be seen from the calculation

Table 7. $\sigma(^{13}\text{C})$ and $\sigma(^{17}\text{O})$ NMR Isotropic Shielding Constants of Formaldehyde Calculated Using MP2^a

basis	complex		monomer		induced	
	$\sigma(^{13}\text{C})$	$\sigma(^{17}\text{O})$	$\sigma(^{13}\text{C})$	$\sigma(^{17}\text{O})$	$\Delta\sigma(^{13}\text{C})$	$\Delta\sigma(^{17}\text{O})$
aug-cc-pVDZ	19.47	-217.31	28.22	-267.74	-8.75	50.43
aug-cc-pCVDZ	14.64	-228.33	23.52	-279.42	-8.88	51.09
aug-cc-pVTZ	1.00	-269.29	9.91	-325.28	-8.91	55.99
aug-cc-pCVTZ	-3.19	-277.84	5.94	-335.43	-9.13	57.59
aug-cc-pVTZ/aug-cc-pVDZ	1.02	-270.38	9.91	-325.28	-8.89	54.90
aug-cc-pVQZ/aug-cc-pVDZ	-5.15	-282.03	3.92	-338.50	-9.07	56.47

^a In case of different basis sets used on formaldehyde or water the nomenclature follows formaldehyde/water. Results are in units of ppm.

Table 8. $\sigma(^{13}\text{C})$ and $\sigma(^{17}\text{O})$ NMR Isotropic Shielding Constants of Formaldehyde Calculated Using CCSD or CCSD(T)^a

method	basis	complex		monomer		induced	
		$\sigma(^{13}\text{C})$	$\sigma(^{17}\text{O})$	$\sigma(^{13}\text{C})$	$\sigma(^{17}\text{O})$	$\Delta\sigma(^{13}\text{C})$	$\Delta\sigma(^{17}\text{O})$
CCSD	aug-cc-pVDZ	17.17	-248.61	25.73	-321.58	-8.56	72.97
	aug-cc-pVTZ/aug-cc-pVDZ	-0.88	-299.83	7.80	-376.85	-8.68	77.02
CCSD(T)	aug-cc-pVDZ	18.57	-248.31	26.93	-319.44	-8.36	71.13
	aug-cc-pVTZ/aug-cc-pVDZ	0.79	-298.68	9.31	-372.85	-8.52	74.17

^a Results are in units of ppm.

Table 9. $\sigma(^{13}\text{C})$ and $\sigma(^{17}\text{O})$ NMR Isotropic Shielding Constants of Formaldehyde^a

	atom	B3LYP	PBE0	KT3	HF	MP2	CCSD	CCSD(T)
H ₂ CO + 2H ₂ O	O	-362.57	-361.18	-294.36	-336.45	-270.38	-299.83	-298.68
	C	-28.63	-25.62	-4.14	-13.91	1.02	-0.88	0.79
H ₂ CO frozen	O	-451.96	-452.77	-366.06	-446.37	-325.28	-376.85	-372.85
	C	-19.53	-16.51	3.98	-5.78	9.91	7.80	9.31
H ₂ CO relaxed	O	-426.17	-426.87	-343.87	-419.03	-306.17	-354.20	-350.63
	C	-14.95	-11.97	7.64	-0.16	13.08	11.77	12.99

^a The basis set used is aug-cc-pVTZ/aug-cc-pVDZ. Results are in units of ppm.

with the aug-cc-pVDZ basis set on water and the aug-cc-pVTZ basis set on formaldehyde, whose results are only slightly changed compared to the results with the aug-cc-pVTZ basis sets on all atoms in the complex. On the other hand, the results for the shift obtained using the mixed aug-cc-pVTZ/aug-cc-pVDZ basis set are to be considered fairly converged as clearly can be seen from the fact that increasing the cardinal number in the basis set used on formaldehyde from T(3) to Q(4) only changes $\Delta\sigma(^{13}\text{C})$ by around -0.2 ppm and $\Delta\sigma(^{17}\text{O})$ by 1.5 ppm. Including tight core functions in the basis set only gives rise to similar small changes. If not stated differently in the following we will thereby use the mixed aug-cc-pVTZ/aug-cc-pVDZ basis set, that is, aug-cc-pVTZ basis on formaldehyde and aug-cc-pVDZ basis on the water molecules complexing formaldehyde.

To illustrate the effect of further electron correlation we present in Table 8 the corresponding results as reported in Table 7 but employing a higher level of correlation, i.e., using CCSD or CCSD(T). Two basis sets have been used, i.e., the aug-cc-pVDZ and the mixed aug-cc-pVTZ/aug-cc-pVDZ basis sets. Compared to MP2, we observe that the magnitude of $\Delta\sigma(^{13}\text{C})$ is slightly decreased, whereas correlation affects $\Delta\sigma(^{17}\text{O})$ to a much higher level. Thus, using the mixed basis set and changing from MP2 to CCSD leads to an increase in $\Delta\sigma(^{17}\text{O})$ of around 22 ppm, whereas including effects of triples excitations as described by CCSD(T) reduces this increase by about 3 ppm. We thereby already at this stage find that different levels of electronic correlation may affect the computed shifts of NMR shielding constants significantly.

2. Shifts in NMR Shielding Constants due to Hydrogen Bonding. In Table 9 we report the absolute $\sigma(^{13}\text{C})$ and $\sigma(^{17}\text{O})$ NMR isotropic shielding constants of formaldehyde obtained either in the complex with two water molecules (first entry), for isolated formaldehyde employing the in-complex geometry (second entry) or for isolated geometry optimized formaldehyde (third entry). In the property calculations we have used the mixed aug-cc-pVTZ/aug-cc-pVDZ basis set. As seen from Table 9, geometry relaxation of formaldehyde influences the results significantly. For example, at the CCSD(T) level of theory this effect amounts to around 22 ppm for $\sigma(^{17}\text{O})$. The main changes in geometry of formaldehyde upon complexation with two water molecules is an increase in the CO bond length. The effect of variations in the CO bond length in carbonyl compounds on the $\sigma(^{17}\text{O})$ NMR isotropic shielding constants have previously been considered^{39,40} and found to be significant. In general terms we observe from Table 9 that the use of the B3LYP and PBE0 *xc* functionals provide results in reasonable agreement with each other but far from the CCSD(T) predictions. In fact, the magnitude of the B3LYP and PBE0 results is too large which is mainly due to the well-known tendency of DFT to overestimate the paramagnetic contribution to the shielding constants (see for example the discussion in ref 35). However, this artifact is removed by employing the KT3 *xc* functional, which is now seen to provide results in significantly better agreement with CCSD(T). Even the sign of the absolute $\sigma(^{13}\text{C})$ shielding constant, which is predicted wrong by B3LYP and PBE0, is now in agreement with

Table 10. $\Delta\sigma(^{13}\text{C})$ and $\Delta\sigma(^{17}\text{O})$ for the Atoms in the Formaldehyde Computed Using DFT^a

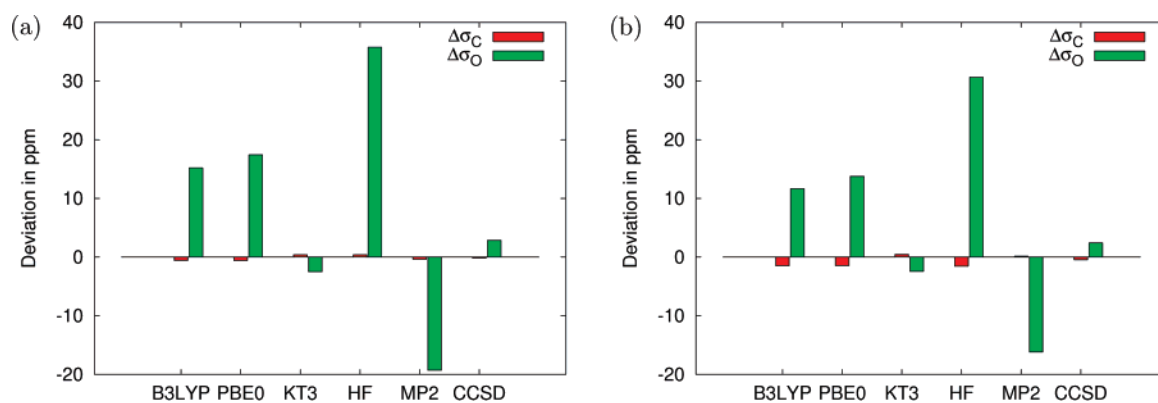
atom	B3LYP		PBE0		PBE0(BSSE)	KT3	
	frozen	relaxed	frozen	relaxed	frozen	frozen	relaxed
O	89.39	63.6	91.59	65.69	92.05	71.70	49.51
C	-9.10	-13.68	-9.11	-13.65	-9.15	-8.12	-11.78

^a The shifts termed "Frozen" are calculated using the formaldehyde geometry as in its complex with two water molecules, whereas the shifts termed "Relaxed" are computed with respect to the isolated geometry optimized formaldehyde molecule. The results indicated by PBE0(BSSE) have been corrected for BSSE. Results are in units of ppm.

Table 11. $\Delta\sigma(^{13}\text{C})$ and $\Delta\sigma(^{17}\text{O})$ for the Atoms in Formaldehyde Computed Using Various Wave Function Methods^a

atom	HF		MP2		CCSD		CCSD(T)	
	frozen	relaxed	frozen	relaxed	frozen	relaxed	frozen	relaxed
O	109.92	82.58	54.90	35.79	77.02	54.37	74.17	51.95
C	-8.13	-13.75	-8.89	-12.06	-8.68	-12.65	-8.52	-12.20

^a The shifts termed "Frozen" are calculated using the formaldehyde geometry as in its complex with two water molecules, whereas the shifts termed "Relaxed" are computed with respect to the isolated geometry optimized formaldehyde molecule. Results are in units of ppm.

**Figure 6.** (a) Frozen and (b) Relaxed $\Delta\sigma(^{13}\text{C})$ and $\Delta\sigma(^{17}\text{O})$ for the atoms in formaldehyde with respect to the corresponding CCSD(T) predictions.

CCSD(T). Concerning the wave function based methods, HF gives exaggerated results even though the HF predictions for the absolute shielding constants show a slight improvement as compared to B3LYP and PBE0. For MP2, on the other hand, we generally observe good agreement for $\sigma(^{13}\text{C})$, as compared to CCSD(T), but the MP2 predictions for $\sigma(^{17}\text{O})$ tend to be underestimated. Thereby, the HF and MP2 results are found to be placed opposite relative to the CCSD(T) predictions. The CCSD results are generally close to the CCSD(T) predictions. In summary we find that the KT3 *xc* functional gives results of near CC quality for $\sigma(^{17}\text{O})$, whereas it is slightly less successful in predicting $\sigma(^{13}\text{C})$ confirming earlier findings for small molecules.²³

Turning now to the effect of the hydrogen bonds on the NMR shielding constants we present in Tables 10 and 11 results based on either DFT (Table 10) or wave function theory (Table 11). As for the water dimer we have included shifts with respect to either a relaxed or frozen (using the in-complex geometry) isolated formaldehyde molecule. For PBE0 we have also included results taking into account the BSSE. Here we find, as for the water dimer, that this only affects the shifts slightly, i.e., around 0.5 ppm for ^{17}O and 0.04 ppm for ^{13}C . As for the case of the absolute NMR shielding constants, we observe from Table 10 a marked difference in the performance of KT3 versus B3LYP or PBE0. The shifts obtained using B3LYP or PBE0 are always larger in magnitude as compared to the KT3 results, i.e.,

using KT3 instead of either B3LYP or PBE0 reduces the magnitude of the frozen $\Delta\sigma(^{17}\text{O})$ and $\Delta\sigma(^{13}\text{C})$ shifts around 18 and 1 ppm, respectively. However, the KT3 shifts are in very good agreement with the results based on CC and specially CCSD(T). Thus we find also for the shift a very good agreement between DFT/KT3 and CCSD(T). The same observation is found for the relaxed shifts. From Table 11 we observe that even though the MP2 results for $\Delta\sigma(^{13}\text{C})$ are in good agreement with CCSD(T), the corresponding MP2 predictions of $\Delta\sigma(^{17}\text{O})$ are severely underestimated. We are thereby left with the conclusion that, for the $\Delta\sigma(^{17}\text{O})$, B3LYP and PBE0 overestimate the shift due to hydrogen bonding, whereas MP2 severely underestimates this quantity. The many-body electronic structure methods are found to provide results for $\Delta\sigma(^{17}\text{O})$ according to

$$\text{HF} > \text{B3LYP} \approx \text{PBE0} > \text{CCSD} \approx \text{CCSD(T)} \approx \text{KT3} > \text{MP2}$$

For $\Delta\sigma(^{13}\text{C})$, on the other hand, all methods give reasonable results although B3LYP and PBE0 tend to overestimate slightly the effect of the water molecules. This is illustrated in Figure 6 where we have plotted the error in the shift in the NMR shielding constants relative to CCSD(T).

As for the water dimer, further potential differences between the performance of B3LYP/PBE0 and KT3 may be explored by varying the effect of the hydrogen bond strength. This may be done, for example, by changing the length or the angle of the hydrogen bond. In Figure 7 we

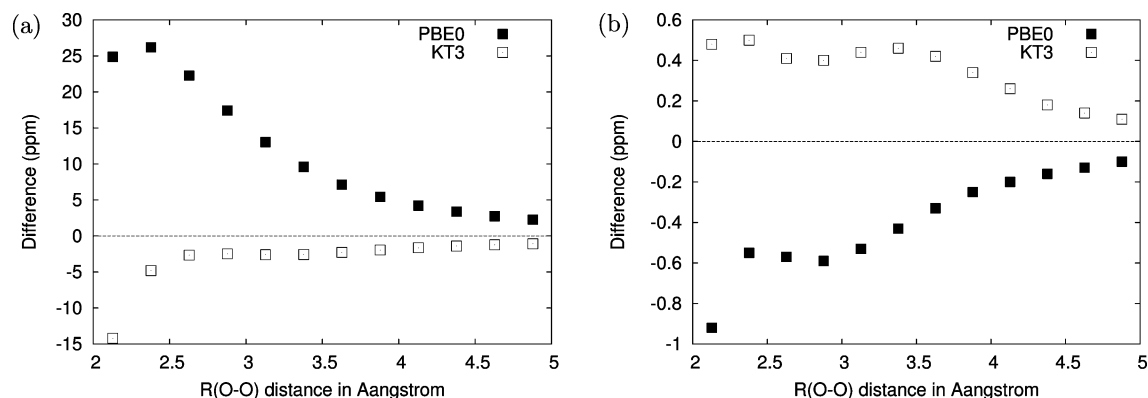


Figure 7. The intrinsic difference between DFT (PBE0 or KT3) and CCSD(T) with respect to the effect of hydrogen bonding on the isotropic NMR shielding constant of the (a) oxygen or (b) carbon atoms in formaldehyde as a function of the distance between the water and formaldehyde oxygen atoms. The water molecules have been displaced symmetrically, and the intramolecular geometries of the individual water molecules have been kept frozen. The difference is defined as $\Delta\sigma_{DFT}^X(R) - \Delta\sigma_{CC}^X(R)$ ($X=C,O$). The equilibrium distance is $R = 2.878 \text{ \AA}$.

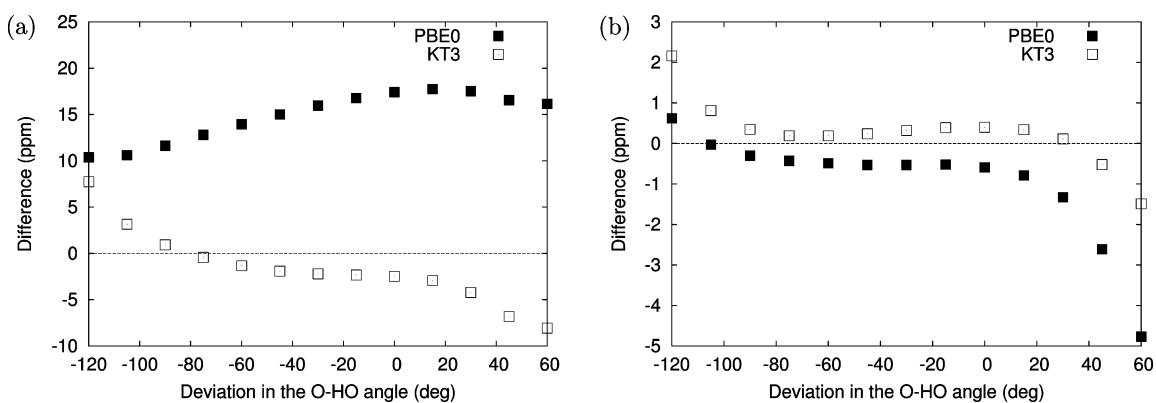


Figure 8. The intrinsic difference between DFT (PBE0 or KT3) and CCSD(T) with respect to the effect of hydrogen bonding on the isotropic NMR shielding constant of the (a) oxygen or (b) carbon atoms in formaldehyde as a function of the deviation in the O–HO angle (Θ) with respect to the equilibrium geometry. This angle is defined as O(formaldehyde)–HO(water) and is in the equilibrium geometry equal to 144.5° . The difference is defined as $\Delta\sigma_{DFT}^X(\Theta) - \Delta\sigma_{CC}^X(\Theta)$ ($X=C,O$). The intramolecular geometries of the individual water molecules have been kept frozen.

have plotted the intrinsic difference between the DFT (PBE0 or KT3) and CCSD(T) isotropic NMR shielding constant of the oxygen (a) or carbon (b) atoms in formaldehyde as a function of the distance between the water and formaldehyde oxygen atoms. The water molecules have been displaced symmetrically, and the intramolecular geometries of the individual water molecules have been kept frozen. The equilibrium distance is $R = 2.878 \text{ \AA}$. From this figure we observe that the use of the KT3 *xc* functional generally leads to smaller errors as introduced by using the PBE0 *xc* functional. In addition, for KT3 this error is relatively constant over a wider range as compared to PBE0. The potential advantages of this observation are the same as discussed for the water dimer. A similar conclusion can be drawn from a set of calculations where the hydrogen bond angle is changed. This is illustrated in Figure 8 which shows the intrinsic difference between DFT (PBE0 or KT3) and CCSD(T) isotropic NMR shielding constant of the oxygen (a) or carbon (b) atoms in formaldehyde as a function of the deviation in the O–HO angle with respect to the equilibrium geometry. This angle is defined as O(formaldehyde)–HO(water) and is in the equilibrium geometry equal to

144.5° . The intramolecular geometries of the individual water molecules have been kept frozen. From this figure we again observe not only that KT3 provides results for the shift due to hydrogen bonding with a smaller error but also that this error stays relatively constant over a wide range in the hydrogen bond angle. Thus we have clearly shown the advantages of using the KT3 *xc* functional in calculations of NMR shielding constants. Furthermore, according to our findings KT3 should provide both absolute and hydrogen bond induced shifts in the NMR shielding constants at the same accuracy obtained from use of high level wave function based methods, e.g., CCSD(T).

We end this section by a discussion concerning the origin of the observed shifts in NMR shielding constants due to hydrogen bonding. We will only consider the case of formaldehyde in complex with two water molecules and focus on the effect of the hydrogen bond length on $\sigma(^{17}\text{O})$. The effect due to the two water molecules on the NMR shielding constant may generally be divided into electrostatic and nonelectrostatic intermolecular interactions. The latter mainly contains dispersion, short-range repulsion, and charge transfer. In the presented calculations both effects are

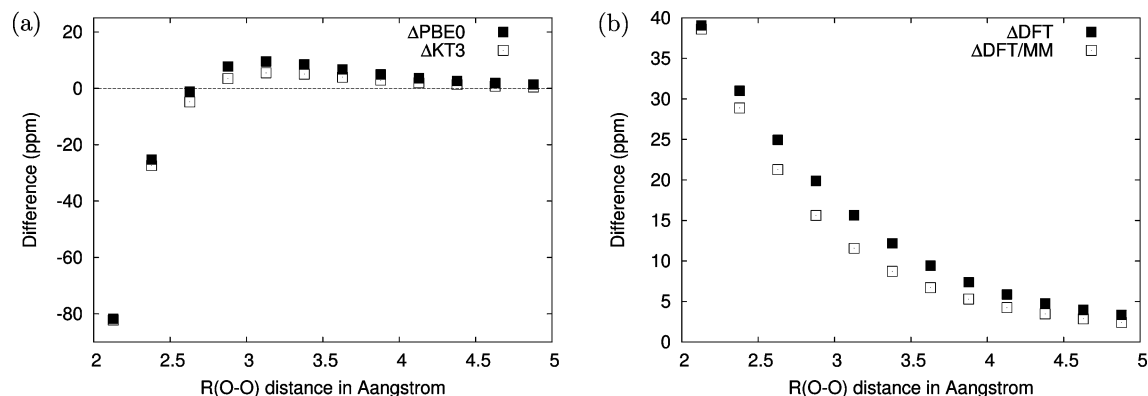


Figure 9. (a) The nonelectrostatic contribution to the $\sigma(^{17}\text{O})$ in formaldehyde due to hydrogen bonding. $\Delta F = \sigma^F - \sigma^{F/MM}$ ($F = \text{PBE0,KT3}$). (b) The difference between the (absolute) $\sigma(^{17}\text{O})$ as calculated using either PBE0 and KT3 (ΔDFT) or the corresponding difference calculated using PBE0/MM and KT3/MM ($\Delta\text{DFT/MM}$).

included in the quantum mechanical calculations on the cluster (supermolecule). It is, however, possible to treat only formaldehyde using quantum mechanics and describe the presence of the water molecules in an effective manner. In the following we will compare the results of such a hybrid quantum-classical approach, in which only electrostatic interactions are accounted for, with the supermolecular results. Thereby, we are in a position to estimate the relative importance of either electrostatic or nonelectrostatic intermolecular effects. In the hybrid quantum-classical approach, generally referred to as the DFT/MM model, we describe each water molecule by assigning partial point charges to the nuclei, and in addition we include an electric polarizability at the water oxygen site. The latter gives rise to induction (many-body) effects, i.e., we do *not* assume a pairwise interaction model. The theoretical and implementational aspects of the DFT/MM model have been detailed in ref 5 as well as the ability to calculate origin independent magnetic properties.³⁶ Different approaches could be used for the derivation of the water molecule parameters describing the electrostatic interactions. For example, partial charges could be calculated using the supermolecule. In this case no polarizability should be assigned to the water molecules since the effect of polarization by formaldehyde is automatically reflected in the charges. However, in such an approach, due to charge transfer between water and formaldehyde, the preceding DFT/MM calculation would generally involved partially charged water molecules. Therefore, we use in the DFT/MM calculation a well-defined water potential.³⁷ In Figure 9(a) we show the effect of mainly nonelectrostatic contributions to $\sigma(^{17}\text{O})$ calculated using either PBE0 or KT3. For each xc functional we have subtracted from the supermolecular prediction of $\sigma(^{17}\text{O})$ the electrostatic component obtained from DFT/MM calculations. Figure 9(a) clearly shows that for short hydrogen bond distances the effect of nonelectrostatic contributions becomes significant. This has previously been discussed by Peralta et al.³⁸ In addition we observe that the two xc functionals describe in a qualitative manner the nonelectrostatic component very similar. This indicates that the difference between the performance of the PBE0 and KT3 xc functionals with respect to CCSD(T) predictions (Figure 7) is mainly due to a different treatment of the electrostatic effects by the two xc functionals. Further

proof for this is found in Figure 9(b) where the differences are shown between the PBE0 and KT3 results for (absolute) $\sigma(^{17}\text{O})$ calculated using either the supermolecular or the quantum-classical approach. From Figure 9(b) it is evident that accounting only for the electrostatic intermolecular interaction effects (DFT/MM) reproduces qualitatively the differences between the PBE0 and KT3 results as obtained from the supermolecular (DFT) calculations.

IV. Discussion and Conclusions

In this paper we have presented the first systematic investigation of the shifts in nuclear magnetic resonance shielding constant due to hydrogen bonds using either the series of wave function based methods HF, MP2, CCSD, and CCSD(T) or DFT employing the B3LYP, PBE0, or KT3 xc functionals. We have considered the water dimer and formaldehyde in complex with two water molecules. For these small prototype hydrogen-bonded molecular systems we have presented a systematic study of the effect of various electronic structure methods on the NMR isotropic shieldings. We have especially focused on the performance of the DFT based methods as compared to the corresponding results derived using CCSD(T). The absolute NMR shielding constants are found to be very dependent on both the choice of the many-body electronic structure method and the basis set used in the calculations. For example we fail to observe a basis set convergence for $\sigma(^{17}\text{O})$ in isolated formaldehyde even when using a basis set of aug-cc-pV5Z size and quality. However, the shift in the NMR shielding constants due to complexation with two water molecules shows a relatively fast basis set convergence which is attributed to a cancellation of errors. While the DFT methods perform reasonably in accounting for the shift in the ^1H (water) and ^{13}C (formaldehyde) NMR shielding constants due to complexation, less satisfactory results are obtained for the ^{17}O NMR shielding constants. Especially in the case of formaldehyde complexed with two hydrogen-bonding water molecules we find, using either B3LYP or PBE0, significantly too large results as compared to CCSD(T). This overestimation is, however, even more severe when using a HF description of the molecular system. On the other hand, the error introduced by using MP2 is of the same magnitude as that of B3LYP/PBE0 but of opposite sign. In contrast to these failures, the KT3 xc

functional is found to provide very accurate results for both the absolute and hydrogen bond shifted ^{17}O NMR shielding constants. Also, when considering intermolecular distortions, KT3 performs reasonably as compared to CCSD(T) and in any case completely outperforms B3LYP and PBE0. This fact is very important when considering calculations of NMR shielding constants based on combined quantum mechanical and statistical methods, where it is mandatory that the NMR shielding constants derived from different solute–solvent configurations are of similar quality, i.e., that the error in the property calculations does not fluctuate between individual calculations.

Even though the molecular systems under scrutiny in this study are small, they represent model systems for more complex or larger samples, for example for acetone or other carbonyl compounds solvated by water. Therefore, our conclusions are of significant importance for the benchmarking of solvent models for quantitative NMR predictions. Recently many popular solvent models, based on either an implicit or explicit description of the solvent, employ DFT. But in fact very little is known about the performance of DFT versus correlated wave function descriptions for solute–solvent interactions. Within this context, the use of DFT has been benchmarked by performing MP2 calculations. This is for example the case in refs 39 and 40, which concern combined quantum mechanics/molecular mechanics or combined quantum mechanics/polarizable continuum model calculations of NMR shielding constants of either formaldehyde or acetone in liquid water. In these studies, DFT was found to give good results for the solvent shift in the ^{17}O NMR shielding constant, particularly, when employing a solvent model which includes electronic polarization explicitly. MP2, on the other hand, was found to underestimate the shifts due to hydrogen bonding. Based on the findings in the present study, part of the success of the theoretical predictions presented in refs 39 and 40 may be attributed to the use of *xc* functionals which artificially overestimate the effect of the solvent on the studied molecular properties. The use of MP2, on the other hand, leads to a severe underestimation of the shifts which, according to the findings presented in this work, is directly attributed to the intrinsic performance of the MP2 model. The overall good agreement between theory and experiment obtained in the DFT based simulations in refs 39 and 40 may on these grounds partly be attributed to error cancellations due to (i) the use of *xc* functionals which overestimate the effect of the solvent, (ii) the use of inaccurate force-fields in the molecular dynamics and combined quantum mechanics/molecular mechanics calculations, and (iii) the neglect of differential zero-point vibrational corrections.⁴¹

Acknowledgment. The authors thank the Danish Center for Scientific Computing (DCSC) for computational resources. J.K. acknowledges support from the Villum Kann Rasmussen Foundation (Denmark). K.V.M. thanks Forskningsrådet for Natur og Univers (FNU) and the EU network NANOQUANT for support. SPAS thanks Forskningsrådet for Natur og Univers (FNU) and the Carlsberg Foundation.

References

- (1) Jeffrey, G. A.; Saenger, W. *Hydrogen bonding in biological structures*; Springer-Verlag: Berlin, 1991.
- (2) Steiner, T. *Angew. Chem., Int. Ed.* **2002**, *41*, 48.
- (3) Ireta, J.; Neugebauer, J.; Scheffler, M. *J. Phys. Chem. A* **2004**, *108*, 5692.
- (4) MacDonald, J. C.; Whitesides, G. M. *Chem. Rev.* **1994**, *94*, 2383.
- (5) Nielsen, C. B.; Christiansen, O.; Mikkelsen, K. V.; Kongsted, J. *J. Chem. Phys.* **2007**, *126*, 154112.
- (6) Becke, A. D. *J. Chem. Phys.* **1993**, *98*, 5648.
- (7) Ernzerhof, M.; Scuseria, G. E. *J. Chem. Phys.* **1999**, *110*, 5029.
- (8) Adamo, C.; Barone, V. *J. Chem. Phys.* **1999**, *110*, 6158.
- (9) Keal, T. W.; Tozer, D. J. *J. Chem. Phys.* **2004**, *121*, 5654.
- (10) Auer, A. A.; Gauss, J.; Stanton, J. F. *J. Chem. Phys.* **2003**, *118*, 10407.
- (11) Parker, L. L.; Houk, A. R.; Jensen, J. H. *J. Am. Chem. Soc.* **2006**, *128*, 9863.
- (12) Krishna, N. R.; Berliner, L. J. *Biological Magnetic Resonance*; Kluwer/Plenum: New York, 1998–2003; Vol. 16–17, p 20.
- (13) Kussmann, J.; Ochsenfeld, C. *J. Chem. Phys.* **2007**, *127*, 054103.
- (14) Helgaker, T.; Jaszunski, M.; Ruud, K. *Chem. Rev.* **1999**, *99*, 293.
- (15) Gauss, J.; Stanton, J. F. *J. Chem. Phys.* **1996**, *104*, 2574.
- (16) Gauss, J.; Stanton, J. F. *J. Chem. Phys.* **1995**, *102*, 251.
- (17) Gauss, J.; Stanton, J. F. *J. Chem. Phys.* **1995**, *103*, 3561.
- (18) Gauss, J. *Chem. Phys. Lett.* **1992**, *191*, 614.
- (19) Cheeseman, J. R.; Trucks, G. W.; Keith, T. A.; Frisch, M. J. *J. Chem. Phys.* **1996**, *104*, 5497.
- (20) Lee, A. M.; Handy, N. C.; Colwell, S. M. *J. Chem. Phys.* **1995**, *103*, 10095.
- (21) Malkin, V. G.; Malkina, O. L.; Salahub, D. R. *Chem. Phys. Lett.* **1993**, *204*, 80.
- (22) Helgaker, T.; Wilson, P. J.; Amos, R. D.; Handy, N. C. *J. Chem. Phys.* **2000**, *113*, 2983.
- (23) Ligabue, A.; Sauer, S. P. A.; Lazzarotti, P. *J. Chem. Phys.* **2007**, *126*, 154111.
- (24) Kendall, R. A.; Dunning, T. H.; Harrison, R. J. *J. Chem. Phys.* **1992**, *96*, 6796.
- (25) Angeli, C.; Bak, K. L.; Bakken, V.; Christiansen, O.; Cimraglia, R.; Coriani, S.; Dahle, P.; Dalskov, E.; Enevoldsen, T.; Fernandez, B.; Hättig, C.; Hald, K.; Heiberg, H.; Helgaker, T.; Hettema, H.; Jensen, H. J. A.; Jonsson, D.; Jørgensen, P.; Kirpekar, S.; Klopper, W.; Kobayashi, R.; Koch, H.; Ligabue, A.; Lutnæs, O. B.; Mikkelsen, K. V.; Norman, P.; Olsen, J.; Packer, M. J.; Pedersen, T. B.; Rinkevicius, Z.; Rudberg, E.; Ruden, T. A.; Ruud, K.; Salek, P.; Sanchez de Merás, A.; Saue, T.; Sauer, S. P. A.; Schimmelpfennig, B.; Sylvester-Hvid, K. O.; Tayler, P. R.; Vahtras, O.; Wilson, D. J.; Ågren, H. *Dalton, a molecular electronic structure program; Release 2.0*; 2005. See <http://www.kjemi.uio.no/software/dalton/dalton.html> ed.

- (26) Aces II Mainz-Austin-Budapest version. Stanton, J. F.; Gauss, J.; Watts, J. D.; Szalay, P. G.; Bartlett, R. J. with contributions from Auer, A. A.; Bernholdt, D. B.; Christiansen, O.; Harding, M. E.; Heckert, M.; Heun, O.; Huber, C.; Jonsson, D.; Jusélius, J.; Lauderdale, W. J.; Metzroth, T.; Michauk, C.; Price, D. R.; Ruud, K.; Schiffmann, F.; Tajti, A.; Varner, M. E.; Vázquez, J. and the integral packages: Molecule (Almlöf, J.; Taylor, P. R.), Props (Taylor, P. R.), and Abacus (Helgaker, T.; Jensen, H. J. A.; Jørgensen, P.; Olsen, J.). See <http://www.aces2.de>.
- (27) Stanton, J. F.; Gauss, J.; Watts, J. D.; Lauderdale, W. J.; Bartlett, R. J. *Int. J. Quantum Chem. Symp.* **1992**, 26, 879.
- (28) Boys, S. F.; Bernardi, F. *Mol. Phys.* **1970**, 19, 553.
- (29) London, F. *J. Phys. Radium* **1937**, 8, 397.
- (30) Hameka, H. F. *Rev. Mod. Phys.* **1962**, 34, 87.
- (31) Ditchfield, R. *Mol. Phys.* **1974**, 27, 789.
- (32) Wolinski, K.; Hinton, J. F.; Pulay, P. *J. Am. Chem. Soc.* **1990**, 112, 8251.
- (33) Helgaker, T.; Jørgensen, P. *J. Chem. Phys.* **1991**, 95, 2595.
- (34) Karadakov, P. B. *J. Mol. Struct.* **2002**, 602–603, 293.
- (35) Wu, A.; Cremer, D.; Gauss, J. *J. Phys. Chem. A* **2003**, 107, 8737.
- (36) Kongsted, J.; Nielsen, C. B.; Mikkelsen, K. V.; Christiansen, O.; Ruud, K. *J. Chem. Phys.* **2007**, 126, 034510.
- (37) Ahlström, P.; Wallqvist, A.; Engström, S.; Jönsson, B. *Mol. Phys.* **1989**, 68, 563.
- (38) Peralta, J. E.; Ruiz de Azua, M. C.; Contreras, R. H. *J. Mol. Struct. (Theochem)* **1999**, 491, 23.
- (39) Pavone, M.; Brancato, G.; Morelli, G.; Barone, V. *Chem. Phys. Chem.* **2006**, 7, 148.
- (40) Aidas, K.; Møgelhøj, A.; Kjær, H.; Nielsen, C. B.; Mikkelsen, K. V.; Ruud, K.; Christiansen, O.; Kongsted, J. *J. Phys. Chem. A* **2007**, 111, 4199.
- (41) Kongsted, J.; Ruud, K. *Chem. Phys. Lett.* **2007**, doi: 10.106/j.cplett.2007.12.008.

CT700285J

DFT Approach to the Calculation of Mössbauer Isomer Shifts

Reshmi Kurian and Michael Filatov*

Theoretical Chemistry, Zernike Institute for Advanced Materials, Rijksuniversiteit Groningen, Nijenborgh 4, 9747 AG Groningen, The Netherlands

Received September 7, 2007

Abstract: With the help of a recently suggested computational scheme [*J. Chem. Phys.* **2007**, *127*, 084101], Mössbauer isomer shifts are calculated within the context of density functional theory, for a series of iron containing compounds. The influence of the choice of a density functional and of the truncation of a basis set on the results of calculations is analyzed. It has been observed that the hybrid density functionals, especially BH&HLYP, provide better correlation with experimental results than pure density functionals. The analysis of basis set truncation reveals that the addition (or removal) of the tightmost primitive functions to a large uncontracted basis set has only a minor influence on the calculated isomer shift values. It is observed that, with the use of a small contracted basis set, a reasonable accuracy for the calculated isomer shifts can be achieved.

I. Introduction

Mössbauer spectroscopy¹ is a powerful analytic tool which enables one to obtain valuable information about the geometric and electronic structure of chemical compounds.^{2–7} The method is based on the Mössbauer effect¹ which is the recoil emission/absorption of γ radiation from a solid sample.^{2–4} The most well-known application of Mössbauer spectroscopy is for the determination of ⁵⁷Fe in metal complexes. However, there exist more than 40 other elements in the periodic table which possess γ -active isotopes and for which the Mössbauer spectra can be obtained.^{2–5} Due to the high sensitivity of the method and its independence on the perfect crystalline structure of the samples, Mössbauer spectroscopy finds an ever increasing number of applications which range from biological chemistry⁶ and nanotechnology⁷ to materials science.⁴

One of the most important characteristics of the Mössbauer spectrum is the so-called Mössbauer isomer shift (MIS).⁸ MIS is the measure of the energy difference between the γ -transitions in the source (E_s) and the absorber (E_a) nuclei. Commonly MIS, δ in eq 1, is measured in terms of the Doppler velocity necessary to achieve resonance absorption of γ -radiation.

$$\delta = \frac{c}{E_\gamma} (E_a - E_s) \quad (1)$$

Within the standard approach to the Mössbauer effect,^{2,3,10–16} the MIS is connected to the electron density at the nucleus via eq 2

$$\delta = \frac{c}{E_\gamma} \frac{4\pi}{5} ZS(Z)R^2 \left(\frac{\Delta R}{R}\right) (\bar{\rho}_e^a - \bar{\rho}_e^s) \quad (2)$$

where E_γ is the energy of the nuclear γ -transition, c is the velocity of light, Z and R are the nuclear charge and radius, ΔR is the variation of the nuclear radius, and $\bar{\rho}_e^a$ and $\bar{\rho}_e^s$ are the average electronic densities inside the absorber and the source nucleus, respectively.

According to eq 2, it is the variation of nuclear volume during Mössbauer γ -transition that is responsible for the occurrence of MIS.^{2,3,9} This equation is most straightforwardly derived within the nonrelativistic formalism. Within this formalism, the electron density remains finite in the vicinity of a point-charge nucleus. With the use of relativistic formalism, the density is divergent at the nuclear position. It is therefore necessary to carry out averaging of the electron density within a sphere of finite radius, which represents nuclear volume.^{3,17} The use of the density at the nuclear position, obtained in relativistic calculations with point-

* Corresponding author e-mail: m.filatov@rug.nl.

charge nucleus, may lead to large errors which manifest in unrealistic contact densities. However, in finite basis set calculations, such errors are difficult to detect especially if the basis set does not contain sufficiently tight basis functions.¹⁸

Most commonly, the contact density obtained in nonrelativistic calculations is corrected for relativistic effects with the use of a scaling factor $S(Z)$ in eq 2.^{2,3,9–11} The contact density can be straightforwardly obtained with the use of a method based on the variational principle, such as the self-consistent field method, the variational configuration interaction, or the Kohn–Sham method. However, with the use of methods based on the perturbation theory, the so-called relaxed density matrix needs to be calculated,¹⁹ which presently is not routinely available for multireference many-body perturbation theory methods.

It is a common practice within the standard approach to the calculation of MIS to treat the factor in front of the density difference in eq 2 as an empirical parameter, the value of which is determined from the fit of the theoretically calculated densities versus the experimentally observed isomer shifts.^{12–16} The so-obtained parameters of nuclear transitions may differ by a factor of 2 from the experimentally obtained values.³

Recently, a new approach²⁰ to the calculation of MIS was suggested. Within this approach, the energy shift of the nuclear γ -transition is expressed in terms of the derivative of the electronic energy with respect to the radius of a finite nucleus. This approach incorporates inherently the effects of relativity and electron correlation. According to the new approach, the MIS is calculated as in eq 3

$$\delta = \frac{c}{E_\gamma} \left(\left. \frac{\delta E_e^a(R_N)}{\delta R_N} \right|_{R_N=R} - \left. \frac{\delta E_e^s(R_N)}{\delta R_N} \right|_{R_N=R} \right) \Delta R \quad (3)$$

where E_e^a and E_e^s are the electronic energies of systems containing the absorber and the source nuclei. In the calculations with eq 3,²⁰ the experimental values of the parameters of nuclear transitions, ΔR and E_γ , were employed which were taken from the compilation in ref 3, and the experimental values of the nuclear radii R were taken from ref 21.

The new method for the calculation of Mössbauer isomer shifts (MIS) has been initially tested in the calculations which employed large uncontracted basis sets and a series of wave function methods ranging from the HF method to the CCSD-(T) method.²⁰ The calculations have been carried out for a number of atoms and a series of iron clusters. The major idea underlying these benchmark calculations was to demonstrate the applicability of the new approach to the calculation of MIS and to demonstrate that the use of empirically adjusted parameters can be avoided with the use of the new method.²⁰

However, several questions remained open in the initial study. In particular, the dependence of the results on the basis set truncation was not addressed. Furthermore, the use of the advanced wave function methods may be prohibitively costly for calculations on large biological systems or on cluster models of solids. The methods based on density

functional theory are more preferable in this respect. Therefore, in the present work, we would like to address two issues: i) sensitivity of the results to the choice of the basis set and ii) utility of density functional methods for the calculation of MIS within the new approach.

II. Computational Details

All calculations were carried out using the COLOGNE 2005²² suite of programs in which the new computational scheme is implemented. The relativistic calculations were carried out within one-electron approximation²³ and using the normalized elimination of the small component (NESC)²⁴ method which was implemented according to ref 25. The nonrelativistic calculations were carried out within the same formalism by setting a high value (10^8 au) for the velocity of light.

The Density Functional Theory methods used here are PBE²⁶ (gradient-corrected correlation functional of Perdew, Burke, and Ernzerhof), BPW91 (Becke 88 exchange²⁷ and Perdew–Wang 91 correlation functionals²⁸), BLYP (Becke 88 exchange and LYP²⁹ correlation functional), B3LYP³⁰ (Becke Three Parameter Hybrid Functionals with LYP correlation functional), and BH&HLYP (B stands for Becke treatment of the exchange functional, H&H means half Hartree–Fock exchange and half Slater exchange,³¹ the correlation part being the LYP functional). The basis sets employed will be specified in the following section.

Throughout this work the Gaussian nucleus model^{21,32} is used in the calculations. The derivatives in eq 3, $(\delta E_e^a(R_N))/(\delta R_N)$, are calculated numerically using the increment of 10^{-6} au for the rms nuclear radius. The use of numeric differentiation helps to avoid the difficulties with obtaining the energy derivatives within the computational schemes for which the Hellmann–Feynman theorem is not satisfied.

When calculating the isomer shifts, the effective electron density inside the nucleus was first calculated using eq 4.²⁰

$$\bar{\rho}_e = \frac{5}{4\pi ZR} \left. \frac{\delta E_e^a(R_N)}{\delta R_N} \right|_{R_N=R} \quad (4)$$

Then the isomer shifts were calculated from eq 5, where the proportionality constant ($a = -0.1573a_0^3 \text{ mm s}^{-1}$) is determined from the experimental parameters of the ⁵⁷Fe nuclear transitions reported in ref 3.

$$\delta = a(\bar{\rho}_e^a - \bar{\rho}_e^s) \quad (5)$$

Note that this value differs by a factor of more than 2 from the proportionality constants calibrated by an empirical fit of the calculated electron densities versus the observed isomer shifts (see, e.g., refs 12–16).

III. Results and Discussion

In the present work, the MIS calculations are carried out for the following series of iron clusters: $[\text{Fe}(\text{H}_2\text{O})_6]^{2+}$, $[\text{FeCl}_4]^{2-}$, $[\text{Fe}(\text{H}_2\text{O})_6]^{3+}$, $[\text{FeF}_6]^{3-}$, $[\text{FeI}_4]^{1-}$, $[\text{FeBr}_4]^{1-}$, $[\text{FeCl}_4]^{1-}$, $[\text{Fe}(\text{CN})_6]^{3-}$, $[\text{Fe}(\text{CO})_5]$, $[\text{Fe}(\text{CO})_4]^{2-}$, $[\text{Fe}(\text{CN})_5\text{NO}]^{2-}$, and $[\text{FeO}_4]^{2-}$. The geometries were taken from the compilation in refs 2 and 12 and from ref 33 ($\text{Fe}(\text{CO})_5$). The MIS values

Table 1. HF Calculations of Mossbauer Isomer Shifts for Different Iron Containing Clusters by Using Relativistic and Nonrelativistic Methods^c

	exptl	ref ^a	24s15p9d3f	23s15p9d3f	22s15p9d3f	21s15p9d3f	20s15p9d3f
1 [Fe(H ₂ O) ₆] ²⁺	1.41	12	0.89(0.63) ^b	0.81(0.63)	0.83 (0.63)	0.81(0.63)	0.79(0.63)
2 [FeCl ₄] ²⁻	0.92	12	0.65(0.35)	0.65(0.35)	0.67(0.37)	0.66(0.37)	0.65(0.37)
3 [Fe(H ₂ O) ₆] ³⁺	0.52	12	0.22(0.16)	0.22(0.16)	0.22(0.16)	0.22(0.16)	0.21(0.15)
4 [FeF ₆] ³⁻	0.50	12	0.26(0.19)	0.26(0.19)	0.26 (0.19)	0.26(0.19)	0.24 (0.19)
6 [FeBr ₄] ¹⁻	0.29	42	0.10(-0.03)	0.08(-0.03)	0.08 (-0.03)	0.04(-0.03)	-0.02(-0.03)
7 [FeCl ₄] ¹⁻	0.22	42	-0.02(-0.02)	-0.02(-0.02)	-0.02(-0.02)	-0.02(-0.02)	-0.02(-0.02)
8 [Fe(CN) ₆] ³⁻	-0.11	12	-0.20(-0.17)	-0.21(-0.17)	-0.22(-0.17)	-0.20(-0.10)	-0.22(-0.17)
9 [Fe(CO) ₅]	-0.12	33	-0.09(-0.07)	-0.09(-0.07)	-0.09(-0.07)	-0.09(-0.07)	-0.10(-0.07)
10 [Fe(CO) ₄] ²⁻	-0.12	33	0.07(0.06)	0.05(0.06)	0.05(0.06)	0.03(0.04)	0.03(0.04)
12 [FeO ₄] ²⁻	-0.67	43	-0.99 (-0.77)	-0.99(-0.77)	-0.99(-0.77)	-0.99(-0.77)	-0.97 (-0.77)

^a Sources of experimental values. ^b In parentheses, the results of nonrelativistic calculations. ^c All shifts are given with respect to [Fe(CN)₆]⁴⁻ ($\delta = -0.02$). See refs 12, 14, and 20.

Table 2. DFT Calculations (PBE) of Mossbauer Isomer Shifts for Different Iron Containing Clusters by Using Relativistic and Nonrelativistic Methods^b

	exptl	24s15p9d3f	23s15p9d3f	22s15p9d3f	21s15p9d3f	20s15p9d3f
1 [Fe(H ₂ O) ₆] ²⁺	1.41	0.70(0.54) ^a	0.70(0.54)	0.58(0.54)	0.69(0.54)	0.67(0.54)
2 [FeCl ₄] ²⁻	0.92	0.37(0.29)	0.37(0.29)	0.38(0.30)	0.38(0.30)	0.38(0.30)
3 [Fe(H ₂ O) ₆] ³⁺	0.52	0.34 (0.27)	0.34 (0.27)	0.34(0.27)	0.34(0.27)	0.33 (0.27)
4 [FeF ₆] ³⁻	0.50	0.34(0.26)	0.34(0.26)	0.33(0.22)	0.32(0.26)	0.33(0.26)
6 [FeBr ₄] ¹⁻	0.29	n.a.(0.20)	n.a.(0.20)	n.a.(0.20)	n.a.(0.20)	0.14(0.20)
7 [FeCl ₄] ¹⁻	0.22	0.21(0.17)	0.19(0.17)	0.21(0.17)	0.20(0.17)	0.20(0.17)
8 [Fe(CN) ₆] ³⁻	-0.11	-0.06(-0.05)	-0.06(-0.05)	-0.04(-0.04)	0.01(-0.05)	-0.06(-0.05)
9 [Fe(CO) ₅]	-0.12	-0.02(-0.03)	-0.02(-0.03)	-0.02(-0.03)	-0.02(-0.03)	-0.02(-0.02)
10 [Fe(CO) ₄] ²⁻	-0.12	0.07(0.06)	0.07(0.06)	0.07(0.06)	0.06(0.05)	0.06(0.06)
12 [FeO ₄] ²⁻	-0.67	-0.40(-0.31)	-0.41(-0.31)	-0.40(-0.31)	-0.41(-0.31)	-0.39(-0.31)

^a In parentheses, the results of nonrelativistic calculations. ^b All shifts are given with respect to [Fe(CN)₆]⁴⁻.

for these compounds range from a large positive value of +1.48 mm/s for [Fe(H₂O)₆]²⁺ to -0.69 mm/s for [FeO₄]²⁻. The sources of experimental values for each of these clusters are reported in Table 1.

First we would like to address the question of the basis set dependence of the MIS calculated according to eqs 3–5.

A. Influence of Basis Sets on Isomer Shift Values. In the preliminary study, reported in ref 20, the large uncontracted basis sets for iron complexes were employed. These basis sets were constructed by augmenting the standard (20s12p9d) Fe basis set of Partridge³⁴ with four tight primitive s-type Gaussian functions and with a set of polarization functions taken from the TZVpp basis set of Ahlrichs and May.³⁵ The so-obtained (24s15p9d3f) basis set for iron was combined with the uncontracted aug-cc-pVDZ basis set of Dunning³⁶ on other atoms with the only exception of iodine for which the 6-311G* basis set³⁷ was used.

In the present work, we carry out calculations with this basis set (denoted further on as basis set A+) for a truncated set of compounds (see Tables 1 and 2) to make a connection to the previous work with this method.²⁰ In the calculations carried out at the Hartree–Fock and PBE density functional levels of theory, we study the effect of truncation of the tight primitive basis functions on the theoretical MISs. The results of the calculations are reported in Tables 1 (Hartree–Fock) and 2 (PBE density functional).

Analysis of the HF results suggests that the MIS calculated with eqs 3–5 are not very sensitive to the truncation of tight primitive basis functions. In most cases, there is only a

modest variation (ca. 10%) in the MIS obtained at the relativistic level of theory. The only marked exception is the iron bromide cluster (see entry 6 in the tables), for which the use of truncated basis sets leads to a certain deterioration of the results obtained with the inclusion of relativity. The nonrelativistic HF results obtained with eqs 3–5 do not show any noticeable dependence on the truncation of the basis set.

The same trends, a weak dependence of the relativistic results and an independence of the nonrelativistic results on the basis set truncation, is observed in the density functional calculations (see Table 2). In most cases, the variation in the calculated MIS is of the order of 10% or less. The use of a basis set augmented with tight s-type primitives led, in the case of relativistic density functional calculations for iron bromide (as well as iodide), to serious convergence problems. The source of these problems is most likely in the use of the numeric quadratures inappropriate for relativistic calculations with tight functions. In the nonrelativistic calculations with eqs 3–5, no convergence problems were observed with the use of the very tight functions in the basis sets.

The results reported in Tables 1 and 2 suggest that the converged theoretical results can be obtained with the use of the (21s15p9d3f) iron basis set which is augmented with only one tight primitive function. This basis set (denoted further on as basis set A) will be used in further study of the accuracy of different density functional methods. This basis set is however too big to be used in practical calculations on large molecular systems. The use of standard basis sets, such as the (14s11p6d3f)/[8s7p4d1f] basis set of

Table 3. Comparison of DFT, HF, and MP2 Results for Basis Sets A+ and B^e

	exptl	A ^a			B ^b		
		PBE	HF	MP2	PBE	HF	MP2
1 [Fe(H ₂ O) ₆] ²⁺	1.41	0.70	0.89	0.96	0.62	0.72	0.82
2 [FeCl ₄] ²⁻	0.92	0.38	0.66	0.56	0.35	0.36	0.49
3 [Fe(H ₂ O) ₆] ³⁺	0.52	0.34	0.22	0.37	0.32	0.21	0.32
4 [FeF ₆] ³⁻	0.50	0.34	0.26	0.41	0.31	0.25	0.35
5 [FeI ₄] ¹⁻	0.31 ^c	n.a.	0.04	0.30	0.48	0.02	0.19
6 [FeBr ₄] ¹⁻	0.29	n.a.	0.10	0.32	0.21	0.00	0.19
7 [FeCl ₄] ¹⁻	0.22	0.21	-0.02	0.18	0.20	0.002	0.17
8 [Fe(CN) ₆] ³⁻	-0.11	-0.06	-0.20	0.05	-0.05	-0.18	0.04
9 [Fe(CO) ₅]	-0.12	-0.02	-0.09	0.00	-0.02	-0.07	0.02
10 [Fe(CO) ₄] ²⁻	-0.12	0.06	0.03	0.05	0.07	0.01	-0.26
11 [Fe(CN) ₅ NO] ²⁻	-0.12 ^d	n.a.	-0.23	-0.17	n.a.	-0.16	0.02
12 [FeO ₄] ²⁻	-0.67	-0.40	-0.99	-0.31	-0.32	-0.82	0.04

^a By using basis set A+. ^b By using basis set B. ^c Reference 42. ^d Reference 5. ^e See text for details of basis sets.

Wachters³⁸ (Fe) and the 6-31+G* Pople's basis set³⁹ on nonmetal atoms, is a common practice in the calculations on large metal complexes.¹³ This basis set is denoted further on as basis set B. In the current work we employed the DZVP basis set⁴⁰ on iodine.

Table 3 reports the results of MIS calculations carried out at the Hartree–Fock, MP2, and DFT (PBE) levels of theory with the use of the basis set B. These results are compared with the results of the calculations carried out with the use of the large A+ basis set. The results obtained with the density functional method are surprisingly stable with respect to the replacement of the large uncontracted basis set A+ with a standard contracted basis B. The greatest difference (ca. 20%) is for the iron tetroxide cluster which may require an extended basis set for the correct description of the ligand back-donation effects. Note however that the effect of relativity is less visible with the use of a small basis set B. This is understandable, because this basis set does not contain tight basis functions needed to describe the relativistic contraction of the electron density.

The HF results in Table 3 are even less sensitive than DFT to the replacement of the uncontracted basis set with the standard contracted basis set. However, the MP2 results show much greater sensitivity to the basis set truncation. The greatest discrepancy is observed for the iron tetroxide cluster (entry 12), which indicates that the proper description of its electronic structure cannot be achieved with the use of the small basis set at the MP2 level.

To summarize this subsection, the calculations of MIS carried out with the use of different basis sets suggest that reasonable results can be obtained at the Hartree–Fock or at the density functional levels of theory with the use of standard contracted basis sets. However, the use of small basis sets in connection with the MP2 method leads to a considerable deterioration of the results for certain compounds. This suggests that extended basis sets, such as the basis sets A or A+, need to be used in connection with MP2.

B. Isomer Shift Variation with Different Theoretical Levels. The results reported in Table 3 show that the inclusion of electron correlation via density functionals has a noticeable effect on the calculated MIS. In almost all cases, there is an improvement in the calculated isomer shifts as

compared to the HF values. Noticeable improvement is obtained for iron halides, cyanides, and oxide clusters. The magnitude of the improvement is comparable with the improvement brought about by MP2 for the large basis set A. For the standard contracted basis set B, the PBE results are noticeably better than the MP2 results with one exception of the Fe(II) aqua complex.

In this subsection, we undertake a study of the dependence of the calculated MIS on the choice of the density functional employed. For this study, we select several popular density functionals: PBE, BPW91, BLYP, B3LYP, and BH&HLYP. In this selection of functionals, there are two series which characterize i) the dependence of the results on specific parametrization of a pure exchange–correlation density functional (series PBE, BPW91, BLYP) and ii) the dependence of the results on the use of varying fraction of the HF exchange in a hybrid HF/DFT functional (series BLYP, B3LYP, BH&HLYP). In our opinion, this selection of functionals enables one to make a reasonable judgment on the performance of different types of density functionals.

The criteria employed to judge the performance of density functionals in the MIS calculations with eqs 3–5 are as follows: a) The mean absolute error which is a characteristic commonly employed to judge the overall performance of computational schemes. b) The slope and the intercept of a least-squares linear fit of the experimental vs calculated isomer shifts, eq 6.

$$\delta^{exp} = \alpha \cdot \delta^{calc} + \beta \quad (6)$$

The latter two parameters characterize the correlation of the calculated MIS with the experimental values (slope of the linear fit, α) and the systematic error in the calculated MIS (the intercept of the linear fit, β).

The results of the density functional and HF calculations are summarized in Tables 4 (basis set A) and 5 (basis set B). Notably the choice of the parametrization of a pure density functional has a negligible effect on the calculated MIS regardless of whether a large (A) or a small (B) basis set is employed. The mean absolute error and the parameters of the linear fit remain nearly the same for different pure density functionals. This observation suggests that it is sufficient to study the effect of hybridization with varying

Table 4. Calculation of Mossbauer Isomer Shifts (mm/s) for Different Iron Containing Clusters by Using Basis Set A^d

	exptl	PBE	BPW91	BLYP	B3LYP	BH&HLYP	HF
1 [Fe(H ₂ O) ₆] ²⁺	1.41	0.69(0.54) ^a	0.69(0.54)	0.67(0.52)	0.71(0.56)	0.77(0.60)	0.81(0.63)
2 [FeCl ₄] ²⁻	0.92	0.38(0.30)	0.38(0.30)	0.37(0.29)	0.39(0.31)	0.43(0.34)	0.66(0.37)
3 [Fe(H ₂ O) ₆] ³⁺	0.52	0.34(0.27)	0.32(0.26)	0.32(0.25)	0.28(0.22)	0.24(0.18)	0.22(0.16)
4 [FeF ₆] ³⁻	0.50	0.32(0.26)	0.32(0.26)	0.32(0.25)	0.30(0.23)	0.28(0.21)	0.26(0.19)
5 [FeI ₄] ¹⁻	0.31	n.a.	n.a.	n.a.	n.a.	n.a.	0.09(0.07)
6 [FeBr ₄] ¹⁻	0.29	n.a.	n.a.	n.a.	n.a.	n.a.	0.04(-0.03)
7 [FeCl ₄] ¹⁻	0.22	0.20(0.17)	0.20(0.34)	0.39(0.33)	0.32(0.29)	0.24(0.23)	-0.02(-0.02)
8 [Fe(CN) ₆] ³⁻	-0.11	0.01(-0.05)	-0.06(-0.05)	0.02(-0.05)	0.00(-0.06)	-0.04(-0.02)	-0.20(-0.10)
9 [Fe(CO) ₅]	-0.12	-0.02(-0.03)	-0.02(-0.03)	-0.03(-0.03)	-0.04(-0.03)	-0.05(-0.04)	-0.09(-0.07)
10 [Fe(CO) ₄] ²⁻	-0.12	0.06(0.05)	0.06(0.05)	0.06(0.05)	0.05(0.04)	0.01(0.02)	0.03(0.04)
11 [Fe(CN) ₅ NO] ²⁻	-0.12	n.a. ^b	n.a.	n.a.	-0.20(-0.16)	-0.28(-0.22)	-0.19(-0.10)
12 [FeO ₄] ²⁻	-0.67	-0.41(-0.31)	-0.41(-0.32)	-0.41(-0.32)	-0.51(-0.40)	-0.63(-0.49)	-0.99(-0.77)
MAE ^c		0.26(0.30)	0.25(0.31)	0.28(0.31)	0.24(0.28)	0.21(0.26)	0.23(0.26)
slope		0.48(0.38)	0.49(0.38)	0.46(0.37)	0.53(0.43)	0.61(0.47)	0.78(0.56)
intercept		0.04(0.02)	0.03(0.04)	0.06(0.04)	0.00(0.00)	-0.05(-0.03)	-0.14(-0.11)

^a In parentheses, the results of nonrelativistic calculations. ^b The results are not available due to poor SCF convergence in the broken-symmetry spin unrestricted method. ^c Mean absolute error of the method. ^d See text for details of basis set. All shifts are given with respect to [Fe(CN)₆]⁴⁻.

Table 5. Calculation of Mossbauer Isomer Shifts (mm/s) for Different Iron Containing Clusters by Using Basis Set B^d

	exptl	PBE	BPW91	BLYP	B3LYP	BH&HLYP	HF
1 [Fe(H ₂ O) ₆] ²⁺	1.41	0.62(0.53) ^a	0.62(0.57)	0.60(0.55)	0.61(0.55)	0.65(0.59)	0.72(0.65)
2 [FeCl ₄] ²⁻	0.92	0.35(0.29)	0.35(0.32)	0.34(0.31)	0.33(0.30)	0.34(0.32)	0.36(0.30)
3 [Fe(H ₂ O) ₆] ³⁺	0.52	0.32(0.26)	0.31(0.28)	0.30(0.28)	0.24(0.21)	0.23(0.17)	0.21(0.17)
4 [FeF ₆] ³⁻	0.50	0.31(0.25)	0.31(0.28)	0.30(0.28)	0.26(0.22)	0.23(0.19)	0.25(0.20)
5 [FeI ₄] ¹⁻	0.31	0.48(0.47)	0.48(0.47)	0.47(0.48)	0.16(0.16)	0.11(0.10)	0.02(0.05)
6 [FeBr ₄] ¹⁻	0.29	0.21(0.19)	0.23(0.23)	0.22(0.21)	0.15(0.14)	0.07(0.07)	0.00(0.00)
7 [FeCl ₄] ¹⁻	0.22	0.20(0.16)	0.20(0.18)	0.19(0.18)	0.13(0.11)	0.06(0.05)	0.00(-0.01)
8 [Fe(CN) ₆] ³⁻	-0.11	-0.05(-0.08)	-0.05(-0.05)	-0.05(-0.05)	-0.09(-0.09)	-0.13(-0.13)	-0.18(-0.18)
9 [Fe(CO) ₅]	-0.12	-0.02(-0.05)	-0.02(-0.02)	-0.02(-0.02)	-0.05(-0.05)	-0.07(-0.07)	-0.07(-0.06)
10 [Fe(CO) ₄] ²⁻	-0.12	0.07(0.06)	0.07(0.06)	0.07(0.06)	0.03(0.02)	-0.01(-0.01)	0.01(0.01)
11 [Fe(CN) ₅ NO] ²⁻	-0.12	n.a. ^b	n.a.	n.a.	-0.16(-0.10)	-0.10(-0.10)	-0.16(-0.15)
12 [FeO ₄] ²⁻	-0.67	-0.32(-0.34)	-0.32(-0.31)	-0.33(-0.31)	-0.44(-0.42)	-0.55(-0.52)	-0.82(-0.77)
MAE ^c		0.25(0.27)	0.25(0.26)	0.25(0.27)	0.24(0.25)	0.23(0.25)	0.25(0.26)
slope		0.43(0.39)	0.43(0.40)	0.42(0.39)	0.47(0.43)	0.52(0.48)	0.63(0.57)
intercept		0.07(0.05)	0.07(0.05)	0.07(0.07)	-0.02(-0.02)	-0.06(-0.07)	-0.13(-0.13)

^a In parentheses, the results of nonrelativistic calculations. ^b See footnote c to Table 4. ^c Mean absolute error of the method. ^d See text for details of basis set. All shifts are given with respect to [Fe(CN)₆]⁴⁻.

fraction of the HF exchange in one series of hybrid density functionals only.

Inclusion of the Hartree-Fock exchange in hybrid functionals leads to a certain increase in the systematic error as given by the intercept of the linear fit for both basis sets, A and B. At the same time, mixing in more HF exchange leads to an improved correlation of the calculated values with the experiment. The slope of the linear fit increases steadily as the fraction of the HF exchange increases. This effect is observed for both basis sets; however, the bigger basis set A provides better overall correlation with the experimental results. The hybrid functional BH&HLYP gives reasonable correlation with experiment and less systematic error compared to HF, for both basis sets A and B.

The improvement brought about by the inclusion of HF exchange in hybrid functionals warrants some discussion. In our opinion, the most plausible explanation for the inferior performance of pure density functionals is the incorrect behavior of the potential generated by such a functional near the nucleus. It is known that the gradient corrected func-

tionals yield the Kohn-Sham potential which is divergent at the nuclear position.⁴¹ Therefore, mixing in the HF exchange (the HF potential remains finite at the nucleus) cures partially this deficiency of pure density functionals and leads to improved results for the properties which critically depend on the electron distribution in the vicinity of the nucleus.

With the use of both basis sets, A and B, the difference between relativistic and nonrelativistic results is clearly visible. From all the parameters employed for the data analysis, it is evident that the inclusion of relativity leads to improved results as compared to the experiment. The difference between relativistic and nonrelativistic results is more pronounced for the large basis set A than for the small basis set B. This is understandable, because the basis set B was optimized and contracted in the nonrelativistic HF calculations and does not possess sufficient flexibility to accommodate changes in the electron distribution due to the inclusion of relativity. This underlines the necessity to develop compact basis sets adapted for the relativistic

Table 6. Comparison of Mossbauer Isomer Shifts (mm/s) from This Work (Using Basis Set B) with That of Ref 13, Recalculated According to the Current Method

	exptl	HF ^a	BH&HLYP ^a	B3LYP ^a	B3LYP ^b	BPW91 ^a	BPW91 ^b
1 [Fe(H ₂ O) ₆] ²⁺	1.41	0.72	0.65	0.61	0.55	0.62	0.53
2 [FeCl ₄] ²⁻	0.92	0.36	0.34	0.33	0.39	0.35	0.38
3 [Fe(H ₂ O) ₆] ³⁺	0.52	0.21	0.23	0.24	0.18	0.31	0.21
4 [FeF ₆] ³⁻	0.50	0.25	0.23	0.26	0.24	0.31	0.27
6 [FeBr ₄] ¹⁻	0.29	0.00	0.07	0.15	0.16	0.23	0.20
7 [FeCl ₄] ¹⁻	0.22	0.02	0.06	0.13	0.15	0.24	0.19
8 [Fe(CN) ₆] ³⁻	-0.11	-0.18	-0.13	-0.09	-0.07	-0.05	-0.05
9 [Fe(CO) ₅]	-0.12	-0.07	-0.07	-0.05	-0.05	-0.02	-0.05
10 [Fe(CO) ₄] ²⁻	-0.12	0.01	-0.01	0.03	-0.08	0.07	-0.06
11 [Fe(CN) ₅ NO] ²⁻	-0.12	-0.16	-0.10	-0.16	-0.09	n.a.	-0.06
12 [FeO ₄] ²⁻	-0.67	-0.82	-0.55	-0.44	-0.40	-0.32	-0.31
MAE ^c		0.25	0.23	0.24	0.24	0.25	0.24
slope		0.63	0.52	0.47	0.45	0.43	0.41
intercept		-0.13	-0.06	-0.02	-0.02	0.07	0.01

^a This work. ^b Reference 13. ^c Mean absolute error of the method.

calculations. Nevertheless, the overall agreement with the experiment is acceptable for both hybrid functionals, B3LYP and BH&HLYP. Although the HF method provides the best correlation with the experimental results (slope of 0.78 and 0.63 with the basis sets A and B, respectively), the systematic error increases in the HF calculations as compared to pure or hybrid density functionals. In the overall assessment, the use of hybrid density functionals with an increased fraction of the HF exchange, such as the BH&HLYP functional, can be recommended for the calculation of MIS in iron complexes.

The computational procedure employed in the present work employs the proportionality constant a in eq 5 which was obtained from the experimentally measured parameters of nuclear transitions in ⁵⁷Fe. Therefore, its comparison with the results of the standard calculations of the MIS, where this constant is treated as an empirical parameter and is fitted against the experimental data, may be not straightforward. However, with the use of the contact densities published in ref 13, it is possible to calculate the MISs with the use of eq 5 and the nonempirical constant a . The so-obtained isomer shifts are compared in Table 6 with the shifts calculated with the use of eqs 3–5 in the present work. From this comparison, it is obvious that the standard approach does not have any numerical advantage before the method used in the present article, if the fitting procedure is excluded. In this sense, the method employed in this paper helps to make an unbiased judgment on the performance of the computational schemes used to calculate the MIS. Because it was not the purpose of the present work to obtain an empirically adjusted proportionality constant in eq 5, the use of a set of 12 molecules seems to be acceptable for making a reasonable judgment on the performance of different computational schemes. The use of the fitting procedure within the standard approach to MIS, although it leads to improved numerical results, does not allow for seeing the true accuracy of a selected quantum chemical method and may result in an unrealistic parameter of nuclear γ -transitions as obtained from the fitted proportionality constant a in eq 5. It is our goal to avoid the empirical fitting and to find out compu-

tational schemes capable of yielding accurate results from first principles.

IV. Conclusion

In the present work, a recently developed approach to the theoretical calculation of Mössbauer isomer shift²⁰ is applied within the context of density functional theory. Within the new approach, the MIS is calculated as a derivative of the electronic energy with respect to the radius of the finite nucleus.²⁰ Note that no empirical parameters are employed in the new approach, and the calibration of the parameters which connect the theoretical electron density at the nucleus with the experimental values of MIS is thus avoided. Therefore, the new approach offers a possibility to carry out an unbiased comparison of different computational methods applied to the MIS calculation. Furthermore, the present method has the advantage that it can be used with any quantum chemical computational scheme regardless of the availability of the relaxed density matrix within this scheme.

In the present work, we carried out calculations of MIS for a series of iron complexes. The computational schemes employed include both hybrid and pure density functionals as well as the HF method. Before the performance of density functional methods was addressed, the dependence of the quality of the calculated MIS on the size of the basis set was studied.

The investigation of the effect of the basis set truncation within the context of the new approach reveals that the MISs are not very sensitive to the removal/addition of the tightest primitive functions from/to a large uncontracted basis set. Therefore, for obtaining converged theoretical values, it is sufficient to employ only one tight s-type primitive function added to the standard uncontracted basis set (see the basis set A). With the use of the small contracted basis set (see the basis set B), an acceptable accuracy in the calculated MIS is obtained for the HF and density functional methods. The use of the small basis set, such as the basis set B, is therefore a reasonable compromise between accuracy and complexity of the calculation.

The investigation of the performance of different density functionals reveals that the pure density functional methods

provide poorer correlation of the calculated MIS with the experimental values. Irrespective of the size of the basis set employed, the hybrid functionals provide a consistently better description of the MIS. Correlation of the calculated MIS with the experimental values improves with the increasing fraction of the HF exchange, however at a price of somewhat greater systematic error. In the overall assessment, the hybrid functionals with a greater fraction of the HF exchange such as the BH&HLYP functional produce a better description of the MIS in iron complexes.

Generally, the density functional methods demonstrate somewhat inferior numeric accuracy as compared to the ab initio wave function methods. A tenable explanation for this is in the incorrect behavior of modern approximate density functionals (and respective potentials) near the nucleus.⁴¹ Mixing in the HF exchange energy partially corrects this deficiency. However, quite a substantial fraction of the HF exchange is needed to achieve a noticeable improvement. It appears that a more universal solution would be to switch to the orbital dependent density functionals which are capable of the exact treatment of a substantial portion of the exchange-correlation energy.

References

- Mössbauer, R. L. *Z. Phys.* **1958**, *151*, 124.
- Gütlich, P.; Link, R.; Trautwein, A. In *Mössbauer Spectroscopy and Transition Metal Chemistry*; Springer: New York, 1978.
- (a) Shenoy, G. K.; Dulap B. D. In *Mössbauer Isomer Shifts*; Shenoy, G. K., Wagner, F. E., Eds.; North-Holland: Amsterdam 1978; pp 869–894. (b) Shenoy, G. K.; Dulap B. D. In *Mössbauer Isomer Shifts*; Shenoy, G. K., Wagner, F. E., Eds.; North-Holland: Amsterdam 1978; pp 17–48.
- Kagan, Yu. M.; Lyubutin, I. S. In *Applications of the Mössbauer effect*; Gordon & Breach: New York, 1985; Vol. 4.
- Gütlich, P.; Ensling, J. In *Inorganic Electronic Structure and Spectroscopy*; Solomon, E. I., Lever, A. B. P., Eds.; John Wiley and Sons: New York, 1999; Vol. 1, pp 161–212.
- (a) Münck, E. In *Physical Methods in Bioinorganic Chemistry: Spectroscopy and Magnetism*; Que, L., Jr., Ed.; University Science Books: Sausalito, 2000; p 287. (b) Münck, E.; Stubna, A. In *Comprehensive Coordination Chemistry II*; Lever, A. B. P., Ed.; Elsevier: New York, 2002; Vol. 2.
- Mørup, S. *Mössbauer Effect Ref. Data J.* **2002**, *25*, 105.
- Kistner, O. C.; Sunyar, A. W. *Phys. Rev. Lett.* **1960**, *4*, 412–415.
- Shirley, D. A. *Rev. Mod. Phys.* **1964**, *36*, 339–351.
- de Vries, J. L. K. F.; Trooster, J. M.; Ros, P. *J. Chem. Phys.* **1975**, *63*, 5256–5262.
- Trautwein, A.; Harris, F. E.; Freeman, A. J.; Descaux, J. P. *Phys. Rev. B* **1975**, *11*, 4101–4105.
- Neese, F. *Inorg. Chim. Acta* **2002**, *337*, 181–192.
- Nemykin, V. N.; Hadt, R. G. *Inorg. Chem.* **2006**, *45*, 8297–8307.
- Nieuwpoort, W. C.; Post, D.; van Duijnen, P. Th. *Phys. Rev. B* **1978**, *17*, 91–98.
- Lovell, T.; Li, J.; Liu, T.; Case, D. A.; Noodleman, L. *J. Am. Chem. Soc.* **2001**, *123*, 12392–12410.
- Lovell, T.; Han, W. G.; Liu, T.; Noodleman, L. *J. Am. Chem. Soc.* **2002**, *124*, 5890–5894.
- Svane, A.; Christensen, N. E.; Rodriguez, C. O.; Methfessel, M. *Phys. Rev. B* **1997**, *55*, 12572–12577.
- Sinnecker, S.; Slep, L. D.; Bill, E.; Neese, F. *Inorg. Chem.* **2005**, *44*, 2245–2254.
- (a) Bartlett, R. J. In *Geometrical Derivatives of Energy Surfaces and Molecular Properties*; Jørgensen, P., Simons, J., Eds.; Reidel: Dordrecht, 1986. (b) Gauss, J.; Cremer, D. *Adv. Quantum Chem.* **1992**, *23*, 205.
- Filatov, M. *J. Chem. Phys.* **2007**, *127*, 084101.
- Visscher, L.; Dyall, K. G. *At. Data Nuc. Data Tables* **1997**, *67*, 207.
- Kraka, E.; Gräfenstein, J.; Filatov, M.; Polo, V.; Wu, A.; He, Y.; Olsson, L.; Konkoli, Z.; He, Z.; Gauss, J.; Reichel, F.; Cremer, D. *COLOGNE 2005*; Göteborg University: Göteborg, 2005.
- (a) Dyall, K. G. *J. Chem. Phys.* **2001**, *115*, 9136–9143. (b) Dyall, K. G. *J. Comput. Chem.* **2002**, *23*, 786–793.
- Dyall, K. G. *J. Chem. Phys.* **1997**, *106*, 9618–9626.
- Filatov, M.; Dyall, K. G. *Theor. Chem. Acc.* **2007**, *117*, 333–338.
- Perdew, J. P.; Burke, K.; Ernzerhof, M. *Phys. Rev. Lett.* **1996**, *77*, 3865–3868.
- Becke, A. D. *Phys. Rev. A* **1988**, *38*, 3098–3100.
- (a) Perdew, J. P.; Wang, Y. *Phys. Rev. B* **1992**, *45*, 13244–13249. (b) Perdew, J. P.; Burke, K.; Wang, Y. *Phys. Rev. B* **1996**, *54*, 16533–16539.
- (a) Lee, C.; Yang, W.; Parr, R. G. *Phys. Rev. B* **1988**, *37*, 785–789. (b) Miehlich, B.; Savin, A.; Stoll, H.; Preuss, H. *Chem. Phys. Lett.* **1989**, *157*, 200–206.
- Stephens, P. J.; Devlin, F. J.; Chabalowski, C. F.; Frisch, M. J. *J. Phys. Chem.* **1994**, *98*, 11623–11627.
- Becke, A. D. *J. Chem. Phys.* **1993**, *98*, 1372–1377.
- Visser, O.; Aerts, P. J. C.; Hegarty, D.; Nieuwpoort, W. C. *Chem. Phys. Lett.* **1987**, *134*, 34–38.
- Kerler, W.; Neuwirth, W.; Fluck, E. *Z. Phys.* **1963**, *175*, 200–220.
- Patridge, H. *J. Chem. Phys.* **1987**, *87*, 6643–6647.
- Ahlrichs, R.; May, K. *Phys. Chem. Chem. Phys.* **2000**, *2*, 943.
- Dunning, T. H., Jr. *J. Chem. Phys.* **1989**, *90*, 1007–1023.
- Glukhovstev, M. N.; Pross, A.; McGrath, M. P.; Radom, L. *J. Chem. Phys.* **1995**, *103*, 1878–1885.
- (a) Wachters, A. J. H. *J. Chem. Phys.* **1970**, *52*, 1033–1036. (b) Wachters, A. J. H. In *IBM Tech. Rept. RJ584*; 1969. (c) Bauschlicher, C. W.; Langhoff, S. R., Jr.; Barnes, L. A. *J. Chem. Phys.* **1989**, *91*, 2399–2411.
- (a) Petersson, G. A.; Al-Laham, M. A. *J. Chem. Phys.* **1991**, *94*, 6081–6090. (b) Petersson, G. A.; Bennett, A.; Tensfeldt, T. G.; Al-Laham, M. A.; Shirley, W. A.; Mantzaris, J. *J. Chem. Phys.* **1988**, *89*, 2193–2218.
- Godbout, N.; Salahub, D. R.; Andzelm, J.; Wimmer, E. *Can. J. Chem.* **1992**, *70*, 560–571.

(41) van Leeuwen, R.; Baerends, E. J. *Phys. Rev. A* **1994**, *49*, 2421–2431.

(42) Friedt, J. M.; Petridis, D.; Sanchez, J. P.; Reschke, R.; Trautwein, A. *Phys. Rev. B* **1979**, *19*, 360–364.

(43) Wertheim, G. K.; Herber, R. H. *J. Chem. Phys.* **1962**, *36*, 2497–2499.

CT700227S

The Shell Structure of Atoms

Georg Eickerling and Markus Reiher*

Laboratorium für Physikalische Chemie, ETH Zurich, Hönggerberg Campus,
Wolfgang-Pauli-Strasse 10, CH-8093 Zurich, Switzerland

Received September 24, 2007

Abstract: The total electron density distribution of an isolated atom or an atom in a molecule does not reveal an atomic shell structure. Many localization functions, such as the radial averaged electron density, the Laplacian of the electron density, or the electron localization function have been proposed to visualize and analyze the shell structure of atoms. It was found that for light main group elements the correct number of shells is revealed by such functions. Later it was recognized that for heavy main group elements and for transition metals many of these diagnostic tools fail to reveal the full set of electronic shells as expected from the periodic table. In this work we focus on the radial structure of isolated atoms as revealed by the Laplacian of the electron density. We will demonstrate that it is the nodal structure of the orbitals of the inner shells which is responsible for the diminishing of at least one valence shell of third row transition metal atoms. Particular attention is paid to the effect of different electronic configurations on the shell structure of atoms and the question if the changes observed in the Laplacian of the radial density are sufficiently large for experimental studies on the topology of the electron density. Our presentation is as general as possible and, hence, employs a fully relativistic, i.e., four-component picture and a multiconfigurational ansatz for the wave function, which is thus valid for the whole periodic table of elements.

1. Introduction

The Aufbau principle for atoms, according to which the electrons in atoms are successively added to form shells and subshells denoted by the principle quantum number n and by the angular quantum number l , is one of the central principles in chemistry. Yet, the shell structure of an atom is not directly observable in the total electron density, which is a monotonically decaying function. In ref 19 this is shown to be true for the electron density outside a sphere with a certain radius r and for $r \rightarrow \infty$. For the region close to the core the Kato cusp condition states that the density is monotonic in this region, and although there is still no formal proof,⁸ there exists further computational evidence that the atomic density is indeed a monotonically decaying function for all values of r .^{1–7,9} Therefore, many functions derived from the total electron density have been proposed as a tool to recover the shell structure and to visualize the Aufbau principle. The first studies focused on the radial density

distribution function $D(r)$ which was shown to exhibit maxima that correspond to the electronic shells of atoms. In a pioneering study, Bartell and Brockway showed by electron diffraction experiments that for argon atoms three local maxima in $D(r)$ corresponding to the three occupied shells with $n = 1, 2,$ and 3 can be found.²⁰ Theoretical investigations later uncovered that the correct number of maxima can only be observed for elements with nuclear charge smaller than or equal to 18.^{21–23}

Therefore, other means have been studied for this purpose like the electron localization function (ELF),²⁴ the electron localization indicator (ELI),²⁵ the Laplacian of the electron density,^{26,27} or the average local electrostatic potential $V(\mathbf{r})/\rho(\mathbf{r})$.²⁸ Of these functions the Laplacian of the electron density has the advantages of (i) not being dependent on any reference definition and (ii) being accessible not only by quantum chemical calculations but also directly from electron density distributions obtained from experiment^{29–33} without the use of further approximations or assumptions. We note

* Corresponding author e-mail: markus.reiher@phys.chem.ethz.ch.

that the first of these points also holds for the one-electron potential^{10–12} and the logarithm or the logarithmic derivative of the electron density.^{13,14,37} These functions might be used as alternatives for the Laplacian of the electron density in future studies.

The capability of the Laplacian of the total electron density to reveal the shell structure of atoms was first reported by Bader et al. for the second row elements Li to Ne and for the argon atom.^{26,27} In two following studies, Sagar et al.³⁴ and Shi and Boyd³⁵ investigated the shell structure as revealed by the Laplacian in more detail. The study of Sagar et al. included the elements He to Ba and Lu to Ra, the one by Shi and Boyd the elements Li to Xe.^{34,35} In both papers the numerical nonrelativistic wave functions by Clementi and Roetti³⁶ were employed. The result of these studies was that at most five shells can be observed in the Laplacian in terms of a pair of regions where the Laplacian is positive and negative. Later, Kohout et al. investigated the Laplacian of the electron density obtained from numerical four-component relativistic calculations for the elements of the 2nd, 11th, 12th, 13th, and 14th groups of the periodic table.³⁷

These previous studies included only one electronic configuration for each atom. The concept of distinguishing between electronic shells in an atom is, however, conceptually related to the definition of the valence configuration of an atom in a molecule. Both are based on a molecular (or atomic) orbital picture derived from quantum-mechanical many electron theory. It is common practice to base general chemical concepts such as the orbital electronegativity introduced by Hinze and Jaffe on such theoretical grounds.^{38–40} But also experimental findings are often interpreted employing these generalized ideas. For instance, Mössbauer spectroscopy can be used to determine the valence configuration of an atom in a molecule.⁴¹ In this case, the conclusions are drawn rather indirectly as the experiment itself is sensitive to the electron density at the position of the nucleus. However, since the total electron density is experimentally accessible for instance by X-ray diffraction experiments, the topological analysis of the Laplacian of the electron density could be a valuable tool to investigate the electronic configuration of an atom in a molecule. The results of experimental studies on the topology of the electron density are in very good agreement with results obtained by quantum chemical calculations,^{42–47} and it might be possible to assess the expected changes in the total electron density due to different valence configuration of atoms.

In this work we therefore investigate to which extent the Laplacian of the electron density is sensitive to different electronic configurations of isolated atoms. This requires a thorough understanding of the features revealed by the Laplacian in the valence region of an atom. Therefore, we introduce the spherically averaged electronic density for closed- and open-shell systems calculated in a relativistic framework based on Dirac's four-component one-electron Hamiltonian⁴⁸ in section 2. The material presented in this section and in section 3 is designed as a self-contained introduction of the theoretical background necessary for the understanding of the later discussion and might be skipped by the expert reader. We then analyze the shell structure of

closed-shell atoms as revealed by the Laplacian in section 4.1. In section 4.2 we will then focus on open-shell atoms by analyzing multiconfiguration wave functions obtained by numerical multiconfiguration self-consistent field (MCSCF) calculations.

2. Theoretical Background

The explicit expression from which the electron density is calculated depends on the type of approximation for the wave function from which it is calculated. In the following it is thus necessary to present these expressions for the general case of an MCSCF wave function in a Dirac-based relativistic theory. In addition, the brief presentation of the theoretical foundations in this section shall also unambiguously introduce the notation required.

2.1. The Spherically Averaged Electron Density. To derive the spherically averaged electron density, which is a central quantity as it can also be obtained for an atom in a molecule, we will start from the general definition of the electron density $\rho(\mathbf{x})$ to be calculated from the total electronic ground state wave function Ψ_0 according to

$$\rho(\mathbf{x}) = N \int d\sigma_1 \int_{-\infty}^{\infty} d^3x_2 \int d\sigma_2 \dots \int_{-\infty}^{\infty} d^3x_N \int d\sigma_N \Psi_0^\dagger(\mathbf{x}, \sigma_1, \mathbf{x}_2, \sigma_2, \dots, \mathbf{x}_N, \sigma_N) \Psi_0(\mathbf{x}, \sigma_1, \mathbf{x}_2, \sigma_2, \dots, \mathbf{x}_N, \sigma_N) \quad (1)$$

where \mathbf{x}_i denotes the spatial coordinates and σ_i the spin coordinates. $\rho(\mathbf{x})$ is only a function of three Cartesian coordinates $\mathbf{x} = (x_1, x_2, x_3)$. However, for the derivation of a spherically averaged electron density for an atom in a molecule one most conveniently uses a representation in the polar coordinates $\mathbf{r} = (r, \varphi, \vartheta)$. Thus, in a first step we seek to find a *radial* electron density $D(r)$ that only depends on the radial coordinate r and for which holds

$$\int_0^{\infty} dr D(r) \equiv N \quad (2)$$

Comparing this definition with the integration of $\rho(\mathbf{r}) = \rho[\mathbf{r}(\mathbf{x})]$ and noting that $d^3x = dx_1 dx_2 dx_3 = r^2 dr \sin \vartheta d\varphi d\vartheta$

$$\int_{-\infty}^{\infty} d^3x \rho(\mathbf{x}) = \int_0^{\infty} r^2 dr \int_0^{2\pi} \int_0^{\pi} \sin \vartheta d\vartheta d\varphi \rho[\mathbf{r}(\mathbf{x})] = N \quad (3)$$

we find

$$D(r) = r^2 \int_0^{2\pi} \int_0^{\pi} \sin \vartheta d\vartheta d\varphi \rho[\mathbf{r}(\mathbf{x})] \quad (4)$$

In order to define a density which may serve our purposes for an atom in a general molecule as well as for a spherically symmetric atom, we need to define a spherically averaged density $\bar{\rho}(r)$ that is the total (electronic) charge in a spherical shell with inner radius r and thickness dr , i.e., $D(r)dr$, divided by the volume of this shell ($4\pi r^2 dr$)

$$\bar{\rho}(r) = \frac{D(r)dr}{4\pi r^2 dr} = \frac{D(r)}{4\pi r^2} \quad (5)$$

so that integration over all shells, $\int \bar{\rho}(r) 4\pi r^2 dr = N$, still yields the total number of electrons. This spherically averaged electron density $\bar{\rho}(r)$ is the quantity one should consider for the investigation of atomic properties when discussing

the electron density along a radial ray in an atom or in an atom of a molecule.

2.2. Wave Function of Spherically Symmetric Atoms.

In the following we will give a brief introduction into the notation needed for our discussion of the spherically averaged electron density $\bar{\rho}(r)$ for atoms with closed- and open-shell configurations. We start from the general representation of the ground state wave function Ψ_0 as a linear combination of configuration state functions Φ_I

$$\Psi_0 = \sum_{I=1}^m \Phi_I C_I \quad (6)$$

For $m = \infty$ the result is the exact full configuration interaction (CI) solution. Each configuration state function Φ_I is constructed from antisymmetrized products of one-electron functions, the orbitals $\psi_i(\mathbf{x})$. For finite m one aims for an MCSCF solution, since orbital relaxation needs to be taken into account. This requires an optimization of the one-particle basis within the truncated CI expansion. For $m = 1$ one would obtain the Hartree–Fock solution. In this case the many-electron function Φ_1 reduces to a single Slater determinant. In the case of atoms the orbitals are either the one-component atomic orbitals⁴⁹

$$\psi_i(\mathbf{x}, \sigma) \rightarrow \psi_{n,l,m_{j,i}}(\mathbf{r}, \sigma) = \frac{P_{n,l}(r)}{r} Y_{l,m_{j,i}}(\vartheta, \varphi) \chi(\sigma) \quad (7)$$

of nonrelativistic Schrödinger quantum mechanics or the four-component spinors⁵⁰

$$\psi_i(\mathbf{x}) \rightarrow \psi_{n,\kappa,m_{j,i}}(\mathbf{r}) = \frac{1}{r} \begin{pmatrix} P_{n,\kappa}(r) \chi_{\kappa,m_{j,i}}(\vartheta, \varphi) \\ i Q_{n,\kappa}(r) \chi_{\kappa,m_{j,i}}(\vartheta, \varphi) \end{pmatrix} \quad (8)$$

of the Dirac theory of the electron (κ_i is the four-component analog to the angular momentum quantum number l and $m_{j(i)}$ is the eigenvalue of the z -component \hat{j}_z of the one-electron total angular momentum operator). In the former case, the atomic configuration state functions Φ_I are eigenfunctions of the total spin operators \hat{L}^2 , \hat{L}_z , \hat{S}^2 , and \hat{S}_z , while in the latter case they are eigenfunctions of $\hat{\mathbf{J}}$ and \hat{J}_z . In general, one obtains the electron density from eq 1 using eq 6 as

$$\rho(\mathbf{x}) = \sum_{ij} \gamma_{ij} \psi_i^\dagger(\mathbf{x}) \psi_j(\mathbf{x}) \quad (9)$$

for any of the above introduced representations of the one-electron functions. Here, k is the total number of orbitals, and $\{\gamma_{ij}\}$ is the first-order density matrix. The density matrix elements are given by

$$\gamma_{ij} = \langle \Psi_0 | \hat{E}_{ij} | \Psi_0 \rangle = \langle a_i \Psi_0 | a_j \Psi_0 \rangle \quad (10)$$

where the excitation operator in second quantization reads⁵¹

$$\hat{E}_{ij} = a_i^\dagger a_j \quad (11)$$

and operates on spin orbitals or spinors, respectively. Note that we have taken advantage in eq 10 of the fact that the adjoint operator of the creator a_i^\dagger is the annihilator a_i . Invoking the formalism of second quantization thus allows

us to conveniently bury the integration of eq 1 over $N - 1$ coordinates in the matrix element $\langle \Psi_0 | \hat{E}_{ij} | \Psi_0 \rangle$. It should be noted that the resulting configuration state functions ($a_i \Phi_I$) are many-particle basis functions for $(N - 1)$ electrons and fulfill all properties that are also fulfilled by the parental Φ_I basis functions.

Expressing Ψ_0 in eq 10 by the linear combination of configuration state functions Φ_I from eq 6 then yields

$$\gamma_{ij} = \sum_{IJ} C_I C_J \langle \Phi_I | \hat{E}_{ij} | \Phi_J \rangle = \sum_{IJ} C_I C_J \langle a_i \Phi_I | a_j \Phi_J \rangle \quad (12)$$

where we assumed the CI expansion coefficients C_I to be real. In the Hartree–Fock case with $m = 1$ eq 9 simplifies to a single summation with $C_I = C_J = 1$, and the diagonal density matrix elements become the occupation numbers

$$\gamma_{ij} \rightarrow \gamma_{ii} = \langle \Phi_1 | \hat{E}_{ii} | \Phi_1 \rangle = \begin{cases} 0 \text{ or } 2 & \text{nonrelativistic} \\ 0 \text{ or } 1 & \text{four-component} \end{cases} \quad (13)$$

due to the orthogonality of the one-electron functions ψ_i from which Φ_1 is constructed. This illustrates explicitly that the integral described by the brackets in eq 12 using the annihilation operators to annihilate one orbital from Φ_1 is equivalent to the integration over all but one electronic coordinate in eq 1. In addition, we should emphasize that in the nonrelativistic theory the last equation refers to the special case of a closed-shell electronic structure such that the excitation operator reads

$$E_{ij} = a_{i\alpha}^\dagger a_{j\alpha} + a_{i\beta}^\dagger a_{j\beta} \quad (14)$$

We now proceed by transforming $\rho(\mathbf{x})$ as given in eq 9 from Cartesian to polar coordinates. In the case of atoms, the angular degrees of freedom can be integrated out analytically, so that we get an explicit expression for $D(r)$ of eq 4

$$D(r) = \sum_{ij} \gamma_{ij} D_{ij}(r) \times \left\{ \begin{array}{l} \langle Y_{l,m_i} | Y_{l,m_j} \rangle \\ \langle \chi_{\kappa,m_{j,i}} | \chi_{\kappa,m_{j,i}} \rangle \end{array} \right\} = \sum_i \gamma_{ii} D_{ii}(r) \quad (15)$$

where

$$D_{ij}(r) = \begin{cases} P_i(r) P_j(r) & \text{nonrelativistic} \\ P_i(r) P_j(r) + Q_i(r) Q_j(r) & \text{four-component} \end{cases} \quad (16)$$

According to eq 5, the spherically averaged density then reads

$$\bar{\rho}(r) = (4\pi r^2)^{-1} D(r) = \begin{cases} (4\pi r^2)^{-1} \sum_{ij} \gamma_{ij} P_i(r) P_j(r) & \text{nonrelativistic} \\ (4\pi r^2)^{-1} \sum_{ij} \gamma_{ij} [P_i(r) P_j(r) + Q_i(r) Q_j(r)] & \text{four-component} \end{cases} \quad (17)$$

and is given in particles per bohr³.

2.3. Closed-Shell Configurations. In the special case of closed-shell molecules with N electrons represented by a single Slater determinant the general expression for $\rho(\mathbf{x})$ given in eq 9 simplifies in the nonrelativistic theory to

$$\rho(\mathbf{x}) = \sum_i^{N/2} 2\psi_i^\dagger(\mathbf{x})\psi_i(\mathbf{x}) \quad (18)$$

and in case of the four-component relativistic theory to

$$\rho(\mathbf{x}) = \sum_i^N \psi_i^\dagger(\mathbf{x})\psi_i(\mathbf{x}) \quad (19)$$

if no additional symmetries (like spherical or point group symmetry) are exploited. In the case of atoms with nsh subshells, the equivalence restriction of one and the same radial function eqs 7 and 8 per subshell (nl) or ($n\kappa$), respectively, allows us to simplify eq 17 even further, and we obtain for the radial and the spherically averaged densities

$$\bar{\rho}(r) = \sum_i^{nsh} d_i \frac{D_{ii}(r)}{4\pi r^2} \quad (20)$$

with the subshell occupation numbers

$$d_i = \begin{cases} 2l_i + 1 & \text{nonrelativistic} \\ 2|\kappa_i| & \text{four-component} \end{cases} \quad (21)$$

2.4. Minimal Model for Open-Shell Structures and Near-Degenerate Configurations. The CI expansion of eq 6 allows us to identify important electronic configurations, i.e., those with large CI coefficients C_l . In the case of two equally important open-shell configurations ($m = 2$) the general expression for $\rho(\mathbf{x})$ given in eq 9 reduces to

$$\rho(\mathbf{x}) = \sum_{ij}^{N+1} \gamma_{ij} \psi_i^\dagger(\mathbf{x})\psi_j(\mathbf{x}) \quad (22)$$

if these two configurations differ by only one orbital. The summation runs over all spin orbitals or spinors, respectively, that enter the two CSFs.

2.5. The Laplacian of the Radial Density. The shell structure of isolated atoms has been previously investigated by means of $D(r)$ and by analyzing the Laplacian ∇^2 of the electron density. The Laplacian operator in spherical coordinates is given by⁵²

$$\nabla^2 = \frac{1}{r^2} \frac{\partial}{\partial r} \left(r^2 \frac{\partial}{\partial r} \right) + \frac{1}{r^2 \sin \vartheta} \frac{\partial}{\partial \vartheta} \left(\sin \vartheta \frac{\partial}{\partial \vartheta} \right) + \frac{1}{r^2 \sin^2 \vartheta} \frac{\partial^2}{\partial \varphi^2} \quad (23)$$

The spherically averaged density $\bar{\rho}(r)$ does not depend on the angular coordinates so that all partial derivatives with respect to ϑ and φ vanish, and thus the Laplacian for this special case simplifies to

$$\nabla^2 \bar{\rho}(r) = \frac{1}{r^2} \frac{d}{dr} \left(r^2 \frac{d}{dr} \right) \bar{\rho}(r) = \frac{d^2}{dr^2} \bar{\rho}(r) + \frac{2}{r} \frac{d}{dr} \bar{\rho}(r) \quad (24)$$

3. Computational Methodology

Atomic four-component Dirac–Hartree–Fock and MCSCF calculations were carried out fully numerically.⁵³ While all angular degrees of freedom are treated analytically, the two radial functions $P_i(r) = P_{n\kappa_i}(r)$ and $Q_i(r) = Q_{n\kappa_i}(r)$ of the

4-spinor are represented on an equidistant, logarithmic grid of points in the new variable s , which is calculated from the original radial variable r (see refs 54 and 55 for details on this type of radial grid). The Laplacian of the spherically averaged electron density was calculated numerically employing a three-point finite difference formula. Concerning the definition of a shell we will use the notation convention to define a shell by the principal quantum number n rather than by a pair of quantum numbers (n, l) , which we denote a subshell.

3.1. Peculiarities of Numerical Solution Methods. For atomic structure calculations the use of an equidistant grid in r for the representation of the radial functions P_i and Q_i is not efficient. Therefore one uses a variable transformation to a new variable $s(r)$ which generates an equidistant grid in s which corresponds to a grid in r with small step sizes h for small values of r and larger step sizes for larger values of r .⁵⁴ The function $s(r)$ for a logarithmic grid used in this work is⁵⁵

$$s(r) = \frac{1}{T} [\ln(r+b) - \ln b] \quad (25)$$

In this equation, T^{-1} is a normalization factor which ensures that $s(r_{\max}) = 1$. The value r_{\max} defines a sphere in which the atom is confined, and the parameter b is used to vary the distribution of grid points on the logarithmic grid.

To calculate the Laplacian in this new radial variable $s(r)$ one needs to transform eq 24 to the new coordinate s . This means we need to rewrite the derivative⁵⁵

$$\frac{d}{dr} = \left(\frac{ds}{dr} \right) \frac{d}{ds} \equiv w^2 \frac{d}{ds} \quad (26)$$

where we introduced w^2 as the square of the weighting function $w(s)$.

For the first term of the sum on the right-hand side of eq 24, we obtain the operator identity⁵⁵

$$\frac{d^2}{dr^2} = w^2 \frac{d}{ds} \left(w^2 \frac{d}{ds} \right) = w^3 \left[\frac{d^2}{ds^2} w - \left(\frac{d^2 w}{ds^2} \right) \right] \quad (27)$$

The Laplacian of the *spherically averaged* radial density [bohr⁻³] in the new radial variable s is then given by

$$\nabla^2 \bar{\rho}(r) = \left\{ w^3 \left[\frac{d^2}{ds^2} w - \left(\frac{d^2 w}{ds^2} \right) \right] + \frac{2}{r} w^2 \frac{d}{ds} \right\} \bar{\rho}(r) [\text{bohr}^{-5}] \quad (28)$$

The multiplication with the elementary charge e which would convert the electron density into the (positive) charge density distribution of N elementary charges has not been made explicit. The negative charge density would then be obtained by multiplication with (-1) . The Laplacian of the (negative) charge density, which corresponds to the negative Laplacian of the electron density, is then defined as

$$L(r) = -e \nabla^2 \bar{\rho}(r) = - \sum_{ij} \frac{1}{4\pi r^2} \nabla^2 D_{ij} [e \text{ bohr}^{-5}] \quad (29)$$

so that local concentration of charge corresponds to positive values of $L(r)$. For unit conversion to eÅ⁻⁵ the results

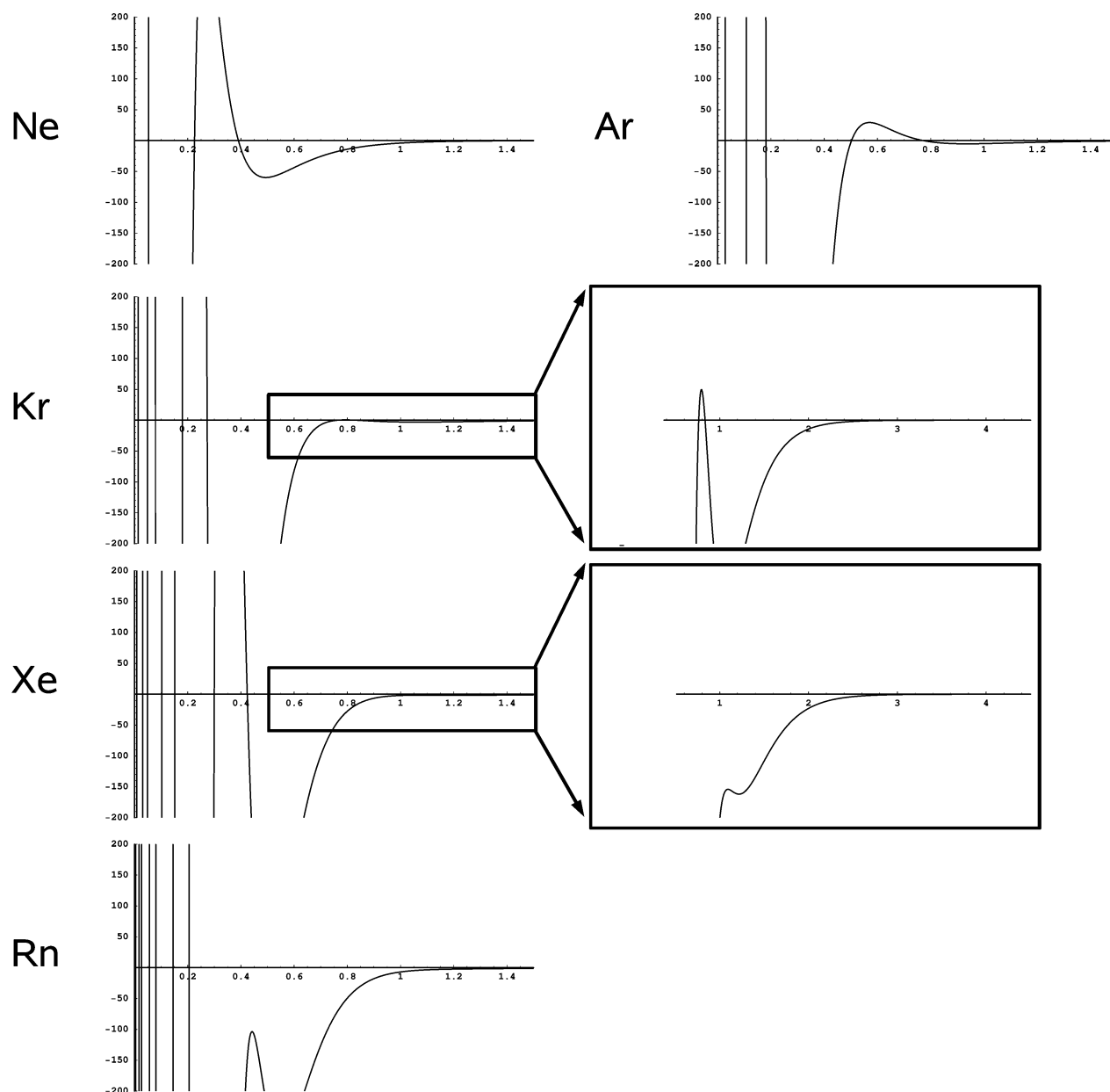


Figure 1. Negative Laplacian of the spherical averaged radial density $L(r)$ of the rare gases Ne–Rn. Comparing the heights of the outermost maxima in $L(r)$ demonstrates the systematic diminishing of the valence shell charge concentration. In the case of Xe the valence shell is only resolved as a local maximum in the negative region of $L(r)$. Units are in $\text{e}\text{\AA}^{-5}$ on the ordinate and \AA on the abscissa. Note the different minimal and maximal values used for the plots for Ne–Rn (-200 to $200 \text{ e}\text{\AA}^{-5}$ and 0 to 1.5\AA) and the two expanded views for Kr and Xe (-2 to $2 \text{ e}\text{\AA}^{-5}$ and 0 to 4.5\AA).

obtained in Hartree atomic units were multiplied by a conversion factor of $24.098731 \text{\AA}^{-5}$. Concerning $\rho(r)$ we note that values given in $\text{e}\text{\AA}^{-3}$ denote a fraction of electrons per cubic angström.

4. Results and Discussion

4.1. Vanishing Valence Shell Structure with Increasing Nuclear Charge. We first consider the shell structure of the closed-shell rare-gas atoms Ne to Rn (the simple case of the He atom with only a single shell has been left aside). Figure 1 depicts $L(r)$ of the electron density in a range of r from 0 to 1.5\AA . From Ne to Kr $L(r)$ resolves the complete electronic shell structure with 2, 3, and 4 pairs of positive and negative regions of $L(r)$ for Ne, Ar, and Kr, respectively. However,

it is obvious from the height of the maxima found for the outermost shell that the degree of local charge concentration, indicated by a positive value of $L(r)$, is systematically reduced with increasing atomic number Z ($L(r) = 369, 29, 0.5,$ and $-1.5 \text{ e}\text{\AA}^{-5}$ for Ne, Ar, Kr, and Xe, respectively).

The reason for the diminishing of the valence shell can be studied considering the Ne atom. Figure 2 depicts the contributions to $L(r)$ due to the $n = 1$ (a) and the $n = 2$ shell (b) together with the total $L(r)$ (c). The maximum of the valence shell at approximately $r = 0.2 \text{\AA}$ ($L(r) = 1325 \text{ e}\text{\AA}^{-5}$) is significantly shifted ($r = 0.26 \text{\AA}$) and reduced in height ($L(r) = 369 \text{ e}\text{\AA}^{-5}$) by the negative contribution of the $1s$ shell in this region. Recall that the Laplacian is a linear operator that allows us to simply add up the individual shell

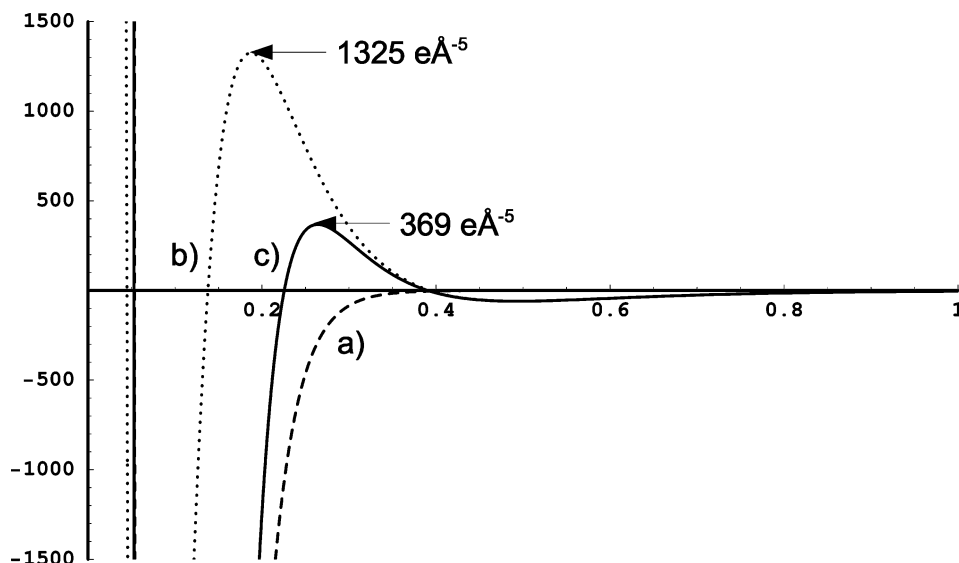


Figure 2. Contributions to the negative Laplacian of the spherical averaged radial density $L(r)$ of (a) the ($n = 1$) shell (dashed line), (b) the ($n = 2$) shell (dotted line), and (c) the total $L(r) = -(4\pi r^2)^{-1} \sum_{i \in \{1s, 2s, 2p\}} \nabla^2 D_{ii}$ of a Ne atom (solid line). Units are in $\text{e}\text{\AA}^{-5}$ on the ordinate and \AA on the abscissa.

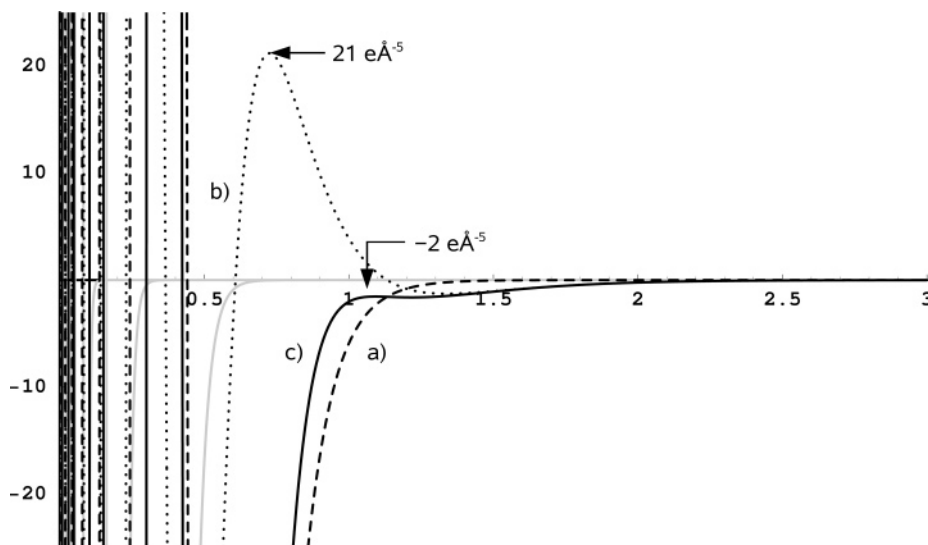


Figure 3. Decomposition of the total Laplacian $L(r)$ of a Xe atom in terms of individual shell contributions (compare eq 29); (a) ($n = 4$) shell (dashed line), (b) ($n = 5$) shell (dotted line), and (c) total $L(r)$ (solid line). The sums of the contributions of the ($n = 1, 2,$ and 3) shells are indicated by light gray lines. Units are in $\text{e}\text{\AA}^{-5}$ on the y - and \AA on the x -axis.

and subshell contributions. Thus, the maximum found for a shell n is not a feature solely to be ascribed to one electronic shell. In fact, the height of the maximum in $L(r)$ and also its position in r is to a large extent affected by the penultimate ($n - 1$) shell.

Accordingly, the reason why only a weak shoulder in the negative region of $L(r)$ can be observed for the $n = 5$ valence shell of Xe lies in the contributions from the $n = 4$ shell. Figure 3 depicts the same scenario for Xe as has been discussed before for Ne. The still pronounced, yet compared to the ($n = 2$) valence shell in Ne weaker maximum in $L(r)$ due to the $n = 5$ valence shell orbitals (dotted line in Figure 3) is severely reduced by the region of charge depletion of the ($n - 1$) shell (dashed line in Figure 3). Figure 3 also depicts the contributions of the $n = 1, 2,$ and 3 shell (light gray lines). As can be seen, $L(r)$ for these three shells already reached values very close to zero in the region around $r =$

1 \AA so that the ($n - 2$) and lower lying shells do not significantly affect the valence shell maximum. At the same time, the maximum in the negative region of the total $L(r)$ is shifted further away from the nucleus, relative to the maximum of the valence shell contribution only. Comparing Figures 2 and 3 it is obvious that it is indeed only the right-hand side tail and thus only a small part of the maximum in $L(r)$ of the valence shell which is remaining as a signature of a valence shell maximum. Thus, not only the magnitude but also the positions of the minima and maxima attributed to one electronic shell are affected by the underlying shells.

The reduction of local charge concentration with increasing nuclear charge number Z due to the contribution from the ($n - 2$) shell is also visible for the ($n - 1$) shell. The corresponding local maximum in $L(r)$ is becoming weaker as Z increases from He to Xe: It reduces from $19\,377 \text{ e}\text{\AA}^{-5}$ in Ar to $8199 \text{ e}\text{\AA}^{-5}$ in Kr and to $1807 \text{ e}\text{\AA}^{-5}$ in Xe. Moving

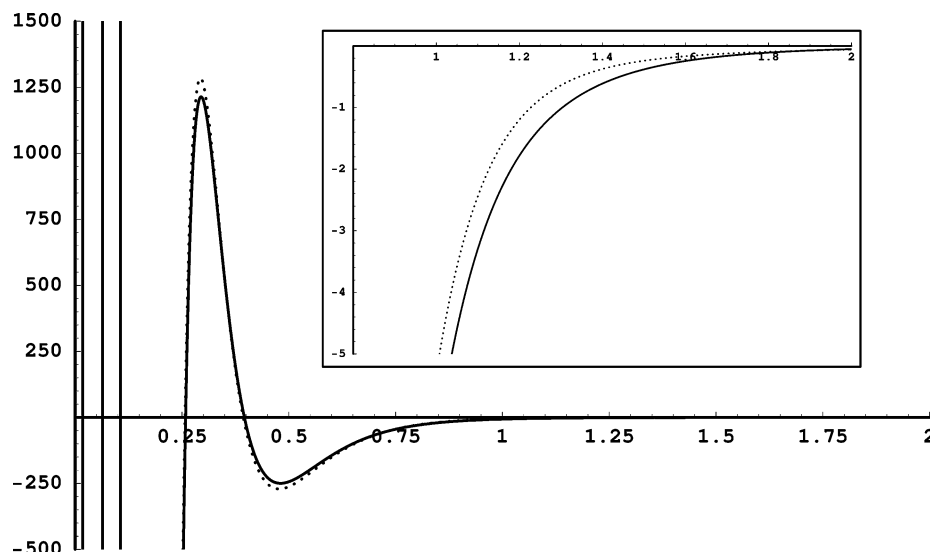


Figure 4. Negative Laplacian of the spherically averaged radial density of a Ni atom with $4s^0 3d^{10}$ configuration (solid line) and $4s^2 3d^8$ configuration (dotted line). Units are in $\text{e}\text{\AA}^{-5}$ on the y - and \AA on the x -axis. The inset shows an enlarged view of the region -5 to $0 \text{ e}\text{\AA}^{-5}$ and 0 to 2 \AA .

finally from Xe to Rn, there is a severe drop in the value of $L(r)$ to $-104 \text{ e}\text{\AA}^{-5}$. This large decrease is caused by the additional f -subshell which is now occupied for the first time. When subtracting the contribution from the $4f$ orbitals to the total $L(r)$, the maximum for the ($n = 5$) shell for Rn increases to $585 \text{ e}\text{\AA}^{-5}$, but still no maximum or shoulder which could be attributed to the ($n = 6$) shell can be detected.

The results presented so far illustrate that when counting and interpreting stationary points in the Laplacian of the radial density as electronic shells one must keep in mind that always the ($n - 1$) shell significantly affects the n th shell, leading for $n > 3$ to the possibility of maxima in the negative region of $L(r)$ or even a complete absence of a local maximum. Now the question arises which feature is indicative of a shell in the Laplacian. Based on similar results, Sager et al. suggested in their study not to use the minima or maxima, but the zero crossings following a maximum as indicators for the atomic shell structure as their positions correlate well with the radius $(n^2/Z)[\hbar/(m_e e^2)]$ from Bohr's theory.³⁴ But this interpretation would then rule out to count the maximum in the *negative* region of $L(r)$ as indicative for the $n = 5$ shell in Xe.

Other authors used the occurrence of a local maximum followed by a local minimum in $L(r)$ as an indicator for a shell.³⁷ This criterion is based on the interpretation of a positive sign of $L(r)$ as a local charge concentration which can be rationalized by the ratio of the kinetic and the potential energy density given by the virial theorem for an atom in a molecule as derived by Bader⁵⁶

$$\nabla^2 \rho(\mathbf{r}) = 2G(\mathbf{r}) + V(\mathbf{r}) \quad (30)$$

According to this, the charge is locally concentrated at a given position \mathbf{r} if the potential energy density $V(\mathbf{r})$, which is a negative-valued function, dominates the positive kinetic energy density $G(\mathbf{r})$ by at least a factor of 2, meaning that the energy of the electrons is dominated by the potential energy at \mathbf{r} . If on the contrary $\nabla^2 \rho(\mathbf{r})$ is positive (and thus

$L(r)$ negative), then the kinetic energy dominates, and a region of charge depletion is assumed. With respect to this interpretation of the sign of $L(r)$ the diminishing of the valence shell maximum corresponds to a reduction of the local charge concentration until the ratio of $G(r)$ and $V(r)$ is smaller than two as observed in the case of Xe. However, this could still mean that the absolute value of $V(r)$ is larger than that of $G(r)$. One must be aware of the fact that eq 30 and the interpretation given above is only valid for a specific choice of the local kinetic energy density. For a detailed discussion see, for example refs 15–18.

As we will demonstrate in the following sections, the maxima found in the negative region of $L(r)$ indeed contain information on the electronic configuration of an atom. The counting of zero crossings alone would rule out an interpretation of these features as indicative for the shell structure. Therefore, keeping in mind the fact that a maximum in $L(r)$ for a given shell n is always (also for light elements) affected by the penultimate shell ($n - 1$), in the following discussion we will assume that any kind of local maximum (and, hence, also in the negative regions of $L(r)$) is indicative for a shell of an atom.

4.2. Open-Shell Atoms. After discussing the general features of the Laplacian in the valence shell of closed-shell rare-gas atoms we will now proceed by considering transition metals with $4s^n 3d^{10-n}$ configuration in order to understand under which circumstances the fourth shell generated by the $4s$ orbital shows up in $L(r)$. We start the discussion of open-shell systems by considering $L(r)$ of a typical transition metal, namely the nickel atom. For elements of the first transition row one would expect to find four shells in the Laplacian of the spherically averaged electron density. However, when looking at the $4s^0 3d^{10}$ and at the $4s^2 3d^8$ configuration in separate open-shell calculations as depicted in Figure 4 one finds only *three* pairs of maxima and minima in *both* cases. Of course, in the case of the $4s^0 3d^{10}$ configuration only the three shells $n = 1, 2$, and 3 are occupied. But for the $4s^2 3d^8$

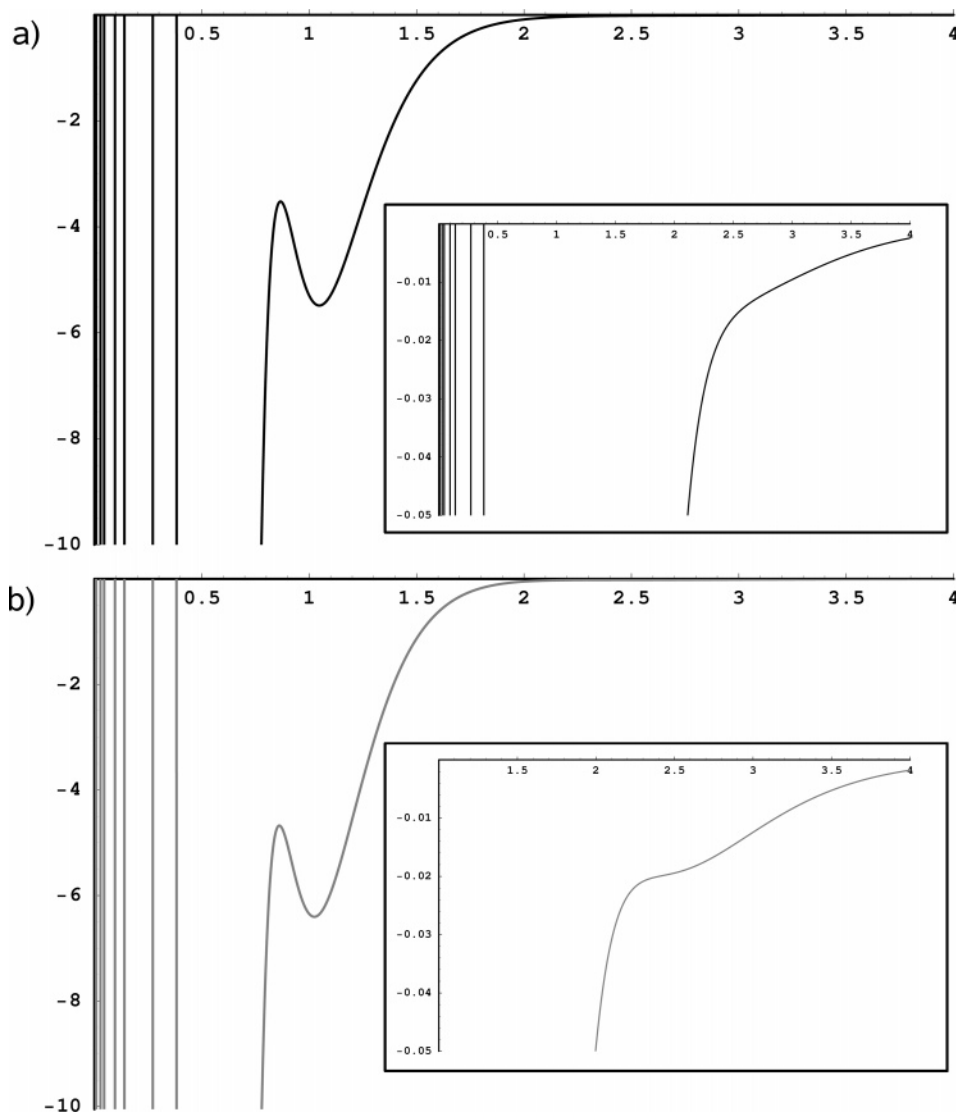


Figure 5. Negative Laplacian $L(r)$ in $\text{e}\text{\AA}^{-5}$ of the spherically averaged radial density $\bar{\rho}(r)$ of a La atom with $5d^16s^2$ single CSF configuration (a) and of a La^+ cation (b). The distance on the x-axis is measured in \AA . The inlays show an enlarged view of the region -0.03 to $0 \text{ e}\text{\AA}^{-5}$ and 0 to 4 \AA .

configuration only three instead of four maxima are found in $L(r)$. The differences due to the different electronic configuration are very small. For instance, the outermost maximum of $L(r)$, denoting the third shell, is more pronounced in the case of the $4s^2 3d^8$ than in the case of the $4s^0 3d^{10}$ configuration (1284 compared to 1214 $\text{e}\text{\AA}^{-5}$, respectively). A difference can also be observed in the region at about $r = 1 \text{ \AA}$ where one would expect the valence shell maximum in $L(r)$. No additional maximum or shoulder can be found if the $4s$ shell is occupied, only a steeper increase to a less negative value of $L(r)$ is found, which again demonstrates the significant contribution of the $(n - 1)$ shell to the valence region of the total Laplacian. An MCSCF calculation which optimizes both of these $J = 0$ configurations simultaneously confirms this picture.

Up to now all calculations were done using a single reference wave function. Especially in the case of open-shell transition metals the description by a single Slater determinant is inadequate. We thus need to look for an example of a transition metal in which two configurations contribute significantly to the total wave function of the atom. The

nickel atom is not a good example in this respect as the contribution of the ground state configuration of $4s^0 3d^{10}$ clearly dominates in an MCSCF calculation over the contribution of a $4s^2 3d^8$ configuration. The first excited-state configuration of a Ni atom starting from a 3F ground state (with $J = 4$) to couple is a 1G state with $4s^2 3d^8$ configuration which are energetically separated by approximately 264 kJ mol^{-1} .⁵⁷ The contribution of this configuration to the total wave function is too small to have an effect on the resulting electron density. In the following section we will therefore investigate a special case for which the energy gap between the electronic ground state and the first excited state is much smaller according to atomic spectroscopy.

4.3. Two Electronic Configurations Contributing Equally to the Total Density. In order to identify a case where two electronic configurations become equally important in a CI expansion, we may consider the data from atomic spectroscopy provided by the Moore tables.⁵⁷ It turns out that the electronic ground state of the lanthanum atom exhibiting a $5d^16s^2$ configuration with $J = 3/2$ and the first excited-state

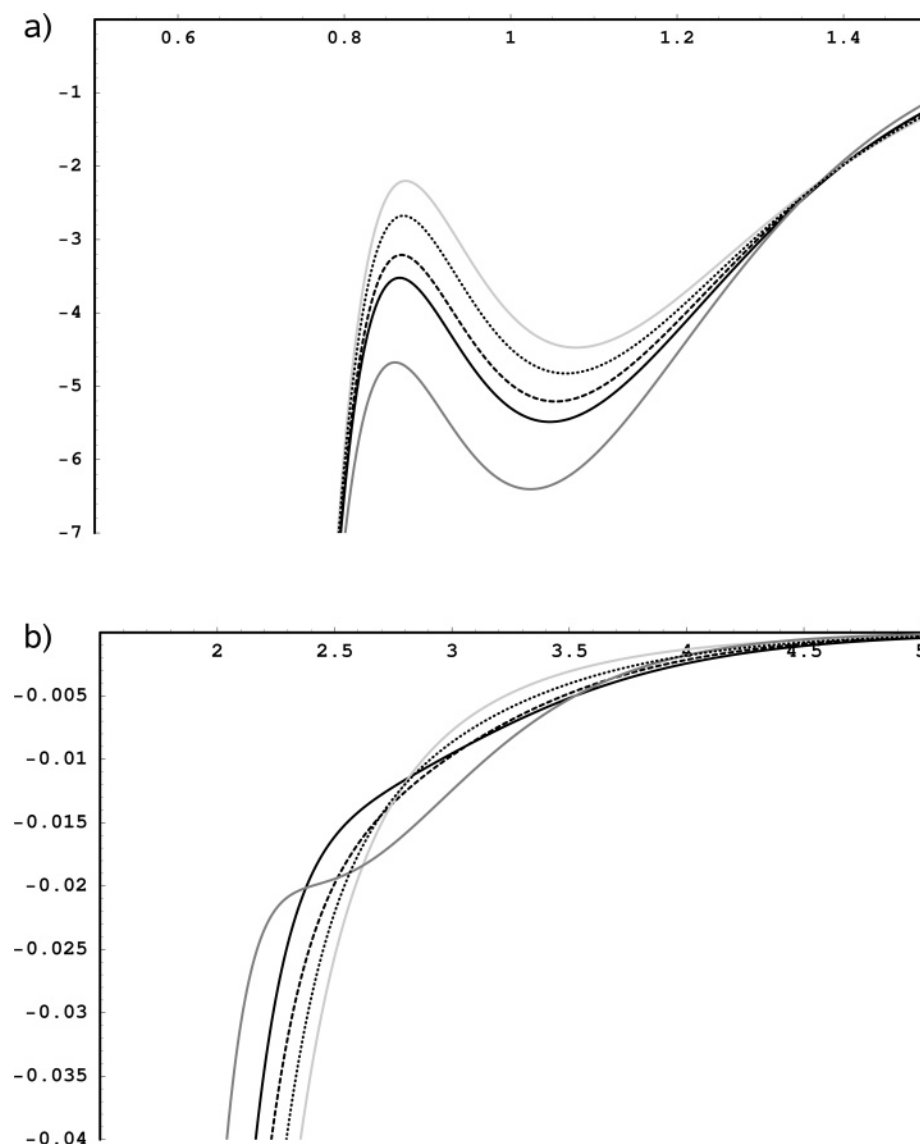


Figure 6. Two selected sections of the negative Laplacian $L(r)$ in $\text{e}\text{\AA}^{-5}$ of the spherically averaged radial density $\bar{\rho}(r)$ of a La atom at $r \in [0.5, 1.5]$ and at $r \in [1.5, 5.0]$. Depicted are the results for the $5d^1 6s^2$ single CSF configuration (black curve), $5d^2 6s^1$ configuration (dotted curve), $5d^3 6s^0$ configuration (light gray curve), and the MCSCF superimposed $5d^1 6s^2$, $5d^2 6s^1$ configurations (dashed curve). In addition, $L(r)$ of a La^+ cation with $5d^0 6s^2$ is shown (dark gray curve). Distances on the x -axis in \AA .

with the same J to couple with the ground state are only separated by 32 kJ mol^{-1} .⁵⁷ Lanthanum is therefore very well suited for the purpose of studying the effect of two equally important configurations on the electron density. We performed several calculations in order to compare the effect of the electronic configuration on the electron density and its Laplacian, starting from a calculation using only one CSF with a $5d^1 6s^2$ ($J = 3/2$) configuration. In this case $L(r)$ features four maxima with $L(r) > 0$ and one additional fifth maximum in the negative region of $L(r)$ (see Figure 5a). This is in accordance with the results discussed in the previous sections. Due to the contribution of the very diffuse $5d$ shell to the total Laplacian the two $6s$ electrons do not give rise to an additional maximum which could be attributed to the sixth shell (see inlay in Figure 5a). That only a single d -electron is sufficient for the maximum of the sixth shell to disappear can be demonstrated by considering the negative Laplacian of the cation La^+ with a $5d^0 6s^2$ configuration where an additional shoulder is found at approximately 2.4 \AA from

the nucleus (see Figure 5b). Obviously, the contribution of the remaining electrons in the fifth shell to the total Laplacian still prevents the formation of a distinct local maximum for the $n = 6$ valence shell. At the same time the maximum in the negative region of $L(r)$ at $r = 0.95 \text{ \AA}$ is less pronounced compared to the neutral La atom (-4.68 and $-3.52 \text{ e}\text{\AA}^{-5}$, respectively). When, in contrast to the cation, which features no $5d$ electrons, assuming a $5d^3 6s^0$ ($J = 5/2$) configuration, $L(r)$ in the region of this latter maximum is less negative resulting in a maximal value of $-2.20 \text{ e}\text{\AA}^{-5}$ (see Figure 6). The negative Laplacian of the neutral La atom with two s and one d electron in its electronic ground state is found in between these two limiting cases. Finally considering the configuration $5d^2 6s^1$, we obtain $L(r) = -2.68 \text{ e}\text{\AA}^{-5}$ which is an intermediate value between the ones of the $5d^1 6s^2$ and the $5d^3 6s^0$ configuration (see Figure 6). Summarizing the results presented so far we note that with an increasing number of d electrons in the $n = 5$ shell the maximum in $L(r)$ attributable to the fifth shell becomes less negative.

Considering the difference between the maximum and the minimum the corresponding values follow the same trend, 2.27, 2.15, 1.96, and 1.73 $\text{e}\text{\AA}^{-5}$ for the $5d^36s^0$, $5d^26s^1$, $5d^16s^2$, and the $5d^06s^2$ configurations, respectively.

This suggests that the Laplacian of the electron density, although not able to fully resolve the shell structure of the La atom as distinct maxima, still provides some information on the electronic configuration of an atom. To investigate this matter further we will in the following compare the results of the single-CSF open-shell calculation to calculations including two CSFs within an MCSCF calculation. Therefore, we performed a calculation employing a $5d^16s^2$ and a $5d^26s^1$ configuration. The resulting CI coefficients are found to be 0.7230 and 0.6909 for the two CSFs, respectively, indicating that both configurations contribute to a similar extent to the final electronic state with $J = 3/2$. The negative Laplacian of the electron density obtained from this calculation also shows the weak maximum at approximately $r = 0.95 \text{ \AA}$ ($L(r) = -3.21 \text{ e}\text{\AA}^{-5}$) which is positioned between the curves obtained for the pure $5d^16s^2$ and the pure $5d^26s^1$ configuration. The same is true considering the value of the difference between the minimum and the maximum ($2.00 \text{ e}\text{\AA}^{-5}$).

Thus, the Laplacian of the electron density is sensitive to the electronic configuration of an atom such that an admixture of approximately 50% of a configuration measured in terms of the (squared) CI coefficients results in a noticeable difference in its course. The relative changes described above follow a clear trend: Starting from a $5d^06s^2$ configuration where the maximum corresponding to the fifth shell is only weakly pronounced, moving electrons from the $5d$ to the $6s$ shell leads to a less negative value of the according maximum in $L(r)$. At the same time, considering a $5d^06s^2$ configuration adding one electron to the $6s$ orbital makes the weak shoulder in the negative Laplacian, which can be attributed to the sixth shell, disappear.

The ability to reconstruct the electronic configuration of an atom from the features shown by the Laplacian would be most important for the interpretation of electron densities obtained from experiment. For such an approach to be feasible, the differences in $L(r)$ for different configurations must be large enough to be unambiguously detectable in the experimental data. This means that when using reference data from quantum chemical calculations the effect due to a change in the valence configuration must exceed the typical deviations between theoretical and experimental topological electron density studies. This appears not to be the case for the La atom. Although the changes in $L(r)$ are large when expressed as percentages (about 30% relative to the single-CSF ground state calculation), the change in the absolute values is rather small (approximately $1 \text{ e}\text{\AA}^{-5}$). In recent experimental charge density studies^{44,45,58} on compounds containing transition metals typical deviations between theory and experiment lie within a range of $0.77\text{--}1.13 \text{ e}\text{\AA}^{-5}$ which would make a clear detection of the differences discussed above difficult. It should be noted that the deviations between experimental and theoretical studies are to some extent due to inadequacies of the multipolar model which is commonly used for the reconstruction of the electron density from the

measured structure factors. These shortcomings can be investigated by comparing the electron densities directly obtained from quantum chemical calculations with those obtained after applying a multipolar model to theoretical structure factors. Similar studies could show whether the precision which can be achieved within the multipolar model as it is used today is in principle accurate enough to reveal the differences in the Laplacian of the electron density due to different electronic configurations.

5. Summary and Conclusion

In this study we have investigated the shell structure of isolated atoms as revealed by the Laplacian of the spherically averaged radial electron density. For heavy elements with $Z > 18$ the electronic shells are not observable as local maxima in the positive region of $L(r)$.^{21–23,59} Our study has shown, however, that also local maxima with a negative sign of $L(r)$ are indicative for a shell. Special attention has been paid to the question whether different electronic configurations can be distinguished in $L(r)$. We could show that when considering also local maxima in the negative region of $L(r)$ as a signature of an electronic shell more than five shells can be observed. Furthermore, a detailed analysis then demonstrated that different electronic configurations may result in qualitative and quantitative changes in the Laplacian of the electron density. This would be of special importance for the interpretation of experimental studies. However, the results of our calculations suggest that the magnitude of the effects due to different electronic configurations is (currently) smaller than the deviations between the topological parameters obtained by quantum chemical calculations and by experiment.

Acknowledgment. The authors thank the Deutsche Forschungsgemeinschaft for the financial support within the SPP 1178 project Re1703/2-1. It is a pleasure for M.R. to acknowledge that it was made possible by the German science foundation DFG to continue funding in Switzerland after the relocation of M.R. from Jena to Zurich. We gratefully acknowledge inspiring discussions with Prof. Paul Ayers and thank Prof. Barbara Kirchner for an early reference to chapter 7.1.3 of Bader's book.

References

- (1) Ayers, P. W.; Morrison, R. C. *Acta Univ. Debreceniensis Ludovico Nominatae Ser. Phys. Chim.* **2002**, 34–35, 197–216.
- (2) Weinstein, H.; Politzer, P.; Srebrenik, S. *Theor. Chim. Acta* **1975**, 38, 159–163.
- (3) Angulo, J. C.; Dehesa, J. S. *Z. Phys. D – Atoms Clusters* **1993**, 25, 287–293.
- (4) Angulo, J. C.; Dehesa, J. S. *Phys. Rev. A* **1991**, 44, 1516–1522.
- (5) Angulo, J. C.; Yanez, R. J.; Romera, E. *Int. J. Quantum Chem.* **1996**, 58, 11–21.
- (6) Angulo, J. C.; Koga, T.; Romera, E.; Dehesa, J. S. *Theochem – J. Mol. Struct.* **2000**, 501–502, 177–182.
- (7) Esquivel, R. O.; Chen, J.; Stott, M. J.; Sagar, R. P.; Smith, V. H. *Phys. Rev. A* **1993**, 47, 936–943.

- (8) Parr, R. G. *J. Chem. Sci.* **2005**, *117*, 613–615.
- (9) Ayers, P. W.; Parr, R. G. *Int. J. Quantum Chem.* **2003**, *95*, 877–881.
- (10) Lassette, E. N. *J. Chem. Phys.* **1985**, *83*, 1709–1721.
- (11) Hunter, G. *Int. J. Quantum Chem.* **1986**, *29*, 197–204.
- (12) Kohout, M. *Int. J. Quantum Chem.* **2001**, *83*, 324–331.
- (13) Wang, W.-P.; Parr, R. G. *Phys. Rev. A* **1977**, *16*, 891–902.
- (14) Sperber, G. *Int. J. Quantum Chem.* **1971**, *5*, 189–214.
- (15) Ayers, P. W.; Parr, R. G.; Nagy, A. *Int. J. Quantum Chem.* **2002**, *90*, 309–326.
- (16) Cohen, L. *J. Chem. Phys.* **1979**, *70*, 788–789.
- (17) Cohen, L. *J. Chem. Phys.* **1984**, *80*, 4277–4279.
- (18) Cohen, L. *Phys. Lett. A* **1996**, *212*, 315–319.
- (19) Hoffmann-Ostenhof, M.; Hoffmann-Ostenhof, T. *Phys. Rev. A* **1977**, *16*, 1782–1785.
- (20) Bartell, L. S.; Brockway, L. O. *Phys. Rev.* **1953**, *90*, 833–838.
- (21) Waber, J. T.; Cromer, D. T. *J. Chem. Phys.* **1965**, *42*, 4116–4123.
- (22) Boyd, R. J. *J. Phys. B* **1976**, *9*, L69–L72.
- (23) Sen, K. D.; Slamet, M.; Sahni, V. *Chem. Phys. Lett.* **1993**, *205*, 313–316.
- (24) Becke, A. D.; Edgecombe, K. E. *J. Chem. Phys.* **1990**, *92*, 5397–5403.
- (25) Kohout, M.; Wagner, F. R.; Grin, Y. *Int. J. Quantum Chem.* **2006**, *106*, 1499–1507.
- (26) Bader, R. F. W.; MacDougall, P. J.; Lau, C. D. H. *J. Am. Chem. Soc.* **1984**, *106*, 1594–1605.
- (27) Bader, R. F.; Essén, H. *J. Chem. Phys.* **1984**, *80*, 1943–1960.
- (28) Sen, K. D.; Gayatri, T. V.; Krishnaveni, R.; Kakkar, M.; Toufar, H.; Janssens, G. O. A.; Baekelandt, B. G.; Schoonheydt, R. A.; Mortimer, W. J. *Int. J. Quantum Chem.* **1995**, *56*, 399–408.
- (29) Coppens, P. *X-Ray Charge Densities and Chemical Bonding*; Oxford University Press: Oxford, New York, 1997.
- (30) Gatti, C. Z. *Kristallogr.* **2005**, *220*, 399–457.
- (31) Tsirelson, V. G.; Ozerov, R. P. *Electron Density and Bonding in Crystals*; Institute of Physics Publishing: Bristol, 1996.
- (32) Koritsanszky, T. S.; Coppens, P. *Chem. Rev.* **2001**, *101*, 1583–1627.
- (33) Coppens, P. A. V. *Acta Crystallogr.* **2004**, *A60*, 357–364.
- (34) Sagar, R. P.; Ku, A. C. T.; Smith, V. H.; Simas, A. M. J. *Chem. Phys.* **1988**, *88*, 4367–4374.
- (35) Shi, Z.; Boyd, R. J. *J. Chem. Phys.* **1988**, *88*, 4375–4377.
- (36) Clementi, E.; Roetti, C. *At. Data Nucl. Data Tables* **1974**, *14*, 177–478.
- (37) Kohout, M.; Savin, A.; Preuss, H. *J. Chem. Phys.* **1991**, *95*, 1928–1942.
- (38) Hinze, J.; Jaffé, H. H. *J. Am. Chem. Soc.* **1962**, *84*, 540–546.
- (39) Hinze, J.; Jaffé, H. H. *Can. J. Chem.* **1963**, *41*, 1315–1328.
- (40) Hinze, J.; Jaffé, H. H. *J. Phys. Chem.* **1963**, *67*, 1501–1506.
- (41) Neese, F. *Inorg. Chim. Acta* **2002**, *337*, 181–192.
- (42) Scherer, W.; Sirsch, P.; Shorokhov, D.; Tafipolsky, M.; McGrady, G. S.; Gullo, E. *Chem. Eur. J.* **2003**, *9*, 6057–6070.
- (43) Scherer, W.; Eickerling, G.; Shorokhov, D.; Gullo, E.; McGrady, G. S.; Sirsch, P. *New J. Chem.* **2006**, *30*, 309–312.
- (44) Scherer, W.; Eickerling, G.; Tafipolsky, M.; McGrady, G. S.; Sirsch, P.; Chatterton, N. P. *Chem. Commun.* **2006**, 2986–2988.
- (45) Rohrmoser, B.; Eickerling, G.; Presnitz, M.; Scherer, W.; Eyert, V.; Hoffmann, R.-D.; Rodewald, U. C.; Vogt, C.; Pöttgen, R. *J. Am. Chem. Soc.* **2007**, *129*, 9356–9365.
- (46) Reisinger, A.; Trapp, N.; Krossing, I.; Altmannshofer, S.; Herz, V.; Presnitz, M.; Scherer, W. *Angew. Chem., Int. Ed.* **2007**, *46*, 8295–8298.
- (47) Hebben, N.; Himmel, H.-J.; Eickerling, G.; Herrmann, C.; Reiher, M.; Herz, V.; Presnitz, M.; Scherer, W. *Chem. Eur. J.* **2007**, *13*, 10078–10087.
- (48) Reiher, M.; Hinze, J. Four-component ab initio Methods for Electronic Structure Calculations of Atoms, Molecules and Solids. In *Relativistic Effects in Heavy-Element Chemistry and Physics*; Hess, B. A., Ed.; Wiley-VCH: Weinheim, 2003; pp 61–88.
- (49) Froese-Fischer, C. *The Hartree-Fock Method for Atoms: A Numerical Approach*; Wiley: Sussex, 1977.
- (50) Grant, I. P. *Adv. Phys.* **1970**, *19*, 747–811.
- (51) Helgaker, T.; Jorgensen, P.; Olsen, J. *Molecular Electronic-Structure Theory*; Wiley: Sussex, 2002.
- (52) Margenau, H.; Murphy, G. M. *The Mathematics of Physics and Chemistry*, 2nd ed.; D. van Nostrand: Princeton, 1956; Vol. 1.
- (53) Reiher, M. Ph.D. Thesis, University of Bielefeld, 1998.
- (54) Andrae, D.; Reiher, M.; Hinze, J. *Int. J. Quantum Chem.* **2000**, *76*, 473–499.
- (55) Andrae, D.; Hinze, J. *Int. J. Quantum Chem.* **1997**, *63*, 65–91.
- (56) Bader, R. F. W. *J. Chem. Phys.* **1980**, *73*, 2871–2883.
- (57) Moore, C. E. *Atomic Energy Levels Volume 2 and 3*; Nat. Stand. Ref. Data Ser.: Nat. Bur. Stand. 1971.
- (58) Eickerling, G.; Mastalerz, R.; Herz, V.; Scherer, W.; Himmel, H.-J.; Reiher, M. *J. Chem. Theory Comput.* **2007**, *3*, 2182–2197.
- (59) Bader, R. *Atoms in Molecules*; Clarendon Press: Oxford, 1990.

CT7002447

Performance of B3LYP Density Functional Methods for a Large Set of Organic Molecules

Julian Tirado-Rives* and William L. Jorgensen*

Department of Chemistry, Yale University, New Haven, Connecticut 06520-8107

Received September 24, 2007

Abstract: Testing of the commonly used hybrid density functional B3LYP with the 6-31G(d), 6-31G(d,p), and 6-31+G(d,p) basis sets has been carried out for 622 neutral, closed-shell organic compounds containing the elements C, H, N, and O. The focus is comparison of computed and experimental heats of formation and isomerization energies. In addition, the effect of an empirical dispersion correction term has been evaluated and found to improve agreement with the experimental data. For the 622 compounds, the mean absolute errors (MAE) in the heats of formation are 3.1, 2.6, 2.7, and 2.4 kcal/mol for B3LYP/6-31G(d), B3LYP/6-31G(d,p), B3LYP/6-31+G(d,p), and B3LYP/6-31+G(d,p) with the dispersion correction. A diverse set of 34 isomerizations highlights specific issues of general interest, such as performance on differences in steric effects, conjugation, and bonding. The corresponding MAEs for the isomerizations are 2.7, 2.4, 2.2, and 1.9 kcal/mol. Improvement is obtained for isomerizations of amines and alcohols when both polarization and diffuse functions are used, but the over-stabilization of linear alkanes compared to branched isomers can be relieved only with the dispersion correction. Besides the insights on DFT methods, the study also aimed to quantify the gains in accuracy that can be achieved by replacing energetics from NDO-based semiempirical methods with DFT results. Since the MAEs obtained with the PDDG/PM3 method for the 622 heats of formation and 34 isomerizations are 2.8 and 2.3 kcal/mol, negligible advantage in accuracy for the B3LYP-based methods emerged in the absence of the dispersion corrections.

Introduction

Density functional methods have been gaining popularity in the past decade. They scale similarly to Hartree–Fock (HF) methods, though they account for some electron correlation effects.^{1,2} Among the ever increasing number of DFT methods, the hybrid functional B3LYP,³ first developed to study vibrational absorption and circular dichroism, has emerged as a good compromise between computational cost, coverage, and accuracy of results. It has become a standard method used to study organic chemistry in the gas phase. It is important, particularly for methods with empirical components, to assess performance on large sets of compounds for which reliable reference data are available. Results of such comparisons should be examined not only for overall

accuracy, usually expressed in statistical terms such as the mean average error (MAE or MAD) or root-mean-square (rms) deviation, but since these overall metrics can be dominated by a few large errors, performance should also be evaluated for specific cases of interest. The present study concentrates on comparisons for a diverse database of 622 neutral, closed shell organic compounds containing only C, H, N, and O, which was gathered in the development of the PDDG/PM3 semiempirical molecular orbital method.^{4–6} Particular comparisons extracted from this database include 34 isomerization reactions that highlight difference in bonding, conjugation, and steric effects of general interest to organic chemists. Besides the insights on the performance of DFT methods, this study was also aimed to address the limits of accuracy that can be expected from semiempirical quantum methods. Specifically, the goal was to quantify the possible gains in accuracy that can be achieved by replacing

* Corresponding author e-mail: julian.tirado-rives@yale.edu (J.T.-R.) and william.jorgensen@yale.edu (W.L.J.).

the semiempirical energetics with DFT results in the computation of heats of formation for the large data set and for the isomerization energies.

Recently, Riley et al.⁷ published an extensive evaluation of 37 DFT methods with 11 different basis sets in which they compared their overall performance on structures, heats of formation, ionization potentials, electron affinities, vibrational frequencies, conformational and hydrogen-bonding energies, and reaction barriers from the G2/97 test set.⁸ However, the size of the molecules was limited as the G2/97 test set contains only compounds with up to 6 non-hydrogen atoms. It was found that B3LYP ranks consistently well, although not at the top for any one category. Of particular interest is the fact that in calculating many of these properties the B3LYP/6-31G(d) combination gives better results than 6-31G+(d) or 6-31G++G(d) and results of comparable quality such as the larger Dunning-type basis sets, cc-pVDZ, cc-pVTz, aug-cc-pVDZ, or aug-cc-pVTZ. Similar results were noted in the original B3LYP publication.³ This characteristic may be interpreted as giving the right answer for the wrong reason or, more optimistically, as an economical, balanced description. Nevertheless, there are still some significant problems that have been receiving attention, particularly, decreasing accuracy with increasing system size, understabilization of branched vs linear alkanes, and underestimation of weak interactions.

The problem with increasing system size undermines one of the reasons for the popularity of DFT methods, i.e., the scaling of computational effort with the number of basis functions (N) is N^4 for B3LYP, while common alternatives such as MP2 scale as N^5 , and MP4 or G2 as N^7 . Curtiss et al. made a general comparison of B3LYP/6-311+G(3df,2p) single-point calculations using MP2(FULL)/6-31G(d) structures and 0.89 scaled HF/6-31G(d) frequencies when developing the G2/97 data set (148 compounds with 1–6 non-hydrogen atoms) and found that it gives a MAE of 3.11 kcal/mol (the G2 method gives 1.58).⁸ Further comparisons using the compounds added to create the newer G3/99 data set (75 additional compounds with 5–10 heavy atoms) using B3LYP/6-311+G(3df,2p) single-point calculations on B3LYP/6-31G(d) geometries with 0.96 scaled B3LYP/6-31G(d) frequencies gave a MAE of 8.21 kcal/mol (G3 gives 1.01).⁹ The net is a MAE of 4.8 kcal/mol with B3LYP for the full G3/99 data set of 223 heats of formation.

Similar evaluations and comparisons have been carried out in the development of other methodologies. For instance, in the development of the X3LYP extended functional, Xu et al.¹⁰ reported a MAE of 3.1 kcal/mol for B3LYP/6-311+G(3df,2p) on the G2/97 set, while the X3LYP functional yielded 2.8 kcal/mol. Kafafi developed the K2-BVWN functional, which includes the use of fitted atom equivalents; for a larger set of 350 atoms and molecules including the G2 set (nitrobenzene being the largest compound), B3LYP/6-311+G(3df,2p)//B3LYP/6-31G(d) yielded a MAE of 3.0 kcal/mol, which was reduced to 1.4 kcal/mol with K2-BVWN.¹¹ A significantly larger basis set was also used in the comparison of the spin-component scaled (SCS) variant of MP2 with B3LYP by Grimme on an extended G2/97' set that included 160 molecules with 6 or fewer heavy atoms as

a training set and 70 additional molecules, including some larger compounds such as naphthalene, azulene, and anthracene, as a test set.¹² The MAEs obtained using B3LYP/QZV3P for the training and test sets were 2.1 and 8.5 kcal/mol, while an extrapolation from TZV2P and QZV3P to obtain close to the basis-set-limit treatment for MP2 produced 1.7 and 4.6 kcal/mol and 1.2 and 2.8 kcal/mol for SCS-MP2. It should be noted that optimized atomic energy corrections were used in these calculations.¹² The system-size issue was also raised in the original report of the PDDG/PM3 method where it was found that the MAE with B3LYP/6-311+G(3df,2p) for heats of formation increases from 2.2 kcal/mol for 60 neutral molecules in the G2 set to 7.2 kcal/mol for 45 molecules in the G3 set, while the MAEs from PDDG/PM3 are 3.2 kcal/mol for both sets.⁴

Concerning linear hydrocarbons, Redfern et al. found that the errors in the calculated heats of formation for the alkanes in the G3 set increase steadily with system size from 0.6 to 30.3 kcal/mol for ethane to hexadecane at the B3LYP/6-311+G(3df,2p)//MP2/6-31G(d) level.¹³ They further noted that using isodesmic reactions to calculate the heats of formation decreases the errors significantly, but the errors become small only with the use of homoisodesmic reactions. For the largest case, hexadecane, the error from the direct calculation of 30.3 kcal/mol is reduced to 16.6 and 2.0 kcal/mol with the isodesmic and homoisodesmic approaches. Wodrich et al. compared experimental bond separation energies with values computed using several functionals, MP2 and CCSD(T), and they found similar systematic errors.¹⁴ The discrepancies for alkane homologation were attributed to deficiencies in the DFT description of “proto-branching” (1,3-interactions),^{14a} which is consistent with the improved performance with the homoisodesmic reactions.

Related problems have emerged in computing the energy differences between branched hydrocarbons and their linear isomers, with the additional characteristic that by their nature these are all isodesmic reactions. The energetic benefits of branching are significantly underestimated with B3LYP. Grimme provided an interesting analysis by comparing SCS-MP2, MP2, B3LYP, and B2PLYP results for isomers of butane, pentane, octane, and undecane that pointed to deficiencies in pair correlation energies between orbitals of the same type, e.g., 1,3-interactions.¹⁵ The same methodology was utilized to study C and Si based chains substituted with H, F, and Cl with similar results.¹⁶

The application of B3LYP to intermolecular interactions also reveals some problems. While hydrogen-bond energies of organic compounds with water are reproduced well,¹⁷ other weakly bonded complexes can be problematic. Tsuzuki and Lüthi found differences in the interaction energies of all three benzene dimers (T-shaped, stacked, or parallel-displaced) with reference CCSD(T)/aug-cc-pVDZ calculations that range from 3.7 to 5.5 kcal/mol; strikingly, the benzene dimer is not bound with B3LYP methods.¹⁸ This deficiency prompted the development of several new functionals. For instance, Zhao and Truhlar developed the PWB6K and PW6B95 alternatives¹⁹ and later M05-2X²⁰ based on a training set that included 115 atomization energies, 13 ionization potentials (IPs), 13 electron affinities (EAs), 76

barrier heights, and 51 complexation energies. The MAE per bond for the atomization energies was 0.92 kcal/mol with B3LYP and 0.41 kcal/mol with PWB6K. The MAEs for heats of formation from M05-2X for the G2 and G3 data sets were later calculated to be 3.2 and 4.2 kcal/mol, respectively.²¹ Development of the B2PLYP and mPW2PLYP functionals by Schwabe and Grimme followed a different approach by including a second-order Møller-Plesset type correction.²² Their training set, expanded from the G3/05 set, included 271 heats of formation, 105 IPs, 63 EAs, 10 proton affinities, and 6 hydrogen-bonded complexes. The MAE for the 271 heats of formation in this set with B3LYP/TZV2P is 5.3 kcal/mol, while their functionals gave 2.7 kcal/mol for B2PLYP/CQZV3P and 2.0 kcal/mol for mPW2PLYP/CQZV3P.

An alternative solution to the deficiencies in the description of π - π and other weakly bound complexes is to apply empirical dispersion corrections based on a scaled C_6/R_{ij}^6 interaction with a distance-dependent damping function. The scaling factors, parameters, combinatory rule, and damping function needed to improve the BLYP, B3LYP, and B97 functionals were determined by Grimme and co-workers based on the interaction energies and distances of increasing number of complexes (29,²³ 40,²⁴ and 161^{25,26}). A comparison of the 148 heats of formation in the G2/97 set using the modified B3LYP functional with TZV2P or TZVPP basis sets gave a MAE of 3.6 kcal/mol. This represents a slight decrease in accuracy for the isolated molecules, but it improves significantly the results for complexes. In a recent publication, addition of this correction to the semiempirical AM1 and PM3 methods was found to improve their performance on weakly bound complexes, when coupled with adjustments for the values of the parameters U_{ss} , β_s , and α for hydrogen and U_{ss} , U_{pp} , β_s , β_p , and α for carbon, nitrogen, and oxygen.²⁷ However, the impact of these modifications on computed heats of formation of neutral isolated molecules was not reported. A very similar method with different combinatory rules was optimized for 22 complexes and verified for 58 additional ones by Jurečka et al.²⁸ Interestingly, adding this correction is more beneficial when larger basis sets or counterpoise corrections are used. Both of these methods provide average improvements of ca. 1.0 kcal/mol for complexes.

Computational Methods

Heats of Formation. All B3LYP calculations were performed with Gaussian03 using the 6-31G(d), 6-31G(d,p), and 6-31+G(d,p) basis sets.²⁹ The PDDG/PM3 calculations were executed with BOSS³⁰ or a local version of MOPAC.^{31,32} Unless indicated otherwise, all energies were obtained using geometries optimized with SCC-DFTB³³ calculations in a prior assessment of it and other semiempirical methods.³⁴ As noted, the molecular structures from SCC-DFTB are generally in excellent agreement with MP2/cc-pVTZ results, showing average deviations for bond lengths, bond angles, and dihedral angles of 0.012 Å, 1.0°, and 2.9°. Optimization was subsequently carried out for the full set of 622 molecules at the B3LYP/6-31G(d) level to assess the effects of the choice of structures on MAE. Comparison with the

SCC-DFTB geometries showed few significant differences except in several cases mostly involving C-C=C angles in alkenes. The B3LYP/6-31G(d) geometries were used in these cases, as noted in the tables. Since the time of the earlier comparative study,³⁴ further optimization of the PDDG/PM3 parameters for C, H, N, and O was also performed on the full training set of molecular structures and properties;⁴ when the reoptimized parameters are applied to the 622 heats of formation, the MAE is reduced from 3.2 to 2.8 kcal/mol. Though the modifications were slight, both the old and the modified PDDG/PM3 parameters are provided in the Supporting Information. The present results use the modified parameters.

Heats of formation at 298 K were computed using the same procedure followed in the development of many semiempirical quantum methods including PDDG/PM3.⁴ Specifically, eq 1 is used where E_{el}^A (also known as *isol*) and ΔH_f^A are the electronic energies and heats of formation of the

$$\Delta H_f^0 = E_{tot}^{mol} - \sum_A E_{el}^A + \sum_A \Delta H_f^A \quad (1)$$

atoms composing the molecule. The experimental values are used for ΔH_f^A , and the E_{el}^A values are treated as adjustable parameters, which were optimized to minimize the unsigned errors for the 622 heats of formation for the HF and DFT-based procedures that were examined here. This approach is used to remove systematic errors in the atomic component of the energy change, and it is expected to yield lower MAEs than alternative computation of heats of formation from the total energy with adjustments for the translational, rotational, vibrational, and $P\Delta V$ changes. The same method has been used in other recent studies to compute heats of formation with conventional DFT methods,³⁵⁻³⁷ SCC-DFTB,³⁴ and in a DFTB approach.³⁸ An additional point is that only the lowest-energy conformer for a molecule is considered in the calculation of the heat of formation (eq 1). As discussed elsewhere,^{34,35} this approximation normally yields errors below 1 kcal/mol for flexible molecules with fewer than 30 atoms. The resultant values for E_{el}^A are reported in Table 1 for all methods considered here.

Dispersion Correction. A promising approach to reduce the errors of DFT proposed by Grimme is the inclusion of an empirical dispersion correction based on eq 2, where $f(R_{ij})$ is an exponential damping function and s_6 is a functional- and basis set-dependent scaling factor.^{23,24} In order to test the possible effects of such a dispersion term, a modified version of the BOSS program³⁰ was used to calculate E_{disp} for all 622 structures, which was then added to the total energies.

$$E_{disp} = -s_6 \sum_i \sum_{j>i} f(R_{ij}) \frac{C_6^{ij}}{R_{ij}^6} \quad (2)$$

Several different variants of this method were tried. In all cases, reoptimization of the scaling factor and the atomic electronic energies, E_{el}^A , in eq 1 was carried out. The first attempt, using Grimme's original C_6 parameters and damping

Table 1. Atomic Heats of Formation and Fitted Electronic Energies for Eq 1

		H	C	N	O
ΔH_f^A (kcal/mol)	all	52.102	170.89	113.00	59.559
E_{el}^A (eV) ^a	HF/6-31G(d)	-13.267830	-1023.471108	-1477.085945	-2032.656503
E_{el}^A (eV) ^a	B3LYP/6-31G(d)	-13.841952	-1029.922686	-1485.365964	-2042.501380
E_{el}^A (eV) ^b	B3LYP/6-31G(d)	-13.846915	-1029.922295	-1485.368385	-2042.523239
E_{el}^A (eV) ^a	B3LYP/6-31G(d,p)	-13.879462	-1029.924616	-1485.414750	-2042.512214
E_{el}^A (eV) ^a	B3LYP/6-31+G(d,p)	-13.872636	-1029.970795	-1485.524958	-2042.646009
E_{el}^A (eV)	B3LYP/6-31+G(d,p)+OC6	-13.884916	-1029.966281	-1485.509729	-2042.662279
E_{el}^A (eV) ^c	PDDG/PM3	-13.248092	-112.796924	-157.693757	-294.712153

^a Using single-point energy evaluations on SCC-DFTB optimized geometries (ref 34). ^b Using B3LYP/6-31G(d) optimized geometries.

Table 2. Mean Absolute Errors in Calculated Heats of Formation for Neutral Molecules Containing the Elements C, H, N, and O (kcal/mol)^a

	N	HF			B3LYP			
		6-31G(d) ^b	6-31G(d) ^b	6-31G(d) ^c	6-31G (d,p) ^b	6-31+ G(d,p) ^b	6-31+G(d,p) +OC6 ^b	PDDG/PM3
all molecules	622	3.9	3.1	3.0	2.6	2.7	2.4	2.8
hydrocarbons	254	2.5	2.2	2.1	2.2	2.5	2.1	2.2
"training set" ^d	134	4.3	3.0	2.9	2.4	2.3	1.9	2.4
"test set" ^d	488	3.8	3.1	3.0	2.7	2.9	2.5	2.9

^a All data are in the Supporting Information. ^b Using single-point energy evaluations on SCC-DFTB optimized geometries (ref 34). ^c Using B3LYP/6-31G(d) optimized geometries. ^d "Training" and "test" sets refer to those used in the development of the PDDG/PM3 parameters (ref 4). All 622 data points were used here in optimizing the E_{el}^A values in Table 1.

function for all atom pairs, produced less than 0.1 kcal/mol improvements for the heats of formation. This lack of improvement may stem from the use of fitted atomic energies E_{el}^A in eq 1. Although a full comparison would require frequency calculations for all 622 molecules, the subset of 97 compounds common to the G3/99 set has a MAE of 4.38 kcal/mol using the published B3LYP/6-311+G(3df,2p) energies and frequencies, while our results at the B3LYP/6-31G(d) level using eq 1 have a MAE of 2.94 kcal/mol. This improvement is numerically similar to that found with previous implementations of the dispersion correction.^{24–26} Different partitions of the corrections depending on bonding arrangements (bonded pairs, pairs bonded to a common atom, pairs separated by two bonds, etc.) and different sets of parameters were tested. The best results were obtained using OPLS-AA generic C, H, N, and O Lennard-Jones parameters ($C_6^{ij} = 4\epsilon_{ij}O_{ij}^6$),³⁹ no damping function ($f = 1$), a single scale factor s_6 of 0.985, and including only the interactions between atom pairs separated by more than three bonds. E.g., for butane, there would be no C–C term, 6 C–H terms, and 21 H–H terms. The resultant MAEs did improve with increasing basis-set size. Thus, the best results were obtained at the 6-31+G(d,p) level, and these are designated as B3LYP/6-31+G(d,p)+OC6 in the tables. Specifically, the ΔH_f MAE for the 622 compounds of 3.0 kcal/mol at the B3LYP/6-31G(d)+OC6 level decreases to 2.5 kcal/mol with the added p-functions in 6-31G(d,p) and to 2.4 kcal/mol with the addition of the diffuse functions. A full tabulation of results is presented in the Supporting Information.

The investigation of the present dispersion correction should be viewed as just a test. It is unsatisfactory from our perspective since it is not general in that it requires assigning atom pairs as bonded or not. This creates ambiguities or discontinuities for application to transition structures or

complexes. However, one could devise a closely related continuous version using an appropriate damping function in eq 2.

Results and Discussion

Heats of Formation. The mean absolute errors for the different methods are recorded in Table 2. The second column contains the number of structures in the molecule sets of the first column. The "training" and "test" sets refers to those used in the original PDDG/PM3 parametrization;⁴ this is an informative separation, since the 134 compounds in the "training" set contain 1–10 non-hydrogen atoms (the average is 5.0), while the 488 in the "test" set are somewhat larger, from 2 to 15 with an average of 7.4 non-hydrogen atoms.

There are several points to note. (1) The B3LYP-based results are uniformly better than those from HF/6-31G(d). (2) The 5–7 kcal/mol MAEs that are regularly found for B3LYP-based heats of formation are readily reduced to 3 kcal/mol using eq 1 with optimization of the atomic energies. The problems with larger systems, as evidenced by the consistency of the results for the "training" and "test" sets, are no longer striking. Substantial improvements with the use of optimized atomic energies have been noted in other studies.^{34–38} (3) All methods yield MAEs of 2.1–2.5 kcal/mol for the 254 hydrocarbons. Wodrich et al. computed bond separation energies, which can be converted to heats of formation, for 72 hydrocarbons with 9 different functionals and the 6-311+G(d,p) basis set.^{14b} Their MAE of ca. 4 kcal/mol for B3LYP is greater than the present result owing to a systematic (mean signed error) of ca. -2 kcal/mol that is relieved by use of eq 1. They obtained the best results with the M05-2X functional, which yields a MAE of 2.13 kcal/mol and a negligible mean signed error. Thus, it appears that current DFT methods and PDDG/PM3 are reaching a

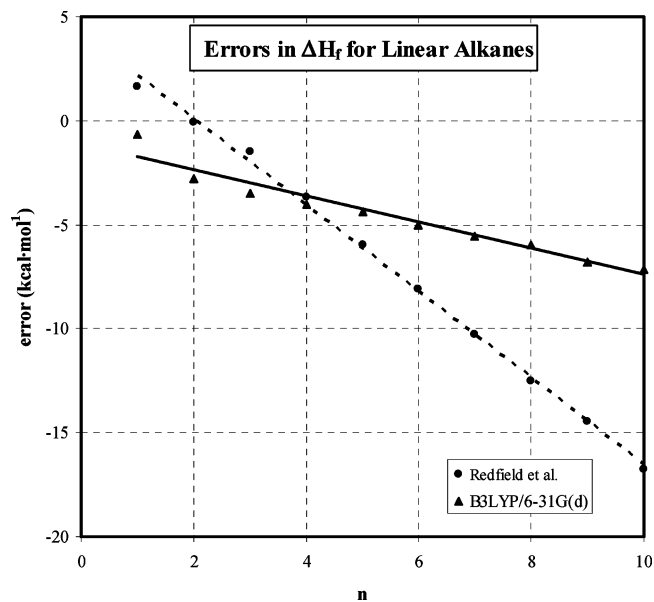


Figure 1. Errors in computed heats of formation for linear alkanes as a function of the number of carbon atoms, n . The present B3LYP/6-31G(d) results are compared with prior B3LYP-based results from ref 13.

MAE limit near 2.0 kcal/mol for hydrocarbons. (4) In comparing the results in columns 4 and 5, it is found that the use of SCC-DFTB or B3LYP/6-31G(d) optimized geometries has a negligible effect on the results. (5) The quality of the B3LYP-based results is not very sensitive to the choice of basis set. Without the dispersion correction, the best results here are obtained with B3LYP/6-31G(d,p). (6) However, none of these results is significantly better than that from the much less computationally demanding PDDG/PM3 method. This was unexpected and, actually, somewhat disappointing in that it does not point to an obvious path forward to a further improved semiempirical method, e.g., by increasing the basis set size or adding B3LYP-like electron repulsion terms. As noted previously, PDDG/PM3 does represent a significant improvement over AM1, PM3, and SCC-DFTB for the 622 heats of formation; these alternatives yield MAEs of 6.8, 4.4, and 5.8 kcal/mol, respectively.³⁴ (7) The lowest MAEs are obtained at the B3LYP/6-31+G(d,p) level with addition of the dispersion terms from eq 2. The overall MAE for the 622 heats of formation is 2.4 kcal/mol in this case. It appears to be difficult to go below this limit without resorting to more complex procedures such as G2 or G3, which better represent electron correlation, or to nongeneral methods using bond and group corrections.

Specific Problem Cases. An examination of the complete results indicates that some of the largest systematic errors in the B3LYP calculations occur in bridged polycyclic systems, particularly diamantane, diamantanone, adamantane, adamantanone, protoadamantane, bullvalene, cubane, camphor, and norbornadiene, which have errors in the 4–13 kcal/mol range at the different levels and contribute about 0.1 kcal/mol to the overall MAEs. Another problem case is molecules with multiple N–N bonds; nitrogen, tetramethyltetrazene, azidomethylbenzene, methyl azide, *trans*-diazene, azoisopropane, cyclopentyl azide, cyclohexyl azide, diazirine,

and azopropane yield errors ranging between 4 and 15 kcal/mol, and their contribution to the average MAE is up to 0.1 kcal/mol. Some of these problems have been reported in other studies, e.g., the heat of formation of norbornadiene calculated with B3LYP/6-311+G(3df,2p) is 66.5 kcal/mol, which is 10 kcal/mol greater than the experimental value or the result of a G2 calculation.⁴⁰ It was also previously noted that there is a 10 kcal/mol error in the isomerization energy for toluene going to norbornadiene using B3LYP/6-31G(d).³⁴ Indeed, Schreiner et al. have found numerous problems with relative energies from B3LYP calculations for polycyclic hydrocarbon isomers.⁴¹ Curiously, the computed heats of formation for norbornane with the present B3LYP-based methods are within 1–2 kcal/mol of experiment. As another example, although other calculated heats of formation for dimethyldiazene are not available, the energy change for the *trans* to *cis* isomerization was found to be 9.8 kcal/mol at the B3LYP/DZP level and 5.0 kcal/mol with G2.⁴² In addition, the error reported in the G2/97 data set for nitrogen (N_2) is 1.4 kcal/mol with B3LYP/6-311+G(3df,2p), so the present errors of ca. 5 kcal/mol may reflect basis-set insufficiency. The largest error for all levels of calculation is for isophthalamide (20–27 kcal/mol, accounting for ca. 0.04 of the total MAEs). It has been a consensus outlier; Stewart's analysis points to a possible experimental error of ca. 20 kcal/mol in this case.³⁵

Concerning hydrocarbon homologation, there have been several attempts to address the scaling problem in B3LYP calculations. Already in 1996, Mole et al. fitted atom equivalents to the experimental values of heats of formation of 23 hydrocarbons and achieved rmsd values of 1.7 and 1.0 kcal/mol with the 6-31G(d) and 6-311G(d,p) basis sets.⁴³ The reasonable trend of increasing accuracy with the bigger basis set was obtained. However, Saeys et al. carried out a similar study with a larger set of 58 hydrocarbons with 10 or fewer carbon atoms.⁴⁴ After fitting the atomic energies, they were able to reduce the MAE for B3LYP/6-31G(d) from 7.4 to 2.2 kcal/mol, while the error with B3LYP/6-311G(d,p) decreased from 12.0 to only 3.1 kcal/mol. CBS-QB3 performed particularly well with the MAE declining from 2.2 to 0.6 kcal/mol. An apparently different approach was followed by Duan et al.⁴⁵ They based their corrections on the number of electrons for each atom at different levels and in different chemical environments (lone pairs, bonds). After fitting to experimental values this is equivalent to atom-based corrections. Recently, the smallest MAE for the full G3 set (222 molecules) reported so far has been given by Friesner et al.⁴⁶ Their method includes utilization of 22 optimized parameters that depend on atomic hybridization and bond types. This allows reduction of the MAE for B3LYP/6-311+G(3df,2p)-based calculations from 4.8 to 0.8 kcal/mol. However, methods that use such bonding corrections are not generally applicable, e.g., to nonequilibrium geometries or to bonding arrangements that have not been tested. Even with semiempirical MO methods, one can obtain average errors in heats of formation of 2 kcal/mol with the use of atom and bond corrections.⁴⁷

In the present case, the homologation problem was not specifically addressed since the optimization of the atomic

Table 3. Isomerization Enthalpies for Hydrocarbons (kcal/mol)

	Exp. ^a	B3LYP						PDDG/ PM3 ^b
		HF 6-31G (d) ^b	6-31G (d) ^b	6-31G (d) ^c	6-31G (d,p) ^b	6-31+ G(d,p) _b	6-31+ G(d,p) _b +OC6	
	1.24	2.18	-2.70	-2.76	-2.83	-2.73	-2.74	6.12
	21.81	27.44	22.22	21.48	21.98	23.16	23.17	21.27
	7.85	8.47	8.29	7.75	8.33	9.04	9.20	7.89
	1.13	1.81	1.40	1.35	1.37	1.34	0.77	1.94
	1.27	1.12	0.75	0.23	0.71	0.86	1.04	1.18
	2.79	2.62	3.68	3.67	3.62	3.17	3.17	4.62
	11.34	12.94	11.95	11.85	12.26	13.90	14.18	8.99
	22.17	22.59	21.63	22.19	21.22	19.92	19.54	25.16
	7.13	8.47	10.38	9.78	9.54	9.52	9.54	5.36
	5.06	1.42	1.43	0.75	1.53	1.70	2.37	5.76
	4.09	-9.81	-6.83	-7.54	-6.64	-6.79	-0.36	4.03
	46.65	56.37	57.30	56.06	57.11	57.11	57.58	45.59
	35.83	39.23	41.06	40.61	41.00	40.04	39.62	30.52
MAE		3.2	3.2	3.1	3.1	3.4	2.9	1.7

^a From experimental heats of formation; see ref 4 and the Supporting Information. ^b Single-point energy evaluations on SCC-DFTB optimized geometries except B3LYP/6-31G(d) geometries were used for propene, 2-methylpropene, and penta-1,3-diene. ^c Using geometries optimized at the B3LYP/6-31G(d) level.

energies considered all 622 data points. Nevertheless, the MAE for the G3 linear alkane series (methane to decane) declines to 4.6 kcal/mol for the present B3LYP/6-31G(d) procedure from the 7.5 kcal/mol in the original B3LYP/6-311+G(3df,2p) study by Redfern et al.¹³ The results still reflect a cumulative error, although it is greatly decreased. As shown in Figure 1, the slope for the line fitted to the error vs the number of carbon atoms decreases from -2.1 kcal \cdot mol $^{-1}$ per carbon atom with Redfern's data to -0.6 in the present calculations.

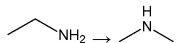
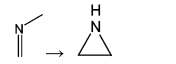
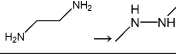
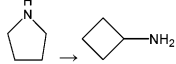
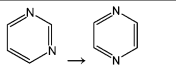
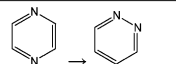
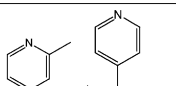
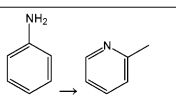
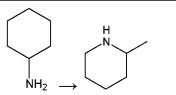
For a more general comparison of the effects of system size, it may be noted that the G2/97 set contains 148 heats of formation including 59 neutral, closed-shell, C, H, N, and O-containing molecules, which happen to have 1–6 heavy atoms.⁸ The MAE obtained for this subset using the published data is 2.2 kcal/mol,⁸ while the corresponding MAE from the present B3LYP/6-31G(d) calculations is 3.0 kcal/mol. However, for G3/99 heats of formation were added for an additional 38 neutral C, H, N, and O-containing molecules (5–10 heavy atoms).⁹ The original B3LYP/6-31G(d) calculations yielded an MAE of 7.8 kcal/mol for this set, while the present approach with eq 1 reduces the MAE for these larger molecules to 2.9 kcal/mol.

Isomerization Energies. Results for the same three sets of isomerization reactions, which were used in ref 34, are given in Tables 3–5. The changes in structure and bonding

for the 34 isomerizations are notably diverse and potentially challenging for the quantum methods. The experimental data and PDDG/PM3 results correspond to enthalpy changes at 25 °C, while the B3LYP results are the change in electronic energy. In the previous study,³⁴ it was found that including the zero-point corrections to the B3LYP/6-31G(d) results using B3LYP/6-31G(d) vibrational frequencies left the MAE for the 13 isomerizations in Table 3 unchanged at 3.1 kcal/mol, and inclusion of the thermal corrections to the vibrational energies only reduced the MAE to 2.9 kcal/mol. Consequently, these adjustments were neglected. Grimme et al. have also recently examined the 34 isomerizations with a variety of DFT procedures and their SCS-MP2 method.⁴⁸ They also performed reference calculations at the CCSD-(T)-cc-PV(DT)Z//B3LYP/TZV(d,p) level, which called into question four of the experimental enthalpy changes in ref 34. The corresponding revised differences in enthalpies of isomerization for the four cases have been adopted here, as noted in Tables 4 and 5.

For the hydrocarbons in Table 3, there are no striking problems with small ring compounds. However, the greatest errors with the B3LYP methods are for the largest molecules, the last four entries. The conversions of neopentane to pentane and tetramethylbutane to octane, with errors of 3.5 and 10.5 kcal/mol, reflect the now well-known branching error. As in most of the entries in this table, the increase in

Table 4. Isomerization Enthalpies (kcal/mol) for Nitrogen-Containing Molecules

	Exp. ^a	B3LYP						PDDG/ PM3 ^b
		HF 6-31G (d) ^b	6-31G (d) ^b	6-31G (d) ^c	6-31G (d,p) ^b	6-31+G (d,p) ^b	6-31+G (d,p) +OC6 ^b	
CH ₃ CN → CH ₃ NC	24.2 ^d	21.16	24.94	24.07	25.17	23.12	23.12	25.78
	6.92	5.33	4.26	4.51	5.65	6.82	6.69	7.11
	11.71	14.63	14.91	14.40	13.47	13.34	13.61	17.83
	26.06	22.53	19.29	20.31	21.98	24.54	25.23	30.58
	10.65	15.43	14.43	13.89	12.94	11.78	11.42	5.03
	4.6 ^d	6.02	3.65	4.07	3.65	3.69	3.70	2.95
	19.66	20.23	18.41	18.60	18.26	18.33	18.33	16.06
	1.10	1.44	1.14	0.89	1.22	1.49	1.40	-0.27
	2.89	-4.31	-2.95	-2.53	-0.18	1.66	1.79	1.12
	4.88	2.01	1.00	1.26	2.30	3.21	3.26	5.64
MAE		2.8	2.9	2.5	1.9	1.1	1.0	2.7

^a From experimental heats of formation; see ref 4 and the Supporting Information. ^b Single-point energy evaluations on SCC-DFTB optimized geometries. ^c Using geometries optimized at the B3LYP/6-31G(d) level. ^d Revised value based on ref 48.


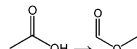
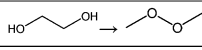
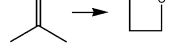
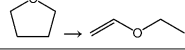
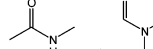

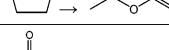
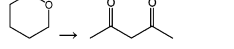
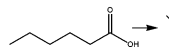
basis set seems to have mixed effects. It does improve slightly the agreement for the neopentane to pentane isomerization, but it has a negligible effect on the tetramethylbutane to octane case. However, strikingly, the dispersion correction reduces these errors by 0.7 and 6.4 kcal/mol, respectively. The 10 kcal/mol error for the toluene-norbornadiene conversion is dominated by the error in the heat of formation in the latter, as described above. The problem is not relieved with the larger basis sets. Owing to the compactness of the bicyclic molecule, the present dispersion correction also provides no help in this case, though overall it lowers the MAE by 0.5 kcal/mol at the B3LYP/6-31+G(d,p) level.

The isomerizations of nitrogen containing molecules reported in Table 4 show a general pattern of having large errors at the B3LYP/6-31G(d) level, e.g., 7 kcal/mol for ethylenediamine to 1,2-dimethylhydrazine and 6 for aniline to 2-methylpyridine. In fact, the problem is general to cases where the number of N–H bonds change; N–H bonds appear to not be energetically favorable enough. As noted previously, zero-point corrections are not the issue here; their addition actually worsens the accord by about 1 kcal/mol.³⁴ However, an increase in the size of the basis set in these cases has very favorable effects. The improvement is sufficient to lower the B3LYP MAE of the set from 2.5 at the 6-31G(d) level to 1.9 at 6-31G(d,p) and 1.1 kcal/mol at 6-31+G(d,p). It is noted that the experimental value for pyrimidine to pyrazine that was quoted previously, 0.03 kcal/

mol,³⁴ has been separately brought into question by Grimme et al.,⁴⁸ who obtained a value of 4.6 kcal/mol from CCSD-(T)-cc-PV(DT)Z//B3LYP/TZV(d,p), and by Cheng et al., who obtained 4.5 kcal/mol using G3 calculations.⁴⁹ The present B3LYP and PDDG/PM3 results support their higher estimates. The results of Grimme et al.⁴⁸ also indicate that the correct value for the acetonitrile to methyl isocyanide conversion should be 24.2 kcal/mol rather than the former 21.4 kcal/mol,³⁴ which is also supported by the B3LYP/6-31+G(d,p) and PDDG/PM3 estimates.

In Table 5, an analogous pattern is found as in Table 4 with the largest errors occurring for isomerizations that change the number of O–H bonds. The 12-kcal/mol error for the 1,2-ethanediol to dimethyl peroxide transformation is striking at the B3LYP/6-31G(d) level. Again, the problem is largely removed with an increase in the basis set size. There is also a 6-kcal/mol error for the acetic acid to methyl formate conversion with B3LYP/6-31G(d). However, the acid to ester conversion for hexanoic acid to methyl pivalate seems remarkably on target until one realizes that there is a cancellation with the alkyl branching error (ca. 4 kcal/mol for neopentane to pentane). So, as noted before,³⁴ a particularly bad case for B3LYP/6-31G(d) would be to consider the pivalic acid to ethyl propanoate isomerization, (CH₃)₃-CCOOH → CH₃CH₂COOCH₂CH₃. The experimental enthalpy change is +6.3 kcal/mol, while the B3LYP/6-31G(d) energy difference is –5.2 kcal/mol. For the entries in Table

Table 5. Isomerization Enthalpies (kcal/mol) for Oxygen-Containing Molecules

	Exp. ^a	HF/	B3LYP/					PDDG/ PM3 ^b
		6-31G (d) ^b	6-31G (d) ^b	6-31G (d) ^c	6-31G (d,p) ^b	6-31+G (d,p) ^b	6-31+G (d,p) +OC6 ^b	
<chem>C2H5OH -> (CH3)2O</chem>	12.25	7.90	5.81	5.50	8.55	10.59	10.27	10.01
	27.15	32.49	27.52	27.52	27.49	27.64	27.64	32.27
	18.30	15.98	13.05	11.79	15.67	17.21	16.56	16.12
	62.57	64.04	50.50	50.12	55.62	59.86	60.63	61.36
	32.65	38.29	33.72	31.80	33.89	34.34	34.51	30.46
	10.39	17.44	13.21	12.26	12.61	11.32	10.93	15.60
	9.4 ^d	10.09	7.30	7.10	8.72	9.80	9.51	10.57
	12.33	14.16	12.59	12.61	11.99	11.12	10.07	15.90
	5.0 ^d	0.91	3.64	5.53	3.43	1.74	0.59	3.19
	4.39	7.35	4.87	4.83	7.41	9.59	7.42	8.82
	8.13	6.14	8.43	8.11	8.43	7.55	7.61	8.64
MAE		3.3	2.6	2.6	1.9	1.8	1.7	2.7

^a From experimental heats of formation; see ref 4 and the Supporting Information. ^b Single-point energy evaluations on SCC-DFTB optimized geometries except B3LYP/6-31G(d) geometries were used for THF and acetylacetone. ^c Using geometries optimized at the B3LYP/6-31G(d) level. ^d Revised value based on ref 48.

5, the results of Grimme et al.⁴⁸ provide revision of the value for the *N*-methacetamide to dimethylformamide conversion to 9.4 kcal/mol from 13.5 kcal/mol,³⁴ again closer to the B3LYP/6-31+G(d,p) and PDDG/PM3 results, and for the valerolactone to acetylacetone isomerization from 0.3 to 5.0 kcal/mol, in better agreement with the PDDG/PM3 result.

Overall, the B3LYP/6-31+G(d,p) results in Tables 4 and 5 are impressive, and for these relatively small molecules the dispersion correction has little impact. The greater impact for the hydrocarbons in Table 3 is dominated by the improvement for the tetramethylbutane isomerization. For the 34 isomerizations the overall MAEs in kcal/mol are 3.2 (HF/6-31G(d)), 2.7 (B3LYP/6-31G(d)), 2.4 (B3LYP/6-31G(d,p)), 2.2 (B3LYP/6-31+G(d,p)), 1.9 with the OC6 term, and 2.3 (PDDG/PM3). If the comparisons are made to the 34 energy changes from Grimme et al.⁴⁸ instead of the present enthalpy changes, the overall MAEs for the 34 isomerizations are 3.0, 2.9, 2.6, 2.4, 2.2, and 2.4 kcal/mol, respectively.

Grimme et al. also studied the 34 isomerization reactions with their modified SCS-MP2 procedure and with several functionals and many basis sets.⁴⁸ For B3LYP, starting from 6-31G(d) the rmsd improves from 4.33 to 3.32 kcal/mol by using the Dunning type *aug-cc-pVTZ* basis set, though it requires 211 times more CPU time. The corresponding SCS-MP2 calculations show rmsd values of 2.67 and 1.25 kcal/mol, respectively. However, the isomerization of tetrame-

thylbutane to octane still favors the linear isomer by 8.0 kcal/mol. In a very recent paper, Schwabe and Grimme described the implementation of their empirical dispersion term with the B3LYP, B2PLYP, and mPWPLYP functionals. When tested on the full G3/99 set of 223 heats of formation they obtained reductions in the MAEs from 5.6 to 3.1, 2.4 to 1.7, and 2.1 to 1.7 kcal/mol, respectively.⁵⁰

Conclusions

The present evaluation of the performance of B3LYP with different basis sets on 622 neutral, closed-shell organic compounds containing C, H, N, and O has provided a clearer assessment of its capabilities and limitations for organic molecules. When used with the popular 6-31G(d) basis set, the average errors are about 3.0 kcal/mol for both isomerization energies and heats of formation, when the latter are computed via eq 1. Optimization of the atomic energies in eq 1 helps alleviate the systematic homologation errors with B3LYP (Figure 1). Nevertheless, improvement with increasing basis-set size is modest for the heats of formation, though addition of the dispersion correction with 6-31+G(d,p) lowers the MAE to 2.4 kcal/mol (Table 2). There is greater improvement for the 34 isomerization reactions with a MAE of 2.2 kcal/mol for B3LYP/6-31+G(d,p) and a MAE of 1.9 kcal/mol with addition of the dispersion terms (Tables 3–5). The greatest benefit of the dispersion terms is in reducing

the underestimate of the stability of branched over linear alkyl groups; however, significant problems remain for bridged polycyclic molecules. It is clear that the 2.0-kcal/mol barrier in MAEs cannot be overcome without the use of a functional other than B3LYP and/or resorting to compound methods and empirical corrections.

A second key motivation for the present study was to ascertain the possible improvements in accuracy that could be obtained from the DFT calculations over the semiempirical PDDG/PM3 method when they are put on an even footing by use of eq 1 for computation of the 622 heats of formation. As it turned out, there is no significant difference in quality between the B3LYP-based results and those from PDDG/PM3 for the heats of formation and isomerization energies. Though this confirms that PDDG/PM3 is an efficient alternative for evaluation of the energetics of organic reactions, obvious guidance has not emerged on how to create a further-improved semiempirical method. There are no striking, general errors with PDDG/PM3, though gains could be sought in performance for small heterocycles (Tables 4 and 5) as well as for conformational energetics and hydrogen bonding.^{4–6,34} The recent scrutiny of the performance of quantum chemistry methods has demonstrated the importance of testing on large, diverse data sets. This does appear to be leading to the generation of improved DFT methodology such as the M05-2X functional.²⁰ In view of the need for rapid methods that can be applied to very large systems, as in the examination of enzymatic reactions or design of new materials, greater development efforts in the semiempirical arena also appear warranted.

Acknowledgment. The authors thank Dr. M. Elstner for the SCC-DFTB code used in this work and the National Science Foundation (CHE-0446920) for financial support.

Supporting Information Available: Computed and experimental data. This material is available free of charge via the Internet at <http://pubs.acs.org>.

References

- (1) Kohn, W.; Sham, L. J. *Phys. Rev.* **1965**, *140* (4A), 1133–1138.
- (2) Hohenberg, P.; Kohn, W. *Phys. Rev.* **1964**, *136* (3B), 864–871.
- (3) Stephens, P. J.; Devlin, F. J.; Chabalowski, C. F.; Frisch, M. J. *J. Phys. Chem.* **1994**, *98*, 11623–11627.
- (4) Repasky, M. P.; Chandrasekhar, J.; Jorgensen, W. L. *J. Comput. Chem.* **2002**, *23*, 1601–1622.
- (5) Tubert-Brohman, I.; Guimaraes, C. R. W.; Repasky, M. P.; Jorgensen, W. L. *J. Comput. Chem.* **2004**, *25*, 138–150.
- (6) Tubert-Brohman, I.; Guimaraes, C. R. W.; Jorgensen, W. L. *J. Chem. Theory Comput.* **2005**, *1*, 817–823.
- (7) Riley, K. E.; Op't Holt, B. T.; Merz, K. M., Jr. *J. Chem. Theory Comput.* **2007**, *3*, 407–433.
- (8) Curtiss, L. A.; Raghavachari, K.; Redfern, P. C.; Pople, J. A. *J. Chem. Phys.* **1997**, *106*, 1063–1079.
- (9) Curtiss, L. A.; Raghavachari, K.; Redfern, P. C.; Pople, J. A. *J. Chem. Phys.* **2000**, *112*, 7374–7383.
- (10) Xu, X.; Zhang, Q.; Muller, R. P.; Goddard, W. A., III. *J. Chem. Phys.* **2005**, *122*, 014105.
- (11) Kafafi, S. A. *J. Phys. Chem.* **1998**, *102*, 10404–10413.
- (12) Grimme, S. *J. Phys. Chem. A* **2005**, *109*, 3067–3077.
- (13) Redfern, P. C.; Zapol, P.; Curtiss, L. A.; Raghavachari, K. *J. Phys. Chem. A* **2000**, *104*, 5850–5854.
- (14) (a) Wodrich, M. D.; Corminboeuf, C.; Schleyer, P. v. R. *Org. Lett.* **2006**, *8*, 3632–3634. (b) Wodrich, M. D.; Corminboeuf, C.; Schreiner, P. R.; Fokin, A. A.; Schleyer, P. v. R. *Org. Lett.* **2007**, *9*, 1851–1854.
- (15) Grimme, S. *Angew. Chem., Int. Ed.* **2006**, *45*, 4460–4464.
- (16) Grimme, S.; Steinmetz, M.; Korth, M. *J. Chem. Theory Comput.* **2007**, *3*, 42–45.
- (17) Rablen, P. R.; Lockman, J. W.; Jorgensen, W. L. *J. Phys. Chem. A* **1998**, *102*, 3782–3797.
- (18) Tsuzuki, S.; Lüthi, H. P. *J. Chem. Phys.* **2001**, *114*, 3949–3957.
- (19) Zhao, Y.; Truhlar, D. G. *J. Phys. Chem. A* **2005**, *109*, 5656–5667.
- (20) Zhao, Y.; Schultz, N. E.; Truhlar, D. G. *J. Chem. Theory Comput.* **2006**, *2*, 364–382.
- (21) Vydrov, O. A.; Scuseria, G. E. *J. Chem. Phys.* **2006**, *125*, 234109–1 to 234109–9.
- (22) Schwabe, T.; Grimme, S. *Phys. Chem. Chem. Phys.* **2006**, *8*, 4398–4401.
- (23) Grimme, S. *J. Comput. Chem.* **2004**, *25*, 1463–1473.
- (24) Grimme, S. *J. Comput. Chem.* **2006**, *27*, 1787–1799.
- (25) Antony, J.; Grimme, S. *Phys. Chem. Chem. Phys.* **2006**, *8*, 5287–5393.
- (26) Grimme, S.; Antony, J.; Schwabe, T.; Mück-Lichtenfeld, C. *Org. Biomol. Chem.* **2007**, *5*, 741–758.
- (27) McNamara, J. P.; Hillier, I. H. *Phys. Chem. Chem. Phys.* **2007**, *9*, 2362–2370.
- (28) Jurečka, P.; Černý, J.; Hobza, P.; Salahub, D. R. *J. Comput. Chem.* **2007**, *28*, 555–569.
- (29) Frisch, M. J.; Trucks, G. W.; Schlegel, H. B.; Scuseria, G. E.; Robb, M. A.; Cheeseman, J. R.; Montgomery, J. A., Jr.; Vreven, T.; Kudin, K. N.; Burant, J. C.; Millam, J. M.; Iyengar, S. S.; Tomasi, J.; Barone, V.; Mennucci, B.; Cossi, M.; Scalmani, G.; Rega, N.; Petersson, G. A.; Nakatsuji, H.; Hada, M.; Ehara, M.; Toyota, K.; Fukuda, R.; Hasegawa, J.; Ishida, M.; Nakajima, T.; Honda, Y.; Kitao, O.; Nakai, H.; Klene, M.; Li, X.; Knox, J. E.; Hratchian, H. P.; Cross, J. B.; Adamo, C.; Jaramillo, J.; Gomperts, R.; Stratmann, R. E.; Yazyev, O.; Austin, A. J.; Cammi, R.; Pomelli, C.; Ochterski, J. W.; Ayala, P. Y.; Morokuma, K.; Voth, G. A.; Salvador, P.; Dannenberg, J. J.; Zakrzewski, V. G.; Dapprich, S.; Daniels, A. D.; Strain, M. C.; Farkas, O.; Malick, D. K.; Rabuck, A. D.; Raghavachari, K.; Foresman, J. B.; Ortiz, J. V.; Cui, Q.; Baboul, A. G.; Clifford, S.; Cioslowski, J.; Stefanov, B. B.; Liu, G.; Liashenko, A.; Piskorz, P.; Komaromi, I.; Martin, R. L.; Fox, D. J.; Keith, T.; Al-Laham, M. A.; Peng, C. Y.; Nanayakkara, A.; Challacombe, M.; Gill, P. M. W.; Johnson, B.; Chen, W.; Wong, M. W.; Gonzalez, C.; Pople, J. A. *Gaussian 03, Revision B.03*; Gaussian, Inc.: Pittsburgh, PA, 2003.
- (30) Jorgensen, W. L.; Tirado-Rives, J. *J. Comput. Chem.* **2005**, *26*, 1689–1700.

- (31) Stewart, J. J. P. *J. Comput.-Aided Mol. Des.* **1990**, *4*, 1–105.
- (32) Code and parameter files to modify MOPAC for PDDG/PM3 calculations are available at <http://www.jorgensenresearch.com>.
- (33) Elstner, M.; Porezag, D.; Jungnickel, G.; Elsner, J.; Haugk, M.; Frauenheim, T.; Suhai, S.; Seifert, G. *Phys. Rev. B* **1998**, *58*, 7260–7268.
- (34) Sattelmeyer, J. W.; Tirado-Rives, J.; Jorgensen, W. L. *J. Phys. Chem. A* **2006**, *110*, 13551–13559.
- (35) Stewart, J. J. P. *J. Mol. Model.* **2004**, *10*, 6–12.
- (36) Csonka, G. I.; Ruzinsky, A.; Tao, J.; Perdew, J. P. *Int. J. Quantum Chem.* **2005**, *101*, 506–511.
- (37) Brothers, E. N.; Scuseria, G. E. *J. Chem. Theory Comput.* **2006**, *2*, 1045–1049.
- (38) Voityuk, A. A. *J. Chem. Theory Comput.* **2006**, *2*, 1038–1044.
- (39) Jorgensen, W. L.; Maxwell, D. S.; Tirado-Rives, J. *J. Am. Chem. Soc.* **1996**, *118*, 11225–11236. The generic parameters are (σ in Å, ϵ in kcal/mol) are as follows: C (3.55, 0.07), H (2.46, 0.03), N (3.25, 0.17), and O (3.00, 0.17).
- (40) Rogers, D. W.; McLafferty, F. J. *J. Phys. Chem. A* **1999**, *103*, 8733–8737.
- (41) Schreiner, P. R.; Fokin, A. A.; Pascal, R. A., Jr.; de Meijere, A. *Org. Lett.* **2006**, *8*, 3635–3638.
- (42) Vrábel, I.; Biscupič, S.; Staško, A. *J. Phys. Chem. A* **1997**, *101*, 5805–5812.
- (43) Mole, S. J.; Zhou, X.; Liu, R. *J. Phys. Chem.* **1996**, *100*, 14665–14671.
- (44) Saeys, M.; Reyners, M.-F.; Marin, G.; Van Speybroeck, V.; Waroquier, M. *J. Phys. Chem. A* **2003**, *107*, 9147–9159.
- (45) Duan, X.-M.; Song, G.-L.; Li, Z.-H.; Wang, X.-J.; Chen, G.-H.; Fan, K.-N. *J. Chem. Phys.* **2004**, *121*, 7086–7095.
- (46) Friesner, R. A.; Knoll, E. H.; Cao, Y. *J. Chem. Phys.* **2006**, *125*, 124107-1–124107-24.
- (47) Repasky, M. P.; Chandrasekhar, J.; Jorgensen, W. L. *J. Comput. Chem.* **2002**, *23*, 498–510.
- (48) Grimme, S.; Steinmetz, M.; Korth, M. *J. Org. Chem.* **2007**, *72*, 2118–2126.
- (49) Cheng, M.-F.; Ho, H.-O.; Lam, C.-S.; Lee, W.-K. *J. Serb. Chem. Soc.* **2002**, *67*, 257–264.
- (50) Schwabe, T.; Grimme, S. *Phys. Chem. Chem. Phys.* **2007**, *9*, 3397–3406.

CT700248K

JCTC

Journal of Chemical Theory and Computation

Density Functional Theory in Transition-Metal Chemistry: Relative Energies of Low-Lying States of Iron Compounds and the Effect of Spatial Symmetry Breaking

Anastassia Sorokin, Mark A. Iron, and Donald G. Truhlar*

Department of Chemistry and Supercomputing Institute, University of Minnesota,
Minneapolis, Minnesota 55455-0431

Received September 25, 2007

Abstract: The ground and lower excited states of Fe_2 , Fe_2^- , and FeO^+ were studied using a number of density functional theory (DFT) methods. Specific attention was paid to the relative state energies, the internuclear distances (r_e), and the harmonic vibrational frequencies (ω_e). A number of factors influencing the calculated values of these properties were examined. These include basis sets, the nature of the density functional chosen, the percentage of Hartree–Fock exchange in the density functional, and constraints on orbital symmetry. A number of different types of generalized gradient approximation (GGA) density functionals (straight GGA, hybrid GGA, meta-GGA, and hybrid meta-GGA) were examined, and it was found that the best results were obtained with hybrid GGA or hybrid meta-GGA functionals that contain nonzero fractions of HF exchange; specifically, the best overall results were obtained with B3LYP, M05, and M06, closely followed by B1LYP. One significant observation was the effect of enforcing symmetry on the orbitals. When a degenerate orbital (π or δ) is partially occupied in the $^4\Phi$ excited state of FeO^+ , reducing the enforced symmetry (from C_{6v} to C_{4v} to C_{2v}) results in a lower energy since these degenerate orbitals are split in the lower symmetries. The results obtained were compared to higher level ab initio results from the literature and to recent PBE+U plane wave results by Kulik et al. (*Phys. Rev. Lett.* **2006**, *97*, 103001). It was found that some of the improvements that were afforded by the semiempirical +U correction can also be accomplished by improving the form of the DFT functional and, in one case, by not enforcing high symmetry on the orbitals.

1. Introduction

Transition-metal centers have great versatility in their bonding. Consequently, accurate theoretical treatment of transition-metal chemistry demands a flexible theoretical framework that treats all energetically accessible spin states, spin couplings, and valence states in an even-handed fashion, which in wave function theory requires a multiconfigurational treatment. This poses a difficult problem for the Kohn–Sham density functional theory (DFT) because all information on the multiconfigurational character of the wave function is contained in the exchange–correlation energy E_{XC} , which is computed from an electron density that is in turn obtained

from a single Hartree product of orbitals.^{1,2} Even when a single antisymmetrized product (Slater determinant) of orbitals does not describe the true electronic wave function well, the Kohn–Sham ground-state energy is correct if one solves the Kohn–Sham equations for the orbitals that give the lowest-energy solution,¹ even though the Kohn–Sham orbitals and eigenvalues, except for the highest orbital eigenvalue,³ do not have any strict physical significance,^{4–6} and the Kohn–Sham Slater determinant that generates the accurate electron density may have different spin properties than the true wave function.^{7–9} Nevertheless, great progress has been made in understanding transition-metal chemistry in terms of the Kohn–Sham theory.^{10–13}

* Corresponding author e-mail: truhlar@umn.edu.

One especially difficult issue for the Kohn–Sham theory (as well as multiconfigurational wave function theory) is the calculation of relative spin-state energetics.^{9,11,12,14–17} Hartree–Fock exchange¹⁸ and Hubbard-like corrections¹⁹ have been found^{9,14,15,17} to have large effects on the ordering of the various spin-coupled states predicted by the Kohn–Sham theory.

In an effort to obtain practical and accurate predictions of relative spin-state energies of polynuclear transition-metal complexes or to determine which spin state is the ground state, it has become common to use an analysis based on the approximate (and not uniquely defined) Heisenberg–Dirac spin Hamiltonian.^{12,20–22} In this analysis, a broken-spatial-symmetry spin-unrestricted Kohn–Sham determinant is treated as a weighted average of spin multiplets. The method is often considered an improvement over treating the variationally fully optimized broken-symmetry-solution to the Kohn–Sham equations as the best approximation to the ground state.¹² A key feature of the broken-spatial symmetry solution used in this method is that electrons with opposite spins may localize on different metal centers so that the Slater determinant corresponds to an antiferromagnetically coupled state.²³ A large literature has developed on this and related broken-symmetry approaches.^{24–33} Broken-symmetry solutions have also been studied in other contexts, and it has often been found that it is important to allow the orbitals to break symmetry in order to get a qualitatively correct description of the system.^{33–42} The energies of the broken-symmetry states are often used without correcting for their spin character.^{34–42} In fact, it has been argued on theoretical grounds that the fully self-consistent broken-symmetry single Slater determinant of lowest total energy is the correct solution to the problem.⁷ Other aspects of broken-symmetry solutions have also been discussed recently, usually in the context that broken symmetry is considered to be an artifact best avoided.^{43–47} Thus, there is not a unified consensus on the use and interpretation of broken-symmetry solutions.

There have been several recent studies of the accuracy of various density functionals for transition-metal–ligand bond energies, relative spin-state energetics, and geometries,^{48–70} and the interpretation of these studies depends in part on how one considers symmetry. The present paper uses the Kohn–Sham theory to calculate spin-state energies and geometries for Fe₂, Fe₂[−], and FeO⁺ (which were chosen to allow comparison to the results of ref 15), and in each case we studied the stability of the solution to breaking symmetry. When symmetry is broken, we compare results for broken-symmetry and restricted solutions.

2. Methods

All calculations in this paper were carried out using the *NWChem* version 5.0 quantum chemistry package,^{71,72} to which the M06 patch⁷³ was applied.

We carried out calculations with several density functionals,^{18,61,70,74–78} which are explained in Table 1. In this Table, *X* denotes the percentage of Hartree–Fock exchange. We will also include Hartree–Fock (HF) calculations⁷⁹ for comparison. The typing of density functionals in Table 1

Table 1. Density Functionals Used for the Present Calculations

type	functional	<i>X</i>	ref
GGA	BLYP	0	74,75
	PBE	0	77
meta-GGA ^a	M06-L	0	67
hybrid GGA	B3LYP	20	74–76
	B1LYP	25	74,75,78
	BHandHLYP	50	18 ^b
	HFLYP	100	75,79 ^c
hybrid meta-GGA ^a	M06	27	70
	M05	28	61

^a Meta-GGA and hybrid meta-GGA functionals depend on spin kinetic energy density, but the other functionals do not. ^b As modified in the *Gaussian* computer package. ^c HF exchange with LYP correlation.

Table 2. Sizes of Basis Sets Employed for Fe

basis	primitive	contracted
TZQ	15s11p6d1f	10s7p4d1f
TZQ(3df)	15s11p6d3f1g	10s7p4d3f1g
QZVP	25s19p11d3f1g	12s7p6d3f1g

follows the usual notation. Thus, generalized gradient approximation (GGA) functionals depend only on the local spin densities for up-spin and down-spin electrons and the magnitudes of the gradients of these spin densities. Meta-GGAs also depend on spin kinetic energy densities, and hybrid GGAs and hybrid meta-GGAs also include Hartree–Fock exchange.

The BLYP, B3LYP, B1LYP, BHandHLYP, and HFLYP functionals^{18,74–76,78} form a sequence differing mainly in the value of *X* (in addition, B3LYP incorporates empirical scaling in the correlation energy). PBE is similar in spirit to BLYP but with theoretically more justifiable exchange and correlation functionals.⁷⁷ M05 and M06, in contrast, are more complicated functionals in which kinetic energy density and improved functional forms are employed in the exchange functional to make it more compatible with a wide range of *X*, and this in turn allows the correlation functional, which also depends on kinetic energy density and which is optimized simultaneously with exchange, to become more physical by not being required to be consistent with less physical exchange.^{61,70} In contrast, the GGA correlation is more compatible with GGA exchange than with exact exchange.⁸⁰

Three different basis sets were used for Fe: the basis called TZQ by Schultz et al.^{36,59} which is taken from Wachters, Hay, Raghavachari, and Trucks⁸² and is denoted 6-311+G* in *Gaussian*;⁸² a basis we call TZQ(3fg), which is called 6-311+G(3df) in *Gaussian*; and the QZVP basis of Weigend et al.⁸³ The sizes of these basis sets are compared in Table 2. For O, the 6-311+G(3df) basis set⁸⁴ was used in all calculations.

All calculations are spin unrestricted; thus HF could be called UHF, B3LYP could be called UB3LYP, etc. We assign spin in the usual way,⁵ where *S* is taken as *M_S* rather than attempting to assign spin states by interpreting the Kohn–Sham determinant as if it were a wave function.

Table 3. Electronic Configurations of the Various Spin States of Fe₂, Fe₂⁻, and FeO⁺

molecule	symmetry	electronic configuration
Fe ₂	⁹ Σ _g ⁻	3d ¹³ : σ _g ² π _u ⁴ δ _g ² π _g ² δ _u ² σ _u ; 4s ³ : σ _g ² σ _u
	⁷ Σ _g ⁻	3d ¹³ : σ _g ² π _u ⁴ δ _g ² π _g ² δ _u ² σ _u ; 4s ³ : σ _g ² σ _u
	⁷ Δ _u	3d ¹⁴ : σ _g ² π _u ⁴ δ _g ³ π _g ² δ _u ² σ _u ; 4s ² : σ _g ²
	⁹ Δ _g	3d ¹³ : σ _g ² π _u ⁴ δ _g ² π _g ² δ _u ² σ _u ; 4s ³ : σ _g ² σ _u
Fe ⁻	⁸ Σ _u ⁻	3d ¹³ : σ _g ² π _u ⁴ δ _g ² π _g ² δ _u ² σ _u ; 4s ⁴ : σ _g ² σ _u
	⁸ Δ _g	3d ¹⁴ : σ _g ² π _u ⁴ δ _g ³ π _g ² δ _u ² ; 4s ³ : σ _g ² σ _u
FeO ⁺	⁶ Σ ⁺	1σ ² 2σ ² 1π ⁴ 1δ ² 3σ ¹ 2π ²
	⁴ Φ	1σ ² 2σ ² 1π ⁴ 1δ ³ 3σ ¹ 2π ¹

(Setting $S = M_S$ would be correct for spin-restricted orbital products with the highest possible M_S of a given configuration.⁸⁵)

The calculations were carried out for the spin states of Fe₂, Fe₂⁻, and FeO⁺ listed in Table 3. The diatomic molecules studied in this paper have $D_{\infty h}$ (Fe₂, Fe₂⁻) and $C_{\infty v}$ (FeO⁺) symmetries, but most electronic structure codes do not allow the use of these high symmetries. For Fe₂, we performed checks on some of the states (namely ⁹Σ_g⁻, ⁹Δ_g, and ⁷Δ_u), and for Fe₂⁻ we performed checks for the ⁸Δ_g state; we found that one gets the same results in C_{2v} and D_{4h} symmetries, so only the D_{4h} results are presented for Fe₂ and Fe₂⁻. For FeO⁺ we present results for three different symmetries: C_{2v} , C_{4v} , and C_{6v} .

All calculations are nonrelativistic. One would expect that relativistic effects would be small but not completely negligible.^{69,86} Relativistic effects should be included for quantitative comparison with experiment, but one of our main goals here was to compare to previous theoretical calculations, which all neglected relativistic effects.^{15,87–92}

It should also be noted that in *NWChem*, while analytical gradients are available for open-shell DFT, analytical Hessians are not. Therefore, the DFT harmonic vibrational frequencies ω_e were calculated by numerical central differences.

We checked that the results are independent of the starting guesses for the orbitals.

3. Results and Discussion

Our results for relative state energies ΔE , equilibrium internuclear distance r_e , and harmonic vibrational frequencies ω_e are given in Tables 4–9, where they are also compared to previous theoretical^{15,87–92} and experimental^{93–95} results. A point of special interest is the comparison to DFT+U^{19,96} calculations,^{15,92} in particular PBE+U, where +U denotes a Hubbard-like⁹⁶ correction, carried out with a plane wave (PW) basis. The DFT+U model has become very popular in solid-state physics where it is intended to correct for excessively delocalized states sometimes predicted by Kohn–Sham calculations with the local spin density approximation or with GGA functionals.^{19,96,98–108}

All energies in tables are electronic energy plus nuclear repulsion and do not include vibrational energy.

In the tables, “/3fg” denotes use of the TZQ(3df) basis for Fe and “/f” denotes use of the TZQ basis for Fe; both are combined with 6-311+G(3df) for O in FeO⁺.

3.1. Fe₂. Experimental spectra⁹⁴ show that the ground state of Fe₂ is the $4s^33d^{13} \ ^9\Sigma_g^-$ state, there are only two states below 1 eV (namely the ground state and a state with an excitation energy of 0.53 eV),⁹⁴ the ground-state harmonic vibrational frequency ω_e is 300 cm⁻¹,⁹³ and r_e and ω_e are almost the same for the two lowest electronic states.⁹⁴ These results were reasonably well confirmed by Hübner and Sauer⁸⁹ employing wave function theory (WFT) calculations, in particular multireference configuration interaction with single and double excitations¹⁰⁹ and a Pople cluster correction¹¹⁰ (MRCISD+Q^P) with an atomic natural orbital¹¹¹ (ANO) basis set. Shortly afterward though, Bauschlicher and Ricca⁹⁰ presented an internally contracted multireference configuration interaction¹¹² with Davidson correction¹¹³ (IC-MRCI+Q) calculations with a different ANO basis set.¹¹⁴ They also presented some corrections for additional correlation effects and for basis set extension; we will call these corrected MRCI or “cor. MRCI”. These calculations⁹⁰ agree with previous work^{89,94} that the ⁹Σ_g⁻ state is the ground state, but the authors cautioned that the calculations are not definitive and raised the possibility of a ⁷Δ_u ground state. Based on the experimental⁹⁴ and high-level theoretical^{89,90} results, we will consider, for the purposes of evaluating our DFT result, the ⁹Σ_g⁻ state to be the ground state.

The PBE calculations with the TZQ/3fg and TZQ/f Gaussian-basis-set choices in Table 4 agree well with each other and reasonably well with the PBE plane wave calculations of Rollman et al.⁹² but less well with the plane wave calculations of Kulik et al.¹⁵ (The requirements for agreement between such calculations on molecules have been studied recently.¹¹⁵)

The relative state energies are particularly interesting because they include three states with three electrons in 4s orbitals and 13 electrons in 3d orbitals (⁹Σ_g⁻, ⁷Σ_g⁻, and ⁹Δ_g, see Table 3) and one state with two electrons in 4s orbitals and 14 in 3d orbitals states (⁷Δ_u). The ⁷Σ_g⁻ state has the same dominant configuration as the ⁹Σ_g⁻ state but differs in the spin coupling between the 3d and 4s subshells.⁸⁹ Table 4 shows that certain DFT methods predict negative values for $\Delta E(^7\Sigma_g^-)$, $\Delta E(^7\Delta_u)$, or $\Delta E(^9\Delta_g)$ and thus predict the wrong ground state. The PBE functional predicts the wrong ground state, whereas PBE+U corrects this. Furthermore, the BLYP and M06-L density functionals, which are the other two functionals studied (besides PBE) that have neither Hartree–Fock exchange nor a Hubbard correction, also predict the incorrect ground state. In contrast, the hybrid GGA (B3LYP and BHandHLYP) and the hybrid meta-GGA (M06 and M05) functionals, like PBE+U, predict the correct ground state. Of the methods that predict the correct ground state, M05 and PBU+U predict the most accurate bond distances, but only PBE+U gets the correct order of all four states studied.

It is well-known that, all other factors being equal, Hartree–Fock exchange favors high-spin states relative to low-spin ones. One reason for this is that Hartree–Fock exchange introduces the Fermi hole¹¹⁶ (by which same-spin electrons avoid one another), and high-spin states have more same-spin interactions. For the sequence BLYP, B1LYP, BHandHLYP, and HFLYP, all factors other than X are

Table 4. Relative State Energies (Relative to the ${}^9\Sigma_g^-$ Ground State) and Bond Distances of Fe_2

method	ref	ΔE (eV) ^a			r_e (Å)			
		${}^7\Sigma_g^-$	${}^7\Delta_u$	${}^9\Delta_g$	${}^9\Sigma_g^-$	${}^7\Sigma_g^-$	${}^7\Delta_u$	${}^9\Delta_u$
HF/3fg	present	-1.09	3.43	1.08	2.187	2.426	2.109	2.286
/f	present	-1.10	3.40	1.13	2.186	2.422	2.114	2.299
BLYP/3fg	present		-0.61	0.05	2.166		2.019	2.277
/f	present	0.31	-0.62	0.04	2.168	2.163	2.023	2.282
PBE/3fg	present		-0.48	0.06	2.147		2.004	2.250
/f	present		-0.50	0.05	2.148	2.145	2.010	2.256
/PW	Rollmann et al. ⁹²		-0.32		2.144		2.005	
/PW	Kulik et al. ¹⁵	0.65	-0.12	0.28	2.11	2.10	1.99	2.26
M06-L/3fg	present		0.09	-0.11	2.150		2.006	2.273
/f	present	0.55	0.07	-0.12	2.151	2.143	2.009	2.280
B3LYP/3fg	present	0.36	0.20	0.36	2.111	2.118	1.979	2.232
/f	present	0.35	0.18	0.36	2.113	2.119	1.984	2.237
/6-311++G(3df)	Kulik et al. ¹⁵	0.34	0.18	0.36				
B1LYP/3fg	Present	0.37	0.43	0.42	2.106	2.114	1.977	2.227
/f	present	0.36	0.41	0.42	2.108	2.116	1.983	2.233
BHandHLYP/3fg	present	0.43	1.32	0.70	2.073	2.087	1.959	2.182
/f	present	0.42	1.30	0.71	2.074	2.089	1.965	2.188
HFLYP/3fg	present	-1.45	2.73	1.13	2.076	2.323	1.999	2.164
/f	present	-1.42	2.72	1.17	2.076	2.319	2.006	2.171
M06/3fg	present	0.09	0.47	0.59	2.119	2.122	1.980	2.232
/f	present	0.10	0.47	0.58	2.118	2.121	1.982	2.234
M05/3fg	present	0.10	0.32	0.74	2.135	2.145	2.005	2.238
/f	present	0.11	0.33	0.73	2.137	2.144	2.008	2.244
PBE+U/PW	Rollmann et al. ⁹²				2.143		2.005	
/PW	Kulik et al. ¹⁵	0.60	0.72	0.41	2.13	2.12	2.00	2.26
CCSD(T)/GTO ^b	Kulik et al. ¹⁵	0.55	0.86	0.38	2.17	2.16	2.00	2.18
MRCISD+Q ^P /ANO	Hübner and Sauer ⁸⁹	0.48 ^c	0.70 ^d	~0.4	2.187	2.180	2.140	>2.3
IC-MRCI+Q/ANO	Bauschlicher and Ricca ⁹⁰	0.53	0.58	<1.05	2.178	2.093	2.081	>2.3
cor. MRCI	Bauschlicher and Ricca ⁹⁰		0.30					
experiment	Leopold et al. ⁹⁴	0.53						

^a Relative to the ${}^9\Sigma_g^-$ ground state. ^b GTO denotes the 6-311++G(3df,3pd) Gaussian-type-orbital basis set. ^c 0.34 eV if corrected for the MRCISD+Q^P error in the separated atoms. ^d 0.56 eV if corrected for MRCISD+Q^P error in the separated atoms.

invariant, and for B3LYP there is only a relatively small change in the correlation functional. However, Table 4 shows that the septet–nonet energy differences do not vary monotonically with X . Thus other features in the orbital interactions and in the density functional cannot be ignored in analyzing the predicted spin states.

The frequencies in Table 5 show no great surprise for the ${}^9\Sigma_g^-$ and ${}^7\Delta_u$ states, at least based on experience with main-group molecules, because for main-group molecules density functionals with no Hartree–Fock exchange have smaller systematic errors for frequencies,¹¹⁷ and they do better here as well. It is not clear why the MRCISD+Q^P and IC-MRCI+Q calculations give a much lower frequency for the ${}^7\Delta_u$ state than all other methods; this low-frequency results from a very flat potential curve for this state in the MRCISD+Q^P calculations—perhaps the static correlation is unbalanced in these calculations. In fact, Bauschlicher and Ricca,⁹⁰ because of their concern about this aspect, reported averaged coupled pair functional¹¹⁸ (ACPF) calculations that yield 2.038 Å and 335 cm⁻¹ for the ${}^7\Delta_u$ state and complete active space second-order perturbation theory¹¹⁹ (CASPT2) calculations that yield 1.979 Å and 429 cm⁻¹, both in much better agreement with the Kohn–Sham calculations.

An interesting conclusion that emerges from Table 4 is

Table 5. Harmonic Vibrational Frequencies for Fe_2

method	ref	${}^9\Sigma_g^-$	${}^7\Sigma_g^-$	${}^7\Delta_u$	${}^9\Delta_g$
HF/f	present	369	289	394	308
BLYP/f	present	320	332	393	268
PBE/f	present	331	340	417	279
/PW	Rollman et al. ⁹²	329		414	
/PW	Kulik et al. ¹⁵	339	335	413	285
M06-L/f	present	337	341	402	281
B3LYP/f	present	361	359	427	301
B1LYP/f	present	367	364	432	304
BHandHLYP/f	present	402	393	459	338
HFLYP/f	present	433	331	451	370
M06/f	present	357	364	429	306
M05/f	present	352	355	417	309
PBE+U/PW	Rollmann et al. ⁹²	346		414	
PBE+U/PW	Kulik et al. ¹⁵	335	331	419	280
CCSD(T)/GTO	Kulik et al. ¹⁵	296	304	404	220
MRCISD+Q ^P /ANO	Hübner and Sauer ⁸⁹	303	310	224	
IC-MRCI+Q/ANO	Bauschlicher and Ricca ⁹⁰	327	296	291	
experiment	Moskovits and DiLello ⁹³	300			

that functionals with a large percentage of Hartree–Fock exchange are the most sensitive to changes in the basis set.

Table 6. Excitation Energy (Relative to the ⁸Σ_u⁻ Ground State), Equilibrium Intermolecular Distances, and Harmonic Vibrational Frequencies for Fe₂⁻

method ^a	ΔE ^b (eV) ⁸ Δ _g	r _e (Å)		ω _e (cm ⁻¹)	
		⁸ Σ _u ⁻	⁸ Δ _g	⁸ Σ _u ⁻	⁸ Δ _g
HF/f	4.79	2.640	2.330	206	297
BLYP/3fg			2.076		
/f	-0.02	2.231	2.081	281	349
PBE/3fg			2.063		
/f	-0.68	2.209	2.068	295	357
/PW ¹⁵	-0.52	2.20	2.07	305	360
M06-L/3fg		2.097			
/f	-0.12	2.212	2.099	299	337
B3LYP/3fg	0.15	2.176	2.041		
/f	0.14	2.178	2.046	316	375
/6-311++G(3df) ¹⁵	0.14				
B1LYP/3fg	0.36	2.172	2.044		
/f	0.35	2.174	2.048	316	375
BHandHLYP/3fg	1.08	2.171	2.052		
/f	1.07	2.176	2.056	321	374
HFLYP/3fg	1.43	2.227	2.141		
/f	4.50	2.508	2.146	247	388
M06/3fg	0.60	2.188	2.045		
/f	0.72	2.188	2.048	315	375
M05/3fg	0.74	2.196	2.059		
/f	0.73	2.198	2.064	316	371
PBE+U/PW ¹⁵	0.38	2.20	2.08	301	355
CCSD(T)/GTO ¹⁵	0.40	2.24	2.12	276	321
MRCI+Q ^p /ANO ⁸⁹	0.8	2.266		255	
IC-MRCI+Q/ANO ⁹⁰	0.70	2.350	2.233	261	165
experiment ⁹⁴				250	

^a References are the same as in Tables 3 and 4. ^b Relative to the ⁸Σ_u⁻ ground state.

3.2. Fe₂⁻. The anion presents a slightly different kind of test because the two states studied have the same multiplicity. The ground state is the ⁸Σ_u⁻ state with a dominant 3d¹³: σ_g²π_u⁴δ_g²π_g²δ_u²σ_u; 4s⁴: σ_g²σ_u² configuration, whereas the ⁸Δ_g state is 3d¹⁴4s³.^{89,94} The high-level calculations (CCSD(T) and MRCI+Q^p) in Table 6 indicate an energy spacing of 0.4–0.8 eV. The PBE plane wave and TZQ calculations in Table 6 agree reasonably well (better than in Table 4), but again the GGA and meta-GGA functionals predict the wrong ground state, while the hybrid GGAs, hybrid meta-GGAs, and PBE+U methods predict the correct ground state. B1LYP, M06, M05, and PBE+U appear to be the most accurate methods for the relative energies. Despite the poor performance for relative energies, M06-L is the most accurate functional for internuclear distances and vibrational frequencies (as already mentioned, functionals with no Hartree–Fock exchange often have small systematic errors for frequencies¹¹⁷). Of the three functionals with the best performance for relative state energies, PBE+U is best for bond distances and frequencies closely followed by M05.

The case of Fe₂⁻ is very illuminating. The prediction of relative state energies in transition-metal chemistry is often discussed entirely in terms of the competition between high spin and low spin, but here both states are octets and the key role of the relative energies of the 3d and 4s orbitals is clearly exposed. Hartree–Fock theory and functionals with

Table 7. Excitation Energy (E(⁴Φ) – E(⁶Σ⁺), in eV) of FeO⁺ Calculated in C_{6v}, C_{4v}, and C_{2v} Symmetries

method	symmetry			not stated
	C _{6v}	C _{4v}	C _{2v}	
HF/3fg	11.21	1.80	-1.80	
/f	11.12	1.82	-1.76	
BLYP/3fg	0.85	0.53	0.44	
/f	0.86	0.54	0.45	
PBE/QZVP	0.94			
/3fg	0.94	0.63	0.56	
/f	0.94	0.52	0.55	
/PW ^a				0.84
M06-L/3fg	1.48	0.96	0.59	
/f	1.49	0.97	0.60	
B3LYP/3fg	2.57	1.24	0.32	
/f	2.58	1.27	0.33	
/TZ2P ^b				0.34 ^c
B1LYP/3fg	2.91	1.33	0.19	
/f	2.92	1.35	0.21	
BHandHLYP/3fg	4.44	1.63	-0.43	
/f	4.45	1.65	-0.41	
HFLYP/3fg	7.16	1.98	-1.70	
/f	7.17	2.01	-1.67	
M06/3fg	2.85	1.67	0.55	
/f	2.86	1.69	0.56	
M05/3fg	2.82	1.78	0.64	
/f	2.83	1.79	0.63	
PBE+U/PW ^a				0.54
CCSD(T)/GTO ^a				0.57
CCSD(T)/3df+//B3LYP ^{d,e}				0.54
QMC//B3LYP ^f				0.36

^a Kulik et al.¹⁵ ^b Filatov and Shaik.⁸⁷ ^c C_s symmetry. ^d Irigoras et al.⁸⁸ ^e CCSD(T)/3df+//B3LYP denotes CCSD(T)/TZVP+G(3df,2p) single-point energy calculations at B3LYP/TZVP+G(3df,2p) geometries. ^f Matxain et al.⁹¹

a high percentage of Hartree–Fock exchange yield a higher energy for the 4s(σ_u) orbital relative to the energies of orbitals with 3d parentage.

3.3. FeO⁺. The FeO⁺ molecule has been carefully studied in the past, primarily to explain the low efficiency of its gas-phase reaction with H₂ to make Fe⁺ + H₂O^{91,120} and the related reverse reaction.⁸⁸ CCSD(T) calculations with an augmented TZQ(3df) basis on Fe and a 6-311++G(2df) basis on O (this basis will be abbreviated “3df+”) were carried out by Irigoras et al.⁸⁸ and yielded a state splitting E(⁴Φ) – E(⁶Σ⁺) of 0.54 eV. Quantum Monte Carlo (QMC) calculations with a fixed-mode approximation by Matxain et al.⁹¹ lowered the calculated splitting to 0.36 eV. These results are compared to our HF and Kohn–Sham calculations and to calculations by Kulik et al.¹⁵ in Table 7. The immediately obvious conclusion is that the lower-symmetry Kohn–Sham solutions (“broken-symmetry” solutions) are in much better agreement with the high-level results than the results where spatial symmetry of the orbitals is enforced.

A complicating issue in Table 7 is the spatial symmetry in the plane wave calculations. For example, the PBE+U/PW calculations have a state splitting 0.30 eV lower than PBE/PW and are in good agreement with the CCSD(T) results, but the PBE/PW calculations do not agree well with the fully optimized (C_{2v}) PBE calculations with Gaussian-

Table 8. Internuclear Distance for the ${}^6\Sigma^+$ Ground State of FeO^+

method	r (Å)
HF/3fg	1.822
BLYP/3fg	1.648
PBE/3fg	1.631
/PW ^b	1.620
M06-L/3fg	1.634
B3LYP/3fg	1.635
/TZ2P ^c	1.643
/DZVP ^d	1.655
/3fg+ ^d	1.637
B1LYP/3fg	1.640
BHandHLYP/3fg	1.655
HFLYP/3fg	1.705
M06/3fg	1.617
M05/3fg	1.623
PBE+U/PW ^b	1.660
CCSD(T)/GTO ^b	1.660
experiment ^e	1.643

^a Results for the $/f$ basis (not shown) are all very similar to those for the $/3fg$ basis. ^b Kulik et al.¹⁵ ^c Filatov and Shaik.⁸⁷ ^d Irigoras et al.⁸⁸ ^e Aguirre et al.⁹⁵

type orbital (GTO) basis sets. If the +U correction were to reduce the PBE/GTO state splitting by 0.30 eV, the resulting splitting would be 0.14 eV, which would be too low. Thus, unless careful attention is paid to symmetry breaking, one can draw spurious conclusions about the validity of various functionals.

Table 8 compares the calculated r_e values of the ${}^6\Sigma^+$ ground state of FeO^+ to the experimental r_0 value⁹⁵ of 1.643 Å. In general, there is reasonable agreement between the calculated and experimental bond distances. One striking exception is the class of methods that involve large fractions of HF exchange (i.e., HF, HFLYP and BHandHLYP). The high fraction of HF exchange results in bond lengths that are significantly lengthened. A second exception is the hybrid meta-GGA functionals (M05 and M06) that give significant bond contraction. However, the more traditional hybrid GGA functions (B1LYP and B3LYP), and to a lesser extent the sole meta-GGA functional (M06-L), yield bond lengths consistent with experiment. It should also be noted that CCSD(T) predicts a bond length that is somewhat larger than experiment, and it is to this number that Kulik et al. favorably compare their PBE+U/PW value.¹⁵

Table 9 shows equilibrium internuclear distances for the ${}^4\Phi$ state. When the symmetry is lowered, the equilibrium internuclear distance increases for the GGAs, the meta-GGA, and the hybrid meta-GGAs with 20–50% Hartree–Fock exchange but decreases for HF and HFLYP. It is nonmonotonic for M06 and M05. Nevertheless, except for B1LYP, amazingly it is always closer to CCSD(T) for the C_{2v} solution than for C_{6v} . An experimental value for the bond length in the excited ${}^4\Phi$ state could not be found in the literature.

If we assume that the correct state splitting for FeO^+ is in the range 0.36–0.56 eV, we would single out any method predicting state splittings in the range 0.26–0.66 eV as performing acceptably. Seven of the ten methods meet this criterion.

Table 9. Equilibrium Internuclear Distances for the ${}^4\Phi$ Excited State of FeO^+ Calculated in C_{6v} , C_{4v} , and C_{2v} Symmetries^a

	C_{6v}	C_{4v}	C_{2v}	not stated
HF/3fg	2.273	1.803	1.814	
BLYP/3fg	1.596	1.601	1.614	
PBE/3fg	1.582	1.588	1.600	
/PW ^b				1.560
M06-L/3fg	1.624	1.625	1.676	
B3LYP/3fg	1.663	1.671	1.694	
/TZ2P ^c				1.703 ^c
/DZVP ^d				1.698
/3fg+ ^d				1.696
B1LYP/3fg	1.687	1.690	1.713	
BHandHLYP/3fg	1.742	1.744	1.746	
HFLYP/3fg	1.798	1.788	1.773	
M06/3fg	1.675	1.668	1.699	
M05/3fg	1.689	1.678	1.708	
PBE+U/PW ^b				1.750
CCSD(T)/PW ^b				1.700

^a Results for the $/f$ basis (not shown) are all very similar to those for the $/3fg$ basis. ^b Kulik et al.¹⁵ ^c Filatov and Shaik, C_s .⁸⁷ ^d Irigoras et al.⁸⁸

Table 10. Absolute Energies (in Hartrees) of the ${}^4\Phi$ Excited State of FeO^+ as Calculated in C_{6v} , C_{4v} , and C_{2v} Symmetries

method	C_{6v}	C_{4v}	C_{2v}
BLYP/3fg	−1338.6092	−1338.6212	−1338.6245
$/f$	−1338.6063	−1338.6181	−1338.6214
B3LYP/3fg	−1338.4902	−1338.5390	−1338.5729
$/f$	−1338.4874	−1338.5356	−1338.5698
M06/3fg	−1338.3478	−1338.3910	−1338.4324
$/f$	−1338.3456	−1338.3886	−1338.4301

For all functionals, the energy of the ${}^4\Phi$ state decreases strongly when we lower the symmetry from C_{6v} to C_{4v} to C_{2v} . Examples are given in Table 10. Notice that the effect of symmetry is larger than the effect of the basis set. The nature of the symmetry breaking in FeO^+ is very unusual and very interesting. The energies of the ${}^4\Phi$ state strongly depend on the symmetry, while those of the ${}^6\Sigma^+$ ground state, like those for Fe_2 and Fe_2^- , do not. A Φ state corresponds to B_1 , E , and B_2 , in C_{6v} , C_{4v} , and C_{2v} , respectively.¹²¹ The energy decreases because orbitals that are degenerate in $C_{\infty v}$ and C_{6v} symmetries can be split in lower symmetries. The electronic configuration of the ${}^4\Phi$ state is $1\sigma^2 2\sigma^2 1\pi^4 1\delta^3 3\sigma^1 2\pi^1$. The π and δ orbitals are degenerate in $C_{\infty v}$ and C_{6v} . In C_{6v} the π and δ orbitals have e_1 and e_2 symmetry, respectively, whereas in C_{4v} , the δ orbitals are split into b_1 and b_2 , while π remains degenerate in e symmetry. In C_{2v} symmetry, the δ orbitals transform as a_1 and a_2 , and the π orbitals are also split, transforming as b_1 and b_2 .¹²¹ An example of the splitting in orbital energies is shown in Table 11. In general, GGA exchange includes static correlation,¹²² and functionals with small X (that is, with a high percentage of GGA exchange) show less dependence on symmetry. The greater tendency to symmetry breaking in the calculations with a higher percentage of Hartree–Fock exchange may be attributable to the tendency of higher Hartree–Fock

Table 11. Energies of the Outer Orbitals (in Hartrees) for the ⁴Φ State of FeO⁺ Calculated in C_{6v}, C_{4v}, and C_{2v} Symmetries Using B3LYP/3fg

spin	orbital	C _{6v}	C _{4v}	C _{2v}
α	1 σ	-1.169	-1.169	-1.159
	2 σ	-0.719	-0.717	-0.708
	1 π	-0.702	-0.698	-0.700
	1 π	-0.702	-0.698	-0.685
	1 δ	-0.657	-0.670	-0.640
	1 δ	0.657	-0.634	-0.628
	3 σ	-0.567	-0.565	-0.561
	2 π	-0.497	-0.496	-0.558
	β	1 σ	-1.210	-1.210
2 σ		-0.646	-0.645	-0.639
1 π		-0.634	-0.634	-0.660
1 π		-0.634	-0.634	-0.595
1 δ		-0.468	-0.562	-0.554

exchange to relatively favor greater electronic localization on the atomic sites.

3.4. Overall Assessment. Considering Tables 4–9 as a whole, the PBE+U calculations perform quite well. A particular difficulty with the DFT+U, though, is the necessity to choose a value for the parameter *U*, which is system dependent and often highly uncertain, as emphasized, for example, in a recent study of Fe₃O₄.¹²³ (Progress in making *U* less arbitrary has been reported recently, but it is still system dependent.¹⁰³) The density functionals without +U contain parameters, but these parameters do not depend on the system. Among the functionals without system-dependent parameters, B3LYP, M06, and M05 do best, followed closely by B1LYP. In fact, given the uncertainty in the accurate data, one could argue that M05 does as well as PBE+U. For example, it agrees very well with the cor. MRCI value of Δ*E* for the ⁷Δ_g state in Table 4 and with the IC-MRCI+Q/ANO value of Δ*E* for the ⁸Δ_g state in Table 6.

4. Conclusions

We carried out DFT calculations on various states of Fe₂, Fe₂⁻, and FeO⁺, using GGA, hybrid GGA, meta-GGA, and hybrid meta-GGA DFT functionals. No single functional was found to yield a satisfactory description of all characteristics for all states of these species. The DFT+U calculations performed previously by Kulik et al.¹⁵ are more accurate than DFT in comparison with CCSD(T) and MRCI calculations, although DFT calculations with the M05 functionals are also reasonably accurate; a definitive comparison of these functionals is precluded by uncertainties in the most accurate available data. Functionals with larger percentages of Hartree–Fock exchange are found to be more sensitive to the choice of the basis set.

The FeO⁺ calculations were carried out in three different symmetries (C_{6v}, C_{4v}, and C_{2v}). The quartet spin state ⁴Φ shows spatial-symmetry-breaking, which is especially prominent in functionals with large percentages of Hartree–Fock exchange. Of particular interest is that accurate results can be obtained for the ⁴Φ state of FeO⁺ only when symmetry-breaking solutions are allowed, a situation that has also been observed in some other problems.^{7,33–37,40}

Acknowledgment. We wish to thank Matteo Cococcioni, Christopher Cramer, Laura Gagliardi, Andreas Heyden, Zhen Hua Li, Rosendo Valero, Oksana Tischenko, and Yan Zhao for helpful discussions. This work was supported in part by NSF Grant no. ITR-0428774. M.A.I. acknowledges support of a research grant from the Herbert J. Seligman Charitable Trust. Computer resources were provided by the Minnesota Supercomputing Institute and by a Molecular Science Computing Facility Computational Grand Challenge grant for Computational Chemical Dynamics of Complex Systems at the Environmental Molecular Sciences Laboratory of Pacific Northwest National Laboratory.

References

- (1) Kohn, W.; Sham, L. J. *Phys. Rev.* **1965**, *140*, A1133.
- (2) Kohn, W.; Becke, A. D.; Parr, R. G. *J. Phys. Chem.* **1996**, *100*, 12974.
- (3) Perdew, J. P.; Parr, R. G.; Levy, M.; Balduz, J. L., Jr. *Phys. Rev. Lett.* **1982**, *49*, 1691.
- (4) Chong, D. P.; Gritsenko, O. V.; Baerends, E. J. *J. Chem. Phys.* **2002**, *116*, 1760.
- (5) Gritsenko, O. V.; Braïda, B.; Baerends, E. J. *J. Chem. Phys.* **2003**, *119*, 1937.
- (6) Zhan, C.-G.; Nichols, J. A.; Dixon, D. A. *J. Phys. Chem. A* **2003**, *107*, 4184.
- (7) Perdew, J. P.; Savin, A.; Burke, K. *Phys. Rev. A* **1995**, *51*, 4531.
- (8) Staroverov, V. N.; Davidson, E. R. *Chem. Phys. Lett.* **2001**, *340*, 142.
- (9) Herrmann, C.; Yu, L.; Reiher, M. *J. Comput. Chem.* **2006**, *27*, 1223.
- (10) Zeigler, T. In *Computational Thermochemistry: Prediction and Estimation of Molecular Thermodynamics*; Irikura, K. K., Frurip, D. J., Eds.; ACS Symposium Series 677; American Chemical Society: Washington, DC, 1998; pp 369–382.
- (11) Harvey, J. N. *Struct. Bonding (Berlin)* **2004**, *112*, 151.
- (12) Noodleman, L.; Han, W.-G. *J. Biol. Inorg. Chem.* **2006**, *11*, 674.
- (13) Niu, S.; Hall, M. B. *Chem. Rev.* **2000**, *100*, 353.
- (14) Reiher, M.; Salomon, O.; Hess, B. A. *Theor. Chem. Acc.* **2001**, *107*, 48.
- (15) Kulik, H. J.; Cococcioni, M.; Scherlis, D. A.; Marzari, N. *Phys. Rev. Lett.* **2006**, *97*, 103001.
- (16) Song, J.; Aprá, E.; Khait, Y. G.; Hofmann, M. R.; Kowalski, K. *Chem. Phys. Lett.* **2006**, *428*, 277.
- (17) Lewin, J. L.; Heppner, D. E.; Cramer, C. J. *J. Biol. Inorg. Chem.* In press (DOI: 10.1007/s00775-007-0290-2).
- (18) Becke, A. D. *J. Chem. Phys.* **1993**, *98*, 1372.
- (19) Anisimov, V. I.; Zaanen, J.; Andersen, O. K. *Phys. Rev. B* **1991**, *44*, 943.
- (20) Heisenberg, W. *Z. Physik* **1928**, *49*, 619; Dirac, P. A. M. *Proc. R. Soc. London, Ser. A* **1929**, *123*, 714. Van Vleck, J. H. *Rev. Mod. Phys.* **1945**, *17*, 27. Slater, J. C. *Rev. Mod. Phys.* **1953**, *25*, 199.

- (21) Noodleman, L. *J. Chem. Phys.* **1981**, *74*, 5737. Noodleman, L.; Baerends, E. J. *J. Am. Chem. Soc.* **1984**, *106*, 2316. Noodleman, L.; Davidson, E. R. *Chem. Phys.* **1986**, *109*, 131. Noodleman, L.; Peng, C. Y.; Case, D. A.; Mouesca, J.-M. *Coord. Chem. Rev.* **1995**, *144*, 199.
- (22) Davidson, E. R.; Clark, A. E. *J. Phys. Chem.* **2002**, *106*, 7456.
- (23) Terakura, K.; Oguchi, T.; Williams, A. R.; Kübler, J. *Phys. Rev. B* **1984**, *30*, 4734.
- (24) Caballol, R.; Castell, O.; Illas, F.; de P. R. Moreira, I.; Malrieu, J. P. *J. Phys. Chem. A* **1997**, *101*, 7860.
- (25) Soda, T.; Kitagawa, Y.; Onishi, T.; Takano, Y.; Shigeta, Y.; Nagao, H.; Yoshioka, Y.; Yamaguchi, K. *Chem. Phys. Lett.* **2000**, *319*, 223.
- (26) Gräfenstein, J.; Hjerpe, A. M.; Kraka, E.; Cremer, D. *J. Phys. Chem. A* **2000**, *104*, 1748.
- (27) Lovell, T.; Liu, T.; Case, D. A.; Noodleman, L. *J. Am. Chem. Soc.* **2003**, *125*, 8377.
- (28) Noh, E. A. A.; Zhang, J. *Chem. Phys.* **2006**, *330*, 82.
- (29) Ali, M. E.; Datta, S. N. *J. Phys. Chem. A* **2006**, *110*, 2776.
- (30) Moreira, I. de P. R.; Illas, F. *Phys. Chem. Chem. Phys.* **2006**, *8*, 1645. de P. R. Moreira, I.; Costa, R.; Filatov, M.; Illas, F. *J. Chem. Theory Comput.* **2007**, *3*, 764.
- (31) Shoji, M.; Koizumi, K.; Taniguchi, T.; Kitagawa, Y.; Yamanaka, S.; Okumura, M.; Yamaguchi, K. *Int. J. Quantum Chem.* **2007**, *107*, 116.
- (32) Niu, S.; Ichiye, T. *Theor. Chem. Acc.* **2007**, *117*, 275.
- (33) Edgecombe, K. E.; Becke, A. D. *Chem. Phys. Lett.* **1995**, *244*, 427.
- (34) McGrady, J. E.; Lovell, T.; Stranger, R. *Inorg. Chem.* **1997**, *36*, 3242.
- (35) Lovell, T.; Stranger, R.; McGrady, J. E. *Inorg. Chem.* **2001**, *40*, 39.
- (36) Stranger, R.; Lovell, T.; McGrady, J. E. *Polyhedron* **2002**, *21*, 1969.
- (37) Schultz, N. E.; Zhao, Y.; Truhlar, D. G. *J. Phys. Chem. A* **2005**, *109*, 4388.
- (38) Hermann, A.; Vest, B.; Schwerdtfeger, P. *Phys. Rev. B* **2006**, *74*, 224402.
- (39) Saito, K.; Nakao, Y.; Sato, H.; Sakaki, S. *J. Phys. Chem. A* **2006**, *110*, 9710.
- (40) Rinaldo, D.; Philipp, D. M.; Lippard, S. J.; Friesner, R. A. *J. Am. Chem. Soc.* **2007**, *129*, 3135.
- (41) Larson, P.; Lambrecht, W. R. L.; Chantis, A.; van Schilf-gaarde, M. *Phys. Rev. B* **2007**, *75*, 045114.
- (42) Batista, E. R.; Martin, R. L. *J. Am. Chem. Soc.* **2007**, *129*, 7224.
- (43) Orlova, G.; Goddard, J. D. *Mol. Phys.* **2000**, *98*, 961. Orlova, G.; Goddard, J. D. *Chem. Phys. Lett.* **2002**, *363*, 486.
- (44) Cohen, R. D.; Sherrill, C. D. *J. Chem. Phys.* **2001**, *114*, 8257.
- (45) Dunietz, B. D.; Head-Gordon, M. *J. Phys. Chem. A* **2003**, *107*, 9160.
- (46) Harju, A.; Räsänen, E.; Saarikoski, H.; Puska, M. J.; Nieminen, R. M.; Niemelä, K. *Phys. Rev. B* **2004**, *69*, 153101.
- (47) Fuchs, M.; Niquet, Y.-M.; Gonze, X.; Burke, K. *J. Chem. Phys.* **2005**, *122*, 094116.
- (48) Li, J.; Schreckenbach, G.; Ziegler, T. *J. Phys. Chem.* **1994**, *98*, 4838.
- (49) Barone, V. *Chem. Phys. Lett.* **1995**, *233*, 129.
- (50) Holthausen, M. C.; Mohr, M.; Koch, W. *Chem. Phys. Lett.* **1995**, *240*, 245.
- (51) Chermette, H. *Coord. Chem. Rev.* **1998**, *178*, 699.
- (52) Sosa, R. M.; Gardiol, P.; Beltrame, G. *Int. J. Quantum Chem.* **1998**, *69*, 371.
- (53) Barden, C. J.; Rienstra-Kiracofe, J. C.; Schaefer, H. F., III. *J. Chem. Phys.* **2000**, *113*, 690.
- (54) Hu, Z.; Boyd, R. J. *J. Chem. Phys.* **2000**, *113*, 9393.
- (55) Legge, F. S.; Nyberg, G. L.; Peel, J. B. *J. Phys. Chem. A* **2001**, *105*, 7905.
- (56) Reiher, M. *Inorg. Chem.* **2002**, *41*, 6928.
- (57) Rulisek, L.; Havlas, Z. *Int. J. Quantum Chem.* **2003**, *91*, 504.
- (58) Gutsev, G. L.; Andrews, L.; Bauschlicher, C. W., Jr. *Chem. Phys.* **2003**, *290*, 47.
- (59) Schultz, N. E.; Zhao, Y.; Truhlar, D. G. *J. Phys. Chem. A* **2005**, *109*, 11127.
- (60) Holthausen, M. C. *J. Comput. Chem.* **2005**, *26*, 1505.
- (61) Zhao, Y.; Schultz, N. E.; Truhlar, D. G. *J. Chem. Phys.* **2005**, *123*, 161103.
- (62) Zhao, Y.; Schultz, N. E.; Truhlar, D. G. *J. Chem. Theory Comput.* **2006**, *2*, 364.
- (63) Quintal, M. M.; Karton, A.; Iron, M. A.; Boese, D. A.; Martin, J. M. L. *J. Phys. Chem. A* **2006**, *110*, 709.
- (64) Furche, F.; Perdew, J. P. *J. Chem. Phys.* **2006**, *124*, 044103.
- (65) Zhao, Y.; Truhlar, D. G. *J. Chem. Phys.* **2006**, *124*, 224105.
- (66) Schultz, N. E.; Gherman, B. F.; Cramer, C. J.; Truhlar, D. G. *J. Phys. Chem. B* **2006**, *110*, 24030.
- (67) Zhao, Y.; Truhlar, D. G. *J. Chem. Phys.* **2006**, *125*, 194101.
- (68) Song, P.; Guan, W.; Yao, C.; Su, Z. M.; Wu, Z. J.; Feng, J. D.; Yan, L. K. *Theor. Chem. Acc.* **2007**, *117*, 407.
- (69) Schultz, N. E.; Zhao, Y.; Truhlar, D. G. *J. Comput. Chem.* In press (DOI: 10.1002/jcc.20717).
- (70) Zhao, Y.; Truhlar, D. G. *Theor. Chem. Acc.* In press (DOI: 10.1007/s00214-007-0310-x).
- (71) Bylaska, E. J.; de Jong, W. A.; Kowalski, K.; Straatsma, T. P.; Valiev, M.; Wang, D.; Aprà, E.; Windus, T. L.; Hirata, S.; Hackler, M. T.; Zhao, Y.; Fan, P.-D.; Harrison, R. J.; Dupuis, M.; Smith, D. M. A.; Nieplocha, J.; Tipparaju, V.; Krishnan, M.; Auer, A. A.; Nooijen, M.; Brown, E.; Cisneros, G.; Fann, G. I.; Früchtl, H.; Garza, J.; Hirao, K.; Kendall, R.; Nichols, J. A.; Tsemekhman, K.; Wolinski, K.; Anchell, J.; Bernholdt, D.; Borowski, P.; Clark, T.; Clerc, D.; Dachsel, M.; Deegan, K.; Dylla, D.; Elwood, E.; Glendening, M.; Gutowski, A.; Hess, J.; Jaffe, B.; Johnson, J.; Ju, R.; Kobayashi, R.; Kutteh, H.; Lin, Z.; Littlefield, R.; Long, X.; Meng, B.; Nakajima, T.; Niu, S.; Pollack, L.; Rosing, M.; Sandrone, G.; Stave, M.; Taylor, H.; Thomas, G.; van Lenthe, J.; Wong, A.; Zhang, Z. *NWChem, A Computational Chemistry Package for Parallel Computers, version 5.0*; a modified version, Pacific Northwest National Laboratory: Richland, WA 99352-0999, U.S.A., 2006.
- (72) Kendall, R. A.; Aprà, E.; Bernholdt, D. E.; Bylaska, E. J.; Dupuis, M.; Fann, G. I.; Harrison, R. J.; Ju, J.; Nichols, J. A.; Nieplocha, J.; Straatsma, T. P.; Windus, T. L.; Wong, A. T. *Comput. Phys. Comm.* **2000**, *128*, 260.

- (73) Zhao, Y.; Truhlar, D. G. *MN-NWCHEMFM, version 2.0*; University of Minnesota: Minneapolis, MN, 2007.
- (74) Becke, A. D. *Phys. Rev. A* **1988**, *38*, 3098.
- (75) Lee, C.; Yang, W.; Parr, R. G. *Phys. Rev. B* **1988**, *37*, 785.
- (76) Becke, A. D. *J. Chem. Phys.* **1993**, *98*, 5648. Stephens, P. J.; Devlin, F. J.; Chabalowski, C. F.; Frisch, M. J. *J. Phys. Chem.* **1994**, *98*, 11623.
- (77) Perdew, J. P.; Burke, K.; Ernzerhof, M. *Phys. Rev. Lett.* **1996**, *77*, 3865.
- (78) Adamo, C.; Barone, V. *Chem. Phys. Lett.* **1997**, *274*, 242.
- (79) Roothaan, C. C. J. *Rev. Mod. Phys.* **1951**, *23*, 69. Pople, J. A.; Nesbet, R. K. *J. Chem. Phys.* **1954**, *22*, 571.
- (80) Perdew, J. In *Density Functional Theory: A Bridge Between Chemistry and Physics*; Geerlings, P., De Proft, F., Langenaeker, W., Eds.; VUB University Press: Brussels, 1999; pp 87–109.
- (81) Wachters, A. J. H. *Chem. Phys.* **1970**, *52*, 1033. Hay, P. J. *J. Chem. Phys.* **1977**, *66*, 4377. Raghavachari, K.; Trucks, G. W. *J. Chem. Phys.* **1989**, *91*, 1062.
- (82) *Gaussian 03 Online Manual*. http://www.gaussian.com/g_ur/g03mantop.htm (accessed August 2, 2007).
- (83) Weigend, F.; Furche, F.; Ahlrichs, R. *J. Chem. Phys.* **2003**, *119*, 12753.
- (84) Krishnan, R.; Binkley, J. S.; Seeger, R.; Pople, J. A. *J. Chem. Phys.* **1980**, *72*, 650. Frisch, M. J.; Pople, J. A.; Binkley, J. S. *J. Chem. Phys.* **1984**, *80*, 3265.
- (85) Staroverov, V.; Davidson, E. R. *Chem. Phys. Lett.* **2001**, *340*, 142.
- (86) Balabanov, N. B.; Peterson, K. A. *J. Chem. Phys.* **2005**, *123*, 064107.
- (87) Filatov, M.; Shaik, S. *J. Phys. Chem. A* **1998**, *102*, 3835.
- (88) Irigoras, A.; Fowler, J. E.; Ugalde, J. M. *J. Am. Chem. Soc.* **1999**, *121*, 8549.
- (89) Hübner, O.; Sauer, J. *Chem. Phys. Lett.* **2002**, *358*, 442.
- (90) Bauschlicher, C. W., Jr.; Ricca, A. *Mol. Phys.* **2003**, *101*, 93.
- (91) Matxain, J. M.; Mercero, J. M.; Irigoras, A.; Ugalde, J. M. *Mol. Phys.* **2004**, *102*, 2635.
- (92) Rollmann, G.; Herper, H. C.; Entel, P. *J. Phys. Chem. A* **2006**, *110*, 10799.
- (93) Moskovits, M.; DiLella, D. P. *J. Chem. Phys.* **1980**, *73*, 4917.
- (94) Leopold, D. G.; Lineberger, W. C. *J. Chem. Phys.* **1986**, *85*, 51. Leopold, D. G.; Almlöf, J.; Lineberger, W. C.; Taylor, P. R. *J. Chem. Phys.* **1988**, *88*, 3780.
- (95) Aguirre, F.; Husband, J.; Thompson, C. J.; Stringer, K. L.; Metz, R. B. *J. Chem. Phys.* **2003**, *119*, 10194.
- (96) Liechtenstein, A. I.; Anisimov, V. I.; Zaanen, J. *Phys. Rev. B* **1995**, *52*, R5467.
- (97) Hubbard, J. *Proc. Roy. Soc. A* **1963**, *276*, 238.
- (98) Dudarev, S. L.; Botton, G. A.; Savrasov, S. Y.; Humphreys, C. J.; Sutton, A. P. *Phys. Rev. B* **1998**, *57*, 1505.
- (99) Pickett, W. E.; Erwin, S. C.; Ethridge, E. C. *Phys. Rev. B* **1998**, *58*, 1201.
- (100) Rohrbach, A.; Hafner, J.; Kresse, G. *Phys. Rev. B* **2004**, *69*, 75413.
- (101) Rollmann, G.; Rohrbach, A.; Entel, P.; Hafner, J. *Phys. Rev. B* **2004**, *69*, 165107.
- (102) Zhou, F.; Cococcioni, M.; Marianetti, C. A.; Morgan, D.; Ceder, G. *Phys. Rev. B* **2004**, *70*, 235121.
- (103) Cococcioni, M.; de Gironcoli, S. *Phys. Rev. B* **2005**, *71*, 035105.
- (104) Franchini, C.; Bayer, V.; Podloucky, R.; Paier, J.; Kresse, G. *Phys. Rev. B* **2005**, *72*, 045132.
- (105) Knížek, K.; Novák, P.; Küpferling, M. *Phys. Rev. B* **2006**, *73*, 153103.
- (106) Wang, L.; Maxisch, T.; Ceder, G. *Phys. Rev. B* **2006**, *73*, 195107.
- (107) Tran, F.; Blaha, P.; Schwarz, K.; Novák, P. *Phys. Rev. B* **2006**, *74*, 155108.
- (108) Jeng, H.-T.; Guo, G. Y.; Huang, D. J. *Phys. Rev. B* **2006**, *74*, 195115.
- (109) Shavitt, I. In *Advanced Theories and Computational Approaches to the Electronic Structure of Molecules*; Dykstra, C. E., Ed.; Reidel: Dordrecht, 1984; p 185.
- (110) Pople, J. A.; Seeger, R.; Krishnan, R. *J. Quantum Chem. Symp.* **1977**, *11*, 149.
- (111) Almlöf, J. E.; Taylor, P. R. *J. Chem. Phys.* **1987**, *86*, 4070. Pou-Amérgo, R.; Merchán, M.; Nebot-Gil, I.; Widmark, P.-O.; Roos, B. O. *Theor. Chim. Acta* **1995**, *92*, 149.
- (112) Knowles, P. J.; Werner, H.-J. *Chem. Phys. Lett.* **1988**, *145*, 514. Werner, H.-J.; Knowles, P. J. *J. Chem. Phys.* **1988**, *89*, 5803.
- (113) Langhoff, S. R.; Davidson, E. R. *Int. J. Quantum Chem.* **1974**, *8*, 61.
- (114) Bauschlicher, C. W., Jr. *Theor. Chim. Acta* **2001**, *106*, 314.
- (115) Paier, J.; Hischl, R.; Marsman, M.; Kresse, G. *J. Chem. Phys.* **2005**, *122*, 234102.
- (116) Slater, J. C. *Phys. Rev.* **1951**, *81*, 385. McWeeny, R. *Rev. Mod. Phys.* **1960**, *32*, 335.
- (117) Cramer, C. J. *Computational Chemistry, Theories and Models*; John Wiley & Sons: 2004; pp 339–340.
- (118) Gdanitz, R. J.; Ahlrichs, R. *Chem. Phys. Lett.* **1988**, *143*, 413.
- (119) Andersson, K.; Malmqvist, P.-Å.; Roos, B. O.; Sadlej, A. J.; Wolinski, K. *J. Phys. Chem.* **1990**, *94*, 5483. Andersson, K.; Malmqvist, P.-Å.; Roos, B. O. *J. Chem. Phys.* **1992**, *96*, 1218.
- (120) Clemmer, D. E.; Chen, Y.-M.; Khan, F. A.; Armentrout, P. B. *J. Phys. Chem.* **1994**, *98*, 6522. Fiedler, A.; Schröder, D.; Shaik, S.; Schwarz, H. *J. Am. Chem. Soc.* **1994**, *116*, 10734. Danovich, D.; Shaik, S. *J. Am. Chem. Soc.* **1997**, *119*, 1773.
- (121) Herzberg, G. *Molecular Spectra and Molecular Structure*; New York, NY, 1966; Vol. 3, p 576.
- (122) Schipper, P. R. T.; Gritsenko, O. V.; Baerends, E. J. *Phys. Rev. A* **1998**, *57*, 1729.
- (123) Wentzel, M. J.; Steinle-Neumann, G. *Phys. Rev. B* **2007**, *75*, 214430.

On the Catalytic Role of Ge⁺ and Se⁺ in the Oxygen Transport Activation of N₂O by CO

S. Chiodo, F. Rondinelli, N. Russo, and M. Toscano*

Dipartimento di Chimica and Centro di Calcolo ad Alte Prestazioni per Elaborazioni Parallele e Distribuite-Centro d'Eccellenza MIUR, Universita' della Calabria, I-87030 Arcavacata di Rende (CS), Italy

Received July 25, 2007

Abstract: The different reactivity of two first row cations selenium and germanium, in activating the reduction of nitrous oxide by carbon monoxide, was theoretically investigated at the density functional level using large basis sets and pseudopotential for metal atoms. In the two examined cases, the reaction mechanisms appeared to be quite different. Germanium shows a very good performance as far as thermodynamic and kinetic aspects are concerned. Selenium, experimentally recognized as an inactive catalyst, was instead found potentially able to catalyze the process through a mechanism of spin orbit coupling involving species with doublet multiplicity.

Introduction

Among the main agents of global warming, the long-lived greenhouse gases such as carbon dioxide, methane, nitrous oxide, and halogenated chlorofluorocarbons contribute to an increase in solar radiation estimated as more than 1%. In particular, the N₂O impact toward the environment is even more negative than CO₂ and methane effects because of several factors. The considerable absorption of infrared radiation from the earth by nitrous oxide is due to its persistence in the atmosphere for about 130 years. Moreover, N₂O is so stable to reach the troposphere, where it gives rise to nitric oxide which is responsible for the depletion of the ozone layer. The tropospheric concentration of nitrous oxide has recently increased by about 0.2–0.3% per year. For the next decades more than 80% of primary energy will still be of a fossil nature, so in the near future it will not be easy to reduce N₂O emissions. Many interesting strategies to limit, at least partly, the damages connected to the greenhouse problem were proposed, like a rational use of energy and the improvements in the automobile technology. Nevertheless, the most promising way to reduce the N₂O environmental impact is its catalytic reduction. Recently, experimental measurements carried out by using an inductively coupled plasma/selected-ion flow tube (ICP/SIFT) tandem mass spectrometer, tested the efficiency of many

atomic cations to catalyze the activation of nitrous oxide by carbon monoxide.^{1–3} While the experimental procedure and the rate coefficients for this kind of O-atom transport reactions are well-known, few theoretical investigations were performed to compute the potential-energy landscapes for the catalytic cycle, illustrated in Scheme 1.

So far, 26 atomic cations were experimentally checked for their catalytic performance.¹

The elucidation of the processes activation barriers is very attractive because all of them are characterized by an O-atom affinity which should make the catalytic cycle happen, but only ten activate nitrous oxide at room temperature.¹ Therefore, the theoretical study of the PES is the only tool to understand the reason of the cations different catalytic efficiency. In our work, we considered the performance of selenium and germanium monocations. The case of selenium and germanium is very remarkable because, although they belong to the same period, selenium gives rise to a very slow reaction while germanium is the most efficient main group catalyst.

Furthermore, the analysis of the species involved in the mechanism, apart from the elucidation of the catalytic activity, is worthwhile for catalytic bond activation of ions with small molecules.

Computational Strategy

All calculations presented here were carried out using the Gaussian03 suite of programs.⁴

* Corresponding author fax: +39-0984-492044; e-mail: m.toscano@unical.it.

Scheme 1. N₂O Activation Cycle by CO in the Presence of Cationic Catalysts



The hybrid nonlocal B3LYP functional,^{5,6} the Stuttgart RLC ECP⁷ for selenium and germanium, and the 6-311+G-(d) basis set for all other atoms were used to perform complete optimizations of geometries without any constraints. Minima and transition states on the potential energy profiles were determined examining a large number of initial structures and then characterized through vibrational analysis. Minima were connected to the transition state by means of an intrinsic reaction coordinate (IRC)⁸ procedure implemented in the Gaussian03 code.

Zero point energy corrections were included in all B3LYP energetic data.

NBO analysis as implemented in the Gaussian03 code⁹ was performed to give better insight in the metal ion–ligand bond nature.

For germanium reaction profile, single point energy refinement on the B3LYP 6-311+G(d)/SDD optimized geometries was performed using the QCISD(T)¹⁰ method, an iterative treatment of single and double excitations followed by a noniterative perturbative treatment of triple excitations to fifth order. The QCISD(T) scheme includes the same fifth order terms as the CCSD(T)^{11,12} method and shows a very similar performance with it, giving reliable results as far as molecular structure, vibrational frequencies, and energetics are concerned.^{13–16}

Since in the case of the selenium catalyzed reaction we were interested also in the spin–orbit coupling (SOC) interaction which lends probabilities to crossovers between doublet and quartet states, a method developed recently by our research group to calculate these SOC contributions¹⁷ using the full Breit-Pauli (BP) operator¹⁸ was applied.

As inherent to the Kohn–Sham approach, this scheme of calculation was originally employed to handle pure and hybrid density functional (DF) monodeterminantal wave functions. The SOC matrix elements are calculated by the formula

$$\langle \hat{H}_{BP}^{SO} \rangle = \langle {}^2\Psi_1 | \hat{H}_{BP}^{SO} | {}^4\Psi_2 \rangle \quad (1)$$

using restricted wave functions. However, due to the monodeterminantal nature of the method, it was possible to produce only one value of the SOC matrix elements. Furthermore, since at the present time, the mentioned procedure requires the use of an all electrons basis set, single point calculations on the involved structure at the crossing point were performed at the B3LYP level employing the DZVP and TZVP basis sets for Se, N, and O¹⁹ atoms, respectively. The structure of the minimum energy crossing point (MECP) was determined employing the methodology developed by Harvey et al.²⁰

A crude estimation of the transition probability at the MECP can be done using the Landau–Zener formula²¹ which is often used for this purpose.

$$P = 1 - e^{-2\delta}$$

$$\delta = \frac{\pi |H_{ij}^{SO}|^2}{\hbar \nu |\Delta g_{ij}|} \quad (2)$$

Here H_{ij}^{SO} is the SOC matrix element between the electronic states, Δg_{ij} is the difference in the slopes of the two intersecting surfaces at the crossing point, and ν is the effective velocity with which the system is passing through the crossing point that can be calculated from the kinetic theory of gases at 298 K.

This formula can only be used for qualitative treatment, thus we have used the obtained information only to gain insight over the most probable reaction path. Following the Gonzalez-Schlegel algorithm²² geometry optimization was performed at each point along the reaction path, starting from the saddle point up to the stationary point in the reverse direction. A step size δs (where s denotes the distance along the minimum energy path) of 0.01 Å was used. The gradients of the two surfaces at the crossing point were computed by polynomial interpolation.

Results and Discussion

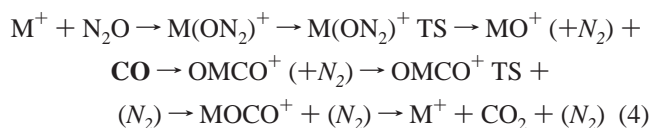
Before evaluating the influence of the two cations on the kinetic features of the process, we analyzed the reaction path relating to the reduction of nitrous oxide by CO in the absence of any catalyst. In this case, the reactive process to evaluate is the following:



According to our calculations, the mechanism is characterized by the only activation barrier of 47.6 kcal/mol. The potential energy curve, computed at the same level of theory by Böhme et al., shows an energy barrier of 47.2 kcal/mol.³ Our investigation highlights that the process is very exothermic. We found a ΔH_0 equal to 86.2 kcal/mol, in agreement with the experimental indication of 87.0 kcal/mol.²³

Catalyzed reaction potential energy surfaces are illustrated in Figure 1. In this figure, we also reported the spectroscopic term symbols for each species and the relative energy values computed with respect to reactants.

For both selenium and germanium catalysts, the reaction mechanism is summarized as follows



where M corresponds to Se or Ge. Both cations were first considered in their ground state, ²P (4s² 4p¹) for Ge⁺ and ⁴S (4s² 4p³) for Se⁺ owing to the fact that the first excited states of these ions lie at very high energies. In particular, the Ge⁺ ⁴P (4s¹ 4p²) and Se⁺ ²P (4s² 4p³) electronic configurations were found 146.7 and 50.3 kcal/mol above the corresponding ground states.

In mechanism 4, N₂ (in italics) is released when monoxide cation is formed, and, after that, CO (in boldface) is

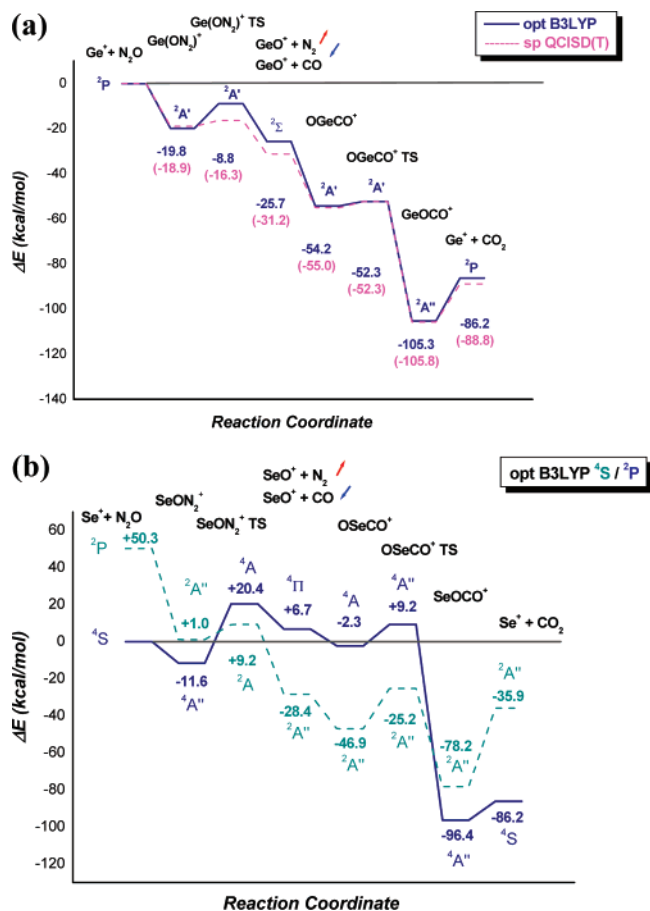


Figure 1. Potential energy surfaces relating to N₂O activation by Ge⁺ (a) and Se⁺ (b). For Ge⁺, solid and dotted lines correspond to the B3LYP and QCISD(T) profiles, while for Se⁺ they represent the ground- and excited-state paths, respectively. Blue and red arrows indicate N₂ leaving and CO incoming molecules, respectively.

introduced in the reaction environment. Therefore, the whole process is made up of two steps: MO⁺ formation and its coordination to CO until CO₂ is produced and the catalyst is released. Two activation barriers have to be overcome to complete the cycle illustrated in Scheme 1.

Optimized structures for minima and transition states, together with their geometrical parameters, are collected in Figure 2.

In the germanium catalyzed N₂O activation, the first step consists of the coordination of nitrous oxide to the cation. The most favored coordination occurs by the oxygen side. The species Ge(ON₂)⁺ lies at 19.8 kcal/mol below the reactants asymptote. As it was experimentally proved,¹ GeO⁺ does not give rise to N₂O adduct ions. Thus, we excluded the presence of the Ge(N₂O)_n⁺ species that give rise to the OGe(N₂O)_{n-1}⁺ compounds. This kind of nitrous oxide multiple coordination was instead observed for other monocations, i.e., for iron.^{1,3}

Through an activation barrier of 11.0 kcal/mol, the Ge(ON₂)⁺ compound evolves in the cation monoxide GeO⁺, releasing the inert molecule of N₂.

The imaginary frequency of Ge(ON₂)⁺ TS, equal to 865 cm⁻¹, corresponds to the stretching of the O–N bond that has to be broken to obtain the nitrogen molecule.

The introduction of carbon monoxide in the reaction environment yields the OGeCO⁺ adduct lying 54.2 kcal/mol below the reactants. In this species, the coordination of CO to GeO⁺ occurs by the metal side. The next minimum GeOCO⁺, having the CO coordinated from the oxygen side, appears to be more stable to about 3 kcal/mol.

The barrier between the two adducts is very small, as the activation energy corresponds to 1.9 kcal/mol. The imaginary frequency characterizing the OGeCO⁺ TS, having the value of 165 cm⁻¹, corresponds to the stretching vibrational mode indicating the formation of the new O–C bond and the breaking of the Ge–C bond.

As we observed in our previous studies concerning different metals performances,²⁴ also for germanium the release of the final products, catalyst and carbon dioxide, is a barrierless step. This finding is not unexpected, as the adduct GeOCO⁺ shows a linear structure with a quite long metal–oxygen distance (2.272 Å). Besides, the two carbon–oxygen distances are very similar than in the CO₂ free molecule (1.180 and 1.141 Å versus 1.161 Å). Looking at the whole Ge⁺ reaction path, in Figure 1(a), the experimental efficiency of the cation in activating nitrous oxide¹ is explained by the fact that the path lies below the reactants asymptote. In fact, what we call the “activation barrier” is not the real barrier of the process in the gas phase. In these conditions there is no possibility for the molecules to lose energy through collisions, so the energy gained in the formation of intermediates is used entirely in the course of reaction.

NBO analysis shows that the bond between the germanium ion and the oxygen atom is ionic in both the GeON₂⁺ and GeOCO⁺ species because of the lack of charge transfer from ligand to metal center. This is confirmed by the net charge value on cation (0.96 |e|). On the contrary, this same bond is characterized by a covalent contribution into the GeO⁺ and OGeCO⁺ minima. Into the oxide, a charge transfer of 0.74 |e| occurs from oxygen to germanium ion. The bond originates from the overlap between the two hybrid s(12%)p(88%) and s(25%)p(75%) orbitals belonging to the germanium ion and oxygen, respectively.

A charge transfer of 0.34 |e| on germanium justifies the presence of a covalent contribution in the Ge–O bond involved in the OGeCO⁺ system. This bond is due to the overlap of two pure p orbitals. Finally, the NBO analysis suggests that the interaction between germanium ion and carbon atom has an electrostatic nature.

Despite the high energetic difference between the ground and first excited states of Ge⁺, we have however ascertained the absence of the two state reactivity phenomenon performing calculations on the stationary points belonging to the most meaningful part (oxide formation) of the quartet pathway, namely the ⁴A' GeON₂⁺ and ⁴Σ GeO⁺. Results indicated that these species lie at 115.9 and 53.3 kcal/mol above the corresponding doublets confirming the lack of any crossing between the PESs having different multiplicity.

Because of the excellent catalytic performance of germanium, we found interesting to calculate the stationary points energies by the QCISD(T) method.

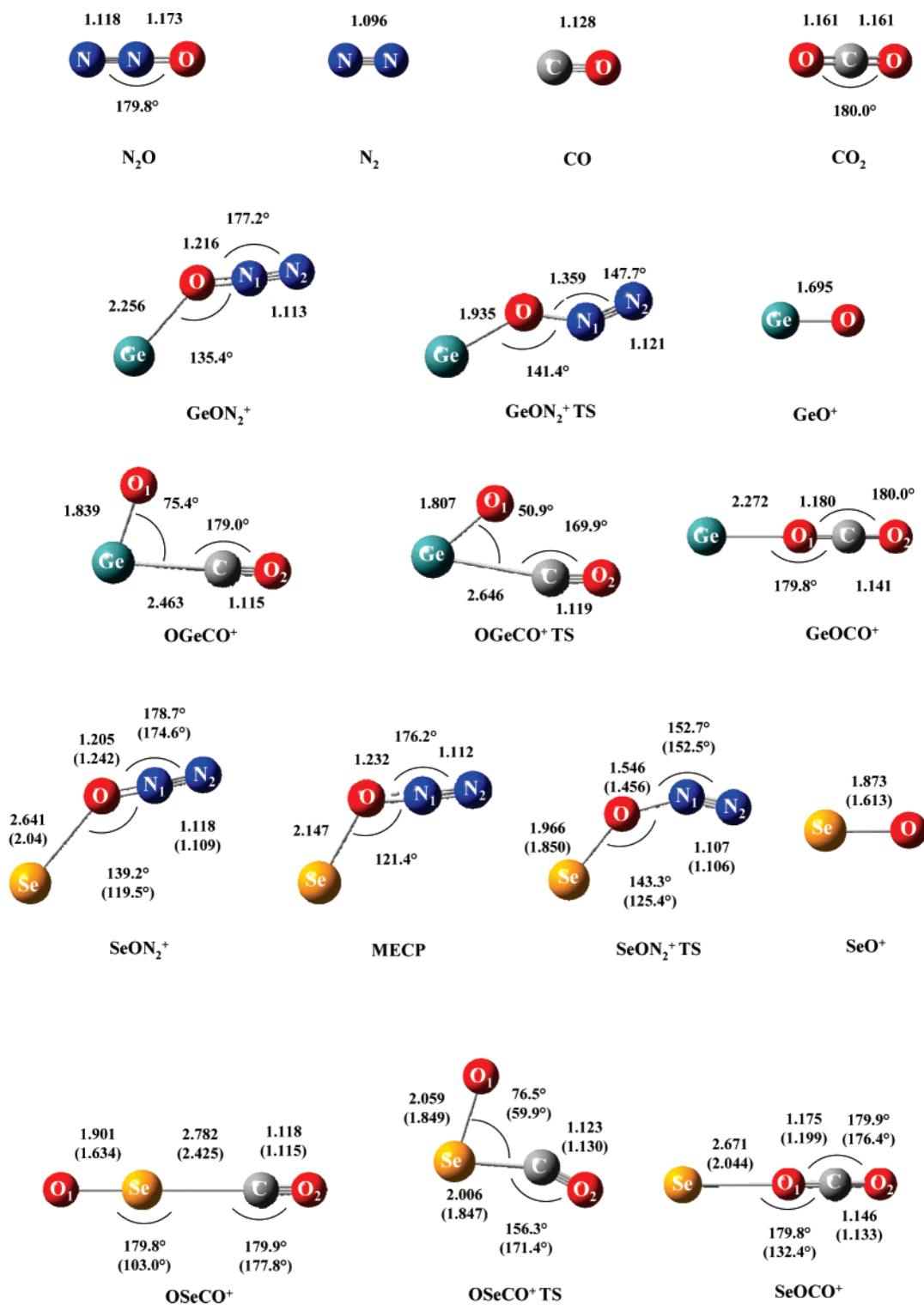


Figure 2. Optimized geometries of species involved in Ge⁺ and Se⁺ PES. Values in parentheses are referred to selenium adducts in the excited state. Bond lengths are given in Å and angles in deg.

The energetic path obtained at the QCISD(T) level is very similar to the B3LYP one, especially after the oxide formation. In the first part of the profile, the main difference concerns the barrier height to overcome for reaching the GeO⁺ species. In fact, it decreases 8.4 kcal/mol with respect to that obtained using the DF approach. However, this does not change the general reaction mechanism. On the other hand, it should be remembered that the QCISD(T) energetic path is the result of a single point computation.

The features of the B3LYP selenium ground state PES, illustrated in Figure 1(b), are completely different than those of germanium. Looking at this reaction path, it seems that Se⁺ can give rise only to small amounts of the cation monoxide. Experimentally, because of too small signal intensity SeO⁺ presence in the reaction environment was not appreciated by any kind of ICP/SIFT measurement.¹

In the selenium case, both the activation barriers of the reaction path lie above the reactants asymptote. This indicates

that the reaction is not kinetically favored. The first step consists of the coordination of N_2O to the selenium cation. As for germanium, the most stable adduct resulting from this interaction is characterized by the oxygen–selenium bond, and there is no experimental evidence of other N_2O coordination compounds. The corresponding minimum, SeON_2^+ , lies at 11.6 kcal/mol below the reactants asymptote.

The coordination to selenium does not substantially change the structure of free N_2O . The N–N distance is exactly the same both in the free molecule and in the SeON_2^+ compound (see Figure 2). N_2O is still linear. As a result of the interaction with selenium, we can just note a slight change of the N–N–O angle (179.8° in the free molecule versus 178.7° in the coordination compound).

The detachment of the N_2 molecule involves the overcoming of a considerable activation barrier. In fact, the transition state, indicated in Figure 1(b) as $\text{Se}(\text{ON}_2)^+$ TS, is located on the PES at 20.4 kcal/mol above the reactants asymptote. This high barrier (32.0 kcal/mol) implies the lack of an appreciable quantity of monoxide cation, as it was experimentally observed. The transition state structure shows, as expected, the increase of the O–N distance that reaches the value of 1.546 Å, while the O–N–N angle assumes the width of 152.7° . The imaginary frequency of 861 cm^{-1} corresponds to the stretching vibrational mode of O–N bond.

The introduction of the carbon monoxide in the reaction environment leads to OSeCO^+ formation. Selenium-side CO coordination to the SeO^+ monoxide gives rise to a linear molecule located at 2.3 kcal/mol below the reactants asymptote.

In the next transition state, located at 9.2 kcal/mol above the reactants asymptote, the O–Se–C angle is equal to 76.5° , and the distance between C and O that will form a new bond in the SeOCO^+ adduct is 2.520 Å. The imaginary frequency, describing the incoming C–O bond stretching, is 611 cm^{-1} .

As for the other cations we previously studied, the SeOCO^+ adduct in which coordination of carbon monoxide occurs by the oxygen side is energetically favored with the respect to the OSeCO^+ species. In this case, it lies 96.4 kcal/mol below the reactants energy. SeOCO^+ is a linear molecular system in which, as for GeOCO^+ , the geometrical parameters indicate that the next step does not imply the presence of an activation barrier. In fact, the Se–O distance is 2.671 Å, and the carbon–oxygen bond lengths are very similar than in carbon dioxide molecule (1.146 and 1.175 versus 1.161 Å). Once again, the carbon dioxide detachment is a barrierless step.

The NBO analysis for the species involving selenium ion gives information similar to that obtained for germanium. In particular, the Se–O bond is ionic in the SeON_2^+ and SeOCO^+ adducts and characterized by a small covalent contribution in the other two minima. The charge transfer from oxygen to selenium ion in the oxide is of about 0.2 |e|. Also in this case, the bond originates from the overlap between two hybrid sp orbitals of the two involved atoms that have a more pronounced p character than in the case of germanium. The covalent bond in the OGeCO^+ species is

still obtained by the overlap of two pure p orbitals. The net charge on the selenium ion is 0.1 |e|. The Ge–C bond is ionic.

As in the case of the germanium and also for the selenium cation, computations on species lying on the path of the excited state were performed to exclude the existence of crossing between the PESs. $^2A''$ SeON_2^+ and $^2A''$ SeO^+ adducts were found at 12.6 above and 35.1 kcal/mol below the corresponding quartets, respectively (see Figure 1(b)), suggesting a greater stability of SeO^+ in the excited rather than in the ground state. The transition state connecting the two examined minima was located at only 8.2 kcal/mol above the $^2A''$ SeON_2^+ system. The next doublets OSeCO^+ minimum and transition state were found still more stable than the quartets (of 44.7 and 34.4 kcal/mol, respectively). Finally, the last SeOCO^+ species and the final products were located at 18.2 and 50.3 kcal/mol above the corresponding ground-state adducts.

These results indicate clearly the presence of two crossings between the profiles at different multiplicities. Actually, on the basis of the new set of data, the reduction of nitrous oxide by carbon monoxide catalyzed by selenium ion becomes possible.

The process should start from the formation of the first SeON_2^+ species in the electronic state of the quartet and afterwards proceed on the doublet PES until the SeOCO^+ is formed. The second crossing is irrelevant for the reaction kinetics, while the first one changes significantly the conclusions about the performance of selenium as catalysts. In fact, as a consequence of a PES lying almost entirely (see Figure 1(b)) below the reaction asymptote, the real energetic expense for the oxide formation decreases considerably with respect to that required in the quartet case (9.2 versus 20.4 kcal/mol). This means that, although with minor efficiency than germanium, the selenium ion could also be active in catalyzing the reaction. All depends on the probability of the SOC between the doublet and quartet surfaces at the crossing point. For this reason we have retained an interest to evaluate this possibility.

The SOC matrix element was found to be, irrespective of its sign, 1034.35 cm^{-1} . The coupling between $^2A''$ and $^4A''$ is due to the z component of the SOC operator (H_{LzSz}). Coordinates of the SeON_2^+ species at the minimum energy crossing point (MECP) geometry are defined in the x,y plane. A large contribution to the orbitals involved in the coupling mechanism arises from p_x and p_y orbitals of selenium which are mainly responsible for the increase in the value of the SOC matrix element. The difference in the slopes of the quartet and doublet curves was found to be of 12.49 kcal/(mol Å), irrespective of its sign. All computed data robustly deliver a value of probability strictly close to one.

Thus one can assert that the selenium ion can work as a catalyst thanks to the two state reactivity phenomenon.

This result appears to be in slight disagreement with experimental determination¹ despite the conclusions of the ICP/SIFT study, as far as the inactivity of selenium cation is concerned, are not so categorical. The authors of this study underline that “for some atomic ions (such as Se^+ , Re^+ , etc.)

that react slowly there is insufficient information to provide an explanation for their low O-atom transfer reactivity”.

We think that some explanation can be derived from our calculations that highlight a significant participation of the excited state of the selenium.

Conclusions

The oxygen transport mechanism from nitrous oxide to carbon monoxide in the presence of Ge⁺ and Se⁺ catalysts was elucidated at the DFT level. The opposite performances of selenium and germanium, claimed by experimental studies, do not find here complete confirmation.

The whole germanium doublet PES lies below the reactants asymptote, indicating that the reaction is thermodynamically and kinetically favored. The rate determining step, in which a fictitious barrier of 11.0 kcal/mol have to be crossed, is the oxide formation. B3LYP computations exclude any participation of the quartet excited state to the catalytic process.

Very similar conclusions can be derived also from single point QCISD(T) profiles, although some part of the paths suffer from the lack of optimization.

On the basis of results concerning the ground state, the selenium ion appears to be inefficient in catalyzing the reduction of N₂O. In fact, both transient key structures were located above the reactants energy and the rate controlling step, corresponding to the formation of SeO⁺ cation monoxide, demands an activation energy of 20.4 kcal/mol. Instead, new very interesting conclusions can be derived from the computations concerning the excited doublet state energetic profile. These show that, in agreement with the presence of a spin orbit coupling at the crossing point of two considered energetic paths, whose probability to occur was computed to be equal to one, the reaction proceeds more easily being now the energetic barrier for the oxide formation of only 9.2 kcal/mol.

However, the general conclusions support the experimental data that indicate in germanium ion a better catalyst than selenium.

Acknowledgment. We gratefully acknowledge the Dipartimento di Chimica, Università della Calabria for financial aid.

References

- Blagojevic, V.; Orlova, G.; Böhme, D. K. *J. Am. Chem. Soc.* **2005**, *127*, 3545.
- Lavrov, V. V.; Blagojevic, V.; Gregory, K. K.; Orlova, G.; Böhme, D. K. *J. Phys. Chem.* **2004**, *108*, 5610.
- Böhme, D. K.; Schwarz, H. *Angew. Chem., Int. Ed.* **2005**, *44*, 2336.
- Frisch, M. J.; Trucks, G. W.; Schlegel, H. B.; Scuseria, G. E.; Robb, M. A.; Cheeseman, J. R.; Montgomery, J. A., Jr.; Vreven, T.; Kudin, K. N.; Burant, J. C.; Millam, J. M.; Iyengar, S. S.; Tomasi, J.; Barone, V.; Mennucci, B.; Cossi, M.; Scalmani, G.; Rega, N.; Petersson, G. A.; Nakatsuji, H.; Hada, M.; Ehara, M.; Toyota, K.; Fukuda, R.; Hasegawa, J.; Ispida, M.; Nakajima, T.; Honda, Y.; Kitao, O.; Nakai, H.; Klene, M.; Li X.; Knox, J. E.; Hratchian, H. P.; Cross, J. B.; Adamo, C.; Jaramillo, J.; Gomperts, R.; Stratmann, R. E.; Yazyev, O.; Austin, A. J.; Cammi, R.; Pomelli, C.; Ochterski, J. W.; Ayala, P. Y.; Morokuma, K.; Voth, G. A.; Salvador, P.; Dannenberg, J. J.; Zakrzewski, V. G.; Dapprich, S.; Daniels, A. D.; Strani, M. C.; Farkas, O.; Malick, D. K.; Rabuck, A. D.; Raghavachari, K.; Foresman, J. B.; Ortiz, J. V.; Cui, Q.; Baboul, A. G.; Clifford, S.; Cioslowski, J.; Stefanov, B. B.; Liu, G.; Liashenko, A.; Piskorz, P.; Komaromi, V.; Martin, R. L.; Fox, D. J.; Keith, T.; Al-Laham M. A.; Peng C. Y.; Nanayakkara, A.; Challacombe, M.; Gill, P. M. W.; Johnson, B.; Chen, W.; Wong, M. W.; Gonzalez, C.; Pople, J. A. Gaussian, Inc.: Wallingford, 2004.
- Becke, A. D. *J. Chem. Phys.* **1993**, *98*, 5648.
- Lee, C.; Yang, W.; Parr, R. G. *Phys. Rev. B* **1988**, *37*, 785.
- Miehlich, B.; Savin, A.; Stoll, H.; Preuss, H. *Chem. Phys. Lett.* **1989**, *157*, 200.
- Gonzalez, C.; Schlegel, H. B. *J. Chem. Phys.* **1989**, *90*, 2154.
- Glendening E. D.; Reed A. E.; Carpenter J. E.; Weinhold F. *NBO 3.0 Program Manual*; Madison, WI, 1995.
- Pople, J. A.; Head-Gordon, M.; Raghavachari, K. *J. Chem. Phys.* **1987**, *87*, 5968.
- Raghavachari, K.; Trucks, G. W.; Pople, J. A.; Head-Gordon, M. *Chem. Phys. Lett.* **1989**, *157*, 479.
- Lee, T. J.; Rendell, A. P.; Taylor, P. R. *J. Phys. Chem.* **1990**, *94*, 5463.
- Martin, J. M. L. *J. Chem. Phys.* **1994**, *100*, 8186.
- Bartlett, R. J.; Stanton, J. F. *Review of Computational Chemistry*; Lipkowitz, K. B., Boyd, D. B., Eds.; VCH: New York, 1994; Vol. V, pp 65–169.
- Lee, T. J.; Scuseria, G. E. *Quantum Mechanical Electronic Structure Calculations with Chemical Accuracy*; Langhoff, S. R., Ed.; Kluwer Academic: Dordrecht, The Netherlands, 1994; pp 47–108.
- Bartlett, R. J. In *Modern Electronic Structure Theory, Part I, Yarkony*; World Scientific: Singapore, 1995; pp 1047–1055.
- Chiodo, S.; Russo, N. *J. Comput. Chem.* In press.
- Bethe, H. A.; Salpeter, E. E. *Quantum Mechanics of the One and Two Electron Atoms*; Plenum: New York, 1977.
- Godbout, N.; Salahub, D. R.; Andzelm, J.; Wimmer, E. *Can. J. Chem.* **1992**, *70*, 560.
- Harvey, J. N.; Aschi, M.; Schwarz, H.; Koch, W. *Theor. Chem. Acc.* **1998**, *99*, 95.
- (a) Zener, C. *Proc. R. Soc. London, Ser. A* **1932**, *137*, 595.
(b) Zener, C. *Proc. R. Soc. London, Ser. A* **1933**, *140*, 1174.
- Gonzalez, C.; Schlegel, H. B. *J. Phys. Chem.* **1990**, *94*, 5523.
- Lias, S. G.; Bartmess, J. E.; Liebmann, J. F.; Holmes, J. L.; Levin, R. D.; Mallard, W. G. *J. Phys. Chem.* **1988**, Ref, Data *17*, Suppl 1.
- Rondinelli, F.; Russo, N.; Toscano, M. *Inorg. Chem.* **2007**, *46*, 7489.

CT700184Q

JCTC Journal of Chemical Theory and Computation

Branching Ratios of Aliphatic Amines + OH Gas-Phase Reactions: A Variational Transition-State Theory Study

Annia Galano*[†] and J. Raul Alvarez-Idaboy[‡]

Departamento de Química, Universidad Autónoma Metropolitana-Iztapalapa, San Rafael Atlixco 186, Col. Vicentina, Iztapalapa, C. P. 09340 México D. F., México, and Facultad de Química, Departamento de Física y Química Teórica, Universidad Nacional Autónoma de México, México DF 04510, México

Received October 19, 2007

Abstract: A theoretical study on the mechanism of the OH + aliphatic amines reactions is presented. Geometry optimization and frequencies calculations have been performed at the BHandHLYP/6-311++G(2d,2p) level of theory for all stationary points. Energy values have been improved by single-point calculations at the above geometries using CCSD(T) and the same basis set. All the possible hydrogen abstraction channels have been modeled, involving the rupture of C–H and N–H bonds. It was found that as the temperature decreases the contributions of the channels involving NH sites to the overall reaction also decrease, suggesting that for upper layers in the troposphere these channels become less important. Their percentage contributions to the overall reaction, at 298 K, were found to be about 20%, 2%, and 48% for methylamine, ethylamine, and dimethylamine, respectively.

Introduction

Aliphatic amines play an important role in the context of atmospheric and environmental sciences due to their potential role as precursors of HCN and particularly N₂O, which is both an important greenhouse gas¹ and the main source of stratospheric NO_x.^{2,3} The products of the degradation of (CH₃)₂NH can also lead to the production of carcinogenic nitrosamines in the polluted environment.⁴ In contrast to ammonia (NH₃), alkylamines rapidly react with the major initiator of trace gas oxidation in the troposphere: the OH radical. However, there is scarce data available on the reactions between OH and alkylamines.

There are only two experimental studies on each of the amines studied in the present work. They are methylamine (CH₃NH₂),^{5,6} ethylamine (CH₃CH₂NH₂),^{6,7} and dimethylamine [(CH₃)₂NH].^{6,7} It has been suggested that the lack of data is caused, to some extent, by experimental problems that arise from mixing amines and suitable OH precursors, which are often acidic gases that form aerosols in the presence of the basic amines.⁶ Accordingly, in ref 6 the

kinetics of some OH + amine reactions has been investigated, at room temperature, using a novel two-photon OH source that overcomes these problems. On the other hand, no theoretical studies have been reported on these systems.

The reactions of the OH radical with amines are thought to proceed via hydrogen atom abstraction from either C–H or N–H bonds. However, the available information on the branching ratios of these reactions is even more limited. Actually there is scarce information on branching ratios for Volatile Organic Compounds (VOCs) reactions in general. However it has been established that branching ratios between different products in multichannel reactions are as important as the overall rate of reaction, in terms of practical applications and in the understanding of the fundamental mechanisms of chemical reactions.^{8,9} In the case of amines there is only one previous study on this subject,⁴ dating from 1979. In that work the H abstraction from the NH group was estimated to contribute by (37 ± 5)% to the overall rate constant of dimethylamine. For the other studied amines there are no previous reports on their branching ratios. Based on the C–H and N–H bond strengths (Table 1), the reactions are assumed to occur by H abstractions, mainly from the C–H sites.¹⁰ This would explain the slight increase in the

* Corresponding author e-mail: agalano@prodigy.net.mx.

[†] Universidad Autónoma Metropolitana-Iztapalapa.

[‡] Universidad Nacional Autónoma de México.

Table 1. C–H and N–H Bond Strengths in the Studied Amines (kcal/mol)

		C–H	N–H
CH ₃ NH ₂		93.3 ± 2 ^a	100.0 ± 2.5 ^a
CH ₃ CH ₂ NH ₂	CH ₂	90.1 ^b	98.7 ^b
	CH ₃	99.0 ^b	
(CH ₃) ₂ NH		87 ± 2 ^a	91.5 ± 2 ^a

^a From ref 11. ^b From ref. 12.

rate coefficient of OH + C₂H₅NH₂ reaction, compared to that of CH₃NH₂. For (CH₃)₂NH the N–H bond is weaker and closer in energy to the C–H bond. Accordingly, the enhanced reactivity of this amine, compared to CH₃NH₂ and C₂H₅NH₂, is assumed to be caused by a larger contribution of N–H path to the overall rate coefficient.

The principal aim of this work is to model the different reactive pathways of the OH reactions with the above-mentioned amines and to estimate the proportion of their contribution to the overall reactions.

Computational Details

Full geometry optimizations were performed with the Gaussian 03¹³ program using the 6-311++G(2d,2p) basis set and the BHandHLYP hybrid HF-density functional, as implemented in Gaussian 03.¹⁴ The energies of all the stationary points were improved by single point calculations using CCSD(T)¹⁵ method and the same basis set mentioned above. Based on our previous experience,¹⁶ the use of the CCSD(T)/BHandHLYP approach properly describes the energetic and kinetics features of VOCs + OH hydrogen abstraction reactions. In addition, for this kind of reactions it has been proved that the differences in geometries between several DFT methods compared to CCSD and QCISD are minimal for BHandHLYP.¹⁷ Unrestricted calculations were used for open shell systems. Frequency calculations were carried out for all the stationary points at the DFT level of theory, and local minima and transition states were identified by the number of imaginary frequencies (NIMAG = 0 or 1, respectively). Intrinsic Reaction Coordinate (IRC)¹⁸ calculations were carried out at the BHandHLYP/6-311G++(2d,2p) level of theory to confirm that the transition states structures connect the proper reactants and products. The paths have been computed by following the Gonzalez-Schlegel steepest descent path,¹⁹ in mass-weighted internal coordinates. Fifty points were modeled on each side of the saddle points, with a gradient step size of 0.02 amu^{1/2}bohr. Thermodynamic corrections to the energy at 298.15 K were included in the determination of the activation energies and of the heats of reaction, which have been reported in terms of Gibbs free energies.

Rate coefficients were calculated using the Canonical Variational Theory (CVT),^{20–26} as implemented in The Rate program at Computational Science and Engineering Online Web site (www.cseo.net).²⁷ For H abstractions from the methyl group in ethyl amine the Conventional Transition State Theory (TST)^{28,29} was used since the corresponding reaction barrier is high enough to avoid significant recrossing effects. The Minimum-Energy Paths (MEP)³⁰ were obtained from IRC calculations at the BHandHLYP/

Table 2. Classical Potential Energies of Reaction (ΔE) and Barriers (ΔE^\ddagger) and Gibbs Free Energies of Reaction (ΔG) and Barriers (ΔG^\ddagger) at 298.15 K^a

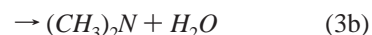
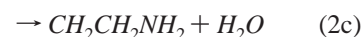
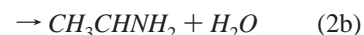
	ΔE^\ddagger	ΔE	ΔG^\ddagger	ΔG	<i>L</i>
(1a)	0.97	–17.00	7.00	–19.08	0.27
(1b)	0.36	–23.19	6.73	–24.48	0.14
(2a)	0.95	–16.99	6.93	–19.01	0.27
(2b)	–0.79	–24.01	5.89	–25.51	0.10
(2c)	5.51	–14.29	10.79	–16.35	0.43
(3a)	–2.23	–22.43	3.76	–25.16	0.12
(3b)	–0.73	–23.86	5.98	–25.19	0.13

^a All in kcal/mol.

6-311G++(2d,2p) level of theory. Force constants, harmonic vibrational frequencies, and normal-mode vectors for the 3N-7 degrees of freedom that are orthogonal to the reaction path were computed at selected points along the IRC, for which the energies were improved by CCSD(T) single point calculations.

Results and Discussion

All the possible reactive channels of the OH hydrogen abstraction reactions from the studied amines have been modeled:



Energies and Geometries. The calculated classical potential energies of reaction (ΔE), the reaction free energies at 298.15 K (ΔG), the classical potential energy barriers (ΔE^\ddagger), and the Gibbs free energy barriers at 298.15 K (ΔG^\ddagger) for all the studied channels are reported in Table 2. All the reactions were found to be exergonic ($\Delta G < 0$) with products more than 16 kcal/mol more stable than the corresponding reactants. A relationship is expected between the calculated classical potential energies of reaction and the strength of the broken bonds. Comparing values in Tables 1 and 2 it can be observed that for the N–H bonds the weakest is that of dimethylamine (DMA), which also correspond to the largest ΔE , while the N–H bond strengths in ethylamine (EA) and methylamine (MA) are of similar magnitude and so are the corresponding classical potential energies of reaction. The same trend is also observed for C–H bonds. In addition, comparing reaction channels that involves different kind of bonds for the same amine it can be seen that the difference in experimentally determined bond strengths for channels (1a) and (1b), (2a) and (2b), and (3a) and (3b) are 6.7 ± 4.5 ,¹¹ 8.6 (error not reported),¹² and 4.5 ± 4 kcal/mol,¹¹ respectively, while the calculated differences

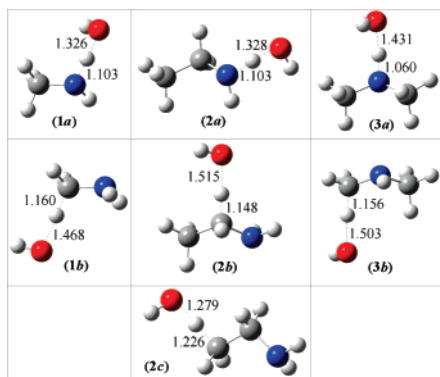


Figure 1. Fully optimized geometries of the transition states.

in ΔE are about 6.7, 7.0, and 1.5 kcal mol, i.e., there is a good agreement between both kind of results. The highest calculated barrier corresponds to path (2c), which is a logical finding since it corresponds to the only H abstraction from a primary carbon that is not next to an amino group, i.e., this is an alkane-like methyl site. Comparing channels 1b and 2c, which involve primary $-\text{CH}_3$ groups, $\Delta E^\ddagger(2c)$ is larger than $\Delta E^\ddagger(1b)$ by about 4.2 kcal/mol, which is in agreement with the 5.7 kcal/mol difference between the corresponding bond strengths. This is also in line with the fact that the amino group activates H abstractions from carbon sites directly bonded to it, i.e., alpha sites.

The L parameters for all the studied channels have also been included in Table 2. The L parameter denotes if a transition state structure is reactant-like ($L < 1$) or product-like ($L > 1$) and also quantifies the corresponding trend. Therefore, according to the Hammond postulate,³¹ there must be a direct relationship between the L value and the heat of reaction of a specific path. The L parameters were calculated for each reaction channel, following refs 32 and 33 as

$$L(N-H) = \frac{\delta r(N-H)}{\delta r(H-O)} \quad (1)$$

and

$$L(C-H) = \frac{\delta r(C-H)}{\delta r(H-O)} \quad (2)$$

where $\delta r(N-H)$ and $\delta r(C-H)$ represent the variation in the breaking bond distance between transition states and reactants; while $\delta r(H-O)$ stands for the variation in the forming bond distance between transition states and products.

According to the L parameters in Table 2, all the transition states structures are reactant-like. The relationships between L and ΔE or ΔG are well accomplished. The lowest (highest) value of L actually corresponds to the most (less) negative energy of reaction, while L values of similar magnitudes correspond to comparable energy values. It seems worthwhile to point out that these are qualitative criteria and when there are very small differences between two L (or energy) values the strict order might change. The transition states (TS) structures and the main bond distances in their fully optimized geometries are shown in Figure 1. From all the TS involved in H abstractions from N-H sites the earliest one (most reactant-like) is that corresponding to channel (3a)

with and the largest H-O distance: $r(N-H)=1.06$ and $r(H-O)=1.43$ Å, respectively. This is an indication of the higher reactivity of the N-H site in DMA compared to MA and EA. On the other hand, the TS with the lowest L , from all those involved in H abstractions from C-H sites, is that corresponding to channel (2b) with $r(C-H)=1.15$ Å, indicating that EA has the highest reactive C-H site among all the modeled ones. At this point, and based on the previous analysis, it is possible to hypothesize that DMA would have the largest contribution of the H abstractions from N-H to the overall reaction, while EA should have the lowest one, within the studied set of amines. This is in line with chemical intuition which indicates that the amine with secondary nitrogen (carbon) would have the most reactive N-H (C-H) site.

Minimum Energy Paths. Intrinsic reaction coordinate calculations (IRC) were performed at the BHandHLYP/6-311++G(2d,2p) level of theory in order to obtain the minimum energy paths (MEP) for the studied channels of reaction. The calculations were carried out starting from the fully optimized saddle-point geometries and then moving downhill along the reactant and product sides, in mass-weighted internal coordinates. Neither reorientation nor symmetry were used to construct the IRC. An even gradient step size of 0.02 amu^{1/2} bohr was used, and fifty points were calculated in each direction. The reaction coordinate s is defined as the signed distance from the saddle point (where $s < 0$ refers to the reactants' side and $s > 0$ refers to the products' side). As a reasonable compromise between speed and accuracy, and based on the curvature of the surface, five points on each side of the saddle point were chosen to construct the MEP. Their energies were improved by single-point calculations at the CCSD(T)/6-311++G(2d,2p) level of theory, and they were used in conjunction with gradients and frequencies computed at the BHandHLYP/6-311++G(2d,2p) level.

The adiabatic minimum energy potential surfaces were obtained within the B//A approach,³⁴ which has become common in the study of polyatomic systems because it is relatively inexpensive from a computational point of view and it usually reproduces correctly the main features of the reaction path. It consists of geometry optimizations at a given level (A) followed by single point calculations, without optimization, at a higher level (B). The MEP obtained using this technique presents a maximum that is shifted toward the reactants valley by about -0.2 bohr with respect to the maximum at the A level of calculation. Espinosa-Garcia and Corchado³⁵ argue that, when the MEP is constructed using the B//A technique, the energy maximum is artificially located away from the saddle point corresponding to the level of optimization (A). This shift, that is simply a numerical effect, could be mistaken with a variational effect and mislead the kinetic calculations. Consequently, we have corrected the position of the maxima as suggested by these authors. The calculated MEPs corresponding to abstractions from C-H sites are almost barrierless processes, while those corresponding to N-H abstractions show barriers that are still low but noticeable. When reaction profiles involve low and broad classical barriers, it causes large variational effects (see

Table 3. Calculated Overall Rate Coefficients (k , $\text{cm}^3 \text{molecule}^{-1} \text{s}^{-1}$) for Amines + OH Reactions, within the Temperature Range 290–310 K, and Experimental Values at 298 K^a

T (K)	k_{MA}	k_{EA}	k_{DMA}
290	4.86×10^{-12}	1.18×10^{-11}	5.21×10^{-11}
292	4.95×10^{-12}	1.19×10^{-11}	5.23×10^{-11}
294	5.03×10^{-12}	1.19×10^{-11}	5.25×10^{-11}
296	5.11×10^{-12}	1.19×10^{-11}	5.20×10^{-11}
298.15	5.20×10^{-12}	1.19×10^{-11}	5.17×10^{-11}
300	5.28×10^{-12}	1.19×10^{-11}	5.15×10^{-11}
302	5.37×10^{-12}	1.19×10^{-11}	5.12×10^{-11}
304	5.45×10^{-12}	1.19×10^{-11}	5.10×10^{-11}
306	5.54×10^{-12}	1.19×10^{-11}	5.07×10^{-11}
308	5.63×10^{-12}	1.20×10^{-11}	5.05×10^{-11}
310	5.72×10^{-12}	1.20×10^{-11}	5.03×10^{-11}
exp ^{5,7}	2.20×10^{-11}	2.77×10^{-11}	6.54×10^{-11}
exp ⁶	1.73×10^{-11}	2.37×10^{-11}	6.49×10^{-11}

^a MA = methylamine, EA = ethylamine, DMA = dimethylamine.

ref 36 for more details). In these cases, the recrossing problem is essential, and variational transition state theory is needed to obtain reliable values of the rate constants (k). Accordingly the CVT approach has been used to compute the rate constant corresponding to all channels but the (2c). In this particular case the reaction barrier (ΔE^\ddagger) is high enough (Table 2) to avoid substantial recrossing effects and the conventional transition state theory, which can be considered as an upper limit of CVT, is adequate to compute k . In addition the (2c) is a minor path that hardly contributes to the overall reaction of ethylamine.

Kinetics and Branching Ratios. The rate coefficients have been calculated within the temperature range 290–310 K (Table 3), to obtain kinetic parameters corresponding to the 298 K vicinity. We have assumed that neither mixing nor crossover between different pathways occurs and that the overall rate constant (k) corresponding to each amine + OH can be calculated as the sum of the rate coefficients of each path:

$$k_{MA} = k_{(1a)} + k_{(1b)} \quad (4)$$

$$k_{EA} = k_{(2a)} + k_{(2b)} + k_{(2c)} \quad (5)$$

$$k_{DMA} = k_{(3a)} + k_{(3b)} \quad (6)$$

Tunneling corrections were significant only for channel 2c, with transmission coefficients (κ) ranging from 5.17 at 290 K to 4.16 at 310 K. For all the other channels tunneling corrections were found to be negligible, even at the lowest temperature. This is a logical finding since their adiabatic barriers (ΔE^\ddagger) are negative or close to zero. The branching ratios of the different reaction channels, which represent the percent of their contribution to the overall reaction, have been calculated for each amine as

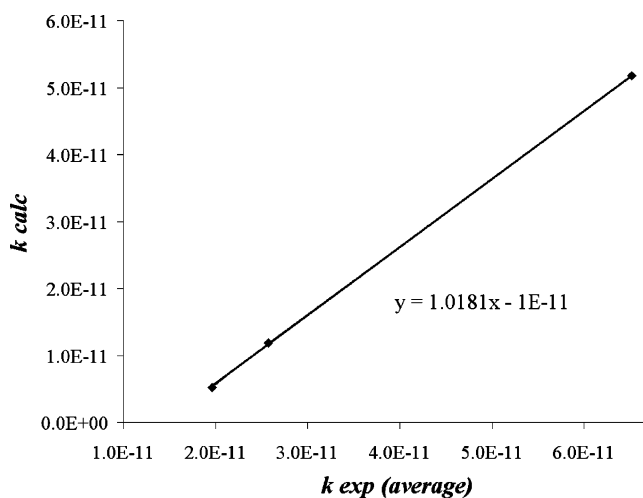
$$\Gamma_{a,b \text{ or } c} = \frac{k_{a,b \text{ or } c}}{k_{\text{overall}}} \times 100 \quad (7)$$

The values of the rate constants and branching ratios for the studied temperature range are reported in Tables 3 and 4.

Table 4. Calculated Branching Ratios (Γ) within the Temperature Range 290–310 K

T (K)	MA		EA			DMA	
	Γ_{1a}	Γ_{1b}	Γ_{2a}	Γ_{2b}	Γ_{2c}	Γ_{3a}	Γ_{3b}
290	20.3	79.7	1.5	98.2	0.3	51.2	48.8
292	20.3	79.7	1.5	98.2	0.3	51.0	49.0
294	20.3	79.7	1.5	98.1	0.4	50.8	49.2
296	20.3	79.7	1.5	98.1	0.4	48.7	51.3
298.15	20.3	79.7	1.9	97.7	0.4	48.4	51.6
300	20.3	79.7	1.9	97.7	0.4	48.0	52.0
302	20.3	79.7	1.9	97.7	0.4	47.7	52.3
304	20.4	79.6	1.9	97.7	0.4	47.3	52.7
306	20.4	79.6	2.0	97.6	0.4	47.0	53.0
308	20.4	79.6	2.0	97.6	0.4	46.6	53.4
310	20.4	79.6	2.0	97.6	0.4	46.3	53.7

^a MA = methylamine, EA = ethylamine, DMA = dimethylamine.

**Figure 2.** Correlation between calculated and average experimental values of k_{298} ($\text{cm}^3 \text{molecule}^{-1} \text{s}^{-1}$).

The calculated rate coefficients agree well with the previously reported experimental values, differing by less than 1 order of magnitude and following the same tendency. The largest discrepancy was found for methylamine with a calculated value that is about one-third of the experimental one. The good correlation between calculated and the average experimental values of the overall rate constants is shown in Figure 2. This good agreement supports the reliability of the present calculations. However the calculated values are more in line with bond dissociation energies than the experimental ones, see Table 1. The ratio between the experimental rate coefficients of ethylamine/methyl amine is only 1.3. This has no precedent in other VOCs + OH reactions when H abstractions from $-\text{CH}_3$ and $-\text{CH}_2-$ are compared. This could be rationalized only if H abstractions mainly occur from NH sites, which is not the case. On the other hand, the ratio of the calculated rate coefficients is 2.3, which is more in line with the equivalent ratio ethanol/methanol which is 3.3 and for which the H abstraction from the OH group is expected to contribute to a very low extent to the overall reaction. Within the studied temperature range the variations of k with temperature are quite small suggesting that activation energies around 298 K should be close to zero. The largest variation was found for MA. The Arrhenius

equation best fitting the calculated data for the studied amines in the 290–310 K temperature range are

$$k_{\text{overall}}^{\text{MA}} = 5.89 \times 10^{-11} e^{-757/RT}$$

$$k_{\text{overall}}^{\text{EA}} = 1.39 \times 10^{-11} e^{-49/RT}$$

$$k_{\text{overall}}^{\text{DMA}} = 2.72 \times 10^{-11} e^{200/RT}$$

According to these equations the Arrhenius activation energies are 1.43, 0.09, and -0.38 kcal/mol for the OH reaction with methylamine, ethylamine, and dimethylamine, respectively. The only experimental values available are (-0.46 ± 0.3) ,⁵ (-0.38 ± 0.3) ,⁷ and (-0.49 ± 0.3) .⁷ For DMA the calculated value is within the error range of the experimental determination. However for MA and EA the calculated Arrhenius activation energies are higher than the experimental ones, with the largest discrepancy for MA, for which it seems to be overestimated. That the experimental activation energy of MA is lower than that corresponding to EA seems to be difficult to rationalize. The calculated values are in agreement with the expected trend, based on the structure reactivity relationship, i.e., the abstraction from a secondary carbon should be energetically more favored than from a primary one, in a similar way to what occurs when comparing ethanol and methanol: 0.14 kcal/mol and 0.72 kcal/mol, respectively. The same applies for secondary and primary amino group when DMA and MA are compared, moreover the activation effect of $\text{CH}_3\text{-NH-}$ group should be larger than that of $\text{NH}_2\text{-}$ group, in a similar way that the activation energy, according to recommended values, for dimethyl ether (0.43 kcal/mol) is lower than for methanol (0.72 kcal/mol). Accordingly, both channels in DMA are expected to be activated with respect to the equivalent channels in MA, i.e., the activation energy of the overall reaction is expected to be lower. Our results are also in agreement with the bond dissociation energies experimentally determined (Table 1) and with the assumption that activation energies should correlate with bond dissociation energies, except when different channels have different tunneling corrections which is not the case. Since in the last decades not only the calculation resources but also the experimental techniques have evolved, new experiments dealing with Arrhenius parameters for aliphatic amines + OH reactions would be desirable.

As it can be seen from the values in Table 4, abstractions from the $-\text{CH}$ sites make the largest contribution to the overall rate constant, with the exception of dimethylamine at temperatures below 294 K. In all the cases the increase in temperature also increases the contribution of N–H sites abstractions. Therefore moving upward in the troposphere, which implies a lowering in temperatures, the abstraction reactions from NH sites are expected to become less and less important. For ethylamine, in particular, even at room temperature the contribution of 2a channel to the overall rate constant is less than 2%. Accordingly, it could be expected that the OH reactions with secondary amines mainly occur by H abstraction from CH sites, especially from those involving secondary carbons. On the other hand, being that DMA is the only secondary amine from all the modeled ones

it seems logical that it shows the largest contribution of H abstractions from N–H sites to the overall rate constant. At 298 K the calculations predict that about 48% of the reaction would involve the NH site. The only experimental report⁴ on branching ratios propose that $(37 \pm 5)\%$ of the DMA + OH reaction takes place through this channel. Taking into account that this determination dates from 1979 and the error inherent to electronic calculations, there is good agreement between these two values. Accordingly, it seems reasonable to assume that the branching ratios proposed here for the first time are reliable enough to describe the product distribution expected for MA and EA.

Conclusion

Different channels have been modeled for the OH + aliphatic amines reactions, involving the rupture of C–H and N–H bonds. According to our results, for ethylamine the only channel that significantly contributes to the overall reaction is that involving abstractions from the secondary carbon. For methylamine and dimethylamine a mixture of products is expected. For the first one the H abstraction take place mainly from the $-\text{CH}_3$ group, while for the second one products involving abstractions from NH and CH sites are expected to be formed in similar proportions. Even though the reaction was studied in a relative short interval of temperatures, around 298 K, and within this interval the rate constants change smoothly with temperature, it seems that as the temperature decreases the contributions of the channels involving NH sites to the overall reaction also decrease. This finding suggests that for upper layers in the troposphere these channels become less important. Their percentage contributions to the overall reaction, at 298 K, were found to be about 20%, 2%, and 48% for methylamine, ethylamine, and dimethylamine, respectively.

Acknowledgment. The authors would like to thank the Dirección General de Servicios de Cómputo Académico (DGSCA) at Universidad Nacional Autónoma de México. This work was partially supported by a grant from the DGAPA UNAM (PAPIIT-IN203206-2) and SEP/CONACYT grant SEP-2004-C01-46167.

References

- (1) Intergovernmental Panel on Climatic Change (IPCC). *Climate Change*; The supplementary report to the IPCC Scientific Assessment; Houghton, J. T., Rasmussen, Callander, B. A., Varnay, S. K., Eds.; Cambridge University Press: New York, 1992.
- (2) Crutzen, P. J. *J. Geophys. Res.* **1971**, *76*, 7311.
- (3) McElroy, M. B.; McConnell, J. C. *J. Atmos. Sci.* **1971**, *28*, 1095.
- (4) Lindley, C. R. C.; Calvert, J. G.; Shaw, J. H. *Chem. Phys. Lett.* **1979**, *67*, 57.
- (5) Atkinson, R.; Perry, R. A.; Pitts, J. N., Jr. *J. Chem. Phys.* **1977**, *66*, 1578.
- (6) Carl, S. A.; Crowley, J. N. *J. Phys. Chem. A* **1998**, *102*, 8131.
- (7) Atkinson, R.; Perry, R. A.; Pitts, J. N., Jr. *J. Chem. Phys.* **1978**, *68*, 1850.

- (8) Seakins, P. W. *Annu. Rep. Prog. Chem., Sect. C: Phys. Chem.* **2007**, *103*, 173.
- (9) (a) Butkovskaya, N. I.; Kukui, A.; Le Bras, G. *J. Phys. Chem. A* **2004**, *108*, 1160. (b) Butkovskaya, N. I.; Setser, D. W. *J. Phys. Chem. A* **1999**, *103*, 6921. (c) Butkovskaya, N. I.; Kukui, A.; Pouvesle, N.; Le Bras, G. *J. Phys. Chem. A* **2004**, *108*, 7021.
- (10) Atkinson, R. *Chem. Rev.* **1986**, *86*, 69.
- (11) McMillen, D. F.; Golden, D. M. *Annu. Rev. Phys. Chem.* **1982**, *33*, 493.
- (12) Gribov, L. A.; Novakov, I. A.; Pavlyuchko, A. I.; Korolkov, V. V.; Orlinson, B. S. *J. Struct. Chem.* **2004**, *45*, 951.
- (13) M. J.; Frisch, G. W.; Trucks, H. B.; Schlegel, G. E.; Scuseria, M. A.; Robb, J. R.; Cheeseman, J. A.; Montgomery, T., Jr.; Vreven, K. N.; Kudin, J. C.; Burant, J. M.; Millam, S. S.; Iyengar, J.; Tomasi, V.; Barone, B.; Mennucci, M.; Cossi, G.; Scalmani, N.; Rega, G. A.; Petersson, H.; Nakatsuji, M.; Hada, M.; Ehara, K.; Toyota, R.; Fukuda, J.; Hasegawa, M.; Ishida, T.; Nakajima, Y.; Honda, O.; Kitao, H.; Nakai, M.; Klene, X.; Li, J. E.; Knox, H. P.; Hratchian, J. B.; Cross, V.; Bakken, C.; Adamo, J.; Jaramillo, R.; Gomperts, R. E.; Stratmann, O.; Yazyev, A. J.; Austin, R.; Cammi, C.; Pomelli, J. W.; Ochterski, P. Y.; Ayala, K.; Morokuma, G. A.; Voth, P.; Salvador, J. J.; Dannenberg, V. G.; Zakrzewski, S.; Dapprich, A. D.; Daniels, M. C.; Strain, O.; Farkas, D. K.; Malick, A. D.; Rabuck, K.; Raghavachari, J. B.; Foresman, J. V.; Ortiz, Q.; Cui, A. G.; Baboul, S.; Clifford, J.; Cioslowski, B. B.; Stefanov, G.; Liu, A.; Liashenko, P.; Piskorz, I.; Komaromi, R. L.; Martin, D. J.; Fox, T.; Keith, M. A.; Al-Laham, C. Y.; Peng, A.; Nanayakkara, M.; Challacombe, P. M. W.; Gill, B.; Johnson, W.; Chen, M. W.; Wong, C.; Gonzalez, J. A.; Pople, *Gaussian 03, Revision D.01*; Gaussian, Inc.: Wallingford, CT, 2004.
- (14) Gaussian03 Online Manual. http://www.gaussian.com/g_ur/k_dft.htm.
- (15) (a) Cizek, J. *Adv. Chem. Phys.* **1969**, *14*, 35. (b) Purvis, G. D.; Bartlett, R. J. *J. Chem. Phys.* **1982**, *76*, 1910. (c) Scuseria, G. E.; Janssen, C. L.; Schaefer III, H. F. *J. Chem. Phys.* **1988**, *89*, 7382. (d) Scuseria, G. E.; Schaefer III, H. F. *J. Chem. Phys.* **1989**, *90*, 3700.
- (16) See for example: (a) Alvarez-Idaboy, J. R.; Galano, A.; Bravo-Pérez, G.; Ruiz-Santoyo, M. E. *J. Am. Chem. Soc.* **2001**, *123*, 8387. (b) Alvarez-Idaboy, J. R.; Cruz-Torres, A.; Galano, A.; Ruiz-Santoyo, M. E. *J. Phys. Chem. A* **2004**, *108*, 2740. (c) Galano, A.; Alvarez-Idaboy, J. R.; Ruiz-Santoyo, M. E.; Vivier-Bunge, A. *Chem. Phys. Chem.* **2004**, *5*, 1379. (d) Galano, A.; Alvarez-Idaboy, J. R.; Ruiz-Santoyo, M. E.; Vivier-Bunge, A. *J. Phys. Chem. A* **2005**, *109*, 169. (e) Galano, A.; Cruz-Torres, A.; Alvarez-Idaboy, J. R. *J. Phys. Chem. A* **2006**, *110*, 1917.
- (17) Szori, M.; Fittschen, C.; Csizmadia, I. G.; Viskolcz, B. *J. Chem. Theory Comput.* **2006**, *2*, 1575.
- (18) Gonzalez, C.; Schlegel, H. B. *J. Phys. Chem.* **1990**, *94*, 5523.
- (19) (a) Gonzalez, C.; Schlegel, H. B. *J. Chem. Phys.* **1989**, *90*, 2154. (b) Gonzalez, C.; Schlegel, H. B. *J. Phys. Chem.* **1990**, *94*, 5523.
- (20) Keck, J. C. *J. Chem. Phys.* **1960**, *32*, 1035.
- (21) Baldrige, K. M.; Gordon, M. S.; Steckler, R.; Truhlar, D. G. *J. Phys. Chem.* **1989**, *93*, 5107.
- (22) Garrett, B. C.; Truhlar, D. G.; Grev, R. S.; Magnuson, A. W. *J. Phys. Chem.* **1980**, *84*, 1730; Erratum: **1983**, *87*, 4554.
- (23) Isaacson, A. D.; Truhlar, D. G. *J. Chem. Phys.* **1982**, *76*, 1380.
- (24) Truhlar, D. G.; Isaacson, A. D.; Garrett, B. C. *Theory of Chemical Reaction Dynamics*; Baer, M., Ed.; CRC Press: Boca Raton, FL, 1985; Vol. 4, pp 65–137.
- (25) Truhlar, D. G.; Garrett, B. C. *Annu. Rev. Phys. Chem.* **1984**, *35*, 159.
- (26) Lu, D.-h.; Truong, T. N.; Melissas, V.; Lynch, G. C.; Liu, Y.-P.; Garrett, B. C.; Steckler, R.; Isaacson, A. D.; Rai, S. N.; Hancock, G. C.; Lauderdale, J. G.; Joseph, T.; Truhlar, D. G. *Comput. Phys. Commun.* **1992**, *71*, 235.
- (27) Zhang, S.; Truong, T. N. *VKLab version 1.0*; University of Utah, 2001.
- (28) Eyring, H. *J. Chem. Phys.* **1935**, *3*, 107.
- (29) Truhlar, D. G.; Hase, W. L.; Hynes, J. T. *J. Phys. Chem.* **1983**, *87*, 2664.
- (30) Truhlar, D. G.; Kupperman, A. *J. Am. Chem. Soc.* **1971**, *93*, 1840.
- (31) Hammond, G. S. *J. Am. Chem. Soc.* **1955**, *77*, 334.
- (32) Rayez, M. T.; Rayez, J. C.; Sawerysyn, J. P. *J. Phys. Chem.* **1994**, *98*, 11342.
- (33) Talhaoui, A.; Louis, F.; Devolder, P.; Meriaux, B.; Sawerysyn, J. P.; Rayez, M. T.; Rayez, J. C. *J. Phys. Chem.* **1996**, *100*, 13531.
- (34) (a) Truhlar, D. G. In *The Reaction Path in Chemistry: Current Approaches and Perspectives*; Heidrich, D., Ed.; Kluwer: Dordrecht, The Netherlands, 1995; p 229. (b) Truhlar, D. G.; Garrett, B. C.; Klippenstein, S. J. *J. Phys. Chem.* **1996**, *100*, 2771. (c) Hu, W. P.; Truhlar, D. G. *J. Am. Chem. Soc.* **1996**, *118*, 860.
- (35) Espinosa-Garcia, J.; Corchado, J. C. *J. Phys. Chem.* **1995**, *99*, 8613.
- (36) Rosenman, E.; McKee, M. L. *J. Am. Chem. Soc.* **1997**, *119*, 9033.

JCTC

Journal of Chemical Theory and Computation

Application of the Correlation Consistent Composite Approach (ccCA) to Third-Row (Ga–Kr) Molecules

Nathan J. DeYonker,* Benjamin Mintz, Thomas R. Cundari, and Angela K. Wilson*

Center for Advanced Scientific Computing and Modeling (CASCaM), Department of Chemistry, University of North Texas, Denton, Texas 76203-5070

Received September 24, 2007

Abstract: The correlation consistent composite approach (ccCA) has been applied to the G3/05 training set of 51 energetic properties for the atoms and molecules that contain the 4p elements, Ga–Kr. When atomic and molecular first-order spin orbit coupling corrections are added to open shell atoms and molecules, the ccCA has a mean absolute deviation from experiment (MAD) of 0.95 kcal mol⁻¹, an improvement of 0.10 kcal mol⁻¹ over G3 and G3X model chemistries. The performance of the ccCA on third-row-containing atoms and molecules is, therefore, commensurate in accuracy with previous studies on lighter main group elements H–Ar. While the typical methods used to compute theoretical molecular spin orbit corrections may go against the spirit of “black box” model chemistries, such corrections may be necessary for molecules containing heavy elements such as Ga–Kr. For example, when second-order spin orbit corrections are added to the atomic and molecular energies, the ccCA MAD is reduced to 0.88 kcal mol⁻¹.

Introduction

Sophisticated ab initio techniques that include electron correlation generally scale as N^5 or higher, where N is the number of basis functions included in the basis set. Due to this high scaling, correlated methods, such as coupled cluster including single, double, and quasiperturbative triple excitations [CCSD(T)], are not computationally tractable for large molecules when combined with large basis sets. Model chemistries, also called composite methods, attempt to effectively reproduce a more sophisticated level of ab initio theory by using combinations of more efficient levels of theory and basis sets in an additive manner. These additive corrections form the foundation of composite model chemistries and have repeatedly been shown to be a valid and cost-effective approximation to the electronic Schrödinger equation. Model chemistries allow for quantitative computational studies on significantly larger chemical systems that would normally be inaccessible.

The correlation consistent Composite Approach (ccCA) has been recently developed in our laboratories and is a

model chemistry based on second-order Møller-Plesset perturbation theory computations extrapolated to the complete basis set (CBS) limit.^{1,2} The ccCA utilizes the family of correlation consistent basis sets pioneered by Dunning and co-workers.^{3–10} The initial purpose for creating the ccCA was to provide an efficient MP2-based model chemistry that did not require parametrization. Benchmark studies utilizing the ccCA have shown that it reliably achieves “chemical accuracy”, defined as obtaining energetic properties within 1 kcal mol⁻¹ of well-established experimental values for main group species, without relying on optimized or semiempirical parameters.

Since its initial implementation, the ccCA generally has been shown to provide results that are comparable to G3^{11–14} and G3X¹⁵ for organic species^{1,2,16} and more reliable than these widely used model chemistries for inorganic s-block species.¹⁷ Since the suite of correlation consistent basis sets also exists for transition metals Sc–Zn,⁵ the ccCA has also been applied to a test set of transition metal-containing species, and an accuracy of ± 3 kcal mol⁻¹ has been achieved for enthalpies of formation.¹⁸ The ccCA can also be utilized for high-accuracy studies on larger molecular species such as magnesocene [Mg(C₅H₅)₂] and beryllium bis(acetyl-

* Corresponding author e-mail: ndeyonk@unt.edu (N.J.D.), akwilson@unt.edu (A.K.W.).

acetate) $[\text{Be}(\text{C}_5\text{H}_7\text{O}_2)_2]^{19}$ that are currently computationally intractable for studies employing large basis set coupled cluster computations, such as those within the W_n ,^{20,21} HEAT,²² and Dixon/Feller/Peterson^{23–30} model chemistries.

Thus far, the ccCA method has been benchmarked using the G_n training sets.^{1,2} The most current iteration of the G_n training sets, G3/05, contains 464 first-, second-,¹¹ and third-row^{14,31–34} atomic and molecular species and includes experimental enthalpies of formation, ionization potentials, electron affinities, and proton affinities. However, because of a lack of core-valence correlation consistent basis sets, atomic and molecular properties of species that contain third-row (K–Kr) atoms have not yet been examined with the ccCA model chemistry. Recently, we have developed the necessary cc-pCVnZ basis sets for Ga–Kr.³⁵ Thus, with the addition of these basis sets to the suite of correlation consistent basis sets, ccCA calculations are now possible for all elements up to krypton ($Z = 36$) with the exception of potassium and calcium. We now extend the investigation of the ccCA model chemistry to the properties of G3/05 molecules that contain the elements Ga through Kr.

Theoretical Methods

Ab initio and DFT computations were carried out with the Gaussian03 software package.³⁶ Structures were optimized at the B3LYP level of theory with the cc-pVTZ basis sets. Harmonic vibrational frequencies were then computed using the B3LYP/cc-pVTZ level of theory at the geometric stationary points. To obtain the required zero-point vibrational energies (ZPE) and temperature-dependent enthalpy corrections, the harmonic frequencies were scaled by a factor of 0.9854 to account for known deficiencies in the harmonic approximation. The use of B3LYP/cc-pVTZ for optimizing geometries and obtaining harmonic frequencies provides results that are quite similar to those obtained via 6-31G(2df,p) optimizations that are computed with the G3X and G4 model chemistries. The current formulation of the ccCA employs MP2 extrapolations to the complete basis set limit (CBS) and the previous ccCA benchmark study found that two types of CBS extrapolations provided the most reliable results for the main group G3/99 training set.² The first is the Peterson mixed exponential/Gaussian function extrapolation scheme³⁷ defined by the formula

$$E(x) = E_{\text{CBS}} + B \exp[-(x - 1)] + C \exp[-(x - 1)^2] \quad (1.1)$$

where $x = 2, 3,$ and 4 come from aug-cc-pVDZ, aug-cc-pVTZ, and aug-cc-pVQZ MP2 energies, respectively. The other CBS extrapolation is the two-point Schwartz $1/(l_{\text{max}}^4)$ scheme^{38–40} using aug-cc-pVTZ and aug-cc-pVQZ MP2 energies and is determined using the formula

$$E(l_{\text{max}}) = E_{\text{CBS}} + \frac{B}{\left(l_{\text{max}} + \frac{1}{2}\right)^4} \quad (1.2)$$

where l_{max} is the maximum angular momentum value within the basis set. In this study, $l_{\text{max}} = 3$ for aug-cc-pVTZ and $l_{\text{max}} = 4$ for aug-cc-pVQZ energies. We refer to the ccCA which utilizes the extrapolation function in eq 1.1 as ccCA-

P, and the ccCA which utilizes the extrapolation function in eq 1.2 as ccCA-S4.

After the MP2 CBS energy is determined, a series of additive corrections is computed. In order to properly account for high-order electron correlation effects, a single point energy is computed at the triple- ζ level with the CCSD(T) wave function. The $\Delta E(\text{CC})$ correction for the ccCA methods can be expressed as

$$\Delta E(\text{CC}) = E[\text{CCSD(T)/cc-pVTZ}] - E[\text{MP2/cc-pVTZ}] \quad (1.3)$$

Next, scalar relativistic corrections are obtained from frozen-core MP2 wave functions using the cc-pVTZ-DK⁴¹ basis sets and the spin-free, one-electron Douglas-Kroll-Hess (DKH) Hamiltonian.^{42–44} The MP2 relativistic correction to the ccCA energy, $\Delta E(\text{DK})$,⁴⁵ is formulated as

$$\Delta E(\text{DK}) = E[\text{MP2/cc-pVTZ-DK}] - E[\text{MP2/cc-pVTZ}] \quad (1.4)$$

The final computation is a correction for core-valence correlation effects. This energy, $\Delta E(\text{CV})$, is computed as

$$\Delta E(\text{CV}) = E[\text{MP2(full)/aug-cc-pCVTZ}] - E[\text{MP2/aug-cc-pVTZ}] \quad (1.5)$$

Including the zero-point energy [$\Delta E(\text{ZPE})$] determined by the scaled B3LYP/cc-pVTZ harmonic vibrational frequencies, the ccCA-CBS energy is defined as

$$E_0(\text{ccCA-CBS}) = E[\text{MP2/aug-cc-pV}\infty\text{Z}] + \Delta E(\text{CC}) + \Delta E(\text{DK}) + \Delta E(\text{CV}) + \Delta E(\text{ZPE}) \quad (1.6)$$

For atomic species,⁴⁶ and some linear molecules (discussed below), a spin orbit correction, taken from previous theoretical studies, $\Delta(\text{SO})$,^{14,31} is also added to the ccCA energy.

Evaluation of ccCA Methods for Species with Elements Ga–Kr

A. Application of ccCA to G3/05 Set of Atoms and Molecules with Elements Ga–Kr. Tabulated experimental uncertainties of ± 1.0 kcal mol⁻¹ or less is a main criterion for inclusion within the G_n test sets. Therefore, the G3/05 training set is a very stringent test of any new ab initio methodology.¹¹ The third-row molecules investigated are obtained from the G3/05 set but do not include the K- and Ca-containing molecules (and their respective ions) as full sets of core-valence correlation consistent basis sets currently do not exist for those elements. However, development of the complete set of correlation consistent basis sets necessary for ccCA computations of molecules containing potassium and calcium is currently in progress in our laboratory, and the ccCA model chemistry will soon be available and benchmarked for the entire periodic table through krypton.

In all, the G3/05 test set for elements Ga–Kr contains 51 systems: 19 atomization energies (D_0), 11 enthalpies of formation (ΔH_f), 15 ionization potentials (IP), 4 electron affinities (EA), and 2 proton affinities (PA). Table 1 shows ccCA energies for the atoms Ga–Kr as well as the spin-orbit correction energies. Geometric parameters for the 51

Table 1. Atomic ccCA Energies for the Elements Ga–Kr

	ccCA-P	ccCA-S4	ΔE (SO) ^a	$\Delta E^{(2)}$ (SO) ^b
Ga ² P _{1/2}	-1943.067544	-1943.069629	-0.00251	-0.00002
Ge ³ P ₀	-2097.939639	-2097.941788	-0.00441	-0.00020
As ⁴ S _{3/2}	-2259.905472	-2259.907698	0.0	-0.00047
Se ³ P ₂	-2428.979165	-2428.981410	-0.00430	-0.00081
Br ² P _{3/2}	-2605.350744	-2605.352995	-0.00560	-0.00049
Kr ¹ S ₀	-2789.137674	-2789.139744	0.0	-0.00076

^a Experimental first-order atomic SO corrections are obtained from ref 46. ^b Theoretical second-order atomic SO corrections are obtained from ref 31.

systems in the third-row set are given in Table S1 (Supporting Information).

When applying the ccCA model chemistry to atoms and molecules with third-row elements, a caveat of the frozen core approximation must be discussed. The valence correlation consistent basis sets for elements Ga–Kr were developed with frozen 1s, 2s, 2p, 3s, 3p, and 3d molecular orbitals (MOs); therefore, “valence” correlated MOs of the atoms and molecules in this training set include only 4s and 4p MOs. The recently created core-valence basis sets have active 3s, 3p, 4s, 3d, and 4p MOs, which will be necessarily correlated in order to compute the ΔE (CV) additive correction, shown in eq 1.5.

For the third-row G3/05 training set (with third-row elements Ga–Kr only), deviations from experimental values are given in Table 2 for ccCA-P, ccCA-S4, G3, G3X, and G4 theories. For the Ga–Kr containing species in the G3/05 training set, the ccCA can reliably predict energetic properties to within chemical accuracy. The mean signed deviation (MSD) is -0.02 kcal mol⁻¹ for ccCA-P and 0.07 kcal mol⁻¹ for ccCA-S4, indicating almost no overall bias in the reliability of the ccCA. The mean absolute deviation (MAD) for ccCA-P is 0.95 kcal mol⁻¹, and slightly larger for ccCA-S4, 1.00 kcal mol⁻¹. The maximum absolute deviations for the ccCA model chemistries are for the ΔH_f of C₅H₈Br₂ (2.9 and 3.4 kcal mol⁻¹ for ccCA-P and ccCA-S4, respectively) and the IP of NaBr (5.2 and 5.0 kcal mol⁻¹ for ccCA-P and ccCA-S4, respectively). Absolute deviation from experiment for the properties of these two molecules is quite large for G3 methods as well (3.2 and 4.9 kcal mol⁻¹, respectively), but the G4 ΔH_f value of C₅H₈Br₂ is only 1.9 kcal mol⁻¹ away from experiment.⁴⁷

For the 51 quantities computed in the training set, the ccCA-P is an improvement of 0.10 kcal mol⁻¹ over the G3X model chemistry, which has a MAD of 1.07 kcal mol⁻¹. The ccCA methods also outperform all of the CBS-*n* methods^{48–50} that have been benchmarked for the 40 third-row-containing atoms and molecules in the older G3/99 set.⁵¹ For these same 40 energetic properties (19 *D*₀, 15 IPs, 4 EAs, and 2 PAs), the ccCA-P and ccCA-S4 MADs are 0.79 and 0.78 kcal mol⁻¹, respectively, while the best CBS-*n* method, CBS-QB3, has a MAD of 1.12 kcal mol⁻¹. Previous CBS CCSD(T) studies in our laboratory have been carried out on the G3 test set of molecules containing Ga–Kr.^{52,53} Interestingly, the ccCA model chemistry has a lower MAD with the third-row test set than most CBS CCSD(T) methods using valence aug-cc-pVnZ and relativistic pseudopotential aug-cc-pVnZ basis sets. Depending on the CBS extrapolation

Table 2. Deviations of ccCA and G*n* Methods from Experiment (Expt–Theory) in kcal mol⁻¹ for the Third-Row G3/05 Training Set

	property	species	expt ^a	ccCA-P	ccCA-S4	G3 ^b	G3X ^b	G4 ^c	
<i>D</i> ₀		GeH ₄	270.5	-2.7	-2.8	-2.5	-2.8	-2.5	
		AsH	64.6	1.6	1.6	-0.1	-0.4	0.7	
		AsH ₂	131.1	-0.7	-0.7	-0.8	-1.2	-0.7	
		AsH ₃	206.0	0.3	0.3	1.4	0.8	1.3	
		SeH	74.3	-0.7	-0.7	-1.1	-1.1	-0.7	
		SeH ₂	153.2	-0.4	-0.4	0.9	0.6	1.1	
		HBr	86.5	-0.8	-0.8	-0.2	0.0	0.4	
		GaCl	109.9	0.4	0.4	-1.5	-1.3	-0.6	
		GeO	155.2	-2.1	-2.1	-1.6	-3.0	-1.0	
		As ₂	91.3	-1.1	-1.0	-0.4	-1.6	-0.4	
		BrCl	51.5	-0.2	-0.2	0.3	0.5	0.5	
		BrF	58.9	-0.2	-0.2	0.3	-0.2	-0.4	
		BrO	55.3	0.6	0.6	0.1	-0.1	0.3	
		Br ₂	45.4	-0.5	-0.6	-0.1	0.1	0.9	
		BBr	103.5	1.2	1.2	0.7	1.1	1.5	
		NaBr	86.2	-0.4	-0.3	-2.1	-1.9	-0.7	
		CH ₃ Br	358.2	-0.7	-0.9	-0.3	-0.1	0.4	
		GeS ₂	191.7	1.5	1.6	-1.9	-2.5	-1.2	
	ΔH_f (298.15 K)		KrF ₂	21.9	-0.2	-0.2	-0.6	-1.3	-1.7
		CF ₃ Br	-155.0	0.8	1.1	2.3	1.3	0.4	
		CCl ₃ Br	-10.0	1.2	1.2	2.9	2.2	1.4	
		C ₂ H ₃ Br	18.9	1.8	2.0	2.0	1.9	1.4	
		C ₂ H ₅ Br	-14.8	1.6	1.9	1.2	0.9	0.3	
		C ₃ H ₇ Br	-23.8	0.9	1.3	0.6	0.1	-0.5	
		C ₆ H ₅ Br	25.2	0.1	0.5	1.5	1.4	1.2	
		C ₆ H ₁₃ Br	-35.4	1.9	2.6	1.2	0.7	0.3	
		C ₃ H ₆ Br ₂	-17.1	2.8	3.1	2.7	2.2	1.0	
		CHF ₂ Br	-101.6	0.6	0.7	1.2	0.4	-0.4	
		COBr ₂	-27.1	2.1	2.0	2.7	2.6	1.2	
		C ₅ H ₈ Br ₂	-13.1	2.9	3.4	3.2	3.1	1.9	
IP			Ga	138.3	-0.2	-0.1	-0.2	-0.2	-0.6
			Ge	182.2	0.0	0.0	-0.1	-0.1	-0.2
			As	225.7	-0.4	-0.4	-0.4	-0.3	-0.3
			Se	224.9	0.6	0.6	1.0	0.5	0.7
			Br	272.4	-0.4	-0.2	0.5	0.9	0.4
			Kr	322.8	0.3	0.5	1.3	0.9	1.2
			AsH	222.3	0.1	0.0	-1.0	-1.0	-0.5
		AsH ₂	217.8	0.3	0.3	-0.8	-0.8	-0.6	
		SeH	227.0	-1.3	-1.2	0.1	-0.1	-0.6	
		SeH ₂	228.0	-1.2	-1.1	-0.3	-0.4	-0.4	
		HBr	268.9	-0.3	-0.2	0.8	0.8	1.0	
EA		Br ₂	242.6	-0.1	0.1	-0.2	-0.2	0.4	
		HOBr	245.3	-1.6	-1.4	-0.4	-0.6	-0.2	
		BrF	271.7	-0.1	0.1	0.7	0.8	1.4	
		NaBr	191.6	-5.2	-5.0	-4.9	-5.1	-4.7	
		Ge	28.4	0.0	0.0	-0.5	-0.4	-0.7	
		Br	77.6	0.1	0.3	-0.5	-0.9	-0.7	
		BrO	54.5	-1.6	-1.5	-1.3	-1.2	-1.5	
		SeH	51.0	-0.5	-0.5	-0.4	-0.5	-0.5	
	PA		Br	322.6	-1.0	-1.2	-0.3	0.3	0.2
			CH ₃ Br	157.3	0.1	0.0	0.4	0.4	0.2
	MSD			-0.02	0.07	0.11	-0.09	-0.01	
MAD				0.95	1.00	1.07	1.05	0.86	

^a Experimental results are obtained from ref 14. ^b G3 and G3X results are obtained from refs 14 and 11, respectively. ^c G4 results are obtained from ref 47.

scheme, the aug-cc-pVnZ MADs range from 0.89 – 1.21 kcal mol⁻¹ and the aug-cc-pVnZ-PP MADs range from 0.98 –

1.42 kcal mol⁻¹. While the MP2-based ccCA method might be expected to be inferior to CCSD(T)-based CBS extrapolations, the treatment of core-valence effects in ccCA is likely the source of improved results over the previous large basis set coupled cluster data applied to the valence correlation space only. Last, a few popular density functional theories have MADs for the third-row set ranging from 2.50–5.41 kcal mol⁻¹ and are much less reliable than ccCA and current-generation *Gn* model chemistries (cf. ref 11, Table 2).

Using first-order atomic and molecular spin orbit corrections, the ccCA MAD of 0.95–1.00 kcal mol⁻¹ is worse than the new G4 method, which has a MAD of 0.86 kcal mol⁻¹.⁴⁷ However, it is perhaps unsurprising that G4 is a significant improvement over ccCA as well as G3 and its variants. The G4 is parametrized with third-row species included in the HLC optimization, and the G4 HLC also contains *six* optimized parameters, rather than four as in the G3 generation. Unlike the study of s-block containing first- and second-row molecules, where ccCA model chemistries obtain a greater number of energetic properties to within chemical accuracy than *Gn* methods,^{17,19} the number of instances in *Gn* and ccCA methods where the deviation has a magnitude less than ±1.0 kcal mol⁻¹ is similar, with a range of 31–36 instances.

As shown in previous ccCA papers, *Gn* theories rely on the HLC to provide a significant contribution to thermodynamic properties (such as atomization energies and enthalpies of formation).^{1,47} It is known that the magnitude of this empirical contribution can be very large, especially with larger molecules, and that it is unable to fully account for basis set and electron correlation deficiencies. While the ccCA is an MP2-based model chemistry and lacks empirical parametrization, it is approximately an order of magnitude more computationally expensive for small- to medium-sized molecules than *Gn* methods. For example, on eight SGI Origin MIPS R16000 processors, the ccCA energy of 1-bromohexane took 109 h to complete versus 9 h for the G3 energy on the same system. Again, it is pertinent to note that the most computationally expensive step of the ccCA method is usually the CCSD(T) cc-pVTZ computations. Thus ccCA is much less expensive than composite methods that are based on CBS limits of CCSD(T) energies.

B. Discussion of First- and Second-Order Spin Orbit Coupling. It was shown that first-order SOC corrections can alter molecular energies by up to 4.1 kcal mol⁻¹ and that even second-order molecular SOC effects, computed in a study by Blaudeau and Curtiss,³¹ can affect atomization energies of molecules containing elements Ga–Kr by up to 0.8 kcal mol⁻¹. Inclusion of theoretical SOC corrections requires accurate computation of multireference wave functions, which in turn is troublesome for the development and benchmarking of single reference “black box” composite methods such as ccCA and *Gn*. Examples are detailed in Hess’s comprehensive review of spin–orbit coupling computations⁵⁴ as well as in work by Peterson which describes severe active space difficulties for ground and excited electronic states of a seemingly innocuous first-row diatomic (BO⁺).⁵⁵ The inclusion of SOC energies is, however, necessary for a proper ab initio treatment of open-shell heavy

Table 3. Deviations of ccCA Methods from Experiment (Expt–Theory) in kcal mol⁻¹ for the Third-Row G3/05 Training Set When Atomic and Molecular Second-Order Spin Orbit Corrections Are Included in the Energies^a

property	species	expt ^b	ccCA-P	ccCA-S4	
<i>D</i> ₀	GeH ₄	270.5	-2.7	-2.7	
	AsH	64.6	1.5	1.5	
	AsH ₂	131.1	-0.5	-0.6	
	AsH ₃	206.0	0.6	0.6	
	SeH	74.3	-0.2	-0.2	
	SeH ₂	153.2	-0.2	-0.2	
	HBr	86.5	-0.9	-0.9	
	GaCl	109.9	0.4	0.4	
	GeO	155.2	-2.0	-2.0	
	As ₂	91.3	-0.5	-0.4	
	BrCl	51.5	0.1	0.1	
	BrF	58.9	0.1	0.1	
	BrO	55.3	0.9	0.9	
	Br ₂	45.4	-0.6	-0.6	
	BBr	103.5	1.5	1.5	
	NaBr	86.2	-0.1	0.0	
	CH ₃ Br	358.2	-0.4	-0.6	
	GeS ₂	191.7	1.6	1.7	
	KrF ₂	21.9	0.3	0.2	
	$\Delta H(298.15\text{ K})$	CF ₃ Br	-155.0	0.5	0.7
CCl ₃ Br		-10.0	0.9	0.9	
C ₂ H ₃ Br		18.9	1.5	1.7	
C ₂ H ₅ Br		-14.8	1.3	1.6	
C ₃ H ₇ Br		-23.8	0.6	1.0	
C ₆ H ₅ Br		25.2	-0.2	0.2	
C ₆ H ₁₃ Br		-35.4	1.6	2.2	
C ₃ H ₆ Br ₂		-17.1	2.2	2.5	
CHF ₂ Br		-101.6	0.2	0.4	
COBr ₂		-27.1	1.4	1.4	
C ₅ H ₈ Br ₂		-13.1	2.3	2.8	
IP		Ga	138.3	-0.2	-0.2
		Ge	182.2	-0.1	-0.1
	As	225.7	-0.7	-0.7	
	Se	224.9	0.7	0.8	
	Br	272.4	0.2	0.3	
	Kr	322.8	-0.2	0.1	
	AsH	222.3	-0.3	-0.3	
	AsH ₂	217.8	0.4	0.4	
	SeH	227.0	-0.4	-0.4	
	SeH ₂	228.0	-1.1	-1.1	
	HBr	268.9	-0.7	-0.6	
	Br ₂	242.6	-0.8	-0.6	
	HOBr	245.3	-1.6	-1.4	
	BrF	271.7	-0.1	0.1	
NaBr	191.6	-5.1	-5.0		
EA	Ge	28.4	0.1	0.1	
	Br	77.6	0.4	0.6	
	BrO	54.5	0.9	0.9	
	SeH	51.0	-0.5	-0.5	
PA	Br	322.6	-1.4	-1.6	
	CH ₃ Br	157.3	0.1	0.0	
MSD			-0.03	0.05	
MAD			0.88	0.92	

^a Molecular second-order SO corrections are from ref 31. ^b Experimental results are obtained from ref 14.

element-containing molecules, which unfortunately describes the majority of the third-row G3/05 ionic species.

In Table 3, ccCA-P and ccCA-S4 deviations are given when second-order atomic and molecular SO corrections are included in the energies. Clearly these effects are important in determining ionization energies, atomization energies, and ΔH_f values for third-row species. Inclusion of these effects improves the MAD of ccCA-P from 0.95 to 0.88 kcal mol⁻¹ and ccCA-S4 from 1.00 to 0.92 kcal mol⁻¹, putting them on par with the G4 model chemistry. By including second-order SOC corrections, 25 of the ccCA-P deviations are improved by more than 0.1 kcal mol⁻¹, while the errors are worse for 18 species. Overall, atomic second-order SOC corrections seem to improve the reliability of enthalpies of formation computed for larger molecules in the G3/05 training set.

C. Systems that Contain Gallium and Germanium Atoms and Electronegative Ligands. For gallium and germanium compounds, the 2s basis functions on electronegative ligand atoms can substantially mix with the 3d basis functions on the electropositive elements Ga and Ge. Yamaguchi, Schaefer, and co-workers^{56,57} originally suggested that including the 3d MOs in the correlation space when carrying out ab initio studies on Ga-containing molecules is a necessity, and further examples were presented by Duke and Radom⁵⁸ and Bauschlicher and co-workers.⁵⁹ Petersson and co-workers have devised an MO overlap scheme to determine a priori if molecules containing Ga–Kr atoms might be problematic.⁶⁰ Martin and Sundermann have created a set of relativistic effective core potentials that include 3d core correlation for Ga and Ge.⁶¹ There is a history of challenges in the study of these molecules including large uncertainties in the experimental enthalpies of formation, and we believe that relativistic coupled cluster calculations employing core-valence correlation effects (with the newly created core-valence basis sets) will be necessary to help pinpoint the source of errors.

Difficulties in computing energetics of molecules containing elements Ga–Kr is thus far limited to systems with Ga–O, Ga–F, and Ge–F bonds. If the 3d electrons are treated in the frozen core approximation, errors in energetic properties of more than 90 kcal mol⁻¹ can occur, as in the case of the G2 atomization energy of GaF₃.⁵⁹ Unfortunately, preliminary results indicate the ccCA model chemistry may also be susceptible to unusually large errors when determining the correlation energy of such species. Using ccCA-P, the deviation from experiment for the atomization energy of GaF₃ is 12.4 kcal mol⁻¹. Inclusion of the 3d MO space in valence energy computations also improves some ccCA atomization energies but is not a panacea. More research is currently underway to provide a detailed analysis of the ccCA performance upon these Ga- and Ge-containing species.

Conclusions

The correlation consistent composite approach (ccCA) methodology has been applied to 51 atomic and molecular properties for elements Ga–Kr in the G3/05 training set. The ccCA energies have been compared to other widely used model chemistries. Several conclusions have resulted from this research, the most important of which are summarized here.

(1) The ccCA methodology performs better than the G3 and G3X model chemistries, with a mean absolute deviation of 0.95–1.00 kcal mol⁻¹ when first-order spin–orbit corrections are used.

(2) The core-valence additive correction to the ccCA energy is essential for a proper description of the relevant properties contained in the G3/05 training set. In fact, the MP2-based ccCA method is competitive with valence basis set CBS extrapolated CCSD(T) studies. We propose that this is due to the better modeling of core-valence electron correlation in the ccCA method as compared to the published CBS coupled cluster approaches.

(3) While adding spin–orbit corrections to atoms and molecules containing 4p and heavier elements detracts from the “black box” nature of ccCA and *Gn* methods, spin–orbit coupling is a physical phenomenon that cannot be ignored when computing thermodynamic and energetic properties of such species. The addition of second-order spin orbit corrections results in a substantial improvement to the accuracy of the ccCA, as the MAD drops from 0.95 and 1.00 kcal mol⁻¹ to 0.88 and 0.92 kcal mol⁻¹ for ccCA-P and ccCA-S4, respectively.

For well-behaved third-row p-block molecules, the ccCA is thus a viable alternative to other model chemistries that rely on semiempirical corrections to the correlation energy. Furthermore, the modeling of heavier p-block elements is an important step on the way to developing a pan-periodic table composite method that is capable of yielding accurate thermodynamics.

Acknowledgment. CASCaM is supported by a grant from the United States Department of Education. This research is partially supported by a grant from the United States Department of Energy, Office of Basic Energy Sciences (to T.R.C.), Grant No. DE-FG02-03ER15387, and by a National Science Foundation CAREER Award CHE-0239555 (to A.K.W.). Computational resources were provided via the National Science Foundation (CHE-0342824) and by the National Computational Science Alliance under #CHE010021 and utilized the NCSA IBM p690. Some computations employed the UNT computational chemistry resource, whose purchase was supported by a CRIF grant from the U.S. National Science Foundation (CHE-0342824).

Supporting Information Available: Equilibrium B3LYP/cc-pVTZ equilibrium geometries (Table S1) and the complete citation for ref 36. This material is available free of charge via the Internet at <http://pubs.acs.org>.

References

- (1) DeYonker, N. J.; Cundari, T. R.; Wilson, A. K. *J. Chem. Phys.* **2006**, *124*, 114104.
- (2) DeYonker, N. J.; Grimes, T.; Yockel, S.; Dinescu, A.; Mintz, B.; Cundari, T. R.; Wilson, A. K. *J. Chem. Phys.* **2006**, *125*, 104111.
- (3) Dunning, T. H., Jr. *J. Chem. Phys.* **1989**, *90*, 1007.
- (4) Dunning, T. H., Jr.; Peterson, K. A.; Wilson, A. K. *J. Chem. Phys.* **2001**, *114*, 9244.
- (5) Balabanov, N. B.; Peterson, K. A. *J. Chem. Phys.* **2005**, *123*, 064107.

- (6) Peterson, K. A.; Dunning, T. H., Jr. *J. Chem. Phys.* **2002**, *117*, 10548.
- (7) Woon, D. E.; Dunning, T. H., Jr. *J. Chem. Phys.* **1993**, *98*, 1358.
- (8) Woon, D. E.; Dunning, T. H., Jr. *J. Chem. Phys.* **1994**, *100*, 2975.
- (9) Woon, D. E.; Dunning, T. H., Jr. *J. Chem. Phys.* **1995**, *103*, 4572.
- (10) Wilson, A. K.; Woon, D. E.; Peterson, K. A.; Dunning, T. H., Jr. *J. Chem. Phys.* **1999**, *110*, 7667.
- (11) Curtiss, L. A.; Redfern, P. C.; Raghavachari, K. *J. Chem. Phys.* **2005**, *123*, 124017.
- (12) Curtiss, L. A.; Raghavachari, K.; Redfern, P. C.; Rassolov, V.; Pople, J. A. *J. Chem. Phys.* **1998**, *109*, 7764.
- (13) Curtiss, L. A.; Raghavachari, K. *Theor. Chem. Acc.* **2002**, *108*, 61.
- (14) Curtiss, L. A.; Redfern, P. C.; Rassolov, V.; Kedziora, G.; Pople, J. A. *J. Chem. Phys.* **2001**, *114*, 9287.
- (15) Curtiss, L. A.; Redfern, P. C.; Raghavachari, K.; Pople, J. A. *J. Chem. Phys.* **2001**, *114*, 108.
- (16) DeYonker, N. J.; Cundari, T. R.; Wilson, A. K.; Sood, C. A.; Magers, D. H. *J. Mol. Struct. (Theochem)* **2006**, *775*, 77.
- (17) Ho, D. S.; DeYonker, N. J.; Wilson, A. K.; Cundari, T. R. *J. Phys. Chem. A* **2006**, *110*, 9767.
- (18) DeYonker, N. J.; Peterson, K. A.; Steyl, G.; Wilson, A. K.; Cundari, T. R. *J. Phys. Chem. A* **2007**, *111*, 11269.
- (19) DeYonker, N. J.; Ho, D. S.; Wilson, A. K.; Cundari, T. R. *J. Phys. Chem. A* **2007**, *111*, 10776.
- (20) Martin, J. M. L.; de Oliveira, G. *J. Chem. Phys.* **1999**, *111*, 1843.
- (21) Karton, A.; Rabinovich, E.; Martin, J. M. L.; Ruscic, B. *J. Chem. Phys.* **2006**, *125*, 144108.
- (22) Tajti, A.; Szalay, P. G.; Császár, A. G.; Kállay, M.; Gauss, J.; Valeev, E. F.; Flowers, B. A.; Vazquez, J.; Stanton, J. F. *J. Chem. Phys.* **2004**, *121*, 11599.
- (23) Dixon, D. A.; Feller, D.; Francisco, J. S. *J. Phys. Chem. A* **2003**, *107*, 186.
- (24) Feller, D.; Dixon, D. A. *J. Phys. Chem. A* **2000**, *104*, 3048.
- (25) Feller, D.; Dixon, D. A.; Francisco, J. S. *J. Phys. Chem. A* **2003**, *107*, 1604.
- (26) Feller, D.; Peterson, K. A. *J. Chem. Phys.* **1998**, *108*, 154.
- (27) Feller, D.; Peterson, K. A. *J. Chem. Phys.* **1999**, *110*, 8384.
- (28) Feller, D.; Peterson, K. A.; Crawford, T. D. *J. Chem. Phys.* **2006**, *124*.
- (29) Feller, D.; Peterson, K. A.; de Jong, W. A.; Dixon, D. A. *J. Chem. Phys.* **2003**, *118*, 3510.
- (30) Pollack, L.; Windus, T. L.; de Jong, W. A.; Dixon, D. A. *J. Phys. Chem. A* **2005**, *109*, 6934.
- (31) Blaudeau, J. P.; Curtiss, L. A. *Int. J. Quantum Chem.* **1997**, *61*, 943.
- (32) Redfern, P. C.; Blaudeau, J. P.; Curtiss, L. A. *J. Phys. Chem. A* **1997**, *101*, 8701.
- (33) Blaudeau, J. P.; McGrath, M. P.; Curtiss, L. A.; Radom, L. *J. Chem. Phys.* **1997**, *107*, 5016.
- (34) Curtiss, L. A.; McGrath, M. P.; Blaudeau, J. P.; Davis, N. E.; Binning, R. C., Jr.; Radom, L. *J. Chem. Phys.* **1995**, *103*, 6104.
- (35) DeYonker, N. J.; Peterson, K. A.; Wilson, A. K. *J. Phys. Chem. A* **2007**, *111*, 11383.
- (36) Frisch, M. J. et al. *Gaussian 03, Revision C.02*; Gaussian, Inc.: Wallingford, CT, 2004.
- (37) Peterson, K. A.; Woon, D. E.; Dunning, T. H., Jr. *J. Chem. Phys.* **1994**, *100*, 7410.
- (38) Martin, J. M. L.; Lee, T. J. *Chem. Phys. Lett.* **1996**, *258*, 136.
- (39) Martin, J. M. L. *Chem. Phys. Lett.* **1996**, *259*, 669.
- (40) Helgaker, T.; Klopper, W.; Koch, H.; Noga, J. *J. Chem. Phys.* **1997**, *106*, 9639.
- (41) de Jong, W. A.; Harrison, R. J.; Dixon, D. A. *J. Chem. Phys.* **2001**, *114*, 48.
- (42) Hess, B. A. *Phys. Rev. A* **1986**, *33*, 3742.
- (43) Hess, B. A. *Phys. Rev. A* **1985**, *32*, 756.
- (44) Douglas, M.; Kroll, N. M. *Ann. Phys.* **1974**, *82*, 89.
- (45) The algorithm of ccCA in ref 2 uses an ROHF reference wave function for the scalar relativistic correction. We have found that using a UHF reference with a Douglas-Kroll-Hess Hamiltonian in Gaussian03 for the DK energies shifts enthalpies of formation by less than 0.01 kcal mol⁻¹. This modification can be substituted for consistency and/or convenience.
- (46) Moore, C. E. *Atomic Energy Levels*; U.S. Department of Commerce: Washington, DC, 1971; Vol. 2.
- (47) Curtiss, L. A.; Redfern, P. C.; Raghavachari, K. *J. Chem. Phys.* **2007**, *126*.
- (48) Petersson, G. A.; Bennett, A.; Tensfeldt, T. G.; Al-Laham, M. A.; Shirley, W. A.; Mantzaris, J. *J. Chem. Phys.* **1988**, *89*, 2193.
- (49) Ochterski, J. W.; Petersson, G. A.; Montgomery, J. A. *J. Chem. Phys.* **1996**, *104*, 2598.
- (50) Petersson, G. A.; Al-Laham, M. A. *J. Chem. Phys.* **1991**, *94*, 6081.
- (51) Ramakrishna, V.; Duke, B. J. *J. Chem. Phys.* **2003**, *118*, 6137.
- (52) Yockel, S.; Wilson, A. K. *J. Chem. Phys.* **2005**, *122*.
- (53) Yockel, S.; Mintz, B.; Wilson, A. K. *J. Chem. Phys.* **2004**, *121*, 60.
- (54) Hess, B. A.; Marian, C. M.; Peyerimhoff, S. D. Ab initio Calculation of Spin-Orbit Effects in Molecules Including Electron Correlation. In *Modern Electronic Structure Theory, Vol. 2 of Advanced Series in Physical Chemistry*; Yarkony, D. R., Ed.; World Scientific: Singapore, 1995; Vol. 2, p 152.
- (55) Peterson, K. A. *J. Chem. Phys.* **1995**, *102*, 262.
- (56) Yamaguchi, Y.; Schaefer, H. F. *J. Chem. Phys.* **1996**, *104*, 9841.
- (57) Richards, C. A. J.; Yamaguchi, Y.; Kim, S.-J.; Schaefer, H. F. *J. Chem. Phys.* **1996**, *104*, 8516.
- (58) Duke, B. J.; Radom, L. *J. Chem. Phys.* **1998**, *109*, 3352.

(59) Bauschlicher, C. W., Jr.; Melius, C. F.; Allendorf, M. D. *J. Chem. Phys.* **1999**, *110*, 1879.

(60) Austin, A. J.; Frisch, M. J.; Montgomery, J. A.; Petersson, G. A. *Theor. Chem. Acc.* **2002**, *107*, 180.

(61) Martin, J. M. L.; Sundermann, A. *J. Chem. Phys.* **2001**, *114*, 3408.

CT7002463

Molecular Dynamics Simulation Study of the Influence of Cluster Geometry on Formation of C₆₀ Fullerene Clusters in Aqueous Solution

Hojin Kim,[†] Dmitry Bedrov,[‡] and Grant D. Smith^{*,†,‡}

*Departments of Chemical Engineering and Materials Science and Engineering,
122 South Central Campus Drive Room 304, University of Utah,
Salt Lake City, Utah 84112*

Received August 22, 2007

Abstract: We have performed atomistic molecular dynamics simulations of linear (1-dimensional), planar (2-dimensional), and icosahedral (3-dimensional) clusters of C₆₀ fullerenes in aqueous solution in order to investigate the influence of cluster geometry on their free energy of formation. As was found in our previous study of the potential of mean force (PMF) as a function of separation for a single pair of fullerenes in aqueous solution, the interaction between fullerenes for all cluster geometries was dominated by direct fullerene–fullerene interactions and not by water-induced hydrophobic interactions. A coarse-grained implicit solvent (CGIS) potential, given by the PMF for the fullerene pair in water obtained from atomistic simulations, was found to describe well the free energy of formation of the linear cluster, indicating that many-body effects, i.e., the influence of neighboring fullerenes on the water-induced interaction between a fullerene pair, are negligible for the 1-dimensional geometry. For the 2-dimensional and particularly the 3-dimensional geometry, however, many-body effects were found to strongly influence hydration, leading to complete dehydration of the central fullerene at close fullerene–fullerene separations for the icosahedral cluster. This strong influence of geometry on hydration translates into water-induced interactions that, while remaining repulsive, as is found for the fullerene pair, are not well described by the two-body CGIS potential obtained from the isolated fullerene pair, particularly for the 3-dimensional geometry.

I. Introduction

Because of their nonpolar character and extremely low solubility in water, C₆₀ fullerenes are often considered to be hydrophobic molecules. However, in recent simulation studies^{1,2} we found that the attraction between two fullerenes, given by the potential of mean force (PMF) as a function of their separation, is actually *weaker* in water than in vacuum. Hence, in contrast to hydrophobic particles of the same size (e.g., one nanometer diameter oil droplets), water actually promotes dispersion of the fullerene pair. The favorable water–fullerene interaction is due to the strong van der Waals

interactions between the fullerenes and water resulting from the high atomic surface density of fullerene. The strong van der Waals interaction of fullerenes with various gas molecules has also been observed in ab initio and density functional calculations.³ These favorable interactions overcome loss of hydrogen bonding and entropic restrictions on water at the fullerene surface. Nevertheless, despite the water-induced repulsion, the strong direct van der Waals interactions between two fullerenes dominate the PMF resulting in a strong attractive interaction (−4.2 kcal/mol) for two fullerenes in direct contact.¹ These strong direct fullerene–fullerene van der Waals interactions are the primary reason for the insolubility of fullerenes in water.

From the PMF studies of two fullerenes in water we have derived a coarse-grained implicit solvent (CGIS) potential¹

* Corresponding author e-mail: gsmith2@cluster2.mse.utah.edu.

[†] Department of Chemical Engineering.

[‡] Department of Materials Science and Engineering.

that describes both direct fullerene–fullerene interactions and effective fullerene–fullerene interactions due to water. We have utilized this potential to study the self-assembly of bare and polymer modified C_{60} fullerenes in water.⁴ This two-body potential assumes that the free energy of formation of fullerene aggregates (clusters) can be described as the sum of the CGIS potential over all fullerene pairs. However, it can be anticipated that as the fullerene cluster size and dimensionality increase the structure of water hydrating each fullerene pair can depend on the relative position of neighboring fullerenes and therefore the water-induced interactions can be different from those obtained for an isolated pair of fullerenes. In this work, we investigate the free energy of formation of 1-dimensional, 2-dimensional, and 3-dimensional fullerene aggregates in aqueous solution and the applicability of the two-body CGIS potential to these geometries. For this purpose we have performed fully atomistic molecular dynamics (MD) simulations to determine the free energy for formation of the fullerene aggregates. MD simulations are suitable to study a small fullerene cluster and previously have been utilized to investigate the phase behavior of the small fullerene cluster, $(C_{60})_7$, in vacuum.^{5,6} Discrepancies between the CGIS and atomistic predictions indicate the existence of a many-body effect in fullerene clusters whose nature is discussed in detail.

II. Methodology

A. Atomistic Simulations. All MD simulations have been carried out using the simulation package *Lucretius*.⁷ For atomistic simulations of the fullerene-water solution, interactions were described by a Lennard-Jones potential⁸

$$U_{LJ}(r) = 4\epsilon \left[\left(\frac{\sigma}{r} \right)^{12} - \left(\frac{\sigma}{r} \right)^6 \right] \quad (1)$$

where r is a distance between atoms, while σ and ϵ are the parameters related to the atomic size and the strength of attraction, respectively. For carbon–carbon interactions the parameters $\sigma_{c-c} = 3.47 \text{ \AA}$ and $\epsilon_{c-c} = 0.275 \text{ kJ/mol}$ were utilized. For water, the transferable intermolecular four-point potential (TIP4P)⁹ water model was employed, and C_{60} -water interactions were represented by a Lennard-Jones potential ($\sigma_{c-o} = 3.19 \text{ \AA}$ and $\epsilon_{c-o} = 0.392 \text{ kJ/mol}$) which was empirically parametrized to recover the macroscopic contact angle of a water droplet on graphite.¹⁰ All bond lengths were constrained using the SHAKE algorithm,¹¹ and the C_{60} fullerenes were made completely rigid through addition of additional bonds. The particle mesh Ewald algorithm (PME)¹² was used to handle the long-range water–water Coulomb interactions. Production runs were carried out in the NVT ensemble (constant volume and temperature) using a multiple-time-step reversible reference system propagator algorithm.^{13,14} A time step of 0.75 fs was used for nonbonded (Lennard-Jones and real part of Coulomb) interactions within a cut off radius of 7 \AA , while a time step of 3 fs was used for nonbonded interactions for separations between 7 and 10 \AA and reciprocal part of the Coulomb interactions.

B. Systems Studied. In this study, the fullerene clusters consisted of 3, 7, and 13 C_{60} fullerenes labeled $(C_{60})_3$, $(C_{60})_7$, and $(C_{60})_{13}$, as illustrated in Figure 1. The $(C_{60})_3$ cluster is

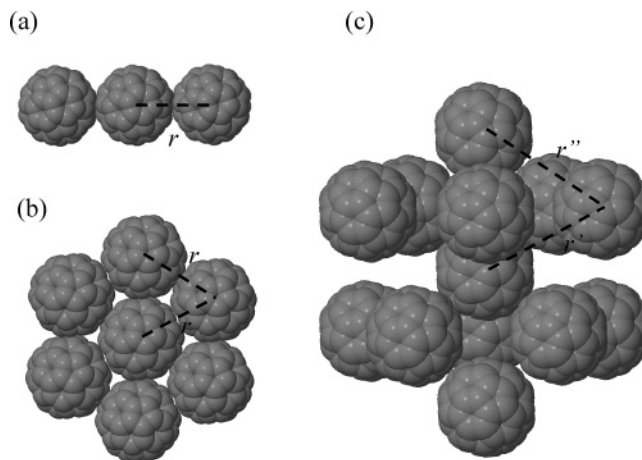


Figure 1. Geometries of the (a) $(C_{60})_3$, (b) $(C_{60})_7$, and (c) $(C_{60})_{13}$ fullerene clusters. r represents the fullerene–fullerene separation distance for clusters (a) and (b) and an average (over all 42 nearest neighbor pairs) of r' and r'' for cluster (c). Here, r' is the separation between shell fullerenes and the central fullerene, and r'' ($r'' = 1.05r'$) is the nearest neighbor shell–shell separation.

linear, the $(C_{60})_7$ cluster is close-packed planar, and the $(C_{60})_{13}$ cluster has an icosahedral geometry. In the $(C_{60})_3$ and $(C_{60})_7$ clusters, dummy atoms that do not interact with any other atoms were used to constrain the clusters to linear or planar geometries, respectively. All fullerenes (center-of-mass) were maintained at an equal distance from the center-of-mass of the central fullerene of the cluster with a range of separations of 9.25–17.0 \AA at increments in spacing of 0.5 or 0.25 \AA , depending upon the separation. All fullerene–fullerene distances in the clusters were constrained by the SHAKE method to maintain both the distance of the fullerenes to the central fullerene as well as the cluster geometry (linear, close-packed planar, or icosahedral).

Equilibration of the systems, which consisted of a single cluster and 6000 water molecules, to yield equilibrium densities was carried out using a periodic cubic cell in the NPT (constant pressure and temperature) ensemble at 298 K and 1 atm with a separation distance (of all shell fullerenes to the center of the cluster) of 17.0 \AA for 500 ps. Following equilibration, NVT simulations were performed at the various separation distances for a sampling time of 5–15 ns. In addition to the clusters, a single fullerene pair, $(C_{60})_2$, was also examined in a cubic cell containing 2000 water molecules using the same simulation protocol.

C. Determination of the Potential of Mean Force. The potential of mean force (PMF) was obtained from integration of the mean constraint force

$$PMF(r) = -n_{shell} \int_r^{r_{max}} \left[\langle F_{con}(r) \rangle - \frac{2k_B T}{r} \right] dr \quad (2)$$

where r is the separation distance between the center-of-mass position of the shell fullerenes (those surrounding the central fullerene of the cluster) and the center-of-mass of the cluster, $\langle F_{con}(r) \rangle$, is the mean constraint force experienced by each shell fullerene along the bond connecting it to the central fullerene, and r_{max} is a distance sufficiently

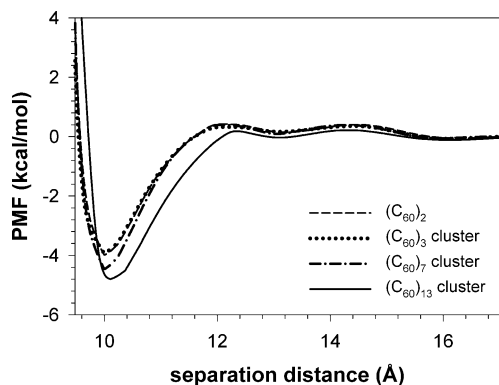


Figure 2. The potential of mean force (PMF) for various fullerene clusters as a function of separation. Each PMF has been normalized by the number of nearest neighbor fullerene pairs in the cluster.

large (17.0 Å) such that $\langle F_{con}(r) \rangle - 2k_B T/r \approx 0$. The parameter n_{shell} is the number of fullerenes surrounding the central fullerene, with $n_{shell} = 2, 6,$ and 12 for the linear, planar, and icosahedral geometries, respectively, and k_B is the Boltzmann constant. Note that by symmetry the only constraint force experienced by a fullerene on average lies along the bond connecting it to the central fullerene. $\langle F_{con}(r) \rangle$ represents an average over both time and all n_{shell} fullerenes. The quantity $PMF(r)$ is the free energy change associated with bringing the fullerenes of the cluster together to a separation r from the central fullerene (with the correct geometry) from a far separation and hence is referred to as the free energy of formation for the cluster.

III. Results

A. Potential of Mean Force. In order to understand the influence of cluster geometry on the free energy of cluster formation, it is useful to normalize the PMF given by eq 2 by the number of nearest neighbor pairs in the cluster, which is 1 for (C₆₀)₂, 2 for (C₆₀)₃, 12 for (C₆₀)₇, and 42 for (C₆₀)₁₃. Furthermore, while all nearest neighbor pair separations are equal to the separation r between the shell and central fullerenes for the (C₆₀)₂, (C₆₀)₃, and (C₆₀)₇ clusters, this is not the case for the (C₆₀)₁₃ cluster. Here, the nearest neighbor distance between shell fullerenes is slightly greater (by 5%) than the separation between shell and central fullerenes as required by the icosahedral geometry. The separation distance r for this cluster for all plots in this paper is an average over all (42) nearest neighbor pairs.

The (normalized by the number of nearest neighbor pairs) PMF as a function of separation is shown for all cluster geometries in Figure 2. All PMFs exhibit one deep minimum at a separation distance of around 10 Å, indicating the van der Waals contact distance for the fullerenes, and oscillatory features at larger separation that reflect the structure of the hydrating water, as discussed previously for the fullerene pair.² The shallow minimum at about 13 Å corresponds to a single layer of hydrating water between the fullerenes while that at about 16 Å to two layers of hydrating water. The slight shifting of the contact minimum to larger separation for the (C₆₀)₁₃ cluster reflects the fact that the distance between nearest neighbor fullerene pairs in the shell is

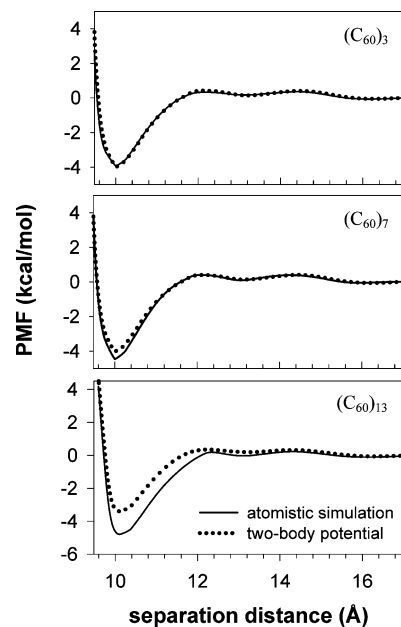


Figure 3. Comparison of the potential of mean force (PMF) obtained from atomistic molecular dynamics simulations and as predicted by the two-body coarse-grained implicit solvent potential.

slightly greater than that between the central fullerene and the shell fullerenes.

While all PMFs show qualitatively similar behavior, it is clear from Figure 2 that the free energy of formation depends upon cluster geometry. As the dimension of the cluster increases the depth of the primary minimum increases. Furthermore, the position of the first peak in the PMF for the (C₆₀)₁₃ cluster is shifted to a larger separation distance than for the 1- and 2-dimensional clusters. This shift is greater than that observed for the contact minimum position, indicating that the shifting reflects not only the difference between shell–shell fullerene and shell–central fullerene separations but also a significant fundamental difference in the effective interactions between the fullerenes of the 3-dimensional cluster compared to the 1- and 2-dimensional aggregates.

B. Comparison with the Coarse-Grained Implicit Solvent Two-Body Potential. Insight into the effect of cluster geometry, and hence into the influence of many-body interactions, on the free energy of formation of fullerene clusters in aqueous solution can be gleaned by comparing the free energy of formation obtained from atomistic simulations with that predicted using the two-body coarse-grained implicit solvent (CGIS) potential. In the CGIS model we assume that the free energy associated with forming nearest neighbor fullerene pairs in each cluster is described (as a function of separation) by the PMF for the (C₆₀)₂ cluster obtained from atomistic simulations (see Figure 2). The resulting (normalized by the number of nearest neighbor pairs) CGIS PMF for the (C₆₀)₃, (C₆₀)₇, and (C₆₀)₁₃ clusters is compared with that from fully atomistic simulations in Figure 3.

For the (C₆₀)₃ cluster the PMF obtained from the two-body CGIS model is nearly identical to that obtained from atomistic simulations. In this linear 1-dimensional geometry,

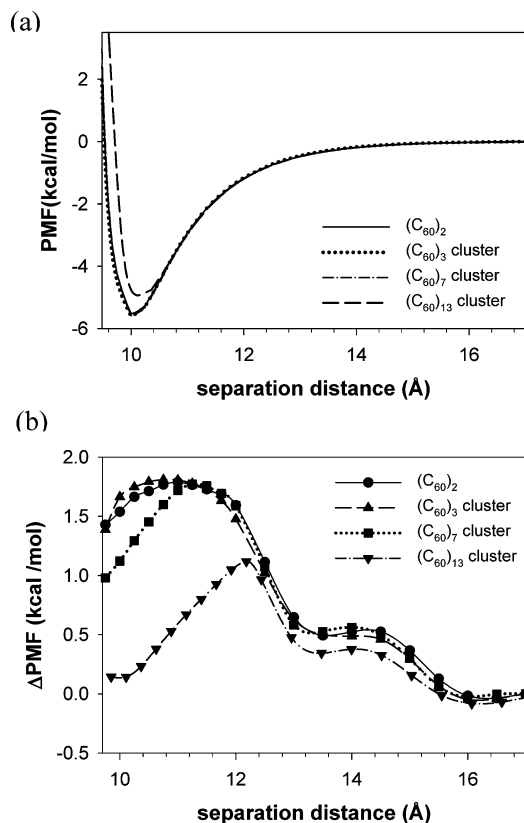


Figure 4. The (a) in vacuo and (b) water-induced contribution to the potential of mean force (PMF) for each cluster geometry. Each PMF has been normalized by the number of nearest neighbor fullerene pairs in the cluster.

the presence of the third fullerene does not perturb the interaction between the (two) nearest neighbor pairs. For the planar (C₆₀)₇ cluster, the fully atomistic simulation predicts a slightly stronger attractive interaction between fullerenes at the close contact position but no discernible difference from the two-body prediction for separations greater than about 11 Å. In contrast, significant differences in the PMF can be seen between the two-body prediction and the atomistic simulations for the 3-dimensional (C₆₀)₁₃ cluster, indicating that pair interactions are strongly perturbed by the presence of other fullerenes (i.e., the existence of many-body effects). The primary minimum is significantly deeper and broader than predicted by the two-body potential, indicating that many-body effects promote fullerene–fullerene attraction at short separation.

C. Water-Induced Interactions. The PMF for the fullerene clusters in vacuum was determined using a Brownian dynamics integrator and the same constraint protocol described above for the clusters in aqueous solution. The (normalized per nearest neighbor pair) PMF in vacuo is shown in Figure 4a. The in vacuo PMF for all clusters is described nearly perfectly by the two-body (pair) PMF, implying that any dependence of the free energy of formation of clusters in water on cluster geometry is due to differences in water-induced interactions.

Figure 4b shows the water-induced contribution to the PMF for each cluster, obtained by subtracting the in vacuo PMF from the PMF obtained in aqueous solution. We first note that the water-induced contribution is a minor compo-

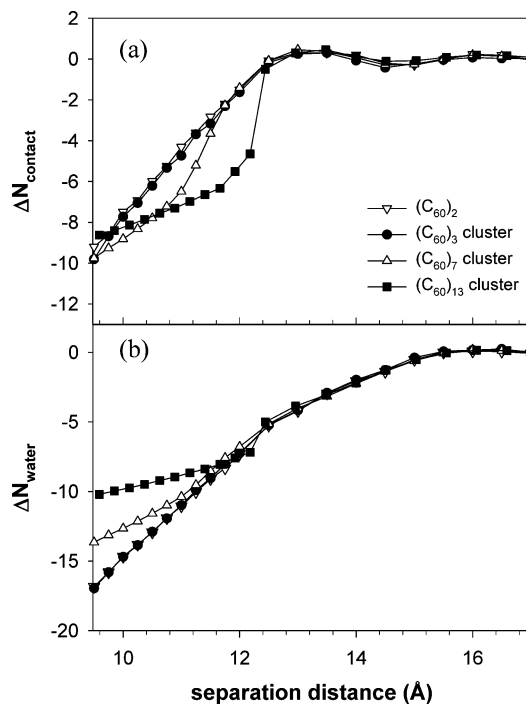


Figure 5. The change in the number of (a) water-fullerene contacts (see text) and (b) hydrating water molecules for each cluster as a function of fullerene separation, normalized by the number of nearest neighbor fullerene pairs.

nent of the total PMF for all clusters (compare to the total PMF in Figure 2), indicating that fullerene–fullerene interactions are dominated by direct van der Waals interactions and not by solvent effects. For all cluster geometries the influence of water on fullerene interaction is repulsive, i.e., water leads to a positive contribution to the free energy of pair formation for all separations, as discussed in our previous work^{1,2} and in the Introduction to this paper for (C₆₀)₂.

In Figure 5a the number of water-fullerene contacts for all cluster geometries, normalized by the number of nearest neighbor pairs, is shown as a function of separation relative to that for large separation. In other words, Figure 5a shows the change in the number of water-fullerene contacts as the separation between fullerenes decreases from large separation. A water-fullerene contact is considered to exist whenever a water molecule is within the first hydration shell of fullerene, i.e., within 8.38 Å of the center of the fullerene.¹ Figure 5b shows the change in the number of hydrating water molecules as a function of separation, again normalized by the number of nearest neighbor pairs. For all cluster geometries the number of contacts is almost constant down to a separation of about 12–12.5 Å, at which point the single layer of hydrating water between the fullerenes (which has contact with two or more fullerenes) begins to be squeezed out and the number of water contacts drops with decreasing separation. In contrast, the number of hydrating water begins to decrease at separations around 15 Å when the second layer of hydrating water starts to be squeezed out and fullerenes begin to share hydrating water molecules.

Figure 4b reveals that the water-induced contribution to the PMF for the fullerene pair (C₆₀)₂ has maxima at

separations of around 11 Å and 14.5 Å. At these separations, neither a single hydration layer nor two hydration layers, respectively, can be well accommodated between the fullerenes, while the minima at 13 Å and 16 Å correspond to distances that can accommodate the hydrating water structure well. The water-induced contribution to the free energy of formation for the (C₆₀)₃ cluster is nearly identical to that for the fullerene pair, reflecting the fact that in the linear geometry the shell fullerenes are too far removed from each other to significantly influence hydration of the shell-central fullerene pairs. The similarity in behavior for the linear cluster and (C₆₀)₂ pair is further emphasized in Figure 5, where a nearly identical smooth loss of water contacts and hydrating water is observed with decreasing separation.

For the close-packed planar geometry, (C₆₀)₇, Figure 4b reveals some influence of geometry on the water-induced contribution to the free energy of formation. The maximum in the water-induced contribution to the free energy is shifted slightly to larger separations compared to the fullerene pair and linear cluster, and the unfavorable contribution of water to the free energy of cluster formation drops rapidly with decreasing separation for separations less than 11.5 Å. This difference in behavior of the water-induced contribution to the free energy of formation for the 1-dimensional and 2-dimensional clusters is reflected in a greater loss in the number of water-fullerene contacts for the (C₆₀)₇ cluster (per nearest neighbor pair) and a loss of fewer hydrating water molecules (per nearest neighbor pair) than is observed for the linear geometry for separations less than about 11.5 Å. At this separation the water within the interior of the cluster (as opposed to those water molecules hydrating the exterior surface of the aggregate) becomes unstable, and these relatively constrained, high free energy water molecules, which interact simultaneously with multiple fullerenes and hence form several water-fullerene contacts, are rapidly expelled from the cluster with decreasing separation.

Continued release of constrained water molecules on the surface of the (C₆₀)₇ cluster with decreasing separation (similar to the effect observed for the pair and linear aggregate) for separations less than about 11.5 Å accounts for the decrease in the unfavorable water-induced contribution to the free energy of formation with decreasing separation. This can be thought of as an interfacial effect. Water interacts favorably with isolated fullerenes. As the fullerenes are brought together, relatively high free energy water is created that must interact with multiple fullerenes. The cluster reaches a maximum free energy at the point where the constrained water in the interior to the cluster is the most frustrated. Further decrease in separation results in release of this water. However, constrained water (water interacting with multiple fullerenes) also exists on the surface of the cluster which is only released gradually as the surface area of the cluster decreases, accounting for the decrease in the unfavorable water induced interaction with decreasing separation.

The effect of many-body interactions on the water-induced contribution to the free energy of cluster formation is more dramatic for the 3-dimensional geometry, as can be clearly

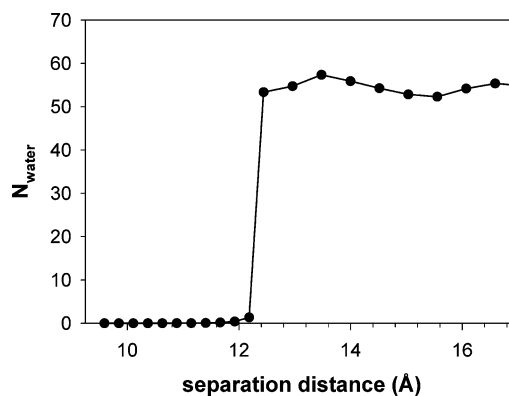


Figure 6. The number of water molecules hydrating the central fullerene in the (C₆₀)₁₃ cluster as a function of fullerene separation.

seen in Figure 4b. The maximum unfavorable contribution of water is shifted to a significantly larger separation, and the magnitude of the maximum decreases dramatically compared to the 1- and 2-dimensional clusters. This difference is reflected in a dramatic drop in the number of water-fullerene contacts and number of hydrating water at separations of around 12 Å as shown in Figure 5. As revealed by Figure 6, which shows the number of water molecules involved with hydrating the central fullerene, this dramatic drop in the number of water-fullerene contacts results from the complete dehydration of the central fullerene. As with the 1-dimensional and 2-dimensional clusters, decrease in the water-induced contribution to the free energy of formation for separations less than 12 Å reflects the continued release of highly constrained water hydrating the exterior surface of the cluster. We anticipate that the latter effect becomes weaker as the size of the 3-dimensional cluster increases and interfacial effects become less important compared to the effects in the cluster interior.

IV. Conclusions

In summary, our investigation of the influence of geometry on the free energy of formation of C₆₀ clusters in aqueous solution reveals that direct fullerene–fullerene interactions dominate over water induced interactions for all dimensionalities. The water-induced repulsion observed for a single fullerene pair is found to weaken with increasing cluster dimension, particularly for the 3-dimensional (icosahedral) cluster. This weakening of the water-induced repulsion reflects the importance of many-body interactions for the more compact geometries, i.e., the important role of neighboring fullerenes on the water-induced interaction between any pair of fullerenes. We believe the reduction in the water-induced repulsion for the 3-dimensional aggregate is due to both the creation of fewer highly constrained, high free energy water molecules, i.e., water solvating more than one fullerene, compared to 1-dimensional and 2-dimensional aggregates, and the overall loss of fewer hydrating water (per contact pair) than is predicted based upon the behavior of a single fullerene pair. Both effects result from the overlap of hydration shells of multiple fullerenes in the compact 3-dimensional geometry.

Acknowledgment. The authors gratefully acknowledge support from the National Science Foundation through grants NSF ITR CHE0312226 and MRSEC (University of Colorado) DMR-0213918.

References

- (1) Li, L.; Bedrov, D.; Smith, G. D. *Phys. Rev. E* **2005**, *71*, 011502.
- (2) Li, L.; Bedrov, D.; Smith, G. D. *J. Chem. Phys.* **2005**, *123*, 204504.
- (3) Slanina, Z.; Pulay, P.; Nagase, S. *J. Chem. Theory Comput.* **2006**, *2*, 782–785.
- (4) Bedrov, D.; Smith, G. D.; Li, L. *Langmuir* **2005**, *21*, 5251–5255.
- (5) Gallego, L. J.; Garcia-Rodeja, J.; Alemany, M. M. G.; Rey, C. *Phys. Rev. Lett.* **1999**, *83*, 5258–5261.
- (6) Piatek, A.; Dawid, A.; Gburski, Z. *J. Phys.: Condens. Matter* **2006**, *18*, 8471–8480.
- (7) <http://www.che.utah.edu/~gdsmith/mdcode/main.html> (accessed Aug 5, 2005).
- (8) Allen, M. P.; Tildesley, D. J. Building the model potential. In *Computer Simulation of Liquids*; Oxford University Press: Clarendon, Oxford, 1989; p 9.
- (9) Jorgensen, W. L.; Chandrasekhar, J.; Madura, J. D.; Impey, R. W.; Klei, M. *J. Chem. Phys.* **1983**, *79*, 926–935.
- (10) Werder, T.; Walther, J. H.; Jaffe, R. L.; Halicioglu, T.; Koumoutsakos, P. *J. Phys. Chem. B* **2003**, *107*, 1345–1352.
- (11) Ryckaert, J. P.; Ciccotti, G.; Berendsen, H. J. C. *J. Comput. Phys.* **1977**, *23*, 327–341.
- (12) Essmann, U.; Perera, L.; Berkowitz, M. L.; Darden, T.; Lee, H.; Pedersen, L. G. *J. Chem. Phys.* **1995**, *103*, 8577–8593.
- (13) Tuckerman, M.; Berne, B. J.; Martyna, G. L. *J. Chem. Phys.* **1991**, *94*, 6811–6815.
- (14) Tuckerman, M.; Berne, B. J.; Martyna, G. L. *J. Chem. Phys.* **1992**, *97*, 1990–2001.

CT700211Y

Structural and Electronic Properties of Selected Rutile and Anatase TiO₂ Surfaces: An *ab Initio* Investigation

Frédéric Labat,[†] Philippe Baranek,[‡] and Carlo Adamo^{*,†}

Laboratoire d'Électrochimie et Chimie Analytique, UMR-7575, ENSCP, 11 rue P. et M. Curie, Paris 75231 Cedex 05, France, and EDF R&D, Département MMC, Avenue des Renardières, 77818 Moret-sur-Loing Cedex, France

Received August 29, 2007

Abstract: Five low-index stoichiometric TiO₂ rutile and anatase surfaces, i.e., rutile (110), (100), and (001) as well as anatase (101) and (100), have been investigated using different Hamiltonians with all-electron Gaussian basis sets, within a periodic approach. Full-relaxations of the aforementioned surfaces have been essentially carried out at the Hartree–Fock (HF) level, but selected surfaces were treated also using pure and hybrid Density Functional Theory (DFT) models. Mulliken charges, band structures, and total and projected-densities of states have been computed both at the HF and the hybrid DFT (B3LYP and PBE0) levels. As regards DFT, the local density (LDA) and generalized gradient approximations (GGA) have been used. No matter which Hamiltonian is considered, as long as sufficiently thick slabs are taken into account, computed atomic relaxations show an overall excellent agreement with the most recent experimental reports. This is especially true when using hybrid functionals which enable the clarification of some conflicting results. Moreover, both at the LDA and HF levels, we were able to classify the surface relative energies in the following sequence: anatase (101) < rutile (110) < anatase (100) < rutile (100) ≪ rutile (001). Instead, when using PBE, B3LYP, or PBE0, the two most stable surfaces are reversed.

I. Introduction

Titanium dioxide (TiO₂) is an excellent model system displaying many of the properties of more complex oxides, readily available and well-characterized experimentally, with a wide range of applications.¹ Its common industrial applications are numerous and varied, ranging from paintings, gas-sensing² to electronics³ or optics.⁴ Recently, great interest has arisen for this material in newer fields such as homogeneous⁵ or heterogeneous catalysis (with the photocatalytic splitting of water⁶ or, by far, degradation of organic molecules in polluted air or waters⁷) and solar cells (with the promising dye-sensitized solar cells^{8,9}). Those latter examples rely mainly on the surface properties of TiO₂ and more precisely on those of its two more stable polymorphs (anatase and rutile). So far, many TiO₂ surfaces investigations

have been reported both experimentally and theoretically (see for instance ref 1 for a recent review of the subject).

The most stable rutile surfaces, namely (110), (100), and (001), have attracted much attention in recent years. The (110) surface, which is the most stable one, has been extensively studied both experimentally^{10–17} and theoretically.^{18–31} Most calculations were carried out at the Density Functional Theory (DFT) level using pure functionals (GGA and LDA),^{19–23,25–28} whereas a few calculations were reported using the Hartree–Fock (HF)^{18,27,29,31} approach or hybrid functionals.^{30,31} Experimentally, the (100) surface has been mainly concerned with its (1 × 1) reconstruction,^{32–39} but recently the stoichiometric (1 × 1) surface has been observed and characterized.^{10,38,39} Several theoretical calculations have also focused on this (1 × 1) surface both at the DFT (pure functionals)^{19,40,41} and the HF^{18,41} levels. On the other hand, the (001) surface has received much less attention, probably because it tends to facet and reconstruct.¹

* Corresponding author e-mail: carlo-adamo@enscp.fr.

[†] UMR-7575, ENSCP.

[‡] EDF.

Experimentally, a LEED-IV study has been reported by Mason et al.⁴² Theoretically, both HF^{18,43} and DFT (LDA and GGA) results can be found in the literature.^{19,43} Despite this obvious lack of available data, the (001) surface is still interesting since it is the crystal orientation of choice for electrochemical studies, as the electrical conductivity is higher along this direction.¹

Works on anatase are few compared to those on rutile, since the former polymorph is thermodynamically less stable than the latter, thus experimental difficulties arise to grow sufficiently large anatase single crystals. Nevertheless, TiO₂ nanoparticles are commonly of the anatase form, and the (101) and (100) surfaces of this polytype are found in dye-sensitized solar cells⁴⁴ due to their high photocatalytic properties. In addition, the (100) surface enhances catalytic activity in industrial supported catalysts.⁴⁵ Experimentally, it has been shown to form a (1 × 2) reconstruction,⁴⁶ while the (101) surface presents a (1 × 1) termination.^{47,48} Theoretically, the clean (101) and (100) surfaces have been investigated at DFT level, using LDA and GGA^{49–51} as well as hybrid approaches.⁵²

General trends regarding the properties of the different surfaces of this model system have been derived from a theoretical point of view. In particular, it has been found that relaxations occur in order to increase effective coordination of undercoordinated atoms, that is, surface energies appear to be related to the presence of undercoordinated Ti atoms (see ref 49 for instance). At the same time, the computed atomic displacements are only weakly sensitive to the adopted Hamiltonian^{27,43} but much more to the thickness of the surface model²⁶ chosen. Indeed, despite these known trends, theory can still clarify some points that deserve a deeper insight. In particular, a coherent analysis of atomic displacements during surface relaxations and of the relative stability of surfaces still requires theoretical investigation. As a matter of fact, most previous calculations have focused on structural and energetics aspects, and only a few investigations of the electronic structures have been reported, especially using hybrid functionals which appear now as good candidates to overcome the shortcomings of both HF and pure DFT approaches in solid-state systems.^{31,53–55} Furthermore, previously reported calculations have been performed using different computational protocols (basis sets, Hamiltonians), making a straightforward comparison of available results difficult.

In this context, we reinvestigate five TiO₂ low-index *clean* surfaces, namely rutile (110), (100), and (001) and anatase (101) and (100) surfaces, using an all-electron LCAO approach both at the DFT and the HF level of theory. Valuable data for almost all surfaces being readily available, we will be able to test the reliability of our calculations and to clarify some conflicting results. It is noteworthy that, even if TiO₂ surfaces have been deeply investigated, this is the first work considering several surfaces of the different polymorphs of TiO₂, using different Hamiltonians.

The paper is structured as follows: computational details are described in section II; structural data, energetics, and electronic properties are reported and discussed in section III. Some conclusions are finally drawn in section IV.

II. Computational Details

All calculations have been performed with the *ab initio* periodic Crystal03 code⁵⁶ which allows for solving self-consistently both the Hartree–Fock (HF) and the Kohn–Sham (KS) equations as well as the use of hybrid schemes, such as B3LYP and PBE0, using pseudopotentials or all-electron Gaussian-type functions basis set through the standard LCAO approach. The oxygen and titanium atoms have been described by (8411/411/1) and (86411/411/3) contractions, respectively, which have previously proven to yield a reliable description of the TiO₂ bulk system.⁵³

At the DFT level, different exchange–correlation functionals, based on the local density (LDA) and generalized gradient approximations (GGA), have been used: LDA for Dirac–Slater⁵⁷ exchange plus Vosko–Wilk–Nusair correlation potential⁵⁸ and PBE for Perdew–Burke–Ernzerhof⁵⁹ (exchange and correlation). Furthermore, two hybrid functionals, B3LYP including Becke’s 3 parameter exchange⁶⁰ and Lee–Yang–Parr correlation,⁶¹ and PBE0, a parameter free hybrid functional mixing 25% HF exchange with PBE exchange–correlation functional,⁶² have also been considered.

From a theoretical point of view, different approaches have been developed to simulate surfaces. Among them, the model usually adopted is that of a slab: a thick slice of material (consisting of several layers), delimited by two free surfaces. In Crystal, two different schemes based on this two-dimensional (2-D) model are available. By forcing a 3-D periodicity, slabs are periodically repeated along the normal to the surface. On the other hand, by imposing 2-D periodic boundary conditions, the system is really two-dimensional and thus isolated. All calculations reported in this paper have been performed using the latter model. Indeed, to provide a faithful description of an ideal surface, sufficiently thick slabs have to be considered, so that the computed structures, energies, and electronic properties can be considered at convergence with respect to the number of atomic layers.⁶³ To this end, slabs of different thickness have been fully relaxed, using a computational protocol based on the evaluation of analytical gradients.^{64,65} Structural optimizations were considered converged when four different convergence criteria^{56,66} are simultaneously satisfied, all computed residual nuclear forces being smaller than 5×10^{-4} au.

Since atomic relaxations are only weakly dependent on the adopted Hamiltonian^{27,43} but much more on the thickness of the slab considered,^{26,31} we have chosen to carry out full relaxations of all of the slabs at the HF level. Atomic displacements obtained in such a way are then used to correct atomic positions obtained from bulk DFT calculations, taken from ref 53, and summarized in Table 1. DFT surface energies were then computed by single-point energies calculations (referred to as DFT//HF data) on such structures. Nevertheless, in selected cases, full-relaxations were also computed at the DFT level (referred to as DFT//DFT). We should note however that, for all surfaces investigated, computed HF displacements are always within 0.1 Å of DFT data (both with pure and hybrid functionals).

Calculations have been performed with a Monkhorst–Pack shrinking factor⁶⁷ of 8, corresponding respectively to 25 points in the irreducible Brillouin zones of the rutile (110),

Table 1. Equilibrium Geometry of Bulk TiO₂ Rutile and Anatase Calculated with Different Hamiltonians^b

	rutile			anatase		
	<i>a</i>	<i>c</i>	<i>u</i>	<i>a</i>	<i>c</i>	<i>u</i>
HF	4.575	2.987	0.307	3.771	9.688	0.204
LDA	4.555	2.929	0.304	3.735	9.580	0.206
PBE	4.653	2.975	0.306	3.786	9.867	0.204
B3LYP	4.639	2.974	0.307	3.783	9.805	0.204
PBE0	4.591	2.955	0.306	3.758	9.704	0.204
expt. ^a	4.593	2.958	0.305	3.789	9.522	0.208

^a See ref 70. ^b Lattice parameters (*a* and *c*) in Å; internal parameter (*u*), referring to the position of the oxygen atom in the asymmetric unit cell, in fractional units. All results are from ref 53.

(100), and anatase (100) surfaces, 15 points for the rutile (001) surface, and 21 points for the anatase (101) surface. For the evaluation of the Coulomb and exchange series, both *fine* and *extrafine* integration schemes were considered.⁶⁸ Crystal drawings have been performed with Schakal.⁶⁹

III. Results

A. TiO₂ Bulk: Geometrical Parameters. Since all initial surface structures have been derived by truncation of the bulk systems, in Table 1 are reported the optimized crystallographic parameters computed using different exchange-correlation functionals for both rutile and anatase structures.⁵³ A detailed analysis of bulk TiO₂, under the same computational conditions can be found in ref 53.

Here, we only recall that rutile and anatase are tetragonal with space groups *PA*₂/*mmm* and *IA*/*amd*, respectively. They are both built from distorted TiO₆ octahedra resulting in threefold coordinated oxygen atoms. In rutile, octahedra share corners in the (001) plane, with their long axial axis alternating by 90°. The structure can therefore be defined as linear chains of edge-sharing octahedra where the chains themselves are connected by the octahedra corners. In anatase, on the other hand, TiO₆ octahedra are sharing four adjacent edges, resulting in zigzagging chains running along the *a* and *b* lattice vectors.

B. Surface Energetics. First, we investigated the effect of the thickness of the slab on the computed surface energy (*E_s*). To this end, we analyzed the dependence of *E_s* on the number (*n*) of Ti-layers taken into account. *E_s* have been computed using the following expression

$$E_s(n) = \frac{1}{2A}(E_n - nE_b) \quad (1)$$

where *E_n* is the total energy of a slab containing *n* Ti-layers, *E_b* is the bulk energy of the infinite system per unit cell (taken from an independent bulk calculation), and *A* is the area of the slab. The (1/2) factor takes into account the existence of two free surfaces for each slab. For sufficiently large values of *n*, *E_s(n)* is expected to converge to the surface energy of the semi-infinite system. We recall that, in rutile (110), a Ti-layer is composed of three planes (O–Ti₂O₂–O motif) as in rutile (100) and anatase (101) (O–Ti–O motif), whereas only one plane forms the Ti-layer in rutile (001) and anatase (100) (TiO₂ and Ti₂O₄ motif, respectively). The labeling scheme adopted is reported in Figures 1–5.

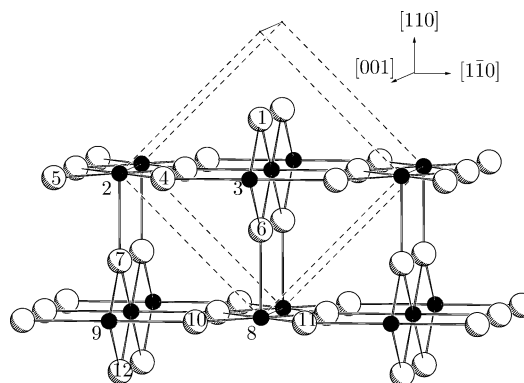


Figure 1. 2-D 2 Ti-layers slab model of the rutile (110) surface. Dashed lines display the position of the (110) surface in the bulk unit cell. Titanium atoms in black.

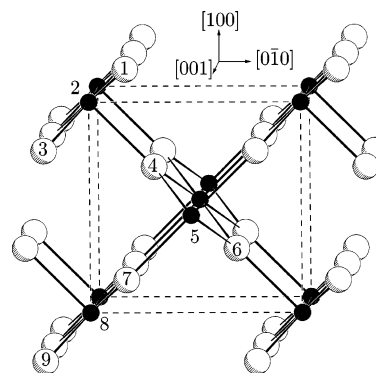


Figure 2. 2-D 3 Ti-layers slab model of the rutile (100) surface. Dashed lines display the position of the (100) surface in the bulk unit cell. Titanium atoms in black.

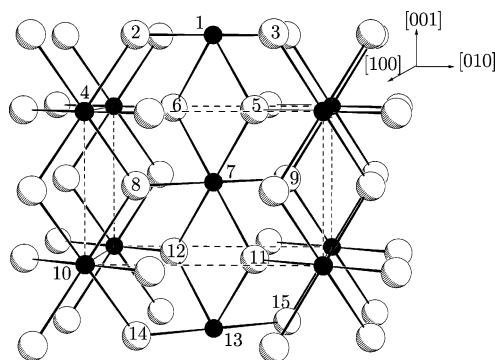


Figure 3. 2-D 5 Ti-layers slab model of the rutile (001) surface. Dashed lines display the position of the (001) surface in the bulk unit cell. Titanium atoms in black.

From the plots of computed HF surface energies vs slab thickness reported in Figures 6 and 7 for rutile and anatase, respectively, some general trends can be drawn.

First, and as expected, for all surfaces, the computed surface energy strongly depends on the number of Ti layers considered in the slab. Furthermore, an oscillation of *E_s* with slab thickness can be noticed. This point, especially evident for the rutile (110) surface, where calculations have been performed for slabs from 1 up to 14 Ti-layers (corresponding to 6 to 84 atoms per unit cell), is in agreement with the results obtained in previous publications.^{19,23,28–30} This oscillating behavior is related to the presence (absence) of a symmetry plane normal to the surface for an odd- (even-) number of

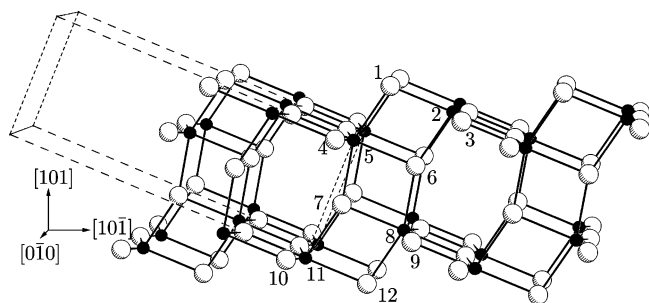


Figure 4. 2-D 4-Ti-layers slab model of the anatase (101) surface. Dashed lines display the position of the (101) surface in the bulk unit cell. Titanium atoms in black. The two motifs, corresponding to the two possible termination of the unit cell, are clearly evident.

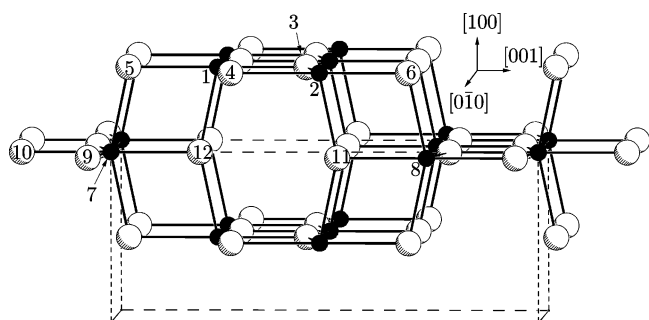


Figure 5. 2-D 3-Ti-layers slab model of the anatase (100) surface. Dashed lines display the position of the (100) surface in the bulk unit cell. Titanium atoms in black.

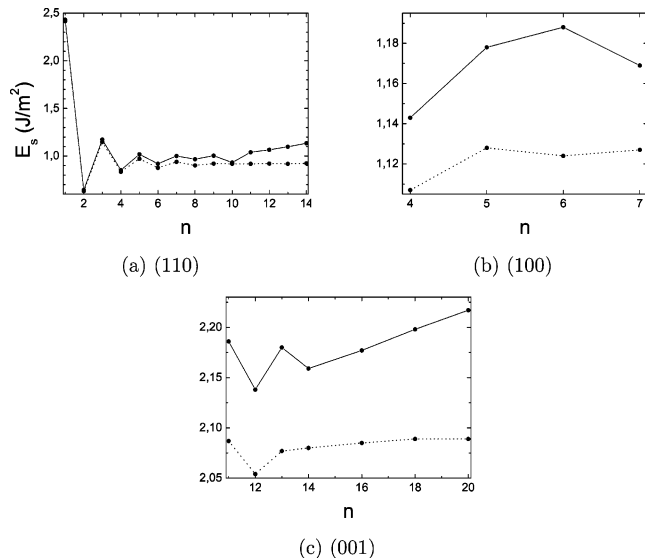


Figure 6. Surface energies E_s (in J/m^2) of fully optimized rutile surfaces as a function of the number n of Ti-layers. HF results. Fine (solid lines) and extrafine (dotted lines) integration⁶⁸ values reported.

Ti-layers in the slabs, that is, to a greater flexibility of slabs with an even number of Ti-layers. Thus, in all cases, the surface energies of the odd Ti-layer slabs converge from above and those of the even Ti-layer slabs from below to the surface energy of infinite layers. The case of the anatase (101) surface is peculiar however, since two sets of data energies are obtained, clearly separated by 0.5 J/m^2 , corresponding to two possible terminations of this surface. Indeed,

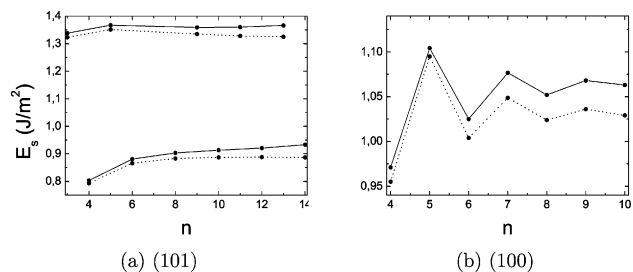


Figure 7. Surface energies E_s (in J/m^2) of fully optimized anatase surfaces as a function of the number n of Ti-layers. HF results. Fine (solid lines) and extrafine (dotted lines) integration⁶⁸ values reported.

along the [010] direction, channels are formed (see Figure 4) which can either be closed (with even number of Ti-layers) or open (with odd number of Ti-layers). In case of open channels, additional undercoordinated Ti (fourfold) and O (twofold) atoms can be observed (compared to the even case), resulting in a significantly higher surface energy. Thus, in the following, for the anatase (101) surface, only slabs with an even number of Ti-layers will be considered since they are the lowest in energy.

From a computational point of view, we note that, for all surfaces, convergence of E_s is achieved only if an *extrafine* integration grid is considered.⁶⁸ More precisely, with the standard *fine* integration grid,⁶⁸ variations of slab total energies are found to be larger than the precision involved in total energies calculations (10^{-5} au). For example, for the rutile (110) surface, variations as large as 10^{-3} au are observed for sufficiently thick slabs. This result is in line with previously reported LCAO surface studies.^{28,29}

Table 2 collects the computed surface energies at the HF, DFT//HF, and DFT//DFT levels on HF-converged thickness.

First, one can notice that the number of Ti-layers needed to converge surface energies varies with the orientation. In particular, the rutile (100) and (001) as well as the anatase (101) surfaces contain only 3 atoms per Ti-layer (that is one TiO_2 unit). In such cases, 5, 13, and 10 Ti-layers were needed to converge E_s to 1.128, 2.077, and 0.887 J/m^2 , respectively. These values accord nicely with previous works carried out at the HF level on slabs constituted by 3 Ti-layers (1.21 J/m^2 , ref 41) and 11 Ti-layers (2.20 J/m^2 , ref 43), for rutile (100) and (001), respectively. The rutile (110) and anatase (100) surfaces, however, contain 6 atoms per Ti layer (2 TiO_2 units), and 9 and 8 Ti-layers were found to be enough to converge the surface energies to 0.921 and 1.029 J/m^2 , respectively. The rutile (110) value is in line with a previous work carried out at the HF level by Swamy et al. (1.00 J/m^2 , ref 27), while no HF results could be found for the anatase (100) surface.

In summary, we find the number of layers enough to converge surface energies as well as values of E_s calculated in HF or in DFT//HF with pure functionals to be in excellent agreement with previous publications. However, computed data with hybrid functionals significantly differ from previously reported calculations. To further clarify this point, we also present in Table 2 surface energies corresponding to full-relaxations carried out with all functionals on HF converged thickness for the two most stable surfaces (rutile

Table 2. Surface Energies (in J/m²), Computed as Single-Point Energies on HF-Corrected DFT Bulk Atomic Geometries (DFT//HF), with Different Hamiltonians and an *Extrafine* Integration^{68 a}

	rutile			anatase	
	(110)-9L	(001)-13L	(100)-5L	(101)-10L	(100)-8L
HF	0.921	2.077	1.128	0.887	1.024
LDA	0.906/(0.890)	1.876	1.197	0.850/(0.828)	0.971
PBE	0.479/(0.417)	1.393	0.694	0.526/(0.495)	0.625
B3LYP	0.461/(0.397)	1.452	0.699	0.575/(0.553)	0.666
PBE0	0.595/(0.552)	1.587	0.833	0.621/(0.601)	0.732
Other LCAO Works					
HF	1.00 ²⁷	2.20 (11L) ⁴³	1.21 (3L) ⁴¹		
LDA	0.90 ²⁷	1.87 (11L) ⁴³	1.30 (3L) ⁴¹		
B3LYP	≈1.00 (8L) ³⁰			≈1.45 (4L) ⁵²	≈1.80 (6L) ⁵²

^a In parentheses, values corresponding to full-relaxations in DFT (DFT//DFT data). Selected previous LCAO works are also obtained. L refers to the number of Ti-layers in the slab.

(110) and anatase (101)). We find DFT//DFT values to be closely related to the DFT//HF ones, with a maximum E_s difference of 0.06 J/m², confirming that our hybrid values are indeed correct. Due to the overall coherency of our results, we cannot give a definitive explanation for discrepancies with respect to data in the literature but only suppose a difference in the expression used for the calculation of surface energy.

Finally, it is interesting to note that the surface relative energies are found to follow the sequence: anatase (101) < rutile (110) < anatase (100) < rutile (100) ≪ rutile (001), both at HF and LDA levels. Using PBE, B3LYP, and PBE0 however, the order of the first two surfaces is reversed, rutile (110) being the most stable surface. The same conclusion holds when DFT//DFT values are considered. In addition, in all cases, the rutile (001) surface is found, by far, as the least stable surface. This result can be easily related to the presence of fourfold Ti atoms on this surface (see Figure 3 and discussion in Section C). Nevertheless, we mention that, from our calculations, the rutile (110) surface is found as the most stable rutile surface, while the corresponding anatase one is the (101) surface. This conclusion is in agreement with experimental findings.¹

C. Surface Geometries. In order to better discuss surface geometries, we will first give a detailed description of each of the unrelaxed surfaces and, next, analyze and discuss the computed atomic relaxations. Since the starting points of the slab geometries are “bulk-truncated” systems, we expect rather large atomic displacements, at least for the atoms in the outermost planes. Unless explicitly stated otherwise, reported geometry optimizations have been performed at the HF level. Subsequent relaxations carried out with hybrid functionals (B3LYP and PBE0) showed that computed HF displacements are within 0.1 Å of hybrid data. In the following subsections, we thus report essentially HF values, but the general conclusions hold for all the considered Hamiltonians.

1. Rutile (110). The rutile (110) surface (see Figure 1) exposes two kinds of titanium and oxygen atoms. Along the [110] direction, fivefold (Ti₂) and sixfold (Ti₃) titanium alternate. Twofold bridging oxygens (O₁) as well as threefold

Table 3. Displacements (in Å, from Bulk-Terminated Positions) for the TiO₂ (110) Rutile Surface (with 6 Atoms per Ti-Layer) Obtained with Different Slab Thickness^c

label	total number of Ti-layers				
	8	9	9-B3LYP	9-PBE0	LEED-IV ^b
O ₁	0.01	0.00	0.09	0.09	0.10 ± 0.05
Ti ₂	-0.17	-0.18	-0.14	-0.13	-0.19 ± 0.03
Ti ₃	0.24	0.22	0.31	0.31	0.25 ± 0.03
O _{4,5}	0.14	0.13	0.22	0.22	0.27 ± 0.08
O _{4,5} [110]	±0.05	±0.05	±0.04	±0.04	0.17 ± 0.15
O ₆	0.02	0.00	0.07	0.08	0.06 ± 0.10
O ₇	0.00	0.00	0.07	0.06	0.00 ± 0.08
Ti ₈	0.16	0.14	0.25	0.24	0.14 ± 0.05
Ti ₉	-0.10	-0.11	-0.08	-0.08	-0.09 ± 0.07
O _{10,11}	0.02	0.01	0.07	0.07	0.06 ± 0.12
O _{10,11} [110]	±0.02	±0.02	±0.03	±0.02	0.07 ± 0.18
O ₁₂	-0.01	-0.02	0.04	0.03	0.00 ± 0.17

^a See ref 30: B3LYP with 86-51G* and 8-411G basis sets for Ti and O, respectively. ^b See ref 17. ^c Labels refer to Figure 1. All displacements are given along the [110] direction, unless explicitly stated.

oxygens (O₄ and O₅) are present. Its unit cell is composed of six atoms with the following sequence of planes: O–Ti₂O₂–O.

The main relaxations, given in Table 3, occur perpendicular to the surface with only oxygen O₄ and O₅ atoms moving laterally (by -0.05 and +0.05 Å, respectively). Sixfold (Ti₃) and fivefold titanium atoms (Ti₂) relax upward and downward, respectively. Relaxations of the bridging oxygen atoms (O₁) are found to be negligible (0.01 Å), while threefold oxygen atoms (O₄ and O₅) relax significantly upward (0.14 Å). It should be noted that displacements decay rapidly with depth into the slab, becoming negligible for the bulklike atoms. Furthermore, values are in excellent agreement with recently reported experimental results,¹⁷ except for the bridging oxygen which is out of the error bar of the experimental data. Harrison et al. attributed this point to anisotropic vibrations in the model,²⁶ not taken into account in our approach. It should be noted, here, that displacements computed at the B3LYP and PBE0 levels are generally close to those obtained at the HF level. In just one case (Ti₃), these latter calculations are in better agreement with the experimental data, but the large experimental deviation prevents

deep comparisons. Moreover, hybrid functionals do give a correct picture of some critical parameters such as the relaxation of the O_1 bridging oxygen atom. Finally, our hybrid values very well compare to those computed by Scaranto et al.³⁰ at the B3LYP level, in the case of an 8 Ti-layers slab.

2. Rutile (100). The rutile (100) surface, displayed in Figure 2, presents fivefold (Ti_2) and sixfold (Ti_5) titanium atoms as well as twofold (O_1) and threefold (O_4) oxygen atoms in a six atoms unit cell with the following sequence of planes: O–Ti–O–O–Ti–O.

The largest relaxations occur along $[0\bar{1}0]$ in the outermost plane with Ti_2 , O_1 , and O_3 atoms moving in opposite directions, as reported in Table 3. Furthermore, an inward relaxation along $[100]$ can be observed for Ti_2 , while O_1 and O_3 relax outward. These relaxations result in an increase of the Ti_2 (fivefold) coordination.^{18,19,40,41} Moreover, one should note that even- or odd-Ti-layers slab lead to different type of relaxations. With odd-Ti-layers slabs, computed atomic displacements mainly concern topmost atomic planes and show a quick decay in amplitude with depth into the surface. With even-Ti-layers slabs however, displacements are much more diffuse and decay much slower. This may be explained by the fact that odd-Ti-layers slabs contain a symmetry plane normal to the $[100]$ direction (see Figure 2). Therefore, relaxations are much more localized than with even-Ti-layers slabs where displacements are delocalized over the whole system. Our results are in good agreement with those obtained with a 3-Ti layer slab,⁴¹ with largest relaxations occurring in the top five atomic planes. Significant differences are, however, found with respect to previous LDA calculations, which may be attributed to the different Hamiltonian (LDA vs HF) and basis set (LCAO vs PW) used. Unfortunately, no experimental data on the TiO_2 (100)- (1×1) relaxation could be found to better clarify this point.

3. Rutile (001). On the flat rutile (001) surface (see Figure 3), all titanium atoms (Ti_1) are coordinated to four oxygen atoms: twofold coordinated oxygen atoms (O_2 and O_3) at the surface level and threefold coordinated oxygens (O_5 and O_6) at the second layer. Its unit cell, with six atoms, consists of two atomic planes, each one composed of one TiO_2 unit.

The main relaxations, given in Table 5, indicate that atomic displacements occur in order to increase effective coordination of Ti cations. Indeed, the outermost Ti_1 cations (Ti-layer 1) relax downward by 0.28 Å with O_2 and O_3 anions moving laterally by 0.10 Å toward it. Ti_4 cations (Ti-layer 2), which effective coordination has therefore been lowered, relax upward by 0.24 Å. Ti_7 cations (Ti-layer 3) are displaced downward to lower Coulomb repulsion induced by the downward displacement of Ti_1 . Therefore, as already mentioned in ref 43, an alternation of the computed displacements is observed in odd and even Ti-layers of the slab. Finally, we should note that major displacements occur in the first two layers, values reported becoming negligible beneath this depth.

4. Anatase (101). The anatase (101) surface (see Figure 4) exposes twofolded oxygen atoms (O_1) bonded to fivefolded titanium atoms (Ti_2) in the second layer. These cations are bonded to threefolded oxygens (O_3) in the $[010]$ direction,

Table 4. Displacements (in Å, from Bulk-Terminated Positions) for the TiO_2 (100) Rutile Surface (with 3 Atoms per Ti-Layer) Obtained with Different Slab Thickness^b

label	total number of Ti-layers							
	5		6		3 ^a		6 ^b	
	$[0\bar{1}0]$	$[100]$	$[0\bar{1}0]$	$[100]$	$[0\bar{1}0]$	$[100]$	$[0\bar{1}0]$	$[100]$
O_1	0.31	0.03	0.26	0.03	0.32	0.04	0.18	0.01
Ti_2	-0.09	-0.03	-0.14	-0.03	-0.09	-0.03	-0.17	-0.07
O_3	0.16	0.04	0.11	0.03	0.15	0.04	0.12	0.02
O_4	0.06	-0.01	0.01	-0.01	0.05	-0.01	0.03	0.02
Ti_5	-0.03	0.00	-0.09	0.00			-0.11	0.00
O_6	0.00	0.00	-0.03	0.00			0.00	0.03
O_7	0.00	0.00	-0.03	0.00			0.00	0.01
Ti_8	0.00	0.00	-0.07	0.00			-0.07	0.02
O_9	0.00	0.00	-0.03	0.00			0.02	0.02
O_{10}	0.00	0.00	-0.03	0.00			0.02	0.02

^a See ref 41: HF/TVAE**. ^b Labels refer to Figure 2.

where channels are formed. Six atoms belong to the unit cell with the following sequence of planes: O–Ti–O–O–Ti–O. Computed relaxations are reported in Table 6. As previously pointed out in refs 49 and 52, the main relaxations occur laterally along the $[10\bar{1}]$ direction. Normal to the surface, fully coordinated atoms (O_3 and Ti_5) relax outward (by 0.16 and 0.13 Å, respectively), while undercoordinated titanium atoms (Ti_2) relax inward by 0.17 Å, leading to a tightening of Ti–O bonds. From our calculations, HF relaxations are in line with previously published data in most cases. However, they significantly disagree with B3LYP results reported by Beltrán et al.⁵² on a 2 Ti-layers slab. In order to verify this point, we fully relaxed the 10 and 12 Ti-layers slabs in B3LYP and PBE0. The results obtained, reported in Table 5, are in excellent agreement with the previously discussed HF data but still are notably different from the data reported in ref 52 for which the very thin slab considered and the small basis sets (6-31 G both on Ti and O atoms) may explain the difference.

5. Anatase (100). The anatase (100) surface is flat and exposes fivefolded titanium atoms (Ti_1 , Ti_2) bonded to twofolded (O_5 , O_6) and threefolded oxygen atoms (O_3 , O_4) in the outermost plane, while sixfold coordinated titanium atoms (Ti_7 , Ti_8) are located in the second layer (see Figure 5). Channels are formed along the $[0\bar{1}0]$ direction. The unit cell has six atoms belonging to the same plane (one Ti_2O_4 unit). The computed atomic relaxations are reported in Table 4.

Fully coordinated oxygen atoms (O_3 , O_4) show an important outward relaxation (0.17 Å), while fivefold and sixfold coordinated titanium atoms relax inward (–0.15 Å) and outward (0.17 Å), respectively, resulting in a surface that is no longer flat. Twofolded oxygen atoms move in opposite directions along $[001]$ to make channels observed in the $[0\bar{1}0]$ direction wider. The relaxation results in an increase of the coordination of the undercoordinated oxygen atoms (O_5 and O_6). All computed values are in excellent agreement with previously published data;⁴⁹ if we except those of Calatayud et al.,⁵⁰ for which the agreement is only qualitative, the thinner slab adopted in such calculations being probably responsible for the difference.

Table 5. Displacements (in Å, from Bulk-Terminated Positions) for the TiO₂ (001) Rutile Surface (with 3 Atoms per Ti-Layer) Obtained with Different Slab Thickness^c

label	total number of Ti-layers								
	11			13			11 ^a		
	[100]	[010]	[001]	[100]	[010]	[001]	[100]	[010]	[001]
Ti ₁	0.00	0.00	-0.28	0.00	0.00	-0.28	0.00	0.00	-0.21
O ₂	-0.10	-0.10	0.01	-0.10	-0.10	0.01	-0.10	-0.10	-0.02
O ₃	0.10	0.10	0.01	0.10	0.10	0.01	0.10	0.10	-0.02
Ti ₄	0.00	0.00	0.24	0.00	0.00	0.24	0.00	0.00	0.21
O ₅	-0.02	0.02	-0.03	-0.02	0.02	-0.04	0.00	0.00	0.01
O ₆	0.02	-0.02	-0.03	0.02	-0.02	-0.04	0.00	0.00	0.01
Ti ₇	0.00	0.00	-0.13	0.00	0.00	-0.13	0.00	0.00	-0.08
O ₈	0.00	0.00	0.02	0.00	0.00	0.01	-0.01	-0.01	0.03
O ₉	0.00	0.00	0.02	0.00	0.00	0.01	0.01	0.01	0.03
Ti ₁₀	0.00	0.00	0.08	0.00	0.00	0.08	0.00	0.00	0.07
O ₁₁	0.00	0.00	-0.02	0.00	0.00	-0.02	0.00	0.00	0.00
O ₁₂	0.00	0.00	-0.02	0.00	0.00	-0.02	0.00	0.00	0.00
Ti ₁₃	0.00	0.00	-0.04	0.00	0.00	-0.05	0.00	0.00	-0.03
O ₁₄	0.00	0.00	0.00	0.00	0.00	0.00	0.00	0.00	0.01
O ₁₅	0.00	0.00	0.00	0.00	0.00	0.00	0.00	0.00	0.01

^a See ref 43: HF/DVSC. ^b See ref 42. ^c Labels refer to Figure 3.**Table 6.** Displacements (in Å, from Bulk-Terminated Positions) for the TiO₂ (101) Anatase Surface (with 3 Atoms per Ti-Layer) Obtained with Different Slab Thickness^a

label	total number of Ti-layers					
	10-HF		10-B3LYP		10-PBE0	
	[10 $\bar{1}$]	[101]	[10 $\bar{1}$]	[101]	[10 $\bar{1}$]	[101]
O ₁	0.32	-0.07	0.37	-0.01	0.41	-0.03
Ti ₂	0.06	-0.17	0.11	-0.17	0.15	-0.19
O ₃	0.18	0.16	0.25	0.21	0.28	0.18
O ₄	0.17	0.04	0.25	0.06	0.28	0.06
Ti ₅	0.20	0.13	0.26	0.20	0.30	0.18
O ₆	0.18	-0.08	0.24	-0.06	0.26	-0.08
O ₇	0.10	0.02	0.15	0.03	0.17	0.03
Ti ₈	0.04	-0.09	0.04	-0.11	0.07	-0.12
O ₉	0.05	-0.04	0.08	-0.04	0.09	-0.05
O ₁₀	0.07	0.00	0.11	0.03	0.13	0.03
Ti ₁₁	0.07	0.04	0.11	0.09	0.13	0.09
O ₁₂	0.04	-0.03	0.06	-0.03	0.07	-0.03

^a Displacements along [0 $\bar{1}$ 0] are null. Labels refer to Figure 4.

D. Surface Electronic Structures. In this section, the convergence of electronic properties with slab thickness is investigated, only for the two most stable surfaces (i.e., rutile (110) and anatase (101)). A Mulliken charge distribution analysis for the undercoordinated titanium (fivefolded) and oxygen (twofolded) ions is presented as well as a minimal band gaps analysis. Since surface energies convergence has been investigated at the HF level, we report results computed both at the HF and the PBE0 levels, this latter approach appearing as a promising candidate to obtain an accurate description of both electronic and structural properties in the solid state.⁵³ Moreover, we note that the effect of the computational scheme chosen, that is, DFT//HF or DFT//DFT, has been investigated and that no significant differences could be evidenced. Therefore, in the following, only PBE0//PBE0 data, simply referred to as PBE0, will be presented.

Table 7. Displacements (in Å, from Bulk-Terminated Positions) for the TiO₂ (100) Anatase Surface (with 6 Atoms per Ti-Layer) Obtained with Different Slab Thickness^c

label	total number of Ti-layers							
	6		6 ^a		8		4 ^b	
	[001]	[100]	[001]	[100]	[001]	[100]	[001]	[100]
Ti ₁ ,Ti ₂	±0.03	-0.15	±0.02	-0.16	±0.04	-0.14	±0.08	-0.01
O ₃ ,O ₄	±0.04	0.17	±0.04	0.18	±0.04	0.18	±0.06	0.34
O ₅ ,O ₆	±0.16	-0.01	±0.16	0.02	±0.16	-0.01	±0.06	0.11
Ti ₇ ,Ti ₈	±0.00	0.13	±0.01	0.17	±0.00	0.11	±0.00	0.18
O ₉ ,O ₁₀	±0.00	0.08	±0.01	0.10	±0.00	0.07	±0.03	0.08
O ₁₁ ,O ₁₂	±0.13	-0.04	±0.13	-0.03	±0.11	-0.03	±0.08	-0.01

^a See ref 49: PW-PBE. ^b See ref 50: PW-PW91, only the top two Ti-layers have been relaxed. ^c Labels refer to Figure 5.**Table 8.** Mulliken Atomic Charges (*q*) and Charge Variation (δq) (in |*e*⁻|) for the Undercoordinated and Fully Coordinated Ti and O Atoms of the Rutile (110) Surface^c

		this work					
		this work		HF ^a		HF ^b	
		<i>q</i>	δq	<i>q</i>	δq	<i>q</i>	δq
O ₁ (2f)	HF	-1.246	+0.117	-1.141	+0.236	-1.11	+0.21
	PBE0	-1.004	+0.178				
O ₄ (3f)	HF	-1.378	-0.015			-1.34	-0.02
	PBE0	-1.204	-0.022				
Ti ₂ (5f)	HF	+2.695	-0.031	+2.635	-0.119	+2.61	-0.03
	PBE0	+2.307	-0.056				
Ti ₃ (6f)	HF	+2.691	-0.035	+2.624	-0.127	+2.52	-0.12
	PBE0	+2.317	-0.046				

^a 5 Ti-layers, see ref 18. ^b 11 Ti-layers, see ref 29. ^c Charge variation δq defined as $q^{\text{surf}} - q^{\text{bulk}}$. Values computed with an *extrafine* integration grid on a 9 Ti-layers slab.

1. Mulliken Charges Analysis. Mulliken atomic charges are collected in Tables 5 and 6 for rutile (110) and anatase (101), respectively. From these data it is clear that both slabs have a strong covalent character, lower in anatase (101) than in rutile (110). Furthermore, and in agreement with what has already been pointed out for bulk structures,⁵³ HF provides

Table 9. Mulliken Atomic Charges (q) and Charge Variation (δq) (in $|e^-|$) for the Undercoordinated and Fully Coordinated Ti and O Atoms of the Anatase (101) Surface^b

		this work		B3LYP ^a	
		q	δq	q	δq
O ₁ (2f)	HF	-1.219	+0.127		
	PBE0	-0.998	+0.162	-0.64	-0.21
O ₃ (3f)	HF	-1.408	-0.062		
	PBE0	-1.226	-0.066	-0.85	0.00
O ₄ (3f)	HF	-1.373	-0.027		
	PBE0	-1.196	-0.036	-0.85	0.00
Ti ₂ (5f)	HF	+2.654	-0.039		
	PBE0	+2.265	-0.055	+1.56	+0.15
Ti ₅ (6f)	HF	+2.678	-0.015		
	PBE0	+2.295	-0.025	+1.64	+0.07

^a 4 Ti-layers, see ref 52. ^b Charge variation δq defined as $q^{\text{surf}} - q^{\text{bulk}}$. Values computed with an *extrafine* integration grid on a 10 Ti-layers slab.

a more ionic picture than PBE0. More than absolute atomic charge values, an easily accessible and more informative feature is the atomic charge variation from bulk to surface (δq), defined as $q^{\text{surf}} - q^{\text{bulk}}$. From the computed δq values, and independently of the computational protocol applied, it is clear that the atomic charge relaxation is very small for all atoms, except for the twofolded oxygens. Furthermore, these atoms are the only ones exhibiting a decrease of their net charges when going from their bulk to slab coordination (threefold to twofold coordination). Actually, a charge reorganization occurs between twofolded oxygen atoms (losing net charge) and neighboring atoms (increasing their net charges). Finally, all q and δq values reported are in line with previously published data,^{18,29} except for the hybrid data

on the anatase (101) slab where our δq behavior is unexpectedly opposite to the one computed by Beltrán et al.⁵²

2. Band Gaps. Band gaps calculations in solids and surfaces still represent a computational challenge for DFT approaches. As it is well-known, LDA and GGA approaches significantly underestimate band gap in solids, as recently shown for instance for TiO₂ bulk.^{53,71} This problem can be corrected at these levels of theory by introducing an atomic parameter, which eventually can be tuned on experimental energies.⁷² More interesting, significant improvements over the GGA results can be directly obtained using hybrids functionals developed (or tuned) for molecular properties. This is the case for instance of the B3LYP or PBE0 approaches.^{53,73} In such cases, the gaps are overestimated (between 0.6 and 1.0 eV for TiO₂ bulk), due to the significant amount of HF exchange.⁵³ The reduction of this latter parameter leads to a better agreement with the experimental data, but, beyond the semiempirical flavor of the parametrization procedure, structural parameters are predicted with larger errors.⁵³ More recently, two new classes of hybrid functionals, namely local and range-dependent hybrids, have been developed and tested on molecular properties and solids.^{74–76} In particular, local hybrid functionals correct the overshooting obtained with the traditional hybrids, but they can also lead in some cases to significant underestimation of the gap, as in ZnO.⁷⁷ To the best of our knowledge, only one study, dealing with TiO₂ bulk properties, has been carried out at such level of theory.⁷⁸ Here, the overshoot has been significantly improved. However, such methods are not yet deeply tested or commonly available.

Figure 8 presents the variation of minimal band gaps and valence band widths as a function of the number of Ti-layers in the slabs. With regards to the band gaps, for the two

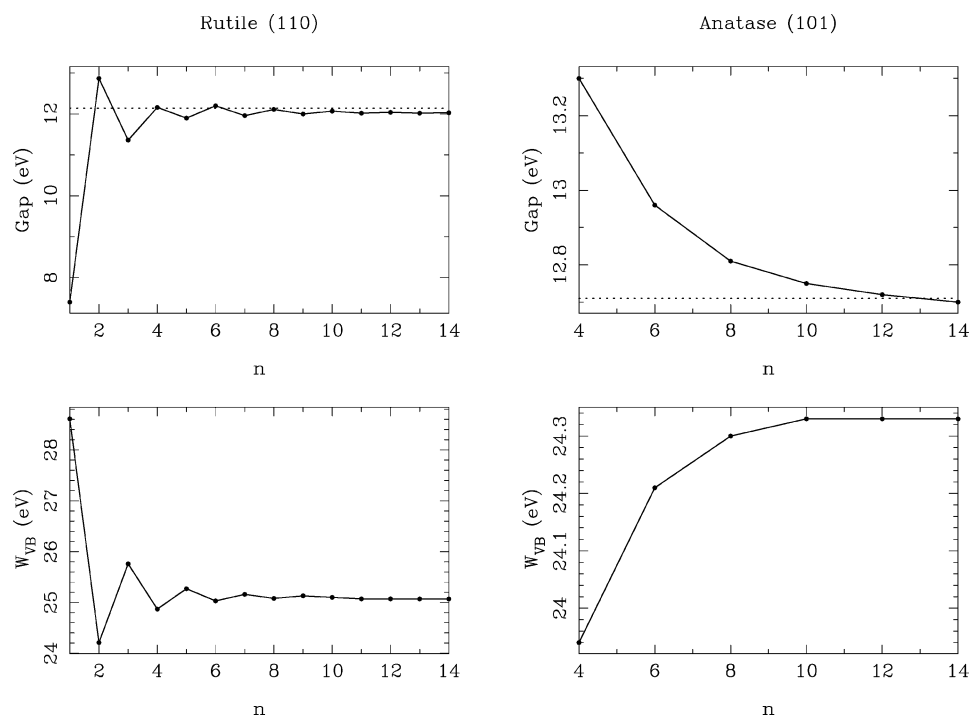


Figure 8. Minimal band gaps (top graphs) and valence band widths (bottom graphs) as a function of the number n of Ti-layers for the rutile (110) and anatase (101) surfaces. Values computed in HF with an *extrafine* integration grid. Dotted lines correspond to bulk values calculated with the same computing conditions.⁵³

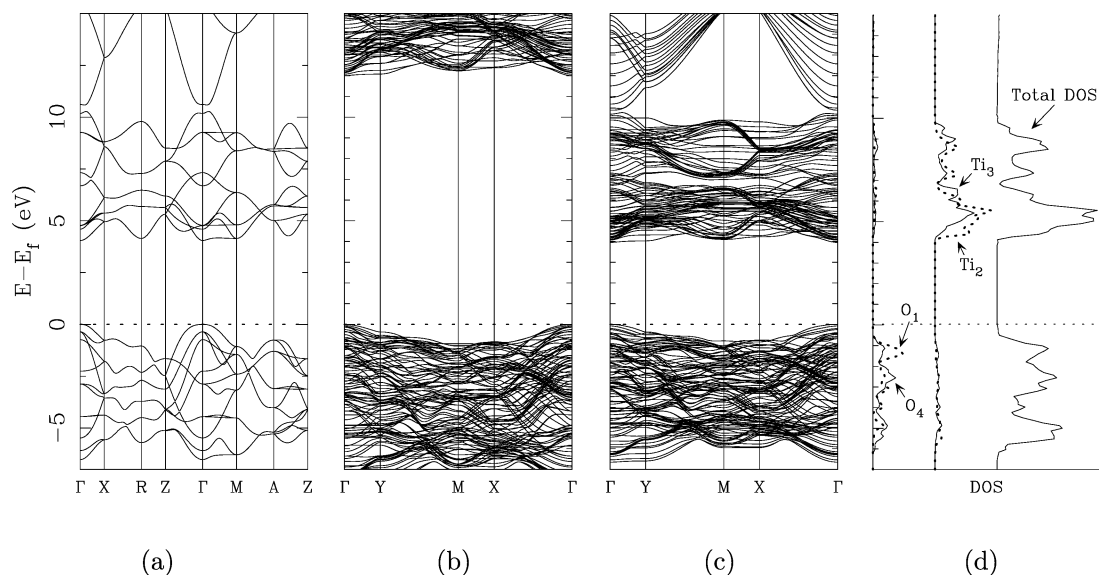


Figure 9. Band structures and DOS of a rutile (110) 9 Ti-layers slab computed in HF (b) and PBE0 (c). The PBE0 band structure of the rutile bulk structure is given in (a) for reference. The DOS and PDOS calculated in PBE0 are shown in (d). The Fermi level is set at 0 eV (dotted lines). All PDOS intensities are multiplied by a factor of 2. Notations correspond to Figure 1.

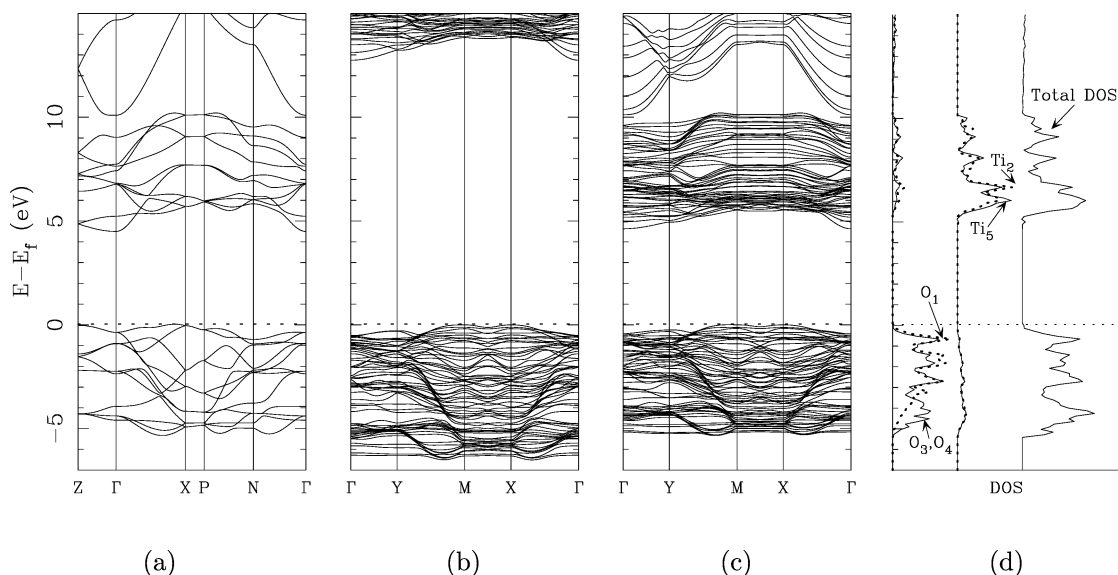


Figure 10. Band structures and DOS of an anatase (101) 10 Ti-layers slab computed in HF (b) and PBE0 (c). The PBE0 band structure of the anatase bulk structure is given in (a) for reference. The DOS and PDOS calculated in PBE0 are shown in (d). The Fermi level is set at 0 eV (dotted lines). Ti and O PDOS intensities are multiplied by a factor of 2 and 4, respectively. Notations correspond to Figure 4.

surfaces investigated in this section, an oscillating trend is only observed for the rutile (110) surface, as already discussed in section IIIB. Nevertheless, in both cases, convergence of the surface band gaps toward the HF bulk gap values (12.14 and 12.71 for rutile and anatase, respectively⁵³) is achieved. Interestingly, in the case of the rutile (110) surface, the oscillating trend reported is exactly opposite to the one obtained for surface energies: the band gaps of the odd Ti-layers slabs converge from below, while those of the even Ti-layers slabs converge from above to the band gap of infinite layers (bulk system). The analysis of the valence bandwidth dependence on the number of Ti-layers reveals that for unconstrained systems (absence of a symmetry plane for an even number of Ti-layers in the slab), the width is lower than for constrained system (presence of

a symmetry plane for odd Ti-layer). This point is in agreement with a previous work by Reinhardt et al.¹⁸ who observed a narrowing of the valence bandwidth in course of the surface relaxation that is to say when going from a constrained to an unconstrained system. We can easily relate this band narrowing to an increase of orbitals hybridization and, more precisely, to a hybridization between O_{2p} and Ti_{3d} orbitals, as pointed out by Bredow et al.²⁸ who found that a rutile (110) slab can “behave” differently as a function of the number of Ti-layers. Indeed, with even Ti-layers, this system can be viewed as weakly interacting bi-Ti-layers, whereas slabs with odd Ti-layers can be considered as truly interacting Ti-layers.

Figures 9 and 10 present band structures as well as densities of states (DOS) and projected-DOS (PDOS) of the

rutile (110) and anatase (101) surfaces calculated both at the HF and PBE0 levels for HF-converged thickness. Since no differences were found between slabs computed at the PBE0 level, using HF or PBE0 structures, the PBE0//HF data are omitted from the figures. Conclusions drawn for the corresponding bulk cases still hold:⁵³ tops of the valence bands (VB) are essentially composed of O_{2p} states with a non-negligible contribution from Ti_{3d} states, whereas the lowest parts of the conduction bands (CB) correspond mainly to Ti_{3d} states, double-peak features for both VB and CB bands (less pronounced for anatase than for rutile), a direct gap at Γ and an indirect one between $\sim X$ and Γ for rutile and anatase, respectively, with overall band structures being flat. From a more quantitative point of view, it is important to note that the gaps computed at the PBE0 level (3.96 and 4.63 eV for rutile (110) and anatase (101), respectively) are in line with corresponding bulk values (4.05 and 4.50 eV for rutile and anatase, respectively). Owing to the presence of undercoordinated atoms on both surfaces, we report herein on the DOS and PDOS computed in PBE0//PBE0. Clearly, for the rutile (110) surface, a shift of both undercoordinated O_{2p} (twofolded) and Ti_{3d} (fivefolded) states toward the band gap is obtained (see Figure 9(d)). Interestingly, in case of the anatase (101) surface, this behavior is not found (see Figure 10(d)), with PDOS of undercoordinated and fully coordinated Ti and O atoms being essentially the same.

IV. Conclusion

In this paper, we have presented a detailed ab initio study of five low-index stoichiometric TiO₂ surfaces. Calculations have been carried out using a periodic approach, at HF, pure, and hybrid DFT levels. Results included surface energies, full-relaxation effects, and electronic properties investigations.

We find our results to be in excellent agreement with most recent publications, both from experimental and theoretical points of view. The relaxation method chosen in this work, that is, fully relaxing slabs in HF and computing single-point energies in DFT from HF-corrected DFT atomic positions, leads to DFT surface energies in agreement with DFT fully relaxed data. Therefore, we were able to confirm the weak sensitivity of atomic displacements to the adopted Hamiltonian. However, displacements as well as surface properties (Mulliken charges and band gaps, in this work) depend strongly on slab thickness. It is therefore important to carefully check convergence of the surface energies before investigating further slab properties.

From a computational point of view, we stress the importance of the accuracy of the calculation of the bielectronic Coulomb and exchange series: convergence of surface energies could only be achieved with an *extrafine* integration grid.⁶⁸ Moreover, we were able to identify the surface relative energies to follow the sequence: anatase (101) < rutile (110) < anatase (100) < rutile (100) \ll rutile (001), both at LDA and HF levels, whereas using PBE, B3LYP, and PBE0, the two most stable surfaces are reversed.

Finally, the oscillating trends of surface energies, band gaps, or atomic displacements with slab thickness are found to be closely related to the presence (absence) of a symmetry plane normal to the surface for odd- (even-) Ti-layers slab for all surfaces. The presence of a symmetry plane results in localized displacements in the top layers and thus higher energies for those constrained systems. From an electronic point of view, a narrowing of the valence band related to an increase of orbital hybridization is observed for unconstrained systems (i.e., without symmetry plane), leading to an oscillation of surface band gaps with slab thickness. Finally, a clear atomic charges reorganization between a slab's topmost atoms is obtained when going from bulk to slab coordination. More precisely, part of the twofolded bridging oxygen atomic charge is redistributed to neighboring atoms for both rutile (110) and anatase (101) surfaces during relaxation.

Acknowledgment. The Crystal team in Torino is acknowledged for technical support. The authors are also grateful to A. V. Bandura and R. A. Evarestov as well as to I. Ciofini and C. Minot for fruitful discussions.

References

- (1) Diebold, U. *Surf. Sci. Rep.* **2003**, *48*, 53.
- (2) Varghese, O. K.; Grimes, C. A. *J. Nanosci. Nanotech.* **2003**, *3*, 277.
- (3) Wu, J. M.; Chen, C. J. *J. Am. Ceram. Soc.* **1990**, *73*, 420.
- (4) Griffin, G. L.; Siefert, K. L. *J. Electrochem. Soc.* **1990**, *137*, 1206.
- (5) Simons, C.; Hanefeld, U.; Arends, I. W. C. E.; Sheldon, R. A.; Maschmeyer, T. *Chem.-Eur. J.* **2004**, *10*, 5829.
- (6) Fujishima, A.; Honda, K. *Nature (London)* **1972**, *238*, 37.
- (7) Kuo, W. S. *J. Environ. Sci. Health B* **2002**, *37*, 65.
- (8) Hagfeldt, A.; Grätzel, M. *Chem. Rev.* **1995**, *95*, 49.
- (9) Kalyanasundaram, K.; Grätzel, M. *Coord. Chem. Rev.* **1998**, *177*, 347.
- (10) Henrich, V. E.; Kurtz, R. L. *Phys. Rev. B* **1981**, *23*, 6280.
- (11) Onishi, H.; Iwasawa, Y. *Surf. Sci.* **1994**, *313*, 1783.
- (12) Murray, P. W.; Condon, N. G.; Thornton, G. *Phys. Rev. B* **1995**, *51*, 10989.
- (13) Diebold, U.; Anderson, J. F.; Ng, K. O.; Vanderbilt, D. *Phys. Rev. Lett.* **1996**, *77*, 1322.
- (14) Charlton, G.; Howes, P. B.; Nicklin, C. L.; Steadman, P.; Taylor, J. S. G.; Muryn, C. A.; Harte, S. P.; Mercer, J.; McGrath, R.; Norman, D.; Turner, T. S.; Thornton, G. *Phys. Rev. Lett.* **1997**, *78*, 495.
- (15) Hird, B.; Armstrong, R. A. *Surf. Sci. Lett.* **1997**, *385*, L1023.
- (16) Bennett, R. A.; Stone, P.; Price, N. J.; Bowker, M. *Phys. Rev. Lett.* **1999**, *82*, 3831.
- (17) Lindsay, R.; Wander, A.; Ernst, A.; Montanari, B.; Thornton, G.; Harrison, N. M. *Phys. Rev. Lett.* **2005**, *94*, 246102.
- (18) Reinhardt, P.; Hess, B. A. *Phys. Rev. B* **1994**, *50*, 12015.
- (19) Ramamoorthy, M.; Vanderbilt, D.; King-Smith, R. D. *Phys. Rev. B* **1994**, *49*, 16721.
- (20) Vogtenhuber, D.; Podloucky, R.; Neckel, A.; Steinemann, S. G.; Freeman, A. J. *Phys. Rev. B* **1994**, *49*, 2099.

- (21) Goniakowski, J.; Holender, J. M.; Kantorovich, L. N.; Gillan, M. J.; White, J. A. *Phys. Rev. B* **1996**, *53*, 957.
- (22) Lindan, P. J. D.; Harrison, N. M.; Gillan, M. J.; White, J. A. *Phys. Rev. B* **1997**, *55*, 15919.
- (23) Bates, S. P.; Kresse, G.; Gillan, M. J. *Surf. Sci.* **1997**, *385*, 386.
- (24) Oliver, P. M.; Watson, G. W.; Kelsey, E. T.; Parker, S. C. *J. Mater. Chem.* **1997**, *7*, 563.
- (25) Bates, S. P.; Kresse, G.; Gillan, M. J. *Surf. Sci.* **1998**, *409*, 336.
- (26) Harrison, N. M.; Wang, X. G.; Muscat, J.; Scheffer, M. *Faraday Discuss.* **1999**, *114*, 305.
- (27) Swamy, V.; Muscat, J.; Gale, J. D.; Harrison, N. M. *Surf. Sci.* **2002**, *504*, 115.
- (28) Bredow, T.; Giordano, L.; Cinquini, F.; Pacchioni, G. *Phys. Rev. B* **2004**, *70*, 035419.
- (29) Evarestov, R. A.; Bandura, A. V. *Int. J. Quantum Chem.* **2004**, *96*, 282.
- (30) Scaranto, J.; Mallia, G.; Giorgianni, S.; Zicovich-Wilson, C. M.; Civalleri, B.; Harrison, N. M. *Surf. Sci.* **2006**, *600*, 305.
- (31) Zhang, Y. F.; Lin, W.; Li, Y.; Ding, K. N.; Li, J. Q. *J. Phys. Chem. B* **2005**, *109*, 19270.
- (32) Murny, C. A.; Hardman, P. J.; Crouch, J. J.; Raiker, G. N.; Thornton, G. *Surf. Sci.* **1991**, *251/252*, 747.
- (33) Murray, P. W.; Leibsle, F. M.; Fisher, H. J.; Flipse, C. F. J.; Murny, C. A.; Thornton, G. *Phys. Rev. B* **1992**, *46*, 12877.
- (34) Hardman, P. J.; Prakash, N. S.; Murny, C. A.; Raiker, G. N.; Thomas, A. G.; Prime, A. F.; Thornton, G.; Blake, R. J. *Phys. Rev. B* **1993**, *47*, 16056.
- (35) Murray, P. W.; Leibsle, F. M.; Murny, C. A.; Fisher, H. J.; Flipse, C. F. J.; Thornton, G. *Phys. Rev. Lett.* **1994**, *72*, 689.
- (36) Murray, P. W.; Leibsle, F. M.; Murny, C. A.; Fisher, H. J.; Flipse, C. F. J.; Thornton, G. *Surf. Sci.* **1994**, *321*, 217.
- (37) Zajonz, H.; Meyerheim, H. L.; Gloege, T.; Moritz, W.; Wolf, D. *Surf. Sci.* **1998**, *398*, 369.
- (38) Raza, H.; Pang, C. L.; Haycock, S. A.; Thornton, G. *Phys. Rev. Lett.* **1999**, *82*, 5265.
- (39) Raza, H.; Pang, C. L.; Haycock, S. A.; Thornton, G. *Appl. Surf. Sci.* **1999**, *140*, 271.
- (40) Lindan, P. J. D.; Harrison, N. M.; Holender, J. M.; Gillan, M. J.; Payne, M. C. *Surf. Sci.* **1996**, *364*, 431.
- (41) Muscat, J.; Harrison, N. M.; Thornton, G. *Phys. Rev. B* **1999**, *59*, 2320.
- (42) Mason, C. G.; Tear, S. P.; Doust, T. N.; Thornton, G. *J. Phys.: Condens. Matter* **1991**, *3*, S97.
- (43) Muscat, J.; Harrison, N. M. *Surf. Sci.* **2000**, *446*, 119.
- (44) Vittadini, A.; Selloni, A.; Rotzinger, F. P.; Grätzel, M. *Phys. Rev. Lett.* **1998**, *81*, 2954.
- (45) Devriendt, K.; Poelman, H.; Fiermans, L. *Surf. Interface Anal.* **2000**, *29*, 139.
- (46) Ruzycki, N.; Herman, G. S.; Boatner, L. A.; Diebold, U. *Surf. Sci.* **2003**, *529*, L239.
- (47) Hebenstreit, W.; Ruzycki, N.; Herman, G. S.; Gao, Y.; Diebold, U. *Phys. Rev. B* **2000**, *62*, R16334.
- (48) Hengerer, R.; Bolliger, B.; Erbudak, M.; Grätzel, M. *Surf. Sci.* **2000**, *460*, 162.
- (49) Lazzeri, M.; Vittadini, A.; Selloni, A. *Phys. Rev. B* **2001**, *63*, 155409.
- (50) Calatayud, M.; Minot, C. *Surf. Sci.* **2004**, *552*, 169.
- (51) Arrouvel, C.; Digne, M.; Breysse, M.; Toulhoat, H.; Raybaud, P. *J. Catal.* **2004**, *222*, 152.
- (52) Beltrán, A.; Sambrano, J. R.; Calatayud, M.; Sensato, F. R.; Andrés, J. *Surf. Sci.* **2001**, *490*, 116.
- (53) Labat, F.; Baranek, Ph.; Domain, C.; Minot, C.; Adamo, C. *J. Chem. Phys.* **2007**, *126*, 154703.
- (54) Beltrán, A.; Gracia, L.; Andrés, J. *J. Phys. Chem. B* **2006**, *110*, 23417.
- (55) Corá, F.; Alfredsson, M.; Mallia, G.; Middlemiss, D. S.; Mackrodt, W. C.; Dovesi, R.; Orlando, R. *Struct. Bonding* **2004**, *113*, 177.
- (56) Saunders, V. R.; Dovesi, R.; Roetti, C.; Orlando, R.; Zicovich-Wilson, C. M.; Harrison, N. M.; Doll, K.; Civalleri, B.; Bush, I.; D'Arco, Ph.; Llunell, M. *Crystal03 User's Manual*; Università di Torino, Torino, 2003.
- (57) Dirac, P. A. M. *Proc. Cambridge Phil. Soc.* **1930**, *26*, 376.
- (58) Vosko, S. H.; Wilk, L.; Nusair, M. *Can. J. Phys.* **1980**, *58*, 1200.
- (59) Perdew, J. P.; Burke, K.; Ernzerhof, M. *Phys. Rev. Lett.* **1996**, *77*, 3865.
- (60) Becke, A. D. *J. Chem. Phys.* **1993**, *98*, 5648.
- (61) Lee, C.; Yang, W.; Parr, R. G. *Phys. Rev. B* **1988**, *37*, 785.
- (62) Adamo, C.; Barone, V. *J. Chem. Phys.* **1999**, *110*, 6158.
- (63) Dovesi, R.; Civalleri, B.; Orlando, R.; Roetti, C.; Saunders, V. R. *Ab Initio Quantum Simulation in Solid State Chemistry I. In Reviews in Computational Chemistry*, 1st ed.; Lipkowitz, K. B., Cundari, T. R., Eds.; Wiley-VCH: New York, 2005; Vol. 21, pp 1–125.
- (64) Doll, K. *Comput. Phys. Commun.* **2001**, *137*, 74.
- (65) Civalleri, B.; D'Arco, Ph.; Orlando, R.; Saunders, V. R.; Dovesi, R. *Chem. Phys. Lett.* **2001**, *348*, 131.
- (66) Four convergence criteria (maximum and root-mean-square (RMS) forces and displacements) are used with default thresholds values of 0.00045, 0.00030 and 0.000180, 0.000120 au, respectively.
- (67) Monkhorst, H.; Pack, J. *Phys. Rev. B* **1976**, *13*, 5188.
- (68) In Crystal, five integers control the accuracy of the calculation of the Coulomb and exchange series, selection of integrals to be computed being performed according to overlap-like criteria (see ITOL keyword in Crystal's manual⁵⁶). Here, the *fine* integration corresponds to the 6 6 6 6 12 settings of the ITOL keyword, while the *extrafine* is 7 7 7 7 14.
- (69) Keller, E. *Schakal99, A Program for the Graphic Representation of Molecular and Crystallographic Models*; Kristallographisches Institut, Universität Freiburg, Freiburg, 1999.
- (70) Burdett, J. K.; Hughbanks, T.; Miller, G. J.; Richardson, J. W.; Smith, J. V. *J. Am. Chem. Soc.* **1987**, *109*, 3639.
- (71) Muscat, J.; Swamy, V.; Harrison, N. M. *Phys. Rev. B* **2002**, *65*, 224112.
- (72) Loschen, C.; Carrasco, J.; Neyman, K. M.; Illas, F. *Phys. Rev. B* **2007**, *75*, 035115.

- (73) Muscat, J.; Wander, A.; Harrison, N. M. *Chem. Phys. Lett.* **2001**, *342*, 397.
- (74) Vydrov, O. A.; Heyd, J.; Krukau, A. V.; Scuseria, G. E. *J. Chem. Phys.* **2006**, *125*, 74106.
- (75) Jacquemin, D.; Perpète, E. A.; Vydrov, O. A.; Scuseria, G. E.; Adamo, C. *J. Chem. Phys.* **2007**, *127*, 94102.
- (76) Heyd, J.; Scuseria, G. E.; Ernzerhof, M. *J. Chem. Phys.* **2003**, *118*, 8207.
- (77) Uddin, J.; Scuseria, G. E. *Phys. Rev. B* **2006**, *74*, 245115.
- (78) Nakai, H.; Heyd, J.; Scuseria, G. E. *J. Comput. Chem. Jpn.* **2006**, *5*, 7.

CT700221W

Properties and 3D Structure of Liquid Water: A Perspective from a High-Rank Multipolar Electrostatic Potential

Steven Y. Liem and Paul L. A. Popelier*

*School of Chemistry, The University of Manchester, Oxford Road, Manchester M13
9PL, Great Britain, and Manchester Interdisciplinary Biocentre (MIB), 131 Princess
Street, Manchester M1 7DN, Great Britain*

Received October 10, 2007

Abstract: We propose a new rigid, nonpolarizable high-rank multipolar potential for the simulation of liquid water. The electrostatic interaction is represented by spherical tensor multipole moments on oxygen and hydrogen, up to hexadecupole. The Quantum Chemical Topology (QCT) method yields the atomic multipole moments from a MP2/aug-cc-p-VTZ electron density of a single water molecule in the gas phase. These moments reproduce the experimental molecular dipole and quadrupole moment within less than 1%. Given its high-rank multipole moments, used in conjunction with a consistent high-rank multipolar Ewald summation, the QCT potential is ideal to assess the performance of exhaustive “gas phase” electrostatics in molecular dynamics simulations of liquids. The current article explores the performance of this potential at 17 temperatures between $-35\text{ }^{\circ}\text{C}$ (238 K) and $90\text{ }^{\circ}\text{C}$ (363 K) and at 7 pressures between 1 and 10 000 atm. The well-known maximum in the liquid’s density at $4\text{ }^{\circ}\text{C}$ is reproduced at $6\text{ }^{\circ}\text{C}$. Six bulk properties are calculated and found to deviate from experiment in a homogeneous manner, that is, without serious outliers, compared to several other potentials. Spatial distribution functions (i.e., $g_{OO}(r, \Omega)$) and the (more common) radial distribution functions are used to analyze the local water structure. At the lone pair side of a central water, neighboring waters form a continuous horseshoe-like distribution, with substantial narrowing in the central part. The latter feature is unique to the QCT potential. Under high pressure, the local structure undergoes dramatic rearrangement and results in the collapse of second shell neighbors into the interstitial region of the first shell, which is in close agreement with experiment. Our results also corroborate the suggestion that the local hydrogen-bonded network remains largely intact even under such conditions.

1. Introduction

Although the properties of liquid water have been the subject of numerous experimental and theoretical studies, this “simple” liquid is still being actively examined. For example, in 2004, Nilsson and co-workers¹ probed the local structure of liquid water by X-ray absorption spectroscopy and X-ray Raman scattering. Perhaps surprisingly their results suggested that most water molecules have only one strong donor and

one strong acceptor hydrogen bond. This picture is in stark contrast with the conventional one of locally tetrahedral liquid structure. Shortly after, Nilsson’s view was challenged by Saykally and co-workers,² who calculated the average number of hydrogen bonds to be 3.3, which is closer to the traditional idea. Nilsson and co-workers then countered this criticism³ but received an immediate reply⁴ from the Saykally group. However, prior to this dispute, both groups could agree⁵ on the presence of such single donor and single acceptor species at the surface of liquid water. This was later

* Corresponding author e-mail: pla@manchester.ac.uk.

confirmed by a Car–Parrinello molecular dynamics study⁶ on the aqueous liquid–vapor interface.

Experimental investigations into the properties of liquid water at nonambient conditions still constitute an area of active research and so does the design of new potentials.⁷ Okhulkov et al.⁸ carried out X-ray scattering studies to examine the structure of liquid at pressures of up to 7.7×10^3 bar. They observed unusual pressure dependence at the shortest intermolecular separation and suggested that under high pressure the second-neighbor shell collapses into the first shell. This explanation was adopted by Eggert et al.⁹ in their recent X-ray diffraction study of liquid water under high pressure. In addition, Eggert et al. also observed a rapid increase in coordination number with pressure. This finding is consistent with the results obtained by Schwegeler et al.,¹⁰ who used first principles molecular dynamics (MD) simulations to study liquid water under pressure.

Experimental studies are rather limited in their ability to depict a detailed picture of the local structure of liquid water. However, molecular simulation techniques are able to produce comprehensive configurational information. Using the SPC/E water potential, Svishchev and Kusalik¹¹ carried out MD simulations to characterize the structure of liquid water by spatial distribution functions (SDF), denoted by $g_{AB}(r, \Omega)$ (where A is always O in our analyses while B can be either O or H . The symbols r and Ω refer to radial and angular coordinates, respectively). Spatial distribution functions contain more information than the more familiar radial distribution functions (RDF), which are obtained from the former by orientational averaging. In their study, SDFs established the precise location of the nearest neighbors, lost in the more familiar RDFs. In a subsequent study, Svishchev and Zassetsky¹² used the polarizable point-charge potential (PPC) function to model liquid water. They performed MD simulations of liquid water and calculated the van Hove function in order to examine the dynamic evolution of the structure of water. The 3D molecular density produced by the polarizable point-charge potential model was consistent with their earlier work¹¹ using the SPC/E model. In addition, they observed that the two H-bond accepting neighbors are less mobile than the H-bond donating neighbors.

Starr et al.¹³ examined the structure of supercooled and glassy water under pressure via MD simulations using the SPC/E potential. They found remarkable agreement with neutron-scattering studies for a wide range of temperatures and pressures. Another study at nonambient conditions was carried out by Kalinichev et al.,¹⁴ who used Monte Carlo (MC) simulations in conjunction with the TIP4P potential and to examine liquid water at pressures up to 10^4 bar. Using density weighted RDFs, they obtained good qualitative and quantitative agreement between simulation and experiment and demonstrated the persistence of a hydrogen-bonded molecular network in water under high pressures.

Our interest in the structure of liquid water was triggered by a concerted effort to design interaction potentials, initially focusing on the electrostatic component, from a theory called Quantum Chemical Topology (QCT).^{15–20} This theory enables an ambiguous partitioning of molecules in atoms, and because of simple atomic additivity, also a partitioning of

van der Waals complexes into their constituent molecules. Work in our group focused on expressing the electrostatic interaction between molecules by atomic QCT multipole moments. Considerable attention^{21–26} was paid to the convergence of the multipole expansion. Geometries of simple van der Waals complexes²³ and natural DNA base pairs²⁷ were successfully predicted with a QCT multipolar potential, including hexadecupole moments. The effects of hydrogen-bonding environment on the polarization and electronic properties of water molecules were also studied²⁸ as well as the asymptotic behavior of the dipole moment of water with increasing water cluster size in liquid water.²⁹ The first dynamical study, using such a high-rank electrostatic QCT potential, appeared³⁰ in 2003, examining liquid HF, soon followed by the first such study on pure liquid water³¹ at ambient conditions. Throughout this article we refer to the latter paper as Paper I.

So far, the repulsive part of the potential has been covered by the Lennard-Jones potential. Our sustained research effort aiming at extraction of *all* contributions to the interaction potential from reduced density matrices demands to abandon those simple potentials ultimately. This will be subject of a future project outside the scope of this paper. Second, polarization is *not* included in the current potential but we presently work on covering it using machine learning. So far, only one simulation³² (on the HF dimer) has been carried out with a polarizable QCT potential, in which neural networks predict atomic multipole moments as a function of the positions of the neighboring atoms.

Here the Coulomb part of the atom–atom interaction is represented by electrostatics only, be it accurate at short range, and in conjunction with a fully multipolar Ewald summation. We stress that the current simulation occurred with rigid water molecules and that no attempt was made to introduce “effective” Coulomb interaction. Indeed, we calculated the wave function of a single water molecule, geometry-optimized it in the gas phase, without artificially enhancing the molecular dipole moment or adding polarizability. The purpose of this study is to assess the overall performance of a potential in which the electrostatic part is parameter-free and “taken to the limit”. In Paper I the assessment of such a potential took place by comparing a number of bulk properties with experiment and by inspecting RDFs. Here, we add a number of bulk properties, but the emphasis is on the inspection of the orientationally nonaveraged structure of liquid water, now explored over a larger portion of the phase diagram. For this purpose the number of temperatures was more than tripled, and the pressure was investigated up to 10^4 atm (approximately 10^4 bar), beyond the previously reported 1 atm.

2. Background and Method

2.1. The QCT Potential. A single water molecule was geometry optimized at the MP2/aug-cc-pVTZ level³³ using GAUSSIAN98,³⁴ yielding an OH distance of 0.9614 Å and an HOH angle of 104.067°. The corresponding electron density yields a molecular dipole moment of 1.852 D (debye) (0.7286 a.u.), which deviates by 0.1% from the oft cited and still quoted experimental value of 1.8546 ± 0.0006 D (0.7297

± 0.0002 a.u.) determined by Stark measurements.³⁵ Although possibly fortuitous, this agreement is excellent in view of the wide range generated by respectable levels of theory.³⁶ For example, a recent CCSD(T) calculation³⁷ with a 9s6p6d3f/6s4p2d1f basis set yielded a dipole moment of 0.7231 a.u. (or 1.838 D), which curiously deviates more from experiment, now by 0.9%. The molecular quadrupole moment at MP2/aug-cc-pVTZ level is 3.604 DÅ (2.679 a.u.), only different by 0.7% from the experimental value of 3.63 ± 0.04 DÅ (2.70 ± 0.03 a.u.), published³⁸ by Verhoeven and Dymanus. The CCSD(T) calculation produces 3.532 DÅ (2.626 a.u.), which is still only 2% different to our level of calculation but almost four times more deviating from experiment than the MP2 calculation.

At this stage of our longer term strategy we can justify the rigid body approach because of the success of other rigid body water potentials.^{39–41} Furthermore, in a dedicated study⁴² on the relative merits of flexible versus rigid models, Tironi et al. highlighted the seriously enhanced computational effort in the presence of high-frequency internal vibrations. They showed that including molecular flexibility and treating it classically does not improve the quality of the models and can even introduce artifacts. This is corroborated by Jorgensen and Tirado-Rives who claim⁴³ that although flexible models have been explored,⁴⁴ classical treatment of the high-frequency vibrations for water is not physically sound. Moreover, Mahoney and Jorgensen stated⁴⁴ that the introduction of quantum mechanical effects alleviates some of the problems created by adding classical flexibility to simple water models, reinforcing the idea that real water is more like rigid water models than classical flexible water models.

Using default parameter values, the program MORPHY98⁴⁵ computes the multipole moments (up to hexadecapole, rank $l = 4$) on each atom from the wave function. This is accomplished via a volume integration⁴⁶ over each atomic basin Ω . An atomic basin is a portion of 3D space spanned by the collection of gradient paths (trajectories of steepest ascent in the electron density) that are attracted to the nucleus.^{15,16,47} The integrand of this volume integration consists of the appropriate spherical tensor ($C(\theta, \varphi)$), weighted by the total charge density $\rho_{tot}(\mathbf{r})$

$$\begin{aligned} Q_{l0} &= \int_{\Omega} d\mathbf{r} \rho_{tot}(\mathbf{r}) r^l C_{l0}(\theta, \varphi) \\ Q_{lmc} &= \int_{\Omega} d\mathbf{r} \rho_{tot}(\mathbf{r}) r^l C_{lmc}(\theta, \varphi) \\ Q_{lms} &= \int_{\Omega} d\mathbf{r} \rho_{tot}(\mathbf{r}) r^l C_{lms}(\theta, \varphi) \end{aligned} \quad (1)$$

where $\rho_{tot}(\mathbf{r}) = \sum_A Z_A \delta(\mathbf{r} - \mathbf{R}_A) - \rho(\mathbf{r})$, Z_A is the charge of nucleus A located at position \mathbf{R}_A , and the functions $C_{lmc}(\theta, \varphi)$ and $C_{lms}(\theta, \varphi)$ are real normalized spherical harmonics of rank l . Other than the atomic charge Q_{00} , there are three dipole moments ($l=1$), denoted by Q_{10} , Q_{11c} , and Q_{11s} , which correspond to the Cartesian components μ_z , μ_x , and μ_y , respectively. Instead of the redundant six Cartesian quadrupole moments there are only five spherical-tensor quadrupole moments ($l=2$), denoted Q_{20} , Q_{21c} , Q_{21s} , Q_{22c} , and Q_{22s} . There are seven octopole moments ($l=3$) and nine hexadecapole moments ($l=4$). The values for all moments are listed

in Table S1 as Supporting Information. We note that our potential shares its multipolar character with Stone's ASP-W2 potential.⁴⁸

The total potential energy (E_{pot}) between any two water molecules has two contributions

$$E_{pot} = E_{elec} + 4\epsilon \left[\left(\frac{\sigma}{r_{OO}} \right)^{12} - \left(\frac{\sigma}{r_{OO}} \right)^6 \right] \quad (2)$$

where E_{elec} corresponds to the electrostatic interaction energy between two water molecules, and r_{OO} is the distance between the two oxygen nuclei. The other contribution is the Lennard-Jones term, containing ϵ and σ , which are the familiar well depth and collision diameter. These are the only two parameters in E_{pot} , and they were fitted to both the density of liquid water and the shape of experimental RDFs at 298 K and 1 atm. The collision diameter turned out to be 3.140 Å and the well depth 0.753 kJ/mol. The two geometric parameters describing the (symmetric) rigid water molecule were fixed at the values mentioned above. The values of the two geometric and two Lennard-Jones parameters are the same as in paper I.

The E_{elec} term can be evaluated from eq 3

$$E_{elec} = \frac{1}{2} \sum_A \sum_{B \neq A} E_{elec}(A, B) \quad (3)$$

where A and B are oxygen or hydrogen atoms, each belonging to different water molecules. In a previous publication²³ we explicitly showed that eq 3 can be re-expressed in terms of a multipole expansion as follows

$$E_{elec}(A, B) = \sum_{l_A l_B m_A m_B} T_{l_A l_B m_A m_B} Q_{l_A m_A}(\Omega_A) Q_{l_B m_B}(\Omega_B) \quad (4)$$

where $T_{l_A l_B m_A m_B}$ is a purely geometric interaction tensor, only depending on the relative orientation of the local frames centered on each nucleus and their internuclear distance, and Q_{lm} are the $2l+1$ multipole moments of rank l with respect to the local frames. The (expansion) rank $L = l_A + l_B + 1$ is typically used to monitor the convergence of an atom-atom electrostatic interaction energy. In Paper I it was shown that L needs to be at least equal to 5 to observe liquidlike behavior, based on oxygen-oxygen pair distribution functions $g_{OO}(r)$. If DLMULTI were (substantially) modified to handle L values larger than 6, which is a major project, then bulk properties could be more completely monitored for convergence. However, we have implemented an open-ended electrostatic interaction code that enables the evaluation of eq 4 for arbitrary rank L . We showed before⁴⁹ that the atom-atom interaction energy profile versus L of a typical O and H in the hydrogen bond between two water molecules in the water dimer had definitely converged at $L = 5$.

2.2. Simulation Details. As with our previous water simulation, the MD simulation was carried out by the DLMULTI program, which is a modified version of the DLPOLY code.^{50,51} A major feature of DLMULTI is the derivation and implementation (by Dr. M. Leslie formerly at Daresbury Labs) of an Ewald summation, generalized beyond point charges, to high rank multipole moments. This Ewald summation is completely consistent with the spherical

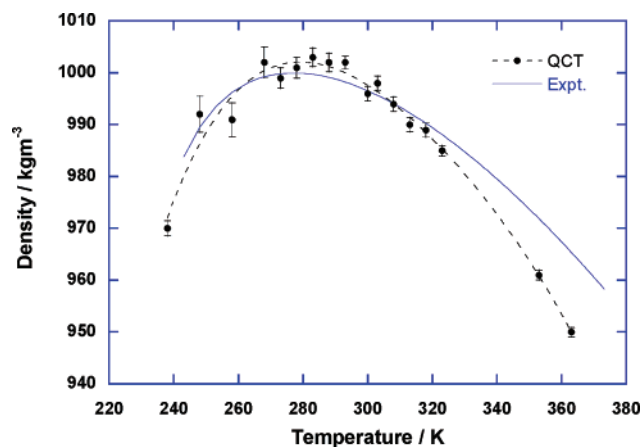


Figure 1. Density of simulated water at 1 atm compared to experimental value.

tensor formalism, which is the basis of the interaction within the simulation box. DLMULTI calculates the long-range contribution of all multipole–multipole interactions using this Ewald summation. A cubic primary cell with full periodic boundary conditions, containing $216 = 6^3$ water molecules, was used for all simulations. Paper I showed that this size is large enough to achieve insignificant system size dependence. We imposed a cutoff distance of 2.5σ for the Lennard-Jones interaction between oxygen atoms. The time-step size used to integrate the equations of motion was 0.5 fs. The results presented in this article are averaged from run lengths of at least 300 ps after an equilibration period of 20–50 ps.

2.3. Analysis of Bulk Properties. In Paper I we already defined and discussed the isobaric heat capacity (C_p), the thermal expansion coefficient (α), the self-diffusion coefficient (D), and the temperature of maximum density. In this study, we evaluated three additional properties of liquid water, namely the constant temperature heat capacity (C_v), the isothermal compressibility (κ_T), and the shear viscosity (η). The constant temperature heat capacity can be calculated from eq 5

$$C_v = \left(\frac{\partial E}{\partial T} \right)_P \quad (5)$$

where E , p , and T are the total energy, temperature, and pressure of the system, respectively. The isothermal compressibility κ_T can be evaluated from eq 6

$$\kappa_T = -\frac{1}{V} \left(\frac{\partial V}{\partial p} \right)_T \quad (6)$$

where V is the volume of the system. The shear viscosity was evaluated from a NVT simulation using the Einstein relation, eq 7,

$$\eta = \frac{1}{2} \frac{V}{k_B T} \lim_{t \rightarrow \infty} \frac{d}{dt} \langle \Delta P_{\alpha\beta}^2(t) \rangle \quad (7)$$

where $\alpha\beta = xy, xz, yz$ and $\Delta P_{\alpha\beta}(t)$ is the “displacement” of $P_{\alpha\beta}(t)$, which is given by eq 8

$$\Delta P_{\alpha\beta}(t) = \int_0^t P_{\alpha\beta}(t') dt' \quad (8)$$

where $P_{\alpha\beta}(t)$ is the off-diagonal elements of the pressure tensor.⁵²

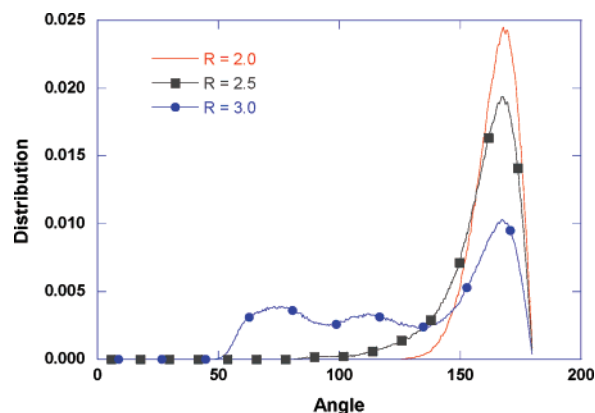


Figure 2. Comparison of the distribution of O–H...O angles at 300 K using different cutoff values for the O...H distances (in Å).

Table 1. Calculated and Experimental Properties of Liquid Water at 300 K (27 °C) and 1 atm

property	QCT	expt	% Δ^e
temperature of maximum density (°C)	6.	4. ^a	-
$D/\times 10^9 \text{ m}^2 \text{ s}^{-1}$	1.44	2.30 ^b	-37
$\alpha/\times 10^5 \text{ K}^{-1}$	28	27.6 ^a	1
$\kappa_T/\times 10^6 \text{ atm}^{-1}$	38	45.6 ^a	-17
$C_p/\text{J K}^{-1} \text{ mol}^{-1}$	82	75.3 ^c	9
$C_v/\text{J K}^{-1} \text{ mol}^{-1}$	106	74.4 ^c	42
density/kg m^{-3}	996.0	996.5 ^a	-
η/cp	1.2	0.85 ^c	41
enthalpy/kJ mol^{-1}	-42.7	-41.5 ^d	-3

^a Reference 58. ^b Reference 72. ^c Reference 73. ^d Reference 74. ^e Percentage deviation from experiment defined as $100(x_{\text{comp}} - x_{\text{exp}})/x_{\text{exp}}$ where x is an experimental or computed property.

2.4. Analysis of Local Structure. The short-range structure in liquid water has been examined by various analysis techniques. These include the RDF $g(r)$, the coordination number $n(r)$, intermolecular structural properties (e.g., angles, distances), and three-dimensional SDFs. The latter tool was employed by Svishchev and Kusalik¹¹ to examine the structure of water using the SPC/E potential. It is a measure of the distribution of neighboring molecules (or a specific type of atoms) around a central molecule. SDFs give a detailed description of the immediate environment adjacent to a molecule by utilizing distribution functions that span both the radial and angular coordinates of the separation vector between species of interest.

Here we describe the procedure of evaluating the SDF of oxygen–oxygen, $g_{OO}(r, \Omega)$. The term *system* refers to the simulation box (which contains 216 molecules). Each molecule in the system is designated as the “central molecule”, one at a time. Since we are interested in the immediate environment of the central molecule, we impose a distance-based selection criterion in order to identify the neighbors. The cutoff distance for the O...O separation was chosen to be 3.5 Å, which is the location of the first minimum in $g_{OO}(r)$. For an arbitrary configuration (“snapshot”) of the system, the neighbors of the central molecule are examined. This examination warrants a common reference orientation for each central molecule and its environment. This is achieved by translating and rotating the system

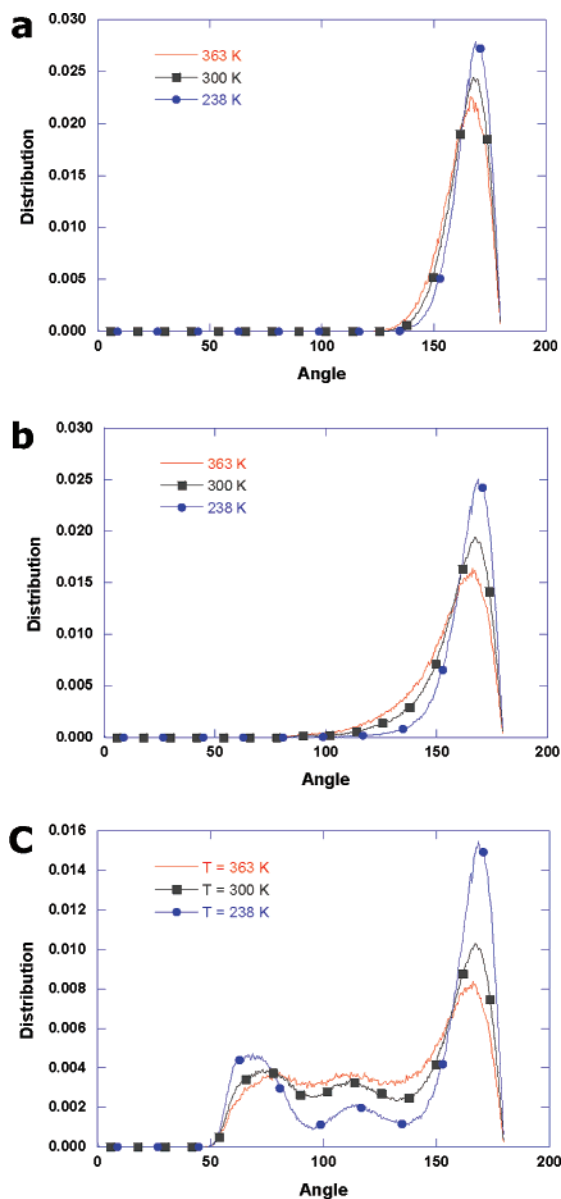


Figure 3. Comparison of the distribution of O–H...O angles at different temperatures. The cutoff distances are (a) 2.0 Å, (b) 2.5 Å, and (c) 3.0 Å.

such that the oxygen atom of the selected central molecule lies at the origin of the system, one O–H bond coincides with the X-axis, and the other O–H bond lies in the XY plane. As a result, all neighboring molecules are viewed from the same perspective. Subsequently, the spherical volume (with radius 5.5 Å) is partitioned into small “grid elements”, by installing a 3D grid centered at the central oxygen. Typically there are $110 \times 110 \times 110$ such grid elements. Then a frequency counter determines the number of oxygens (belonging to neighboring molecules) that are located within each grid element. When all molecules in the system are examined, each being a central molecule in turn, the frequency of oxygen atoms appearing in each grid element, n_o , is known. In order to obtain a distribution of oxygens around a *single* central molecule, this frequency needs to be normalized by the number of oxygen atoms in the system, N_o . The value n_o/N_o then gives the desired mean frequency of neighboring oxygens located around the oxygen of a *single*

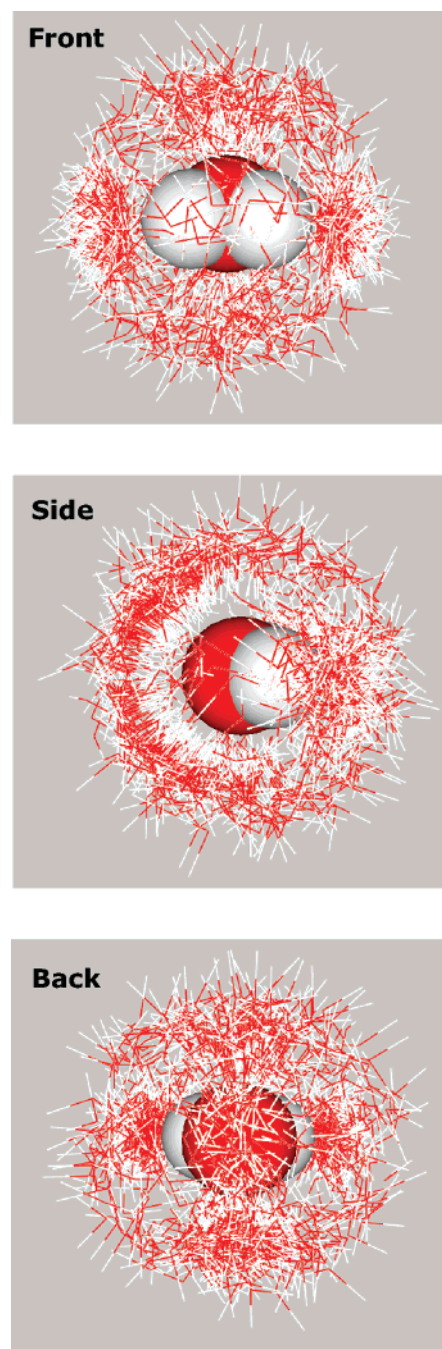


Figure 4. Location of neighboring molecules adjacent to each molecule in the system. Three different views are presented: front, side, and back view.

central molecule. This process can be repeated for all configurations generated from a MD run. However, it is more sensible to use a portion of these configurations (e.g., every 500th configuration). The value n_o is then incremented over all selected configurations. In order to correct for this accumulation, n_o must be divided by the number of configurations included in the evaluation, N_c , resulting in $n_o/[N_oN_c]$.

Finally, the average number of oxygen atoms appearing in each grid element is given by $[N_oV_{elem}]/V_{sys}$ where V_{elem} is the volume of the grid element (assuming a homogeneous distribution of oxygen atoms in the system), and V_{sys} is the volume of the system. We used this factor to normalize the

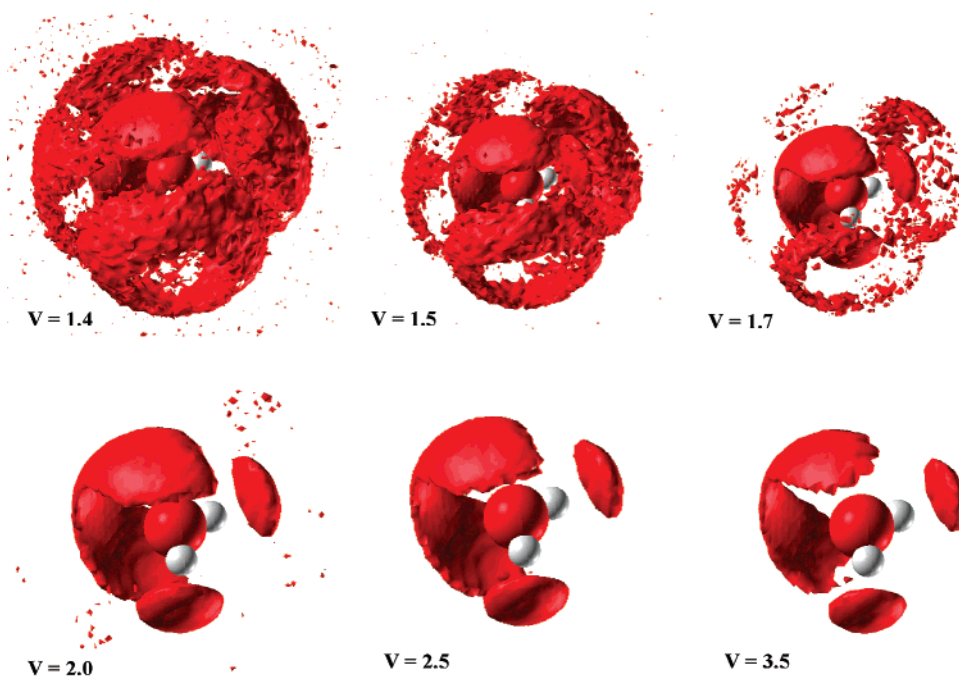


Figure 5. Six different isovalues of the SDF illustrating the variation in the immediate environment of a central water molecule (plotting scales adjusted visually).

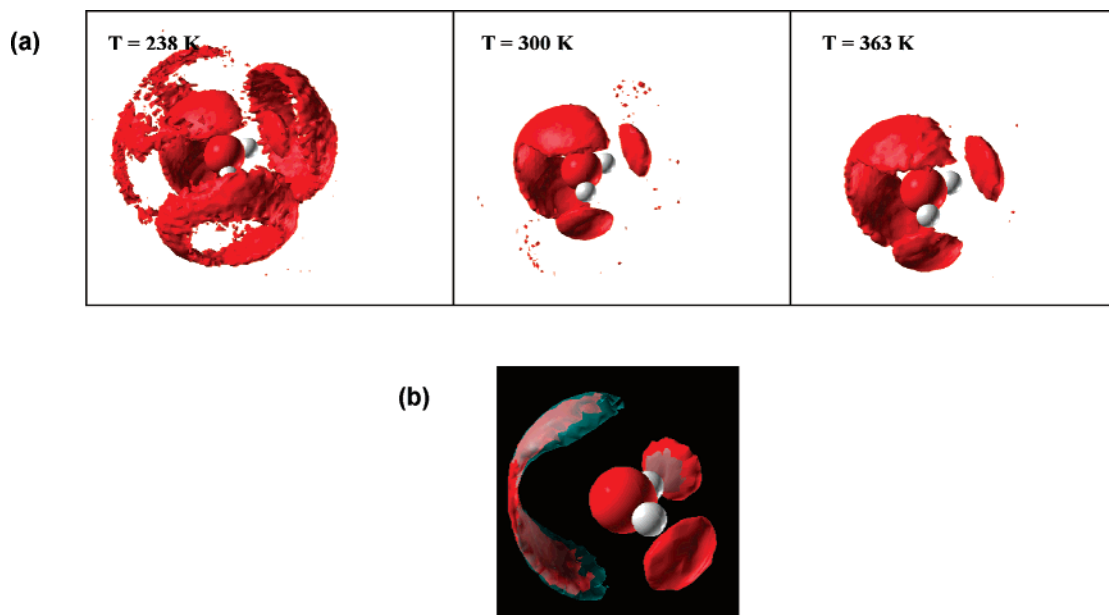


Figure 6. (a) SDF isosurfaces with a value of 2.0 illustrating the variation of the immediate environment of a central water molecule at different temperatures (plotting scales adjusted visually). (b) Comparison of spatial distribution functions of oxygen atoms (showing the first shell neighbors only) $g_{OO}(r,\Omega)=2$, at two different temperatures, 238 K ($-35\text{ }^{\circ}\text{C}$) (cyan) and 363 K ($90\text{ }^{\circ}\text{C}$) (red) (at 1 atm).

mean value, $n_O/[N_O N_C]$, to give a value that is relative to the mean oxygen density of the system. The final quantity, $g_{OO}(r,\Omega)$, is then defined in eq 9. If the grid element size is sufficiently small, then the density function $g_{OO}(r,\Omega)$ appears continuous and meaningful constant-density envelopes can be plotted, as shown in Figures 5, 6, and 9.

$$g_{OO}(r,\Omega) = \frac{n_O}{N_O N_C} \left[\frac{N_O V_{elem}}{V_{syst}} \right]^{-1} \quad (9)$$

The corresponding formula for $g_{OH}(r,\Omega)$ can be easily obtained by replacing n_O by n_H in eq 9, where n_H is the frequency of hydrogen atoms appearing in each grid element. Second, N_O must be replaced by N_H , the number of hydrogen atoms in the system.

3. Results and Discussions

Compared to the NPT simulations of liquid water at ambient pressure in Paper I we extended the temperature range from

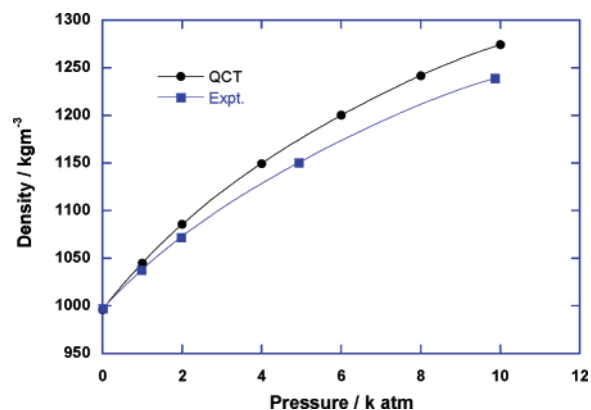
Table 2. Averaged System Density and Calculated Diffusion Coefficient at 300 K at Various Applied Pressures

pressure/atm	density/kgm ⁻³	$D/\times 10^9 \text{ m}^2 \text{ s}^{-1}$
1	996	1.44
1000	1045	1.53
2000	1086	1.42
4000	1149	1.11
6000	1200	0.88
8000	1242	0.70
10000	1274	0.58

238 K to 363 K (−35 °C to 90 °C) with runs at 17 different temperatures. We also conducted several NVT simulations in order to calculate the constant volume heat capacity. Finally, we performed NPT simulations at nonambient pressures (between 1 and 10 000 atm at 300 K, 7 pressures in total) in an attempt to understand the effect of pressure on the structure of liquid water.

3.1. Simulations at Ambient Pressure. *3.1.1. Bulk Properties.* The various properties evaluated from the ambient pressure simulations (1 atm, 300 K) are summarized in Table 1. The variation of the density of the system as a function of temperature is shown in Figure 1 (numerical values in Table S1). The graph clearly shows the existence of a temperature of maximum density at around 280 K. By numerically differentiating a fitted fourth order polynomial, the maximum is determined to be 279 K (6 °C). This maximum is not affected by the presence of the error bars. This value deviates by only 2 °C from the well-known experimental value of 277 K (4 °C). The availability of simulation runs at 12 extra temperatures, compared to the 5 runs of Paper I, improved the quality of the prediction. Indeed, in Paper I the rather slowly converging property of maximum density temperature was overestimated by about 10 °C. When comparing the overall shape of the experimental and simulated density-versus-T curves in this work, the density of the simulated water decreases at a faster rate at both ends of the temperature range (i.e., the curvature of the simulated curve is larger). However, Monte Carlo simulations (at 1 atm) carried out⁵³ for the SPC and TIP3P models showed no maximum at all within the [−50 °C, 100 °C] interval. The TIP4P model put the maximum at −15 °C (258 K), SPC/E at −38 °C (235 K).⁵⁴ In contrast, the TIP5P model, which was specifically designed to correctly predict the temperature of maximum density, does indeed reproduce the correct value of 4 °C at 1 atm.

The self-diffusion coefficient D deviates slightly more from the experimental value compared to Paper I, where $D = 1.5 \times 10^{-9} \text{ m}^2 \text{ s}^{-1}$ was reported. Nevertheless, the current 37% deviation from experiment is still respectable compared to other potentials, which yield values varying from 1.9 (TIP4P-FQ) to 5.2 (TIP3P). Popular point charge models such as TIP3P, TIP4P ($D = 3.3 \times 10^{-9} \text{ m}^2 \text{ s}^{-1}$) and SPC ($D = 3.9 \times 10^{-9} \text{ m}^2 \text{ s}^{-1}$) all substantially overestimate D . The TIP5P model predicts D to be $2.6 \times 10^{-9} \text{ m}^2 \text{ s}^{-1}$, which is only 12% off, and SPC/E scores well with $D = 2.5 \times 10^{-9} \text{ m}^2 \text{ s}^{-1}$. Chaplin provides a continuously updated Web site⁵⁵ comparing a large number of potentials in terms of their performance in predicting bulk properties. In 2002, Guillot⁴⁴

**Figure 7.** Density of simulated water at different pressures compared to experimental value.

compared the self-diffusion coefficient of 32 water potentials and found that about 40% overestimated its value, about 40% underestimated it, whereas about 20% predicted it correctly. The addition of quantum effects^{43,56,57} is known to increase the value of D substantially. Thus it is promising that the QCT model underestimates D , in the absence of quantum effects.

The thermal expansion coefficient, α , has considerably improved compared to Paper I, where it was reported as $35 \times 10^{-5} \text{ K}^{-1}$. Now referring to an experimental⁵⁸ value, evaluated exactly at 300 K (27 °C), the current re-evaluation of α coincides with the experimental value. Other well-known potentials and their recent modifications always overestimate α , sometimes by more than 200%. For example, at 25 °C, TIP3P, TIP4P, and TIP5P predict⁵⁹ it to be 92, 44, and 63, respectively. In the SPC series, SPC, SPC/E, SPC/A, SPC/L,⁴¹ COS/B2, COS/G2, and COS/G3⁶⁰ predict α to be 73, 56, 80, 75, 97, 57, and 70, respectively, at 300 K (27 °C).

The isothermal compressibility, κ_T , predicted by QCT to be $38 \times 10^{-6} \text{ atm}^{-1}$, turns out to underestimate experiment by 17%. From the TIPnP series of potentials, only the TIP5P value of $41 \times 10^{-6} \text{ atm}^{-1}$ comes closer to experiment than the QCT potential, the other TIP potentials overestimating experiment by at least 40%. The SPC series mentioned above predicts values from 39.5 to $51.7 \times 10^{-6} \text{ atm}^{-1}$ and hence scores better than QCT. It is conceivable that a κ_T value computed from QCT simulations at more than 7 different pressures may lead to better agreement with experiment.

The heat capacity at constant pressure, C_p , is a property that clearly benefited from the extra simulation runs at 12 new temperatures. Once predicted to be $105 \text{ J mol}^{-1} \text{ K}^{-1}$ in Paper I, it is now $82 \text{ J mol}^{-1} \text{ K}^{-1}$, overestimating experiment by only 9%. Whereas TIP5P predicted the best κ_T value (out of the TIPnP series), it now predicts the worse C_p value, that is, $122 \text{ J mol}^{-1} \text{ K}^{-1}$, which deviates from experiment by 62%. The SPC model is able to match experiment virtually perfectly, but its recent modifications (mentioned above) overestimate experiment with a value as high as $94.1 \text{ J mol}^{-1} \text{ K}^{-1}$.

The heat capacity at constant volume, C_v , again suffers from the more modest number of pressures at which simulations were conducted. As a result, the QCT prediction

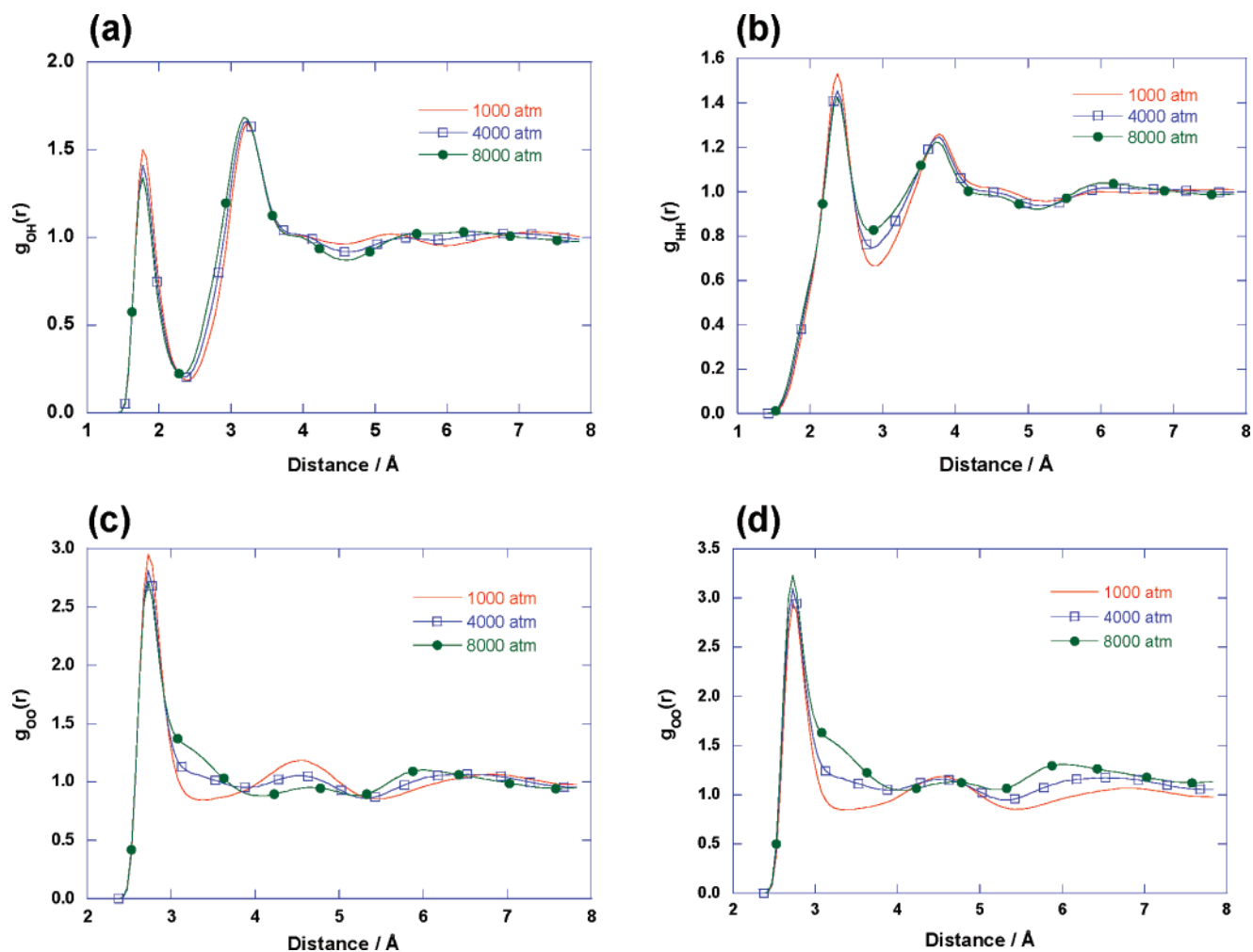


Figure 8. Comparison of RDFs at three different pressures. (a) OH, (b) HH, (c) OO, and (d) density-weighted ("normalized") OO.

of $106 \text{ J mol}^{-1} \text{ K}^{-1}$, is expected to deviate substantially from experiment. Indeed, it does so by 42%. The papers we consulted for the results of familiar potentials, as discussed above, do not report C_v .

The QCT potential predicts shear viscosity (η) only moderately well, overshooting experiment by 41%. However, the SPC model performs equally poor, undershooting experiment by 42%. Only SPC/E does substantially better, predicting a value of 0.91 cp, which is only 7% off the experimental value of 0.85 cp. The TIP5P model predicts 1.49 cp, which is 75% off.

3.1.2. Structure. The local structure of the liquid water was examined by monitoring the distribution of O–H...O angles and the SDFs. The distribution of the O–H...O angle was computed by calculating the angle formed by an H atom from a neighboring molecule with the O–H bond from a given central molecule. We selected neighboring molecules by setting the cutoff values for the O...H distance to 2.0, 2.5, and 3.0 Å. Figure 2 illustrates the variation in the distribution of the O–H...O angle for these three cutoff distances. For 2.0 Å, the distribution is a single well-defined peak centered at approximately 169° . The peak is slightly skewed to the left and tails off rapidly for values smaller than 150° . At the cutoff of 2.0 Å, most water pairs can be

regarded as hydrogen bonded to each other. The distribution at the 2.5 Å cutoff is similar, but the tailing off (at the left of the maximum) is slower. This follows from the fact that the maxima of the two peaks, 2.5 Å and 2.0 Å, practically coincide but the angle at which the distribution vanishes is 86° and 127° , respectively. The distribution for the largest cutoff of 3.0 Å is qualitatively different from the two others. Now there are smaller peaks left of the main one, at angles well below 150° , one centered at 113° and the other at 74° .

The effect of temperature (238, 300, and 363 K) on the O–H...O angle distribution is shown in Figure 3. As expected, the height of the peak near 170° decreases with increasing temperature for all three O...H distance cutoff values. Also, the peaks broaden, while the tail ends located between 50 and 150° become less well defined. The impact of temperature rise is significantly smaller for shorter cutoffs.

A direct way to analyze the local structure of liquid water is visualizing a snapshot of the simulated system. Figure 4 shows the location of neighboring molecules adjacent to each molecule in the system. This picture is generated by selecting all neighboring molecules with a O...O distance of less than 3.5 Å from the central molecule. Note that each selected "central molecule" was rotated and translated (together with the neighbors) to coincide with the position of the large

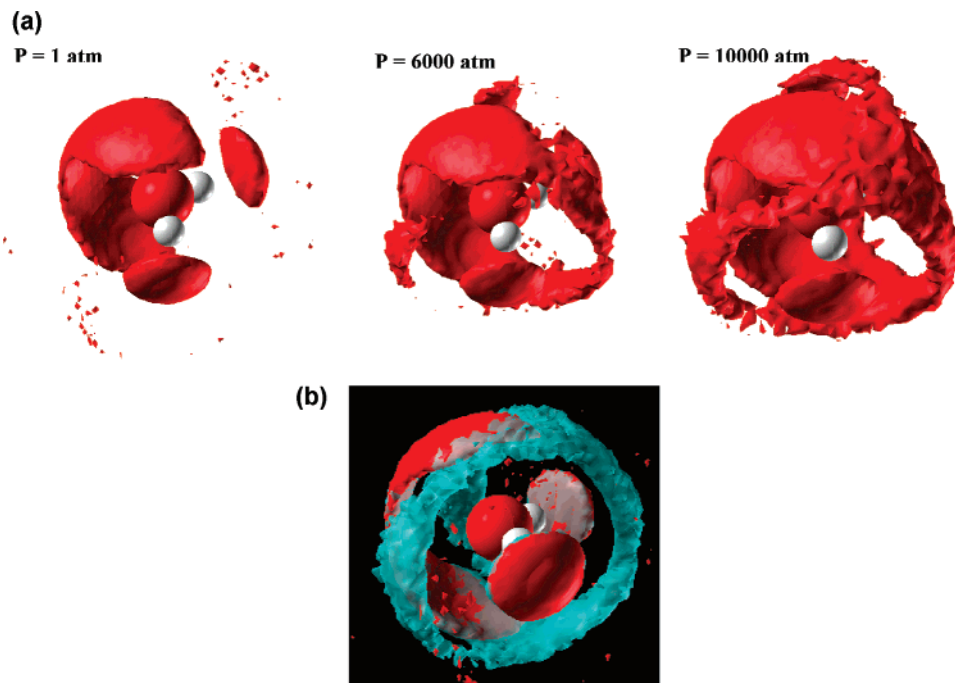


Figure 9. (a) SDF isosurfaces with a value of 2.0 ($g_{OO}(r, \Omega)=2$) illustrating the variation of the local environment of a central water molecule at three different pressures (plotting scales adjusted visually). (b) Comparison of spatial distribution functions of oxygen atoms (showing the 1st shell neighbors only) at two different pressures, 10 000 atm (cyan) and 1 atm (red) (at 300 K).

molecule in the center of Figure 4a–c. Neighbors are concentrated in three regions of space around the central water molecule. Two regions are adjacent to hydrogen atoms of the central water. These regions consist of molecules acting as hydrogen bond acceptors to the central water molecule. The third region encircles the lone pair zone of the central oxygen in the shape of a horseshoe. The “side view” of Figure 4 gives the clearest image of this region, which consists of donor molecules forming hydrogen bonds with the central oxygen atom. This continuous distribution is in agreement with Finney’s observation⁶¹ that the negative charge around the oxygen atom should be regarded as a single (contiguous) zone rather than as two distinguished lobes.

In contrast with many familiar water potentials, the width of the “horseshoe” narrows gradually but significantly toward the middle part, in the plane of the central water molecule (see “back view”). To the best of our knowledge, this feature has not been observed in other water (traditional) potentials. Alternative potentials, such as PPC,^{12,62} SPC/E,¹¹ and TIP4P,⁶³ typically show a *widening* in the middle region. We believe that this is a direct consequence of the multipole nature of our potential, whose improved directionality results in accurate geometry prediction of small water clusters.⁶⁴ Consequently, we believe this is a genuine structural property for liquid water. It should be noted that in the space between these three regions, the existence of water molecules is significantly less likely but not negligible.

An alternative way of examining the local structure is to use the SDFs where the distribution and number of adjacent molecules (in our case oxygen atoms actually) are represented by isosurfaces of specific values. A higher isovalue means a higher oxygen and hence water concentration. Figure

5 shows the distribution at six different isovalues, i.e., 1.4, 1.5, 1.7, 2.0, 2.5, and 3.5. For isovalues above 2.0, the information deduced from the isosurfaces is essentially identical to that in Figure 4, apart from the fact that the three regions are more readily identifiable. For lower values, molecules further away from the central molecule start to appear, corresponding to the second shell of oxygen atoms. This secondary structure becomes more notable at the 1.4 and 1.5 isovalues. Two separate circular rings appear, each centered on a “flattened sphere” (consisting of acceptor oxygens) next to each of the hydrogen atoms of the central water. The secondary structure adjacent to the “horseshoe” shaped region appears as a pair of “wings”.

Let us focus on the relationship between oxygens in a circular ring and oxygens in the flattened sphere beneath it. In particular, we ask if such pairs of oxygen atoms are hydrogen-bonded. A natural criterion to decide on this question is knowledge of the average O...O distance. We know from the $g_{OO}(r)$ curves (Figure S2 in the Supporting Information and also Figure 8c) that hydrogen-bonded oxygens are separated by approximately 2.7 Å and definitely less than 3 Å. Figure 4 enables the measurement of O...O distances, and via the straightforward correspondence between Figures 4 and 5 we can infer distances in Figure 5. Distances between the appropriate oxygen pairs were sampled directly in the snapshots appearing in Figure 4. The spread in a typical sample of distances turned out to be very small. We concluded that the average O...O distance is about 2.9 Å. Hence, this supports the existence of a network of hydrogen bonds between the first and second shell.

The effects of temperature on the local structure of liquid water are illustrated in Figure 6 by means of SDF=2.0 isosurfaces. The distribution of oxygen atoms is slightly more

dispersed (i.e., the volume enclosed by the isosurface is bigger) at 363 K when compared with 300 K. Perhaps more surprisingly is the appearance of the secondary structure at 238 K at the high isovalue of 2.0. This shows that the local tetrahedral network is enhanced by the reduction in temperature.

3.2. Simulations at High Pressure. The results of the nonambient pressure simulations are summarized in Table 2, and the variation of liquid density as a function of pressure is compared with experimental results in Figure 7. The comparison shows that the simulated water mimics its real counterpart reasonably well with larger deviations at higher pressures. Furthermore there is tentative evidence in Table 2 for the reported^{65–68} maximum in diffusion coefficient at elevated pressures, which is one of the well-known anomalies of liquid water.

RDFs are a useful tool to monitor the local structure of a liquid and can be readily obtained by experiment or computer simulations. Figure 8 shows the results of various RDFs derived from the simulations. The effect of pressure on the HH and OH RDFs (in Figure 8a,b) is gradual and small. There is no significant change in the overall form but with only limited decrease in the peak heights and decrease in well depth of the first broad minimum. In contrast, Figure 8c shows that the OO RDF changes substantially with pressure. The second peak at around 4.5 Å gradually disappears (i.e., flattens), while a shoulder starts to develop on the right-hand side of the first peak (at around 3.2 Å) as the pressure is increased. However, a simple comparison of the current RDFs may not be appropriate because the pressure increase causes a considerable change in density. This is why we corrected the OO RDF for this change in density, as shown in Figure 8d. The density-weighted or normalized RDF curves show a different picture. The height of the first peak increases with pressure rather than decreases. More importantly, the disappearance of the second peak (for 1000 atm) is not due to reduction in its peak height. Rather, it can be attributed to the notable increase in the RDF in regions between 3 and 4 Å and between 5 and 7 Å. This bears remarkable resemblance to the molecular distribution functions obtained from X-ray diffraction of liquid water at pressures up to 7700 bar by Okhulkov et al.⁸

Our results also indicate that the coordination number rises from 5 to about 7.5 when the pressure is increased from 1 to 10 000 atm. This is consistent with the findings of Eggert et al.⁹ and a recent first principles MD simulation of liquid water¹⁰ where the coordination number also increases with pressure. Even at 1 atm, previous studies have indicated that the coordination number is greater than four.^{11,69}

A more direct way of examining the effect of pressure on local structure is provided by SDFs, as shown in Figure 9). It can be seen that high pressure has a dramatic effect on the short-range structure. A considerable number of oxygens start to appear in regions where they were rare at ambient pressure. At 10 000 atm, the “horseshoe” region has notably morphed into a complete ring occupying space in between the two hydrogens of the central water. In addition, the isosurface with lower values (e.g., 1.5) shows similar features. However, the secondary ring structure that appeared

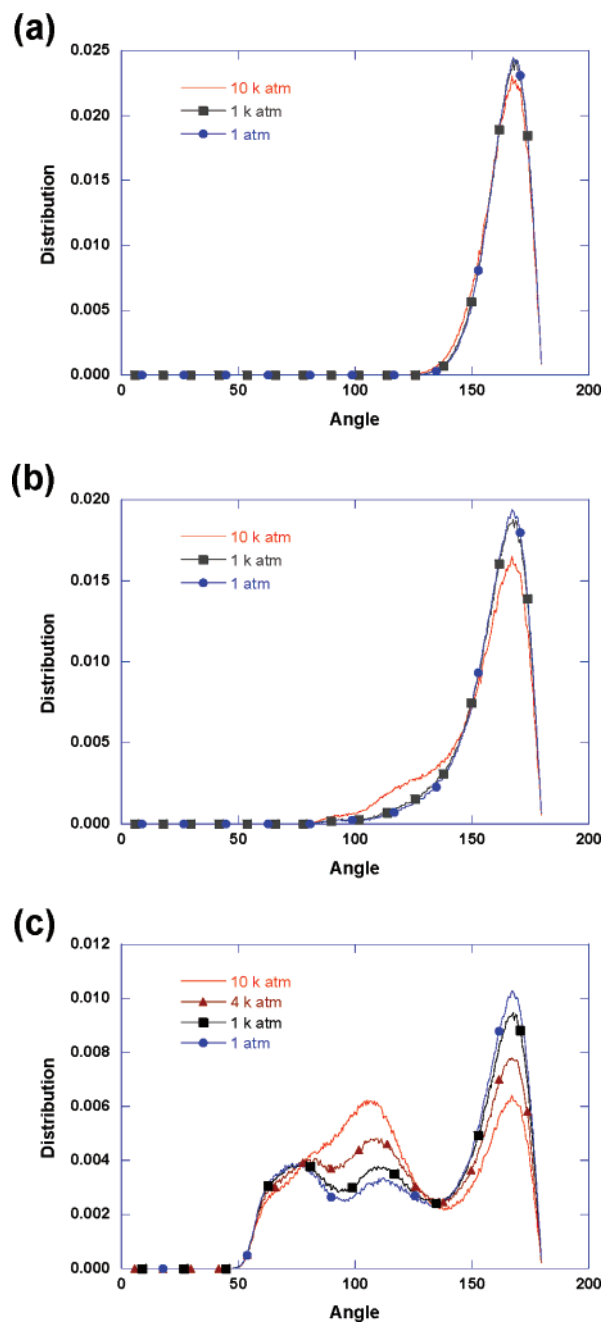


Figure 10. Comparison of the distribution of O–H...O angles at three different pressures. The cutoff distances are (a) 2.0 Å, (b) 2.5 Å, and (c) 3.0 Å.

at ambient pressure is now much less significant indicating a decrease in the amount of water associated with it. Moreover, the secondary “wing”-like structure (see $T = 238$ K in Figure 6) is completely absent at this elevated pressure (10 000 atm). This is a unique piece of evidence that confirms the collapse of second-neighbor shell molecules into the first shell, which is inferred from X-ray diffraction⁹ and X-ray scattering experiments.⁸ These additional molecules also contribute to the OO RDF, and they are responsible for the increase in $g(r)$ between 3 and 4 Å.

The O–H...O angle distributions (see Figure 10) can also shed some light onto the change induced by the applied pressure. As in the ambient pressure case, the change in

distribution for close neighbors (cutoff = 2.0 Å) is minimal even at the highest pressure. However, the impact of increased pressure on the distribution for neighboring molecules of up to 3.0 Å is quite remarkable. There is a substantial reduction in height of the peak at 170° in conjunction with an extensive change in the tail of the distribution (50–140°). Upon pressure increase, the two smaller peaks merge to form one peak centered at 110° and the number of molecules belonging to this range increases dramatically. Again, this is consistent with what one observes in the RDFs and SDFs. This increased angular distortion in the O–H...O angle distribution has also been suggested by Khan et al.⁷⁰

It has been suggested⁷¹ that the hydrogen-bonded molecular network remains almost intact even at extreme high pressures. This is supported by the finding of Kalinichev et al.¹⁴ who used MC simulations in conjunction with the TIP4P water potential to show that the number of hydrogen-bonded neighbors does not change significantly even in such severe conditions. Our SDF results corroborate this result because the regions occupied by the first shell neighbors at 1 atm and 10 000 atm remain invariant (see Figure 9). However, it should be noted that there is a significant difference in the distribution of the nearest neighbors between our QCT potential and the TIP4P one.⁶³

The stability of the hydrogen-bonded molecular network can also be seen in the O–H...O angle distributions because they remain essentially the same for a cutoff up to 2.5 Å, even at the highest pressure. In addition, we believe that the appearance of molecules in the interstitial regions (see Figure 9) is the cause for suggested change in the O...O...O and O–H...O angle distributions as proposed by Urquidi et al.⁷¹ and Khan et al.⁷⁰

4. Conclusions

We carried out extensive simulations of liquid water using a QCT potential. In view of its high-rank multipolar character the description of the electrostatic interaction at short range is expected to be accurate, except for the lack of polarization. We have explored a part of the phase diagram of liquid water by means of NVT and NPT MD simulations. The results confirm the existence of a density maximum at around 6 °C (279 K). Compared to popular potentials, the discrepancy between experiment and simulation for six calculated bulk properties appeared homogeneous, that is, without serious outliers. Much of the remaining work focused on the local 3D structure of liquid water, making full use of 3D snapshots and Spatial Distribution Functions (SDFs), over and above the familiar 1D radial distribution functions. The analysis of O–H...O angle distribution shows that most immediate neighbors (<2.5 Å) are hydrogen-bonded to the central molecule. Perhaps surprisingly, the impact of temperature is only minimal for molecules within 2.0 Å of the central molecule since the distribution changes only slightly at the highest temperature of 90 °C (363 K). We recover the traditional picture of a tetrahedral environment but, distinct for the QCT potential compared to others, a different shape of the SDF contour surfaces at the lone pair side of a central

water. Neighboring molecules at that side form a “horseshoe”-like shape with substantial narrowing in the central part. In addition, “interstitial” molecules do exist but are rare. At lower temperature, well-defined secondary structures (second-shell neighbors) are observed around the central molecule. At nonambient pressures, the local environment undergoes substantial changes. A pressure increase ultimately causes the “collapse” of the second-shell molecules into the “interstitial” region, which has dramatic repercussions for the O–H...O angle distribution. The impact on the RDF is surprisingly small however. Only the OO RDF shows substantial changes, which is in good agreement with previous experimental studies. We confirm that the local hydrogen-bonding network remains largely intact even in such extreme conditions.

Acknowledgment. We thank Fran Painter and Simon Houlding for help with some of the NPT simulations and all NVT simulations and the EPSRC for partial funding.

Supporting Information Available: SDF isosurfaces generated from simulations with the QCT, SPC, and TIP5P potentials (Figure S1), radial distribution function and coordination number for a simulation generated by the QCT and TIP5P potential (Figure S2), cross-sections of the SDF with three different mutually orthogonal planes, each figure comparing three temperatures, three pressures for the QCT potential, and three potentials (Figures S3–S5), two views of the SDF of the first shell of neighboring water molecules generated by the QCT potential (Figure S6), QCT multipole moments of the atoms in water (Table S1), temperature dependence of various bulk properties obtained by NPT simulation (Table S2), and temperature dependence of constant volume heat capacity obtained by NVT simulation (Table S3). This material is available free of charge via the Internet at <http://pubs.acs.org>.

References

- (1) Wernet, P.; Nordlund, D.; Bergmann, U.; Cavalleri, M.; Odelius, M.; Ogasawara, H.; Naslund, L. A.; Hirsch, T. K.; Ojamae, L.; Glatzel, P.; Pettersson, L. G. M.; Nilsson, A. *Science* **2004**, *304*, 995.
- (2) Smith, J. D.; Cappa, C. D.; Wilson, K. R.; Messer, B. M.; Cohen, R. C.; Saykally, R. J. *Science* **2004**, *306*, 851.
- (3) Nilsson, A.; Wernet, P.; Nordlund, D.; Bergmann, U.; Cavalleri, M.; Odelius, M.; Ogasawara, H.; Naslund, L.-A.; Hirsch, T. K.; Ojamae, L. *Science* **2005**, *308*, 793a.
- (4) Smith, J. D.; Cappa, C. D.; Messer, B. M.; Cohen, R. C.; Saykally, R. J. *Science* **2005**, *308*, 793b.
- (5) Wilson, K. R.; Cavalleri, M.; Rude, B. S.; Schaller, R. D.; Nilsson, A.; Pettersson, L. G. M.; Goldman, N.; Catalano, T.; Bozek, J. D.; Saykally, R. J. *J. Phys.: Condens. Matter* **2002**, *14*, L221.
- (6) Kuo, I. F. W.; Mundy, C. J.; McGrath, M. J.; Siepmann, J. I.; VandeVondele, J.; Sprik, M.; Hutter, J.; Chen, B.; Klein, M. L.; Mohamed, F.; Krack, M.; Parrinello, M. *J. Phys. Chem. B* **2004**, *108*, 12990.
- (7) Bukowski, R.; Szalewicz, K.; Groenenboom, G. C.; van der Avoird, A. *Science* **2007**, *315*, 1249.

- (8) Okhulkov, A. V.; Demianets, Y. N.; Gorbaty, Y. E. *J. Chem. Phys.* **1994**, *100*, 1578.
- (9) Eggert, J. H.; Weck, G.; Loubeyre, P. *J. Phys.: Condens. Matter* **2002**, *14*, 11385.
- (10) Schwegler, E.; Galli, G.; Gygi, F. *Phys. Rev. Lett.* **2000**, *84*, 2429.
- (11) Svishchev, I. M.; Kusalik, P. G. *J. Chem. Phys.* **1993**, *99*, 3049.
- (12) Svishchev, I. M.; Zassetsky, A. Y. *J. Chem. Phys.* **2000**, *112*, 1367.
- (13) Starr, F. W.; Bellissent-Funel, M. C.; Stanley, H. E. *Phys. Rev. E* **1999**, *60*, 1084.
- (14) Kalinichev, A. G.; Gorbaty, Y. E.; Okhulkov, A. V. *J. Mol. Liq.* **1999**, *82*, 57.
- (15) Bader, R. F. W. *Atoms in Molecules. A Quantum Theory*; Oxford Univ. Press: Oxford, GB, 1990.
- (16) Popelier, P. L. A. *Atoms in Molecules. An Introduction*; Pearson: London, Great Britain, 2000.
- (17) Popelier, P. L. A.; Aicken, F. M.; O'Brien, S. E. *Atoms in Molecules. In Chemical Modelling: Applications and Theory*; Royal Society of Chemistry Specialist Periodical Report; Hinchliffe, A., Ed.; 2000; Vol. 1, Chapter 3, pp 143–198.
- (18) Popelier, P. L. A.; Smith, P. J. *Quantum Topological Atoms. In Chemical Modelling: Applications and Theory*; Royal Society of Chemistry Specialist Periodical Report; Hinchliffe, A., Ed.; 2002; Vol. 2, Chapter 8, pp 391–448.
- (19) Popelier, P. L. A. *Quantum Chemical Topology: on Bonds and Potentials. In Structure and Bonding Intermolecular Forces and Clusters*; Wales, D. J., Ed.; Springer: Heidelberg, Germany, 2005; Vol. 115, p 1.
- (20) Rafat, M.; Popelier, P. L. A. *Topological atom-atom partitioning of molecular exchange energy and its multipolar convergence. In Quantum Theory of Atoms in Molecules*; Matta, C. F., Boyd, R. J., Eds.; Wiley-VCH: Weinheim, Germany, 2007; Vol. 5, p 121.
- (21) Kosov, D. S.; Popelier, P. L. A. *J. Chem. Phys.* **2000**, *113*, 3969.
- (22) Kosov, D. S.; Popelier, P. L. A. *J. Phys. Chem. A* **2000**, *104*, 7339.
- (23) Popelier, P. L. A.; Joubert, L.; Kosov, D. S. *J. Phys. Chem. A* **2001**, *105*, 8254.
- (24) Popelier, P. L. A.; Rafat, M. *Chem. Phys. Lett.* **2003**, *376*, 148.
- (25) Rafat, M.; Popelier, P. L. A. *J. Chem. Phys.* **2005**, *123*, 204103.
- (26) Joubert, L.; Popelier, P. L. A. *Mol. Phys.* **2002**, *100*, 3357.
- (27) Joubert, L.; Popelier, P. L. A. *Phys. Chem. Chem. Phys.* **2002**, *4*, 4353.
- (28) Devereux, M.; Popelier, P. L. A. *J. Phys. Chem. A* **2007**, *111*, 1536.
- (29) Handley, C. M.; Popelier, P. L. A. *Synthesis and Reactivity in Inorganic, Metal-Organic, and Nano-Metal Chemistry*; in press.
- (30) Liem, S.; Popelier, P. L. A. *J. Chem. Phys.* **2003**, *119*, 4560.
- (31) Liem, S.; Popelier, P. L. A.; Leslie, M. *Int. J. Quantum Chem.* **2004**, *99*, 685.
- (32) Houlding, S.; Liem, S. Y.; Popelier, P. L. A. *Int. J. Quantum Chem.* **2007**, *107*, 2817.
- (33) Dunning, T. H. *J. Chem. Phys.* **1989**, *90*, 1007.
- (34) Frisch, M. J.; Trucks, G. W.; Schlegel, H. B.; Scuseria, G. E.; Robb, M. A.; Cheeseman, J. R.; Zakrzewski, V. G.; Montgomery, J. A., Jr.; Stratmann, R. E.; Burant, J. C.; Dapprich, S.; Millam, J. M.; Daniels, A. D.; Kudin, K. N.; Strain, M. C.; Farkas, O.; Tomasi, J.; Barone, V.; Cossi, M.; Cammi, R.; Mennucci, B.; Pomelli, C.; Adamo, C.; Clifford, S.; Ochterski, J.; Petersson, G. A.; Ayala, P. Y.; Cui, Q.; Morokuma, K.; Malick, D. K.; Rabuck, A. D.; Raghavachari, K.; Foresman, J. B.; Cioslowski, J.; Ortiz, J. V.; Baboul, A. G.; Stefanov, B. B.; Liu, G.; Liashenko, A.; Piskorz, P.; Komaromi, I.; Gomperts, R.; Martin, R. L.; Fox, D. J.; Keith, T.; Al-Laham, M. A.; Peng, C. Y.; Nanayakkara, A.; Gonzalez, C.; Challacombe, M.; Gill, P. M. W.; Johnson, B.; Chen, W.; Wong, M. W.; Andres, J. L.; Gonzalez, C.; Head-Gordon, M.; Replogle, E. S.; Pople, J. A. *GAUSSIAN 98. Gaussian 98, Revision A.7*; Gaussian, Inc.: Pittsburgh, PA, U.S.A., 1998.
- (35) Clough, S. A.; Beers, Y.; Klein, G. P.; Rothman, L. S. *J. Chem. Phys.* **1973**, *59*, 2254.
- (36) Höfner, S.; Wendland, M. *Int. J. Quantum Chem.* **2002**, *86*, 199.
- (37) Maroulis, G. *Chem. Phys. Lett.* **1998**, *289*, 403.
- (38) Verhoeven, J.; Dymanus, A. *J. Chem. Phys.* **1970**, *52*, 3222.
- (39) Millot, C.; Soetens, J.-C.; Martins, Costa, M. T. C.; Hodges, M. P.; Stone, A. J. *J. Phys. Chem. A* **1998**, *102*, 754.
- (40) Burnham, C. J.; Xantheas, S. S. *J. Chem. Phys.* **2002**, *116*, 1500.
- (41) Glaetli, A.; Daura, X.; van Gunsteren, W. F. *J. Chem. Phys.* **2002**, *116*, 9811.
- (42) Tironi, I. G.; Brunne, R. M.; van Gunsteren, W. F. *Chem. Phys. Lett.* **1996**, *250*, 19.
- (43) Jorgensen, W. L.; Tirado-Rives, J. *Proc. Natl. Acad. Sci. U.S.A.* **2005**, *102*, 6665.
- (44) Guillot, B. *J. Mol. Liq.* **2002**, *101*, 219.
- (45) *MORPHY98*; a program written by P. L. A. Popelier with a contribution from R. G. A. Bone; UMIST: Manchester, England, EU, 1998.
- (46) Popelier, P. L. A. *Mol. Phys.* **1996**, *87*, 1169.
- (47) Gillespie, R. J.; Popelier, P. L. A. *Chemical Bonding and Molecular Geometry from Lewis to Electron Densities*; Oxford Univ. Press: New York, U.S.A., 2001.
- (48) Hodges, M.; Stone, A. J.; Xantheas, S. S. *J. Phys. Chem. A* **1997**, *101*, 9163.
- (49) Rafat, M.; Popelier, P. L. A. *J. Chem. Phys.* **2006**, *124*, 144102.
- (50) Smith, W.; Forester, T. R. *J. Mol. Graph.* **1996**, *14*, 136.
- (51) *DLPOLY*; a computer program written by W. Smith, M. Leslie, and T. R. Forester; CCLRC: Daresbury Lab, Daresbury, Warrington WA4 4AD, England, 2003.
- (52) Allen, M. P.; Tildesley, D. J. *Computer Simulation of Liquids*; Clarendon: Oxford, GB, 1987.
- (53) Jorgensen, W. L.; Jenson, C. *J. Comput. Chem.* **1998**, *19*, 1179.
- (54) Baez, L. A.; Clancy, P. *J. Chem. Phys.* **1994**, *101*, 9837.
- (55) Chaplin, M. <http://www.lsbu.ac.uk/water/models.html> 2007.

- (56) Paesani, F.; Iuchi, S.; Voth, G. A. *J. Chem. Phys.* **2007**, *127*, 074506.
- (57) Fanourgakis, G. S.; Schenter, G. K.; Xantheas, S. S. *J. Chem. Phys.* **2006**, *125*, 141102.
- (58) Kell, G. S. *J. Chem. Eng. Data* **1967**, *12*, 66.
- (59) Mahoney, M. W.; Jorgensen, W. L. *J. Chem. Phys.* **2000**, *112*, 8910.
- (60) Yu, H.; van Gunsteren, W. F. *J. Chem. Phys.* **2004**, *121*, 9549.
- (61) Finney, J. L. *Philos. Trans. R. Soc. London, Ser. B* **2004**, *359*, 1145.
- (62) Svishchev, I. M.; Kusalik, P. G.; Wang, J.; Boyd, R. J. *J. Chem. Phys.* **1996**, *105*, 4742.
- (63) Kusalik, P. G.; Svishchev, I. M. *Science (Washington, D. C.)* **1994**, *265*, 1219.
- (64) Shaik, M.; Devereux, M.; Popelier, P. L. A. Submitted for publication.
- (65) Woolf, L. A. *J. Chem. Soc., Faraday Trans I* **1975**, *71*, 784.
- (66) Wilbur, D. J.; Defries, T.; Jonas, J. *J. Chem. Phys.* **1976**, *65*, 1783.
- (67) Jonas, J.; Lee, Y. T. *J. Phys: Condens. Matter* **1992**, *4*, 305.
- (68) Netz, P. A.; Starr, F. W.; Stanley, H. E.; Barbosa, M. C. *J. Chem. Phys.* **2001**, *115*, 344.
- (69) Corongiu, G.; Clementi, E. *J. Chem. Phys.* **1992**, *97*, 2030.
- (70) Khan, A.; Khan, M. R.; Khan, M. F.; Khanam, F. *Theochem* **2004**, *679*, 165.
- (71) Urquidi, J.; Cho, C. H.; Singh, S.; Robinson, G. W. *J. Mol. Struct.* **1999**, *485–486*, 363.
- (72) Krynicki, K.; Green, C. D.; Sawyer, D. W. *Faraday Discuss.* **1978**, *66*, 199.
- (73) Weast, R. C. *Handbook of Chemistry and Physics CRC*; Boca Raton, U.S.A., 1976; Vol. 56th ed.
- (74) Wagner, W.; Pruss, A. *J. Phys. Chem. Ref. Data* **2002**, *31*, 387.

CT700266N

Theoretical Analysis of the Reaction Mechanism of Biotin Carboxylase

Yuko Ito,[†] Hiroki Kondo,^{*†} Yoshihito Shiota,[‡] and Kazunari Yoshizawa^{*‡}

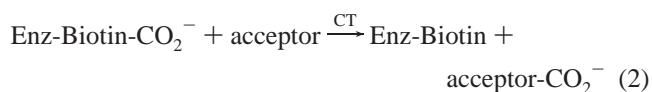
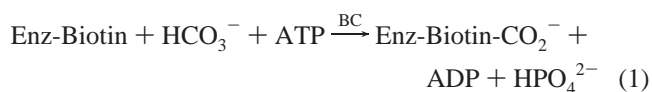
Department of Bioscience and Bioinformatics, Kyushu Institute of Technology, 680-4 Kawazu, Iizuka 820-8502, Japan, and Institute for Materials Chemistry and Engineering, Kyushu University, Nishi-ku, Fukuoka 819-0395, Japan

Received October 6, 2007

Abstract: A computational approach is taken to clarify the reaction mechanism of biotin carboxylase (BC) by using the B3LYP density functional method. The overall reaction of BC is supposed to consist of two steps: in the first step, carboxyphosphate (CP) is generated from bicarbonate and ATP, and it is subject to nucleophilic attack on its carboxyl group by biotin to form carboxybiotin in the second step. The activation energies for the transition states of the first and second steps are computed to be 46.6 and 7.9 kcal/mol, respectively, demonstrating that the first step limits the overall reaction of BC. In the second step, the ureido moiety of biotin undergoes enolization with the aid of general acid–base catalysis by CP, followed by collapse of CP into CO₂ and phosphate. The resulting bent CO₂ is highly labile and condenses quickly with enolic biotin to give carboxybiotin. Implicit in this scheme as they are, ingenious proton movements between the two substrates, CP and biotin, dictate all of the succeeding chemical events.

Introduction

Biotin-dependent carboxylases play an important role in cellular metabolism by converting such key metabolites as pyruvate and acetyl-CoA to oxalacetate and malonyl-CoA, respectively.¹ The reactions mediated by the respective enzymes, i.e., pyruvate carboxylase (PC, EC 6.4.1.1) and acetyl-CoA carboxylase (ACC, EC 6.4.1.2), comprise two partial reactions: In the first partial reaction protein-bound biotin is carboxylated by biotin carboxylase (BC) with ATP and bicarbonate as cosubstrates (eq 1). In the second partial reaction mediated by carboxyl transferase (CT), the carboxyl group bound temporarily on biotin is then transferred to an acceptor substrate (eq 2). The first partial reaction is common to all the biotin-dependent carboxylases and key to accomplishing the overall carboxylation of acceptor substrates.



Since two of the substrates in the reaction of BC, biotin and bicarbonate, are not labile enough to undergo spontaneous condensation, ATP is needed to activate either or both of the substrates. There are several hypotheses to account for the chemical role of ATP in the reaction of BC, as shown in Scheme 1;^{2,3} in mechanism 1 bicarbonate is phosphorylated by ATP to form carboxyphosphate (CP), which is then attacked by the N-1 nitrogen of enzyme-bound biotin.⁴ In mechanism 2 the carbonyl group of biotin is phosphorylated first to yield *O*-phosphobiotin, which then undergoes nucleophilic attack on bicarbonate to give carboxybiotin.⁵ In light of numerous mechanistic studies,^{2,6–14} it would be safe to rule out mechanism 2, and our attention is focused on mechanism 1 as the plausible one for the BC-catalyzed reaction. Nevertheless, since the putative intermediate CP

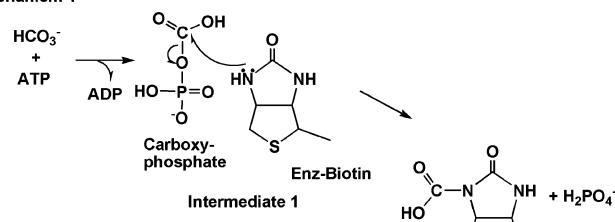
* Corresponding author e-mail: kondo@bio.kyutech.ac.jp (H.K.); kazunari@ms.ifoc.kyushu-u.ac.jp (K.Y.).

[†] Kyushu Institute of Technology.

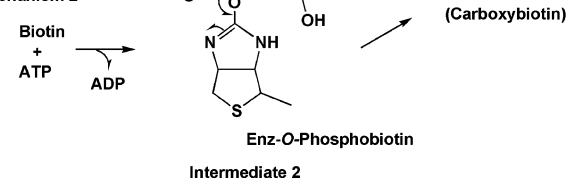
[‡] Kyushu University.

Scheme 1. Mechanistic Possibilities for the ATP-Dependent Carboxylation of Biotin by Bicarbonate, Catalyzed by Biotin Carboxylase (BC)

Mechanism 1



Mechanism 2



is either short-lived or accumulated only in quantities insufficient for experimental validation, the definitive evidence for this hypothesis is still lacking.

Another aspect of BC is the fact that it belongs to the ADP-forming ligase family in which most typically a carboxylic acid and an amine undergo condensation in the presence of ATP to form an amide. A relative closest to BC in this group would be carbamoyl-phosphate synthetase (CPS), and in fact they share primary and tertiary structures.^{15,16} Nonetheless, they do differ in the substrate to be carboxylated; ammonia in CPS and the urea of biotin in BC. Because of this subtle difference it is not certain whether the two reactions proceed by the same mechanism, despite the fact that the CPS reaction is most likely to proceed via a CP intermediate.^{17–21}

These are the rationale behind our theoretical studies of the BC reaction and given the difficulty of proving or disproving the intervention of the intermediate CP in this process experimentally, theoretical treatment would be useful to assess the validity of the proposed mechanisms. In this article, we propose a possible mechanism for the formation of CP and its reaction with biotin using density functional theory (DFT) calculations.

Methods

Computational Methods. The geometries of all stationary points were fully optimized using the B3LYP functional^{22,23} with the 6-31G** basis set²⁴ on the Gaussian 03 software package.²⁵ The structures and energies of the reactants, intermediates, and products are optimized in the first place, and then the transition state search is carried out on the basis of those structures. All optimized structures were characterized as minima or cols by harmonic vibration analyses. In general, the transition state is defined as the first-order stationary point on a potential energy surface that has a single negative Hessian eigenvalue with an imaginary frequency.^{26,27} Therefore, whether a given structure is a transition state or not can be assessed from a calculation of vibrational frequencies. Furthermore, as the reaction goes toward the transition state, the bond involved directly in the

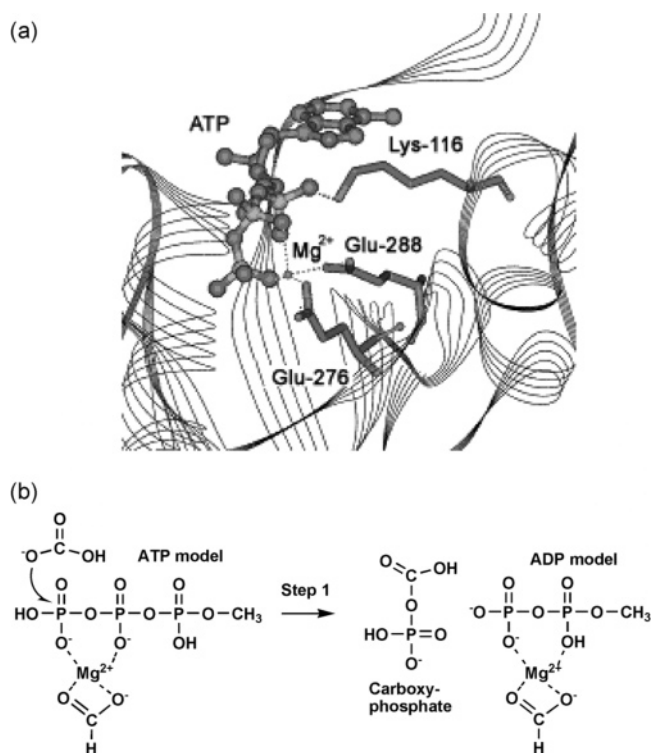


Figure 1. Conformational snapshot of the catalytic site of *Escherichia coli* BC adapted from the structure of mutant E288K (1DV2) by Insight (a) and the ATP model used for the first step of the BC reaction (b).

reaction is elongated with an increase in the amplitude of vibration to give rise to a band at a lower wavenumber.^{26,27} Accordingly, the frequency ought to be lower than that in the steady state. Reaction paths were characterized by intrinsic reaction coordinate (IRC) calculations,^{28–30} where the initial force constants are provided from the frequency calculations for optimized transition states. IRC was constructed from discrete points at intervals of 0.03 or 0.10 $\text{amu}^{1/2}\cdot\text{bohr}$. We confirmed changes in geometrical parameters and energies along reaction paths.

Calculation Models. Calculations were performed for mechanism 1 of the BC reaction illustrated in Scheme 1. The crystal structure of a mutant of *Escherichia coli* BC with ATP bound suggests that the side chain of Lys-116 forms a hydrogen bond with the α -phosphate of ATP and that Mg^{2+} ion is coordinated to the side chain of Glu-288.³¹ Accordingly, a proton was placed on the α -phosphate of ATP, and Mg^{2+} ion bridging the β - and γ -phosphates is coordinated by formate as a ligand, a mimic of the side chain of Glu-288, as shown in Figure 1. At first, the Mg^{2+} –ATP complex was optimized without formate, but the structure was distorted completely during the optimization, presumably because Mg^{2+} forms a hexacoordinate complex. In addition to these alterations from the BC crystal structure, ATP was modeled by methyl triphosphate to simplify the system and to ease calculations. Biotin has a pentanoic acid side chain, and it was also replaced with a methyl group, as the side chain is not involved directly in the reaction. Furthermore, although the negative charges of ATP are neutralized by Mg^{2+} ion, it was essential to consider protonation of ATP and bicarbonate to overcome the charge repulsion, as both

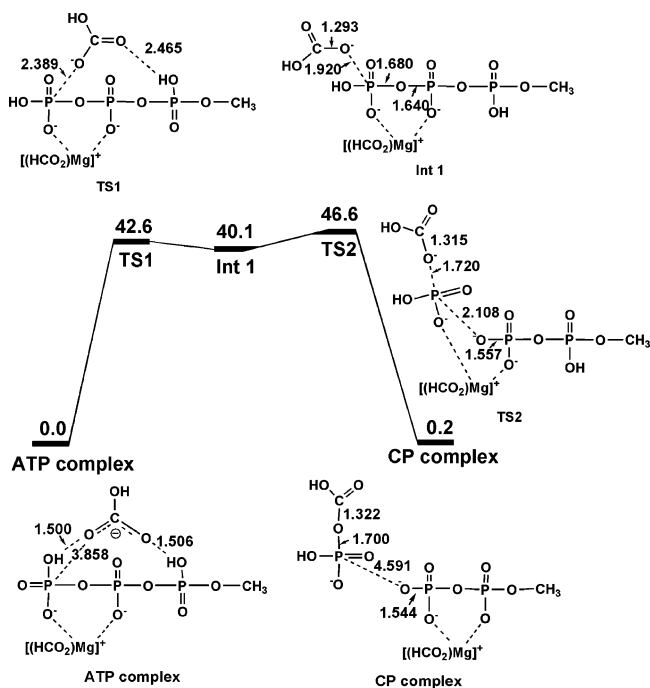


Figure 2. Relative energies and optimized structure computed for the reactant complex, transition states, intermediate, and carboxyphosphate complex for the first partial reaction (step 1) of BC by the B3LYP/6-31G** level of theory. Units are in kcal/mol.

of them are negatively charged. Thus, protons were placed on either or both of the β - and γ -phosphates of ATP and a proton was placed or removed from bicarbonate, but calculations were successful only in the model depicted in Figure 1, where Mg^{2+} is coordinated by the γ -(bidentate) and β -(monodentate) phosphates and formate (bidentate). In addition to this pentacoordinate model, a hexacoordinate complex with another formate or water as ligand was examined, but the energy obtained was not much different.

Results

Carboxylation of biotin is assumed to comprise the following elementary steps: nucleophilic attack of bicarbonate on the γ -phosphate of ATP to form CP and ADP and subsequent reaction of biotin with CP. These two steps were analyzed separately.

Formation of Carboxyphosphate. In light of many experimental results and theoretical considerations of the reactions involving ATP, the nucleophilic attack of bicarbonate on the γ -phosphate of ATP is presumed to proceed by the “inline” mechanism.^{4,8–12} An energy diagram calculated for this step and the optimized structures are illustrated in Figure 2. The entire process contains two transition states (TS1 and TS2) and one intermediate (Int 1). Initially, one of the oxygen atoms of bicarbonate is located 3.858 Å away from the γ -phosphorus atom of ATP. The distance between these two atoms is shortened to 2.389 Å at TS1, and the energy barrier for this state amounts to 42.6 kcal/mol relative to the initial state. The distance is further shortened to 1.920 Å at Int 1 and eventually to 1.720 Å at TS2 whose energy level is located 46.6 kcal/mol higher than that of the initial state and 6.5 kcal/mol relative to Int 1. By contrast, the

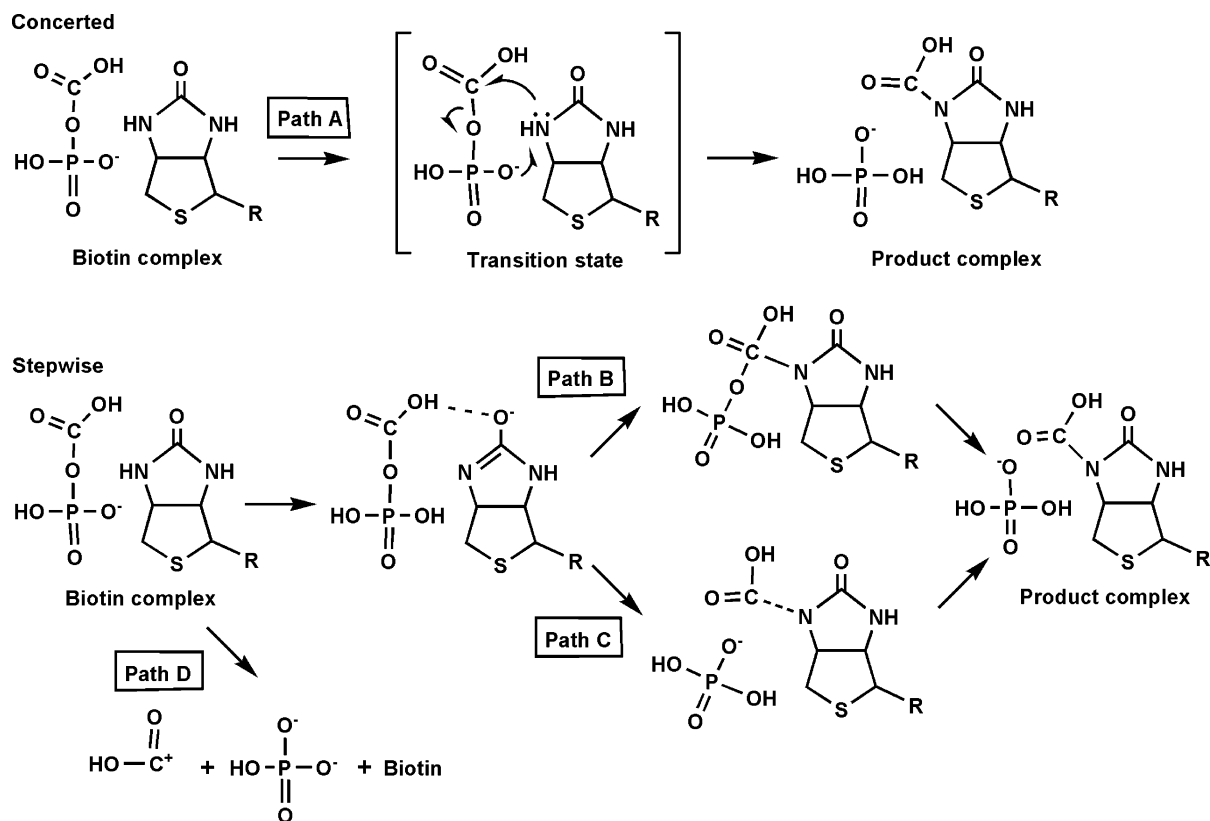
$\text{P}(\gamma)\text{--O}(\beta\gamma)$ bond distance is elongated to 1.680 and 2.108 Å at Int 1 and TS2, respectively, and it is eventually cleaved to produce CP and ADP. As a result of this the $\text{P}(\gamma)\text{--O}(\text{bicarbonate})$ bond formed is shortened slightly from 1.720 Å at TS2 to 1.700 Å in the CP complex. The CP complex lies 0.2 kcal/mol above the ATP complex. The imaginary frequency for TS1 is 89i cm^{-1} , and this vibrational motion is related to the stretching of a bond between the bicarbonate oxygen with the γ -phosphorus atom. The imaginary frequency for TS2 representing an asymmetric stretching vibration of the $\text{P}(\gamma)\text{--O}(\beta\gamma)$ bond being cleaved and the $\text{P}(\gamma)\text{--O}(\text{bicarbonate})$ bond forming was evaluated as 122i cm^{-1} . Compared with the C–O stretching vibration of anhydrides and the asymmetric stretching vibration of the O–P–O groups in inorganic phosphate and nucleotides of a band at 1100 and 1800–850 cm^{-1} , respectively,^{32–36} the results obtained above support the notion that TS1 and TS2 are true transition states.

Our calculations indicate that Mg^{2+} ion plays an important role in the reaction of bicarbonate with ATP. As both bicarbonate and ATP are negatively charged, the positive charges of Mg^{2+} ion facilitate the formation of CP by alleviating the electrostatic repulsion between the negative charges.

Mg^{2+} -mediated hydrolysis of a phosphodiester of a hammerhead ribozyme was studied theoretically at the B3LYP/6-31G** level of theory.³⁷ The hydrolysis reaction is reminiscent of the first step of the BC reaction; the intramolecular nucleophilic attack by an oxygen atom on the phosphorus with charge compensation by Mg^{2+} ion occurs exothermically by only 2.3 kcal/mol with two transition states. The first activation barrier is 18.6 kcal/mol, and the second is 2.2 kcal/mol above the intermediate. The oxygen atom attacks the phosphate from 3.5 Å away in the initial state in this reaction.

Comparison of the first step of the BC reaction with the hydrolysis of the phosphodiester in terms of the type of reaction and the molecular structure involved suggests that the scheme drawn for the first step of BC reaction having two transition states is plausible. Although the energy obtained (46.6 kcal/mol) is fairly high, compared with the 18.6 kcal/mol energy barrier in the hydrolysis of the phosphodiester, the initial state lying nearly at the same energy level as that of the CP complex seems to be reasonable. Since only one bond is reorganized from the phosphoric anhydride O–P–O bond in the ATP complex to a mixed anhydride C–O–P bond in the CP complex, the latter anhydride bond is 2–4 kcal/mol more stable than the former,^{38,39} as shown in Figure 2.

Reaction of Carboxyphosphate with Biotin. Four possible pathways were envisaged as plausible mechanisms for the second partial reaction, as shown in Scheme 2. Path A is a concerted mechanism, in which proton abstraction from biotin by CP, nucleophilic attack by one of the ring nitrogen atoms on CP, and the cleavage of the C–O bond in CP occur in a concerted manner. Paths B and C are stepwise reactions, in which abstraction of a proton from biotin by CP occurs first, and then they separate from each other.^{14,40,41} In path B, nucleophilic attack of enolic biotin on CP precedes

Scheme 2. Four Viable Reaction Pathways for the BC Reaction

expulsion of phosphate from CP, while in path C, CP collapses to CO_2 first, which then reacts with biotin. In the stepwise mechanisms CP will be more susceptible to nucleophilic attack and the nitride of biotin will serve as a more powerful nucleophile. In path D, spontaneous collapse of CP occurs first to yield the protonated form of carbon dioxide, which must be highly labile toward nucleophiles. Subsequently, proton abstraction and the nucleophilic attack occur in the second step.

Energy diagrams representing each of these paths are depicted in Figure 3. DFT calculations for the concerted pathway (path A) reveal that an energy as much as 35.6 kcal/mol is required to form the product complex via **TS3A**, and it is hence unlikely for the reaction to follow this pathway. Since the spontaneous C–O bond cleavage in path D requires 77.7 kcal/mol, this mechanism should also be ruled out. Thus, it is concluded that nucleophilic attack of biotin on CP should take place via **TS3**, resulting in the formation of **Int 2**. In addition to these four paths the intermediate with a quaternary ureido nitrogen was also examined, but the energy obtained was too high to be optimized by the current level of theory.

In the first stage of the stepwise pathway, which is common to paths B and C, biotin is rendered active as a nucleophile by enolization of its ureido moiety. This is achieved by proton abstraction from the ring nitrogen by CP, and it is manifested in a change in the length of the bonds involved in this process. Thus, the bond length of the C–N and C=O in the urea moiety of biotin is shortened or elongated at **TS3**, respectively, upon the biotin enolization. At the same time, the N–H bond is elongated to 2.438 Å from 1.018 Å at **TS3** because of the proton migration from

biotin to CP. The length of the newly formed O–H bond of CP is 0.967 Å, and that of enolic biotin is 1.032 Å at **Int 2**. The optimized structures are shown in Figure 4. At **TS3**, the imaginary frequency representing either the N–H cleaved or the enolic O–H formed is $142i \text{ cm}^{-1}$, a value fairly low compared with 3300 cm^{-1} and 3100 cm^{-1} for the stretching motion of O–H groups with an intermolecular hydrogen bond and of N–H groups in hydrogen-bonded secondary amides, respectively.^{33,35} Nonetheless, the value may be reasonable, as the IRC with a step size of $0.03 \text{ amu}^{1/2} \cdot \text{bohr}$ connected the biotin complex with **Int 2** via **TS3** smoothly. The activation barrier for **TS3** amounts to 7.9 kcal/mol relative to the biotin complex and **Int 2** lies 3.2 kcal/mol above the biotin complex, as shown in Figure 3. The stepwise mechanism is then separated to paths B and C, which give rise to **TS4B** and **TS4C**, respectively, first.

In path B, the second step begins with an intramolecular proton abstraction from the phosphate of CP by the carboxyl group at **TS4B**. This proton transfer occurs in accord with a difference in the $\text{p}K_a$ of phosphates and carboxylic acids, as the $\text{p}K_a$ of inorganic and organic phosphates is around 2.0, while that of carboxylic acids is about 3–4^{42,43} and it enhances the electrophilicity of the carbonyl carbon of CP, thereby facilitating nucleophilic attack of the enolic biotin to give **Int 3B**. Judging from the frequency for the O–H asymmetric stretching vibration in the steady state, the imaginary frequency of $472i \text{ cm}^{-1}$ seems to be reasonable for the proton abstraction at **TS4B**. The activation energies are 1.3 kcal/mol for **Int 2** and 4.5 kcal/mol for the biotin complex. **Int 3B** lies 0.9 kcal/mol and 4.1 kcal/mol above **Int 2** and the biotin complex respectively, as shown in Figure 3.

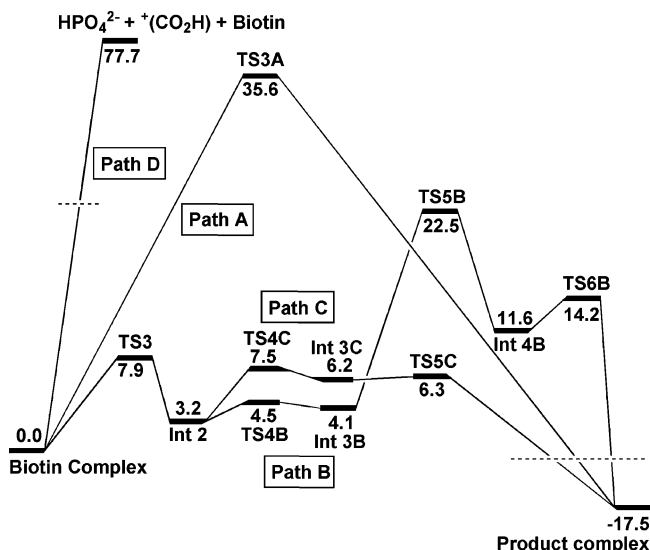


Figure 3. Relative energies computed for the biotin complex, transition states, intermediates, and product complex for the second partial reaction (step 2) of BC by the B3LYP/6-31G** level of theory. Units are in kcal/mol.

In the third stage, the nitrogen of enolic biotin undergoes nucleophilic attack on the carbonyl of CP, concomitant with a proton transfer from the enol to CP to form a tetrahedral intermediate (**TS5B** and **Int 4B**). At the same time, the enolic form of biotin returns to the original keto form. Formation of a tetrahedral intermediate is common in the reaction of carbonyl groups and usually yields the largest activation energy.⁴⁴ Hence, the proton transfer is needed to stabilize the nascent oxyanion of a tetrahedral intermediate. The imaginary frequency associated with the asymmetric stretching vibration of the enolic O–H and the C–N bond forming at **TS5B** is $240i\text{ cm}^{-1}$, a value regarded as reasonable, as the O–H and C–N stretching vibrations give rise to a band at about 3300 cm^{-1} and about 1000 cm^{-1} in the steady state, respectively.^{33,36,45} The activation barrier is 18.4 kcal/mol relative to **Int 3B**, and **Int 4B** lies 7.5 kcal/mol above **Int 3B**.

In the last stage, the C–O bond in CP is gradually elongated and finally cleaved completely upon an intramolecular proton transfer from the carboxyl group of CP to the phosphate. With the expulsion of the phosphate group from the complex, the carbon atom of CP reverts to sp^2 from sp^3 . At the end of this stage through **TS6B**, the C–O bond is cleaved completely along with the proton transfer from the carboxyl group to the phosphate. The imaginary frequency representing the asymmetric O–H stretching for the intramolecular proton transfer and the C–O bond cleavage is $395.1i\text{ cm}^{-1}$ at **TS6B**. The activation barrier amounts to 2.6 kcal/mol relative to **Int 4B**.

In path C, which gives rise to the product complex via the formation of CO_2 and phosphate, CP is split into CO_2 and phosphate spontaneously prior to reaction with biotin (Figure 4). The C–O bond to be cleaved is elongated from 1.426 \AA to 1.965 \AA at **TS4C** and finally to 2.520 \AA at **Int 3C**, where the detached and bent CO_2 is anchored by two hydrogen bonds with the enol of biotin and the detached phosphate. The imaginary frequency associated with the

stretching vibration of the C–O to be cleaved is $126i\text{ cm}^{-1}$ at **TS4C**, a value regarded as reasonable, as the C–O stretching vibrations in anhydrides C–O–C gives rise to a band at about 1100 cm^{-1} in the steady state.^{32,33,36} **TS4C** was confirmed by IRC calculations with a step size of $0.10\text{ amu}^{1/2}\cdot\text{bohr}$. The activation barrier of **TS4C** is only 3.2 kcal/mol relative to **Int 2**. In other words, the C–O cleavage occurs more easily via **TS4C** than via **TS6B** of path B.

The nitrogen of enolic biotin then undergoes nucleophilic attack on bent CO_2 together with a proton transfer from the enol to CO_2 with a six-membered transition state (**TS5C**). The activation barrier is 0.1 kcal/mol relative to **Int 3C**, and the relative energy is 6.3 kcal/mol from the biotin complex. The much lower activation energy for this pathway stems from the higher electrophilicity of the carbon in question, bent CO_2 , than that of CP. In addition, this pathway can avoid formation of a tetrahedral intermediate like **Int 4B**. The imaginary frequency associated with the stretching vibration of the C–N bond forming is $25i\text{ cm}^{-1}$. The low frequency may be associated with the low activation energy, and this notion was proven by IRC calculations with a step size smaller than 1.

Discussion

Biotin-dependent carboxylation is intriguing from chemical as well as biological standpoints, as it enables incorporation of bicarbonate into organic substrates under mild conditions to give carboxylic acids. The first partial reaction of BC plays a key role in this context, and its mechanism has been the target of intensive studies.^{1–12} The CP hypothesis is the only surviving mechanism for BC, but this intermediate is so elusive that it is difficult to prove its intervention by experiments. As described above, the feasibility of this pathway was scrutinized theoretically for the first time. Carboxylation of biotin was supposed to be accomplished in the two partial reactions: formation of CP from bicarbonate and ATP and its subsequent reaction with biotin. Both of these two steps were simulated successfully with energies of activation of 46.6 and at most 7.9 kcal/mol for the first and second transition states, respectively. The former value may look too large for any reaction to take place smoothly, and there will probably be a path or means to lower this energy of activation. For example, solvent effects and the dielectric constant may be taken into account.³⁷ Nonetheless, it seems certain that intermediate CP can form by the reaction of bicarbonate with ATP and that the formation of CP is more laborious than its collapse. In other words, the first step limits the overall reaction of BC, and CP will not accumulate in quantities sufficient for detection experimentally at any stage of the reaction.

One of the most prominent features of the second step is that enolization of the ureido portion of biotin is possible. In light of its chemical structure, enolization of biotin is easy to conceive intuitively, and in fact an enol form of biotin has often been postulated in the carboxylation of biotin and subsequent carboxyl transfer from it.^{40,46,47} Previous theoretical studies were, however, dismissive of the occurrence of an enolic form, as it is too unstable thermodynamically to form.^{48–50} The present study reveals that biotin can undergo

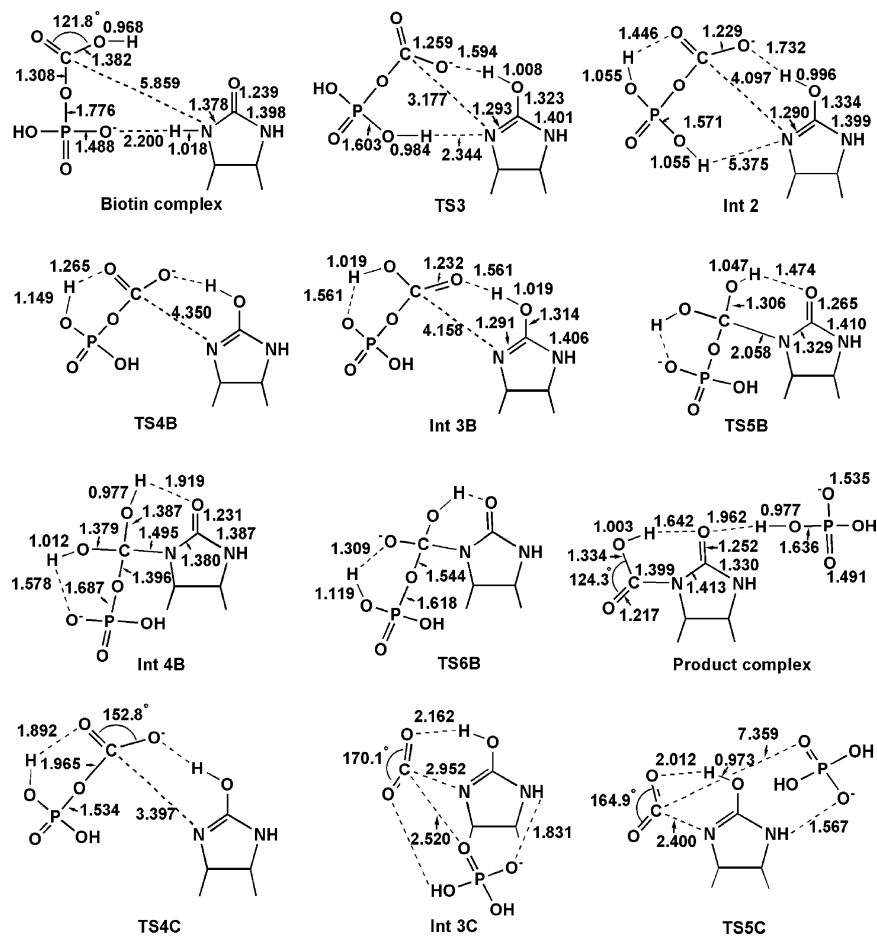


Figure 4. Optimized geometries for the second partial reaction of BC. The tetrahydrothiophene part of biotin is omitted for clarity. Units are in Å.

enolization in the presence of CP with relatively low energy (8 kcal/mol); CP assists this process by serving as a general acid–base catalyst. Thus, the phosphate of CP abstracts a proton from the ureido nitrogen, and the carboxyl group donates a proton to the ureido carbonyl at the transition state (TS3). The resulting **Int 2** will follow either one of the two pathways: CP reacts directly with biotin, thereby forming tetrahedral intermediates, or CP generates bent CO₂ which then reacts with enolic biotin. It turned out that the latter pathway is 15 kcal/mol lower in energy, presumably because it can avoid the formation of a tetrahedral intermediate and because bent CO₂ is more electrophilic than CP.

Although the net reaction of the second step is nucleophilic attack of the ureido nitrogen of biotin on the carboxyl group of CP, mobile protons residing initially on the carboxyl and phosphate of CP and on the ureido group play important roles. Thus, proton transfers from CP to biotin and from biotin to CP trigger the entire second step of BC reaction. This kind of behavior is indeed common in many enzymatic reactions.^{40,51–58} It is noted that though there are only two components, CP and biotin, in the present system, there are protein and water molecules as well in actual enzymatic systems. In addition, Lewis acids such as Mg²⁺ and Mn²⁺ participate in the carboxylation to polarize the scissile bonds.⁵⁹ Some of these components in close contact with substrates at the enzyme active site may reduce the activation

energy by handling proton elaborately or acting as the true proton donor or acceptor.^{60–64}

Finally, carbamoyl-phosphate synthetase, the closest relative of BC in terms of the type of the chemical reactions they mediate, uses ammonia as the nucleophile in the second step in place of biotin. As ammonia (pK_a 9.3 for ammonium) is a much more powerful base than biotin (pK_a 0.18), it would be advantageous for the carboxylases to use ammonia as a nucleophile. Moreover, enzymes contain a number of potential nucleophiles such as imidazole (pK_a 6.8) which may react with CP equally well or even better than biotin. The advantage of using chemically inert biotin as the nucleophile for CP would then be that it becomes labile through enolization only when it is needed, so that it can avoid unnecessary side reactions. In addition, the product, CB (carboxybiotin), is not the ultimate product; rather the carboxyl group placed temporarily on biotin is transferred eventually to acceptor substrates by the reaction of CT. Although the direction is opposite, this reaction is essentially the same as the BC reaction in that it will involve enolization during the carboxyl transfer.^{2,40,41,47,65–68} Hence, it will take place nearly with the same ease as the BC reaction.

Conclusions

We have discussed a possible mechanism of biotin carboxylase (BC) using the B3LYP density functional method. The overall reaction of BC consists of two steps: in the first step,

carboxyphosphate (CP) is generated from bicarbonate and ATP, and it is subject to nucleophilic attack on its carboxyl group by biotin to form carboxybiotin in the second step. Detailed analysis of the potential energy surfaces shows that the first step involves two transition states (**TS1** and **TS2**) and one intermediate. The activation energies for **TS1** and **TS2** were computed to be 42.6 and 46.6 kcal/mol, respectively. In the second step, we considered four possible paths. DFT calculations show that the ureido moiety of biotin undergoes enolization with the aid of general acid–base catalysis by CP, followed by collapse of CP into CO₂ and phosphate. The resulting bent CO₂ is highly labile and condenses quickly with enolic biotin to give carboxybiotin. In the second step the activation energy of the rate-determining step is 10.1 kcal/mol if the reaction traces the stepwise pathway along the most low-lying potential energy surface. Therefore the first transition state in the first step controls the reaction rate in the overall reaction of BC. Our calculations indicate that the structure of biotin is suitable for capturing carbonate from CP.

Acknowledgment. The authors are grateful to Prof. Paul V. Attwood of the University of Western Australia for many helpful discussions. K.Y. acknowledges Grants-in-Aid (No. 18350088, 18G02070005, and 18066013) for Scientific Research from the Japan Society for the Promotion of Science, the Nanotechnology Support Project of the Ministry of Education, Culture, Sports, Science and Technology of Japan (MEXT), the Joint Project of Chemical Synthesis Core Research institution of MEXT, and CREST of Japan Science and Technology Corporation for their support of this work.

Supporting Information Available: Full author list for ref 25; Cartesian coordinates for all optimized geometries; and zero-point energy and thermochemical data at each transition state. This material is available free of charge via the Internet at <http://pubs.acs.org>.

References

- (1) Wood, H. G.; Barden, R. E. Biotin enzymes. *Annu. Rev. Biochem.* **1977**, *46*, 385.
- (2) Knowwood, H. G.; Barden, R. E.; Bioles, J. R. The mechanism of biotin-dependent enzymes. *Annu. Rev. Biochem.* **1989**, *58*, 195.
- (3) Kaziro, Y.; Hass, L. F.; Boyer, P. D.; Ochoa, S. Mechanism of the propionyl carboxylase reaction. *J. Biol. Chem.* **1962**, *237*, 1460.
- (4) Bruice, T. C.; Hegarty, A. F. Biotin-bound CO₂ and the mechanism of enzymatic carboxylation reactions. *Proc. Natl. Acad. Sci. U.S.A.* **1970**, *65*, 805.
- (5) Hansen, D. E.; Knowles, J. R. The stereochemical course at phosphorus of the reaction catalyzed by phosphoenolpyruvate carboxylase. *J. Biol. Chem.* **1982**, *257*, 14795.
- (6) Ogita, T.; Knowles, J. R. On the intermediacy of carboxyphosphate in biotin-dependent carboxylations. *Biochemistry* **1988**, *27*, 8028.
- (7) Hansen, D. E.; Knowles, J. R. N-carboxybiotin formation by pyruvate carboxylase: The stereochemical correspondence at phosphorus. *J. Am. Chem. Soc.* **1985**, *107*, 8304.
- (8) Polakis, S. E.; Guchhait, R. B.; Zwergel, E. E.; Lane, M. D. Acetyl coenzyme A carboxylase system of *Escherichia coli*. *J. Biol. Chem.* **1974**, *249*, 6657.
- (9) Ashman, L. K.; Keech, D. B. Sheep kidney pyruvate carboxylase. Studies on the coupling of adenosine triphosphate hydrolysis and CO₂ fixation. *J. Biol. Chem.* **1975**, *250*, 14.
- (10) Attwood, P. V.; Graneri, B. D. L. A. Pyruvate carboxylase catalysis of phosphate transfer between carbamoyl phosphate and ADP. *Biochem. J.* **1991**, *273*, 443.
- (11) Phillips, N. F. B.; Snoswell, M. A.; Chapman-Smith, A.; Keech, D. B.; Wallace, J. C. Isolation of carboxyphosphate intermediate and the locus of acetyl-CoA action in the pyruvate carboxylase reaction. *Biochemistry* **1992**, *31*, 9445.
- (12) Attwood, P. V. Locus of action of acetyl CoA in the biotin-carboxylation reaction of pyruvate carboxylase. *Biochemistry* **1993**, *32*, 12736.
- (13) Jitrapakdee, S.; Wallace, J. C. Structure function and regulation of pyruvate carboxylase. *Biochem. J.* **1999**, *340*, 1.
- (14) Attwood, P. V.; Wallace, J. C. Chemical and catalytic mechanisms of carboxyl transfer reactions in biotin-dependent enzymes. *Acc. Chem. Res.* **2002**, *35*, 113.
- (15) Kondo, H.; Shiratsuchi, K.; Yoshimoto, T.; Masuda, T.; Kitazono, A.; Tsuru, D.; Anai, M.; Sekiguchi, M.; Tanabe, T. Acetyl-CoA carboxylase from *Escherichia coli*: gene organization and nucleotide sequence of the biotin carboxylase subunit. *Proc. Natl. Acad. Sci. U.S.A.* **1991**, *88*, 9730.
- (16) Waldrop, G. L.; Rayment, I.; Holden, H. M. Three-dimensional structure of the biotin carboxylase subunit of acetyl-CoA carboxylase. *Biochemistry* **1994**, *33*, 10249.
- (17) Powers, S. G.; Meister, A. Identification of Enzyme-Bound Activated CO₂ as Carbonic-Phosphoric Anhydride: Isolation of the Corresponding Trimethyl Derivative from the Active Site of Glutamine-Dependent Carbamyl Phosphate Synthetase. *Proc. Natl. Acad. Sci. U.S.A.* **1976**, *73*, 3020.
- (18) Powers, S. G.; Meister, A. Carbonic-phosphoric anhydride (carboxy phosphate). Significance in catalysis and regulation of glutamine-dependent carbamyl phosphate synthetase. *J. Biol. Chem.* **1978**, *253*, 1258.
- (19) Wimmer, M. J.; Rose, I. A.; Powers, S. G.; Meister, A. Evidence that carboxyphosphate is a kinetically competent intermediate in the carbamyl phosphate synthetase reaction. *J. Biol. Chem.* **1979**, *254*, 1854.
- (20) Stapleton, M. A.; Javid-Majd, F.; Harmon, M. F.; Hanks, B. A.; Grahmann, J. L.; Mullins, L. S.; Rauschel, F. M. Role conserved residues within the carboxy phosphate domain of carbamoyl phosphate synthetase. *Biochemistry* **1996**, *35*, 14352.
- (21) Javid-Majd, F.; Stapleton, M. A.; Harmon, M. F.; Hanks, B. A.; Mullins, L. S.; Rauschel, F. M. Comparison of the functional differences for the homologous residues within the carboxy phosphate and carbamate domains of carbamoyl phosphate synthetase. *Biochemistry* **1996**, *35*, 14362.
- (22) Lee, C.; Yang, W.; Parr, R. G. Development of the Colle-Salvetti correlation-energy formula into a functional of the electron density. *Phys. Rev. B* **1988**, *37*, 785.
- (23) Becke, A. D. Density-functional thermochemistry. III. The role of exact exchange. *J. Chem. Phys.* **1993**, *98*, 5648.

- (24) Muetterties, E. L.; Bleeke, J. R.; Wucherer, E. J.; Albright, T. A. Structural stereochemical, and electronic features of arene-metal complexes. *Chem. Rev.* **1982**, 82, 499.
- (25) Frisch, M. J.; Trucks, G. W.; Schlegel, H. B.; Scuseria, G. E.; Robb, M. A.; Cheeseman, J. R.; Montgomery, J. A., Jr.; Vreven, T.; Kudin, K. N.; Burant, J. C.; Millam, J. M.; Iyengar, S. S.; Tomasi, J.; Barone, V.; Mennucci, B.; Cossi, M.; Scalmani, G.; Rega, N.; Petersson, G. A.; Nakatsuji, H.; Hada, M.; Ehara, M.; Toyota, K.; Fukuda, R.; Hasegawa, J.; Ishida, M.; Nakajima, T.; Honda, Y.; Kitao, O.; Nakai, H.; Klene, M.; Li, X.; Knox, J. E.; Hratchian, H. P.; Cross, J. B.; Adamo, C.; Jaramillo, J.; Gomperts, r.; Stratmann, R. E.; Yazyev, O.; Austin, A. J.; Cammi, R.; Pomelli, C.; Ochterski, J. W.; Ayala, P. Y.; Morokuma, K.; Voth, G. A.; Salvador, P.; Dannenberg, J. J.; Zakrzewski, V. G.; Dapprich, S.; Daniels, A. D.; Strain, M. C.; Farkas, O.; Malick, D. K.; Rabuck, A. D.; Raghavachari, K.; Foresman, J. B.; Ortiz, J. V.; Cui, Q.; Baboul, A. G.; Clifford, S.; Cioslowski, J.; Stefanov, B. B.; Liu, G.; Liashenko, A.; Piskorz, P.; Komaromi, I.; Martin, R. L.; Fox, D. J.; Keith, T.; Al-Laham, M. A.; Peng, C. Y.; Nanayakkara, A.; Challacombe, M.; Gill, P. M. W.; Johnson, B.; Chen, W.; Wong, M. W.; Gonzalez, C.; Pople, J. A. *Gaussian 03*; Gaussian, Inc.: Wallingford, CT, 2004.
- (26) Miller, W. H.; Handy, N. C.; Adams, J. E. Reaction Path Hamiltonian for Polyatomic Molecules. *J. Chem. Phys.* **1980**, 72, 99.
- (27) Page, M.; McIver, J. W., Jr. On evaluating the reaction path Hamiltonian. *J. Chem. Phys.* **1988**, 88, 922.
- (28) Fukui, K. The path of chemical reactions. The IRC approach. *Acc. Chem. Res.* **1981**, 14, 363.
- (29) Gonzalez, C.; Schlegel, H. B. An improved algorithm for reaction path following. *J. Chem. Phys.* **1989**, 90, 2154.
- (30) Gonzalez, C.; Schlegel, H. B. Reaction path following in mass-weighted internal coordinates. *J. Chem. Phys.* **1990**, 94, 5523.
- (31) Thoden, J. B.; Blanchard, C. Z.; Holden, H. M.; Waldrop, G. L. Movement of the biotin carboxylase B-domain as a result of ATP binding. *J. Biol. Chem.* **2000**, 275, 16183.
- (32) Cook, D. The interaction of Friedel-Crafts catalysts with organic molecules: II. Boron trifluoride with benzoic anhydride. *Can. J. Chem.* **1962**, 40, 445.
- (33) Silverstein, R. M.; Webster, F. X. In *Spectrometric Identification of Organic Compounds*, 6th ed.; John Wiley and Sons Ltd.: New York, 1998.
- (34) Fang, Y.; Bai, C.; Wang, T.; Zhong, F.; Tang, Y.; Lin, S. B.; Kan, L. Evidence for the conformational rigidity of triplex d(C⁺T)₈-d(AG)₈-d(CT)₈ on silver electrode revealed by Fourier transform Raman scattering studies. *J. Mol. Struct.* **1996**, 377, 1.
- (35) Mamedov, S.; Stachel, D.; Soltwisch, M.; Quitmann, D. Local environment and dynamics of PO₄ tetrahedra in Na-Al-PO₃ glasses and melts. *J. Chem. Phys.* **2005**, 123, 124515.
- (36) Coates, J. Interpretation of infrared spectra: A practical approach. In *Encyclopedia of Analytical Chemistry*; Meyers, R. A., Ed.; John Wiley and Sons Ltd.: Chichester, U.K., 2000; pp 10815–10837.
- (37) Torres, R. A.; Himo, F.; Bruice, T. C.; Noodleman, L.; Lovell, T. Theoretical Examination of Mg(2+)-Mediated Hydrolysis of a Phosphodiester Linkage as Proposed for the Hammerhead Ribozyme. *J. Am. Chem. Soc.* **2003**, 125, 9861.
- (38) De Meis, L. The concept of energy-rich phosphate compounds: water, transport ATPases and entropic energy. *Arch. Biochem. Biophys.* **1993**, 306, 287.
- (39) De Meis, L. Role of water in the energy of hydrolysis of phosphate compounds: energy transduction in biological membranes. *Biochim. Biophys. Acta* **1989**, 973, 333.
- (40) Attwood, P. V.; Tipton, P. A.; Cleland, W. W. Carbon-13 and deuterium isotope effects on oxalacetate decarboxylation by pyruvate carboxylase. *Biochemistry* **1986**, 25, 8197.
- (41) Attwood, P. V. The structure and the mechanism of action of pyruvate carboxylase. *Int. J. Biochem. Cell Biol.* **1995**, 27, 231.
- (42) Shriver, D. F.; Atkins, P. W.; Langford, C. H. In *Inorganic Chemistry*, 2nd ed.; Oxford University Press: Oxford, 1994.
- (43) Clayden, J.; Greeves, N.; Warren, S.; Wothers, P. In *Organic Chemistry*; Oxford University Press: New York, 2001.
- (44) Williams, A.; Naylor R. A. Hydrolysis of phosphinic esters: general-base catalysis by imidazole. *J. Chem. Soc. B* **1971**, 1967.
- (45) Khanna, R. K.; Moore, M. H. Carbamic acid: molecular structure and IR spectra. *Spectrochim. Acta, Part A* **1999**, 55A, 961.
- (46) Hegarty, A. F.; Bruice, T. C.; Benkovic, S. J. Biotin and the Nucleophilicity of 2-Methoxy-2-Imidazoline Toward the sp² Carbonyl Carbon. *J. Chem. Soc., Chem. Commun.* **1969**, 20, 1173.
- (47) Stallings, W.; Detitta, G. T. Crystallographic investigations of biotin and carboxybiotin derivatives. *Ann. NY Acad. Sci.* **1985**, 447, 152.
- (48) Maggiora, G. M. Theoretical aspects of the structural chemistry of biotin I. The electronic structure of biotin and protonated biotins. *J. Theor. Biol.* **1973**, 41, 523.
- (49) Capon, B.; Rycroft, D. S.; Watson, T. W.; Zucco, C. Simple enols. 1. The generation of vinyl alcohol in solution and its detection and characterization by NMR spectroscopy. *J. Am. Chem. Soc.* **1981**, 103, 1761.
- (50) Capon, B.; Zucco, C. Simple enols 2. Kinetics and mechanism of the ketonization of vinyl alcohol. *J. Am. Chem. Soc.* **1982**, 104, 7567.
- (51) Kraut, J. Serine proteases: structure and mechanism of catalysis. *Annu. Rev. Biochem.* **1977**, 46, 331.
- (52) Lolis, E.; Petsko, G. A. Transition state analogues in protein. crystallography: probes of the structural source of enzyme catalysis. *Annu. Rev. Biochem.* **1990**, 59, 597.
- (53) Fastrez, J.; Fersht, A. R. Demonstration of the acyl-enzyme mechanism for the hydrolysis of peptides and anilides by chymotrypsin. *Biochemistry* **1973**, 12, 2025.
- (54) Sigler, P. B.; Blow, D. M.; Matthews, B. W.; Henderson, R. Structure of crystalline alpha-chymotrypsin. II. A preliminary report including a hypothesis for the activation mechanism. *J. Mol. Biol.* **1968**, 35, 143.
- (55) Carter, P.; Wells, J. A. Dissecting the catalytic triad of a serine protease. *Nature* **1988**, 322, 564.
- (56) Carter, P.; Wells, J. A. Functional interaction among catalytic residues in subtilisin BPN'. *Protein* **1990**, 7, 335.

- (57) Koepke, J.; Ermiler, U.; Warkentin, E.; Wenzl, G.; Flecker, P. Crystal structure of cancer chemopreventive Bowman-Birk inhibitor in ternary complex with bovine trypsin at 2.3 Å resolution. Structural basis of Janus-faced serine protease inhibitor specificity. *J. Mol. Biol.* **2000**, *298*, 477.
- (58) Gaboriaud, C.; Rossi, V.; Bally, I.; Arlaud, G. J.; Fontecilla-Camps, J. C. Crystal structure of the catalytic domain of human complement C1s: a serine protease with a handle. *EMBO J.* **2000**, *19*, 1755.
- (59) Lihs, F. J.; Caudle, M. T. Kinetics and Mechanism for CO₂ Scrambling in a N-Carboxyimidazolidone Analogue for N¹-Carboxybiotin. *J. Am. Chem. Soc.* **2002**, *124*, 11334.
- (60) Levert, K. L.; Lloyd, R. B.; Waldrop, G. L. Do cysteine 230 and lysine 238 of biotin carboxylase play a role in the activation of biotin? *Biochemistry* **2000**, *39*, 4122.
- (61) Kazuta, Y.; Tokunaga, E.; Aramaki, E.; Kondo, H. Identification of lysine-238 of Escherichia coli biotin carboxylase as an ATP-binding residue. *FEBS Lett.* **1998**, *427*, 377.
- (62) Jitrapakdee, S.; Booker, G. W.; Cassady, A. I.; Wallace, J. C. Cloning sequencing and expression of rat liver pyruvate carboxylase. *Biochem. J.* **1996**, *316*, 631.
- (63) Blanchard, C. Z.; Lee, Y. M.; Frantom, P. A.; Waldrop, G. L. Mutations at four active site residues of biotin carboxylase abolish substrate-induced synergism by biotin. *Biochemistry* **1999**, *38*, 3393.
- (64) Sloane, V.; Blanchard, C. Z.; Guillot, F.; Waldrop, G. L. Site-directed Mutagenesis of ATP Binding Residues of Biotin Carboxylase: Insight into the Mechanism of Catalysis. *J. Biol. Chem.* **2001**, *276*, 24991.
- (65) Yong-Biao, J.; Islam, M. N.; Sueda, S.; Kondo, H. Identification of the catalytic residues involved in the carboxyl transfer of pyruvate carboxylase. *Biochemistry* **2004**, *43*, 5912.
- (66) Hall, P. R.; Zheng, R.; Antony, L.; Pustai-Carey, M.; Carey, P. R.; Yee, V. C. Transcarboxylase 5S structures: assembly and catalytic mechanism of a multienzyme complex subunit. *EMBO J.* **2004**, *23*, 3621.
- (67) Blanchard, C. Z.; Waldrop, G. L. Overexpression and kinetic characterization of the carboxyltransferase component of acetyl-CoA carboxylase. *J. Biol. Chem.* **1998**, *273*, 19140.
- (68) Tipton, P. A.; Cleland, W. W. Mechanism of decarboxylation of carboxybiotin. *J. Am. Chem. Soc.* **1988**, *110*, 5866.

CT700260F